



IntechOpen

Heat Exchangers

Basics Design Applications

Edited by Jovan Mitrovic



HEAT EXCHANGERS – BASICS DESIGN APPLICATIONS

Edited by **Jovan Mitrovic**

Heat Exchangers - Basics Design Applications

<http://dx.doi.org/10.5772/1997>

Edited by Jovan Mitrovic

Contributors

Jayakumar J S, Yasuki Kansha, Akira Kishimoto, Atsushi Tsutsumi, Muhammad Aziz, Omid Asgari, Hadis Hemati, Mohammad Hassan Saidi, Mohamed Mansour, Mohammed Hassab, Ignacio Carvajal-Mariscal, Florencio Sanchez-Silva, Georgiy Polupan, Huisheng Zhang, Shilie Weng, Ming Su, Muthuraman Subbiah, Pablo Dolado, Ana Lázaro, José María Marín, Belén Zalba, Trung Thanh Dang, Salim Newaz Kazi, Tomasz Bury, Klaren, Eric. F. De Boer, David Astrain, Alvaro Martinez, Piotr Wais, Kharseh, Ali Bani Kananeh, Julian Peschel, Minato, Béatrice Ledéser, Ronan Hébert, Y. S. Muzychka, M. M. Awad, Agnieszka Chudzik, Dusan D Gvozdenac

© The Editor(s) and the Author(s) 2012

The moral rights of the and the author(s) have been asserted.

All rights to the book as a whole are reserved by INTECH. The book as a whole (compilation) cannot be reproduced, distributed or used for commercial or non-commercial purposes without INTECH's written permission.

Enquiries concerning the use of the book should be directed to INTECH rights and permissions department (permissions@intechopen.com).

Violations are liable to prosecution under the governing Copyright Law.



Individual chapters of this publication are distributed under the terms of the Creative Commons Attribution 3.0 Unported License which permits commercial use, distribution and reproduction of the individual chapters, provided the original author(s) and source publication are appropriately acknowledged. If so indicated, certain images may not be included under the Creative Commons license. In such cases users will need to obtain permission from the license holder to reproduce the material. More details and guidelines concerning content reuse and adaptation can be found at <http://www.intechopen.com/copyright-policy.html>.

Notice

Statements and opinions expressed in the chapters are these of the individual contributors and not necessarily those of the editors or publisher. No responsibility is accepted for the accuracy of information contained in the published chapters. The publisher assumes no responsibility for any damage or injury to persons or property arising out of the use of any materials, instructions, methods or ideas contained in the book.

First published in Croatia, 2012 by INTECH d.o.o.

eBook (PDF) Published by IN TECH d.o.o.

Place and year of publication of eBook (PDF): Rijeka, 2019.

IntechOpen is the global imprint of IN TECH d.o.o.

Printed in Croatia

Legal deposit, Croatia: National and University Library in Zagreb

Additional hard and PDF copies can be obtained from orders@intechopen.com

Heat Exchangers - Basics Design Applications

Edited by Jovan Mitrovic

p. cm.

ISBN 978-953-51-0278-6

eBook (PDF) ISBN 978-953-51-6145-5

We are IntechOpen, the world's leading publisher of Open Access books Built by scientists, for scientists

4,100+

Open access books available

116,000+

International authors and editors

120M+

Downloads

151

Countries delivered to

Our authors are among the
Top 1%

most cited scientists

12.2%

Contributors from top 500 universities



WEB OF SCIENCE™

Selection of our books indexed in the Book Citation Index
in Web of Science™ Core Collection (BKCI)

Interested in publishing with us?
Contact book.department@intechopen.com

Numbers displayed above are based on latest data collected.
For more information visit www.intechopen.com



Meet the editor



Professor Dr Ing. Jovan Mitrovic was a professor and Head of the Department of Thermal Process Engineering and Plant Technology at the University Paderborn, and a professor in Technical Thermodynamics and Thermal Process Engineering at the University Stuttgart, both in Germany. After his retirement, he accepted a position of a visiting professor at the University in East Sarajevo, Republic of Srpska, Bosnia and Herzegovina, lecturing Thermo/Fluid Energetic in Higher Education Programme. He received his degree in Mechanical Engineering from the University of Belgrade (Yugoslavia), and PhD (Dr.-Ing.) from the University Stuttgart, Germany. His main research interests are transport phenomena with phase transitions, falling films heat transfer, and heat transfer improvement. He is author/co-author of more than 120 papers published in refereed journals; in 2004 he edited the book Heat Exchanger and Condenser Tubes. Professor Mitrovic is a member of the Editorial Board of Chemical Engineering and Technology. He has supervised/co-supervised over 20 PhD Theses and over 120 Diploma/Master Dissertations.

Contents

Preface XIII

Part 1 General Aspects 1

- Chapter 1 **Thermodynamic Optimization 3**
M.M. Awad and Y.S. Muzychka
- Chapter 2 **Analytical Solution
of Dynamic Response of Heat Exchanger 53**
D. Gvozdenac
- Chapter 3 **Self-Heat Recuperation: Theory and Applications 79**
Yasuki Kansha, Akira Kishimoto, Muhammad Aziz
and Atsushi Tsutsumi
- Chapter 4 **Development of High Efficiency
Two-Phase Thermosyphons for Heat Recovery 97**
Ignacio Carvajal-Mariscal, Florencio Sanchez-Silva
and Georgiy Polupan
- Chapter 5 **Impact of a Medium Flow Maldistribution
on a Cross-Flow Heat Exchanger Performance 117**
Tomasz Bury
- Chapter 6 **Control of LNG Pyrolysis and Application
to Regenerative Cooling Rocket Engine 143**
R. Minato, K. Higashino, M. Sugioka and Y. Sasayama
- Chapter 7 **Numerical Analysis of the Structural
Stability of Heat Exchangers – The FEM Approach 165**
Agnieszka A. Chudzik

Part 2 Micro-Channels and Compact Heat Exchangers 187

- Chapter 8 **Microchannel Simulation 189**
Mohammad Hassan Saidi, Omid Asgari and Hadis Hemati

- Chapter 9 **Compact Heat Exchange Reformer
Used for High Temperature Fuel Cell Systems 221**
Huisheng Zhang, Shilie Weng and Ming Su
- Chapter 10 **Single-Phase Heat Transfer and Fluid
Flow Phenomena of Microchannel Heat Exchangers 249**
Thanhtrung Dang, Jyh-tong Teng, Jiann-cherng Chu, Tingting Xu,
Suyi Huang, Shiping Jin and Jieqing Zheng
- Chapter 11 **Heat Exchangers for Thermoelectric Devices 289**
David Astrain and Álvaro Martínez
- Part 3 Helical Coils and Finned Surfaces 309**
- Chapter 12 **Helically Coiled Heat Exchangers 311**
J. S. Jayakumar
- Chapter 13 **Fin-Tube Heat Exchanger Optimization 343**
Piotr Wais
- Chapter 14 **Thermal Design of Cooling and Dehumidifying Coils 367**
M. Khamis Mansour and M. Hassab
- Part 4 Plate Heat Exchangers 395**
- Chapter 15 **The Characteristics of Brazed Plate Heat
Exchangers with Different Chevron Angles 397**
M. Subbiah
- Part 5 Energy Storage Heat Pumps Geothermal Energy 425**
- Chapter 16 **PCM-Air Heat Exchangers: Slab Geometry 427**
Pablo Dolado, Ana Lázaro, José María Marín
and Belén Zalba
- Chapter 17 **Ground-Source Heat Pumps and Energy Saving 459**
Mohamad Kharseh
- Chapter 18 **The Soultz-sous-Forêts' Enhanced Geothermal
System: A Granitic Basement Used
as a Heat Exchanger to Produce Electricity 477**
Béatrice A. Ledésert and Ronan L. Hébert
- Part 6 Fouling of Heat Exchangers 505**
- Chapter 19 **Fouling and Fouling Mitigation
on Heat Exchanger Surfaces 507**
S. N. Kazi

- Chapter 20 **Fouling in Plate Heat Exchangers:
Some Practical Experience 533**
Ali Bani Kananeh and Julian Peschel
- Chapter 21 **Self-Cleaning Fluidised Bed Heat Exchangers for Severely
Fouling Liquids and Their Impact on Process Design 551**
Dick G. Klaren and Eric F. Boer de

Preface

As motive force of processes, heat must be transferred from one fluid to other, task that is performed by means of heat exchangers. From this point of view, heat exchangers represent an important element of thermal facilities that has substantially contributed to technical development of the society. Today it is impossible to imagine any branch of process engineering and energy technology without involvement of heat exchangers. Advanced models of these apparatus were proposed in the middle of the 18th century, while theoretical backgrounds have been completed a century later.

Corresponding to practical importance of heat exchangers, innumerable studies and treatises are devoted to processes taking place in these devices and their constructive shaping. The actual development trend in this field is guided by the ideas of reduction of thermal transport resistances and the raise of energy conversion efficiency. These ideas have also guided the conception of the present book. It is a collection of contributions prepared by the specialists. It consists of 21 Chapter that are arranged in 6 Sections:

Section 1: General Aspects,

Section 2: Micro-Channels and Compact Heat Exchangers,

Section 3: Plate Heat Exchangers,

Section 4: Helical Coils and Finned Surfaces,

Section 5: Energy Storage, Heat Pumps and Geothermal Energy,

Section 6: Fouling of Heat Exchangers.

Section 1 - General Aspects

This part comprises 7 Chapters dealing mainly with the questions of fluid flow and heat transfer in heat exchangers. Chapter 1 by Awad and Muzychka addresses the entropy generation arising from heat transfer and fluid flow and provides a basis for thermodynamic optimisation of heat exchangers. Gvozdenac gives in Chapter 2 a detailed analysis of convective heat transfer in heat exchangers at different flow arrangements under transient conditions. Kansha et al. present in Chapter 3 a self-heat recuperation technology for transport of latent and sensible heat of the process streams without heat addition and introduce a theoretical analysis of this technology. Carvajal-Mariscal et al. recommend in Chapter 4 combinations of process parameters that give high efficiency of two-phase thermosyphons. These devices are used for transport of high heat flow rates from heat source to heat sink by connecting the evaporator and

the condenser. The heat flow rate is reduced, if the elements of the heat exchangers are not evenly supplied with the fluid. Bury examined the issue in Chapter 5 and reports an average deterioration factor of 15% for a cross-flow heat exchanger. In Chapter 6, Minato et al. deal with the LNG pyrolysis in connection with regenerative cooling of rocket engines. The processes occurring are exceedingly complex, not only because of high process temperatures, which usually cause large temperature gradients. Thermal stresses thus induced may impair the structural stability of constructions, as is exemplified by A. Chudzik in Chapter 7 for a shell-and-tube heat exchanger.

Section 2 - Micro-Channels and Compact Heat Exchangers

Section 2 clusters the contributions dealing with the processes occurring in micro-channels and apparatus composed of such elements. By using micro-channels, one pursues the idea of shortening the heat transfer paths, thereby trying to copy solutions evolved in the nature. In Chapter 8, Asgari analyses numerically the heat transfer in a heat exchanger, consisting of a number of rectangular micro-channels, connected in parallel, at low Re numbers with fully developed flow. The applied heat flux is orthogonal and uniform on the bottom plane of the apparatus. Zhang et al., in Chapter 9, simulate dynamically a compact heat exchange reformer for high temperature fuel cell systems under catalytic conditions. The modelling technique is suited for quick and real time calculations. With single phase flow, Dang et al. show in Chapter 10 the hydraulic diameter of the micro channel to be the chief parameter governing the thermo-fluid characteristic of the apparatus. Both experimental and numerical treatments confirm advantages of counter-current fluid flow arrangement. The contribution in Chapter 11 deals with the thermoelectric devices, which are used either to generate electric potential in a temperature gradient (Seebeck effect) or to generate a temperature difference by means of electric current (Peltier effect). Astrain and Martínez analysed there the efficiency of the device, mainly focussing on heat transfer. The thermal performances of heat transfer modules are demonstrated to decisively affect the efficiency of the whole system.

Section 3 - Plate Heat Exchangers

Section 3 comprises the contributions dealing with the heat exchangers consisting of helical coils and finned surfaces. Helical coils provide the simplest construction of heat exchangers while fining of surfaces should compensate for the low heat transfer. In Chapter 12 Jayakumar presents a detailed analysis of hydrodynamic and heat transfer of single-phase and two-phase water flow in helical pipes, for various coil parameters and boundary conditions. Basing on the results, correlations for the average and local Nusselt numbers were developed. Wais pursues in Chapter 13 the possibilities of finding the fin shape that should maximize the heat transfer and reduce the fin mass. The results of numerical experiments are used for developing of heat transfer correlations. Chapter 14 by Khamis Mansour deals with the thermal design of cooling and dehumidifying coils. The used row-by-row calculation method provides a better reliability than the common averaging method. This is of particular importance when local data are required as in case of air dehumidifiers.

Section 4 - Helical Coils and Finned Surfaces

Plate heat exchangers consist of a number of plates assembled in parallel next to one another thus forming flow channels such that each plate separates hot from cold fluid stream. Plates are provided with macro structures and the neighbouring plates touch each other on the crests of the structures. The channels are gasketed or brazed on the circumference. In Chapter 15 Muthuraman presents results of the experimental condensation studies of R410A in brazed plate heat exchangers for various plate structures and provides correlations for heat transfer and pressure drop.

Section 5 - Energy Storage, Heat Pumps and Geothermal Energy

Part 5 bundles the contributions dealing with the storage and conversion of thermal energy, focussing on alternative energy sources and clean energy. Thermal radiation of the Sun counts to the cleanest energies; being available mainly seasonally, its storage is becoming increasingly important. If stored as internal energy of a substance, the substance should undergo an endothermic phase transition during storing while exothermic when releasing the heat. Chapter 16 by Dolado et al. deals with the heat exchangers comprising phase change materials, illustrating the processes mainly in form of temperature history diagrams. Thermal energy stored in the ground may be utilized by means of heat pumps. Chapter 17 by Kharseh illustrates an example with surface geothermal energy, while Ledésert and Hébert give in Chapter 18 an overview on the exploitation of deep geothermal energy. The high temperature of energy source in later case allows transformation of geothermal energy in other energy forms.

Section 6 - Fouling of Heat Exchangers

Dissolved solid substances and impurities contained in process streams interact with the heat transfer surfaces, attractively or repulsively. In case of attraction, the concentration of the dissolved may reach the solubility boundary and initiate crystallisation. Starting from this initial state, a solid layer grows on the surface during operation; it diminishes the thermal capacity of heat exchanger, if its thermal conductivity is low. This is referred to as fouling. The contribution devoted to fouling of heat exchangers are grouped in this Part. Chapter 19 by Kazi addresses general questions of fouling, thereby analysing its impacts on heat transfer. Some practical insights into fouling in plate heat exchangers are provided in Chapter 20 by Bani Kananeh and Peschel, while in Chapter 21 Klaren and de Boer report on the self-cleaning fluidised bed heat exchangers.

Prof. Dr. Ing. Jovan Mitrovic
Thermodynamics and Thermal Process Engineering
Germany

Part 1

General Aspects

Thermodynamic Optimization*

M.M. Awad¹ and Y.S. Muzychka²

¹*Mechanical Power Engineering Department,
Faculty of Engineering, Mansoura University,*

²*Faculty of Engineering and Applied Science, St. John's, NL,
Memorial University of Newfoundland,*

¹*Egypt*

²*Canada*

1. Introduction

Second law analysis in the design of thermal and chemical processes has received considerable attention since 1970s. For example, Gaggioli and Petit (1977) reviewed the first and second laws of thermodynamics as an introduction to an explanation of the thesis that energy analyses of plants, components, and processes should be made by application of the second law that deals with the availability of energy or the potential energy. They illustrated their methodology suggested by applying it to an analysis of the Koppers-Totzek gasification system. Optimization of heat exchangers based on second-law rather than first-law considerations ensures that the most efficient use of available energy is being made.

Second-law analysis has affected the design methodology of different heat and mass transfer systems to minimize the entropy generation rate, and so to maximize system available work. Many researchers considered these processes in terms of one of two entities: exergy (available energy) and irreversibility (entropy production). For instance, McClintock (1951) described irreversibility analysis of heat exchangers, designed to transfer a specified amount of heat between the fluid streams. He gave explicit equations for the local optimum design of fluid passages for either side of a heat exchanger. To the knowledge of authors, McClintock (1951) was the first researcher who employed the irreversibility concept for estimating and minimizing the usable energy wasted in heat exchangers design. Bejan (1977) introduced the concept of designing heat exchangers for specified irreversibility rather than specified amount of heat transferred. Many authors used this technique in the field of cryogenic engineering (Bejan and Smith (1974, 1976), Bejan (1975), and Hilal and Boom (1976)).

One of the first examinations of entropy generation in convective heat transfer was conducted by Bejan (1979) for a number of fundamental applications. Much of the early

* The part of this chapter was presented by Y. S. Muzychka in fall 2005 as Part III during the short course: Adrian Bejan, Sylvie Lorente, and Yuri Muzychka, Constructal Design of Porous and Complex Flow Structures, Memorial University of Newfoundland, Faculty of Engineering and Applied Science, St. John's, NL, Canada, September 21-23, 2005.

work is well documented in his books (Bejan, 1982a and 1996a). Since the publication of (Bejan, 1996a), entropy generation in internal structure has been examined by numerous researchers. In this section, we will examine these studies that include the optimization of heat exchangers, and enhancement of internal flows. Also, we will proceed to develop some of the basic principles and examine selected results from the published literature.

1.1 Optimization of heat exchangers

In the past thirty five years, much work relating to heat exchanger design based on the second law of thermodynamics was presented by researchers (Bejan, 1988). Heat exchangers have often been subjected to thermodynamic optimization (or entropy generation minimization) in isolation, i.e., removed from the larger installation, which uses them. Examples include the parallel flow, counterflow, crossflow, and phase-change heat exchanger optimizations. We will talk in details about this in this section.

Bejan (1977) presented a heat exchanger design method for fixed or for minimum irreversibility (number of entropy generation units, N_s). The researcher obtained the number of entropy generation units (N_s) by dividing entropy generation rate by the smallest heat capacity rate of the fluids. The value of N_s can range between 0-∞. The heat exchanger would have a better performance if the entropy generation was at its minimum ($N_s \rightarrow 0$). This dimensionless number can clearly express how a heat exchanger performance is close to an ideal heat exchanger in terms of thermal losses. He showed that entropy generation in a heat exchanger is due to heat transfer through temperature gradient and fluid friction. In contrast with traditional design procedures, the amount of heat transferred between streams and the pumping power for every side became outputs of the N_s design approach. Also, he proposed a methodology for designing heat exchangers based on entropy generation minimization. To illustrate the use of his method, the paper developed the design of regenerative heat exchangers with minimum heat transfer surface and with fixed irreversibility N_s .

The thermal design of counterflow heat exchangers for gas-to-gas applications is based on the thermodynamic irreversibility rate or useful power no longer available as a result of heat exchanger frictional pressure drops and stream-to-stream temperature differences. The irreversibility (entropy production) concept establishes a direct relationship between the heat exchanger design parameters and the useful power wasted due to heat exchanger nonideality.

Bejan (1978) demonstrated the use of irreversibility as a criterion for evaluation of the efficiency of a heat exchanger. The researcher minimized the wasted energy using the optimum design of fluid passages in a heat exchanger. He studied the interrelationship between the losses caused by heat transfer across the stream-to-stream due to differences in temperatures and losses caused by fluid friction. He obtained the following relation for the entropy generation rate per unit length as follows:

$$\frac{d\dot{S}_{gen}}{dx} = \frac{\dot{m}}{\rho T} \left(-\frac{dP}{dx} \right) + \frac{dq}{dx} \frac{\Delta T}{T^2 \left(1 + \frac{\Delta T}{T} \right)} \cong \frac{\dot{m}}{\rho T} \left(-\frac{dP}{dx} \right) + \frac{dq}{dx} \frac{\Delta T}{T^2 \left(1 + \frac{\Delta T}{T} \right)} \geq 0 \quad (1)$$

The first term in expression (1) is the entropy production contribution due to fluid friction in the fluid duct. The second term in expression (1) represents the contribution due to heat transfer across the wall-fluid temperature difference. These two contributions were strongly interrelated through the geometric characteristics of the heat exchanger. It should be noted that the use of density (ρ) instead of the inverse of specific volume (v) in the first term on the right hand side. Also, the denominator of the second term on the right hand side was simplified by assuming that the local temperature difference (ΔT) was negligible compared with the local absolute temperature (T). Heat transfer losses could be reduced by increasing the heat transfer area, but in this case pressure drops in the channels increased. Both heat transfer losses and frictional pressure drops in channels determined the irreversibility level of heat exchanger.

A remarkable feature of Eq. (1) and of many like it for other simple devices is that a proposed design change (for instance, making the passage narrower) induces changes of opposite signs in the two terms of the expression. Then, an optimal trade-off exists between the fluid friction irreversibility and the heat transfer irreversibility contributions, an optimal design for which the overall measure of exergy destruction is minimum, while the system continues to serve its specified function. In order to illustrate this trade-off, use the definition of friction factor (f), Stanton number (St), mass flux (G), Reynolds number (Re), and hydraulic diameter (d_h):

$$f = \frac{\rho d_h}{2G^2} \left(-\frac{dP}{dx} \right) \quad (2)$$

$$St = \frac{dq}{dx} \frac{1}{p \Delta T_c \rho G} \quad (3)$$

$$G = \frac{\dot{m}}{A} \quad (4)$$

$$Re = \frac{G d_h}{\mu} \quad (5)$$

$$d_h = \frac{4A}{p} \quad (6)$$

In Eq. (3), the quantity $(dq/dx)/(p\Delta T)$ is better known as the average heat transfer coefficient. The entropy generation rate, Eq. (1) becomes

$$\frac{d\dot{S}_{gen}}{dx} = \left(\frac{dq}{dx} \right)^2 \frac{d_h}{4T^2 \dot{m} c_p St} + \frac{2\dot{m}^3 f}{\rho^2 T d_h A^2} \quad (7)$$

Where heat transfer rate per unit length and mass flow rate are fixed. The geometric configuration of the exchanger passage has two degrees of freedom, the perimeter (p) and the cross-sectional area (A), or any other pair of independent parameters, like $(Re; d_h)$ or $(G;$

d_h). If the passage is a straight pipe with circular cross-section, p and A are related through the pipe inner diameter d that is the only degree of freedom left in the design process. Writing

$$d_h = d, \quad A = \pi d^2 / 4, \quad \text{and} \quad p = \pi d \quad (8)$$

Equation (7) becomes

$$\frac{d\dot{S}_{gen}}{dx} = \left(\frac{dq}{dx}\right)^2 \frac{d_h}{\pi T^2 k Nu} + \frac{32 \dot{m}^3 f}{\pi^2 \rho^2 T d^5} \quad (9)$$

Where $Re = 4 \dot{m} / \pi \mu d$. The Nusselt number (Nu) definition, and the relation between Nu , St , Re , and the Prandtl number ($Pr = \nu/\alpha$)

$$Nu = \frac{h_{av} d_h}{k} = St \cdot Re \cdot Pr = St \cdot Pe \quad (10)$$

Introducing two classical correlations for fully developed turbulent pipe flow (Bejan, 1993),

$$Nu = 0.023 Re^{0.8} Pr^{0.4} \quad (0.7 < Pr < 160 : Re > 10^4) \quad (11)$$

$$f = 0.046 Re^{-0.2} \quad (10^4 < Re < 10^6) \quad (12)$$

and combining them with Eq. (9), yields an expression for exergy destruction, which depends only on Re . Differentiating the exergy destruction with respect to the Reynolds number (Re) and equaling the result with zero, we find that the entropy generation rate is minimized when the Reynolds number (or pipe diameter) reaches the optimal value (Bejan, 1982a)

$$Re_{opt} = 2.023 Pr^{-0.071} B^{0.358} \quad (13)$$

Equation (13) shows how to select the optimal pipe size for minimal irreversibility. Parameter B is a heat and fluid flow “duty” parameter that accounts for the constraints of heat transfer rate per unit length, and mass flow rate:

$$B = \dot{m} \left(\frac{dq}{dx}\right) \frac{p}{\mu^{5/2} (kT)^{1/2}} \quad (14)$$

Additional results may be obtained for non-circular ducts using the appropriate expressions for the geometry A and p , and appropriate models for heat transfer and friction coefficients.

The Reynolds number (Re) effect on the exergy destruction can be expressed in relative terms as

$$\frac{d\dot{S}_{gen}/dx}{(d\dot{S}_{gen}/dx)_{min}} = 0.856 \left(\frac{Re}{Re_{opt}}\right)^{-0.8} + 0.144 \left(\frac{Re}{Re_{opt}}\right)^{4.8} \quad (15)$$

where the ratio on the left-hand side is known as the entropy generation number (N_s), (Bejan, 1982a). In the denominator of the left hand side of Eq. (15), the minimum exergy destruction is calculated at the optimum Reynolds number (Re_{opt}). Also, $Re/Re_{opt} = d_{opt}/d$ because the mass flow rate is fixed. Using Eq. (15), it is clear that the rate of entropy generation increases sharply on either side of the optimum. The left hand side of the optimum represents the region in which the overall entropy generation rate is dominated by heat transfer effects. The right hand side of the optimum represents the region in which the overall entropy generation rate is dominated by fluid friction effects. The left hand side of Eq. (15) is used to monitor the approach of any design relative to the best design that can be conceived subject to the same constraints. Bejan (1982a, 1988) used this performance criterion extensively in the engineering literature. Also, Mironova et al. (1994) recognized this performance criterion in the physics literature.

Bejan (1978) also made a proposal to use the number of entropy production units (N_s) as a basic yardstick in describing the heat exchanger performance. This dimensionless number was defined as the entropy production rate or irreversibility rate present in a heat exchanger channel. When $N_s \rightarrow 0$, this implied an almost ideal heat exchanger channel. According to his study, it was enough to increase the effectiveness by using design criteria like the minimization of difference wall temperature or maximization of the ratio of heat transfer coefficient to fluid pumping power.

Bejan (1979) illustrated the second law aspects of heat transfer by forced convection in terms of four fundamental flow configurations: pipe flow, boundary layer over flat plate, single cylinder in cross-flow, and flow in the entrance region of a flat rectangular duct. The researcher analyzed in detail the interplay between irreversibility due to heat transfer along finite temperature gradients and, on the other hand, irreversibility due to viscous effects. He presented the spatial distribution of irreversibility, entropy generation profiles or maps, and those flow features acting as strong sources of irreversibility. He showed how the flow geometric parameters might be selected to minimize the irreversibility associated with a specific convective heat transfer process.

Bejan (1980) used the second law of thermodynamics as a basis for evaluating the irreversibility (entropy generation) associated with simple heat transfer processes. In the first part of his paper, he analyzed the irreversibility production from the local level, at one point in a convective heat transfer arrangement. In the second part of his paper, he devoted to a limited review of second law analysis applied to classic engineering components for heat exchange. In this category, the paper included topics like heat transfer augmentation techniques, heat exchanger design, and thermal insulation systems. The researcher presented analytical methods for evaluating and minimizing the irreversibility associated with textbook-type components of heat transfer equipment. Also, he obtained an expression for the entropy generation rate in a balanced counterflow heat exchanger with zero pressure drop irreversibility as follows:

$$N_s = \ln \frac{\left(1 + \frac{T_1}{T_2} NTU\right) \left(1 + \frac{T_2}{T_1} NTU\right)}{(1 + NTU)^2} \quad (16)$$

Using Eq. (16), $N_s = 0$ at both $\varepsilon = 0$ (or at $NTU = 0$) and $\varepsilon = 1$ (or at $NTU = \infty$), and had its maximum value at $\varepsilon = 0.5$ (or at $NTU = 1$). The maximum N_s increases as soon as T_1/T_2 goes above or below 1:

$$N_{s,\max} = \ln \left[\frac{1}{2} + \frac{1}{4} \left(\frac{T_1}{T_2} + \frac{T_2}{T_1} \right) \right] \quad (17)$$

N_s increases with the absolute temperature ratio T_2/T_1 . When $N_s > 1$, the irreversibility decreases sharply as $\varepsilon \rightarrow 1$. On the left side of the maximum $N_s < 1$, the irreversibility decreases due to insufficient heat transfer across a temperature difference of order $(T_1 - T_2)$.

This maximum entropy paradox constitutes an excellent illustration of the importance of the principle of thermodynamic isolation in the optimization of an engineering component.

Chowdhury and Sarangi (1980, 1983) used irreversibility analysis to predict the optimum thermal conductivity of the separating wall in a concentric tube counterflow heat exchanger. The researchers accounted for the entropy generation due to axial conduction in the wall, along with that due to lateral heat transfer and fluid friction. The frictional entropy generation was independent of the thermal conductivity of the wall and also did not affect the thermal effectiveness of the heat exchanger. As a result, they treated it as constant throughout this work. They assumed that the entropy generations due to lateral and axial heat transfer were independent of each other.

Chowdhury and Sarangi (1982) studied the generation of entropy in a counterflow heat exchanger. For nearly ideal heat exchanger with nearly balanced capacity rate, the researchers obtained an expression for the number of entropy generation units, N_s . They compared the results of their expression with exact calculation and results of Bejan (1977). They observed that their new expression gave a much closer approximation and also could be easily incorporated into the new design procedure of Bejan.

Bejan (1982a) showed that the Entropy Generation Minimization (*EGM*) method was dependent on the use of fluid mechanics, heat transfer, and thermodynamics in its application. The difference between the exergy method and the entropy generation minimization method is that exergy method uses only the first law, second law, and the properties of the environment. On the other hand, *EGM* characteristics are system modeling, development of the entropy generation rate as a function of the model parameters and the ability to minimize the entropy generation rate.

The researcher applied the entropy generation balance or entropy imbalance equation to a control volume of an open system. For gas-gas heat exchanger, he explained entropy generation as the sum of the entropy generation caused by finite temperature difference with frictional pressure drop.

$$\dot{S}_{gen} = \dot{S}_{gen,\Delta T} + \dot{S}_{gen,\Delta P} \quad (18)$$

The first term on the right-hand side of Eq. (18) is the entropy generation rate accounting for the heat transfer irreversibility, and the second term for the fluid friction irreversibility. He expressed that entropy generation (S_{gen}) = 0 corresponded to the highest quality while the entropy generation (S_{gen}) > 0 represented poorer quality.

Also, he described the relative importance of the two irreversibility mechanisms using the irreversibility distribution ratio (ϕ) that was defined as:

$$\phi = \frac{\text{fluid - flow irreversibility}}{\text{heat transfer irreversibility}} = \frac{\dot{S}_{gen,\Delta P}}{\dot{S}_{gen,\Delta T}} \quad (19)$$

For example, the irreversibility distribution ratio (ϕ) varies along with the V-shaped curve of entropy generation number (N_s), or relative entropy generation rate in a smooth pipe with heat transfer (Bejan, 1980), increasing in the direction of large Reynolds numbers (small pipe diameters because the mass flow rate is fixed) in which the overall entropy generation rate is dominated by fluid friction effects. At the optimum (corresponding to $N_s = 1$), the irreversibility distribution ratio (ϕ) assumes the value $\phi_{opt} = 0.168$. This means that the optimal trade-off between the irreversibility due to heat transfer effects and the irreversibility due to fluid friction effects does not coincide with the design where the irreversibility mechanisms are in perfect balance, even though setting $\phi = 1$ is a fairly good way of locating the optimum.

Substituting Eq. (19) into Eq. (18) yields

$$\dot{S}_{gen} = (1 + \phi)\dot{S}_{gen,\Delta T} \quad (20)$$

In addition, augmentation entropy generation number ($N_{s,a}$) was given by

$$N_{s,a} = \frac{\dot{S}_{gen,a}}{\dot{S}_{gen,o}} \quad (21)$$

This definition represents the ratio of the augmented to base channel entropy generation rates. Under particular flow conditions and/or constraints, $N_{s,a} < 1$ is desirable, as the augmented system is thermodynamically improved over the basic system, because, in addition to enhancing heat transfer, the irreversibility degree of the apparatus is reduced assuming other factors like heat transfer duty, pressure drop, or pumping power remain the same. If the function of the heat exchanger passage is fixed (i.e. mass flow rate and heat flux are given), this dimensionless number can be written in the more explicit form (Bejan, 1988)

$$N_{s,a} = \frac{1}{1 + \phi_0} N_{s,\Delta T} + \frac{\phi_0}{1 + \phi_0} N_{s,\Delta P} \quad (22)$$

In Eq. (22), ϕ_0 represents the irreversibility distribution ratio of the reference design, whereas $N_{s,\Delta T}$ and $N_{s,\Delta P}$ are the values of $N_{s,a}$ in the limits of pure heat transfer irreversibility and pure fluid-flow irreversibility:

$$N_{s,\Delta T} = \frac{St_0 d_{h,a}}{St_a d_{h,0}} \quad (23)$$

$$N_{s,\Delta P} = \frac{f_a d_{h,0} A_0^2}{f_0 d_{h,a} A_a^2} \quad (24)$$

The geometric parameters (A , d_h) before and after augmentation are linked through the constant mass flow rate constraint that reads

$$Re_a \frac{A_a}{d_{h,a}} = Re_0 \frac{A_0}{d_{h,0}} \quad (25)$$

Substituting Eq. (23) and Eq. (24) into Eq. (22) yields

$$N_{s,a} = \frac{1}{1 + \phi_0} \frac{St_0 d_{h,a}}{St_a d_{h,0}} + \frac{\phi_0}{1 + \phi_0} \frac{f_a d_{h,0} A_0^2}{f_0 d_{h,a} A_a^2} \quad (26)$$

Equation (26) shows that $N_{s,a}$ is, in general, a function of both the heat transfer coefficient ratio (St_a/St_0) and the friction factor ratio (f_a/f_0). The numerical value of ϕ_0 dictates the relative importance of the friction factor ratio (f_a/f_0). ϕ_0 is known because the reference design is known. It should be noted that ϕ_0 describes the thermodynamic regime of operation of the heat exchanger passage (ΔT losses versus ΔP losses), much in the way that Re_0 indicates the fluid mechanics regime (laminar versus turbulent).

For the case of no change in hydraulic diameter and the cross-sectional appreciably ($d_{h,a} \cong d_{h,0}$, $A_a \cong A_0$), the augmentation entropy generation number ($N_{s,a}$) has this simple form

$$N_{s,a} = \frac{1}{1 + \phi_0} \frac{St_0}{St_a} + \frac{\phi_0}{1 + \phi_0} \frac{f_a}{f_0} \quad (27)$$

Bejan (1982b) summarized an important contemporary trend in the field of heat transfer and thermal design. The researcher represented this trend using the infusion of the second law of thermodynamics and its design-related concept of entropy generation minimization. This new trend was important and, at the same time, necessary, if the heat transfer community was to contribute to a viable engineering solution to the energy problem. The examples considered in his article ranged from the irreversibility associated with some of the most fundamental convective heat transfer processes, to the minimum irreversibility design of one-dimensional insulations like the main counterflow heat exchanger of a helium liquefaction plant.

Bejan (1983) discussed the irreversibility characteristics of the heat exchangers in which at least one of the streams was a two-phase mixture.

Witte and Shamsundar (1983) defined a thermodynamic efficiency based on the second law of thermodynamics for heat exchange devices. The efficiency could be simply written in terms of the mean absolute temperatures of the two fluids exchanging heat, and the appropriate environment temperature, Their expression was

$$\eta_{W-S} = 1 - \frac{T_0 \dot{S}_{gen}}{\dot{Q}} \quad (28)$$

$$\dot{Q} = \dot{m}_h(h_{in} - h_{out})_h = \dot{m}_c(h_{out} - h_{in})_c \quad (29)$$

$\eta_{W-S} = 1$ represented the highest value and corresponded to the reversible process. The examination of this efficiency indicated that η_{W-S} could be negative, and the full range of this efficiency was $-\infty < \eta_{W-S} \leq 1$. Negative values of η_{W-S} characterized counterflow heat exchangers working at cryogenic operational conditions. It should be noticed that this is a conceptually inconvenient result ((Bejan, 1988), (Hesselgreaves, 2000)).

Also, Witte and Shamsundar (1983) showed that for a given ratio of hot to cold inlet temperatures, the efficiency and effectiveness for particular heat exchange configurations were related. They compared this efficiency to second-law efficiencies proposed by other authors, and showed to be superior in its ability to predict the influence of heat exchanger parameter changes upon the efficiency of energy use. They applied this concept to typical heat exchange cases to demonstrate its usefulness and sensitivity.

London and Shah (1983) presented an operationally convenient methodology for relating economic costs to entropy generation. This methodology, in the hands of the heat exchanger designer, allowed an interaction with the system designer to gain insights into the trade-offs allowed between the thermodynamic irreversibilities of flow friction, heat transfer, heat leakage, and mixing. This methodology started with recognition of the appropriate individual irreversibilities. Then, it related the individual costs to system rating and energy penalties by thermodynamic arguments. The analysis loop was closed by considerations related to reduction of the individual irreversibilities in a cost-effective way. On the other hand, the usual energy or "exergy" analysis provided an answer for the overall costs of the collective irreversibilities. This did not provide the engineer with the insight needed to minimize the individual irreversibilities in a cost-effective manner.

Perez-Blanco (1984) discussed irreversibility in heat transfer enhancement. The researcher developed the methods of calculating overall entropy generation rate in a single-flow heat exchanger tube with uniform wall temperature.

Sekulic and Baclic (1984) considered the concept of enthalpy exchange irreversibility (*EEL*). The researchers conducted the optimization of heat exchangers on the basis of entropy generation number for counterflow and crossflow heat exchangers.

da Costa and Saboya (1985) discussed second law analysis for parallel flow and counterflow heat exchangers. In a comparative study of the irreversibility due to heat transfer for imbalanced (i.e. the thermal capacity rates for both fluids are not the same) counterflow and parallel flow heat exchangers, the researchers found that the maximum occurs at effectiveness (ϵ) = 1 in parallel flow heat exchangers.

Sekulic (1985-1986) presented a note on the thermodynamic approach to the analysis of unequally sized passes in two-pass crossflow heat exchangers.

Sekulic and Herman (1986) considered the minimum of enthalpy exchange irreversibility (*EEL*) as a selective criterion in heat exchanger design. The researchers applied this concept in the core sizing procedure of a compact crossflow heat exchanger for gas-to-gas application. In the final analysis, the approach objective was the pressure drop choice in such a way that from the total set of possible heat exchanger core dimensions the thermodynamically optimal one was selected.

Sekulic (1986) applied the entropy generation (irreversibility) concept founded on the second law of thermodynamics in heat exchanger analysis. In this analysis, the quantity termed enthalpy exchange irreversibility norm (*EEIN*) was the measure of the internal heat exchanger irreversibilities. The researcher discussed the behavior of *EEIN* as a function of the heat exchanger thermal size for an arbitrary flow arrangement and more precisely for two characteristic limiting cases: cocurrent and countercurrent heat exchangers.

In the heat exchangers design, the enhancement of heat transfer surface area is effective to reduce the loss due to the fluid-to-fluid temperature difference. On the other hand, this leads to the increase of the pressure loss in the channel. The optimum working condition must be determined by taking these conditions trade into account. As a result, Tsujikawa et al. (1986) presented the design method of the regenerator of the gas turbine cycle applied with the entropy generation from the viewpoint of the second law of thermodynamics. Their study was mainly concerned with the optimization through the choice of the minimum entropy production. For the fixed value of the pressure ratio of the compressor, the researchers calculated the number of entropy generation units and determined the optimum temperature efficiency of the generator that gave the minimum heat transfer surface area.

Krane (1987) applied second law analysis techniques based on the minimization of entropy generation to the optimal design and operation of a sensible heat thermal energy storage system in which the storage element was both heated and cooled by flowing streams of gases. His results showed that (1) an entire operational cycle that consisted of a storage process and a removal process must be considered (as opposed to the storage process alone) to optimize the design and performance of such a system; and (2) a typical optimum system destroyed approximately 70-90% of the entering availability and, therefore, had an extremely low thermodynamic efficiency.

Zubair et al. (1987) presented a closed-form analytical method for the second-law-based thermoeconomic optimization of two-phase heat exchangers used as condensers or evaporators. Due to finite temperature difference heat transfer and pressure drops, the researchers proposed the concept of "internal economy" as a means of estimating the economic value of entropy generated, thus permitting the engineer to trade the cost of entropy generation in the heat exchanger against its capital expenditure. They presented results in terms of the optimum heat exchanger area as a function of the exit/inlet temperature ratio of the coolant, unit cost of energy dissipated, and the optimum overall heat transfer coefficient. The total heat transfer resistance represented by ($U^{-1} = C_1 + C_2 Re^{-n}$) in this analysis was patterned after Wilson (1915) that accommodated the complexities associated with the determination of the two-phase heat transfer coefficient and the buildup of surface scaling resistances. They presented the analysis of a water-cooled condenser and an air-cooled evaporator with supporting numerical examples that were based on the thermoeconomic optimization procedure of this study.

Bejan (1987) presented a review article to outline the most basic steps of the procedure of entropy generation minimization (thermodynamic design) at the system-component level. His current paper was a continuation of his earlier review work (Bejan, 1982a and 1982b). As a result, a further objective was to review the fundamental work published in this area in the 1980s. The researcher focused on the fundamental mechanisms responsible for the generation of entropy in heat and fluid flow and on the design tradeoff of balancing the heat transfer irreversibility against the fluid flow irreversibility. He selected applications from

the fields of heat exchanger design, thermal energy storage, and mass exchanger design. This current article provided a comprehensive, up-to-date review of second-law analyses published in the heat and mass transfer literature during the last decade.

Bejan (1988) summarized the structure of heat exchanger irreversibility as follows:

$$N_s = N_{s,imbalance} + N_{s,\Delta T} + N_{s,\Delta P} \quad (30)$$

The first term on the right hand side represents the remanent (flow-imbalance) irreversibility. The second term on the right hand side represents the heat transfer irreversibility. The third term on the right hand side represents the fluid flow irreversibility. The researcher suggested to calculate the remanent irreversibility ($N_{s,imbalance}$) first in the thermodynamic optimization of any heat exchanger because it is not logic to invest heat exchanger area and "engineering" into minimizing the sum ($N_{s,\Delta T} + N_{s,\Delta P}$) when this sum is already negligible compared with the remanent irreversibility ($N_{s,imbalance}$). Only in very special case does the entropy generation rate of a heat exchanger break into a sum of these three terms. One such case is the balanced counter flow heat exchanger in the nearly balanced and nearly ideal limit ($\omega \rightarrow 1$, $\Delta T \rightarrow 0$, $\Delta P's \rightarrow 0$). This case was discussed in details in Bejan (1977).

The remanent (flow-imbalance) irreversibility of two-stream parallel-flow heat exchangers can be obtained by combining the equation of the entropy generation rate of the entire heat exchanger with the perfect design conditions and the effectiveness relation for parallel flow (Bejan (1993)) as follows:

$$N_{s,imbalance} = \frac{\dot{S}_{gen}}{(\dot{m}c_p)_2} = \ln \left\{ \left(\frac{T_2}{T_1} \right)^\omega \left[1 + \left(\frac{T_1}{T_2} - 1 \right) \frac{\omega}{1 + \omega} \right]^{1+\omega} \right\} \quad (31)$$

In the limit of extreme imbalance ($\omega \rightarrow \infty$), Eq.(31) becomes

$$N_{s,imbalance} = \frac{T_2}{T_1} - 1 - \ln \frac{T_2}{T_1} \quad (32)$$

In this limit, the side 1 stream is so large that its temperature remains equal to T_1 from inlet to outlet. It behaves like a stream that condenses or evaporates at constant pressure.

On the other hand, the remanent (flow-imbalance) irreversibility of two-stream counter flow heat exchangers can be obtained as follows:

$$N_{s,imbalance} = \frac{\dot{S}_{gen}}{(\dot{m}c_p)_2} = \ln \left\{ \left[1 - \frac{1}{\omega} \left(1 - \frac{T_2}{T_1} \right) \right]^\omega \frac{T_1}{T_2} \right\} \quad (33)$$

From Eq. (31) and Eq. (33), it is clear that the remanent (flow-imbalance) irreversibility in parallel flow is greater than in counterflow. Also, both flow arrangement approach the value indicated by Eq. (32) as the flow imbalanced ratio (ω) increases.

Sekulic and Milosevic (1988) investigated entropy generation in heat exchanger networks using the component balance approach.

Witte (1988) used the second-law efficiency to develop a new technique for optimizing the design of heat exchangers. His method related the operating costs of the exchanger to the destruction of availability caused by the exchanger operation. The researcher related directly the destruction of availability to the second-law efficiency of the exchanger. This allowed one to find the NTU at which the benefits of reduced availability losses were offset by the costs of added area; this was the optimal point. In order to determine the proper cost of irreversibility to be used in the optimization process, he included the irreversibility cost in a dimensionless parameter that represented the ratio of annual ownership costs to annual operating costs that included irreversibility costs. In this way, every heat exchanger designer could estimate the costs of irreversibilities for his particular system, and then used the generalized method that was developed herein for determining the optimal heat exchanger size. His method was applicable to any heat exchanger for which the ε - NTU - R relationships were known.

Grazzini and Gori (1988) developed a general expression for entropy generation in counter-current heat exchangers is. Their expression was applicable to incompressible liquids and perfect gases. They defined two new entropy generation numbers, N_M and N_Q .

They investigated the relative position of both the maximum and minimum in the entropy generation numbers. They applied their analysis to an air-air counter-current heat exchanger. The three entropy generation numbers, N_s , N_M and N_Q , had a different variation with NTU at the different values of the capacity flow rate ratio employed in the calculations.

Eğrican (1989) investigated logarithmic mean temperature difference (LMTD) method based on the first law of thermodynamics with effectiveness-transfer unit methods and entropy generation units based on the second law of thermodynamics. To give an example, the researcher applied this method to counter-flow shell and tube heat exchanger.

Poulikakos and Johnson (1989) obtained a general expression for the entropy generation for combined convective heat and mass transfer in external flows. This expression took into account irreversibilities due to the presence of heat transfer across a finite temperature difference, mass transfer across a finite difference in the chemical potential of a species, and flow friction. Minimizing the entropy generation in heat- and fluid-flow devices was a valuable criterion for optimum design. The researchers showed that the same philosophy could be used when in addition to heat transfer and fluid flow irreversibilities, mass transfer irreversibilities existed in the thermal system of interest. They applied the general expression for entropy generation to two fundamental problems of forced convection heat and mass transfer, namely, laminar and turbulent boundary layer forced convection from a flat plate and from a cylinder in crossflow. After minimizing the entropy generation, they drew useful conclusions that were representative of the second law viewpoint for the definition of the optimum operating conditions for the specified applications.

Paoletti et al. (1989) calculated the exergetic losses in compact heat exchanger passages. In their approach, the researchers analyzed the heat exchangers on the basis of second-law and used the entropy generation rate in a local sense. They associated the symbol Be as an alternative irreversibility distribution parameter and defined as the ratio of heat transfer irreversibility to total irreversibility due to heat transfer and fluid friction

$$Be = \frac{\dot{S}_{gen,\Delta T}}{\dot{S}_{gen,\Delta T} + \dot{S}_{gen,\Delta P}} = \frac{1}{1 + \phi} \quad (34)$$

In addition, Benedetti and Sciubba (1993) called it the Bejan number (Be). Later, Natalini and Sciubba (1999) introduced also Bejan number (Be) using Eq. (34). Natalini and Sciubba (1999) solved first the full Navier-Stokes equations of motion for turbulent viscous flow, together with the appropriate energy equation, via a standard finite-element code with a k-epsilon closure, to obtain complete velocity and temperature fields. Then, the researchers used these fields to compute the entropy generation rates corresponding to the viscous and thermal dissipation.

It is clear from Eq. (34) that $Be = 1$ that occurs at $\phi = 0$ corresponds to the case at which the irreversibility is dominated by the heat transfer effects. On the other hand, $Be = 0$ corresponds to the case at which the irreversibility is dominated by the fluid friction effects. Also, $Be = 0.5$ that occurs at $\phi = 1$ corresponds to the case at which the heat transfer irreversibility and the fluid friction irreversibility are equal.

It should be noted that the Be definition in Eq. (34) should not be confused with another Bejan number (Be) used in convection. Petrescu (1994) defined the Bejan number (Be) as follows:

$$Be = \frac{\Delta PL^2}{\mu\alpha} \quad (35)$$

This was similar to the new dimensionless group developed by Bejan and Sciubba (1992) in their study on the optimal spacing between plates cooled by forced convection. Also, the same group appeared in the solutions to other electronic cooling problems involving forced convection (Bejan, 1993). In addition, the group defined in Eq. (35) governed all the phenomena of contact melting and lubrication, in both internal and external contact configurations (Bejan, 1992).

The researcher reported that the Bejan number (Be) was essential in at least four areas of heat transfer: electronic cooling, scale analysis of forced convection, second law analysis of heat exchangers, and contact melting and lubrication. The Be group defined by Eq. (35) was the forced convection ($Pr \geq 1$) analog of the Rayleigh number (Ra) for natural convection in $Pr \geq 1$ fluids.

Sekulic (1990) presented the entropy generation (irreversibility) concept as a convenient method for estimating the quality of the heat exchange process in heat exchanger analysis. The researcher used the entropy generation caused by finite temperature differences, scaled by the maximum possible entropy generation that could exist in an open system with two fluids, as the quantitative measure of the quality of energy transformation (the heat exchange process). This quality was defined as

$$\begin{aligned} \text{Quality of energy transformation} &= 1 - (\text{Entropy generation in the real process}) \\ &\times (\text{Entropy generation in the most disadvantageous case})^{-1} \end{aligned} \quad (36)$$

According to this concept, entropy generation = 0 (reversible process) corresponded to the highest quality, and the quality of energy transformation decreased with increasing entropy generation. Another point that should be considered was that the use of this concept required the determination of the most disadvantageous case. Substituting the entropy generation number (N_s) and the maximum possible dimensionless entropy generation ($N_{s,max}$) into Eq. (36) gives the following quantity termed as “Heat Exchange Reversibility Norm” (*HERN*):

$$Y_s = 1 - \frac{N_s}{N_{s,max}} \quad (37)$$

HERN is a measure of the quality of energy transformation of heat exchangers. In his analysis, it was assumed that the contribution of fluid friction to entropy generation was negligible. If the pressure drop contribution to the total irreversibility was not negligible, then, it must be taken into account. The quality of the heat transfer process in a heat exchanger was dependent on the following three quantities for this special case: the ratio of inlet temperatures, the ratio of heat capacity rates, and the effectiveness of the heat exchanger.

Sekulic (1990) applied the *HERN* measure to a two-fluid heat exchanger of arbitrary flow arrangement. He discussed the effect of various parameters (inlet temperature ratio, fluid flow heat capacity rate ratio, flow arrangements) and the heat exchanger thermal size (number of heat transfer units) on the quality of energy transformation for various types of heat exchangers.

Rispoli and Sciubba (1990) investigated numerically the calculation of local irreversibilities in compact heat exchangers. Their approach to analyze heat exchangers on the basis of second law was to use the entropy generation rate in a local sense. They analyzed two various geometries of compact heat exchanger passages on the basis of local entropy generation rate. The evaluation of the entropy production in a local sense had the following advantages:

- i. it was possible to assess the effect of design changes both on the local and the global irreversibility,
- ii. direct and consistent comparisons between various design configurations, both from the designer’s and from the user’s perspective, could be made,
- iii. entropy production maps of different devices and/or components can be established, and the overall system design rationalized.

The coupled momentum and energy equations should be solved to determine the local entropy production rates. The corresponding entropy production was computed by using the resulting velocity and temperature fields.

The researchers defined local Bejan number as the ratio of entropy generation due to thermal effects to total entropy generation as:

$$Be = \frac{\text{Local entropy generation rate due to thermal effects}}{\text{Total local entropy generation rate}} = \frac{\dot{S}_t}{\dot{S}_t + \dot{S}_v} \quad (38)$$

Bejan number (Be) ≈ 1 for high Re flows, low Pr fluids, high logarithmic mean temperature difference ($LMTD$) while Bejan number (Be) ≈ 0 for low Re flows, high Pr fluids, low logarithmic mean temperature difference ($LMTD$). Theoretically, Bejan number (Be) = 0 only for totally isothermal flows.

Evans and von Spakovsky (1991) set forth two fundamental principles of differential Second Law analysis for heat exchanger design. Their first principle defined a Second Law temperature, while their second principle defined a Second Law temperature difference. The researcher showed that the square of the ratio of the Second Law temperature difference to the Second Law temperature was always to be equal to the negative of the partial derivative of the rate of entropy generation (for heat transfer) with respect to the overall conductance of the heat exchanger. For the basic design of elementary heat exchangers, every of these two Second Law quantities was shown to take the form of a simple geometric average.

Sieniutycz and Shiner (1994) presented a review article on thermodynamics of irreversible processes and its relation to chemical engineering: Second law analyses and finite time thermodynamics. In spite of their focus was on chemical engineering applications, their stated objective was to clarify the connections between the work of different groups in the field.

Later, Bejan (1996c) presented notes on the history of the method of entropy generation minimization (finite time thermodynamics). The researcher mentioned that Professors Sieniutycz and Shiner deserved credit for conducting a review of this wide and active field. Also, credit went to their collaborators, Professors Berry and Ratkje, who had clearly contributed to their review article. In these notes, he wanted to complement Sieniutycz and Shiner's list with a few additional references that shed a somewhat various light on the age and origins of the method. In brief, the method was older than portrayed in Sieniutycz and Shiner (1994) and its roots were in engineering, not in physics.

Bejan (1996b) presented a review article on entropy generation minimization: the new thermodynamics of finite-size devices and finite-time processes. His review traced the development and adoption of *EGM* method in many sectors of mainstream thermal engineering and science: cryogenics, heat transfer, education, storage systems, solar power plants, nuclear and fossil power plants, and refrigerators. The researcher placed emphasis on the fundamental and technological importance of the optimization method and its results, the pedagogical merits of the method, and the chronological development of the field.

Xiong et al. (1996) discussed some conceptual problems in their paper. Firstly, according to the physical meaning of effectiveness, the researchers developed a new expression of effectiveness using an ideal heat exchanger model and temperature histogram method, in which the non-uniform inlet temperature profile was considered. Secondly, they studied the relation of entropy generation number (N_s) to effectiveness (ε). They pointed out that both of them could express the perfect degree of a heat exchanger to the second thermodynamic law. Finally, they presented a criterion named as comprehensive thermal performance coefficient (*CTPE*) to describe both quantity and quality of heat transferred in a heat exchanger.

Xu et al. (1996) demonstrated the difference between the entropy generation number method proposed by Bejan and the method of entropy generation per unit amount of heat

transferred in analyzing the thermodynamic performance of heat exchangers. The researchers pointed out the reason for leading to the above difference. They proposed a modified entropy generation number for evaluating the irreversibility of heat exchangers which was in consistent with the entropy generation per unit amount of heat transferred in entropy generation analysis. Also, they investigated entropy generated by friction. Their results showed that when the entropy generated by friction in heat exchangers was taken into account, there was a minimum total entropy generation number while the NTU and the ratio of heat capacity rates varied. The existence of this minimum was the prerequisite of heat exchanger optimization.

Ogulata and Doba (1998) presented a cross-flow plate type heat exchanger that had been studied and manufactured in the laboratory conditions because of its effective use in waste heat recovery systems. The researchers tested this new heat exchanger with an applicable experimental set up, considering temperatures, velocity of the air and the pressure losses occurring in the system. They measured these variables and determined the efficiency of the system. They took into consideration the irreversibility of the heat exchanger while they performed the heat exchanger design so that the minimum entropy generation number had analyzed with respect to second law of thermodynamics in the cross-flow heat exchanger.

Ogulata et al. (1999) studied and manufactured a cross-flow plate-type heat exchanger in laboratory conditions because of its effective use in waste heat recovery systems. The researcher tested this new heat exchanger with an applicable experimental setup, considering temperatures, velocity of the air, and the pressure losses occurring in the system. They measured these variables and determined the efficiency of the system. The heat exchanger irreversibility was taken into consideration, while the heat exchanger design was such that the minimum entropy generation number was analyzed with respect to the second law of thermodynamics in the cross-flow heat exchanger. The minimum entropy generation number was dependent on the parameters called the optimum flow path length and dimensionless mass flux. They analyzed variations of the entropy generation number with these parameters.

Nafey (2000) presented theoretical analysis of entropy generation and availability destruction of NTU similar cocurrent or countercurrent heat exchangers connected in series. The researcher developed a criterion for comparing the relative performance of any number of in-series connected similar heat exchangers. He presented the effect of various influencing parameters like the number of connected heat exchangers, the individual effectiveness of every unit, the heat capacity rate ratio and flow arrangement on the quality of heat exchange. He found that the maximum of availability destruction (maximum entropy generation) for in-series-connected similar cocurrent heat exchangers was obtained at $\varepsilon^* = (1+R)^{-1}$. However, for counter-current heat exchangers connected in-series; $\varepsilon_n^* = (\sum_{i=0}^n R^i/n)^{-1}$. This analysis might be useful for a proper choice of the number of heat exchangers to be connected together and the choice for the best operating conditions.

Ordóñez and Bejan (2000) determined the main architectural features of a counterflow heat exchanger based on thermodynamic optimization subject to volume constraint. The researchers assumed that the channels were formed by parallel plates, the two fluids were ideal gases, and the flow was fully developed, laminar or turbulent. First, they showed that the irreversibility of the heat exchanger core was minimized with respect to (1) the ratio of

the two-channel spacings, and (2) the total heat transfer area between the two streams. Second, the entropy generation rate also accounted for the irreversibility due to discharging the spent hot stream into the ambient. They showed that the design could be optimized with respect to (1), (2) and (3) the ratio of the capacity rates of the two streams. The optimized features of the geometry were robust with respect to whether the external discharge irreversibility was included in the entropy generation rate calculation.

Hesselgreaves (2000) reviewed the different approaches to second law analysis and presented a rational method that satisfied the physical requirements. His intention was not reviewing all previous work, but presenting an approach that resolved some perceived inconsistencies and paradoxes. The researcher derived entropy generation numbers for different types of two-fluid heat exchangers with zero pressure drop and finite pressure drop. The types of heat exchangers were: heat exchangers with flow imbalance, unbalanced counterflow, parallel flow, condensing on one side, and evaporation on one side. An important result of this investigation was that the basic entropy generation relationship for gas flows was controlled by the flow Mach number. This was consistent with an extension of Shapiro (1953)'s classical one-dimensional flow analysis of a compressible gas with friction and heat addition.

Yilmaz et al. (2001) presented second-law based performance evaluation criteria to evaluate the performance of heat exchangers. First, the researchers recalled and discussed the need for the systematic design of heat exchangers using a second law-based procedure. Then, they classified the evaluation techniques for heat exchangers based on the second law of thermodynamics into two categories: the evaluation techniques using entropy as an evaluation parameter, and the evaluation techniques using exergy as an evaluation parameter. They presented and reviewed collectively both categories, and gave their respective characteristics and constraints. It was shown how some of these criteria were related to every other. Also, emphasis was placed on the importance of second law-based thermoeconomic analysis of heat exchangers, and these methods were discussed briefly.

Vargas et al. (2001) studied the process of determining the internal geometric configuration of a component by optimizing the global performance of the installation, which used the component. The example chosen was the crossflow heat exchanger used in the environmental control system of a modern aircraft. The researchers achieved the optimization of global performance by minimizing the total entropy generation rate of the installation. There were three degrees of freedom in the heat exchanger configuration (the length-to-width and height-to-width aspect ratios, and the separator plate spacing ratio) that was subjected to two global constraints: total component volume, and total wall material volume (or weight/density) of wall material. Their numerical results showed how the optimal configuration responded to changes in specified external parameters like volume, weight, Mach number, diffuser inlet cross-sectional area, and the pressure at which the cabin air was initially bled from the engine compressor. They showed that the optimal configuration was robust and that major features like the ratios of channel spacings and flow lengths were relatively insensitive to changes in some of the external parameters. Also, they showed that the optimal heat exchanger geometry was insensitive to the thermodynamic irreversibility caused by discharging the used ram air into the ambient.

Vargas and Bejan (2001) showed that the main geometric features of a flow component could be deduced from the thermodynamic optimization of the global performance of the

largest flow system that incorporated the component. Their approach represented a departure from the usual approach, where a flow component was optimized in isolation. The researchers chose the counterflow heat exchanger of the environmental control system (ECS) used on modern aircraft as an example. They fitted the heat exchanger with a diffuser and a nozzle for the ram air, and the ECS run on the boot strap air cycle, employing an additional compressor and turbine. They considered two heat transfer surface types, finned and smooth parallel plates. They reported numerical results for the external geometric aspect ratios of the heat exchanger, and for the plate-to-plate spacing of the smooth-plates model. They showed that the optimized geometry for the core with finned surfaces was nearly the same as the optimized geometry for the core with smooth plates. Many optimized geometric features were robust with respect to changes in external parameters that varied from one application to the next. Their method illustrated in this work – the thermodynamic (constructal) optimization of flow geometry – was applicable to any system that run on the basis of a limited amount of fuel (exergy) installed onboard, e.g., automobiles, ships, portable tools.

Bejan and Lorente (2001) reviewed recent developments in thermodynamic optimization by focusing on the generation of optimal geometric form (shape, structure, topology) in flow systems. The flow configuration was free to vary. The researchers drew examples of large classes of applications from different sectors of mechanical and civil engineering: the distribution of heat transfer area in power plants, optimal sizing and shaping of flow channels and fins, optimal aspect ratios of heat exchanger core structures, aerodynamic and hydrodynamic shapes, tree-shaped assemblies of convective fins, tree-shaped networks for fluid flow and other currents, optimal configurations for streams that undergo bifurcation or pairing, insulated pipe networks for the distribution of hot water and exergy over a fixed territory, and distribution networks for virtually everything that moves in society (goods, currency, information). The principle-based generation of flow geometry united the thermodynamic optimization developments known in mechanical engineering with lesser known applications in civil engineering and social organization. Their review article extended thermodynamics, because it showed how thermodynamic principles of design optimization took into account the development of optimal configurations in civil engineering and social organization.

Bejan (2001) discussed the basis for the entropy generation minimization method, and a series of key applications in power generation, refrigeration, and exergy conservation. The researcher started with a review of the concept of irreversibility, entropy generation, or exergy destruction. He used the proportionality between exergy destruction and entropy generation in the search for improved thermodynamic performance subject to finite-size constraints and specified environmental conditions. He gave examples from refrigeration, energy storage systems for sensible heat and latent heat, solar energy, and the generation of maximum power by using a stream of hot gas. He showed that the physical structure (geometric configuration, topology) of the system springed out of the process of global thermodynamic optimization subject to global constraints. This principle generated structure not only in engineering but also in physics and biology (constructal theory).

Shiba and Bejan (2001) showed that the internal geometric configuration of a component could be deduced by optimizing the global performance of the installation, which used the component. The example chosen was the counterflow heat exchanger, which served as

condenser in a vapor-compression-cycle refrigeration system for environmental control of aircraft. The researcher achieved the optimization of global performance by minimizing the total power requirement or the total entropy generation rate. There were three degrees of freedom in the heat exchanger configuration that was subjected to two global constraints: total volume, and total volume (or weight) of wall-material. Their numerical results showed how the optimal configuration responded to changes in specified external parameters like refrigeration load, fan efficiency, and volume and weight. In accordance with constructal theory and design (Bejan, 2000), it was shown that the optimal configuration was robust: major features like the ratio of diameters and the flow length were relatively insensitive to changes in the external parameters.

Bejan (2002) discussed the fundamentals of the methods of exergy analysis and entropy generation minimization (or thermodynamic optimization-the minimization of exergy destruction). The researcher began with a review of the irreversibility concept, entropy generation, or exergy destruction. Examples illustrated the accounting for exergy flows and accumulation in closed systems, open systems, heat transfer processes, and power and refrigeration plants. He gave examples from energy storage systems for sensible heat and latent heat, solar energy, and the generation of maximum power in a power plant model with finite heat transfer surface inventory.

Yuan and Kou (2001) investigated the entropy generation in a crossflow heat exchanger including three gas streams and the influence of longitudinal wall conduction on the entropy generation. Using the numerical method, the researchers calculated the exit mean temperature of every stream, and then computed the number of entropy generation units. Their results indicated that the entropy generation increased with the decrease of inlet temperature of gas stream 3 and the decrease of inlet temperature ratio of gas streams 1 to 2. Also, their results showed that the longitudinal wall conduction raised the entropy generation and that this raising increased with increasing NTU when heat capacity rate ratio of stream 1 was 0.5

Yuan and Kou (2003) investigated the entropy generation on a crossflow heat exchanger including three gas streams with three various arrangements. Using the numerical method, the researchers calculated individually the exit mean temperature of every gas stream in various arrangements, and then computed the number of entropy-generation units of every arrangement. Their results indicated that there was a maximum entropy generation for every arrangement along with the increase in number of transfer units (NTU). Comparing the three arrangements showed that the entropy generation of the third arrangement was the lowest, because this arrangement transferred heat across a smaller temperature difference. Also, this study examined the influence of longitudinal wall conduction on the entropy generation in every arrangement. The largest influence on entropy generation was found in the third arrangement.

Shah and Skiepko (2004) found that the concept of minimum irreversibility was not quite applicable to the heat exchanger analysis although it was associated with the maximum energy efficiency for energy conversion processes in thermal systems. The researchers showed that the heat exchanger effectiveness could be maximum, having an intermediate value or minimum at the maximum irreversibility operating point depending on the flow arrangement of the two fluids. Similarly, the heat exchanger effectiveness could be minimum or maximum at the minimum irreversibility operating point. They illustrated and

discussed such heat exchanger performance and irreversibility trends by combining the temperature difference irreversibility with the P - NTU results for complex flow arrangements.

Strub et al. (2004) evaluated the contribution of second law analysis to the study of a phase changing of ice slurries as secondary refrigerant in cooling systems. First, the researchers calculated the enthalpies and the entropies. Then, they carried out an entropy/exergy analysis of a heat exchanger. Their work attempted to provide a thermodynamic criterion to choose the kind of fluid and the inflow conditions that were more suitable for a particular application. They established the method and obtained the results for an ethyl alcohol-water mixture.

Lerou et al. (2005) studied optimization of counterflow heat exchanger ($CFHX$) geometry through minimization of entropy generation. In their study, the researchers applied another, less familiar design strategy where different loss mechanisms such as pressure drop and parasitic heat flows were all treated as a production of entropy. Thus, it was possible to compare and sum them. In this way, they found that a $CFHX$ configuration was optimal for a certain application, producing a minimum of entropy and thus had minimum losses. For instance, they gave the design steps of a $CFHX$ for the micro cooling project at the University of Twente. Also, they presented a generalization of micro $CFHX$ dimensions for cooling powers between 10 and 120 mW.

Mohamed (2006) realized analysis of heat transfer and fluid flow thermodynamic irreversibilities on an example of a counter flow double pipe heat exchanger utilizing turbulent air flow as a working fluid. During the process of mathematical model creation and for various working and constructing limitations, the researcher studied total thermodynamic irreversibility. His work proved that the irreversibility occurred due to unequal capacity flow rates (flow imbalance irreversibility). He concluded that the heat exchanger should be operated at effectiveness, $\varepsilon > 0.5$ and the well operating conditions would be achieved when $\varepsilon \sim 1$ where low irreversibility was expected. He adopted a new equation to express the entropy generation numbers for imbalanced heat exchangers of similar design with smallest deviation from the exact value. His new equation was the sum of two terms: the first term was the contribution of the pressure terms and the second term was the contribution of the temperature terms. He compared the results obtained from his new equation with the exact values and with those obtained by Bejan (1988). Also, the guide charts presented in his work could be used to determine the most wanted combination of the effects of various parameters to obtain minimal irreversibility.

Naphon (2006) presented the theoretical and experimental results of the second law analysis on the heat transfer and flow of a horizontal concentric tube heat exchanger. The researcher designed and constructed the experiments setup for the measured data. He used hot water and cold water as working fluids. He did the test runs at hot and cold water mass flow rates in the range of 0.02-0.20 kg/s. The inlet hot water and inlet cold water temperatures were between 40 and 50 °C, and between 15 and 20 °C, respectively. He discussed the influences of the inlet conditions of both working fluids flowing through the heat exchanger on the heat transfer characteristics, entropy generation, and exergy loss. Based on the conservation equations of energy, he developed his mathematical model and solved using the central finite difference method to obtain temperature distribution, entropy generation, and exergy

loss. The predicted results obtained from the model were validated by comparing with his measured data. From this comparison, he found that there was reasonable agreement between predicted results and those from the measured data.

Kurtbaşı et al. (2007) investigated the effects of propeller-type turbulators located in the inner pipe of co-axial heat exchanger on entropy generation rate (N_s) and exergy loss rate (E^*). Propeller-type turbulators with blade angles (θ) = 10°, 20° and 40°, also at every angle the propellers with blade diameter (d_b) = 48 mm, 50 mm and 52 mm. The researchers mounted these turbulators in the inner pipe using different distances (L_t). According to the flow observation experiments, they found maximum decaying distance of swirl flow as 30 cm. They performed the experiments with various distances of turbulators. In this system, they investigated heat transfer, entropy generation rate, and exergy loss rate. Then, they investigated the influences of angle, diameter, and number of the blades on the heat transfer, entropy generation rate, and exergy loss rate and compared with every other for various values of the Reynolds number, from 104 to 3×10^4 , and Prandtl number equal to 0.71. They found that Nusselt number and exergy loss rate approximately increased from 95 to 354 and 0.04 to 0.2 depending on blade angle, interturbulator distance and propeller diameter for $104 < Re < 3 \times 10^4$. The heat exchanger efficiency changed at between 0.17 to 0.72 levels.

Khan et al. (2007) were specifically interested in determining an optimal design of the tube banks in cross flow using an entropy generation minimization method that was as a unique measure to study the thermodynamic losses caused by heat transfer and pressure drop for a fluid in cross flow with tube banks. The optimal design of tube banks was very important because of extensive use of high performance compact heat exchangers that were found in many applications like an automobile radiator, an oil cooler, a preheater, an air-cooled steam condenser, a shell and tube type heat exchanger, and the evaporator of an air conditioning system. Usually, tube banks were arranged in an inline or staggered manner, where one fluid moved across the tubes, and the other fluid at a different temperature passed through the tubes. In their study, both inline and staggered arrangements were studied and their relative performance was compared for the same thermal and hydraulic conditions. The researchers employed the crossflow correlations for the heat transfer and pressure drop to calculate entropy generation rate. They obtained a general dimensionless expression for the entropy generation rate by considering a control volume around a tube bank and applying conservation equations for mass and energy with entropy balance. Analytical/empirical correlations for heat transfer coefficients and friction factors were used, where the characteristic length was used as the diameter of the tubes and reference velocity used in Reynolds number and pressure drop was based on the minimum free area available for the fluid flow. Also, they performed a parametric study to show the influences of various design variables on the overall performance of tube banks. They showed that all relevant design parameters for tube banks, including geometric parameters and flow conditions, could be simultaneously optimized.

Gupta and Das (2007) carried out the second law analysis of crossflow heat exchangers in the presence of non-uniformity of flow. The researchers modeled this non-uniformity with the help of axial dispersion model and took into account the back mixing and flow maldistribution. They evaluated an analytical model for exergy destruction for the cross-flow configuration. They carried out a wide range of study of the operating parameters and

non-uniform flow on exergetic behavior of crossflow heat exchangers. Their results clearly brought out not only the reason behind the maximum entropy paradox in heat exchangers but also the proper perspective of exergy destruction and the consequent optimization of crossflow heat exchangers from the second law viewpoint.

Gupta et al. (2007) studied second law analysis of counter flow cryogenic heat exchangers in presence of ambient heat-in-leak and longitudinal conduction through wall. The researchers carried out this study because the performance of highly effective heat exchangers was strongly dependent on these irreversibilities in low temperature applications. They observed that the influence of ambient heat-in-leak was different for the balanced and imbalanced counter flow high NTU heat exchangers. Also, their study made it possible to compare the different irreversibilities for varying range of NTU and analyze the effect of external irreversibilities on the performance of heat exchangers when either hot fluid or cold fluid was minimum capacity fluid.

Pitchandi and Natarajan (2008) described the second law of thermodynamics analysis of a regenerative heat exchanger. Their analysis was based on the fact that the dimensionless parameters, known as the reduced periods and reduced length, were the characteristic variables to describe the heat exchanger. The researcher discretized the solid matrix in the heat exchanger passage using trapezoidal rule and took the elemental matrix as a thermodynamic system. They applied the second law of thermodynamics to the system and obtained the entropy generation equation using the dimensionless numbers Reduced period (Π) and Reduced length (Λ) in every element. They studied the variation of entropy generation due to reduced length and reduced period. Also, the effect of the effectiveness of the heat exchanger on entropy generation was highlighted.

He et al. (2009) applied second-law based thermodynamics analysis to a new heat exchanger with helical baffles. The helical baffles were designed as quadrant ellipses and every baffle occupied one quadrant of the cross-section of the shell side. The researchers carried out experimental tests with cold water in the tube side with a constant flow rate, and hot oil on the shell side with flow rate range from 4–24 m^3/h . They measured the temperatures and pressures for the inlet and outlet of both sides. They investigated heat transfer, pressure drop, entropy generation, and exergy loss of the new heat exchanger and compared with the results for a conventional shell-and-tube heat exchanger with segmental baffles. The computed results indicated that both the entropy generation number and exergy losses of the new heat exchanger design were lower than those of the heat exchanger with segmental baffles that meant that the novel heat exchanger had a higher efficiency than the heat exchanger with segmental baffles, from the second-law based thermodynamics viewpoint.

Fan and Luo (2009) presented the experimental results of second law analysis on the heat transfer and hydraulic characteristics of a mini crossflow heat exchanger equipped with constructal distributor/collector. In their experiments, the researchers used hot and cold water as working fluids. They performed tests for different "distributor-heat-exchanger-collector" configurations at channel Reynolds numbers in the heat exchanger between 800 and 3100. They discussed the integration of constructal component on the thermal performance, entropy generation, exergy loss, and the second law effectiveness of the heat exchanger. Also, they analyzed and discussed the relationship between heat-transfer intensification and system-irreversibility production in this case.

Guo et al. (2009) developed a new shell-and-tube heat exchanger optimization design approach using entropy generation minimization and genetic algorithm. The researchers employed the dimensionless entropy generation rate obtained by scaling the entropy generation on the ratio of the heat transfer rate to the inlet temperature of cold fluid as the objective function. They took some geometrical parameters of the shell-and-tube heat exchanger as the design variables and applied the genetic algorithm to solve the associated optimization problem. They showed that for the case that the heat duty was given, not only could the optimization design increase the heat exchanger effectiveness significantly, but also decreased the pumping power dramatically. In the case that the heat transfer area was fixed, the benefit from the increase of the heat exchanger effectiveness was much more than the increasing cost of the pumping power.

Exergy change rate in an ideal gas flow or an incompressible flow can be divided into two types: a thermal exergy change rate and a mechanical exergy loss rate. San (2010) generalized the mechanical exergy loss rates in the two flows using a pressure-drop factor ($F_{\Delta P}$) because the consumed mechanical exergy is usually more valuable than the recovered thermal exergy for heat exchangers using in waste heat recovery. The researcher proposed a weighing factor to modify the pressure-drop factor. He defined an exergy recovery index (η_{II}) and expressed it as a function of effectiveness (ε), ratio of modified heat capacity rates (C^*), hot stream-to-dead-state temperature ratio (T_h/T_o), cold stream-to-dead-state temperature ratio (T_c/T_o) and modified overall pressure-drop factor ($F_{\Delta P}^*$). This η_{II} - ε relation could be used to find the η_{II} value of a heat exchanger with any flow arrangement. He established the η_{II} - NTU and η_{II} - NTU_h relations of cross-flow heat exchanger with both fluids unmixed respectively. The former provided a minimum NTU design principle and the latter provided a minimum NTU_h design principle. A numerical example showed that, at a fixed heat capacity rate of the hot stream, $(m c_p)_h$, the heat exchanger size yielded by the minimum NTU_h principle was smaller than that yielded by the minimum NTU principle.

Guo et al. (2010) presented a multi-objective optimization of heat exchanger thermal design in the framework of the entropy generation minimization. Their objectives were to minimize the dimensionless entropy generation rates related to the heat conduction under finite temperature difference and fluid friction under finite pressure drop. The researchers specified constraints using the admissible pressure drop and design standards. They employed the genetic algorithm to search the Pareto optimal set of the multi-objective optimization problem. They found that the solutions in the Pareto optimal set were trade-off between the pumping power and heat exchanger effectiveness. The optimal solution in the Pareto optimal set achieved the largest exchanger effectiveness by consuming the least pumping power under the design requirements and standards. In comparison with the single-objective optimization design, the multi-objective optimization design led to the significant decrease in the pumping power for achieving the same heat exchanger effectiveness and presented more flexibility in the design process.

Kotcioglu et al. (2010) studied a second law analysis of a cross-flow heat exchanger (HX) in the presence of a balance between the entropy generation due to heat transfer and fluid friction. The researchers investigated the entropy generation in a cross-flow HX with a new winglet-type convergent-divergent longitudinal vortex generator ($CDLVG$). They presented optimization of HX channel geometry and effect of design parameters regarding the overall

system performance. Based on the entropy generation minimization (EGM), they developed the optimization model for the *HX* flow lengths and *CDLVGs*. They found that increasing the cross-flow fluid velocity enhanced the heat transfer rate and reduced the heat transfer irreversibility. Their test results demonstrated that the *CDLVGs* were potential candidate procedure to improve the disorderly mixing in channel flows of the cross-flow type *HX* for large values of the Reynolds number.

Wang et al. (2010) studied experimentally flow and heat transfer characteristics of the shell-and-tube heat exchanger (*STHXs*) with continuous helical baffles (*CH-STHX*) and segmental baffles (*SG-STHX*). In their experiments, these *STHXs* shared the same tube bundle, shell geometrical structures, different baffle arrangement, and number of heat exchange tubes. Their experimental results suggested that the *CH-STHX* could increase the heat transfer rate by 7-12% than the *SG-STHX* for the same mass flow rate although its effective heat transfer area had 4% decrease. Also, the heat transfer coefficient and pressure drop of the *CH-STHX* had 43-53% and 64-72% increase than those of the *SG-STHX*, respectively. Based on second-law thermodynamic comparisons in which the quality of energy were evaluated by the entropy generation number and exergy losses, the *CH-STHX* decreased the entropy generation number and exergy losses by 30% and 68% on average than the *SG-STHX* for the same Reynolds number. Also, the analysis from nondimensional correlations for Nusselt number and friction factor revealed that if the maximal velocity ratio $R > 2.4$, the heat transfer coefficient of *CH-STHX* was higher than that of *SG-STHX*, and the corresponding friction factor ratio kept at constant $f_{o,CH}/f_{o,SG} = 0.28$.

Assad (2010) presented a theoretical analysis of a heat exchanger with a negligible fluid flow pressure drop to determine whether it was better to operate the heat exchanger with the minimum or maximum heat capacity rate of the hot fluid from entropy generation point of view. The researcher derived entropy generation numbers (N_s) for both cases, and his results showed that they were identical, when the heat exchanger was running at a heat capacity ratio (R) = 0.5 with heat exchanger effectiveness (ε) = 1. He defined an entropy generation number ratio (S^*) by dividing the entropy generation number for minimum heat capacity rate on the hot fluid side to the entropy generation number for maximum heat capacity rate on the hot fluid side. S^* had a maximum value at $\varepsilon = (1+R)^{-1}$ for any inlet temperature ratio (T_r) and R values. This result could be obtained by taking the derivative of S^* with respect to ε and equating it to zero. When $R = 0.1, 0.5$ and 0.9 , the entropy generation number ratio (S^*) received a maximum value at an effectiveness (ε) = 0.91, 0.67 and 0.526, respectively. When $R = 0.9$, the entropy generation number ratio (S^*) was the same for all inlet temperature ratios (T_r) at $\varepsilon = 0.8$. However, when $\varepsilon < 0.8$, S^* increased as T_r decreased, and when $\varepsilon > 0.8$, S^* increased as T_r increased. His results showed that the entropy generation number ratio (S^*) was far from 1 depending on the inlet temperature ratio (T_r) of the cold and hot fluid. When $S^* < 1$, it was better to run the heat exchanger with minimum heat capacity rate on the hot fluid side, whereas when $S^* > 1$, it was better to run the heat exchanger with maximum heat capacity rate on the hot fluid side. These results could be used to determine the wanted combination of the effects of various parameters (R , T_r , and ε) to obtain lower irreversibility. Also, these results were valid for parallel-flow and counterflow heat exchangers.

Fakheri (2010) further explored the topic of an ideal heat exchanger that was still an open question. It was shown that the minimization of entropy production or exergy destruction should not be an objective in heat exchanger design. It was further proven that heat

exchanger effectiveness did not correlate with irreversibility. Therefore, the researcher introduced a new performance measure to characterize the performance of heat exchangers, entropy flux (Γ), which was allowing the comparison of different heat exchangers under varying operating conditions by applying the second law. The entropy flux (Γ) could be defined as

$$\Gamma = \frac{\dot{S}}{UA} \quad (39)$$

As shown in Eq. (39), entropy flux (Γ) incorporated three main features of heat exchangers, namely, entropy generated (\dot{S}) that so far was only a result of heat transfer, overall heat transfer coefficient (U) and the heat exchanger area (A). In heat exchanger design, the goal is to increase the heat transfer while reducing the size so that higher values of entropy flux are desirable. For a given effectiveness, a single stream heat exchanger had the absolute maximum entropy flux, and for capacity ratios (C_r) greater than zero, counterflow had the highest entropy flux, parallel flow the lowest, and the shell and tube heat exchangers were somewhere in between.

On the basis of the first and second laws of thermodynamics, Ruan et al. (2011) derived the general expression of the number of entropy generation units of three-fluid heat exchangers with three thermal communications. The researchers discussed thoroughly the effect of several non-dimensional design parameters on the number of entropy generation units of three-fluid heat exchangers. Furthermore, they gave the detailed comparisons of results for the arrangement of the parallel flow and the counter flow. They showed that the variation tendencies of the number of entropy generation units with the ratio of the thermal resistances, ratio of the thermal capacities, and number of heat transfer units for the parallel-flow arrangement were different from those of the counter-flow arrangement. There was an extremum of the number of entropy generation units for the counter-flow arrangement. Also, the entropy generation for the counter flow was mostly smaller than that of the parallel flow under the same conditions

Arivazhagan and Lokeswaran (2011) investigated the entropy generation rate in shell and tube heat exchanger with porous medium inserted inside the tubes. The researchers used three various waste metal chips made of copper, aluminum, and mild steel as porous medium. There was a trade-off between the pressure drop and heat transfer in the design of enhanced heat exchangers. If Reynolds number increased, the rate of heat transfer would also increase at the expense of reasonable pressure drop in porous flow. Because of turbulent energy dissipation at high Reynolds number, this pressure drop would increase further, resulting in high entropy generation. They developed and used the empirical correlations for the entropy generation minimization of the actual heat exchanger. They derived their conclusions on the basis of the behavior of the entropy generation number (N_s) as a function of the Reynolds number (Re). On the basis of the entropy generation minimization, they found the upper limit of Reynolds number to be 1450, beyond which irreversibility increased.

1.2 Optimization of internal enhancements

In many heat transfer applications, internal enhancements are utilized to promote or enhance heat transfer. However, any enhancement of a primary surface gives rise to an

increase in pressure drop for a given mass flow rate. Using thermodynamic optimization, we may also assess the penalties of improving thermal contact in terms of entropy generation. Since thermal enhancement leads to higher heat transfer rates, a lower mass flow is permissible in most applications. Therefore, in a given application with fixed duty (Q), the temperature difference will be reduced for the same mass flow rate. This tradeoff, potentially allows for the overall entropy generation rate to be reduced below that for the primary surface at the desired duty condition. In this section, we will examine the impact of thermal enhancement devices such as strip fins and ribs on entropy generation.

Bejan and Pfister (1980) used entropy generation as a measure of the relative merit of heat transfer augmentation techniques relative to each other and to the heat exchange apparatus in which they might be incorporated. In this way, heat transfer augmentation techniques were viewed as design changes capable of reducing the irreversible destruction of useful energy (exergy) in heat exchange equipment. The entropy generation rate took into account simultaneously the heat transfer and fluid friction changes associated with implementing a heat transfer augmentation technique. The researchers proposed that the merit of a given heat transfer augmentation technique might be evaluated by comparing the rate of entropy generation of the heat exchange apparatus before and after the implementation of the augmentation technique. Using in-tube roughness as an instance, they showed what specific operating conditions must be met before the destruction of exergy could be reduced via heat transfer augmentation.

Benedetti and Sciubba (1993) presented a novel method that could be helpful in assessing the 'optimal' configuration of finned-tube heat exchangers. Their method was based on the determination on a local basis of the two components of the entropy generation rate: the one caused by viscous dissipations and the one due to thermal irreversibilities. Depending on the engineering purpose for which a technical device was designed, it could be argued that the 'optimal' configuration would be that in which either one (or both) of these two entropy generation rates was minimized. For a heat exchanging device, it was important to minimize thermal irreversibilities, but more important was to minimize the mechanical power lost in achieving a prescribed heat-exchange performance: to this purpose, one could form a 'relative irreversibility index' (named 'Bejan number (Be)' here and use it to assess the merit of a given configuration. In the procedure developed here, the researchers considered a circular, single-tube, finned heat exchanger configuration. They computed the velocity and temperature fields via a standard finite-element package (*FIDAP*) for a realistic value of the Reynolds number and for a variety of geometric configurations (different fin external diameters and fin spacing). Then, they calculated the entropy generation rate from the flow field, and examined both at a local level, to detect possible 'bad' design spots (i.e., locations that corresponded to abnormally high entropy generation rates that could be cured by design improvements), and at an 'overall' (integral) level, to assess the 'entropic' performance of the heat exchanger. They given 'Optimal' curves, and determined the 'optimal' spacing of fins using alternatively the entropy generation rate and the total heat transfer rate as objective functions: different optima arise, and the differences as well as the similarities were discussed in detail.

Another widely used thermal enhancement device used in heat transfer applications is the offset strip fin. Manglik and Fang (1994) applied the second law of thermodynamics to evaluate the heat transfer enhancement of offset strip fin core relative to plain plate fin

compact heat exchangers. The researchers considered single-phase air flow in both laminar and turbulent regimes. examined entropy generation rates using the procedure proposed by Bejan and Pfister (1980). They presented the thermal-hydraulic performance in terms of area goodness factor (j/f) and the entropy generation number ($N_{s,a}$). Due to the irreversibility reduction was a trade-off between the heat transfer enhancement and the corresponding pressure drop penalty, they introduced a new parameter, entropy generation distribution factor (ψ) as

$$\psi = \frac{\dot{S}_{\Delta T,o} - \dot{S}_{\Delta T,a}}{\dot{S}_{\Delta P,a} - \dot{S}_{\Delta P,o}} \quad (40)$$

This new parameter represents the ratio of entropy generation reduction due to heat transfer enhancement and the increase in entropy generation due to the consequent increase in fluid friction. Thermodynamics benefits would be obtained only if $\psi > 1$. The magnitude of ψ was such that a better resolution was obtained for the entropy generation change due to the variations in operating conditions. They reported entropy generation numbers for three types of flow: constant mass flow rate, constant pressure drop, and constant pumping power. They delineated the relative effect of the aspect ratio, fin density, and fin thickness to offset length ratio of the offset strip fins on heat transfer enhancement and entropy generation minimization.

Sciubba (1996) presented a novel method that could be helpful in assessing the optimal configuration of finned-tube heat exchangers. His method was an extension of the local irreversibilities method, and it was based on the determination on a local basis of the two components of the entropy generation rate: the one caused by viscous dissipations and the one due to thermal irreversibilities. Depending on the engineering purpose for which a technical device was designed, it could be argued that the optimal configuration would be that in which either one (or both) of these two entropy generation rates was minimized. For a heat exchanging device, it was important to minimize thermal irreversibilities, but more important was to minimize the mechanical power lost in achieving a prescribed heat-exchange performance: to this purpose, one could form a relative irreversibility index (named Bejan number (Be) here), and use it to assess the merit of a given configuration. Average or global Bejan number (Be_{av}) could be found by integration of Eq. (38) as:

$$Be_{av} = \frac{\int \dot{S}_t}{\int \dot{S}_t + \int \dot{S}_v} = \frac{1}{1 + Br} \quad (41)$$

$$Br = Ec.Pr = \frac{\mu V^2}{k\Delta T} \quad (42)$$

Average Bejan number (Be_{av}) $\rightarrow 0$ in the limit of vanishing average thermal gradient ΔT , and $Be_{av} \rightarrow 1$ in the limit of vanishing mean velocity gradient.

In the procedure presented here, the researcher considered a circular, single-tube, finned heat exchanger configuration. He computed the velocity and temperature fields (via a

standard finite-element package, *FIDAP*) for a realistic value of the Reynolds number and for different geometric configurations (different fin external diameters and fin spacing). Then, he calculated the entropy generation rate from the flowfield, and examined both at a local level, to detect possible bad design spots (i.e., locations that corresponded to abnormally high entropy generation rates that could be cured by design improvements), and at an overall (integral) level, to assess the entropic performance of the heat exchanger. He gave optimal curves and determined the optimal spacing of fins using alternatively the entropy generation rate and the total heat transfer rate as objective functions: different optima arise, and the differences as well as the similarities were discussed in detail.

Tagliafico and Tanda (1996) presented a thermodynamic method for the comparison of plate fin heat exchanger performance. The researchers evaluated and scaled the entropy production of a given heat transfer surface geometry using that of corresponding reference configuration (a parallel-plate channel) with the same frontal area, volume, heat transfer duty, and mass flow rate to relate the relative merit of the surface geometry to corresponding irreversibility level. They applied their method to a number of plate-fin compact heat exchanger surfaces whose performance data were taken from Kays and London (1984). They examined six types of heat exchanger enhancements: the plain fin, louvered fin, strip fin, wavy fin, pin fin, and perforated fin. From this analysis, they found that the thermodynamic performance of the most suitable surfaces, among those considered in this study, turned out to be strongly related to the operating conditions (both heat transfer duty and mass flow rate). Also, they found that the strip fin was the thermodynamically most efficient augmentation device.

Muley and Maglik (1999) investigated performance optimization of plate heat exchangers with chevron plates. In this study, the researchers repeated Manglik and Fang's (1994) analysis but for corrugated rib surfaces used in plate heat exchangers. These devices also known as chevron ribs are widely used in process heat exchangers due to their ease of construction and cleaning for fouling applications. They showed results for constant mass flow, constant pumping power, and constant pressure drop. They found that corrugated ribs at the fixed pumping power and fixed pressure drop constraints, led to a thermodynamically more efficient system.

Su et al. (1999) found a new way of fin design to minimize the irreversibilities due to heat transfer and fluid friction and maximize the available work of the working fluid. First, the researchers derived the general entropy generation formulas for fins according to the first and second law of thermodynamics. Then, they made a theoretical analysis on cylindrical pin fins and rectangular straight fins using the above formulas. They obtained the minimum entropy generation formulas for these two types of fins and proposed a principle for fin optimization, where the minimum entropy generation was chosen to be the objective function to be studied. They discussed in detail the influence of various parameters on fin entropy generation in forced convection heat transfer.

2. External structure

The ability of a designer to minimize the thermal resistance between the source of heat dissipation and the thermal sink is essential in controlling maximum operating temperatures. While the convective heat transfer coefficient could potentially be enhanced

with an increase in the approach velocity, the dependence of heat transfer coefficient on the square root of the velocity in laminar flow results in diminished returns as velocity is increased. The second option for reducing film resistance is achieved by increasing the effective surface area for convective heat transfer. This is typically achieved through the use of heat sinks in single fluid heat exchangers and extended surfaces in two fluid heat exchangers. Heat sinks offer a low cost, convenient method for lowering the film resistance and in turn maintaining junction operating temperatures at a safe level in electronic components. Unfortunately, the selection of the most appropriate heat sink for a particular application can be very difficult given the many design options available. Thermal analysis tools, ranging from simple empirically derived correlations to powerful numerical simulation tools, can be used to analyze the thermal performance of heat sinks for a given set of design conditions. Regardless of which procedure is used, analysis tools only provide a performance assessment for a prescribed design where all design conditions are specified a priori. Following an exhaustive parametric analysis, design options can be assessed with respect to their influence on thermal performance, however, there is no guarantee that an “optimized” solution is obtained since the parametric analysis only provides a ranking of a limited set of test cases. The method of entropy generation minimization, pioneered by Bejan, provides a procedure for simultaneously assessing the parametric relevance of system parameters as they relate to not only thermal performance but also viscous effects.

2.1 Fin shape

Heat exchanger fins are often used in heat exchange devices to increase the heat transfer rate between the heat-exchange surface and the surrounding fluid. Extended surfaces (fins) enhance heat transfer rate by increasing surface area and by inducing turbulent mixing of flow. They can be found in many engineering applications such as the cooling of turbine blades in gas turbine engines, the cooling of electronic components, and different other heat exchange devices used in aerospace, aircraft, chemical processing plants, ..., etc. There are different kinds of heat exchanger fins, ranging from relatively simple shapes, like rectangular, cylindrical, annular, tapered or pin fins, to a combination of various geometries. These fins may protrude from either a cylindrical or rectangular base.

Numerous analysis tools are available for determining the thermal performance of heat sinks given a well defined set of design conditions. Convective optimizations are available, such as those presented in Kraus and Bar-Cohen (1995), however, these models assumes a prescribed heat transfer coefficient over the length of the fins which is constant, while in most heat sink applications, hydrodynamic and thermal entrance effects introduce a variable heat transfer coefficient, at least over a portion of the heat sink. The assumption of a constant value of heat transfer coefficient can no longer be prescribed, since the value will depend upon fin spacing and length in the direction of flow. Optimization routines that lead to changes in fin spacing, fin height or fin length also result in changes in the mean heat transfer coefficient and head loss in such a way that iterative procedures are required. While in some instances parametric studies can be undertaken to obtain a relationship between thermal performance and design parameters, a comprehensive design tool should also take into consideration the effect of viscous dissipation and its relationship on thermal performance. The entropy generation associated with heat transfer and frictional effects serve as a direct measure of lost potential for work or in the case of a heat sinks and other finned systems. A modeling approach that establishes a relationship between entropy

generation and a fin design parameters, can be used in such a manner that all relevant design conditions combine to produce the best possible thermal sink for the given constraints.

Poulikakos and Bejan (1982) established a theoretical framework for the minimization of entropy generation in forced convection for the design of extended surfaces by the use of the first and second laws of thermodynamics. First, the researchers derived the entropy generation rate formula for a general fin. The entropy generation rate for extended surfaces in external flow with conductive resistance was defined by the following relationship:

$$\dot{S}_{gen} = \frac{\dot{Q}\theta_b}{T_\infty^2} + \frac{F_d V_f}{T_\infty} \quad (43)$$

The temperature excess of the fin or heat sink (θ_b) might be related to the overall system thermal resistance:

$$\theta_b = \dot{Q} R_{fin} \quad (44)$$

Based on this general result, they developed analytical methods and graphic results for selecting the optimum dimensions of pin fins, rectangular plate fins, plate fins with trapezoidal cross section, and triangular plate fins with rectangular cross section.

Lee and Lin (1995) examined the performance and the entropy generation rate of a fractal-like fin under crossflow. This fin type was defined as a fin with subfins repeatedly extending in a fixed way.

Khan et al. (2006) examined the role of cross-sectional shape on entropy generation for several widely used fin cross-sections. The cross-sections examined were circular, elliptical, square, and rectangular. The researchers obtained a general dimensionless expression for the entropy generation rate by considering a control volume around the pin fin including base plate and applying the conservation equations for mass and energy with the entropy balance. They developed the formulation for the dimensionless entropy generation rate in terms of dimensionless variables, including the aspect ratio, Reynolds number, Nusselt number, and the drag coefficient. They examined selected fin geometries for the heat transfer, fluid friction, and the minimum entropy generation rate corresponding to various parameters including axis ratio, aspect ratio, and Reynolds number. Their results clearly indicated that the preferred fin profile was very dependent on these parameters. As the fin became more slender two effects contribute to the reduction in entropy generation number, namely increased surface area that reduced the temperature excess, and a reduction in profile drag which in turn reduced the viscous losses.

2.2 Plate fin arrays

It is well known that in plate fin type heat exchangers the backmixing and other deviations from plug flow contribute significantly to the inefficiency of the heat exchanger that is important to heat exchangers working in the cryogenic regime.

Culham and Muzychka (2001) presented a procedure that allowed the simultaneous optimization of heat sink design parameters for electronic applications based on a

minimization of the entropy generation associated with heat transfer and fluid friction. All relevant design parameters for plate fin heat sinks, including geometric parameters, heat dissipation, material properties and flow conditions could be simultaneously optimized to characterize a heat sink that minimized entropy generation and in turn results in a minimum operating temperature. The researchers modified Eq. (43) to account for the overall sink resistance rather than the resistance of a single fin using a simple control volume analysis as follows:

$$\dot{S}_{gen} = \frac{\dot{Q}^2 R_{sink}}{T_\infty^2} + \frac{F_d V_f}{T_\infty} \quad (45)$$

Using Eq. (45), along with the appropriate expressions for the fin resistance, convective heat transfer coefficient, and frictional/drag losses, a model for the entropy generation rate was developed for an array of parallel plates.

Also, they integrated a novel approach for incorporating forced convection through the specification of a fan curve into the optimization procedure, providing a link between optimized design parameters and the system operating point. They presented examples that demonstrated the robust nature of the model for conditions typically found in electronic applications. It was not unusual for a designer to be given an overall maximum heat sink volume. The examples presented in Culham and Muzychka (2001) were assumed to be constrained by a overall maximum volume of 50 mm × 50 mm × 25 mm. In addition, it was assumed that a total heat dissipation of 30 W was uniformly applied over the base plate of the heat sink that had a uniform thickness of 2 mm. Other constraints that were fixed were the thermal conductivity of the heat sink at $k = 200 \text{ W/m.K}$ and the ambient temperature of the surrounding air medium at $T_o = 25^\circ\text{C}$ or 298 K.

Culham and Muzychka (2001) presented several cases that demonstrated the method of entropy generation minimization for sizing plate fin heat sinks. Their examples included single and multi-parameter optimizations. Their results demonstrated the influence of introducing progressively more unconstrained variables into the optimization procedure. The system of non-linear equations for several cases could be solved using numerical procedures like Newton-Raphson solution, contained within many commercially available algebraic software tools. Given the geometric constraints and a uniform heat load to the base plate of the heat sink of 30 W, an optimum number of fins, N , was to be determined when $V_f = 2 \text{ m/s}$, $t = 1 \text{ mm}$, and $H = 25 \text{ mm}$. As shown in Table 1, the estimation of the appropriate number of fins was $N \approx 29$. It was easily seen that decreasing the number of fins led to an increase in the thermal resistance of the heat sink which in turn led to an increase in the temperature excess and a resultant increase in the entropy generation rate. Increasing the number of fins beyond the optimized value would lead to a decrease in the heat sink resistance and temperature excess, but the increase in the head loss associated with fluid drag would result in an increase in the entropy generation rate.

While the optimization procedure estimated the optimum number of fins to be 28.57 the relatively wide range of near minimum entropy generation rate between $20 < N < 35$, provided designers with a range of options when specifying the appropriate number of fins. In subsequent applications of the optimization method, additional design variables were

introduced into the procedure to simultaneously consider multiple parameters that led to an optimization of the temperature excess and the head loss of the heat sink.

Additional parameters were left unconstrained, like velocity (V_f), fin height (H), number of fins (N), and fin thickness (t). Case (ii) examined the influence of relaxing the constraint on free stream velocity prescribed in Case (i) while all other assumed constraints remained unchanged. As shown in Table 1, the optimized number of fins was determined to be $N \approx 27$ and the approach velocity was estimated to be $V_f = 2.81$ m/s for minimum entropy generation. A decrease in the number of fins and an increase in the free stream velocity led to a heat sink with a lower temperature excess but a higher head loss. Overall, the entropy generation rate for this case was lower than in the previous example. Case (iii) examined a three parameter optimization where the constraint on the fin thickness was removed. The results of the optimization gave $N \approx 38$, $V_f = 3.28$ m/s, and $t = 0.4$ mm as shown in Table 1. Further gains had been made in lowering the heat sink temperature excess and head loss that resulted in yet a further decrease in the entropy generation rate. However, the fin thickness might be too thin for practical manufacturing considerations. Finally, none of the variables of interest would be constrained to predetermined values, thus providing a simultaneous optimization of all design variables, including the free stream velocity (V_f), the number of fins (N), the fin thickness (t), and the fin height (H). Their results of the optimization gave $N \approx 19$, $V_f = 1.21$ m/s, $t = 1.6$ mm, and $H = 122$ mm. Once again a more optimal solution had been found. While the approach presented provided an optimized heat sink, the fin height exceeded the maximum allowable height of 25 mm predicated by the board-to-board spacing.

Moreover, it was important to note, that as more variables became unconstrained, the system was progressively seeking a more optimal design. For instance, in cases (ii) and (iii), although the fin count increased, the fin thickness decreased, leading not only to a thermally more efficient design, but also a system that used less material. Finally, one might introduce additional constraints as needed that limited the temperature excess or the mass of the heat sink. Their method outlined was also applicable to fin arrays used in heat exchangers.

Case	N	θ_b ($^{\circ}\text{C}$)	ΔP (mmH ₂ O)	V_f (m/s)	t (mm)	H (mm)	\dot{S}_{gen} (W/ $^{\circ}\text{C}$)
(i)	28.57	11.51	5.62	2.0	1.0	25	0.00435
(ii)	26.77	9.49	7.02	2.81	1.0	25	0.00402
(iii)	38.14	8.66	5.78	3.28	0.4	25	0.00370
(iv)	19.07	7.20	1.90	1.21	1.6	122	0.00290

Table 1. Optimized Conditions for All Test Cases.

Their model was shown to converge to a unique solution that gave the optimized design conditions for the imposed problem constraints.

The specification and design of heat sinks for electronic applications is not easily accomplished through the use of conventional thermal analysis tools because “optimized” geometric and boundary conditions are not known a priori.

Culham et al. (2007) presented an analytical model for calculating the best possible design parameters for plate fin heat sinks using an entropy generation minimization procedure

with constrained variable optimization. The researchers adapted the method to include a thermal spreading resistance in the overall thermal circuit. Their method characterized the contribution to entropy production of all relevant thermal resistances in the path between source and sink as well as the contribution to viscous dissipation associated with fluid flow at the boundaries of the heat sink. The minimization procedure provided a fast, convenient method for establishing the “best case” design characteristics of plate fin heat sinks given a set of prescribed boundary conditions. They showed that heat sinks made of composite materials containing nonmetallic constituents, with a thermal conductivity as much as an order of magnitude less than typical metallic heat sinks, could provide an effective alternative where performance, cost, and manufacturability were of importance. Also, they showed that the spreading resistance encountered when heat flows from a heat source to the base plate of a heat sink, while significant, could be compensated for by making appropriate design modifications to the heat sink.

Iyengar and Bar-Cohen (2003) presented a coefficient of performance (*COPT*) analysis for plate fin heat sinks in forced convection and showed to provide a viable technique for combining least-material optimization with the entropy minimization methodology. The *COPT* metric related the heat sink cooling capability to the invested fan pumping work and the thermodynamic work required to manufacture and assemble the heat sink. The proposed optimization methodology maximized the forced convection cooling that could be achieved by a heat sink occupying a specified volume, with a fixed energy investment and entropy generation rate. Also, their study identified the presence of an optimal resource allocation ratio, providing the most favorable distribution of existing energy resources, between heat sink manufacturing and operation, over a fixed product life cycle.

Abbassi (2007) investigated the entropy generation in a uniformly heated microchannel heat sink (*MCHS*). He used analytical approach to solve forced convection problem across *MCHS*. This analytical approach was a porous medium model based on extended Darcy equation for fluid flow and two-equation model for heat transfer. Simultaneously, closed form velocity solution in a rectangular channel was employed to capture *z*-directional viscous effect diffusion and its pronounced influence on entropy generation through fluid flow. Subsequently, governing equations were cast into dimensionless form and solved analytically. Then, second law analysis of problem was conducted on the basis of obtained velocity and temperature fields and expressions for local and average entropy generation rate were derived in dimensionless form. Then, average entropy generation rate was utilized as a criterion for assessing the system performance. At the end, the effect of influential parameters like, channel aspect ratio (α_s), group parameter (Br/Ω), thermal conductivity ratio (C) and porosity (ε) on thermal and total entropy generation was investigated. In order to examine the accuracy of the analysis, the results of thermal evaluation were compared to one of the previous investigations conducted for thermal optimization of *MCHS*.

Khan et al. (2009) employed an entropy generation minimization (*EGM*) procedure to optimize the overall performance of microchannel heat sinks. The researchers developed new general expressions for the entropy generation rate by considering an appropriate control volume and applying mass, energy, and entropy balances. They investigated the influence of channel aspect ratio, fin spacing ratio, heat sink material, Knudsen numbers, and accommodation coefficients on the entropy generation rate in the slip flow region. They

used analytical/empirical correlations for heat transfer and friction coefficients, where the characteristic length was used as the hydraulic diameter of the channel. In addition, a parametric study was performed to show the effects of various design variables on the overall performance of microchannel heat sinks.

The thermal design of plate fin heat sinks can benefit from optimization procedures where all design variables are simultaneously prescribed, ensuring the best thermodynamic and air flow characteristic possible. While a cursory review of the thermal network established between heat sources and sinks in typical plate fin heat sinks would indicate that the film resistance at the fluid-solid boundary dominates, it is shown that the effects of other resistance elements, such as the spreading resistance and the material resistance, although of lesser magnitude, play an important role in the optimization and selection of heat sink design conditions.

Zhou et al. (2009) proposed the multi-parameter constrained optimization procedure integrating the design of experiments (*DOE*), response surface models (*RSM*), genetic algorithm (*GA*), mixed integer optimization (*MOST*), and computational fluid dynamics (*CFD*) to design the plate finned heat sinks by minimizing their rates of entropy generation. The results of three cases demonstrated that the combination optimization algorithm was feasible. In these cases, the overall rate of entropy generation decreased as the result of introducing the additional constrained variables into the optimization procedure. As a result, the general thermal and fluid performance of the heat sink was dramatically improved.

Based on the results derived by the optimization, the researchers investigated the overall thermal and fluid performance of the plate finned heat sinks with both side and top bypass flow. Also, they established two correlations describing Nusselt number and friction factor, as the functions of geometrical and operational parameters, by means of the multivariate non-linear regression analysis. They deduced the specific expressions to compute the thermal resistance and the rate of entropy generation.

Ganzarollia, and Altemania (2010) performed the thermal design of a counterflow heat exchanger using air as the working fluid with two distinct goals: minimum inlet temperature difference and minimum number of entropy generation units. The researchers constituted the heat exchanger by a double-finned conductive plate closed by adiabatic walls at the fin tips on both sides. The cold and hot air flows were considered in the turbulent regime, driven by a constant pressure head. The thermal load was constant, and an optimization was performed in order to obtain the optimum fin spacing and thickness, according to the two design criteria. They employed a computer program to evaluate the optimum conditions based on correlations from the literature. They compared the results obtained from both design criteria to each other. They performed a scale analysis considering the first design goal and compared the corresponding dimensionless parameters with the results from the correlations.

Zhang et al. (2010) developed a general three-dimensional distributed parameter model (*DPM*) for designing the plate-fin heat exchanger (*PFHE*). The proposed model that allowed for the varying local fluid thermophysical properties inside the flow path could be applied for both dry and wet working conditions by using the uniform enthalpy equations. The researchers generated the grids in the *DPM* to match closely the flow passage of the heat

exchanger. They adopted the classical correlations of the heat transfer and the flow friction to avoid solving the differential equations. As a result, the computation burden of *DPM* became significantly less than that of the Computational Fluid Dynamics method. They performed the optimal design of a *PFHE* based on the *DPM* with the entropy generation minimization taken into consideration. They employed the genetic algorithm to conduct the optimization due to its robustness in dealing with complicated problems. The fin type and fin geometry were selected optimally from a customized fin database. The *PFHE* included in an environmental control system was designed by using the proposed approach in their study. Finally, They evaluated the cooling performance of the optimal *PFHE* under both dry and wet conditions.

Galvis and Culham (2010) used the entropy generation minimization (*EGM*) method to find the optimum channel dimensions in micro heat exchangers with a uniform heat flux. With this approach, pressure drop and heat transfer in the micro channels were considered simultaneously during the optimization analysis. The researchers developed a computational model to find the optimum channel depth knowing other channel geometry dimensions and coolant inlet properties. Their assumptions were laminar and both hydrodynamically and thermally fully developed flow, and incompressible. However, they introduced the Hagenbach factor (*K*) to take into account the developing length effect in the friction losses. The Hagenbach factor (*K*) for rectangular channels obtained by Steinke and Kandlikar (2006) as follows:

$$K = 0.6796 + 1.2197\alpha_s + 3.3089\alpha_s^2 - 9.5921\alpha_s^3 + 8.9089\alpha_s^4 + 2.9959\alpha_s^5 \quad (46)$$

The micro channels were assumed to have an isothermal or isoflux boundary condition, non-slip flow, and fluid properties had dependency on temperature accordingly. For these particular case studies, the pressure drop and heat transfer coefficient for the isothermal boundary condition is lower than the isoflux case. As the channel size decreased, they found higher heat transfer coefficient and pressure drop. The optimum channel geometry that minimized the entropy generation rate tended to be a deep, narrow channel.

Rao and Patel (2010) discussed the use of particle swarm optimization (*PSO*) algorithm for thermodynamic optimization of a cross flow plate-fin heat exchanger. The researchers considered minimization of total number of entropy generation units for specific heat duty requirement under given space restrictions, minimization of total volume, and minimization of total annual cost as objective functions and treated individually. Based on the applications, they considered heat exchanger length, fin frequency, numbers of fin layers, lance length of fin, fin height and fin thickness or various flow length of the heat exchanger for optimization. They included heat duty requirement constraint in the procedure. Also, they presented two application examples to demonstrate the effectiveness and accuracy of the proposed algorithm. They validated the results of optimization using *PSO* by comparing with those obtained by using genetic algorithm (*GA*). In addition, they carried out parametric analysis to demonstrate the influence of heat exchanger dimensions on the optimum solution. Moreover, they presented the influence of variation of *PSO* parameters on convergence and optimum value of the objective.

Ahmadi et al. (2011) conducted a thermal modeling for optimal design of compact heat exchangers to minimize cost and entropy generation. The researchers applied an ε - *NTU*

method for estimation of the heat exchanger pressure drop, and effectiveness. Fin pitch, fin height, fin offset length, cold stream flow length, no-flow length, and hot stream flow length were considered as six decision variables. They applied fast and elitist nondominated sorting genetic algorithm (i.e., nondominated sorting genetic algorithm II) to minimize the entropy generation units and the total annual cost (sum of initial investment and operating and maintenance costs) simultaneously. The results for Pareto-optimal front clearly revealed the conflict between two objective functions, the number of entropy generation units (N_s) and the total annual cost (C_{total}). It revealed that any geometrical changes that decreased the number of entropy generation units, led to an increase in the total annual cost and vice versa. Moreover, they derived an equation for the number of entropy generation units versus the total annual cost for the Pareto curve for prediction of the optimal design of the plate fin heat exchanger as follows:

$$C_{total} (\$) = \frac{-2.819N_s^3 - 4.311N_s^2 + 1.728N_s - 0.04891}{N_s^2 + 21.84N_s - 1.867} \times 10,000 \quad 0.0939 < N_s < 0.13 \quad (47)$$

Considering a numerical value for the number of entropy generation units in the range $0.0939 < N_s < 0.13$ provided the minimum total annual cost for that optimal point along with other optimal design parameters. Also, optimization of heat exchangers based on considering exergy destruction revealed that irreversibilities, like pressure drop and high temperature difference between cold and hot streams, played a key issue in exergy destruction. Thus, more efficient heat exchanger led to have a heat exchanger with higher total cost rate. At the end, the sensitivity analysis of change in the optimum number of entropy generation units and the total annual cost with change in the decision variables of the plate fin heat exchanger was also performed, and the results were reported.

Shuja and Zubair (2011) presented a detailed second-law based thermoeconomic optimization for a finned heat sink array. This involved including costs associated with material and irreversible losses due to heat transfer and pressure drop. The researchers optimized the effect of important physical, geometrical and unit cost parameters on the overall finned array for some typical operating conditions that were representative of electronic cooling applications. They presented the cost optimized results in terms of different parameters for a finned system. Furthermore, they explained the methodology of obtaining optimum design parameters for a finned heat sink system that would result in minimum total cost.

Gielen et al. (2011) discussed the use of second law based cost functions in plate fin heat sink design. The researchers proposed and compared a new entropy-based cost function with existing heat sink cost functions. A case study of a plate fin heat sink pointed out that their newly developed cost function offered a heat sink that was more than twice as efficient as a heat sink designed with the traditional thermal resistance minimization objective. The influences of this new heat sink design on data center cooling systems were considered and found to be significantly improving the system efficiency and waste heat recovery.

Al-Obaidi (2011) used second law analysis for a steady-state cross flow microchannel heat exchanger (MCHX) because this type of heat exchangers was known for its higher heat transfer coefficient and higher area per volume ratio. As a result, broad range studies were being carried out to optimize its performance and minimize its inefficiencies. The researcher

employed entropy generation and exergy loss to investigate a multiport serpentine slab *MCHX* with ethylene glycol-water and air as the working fluids. She used conservation of energy and the increase in entropy principles to create a mathematical model that used various like heat capacity rate ratio, fluids inlet temperatures, effectiveness and pressure drop for obtaining entropy generation. Results were found on the basis of the behavior of the entropy generation number (N_s) with the key parameters. She found a good agreement between the predicted and the measured results.

2.3 Pin fins

For heat transfer enhancement, pin fins are widely used as effective elements. For this purpose, extensive work is being carried out to choose and optimize pin fins for different applications. Any optimization procedure would lead to desirable results only if the parallel pressure drop and heat transfer are considered. Pin fin arrays are another popular geometry used in electronics cooling. Pin fins are attractive as a result of their ability to operate easily in multi-directional fluid streams.

First, Lin and Lee (1997) conducted the second law analysis on a pin-fin array under crossflow to evaluate the entropy generation rate. Increasing the crossflow fluid velocity enhancing the heat transfer rate and hence, reducing the heat transfer irreversibility. Nevertheless, owing to the simultaneous increase in drag force exerting on the fin bodies, the hydrodynamic irreversibility increased also. An optimal Reynolds number thereby existed over wide operating conditions. The researchers searched the optimal design/operational conditions on the basis of entropy generation minimization. Also, they made the comparison of the staggered and the in-line pin-fin alignments.

Şara et al. (2001) presented heat transfer and friction characteristics, and the second law analysis of the convective heat transfer through a rectangular channel with square cross-sectional pin fins attached over a flat surface. The researchers used different clearance ratios and interfin distance ratios and determined optimum pin-fin arrays that minimized entropy generation. They found that average Nusselt number based on the projected area decreased with increasing clearance ratio and interfin distance ratio, whereas average Nusselt number based on the total heat transfer area increased with increasing interfin distance ratio and with decreasing clearance ratio. Also, they found that the friction factor to decrease with increasing clearance ratio and interfin distance ratio. They obtained smaller entropy generation numbers at lower Reynolds number, higher clearance ratio, and higher interfin spacing ratio.

Khan et al. (2005) applied an entropy generation minimization (EGM) technique as a unique measure to study the thermodynamic losses caused by heat transfer and pressure drop in cylindrical pin-fin heat sinks. The researchers obtained a general expression for the entropy generation rate by considering the whole heat sink as a control volume and applying the conservation equations for mass and energy with the entropy balance. They used analytical/empirical correlations for heat transfer coefficients and friction factors in the optimization model, where the characteristic length was used as the diameter of the pin and reference velocity used in Reynolds number and pressure drop was based on the minimum free area available for the fluid flow. They studied both in-line and staggered arrangements and compared their relative performance on the basis of equal overall volume of heat sinks.

The details of the necessary models for heat transfer and drag might be found in Khan et al. (2005) along with the general control volume analysis. It was shown that all relevant design parameters for pin-fin heat sinks, including geometric parameters, material properties and flow conditions could be simultaneously optimized.

Khan et al. (2008) applied an entropy generation minimization (*EGM*) method to study the thermodynamic losses caused by heat transfer and pressure drop for the fluid in a cylindrical pin-fin heat sink and bypass flow regions. The researchers obtained a general expression for the entropy generation rate by considering control volumes around the heat sink and bypass regions. The conservation equations for mass and energy with the entropy balance were applied in both regions. Inside the heat sink, analytical/empirical correlations were used for heat transfer coefficients and friction factors, where the reference velocity used in the Reynolds number and the pressure drop was based on the minimum free area available for the fluid flow. In bypass regions theoretical models, based on laws of conservation of mass, momentum, and energy, were used to predict flow velocity and pressure drop. They studied both in-line and staggered arrangements and compared their relative performance to the same thermal and hydraulic conditions. Also, they performed a parametric study to show the effects of bypass on the overall performance of heat sinks.

Sahiti et al. (2008) derived experimentally the heat transfer and pressure drop characteristics of a double-pipe pin fin heat exchanger. The researchers used the empirical correlations previously validated with their experimental data to develop a mathematical model for the optimization of the actual heat exchanger. They developed the optimization model on the basis of the entropy generation minimization for various heat exchanger flow lengths and various pin lengths. They derived the conclusions on the basis of the behavior of the entropy generation number (N_s) as a function of the Reynolds number (Re). They showed that not all definition forms for the entropy generation number led to the right conclusions.

Nwachukwu and Onyegegbu (2009) derived an expression for the optimum pin fin dimension on exergy basis for a high temperature exchanger employing pin fins. Their result was different from that obtained by Poulikakos and Bejan (1982) for a low temperature heat recovery application. In addition, the researchers established a simple relation between the amounts the base temperature of the optimized pin fin was raised for a range of absorptive coating values. Employing this relation, if the absorptivity of the coating, the plate emissivity, the number of protruding fins, and some area and fluid parameters were known, they obtained immediately the corresponding value for the base temperature of the fin. Their analysis showed that the thermal performance of the exchanger improved substantially with a high absorptivity coating hence could be seen as a heat transfer enhancement feature of the exchanger operating with radiation dominance.

Kamali et al. (2010) used numerical analysis to investigate entropy generation for array of pin-fin heat sink. Technique was applied to study the thermodynamic losses caused by heat transfer and pressure drop in pin-fin heat sinks. The researchers obtained a general expression for the entropy generation rate by considering the whole heat sink as a control volume and applying the conservation equations for mass and energy with the entropy balance. They used analytical and empirical correlations for heat transfer coefficients and friction factors in the numerical modeling. Also, they studied heat transfer and pressure drop effects in entropy generation in control volume over pin-fins. They used numerical

analysis for three different models of pin-fin heat sinks. The models were different in cross section area. These cross section areas were circle, horizontal ellipse, and vertical ellipse. Reference velocity used in Reynolds number and pressure drop was based on the minimum free area available for the fluid flow. As expected, the pressure drop and entropy generation increased with the rise of frontal velocity. Also, they investigated in-line arrangement of fins for numerical analysis and compared their relative performance. Finally, they compared the performance of these three models from the views point of heat transfer and total entropy generation rate. The elliptic pin fin showed the lowest pressure drops. Whereas, the circular geometry appeared as the best from the view point of the total entropy generation rate for low approach velocities and the elliptical geometry was the next favorable geometry from the view point of total entropy generation rate for higher approach velocities. Eventually, vertical elliptic fins showed the highest pressure drop and entropy generation among these different geometries.

Su et al. (2011) studied theoretically the entropy generation during heat transfer of a pin fin array in channels with lateral ejection holes for a turbine blade. The researchers established the entropy generation model based on the second-law analysis. They analyzed the distribution of the entropy generation due to heat transfer and fluid friction irreversibility respectively and made a comparison for three typical short pin fin channels. The entropy generation number component due to heat transfer decreased while Re_d increased, while the component due to fluid friction increased with the increase of Re_d . The entropy generation number (N_s) reached minimum when the two components met and the corresponding Reynolds number (Re_d) was optimal. The ejection holes affected the energy lost of the working fluid. For the three cases studied in this work, case b with short ejection holes gave the best comprehensive thermal performance with comparison to cases with no and long ejection holes. They suggested that their results would be helpful for the design of the heat dissipation of pin fin heat exchangers.

3. Conclusion

This chapter provides a comprehensive, up-to-date review in a chronological order on the research progress made on entropy generation minimization (thermodynamic optimization, or finite time thermodynamics). *EGM* is the method which combines into simple models the most basic concepts of heat transfer, fluid mechanics, and thermodynamics (Bejan, 1982a). These simple models are used in the real (irreversible) devices and processes optimization, subject to finite-size and finite-time constraints. The current review is related to using *EGM* method in heat exchangers for both internal structure and external structure. Examples are drawn from different kinds of applications: parallel flow, counterflow, crossflow, phase-change heat exchanger optimizations, as well as optimization of internal enhancement. Attention is also gives to micro systems such as microchannel heat exchanger (*MCHX*).

4. Acknowledgment

The authors acknowledge the financial support of the Natural Sciences and Engineering Research Council of Canada (NSERC) through the Discovery Grants program. Also, we want to thank the Editor, Prof. Jovan Mitrovic, for inviting us to prepare this chapter.

5. Nomenclature

A	total heat transfer area, m^2
B	duty parameter
Be	Bejan number
Br	Brinkman number = $Ec.Pr$
C	thermal conductivity ratio
C^*	modified ratio of heat capacity rates, $(\dot{m} c_p)_h / (\dot{m} c_p)_c$
C_r	capacity ratios
C_{total}	total annual cost, \$
c_p	constant-pressure specific heat, $J/kg.K$
d	diameter, m
E^*	exergy loss rate
Ec	Eckert number
F_d	total drag force on the fin (or array), N
$F_{\Delta P}$	pressure-drop factor
$F_{\Delta P}^*$	modified pressure-drop factor
f	Fanning friction factor
G	mass flux, $kg/m^2.s$
H	height, m
h	heat transfer coefficient, $W/m^2.K$, enthalpy, J/kg
j	Colburn factor
K	Hagenbach factor
k	thermal conductivity, $W/m.K$
L	length, m
\dot{m}	mass flow rate, kg/s
N	number of fins
N_s, N_M, N_Q	entropy generation numbers
Nu	Nusselt number
NTU	number of heat transfer units, $U_o A_o / (\dot{m} c_p)_{min}$
NTU_h	modified number of heat transfer units, $U_o A_o / (\dot{m} c_p)_h$
P	temperature effectiveness for a fluid, pressure, Pa
p	perimeter, m
Pe	Peclet number = $Re.Pr$
Pr	Prandtl number = ν/α
\dot{Q}	heat dissipation rate, W
dq/dx	heat transfer rate per unit length, W/m
R	heat capacity ratio
R_{fin}	resistance of the fin structure as a function of geometry, K/W
R_{sink}	overall resistance for the sink array, K/W
Ra	Rayleigh number
Re	Reynolds number
\dot{S}_i	entropy generation rate due to thermal effects, W/K

\dot{S}_v	entropy generation rate due to viscous dissipation, W/K
S^*	entropy generation number ratio
St	Stanton number
T	temperature, K
T_o	ambient temperature or dead-state temperature, K
T_r	inlet temperature ratio
T_∞	environment temperature, K
t	fin thickness, m
U	overall heat transfer coefficient, W/m ² .K
V	velocity, m/s
V_f	free stream or approach velocity, m/s
v	specific volume, m ³ /kg
w_C	channel width, m
Y_s	heat exchange reversibility norm (HERN)

Greek

α	thermal diffusivity = $k/\rho c_p$, m ² /s
α_s	channel aspect ratio = H/w_C
Δ	difference
ε	effectiveness, porosity
ϕ	irreversibility distribution ratio
Γ	entropy flux
η	efficiency
η_{II}	exergy recovery index
Λ	Reduced length
μ	dynamic viscosity, kg/m.s
ν	kinematic viscosity, m ² /s
Π	Reduced period
θ	blade angle
θ_b	temperature excess of the fin, ($T_b - T_\infty$)
ρ	density, kg/m ³
Ω	dimensionless temperature difference
ω	capacity ratios
ψ	entropy generation distribution factor

Subscripts

0	without augmentation
1	stream 1
2	stream 2
av	average
b	blade
c	cold stream
gen	generation
h	hydraulic, hot stream
in	in
max	maximum value

<i>min</i>	minimum value
<i>o</i>	dead state or external (air side)
<i>opt</i>	optimum
<i>out</i>	out
W-S	Witte-Shamsundar

Superscripts

* at maximum irreversibility

6. References

- Abbassi, H., 2007, Entropy Generation Analysis in a Uniformly Heated Microchannel Heat Sink, *Energy* 32 (10) pp. 1932-1947.
- Ahmadi, P., Hajabdollahi, H., Dincer, I., 2011, Cost and Entropy Generation Minimization of a Cross-Flow Plate Fin Heat Exchanger Using Multi-Objective Genetic Algorithm, *ASME Journal of Heat Transfer*, 133 (2), Article (021801).
- Al-Obaidi, S., 2011, Second Law Analysis of a Multiport Serpentine Microchannel Heat Exchanger, Master Thesis, University of Windsor, ON, Canada.
- Arivazhagan, M., and Lokeswaran, S., 2011, Entropy Generation Minimization of Shell and Tube Heat Exchanger with Porous Medium, *Experimental Techniques*, doi: 10.1111/j.1747-1567.2011.00758.x.
- Assad, M. El Haj, 2010, Effect of Maximum and Minimum Heat Capacity Rate on Entropy Generation in a Heat Exchanger, *International Journal of Energy Research*, 34 (14), pp. 1302-1308.
- Bejan, A., 1975, Discrete Cooling of Low Heat Leak Supports to 4.2 K, *Cryogenics*, 15 (5), pp. 290-292.
- Bejan, A., 1977, The Concept of Irreversibility in Heat Exchanger Design: Counterflow Heat Exchangers for Gas-to-Gas Application, *ASME Journal of Heat Transfer*, 99 (3), pp. 374-380.
- Bejan, A., 1978, General Criterion for Rating Heat-Exchanger Performance, *International Journal of Heat and Mass Transfer*, 21 (5), pp. 655-658.
- Bejan, A., 1979, A Study of Entropy Generation in Fundamental Convective Heat Transfer, *ASME Journal of Heat Transfer*, 101 (4), pp. 718-725.
- Bejan, A., 1980, Second-Law Analysis in Heat Transfer, *Energy*, 5 (8-9), pp. 721-732.
- Bejan, A., 1982a, *Entropy Generation through Heat and Fluid Flow*, Wiley, New York, NY.
- Bejan, A., 1982b, Second-Law Analysis in Heat Transfer and Thermal Design, *Advances in Heat Transfer*, 15, pp. 1-58.
- Bejan, A., 1983, Second-Law Aspects of Heat Transfer Engineering, Keynote Address to the 3rd Multi-Phase Flow and Heat Transfer Symposium/Workshop, Miami Beach, Florida, April 18-20, 1983. Also published in *Multi-Phase Flow and Heat Transfer III*, ed. Veziroglu, T. N. and Bergles, A. E., Elsevier, Amsterdam, 1984, 1A, pp. 1-22.
- Bejan, B., 1987, The Thermodynamic Design of Heat and Mass Transfer Processes and Devices, *International Journal of Heat and Fluid Flow*, 8 (4), pp. 258-276.
- Bejan, A., 1988, *Advanced Engineering Thermodynamics*, Wiley, New York, NY.

- Bejan, A., 1992, Single Correlation for Theoretical Contact Melting Results in Various Geometries, *International Communications in Heat and Mass Transfer*, 19 (4), pp. 473-483.
- Bejan, A., 1993, *Heat Transfer*, Wiley, New York, NY.
- Bejan, A., 1996a, Entropy Generation Minimization, CRC Press, Boca Raton, FL.
- Bejan, A., 1996b, Entropy Generation Minimization: The New Thermodynamics of Finite-Size Devices and Finite-Time Processes, *Journal of Applied Physics*, 79 (3), pp. 1191-1218.
- Bejan, A., 1996c, Notes on the History of the Method of Entropy Generation Minimization (Finite Time Thermodynamics), *Journal of Non-Equilibrium Thermodynamics*, 21 (3), pp. 239-242.
- Bejan, A., 2000, *Shape and Structure, from Engineering to Nature*, Cambridge University Press, Cambridge, UK.
- Bejan, A., 2001, Entropy Generation Minimization: The Method and Its Applications, *Strojniski Vestnik/Journal of Mechanical Engineering*, 47 (8), pp. 345-355.
- Bejan, A., 2002, Fundamentals of Exergy Analysis, Entropy Generation Minimization, and the Generation of Flow Architecture, *International Journal of Energy Research*, 26 (7), pp. 545-565.
- Bejan, A., and Lorente, S., 2001, Thermodynamic Optimization of Flow Geometry in Mechanical and Civil Engineering, *Journal of Non-Equilibrium Thermodynamics*, 26 (4), pp. 305-354
- Bejan, A. and Pfister, P.A., 1980, Evaluation of Heat Transfer Augmentation Techniques Based on Their Impact on Entropy Generation, *Letters in Heat and Mass Transfer*, 7 (2), pp. 97-106.
- Bejan, A., and Sciubba, E., 1992, The Optimal Spacing of Parallel Plates Cooled by Forced Convection, *International Journal of Heat and Mass Transfer*, 35 (12), pp. 3259-3264.
- Bejan, A., and Smith, J. L. Jr, 1974, Thermodynamic Optimisation of Mechanical Supports for Cryogenic Apparatus, *Cryogenics*, 14 (3), pp. 158-163.
- Bejan, A., and Smith, J. L. Jr, 1976, Heat Exchangers for Vapour Cooled Conducting Supports of Cryostats, *Advances in Cryogenic Engineering*, 21, pp. 247.
- Benedetti, P., and Sciubba, E., 1993, Numerical Calculation of the Local Rate of Entropy Generation in the Flow Around a Heated Finned Tube, *The 1993 ASME Winter Annual Meeting, ASME HTD*, 266, pp. 81-91, New Orleans, LA, USA, 28 November-3 December, 1993.
- Chowdhury, K., and Sarangi, S., 1980, A Second Law Analysis of the Concentric Tube Balanced Counterflow Heat Exchanger: Optimisation of Wall Conductivity, *Proceedings of the 7th National Symposium on Refrigeration and Air Conditioning, India*, pp. 135-138.
- Chowdhury, K., and Sarangi, S., 1983, A Second Law Analysis of the Concentric Tube Counterflow Heat Exchanger: Optimisation of Wall Conductivity, *International Journal of Heat and Mass Transfer*, 26 (5), pp. 783-786.
- Culham, J. R., Khan, W. A., Yovanovich, M. M., and Muzychka, Y. S., 2007, The Influence of Material Properties and Spreading Resistance in the Thermal Design of Plate Fin Heat Sinks, *ASME Journal of Electronic Packaging*, 129 (3), pp. 76-81. Also

- presented at Proceedings of ASME 35th National Heat Transfer Conference (NHTC'01), Fundamentals of Heat Transfer Modes Applied to Electronics Cooling, NHTC2001-20019, Vol. 1, pp. 167-174, Anaheim, CA, June 10-12, 2001.
- Culham, J. R., and Muzychka, Y. S., 2001, Optimization of Plate Fin Heat Sinks Using Entropy Generation Minimization, *IEEE Transactions on Components and Packaging Technologies*, Vol. 24, pp. 159-165. Also presented at Proceedings of the 17th Intersociety Conference, Thermal and Thermomechanical Phenomena in Electronic Systems (ITHERM2000), Vol. 2, pp. 8-15, May 23-26, 2000, Las Vegas, NV.
- da Costa, C. E. S. M. and Saboya, F. E. M., 1985, Second Law Analysis for Parallel Flow and Counterflow Heat Exchangers, Proceedings of the 8th Brazilian Congress of Mechanical Engineering (VIII COBEM), pp. 185-187, Sao Jose dos Campos, S. P., Brazil, December 1985.
- Eğrican, N., 1989, A Heat Exchanger Design Method Based on the Second Law of Thermodynamics, *Journal of Engineer and Machine*, 30 (354), pp. 10-16.
- Evans, R. B., and von Spakovsky, M. R., 1991, Two Principles of Differential Second-Law Analysis for Heat Exchanger Design, *ASME Journal of Heat Transfer*, 113 (2), pp. 329-336. Also presented in AES, Vol. 7, pp. 1-12, Approaches to the Design and Optimization of Thermal Systems, November 27 - December 2, 1988, Chicago, IL.
- Fakheri, A., 2010, Second Law Analysis of Heat Exchangers, *ASME Journal of Heat Transfer*, 132 (11), Article (111802).
- Fan, Y., and Luo, L., 2009, Second Law Analysis of a Crossflow Heat Exchanger Equipped with Constructal Distributor/Collector, *International Journal of Exergy*, 6 (6), pp. 778-792.
- Gaggioli, R. A., and Petit, P. J., 1977, Use the Second Law First, *Chemtech*, 7, pp. 496.
- Galvis, E., and Culham, J. R., 2010, Lower Entropy Generation in Microchannels with Laminar Single Phase Flow, Proceedings of the ASME 2010 3rd Joint US-European Fluids Engineering Summer Meeting and 8th International Conference on Nanochannels, Microchannels, and Minichannels (FEDSM-ICNMM2010), Topic: Single-Phase Liquid Flow, FEDSM-ICNMM2010-30031, August 1-5, 2010, Montreal, Canada.
- Ganzarollia, M. M., and Altemania, C. A. C., 2010, Optimum Fins Spacing and Thickness of a Finned Heat Exchanger Plate, *Heat Transfer Engineering*, 31 (1), pp. 25-32.
- Gielen, R., Rogiers, F., Joshi, Y., and Baelmans, M., 2011, On the Use of Second Law Based Cost Functions in Plate Fin Heat Sink Design, 27th Annual IEEE Semiconductor Thermal Measurement and Management Symposium (SEMI-THERM), Article (5767182), pp. 81-88, 20-24 March 2011, San Jose, CA.
- Grazzini, G., and Gori, F., 1988, Entropy Parameters for Heat Exchanger Design, *International Journal of Heat and Mass Transfer*, 31 (12), pp. 2547-2554.
- Guo, J., Cheng, L., and Xu, M., 2009, Optimization Design of Shell-and-Tube Heat Exchanger by Entropy Generation Minimization and Genetic Algorithm, *Applied Thermal Engineering*, 29 (14-15), pp. 2954-2960.

- Guo, J. F., Cheng, L., and Xu, M. T., 2010, Multi-Objective Optimization of Heat Exchanger Design by Entropy Generation Minimization, *ASME Journal of Heat Transfer*, 132 (8), Article (081801).
- Gupta, A., and Das, S. K., 2007, Second Law Analysis of Crossflow Heat Exchanger in the Presence of Axial Dispersion in One Fluid, *Energy*, 32 (5), pp. 664-672.
- Gupta, P. K., Kush, P. K., and Tiwari, A., 2007, Second Law Analysis of Counter Flow Cryogenic Heat Exchangers in Presence of Ambient Heat-in-Leak and Longitudinal Conduction through Wall, *International Journal of Heat and Mass Transfer*, 50 (23-24), pp. 4754-4766.
- He, Y.-L., Lei, Y.-G., Tao, W.-Q., Zhang, J.-F., Chu, P., and Li, R., 2009, Second-law Based Thermodynamic Analysis of a Novel Heat Exchanger, *Chemical Engineering and Technology*, 32 (1), pp. 86-92.
- Hesselgreaves, J. E., 2000, Rationalisation of Second Law Analysis of Heat Exchangers, *International Journal of Heat and Mass Transfer*, 43 (22), pp. 4189-4204.
- Hilal, M. A., and Boom, R. W., 1976, Optimisation of Mechanical Supports for Large Superconductive Magnets, *Advances in Cryogenic Engineering*, 22, pp. 224-232 (Presented at Proceedings of 1st International Cryogenic Materials Conference, Kingston, Ontario, Canada, July 22-25, 1975).
- Holmberg, R. B., 1989, Sensible and Latent Heat Transfer in Cross-Counterflow Gas-to-Gas Heat Exchanger, *ASME Journal of Heat Transfer*, 111 (1), pp. 173-177.
- Iyengar, M., and Bar-Cohen, A., 2003, Least-Energy Optimization of Forced Convection Plate-Fin Heat Sinks, *IEEE Transactions on Components and Packaging Technologies*, 26 (1), pp. 62-70. Also presented at 8th Intersociety Conference on Thermal and Thermomechanical Phenomena in Electronic Systems, pp. 792-799, May 30, June 1, 2002, San Diego, CA.
- Kamali, R., Barari, B., and Shirazi, A. A., 2010, Numerical Analysis of Entropy Generation in Array of Pin-fin Heat Sinks for Some Different Geometry, *Proceedings of the ASME 2010 3rd Joint US-European Fluids Engineering Summer Meeting and 8th International Conference on Nanochannels, Microchannels, and Minichannels (FEDSM-ICNMM2010)*, Topic: Numerical Methods, FEDSM-ICNMM2010-30011, August 1-5, 2010, Montreal, Canada.
- Kays, W. M. and London, A. L., 1984, *Compact Heat Exchangers*, 3rd ed., Kreiger Publishing, Melbourne, FL.
- Khan, W. A., Culham, J. R., and Yovanovich, M. M., 2005, Optimization of Pin Fin Heat Sinks Using Entropy Generation Minimization, *IEEE Transactions on Components and Packaging Technologies*, 28 (2), pp. 247-254. Also presented in 9th Intersociety Conference on Thermal and Thermomechanical Phenomena in Electronic Systems, Las Vegas, NV, USA, June 1-4, 2004.
- Khan, W. A., Culham, J. R., and Yovanovich, M. M., 2006, The Role of Fin Geometry in Heat Sink Performance, *ASME Journal of Electronic Packaging*, 128 (12), pp. 324-330, Also presented at International Electronic Packaging Technical Conference and Exhibit, InterPACK2003-35014, Maui, Hawaii, July 6-11, 2003.
- Khan, W. A., Culham, J. R., and Yovanovich, M. M., 2007, Optimal Design of Tube Banks in Crossflow Using Entropy Generation Minimization Method, *Journal of*

- Thermophysics and Heat Transfer 21 (2), pp. 372-378. Also presented at AIAA 44th Aerospace Sciences Meeting and Exhibit, Reno, NV, January 9-12, 2006.
- Khan, W. A., Culham, J. R., and Yovanovich, M. M., 2008, Optimization of Pin-Fin Heat Sinks in Bypass Flow Using Entropy Generation Minimization Method, ASME Journal of Electronic Packaging, 130 (3), pp. 0310101-0310107. Also presented at the 2007 ASME-JSME Thermal Engineering Conference and Summer Heat Transfer Conference (HT2007), Vancouver, British Columbia, Canada, July 8-12, 2007.
- Khan, W. A., Culham, J. R., and Yovanovich, M. M., 2009, Optimization of Microchannel Heat Sinks Using Entropy Generation Minimization Method, IEEE Transactions on Components and Packaging Technologies, 32 (2), pp. 243-251. Also presented in 22nd Annual IEEE Semiconductor Thermal Measurement and Management Symposium (Semi-Therm), Dallas, TX, March 14-16, 2006.
- Kotcioglu, I., Caliskan, S., Cansiz, A., and Baskaya, S., 2010, Second Law Analysis and Heat Transfer in a Cross-Flow Heat Exchanger with a New Winglet-Type Vortex Generator, Energy, 35 (9), 3686-3695.
- Krane, R. J., 1987, A Second Law Analysis of the Optimum Design and Operation of Thermal Energy Storage Systems, International Journal of Heat and Mass Transfer, 30 (1), pp. 43-57.
- Kraus, A. D. and Bar-Cohen, A., 1995, Design and Analysis of Heat Sinks, John Wiley and Sons Ltd., New York, NY.
- Kurtbaşı, I., Durmuş, A., Eren, H., and Turgut, E., 2007, Effect of Propeller Type Swirl Generators on the Entropy Generation and Efficiency of Heat Exchangers, International Journal of Thermal Sciences, 46 (3), pp. 300-307.
- Lee, D. J., and Lin, W. W., 1995, Second-Law Analysis on a Fractal-Like Fin under Crossflow, AIChE Journal, 41 (10), pp. 2314-2317.
- Lerou, P. P. M., Veenstra, T. T., Burger, J. F., Ter Brake, H. J. M., and Rogalla, H., 2005, Optimization of Counterflow Heat Exchanger Geometry through Minimization of Entropy Generation, Cryogenics, 45 (10-11), pp. 659-669.
- London, A. L., and Shah, R. K., 1983, Costs and Irreversibilities in Heat Exchanger Design, Heat Transfer Engineering, 4 (2), pp. 59-73.
- Manglik, R. M. and Fang, P. P., 1994, Second Law Analysis of Heat Transfer Enhancement in Offset Strip Fin Compact Heat Exchangers, Proceedings of the 10th International Heat Transfer Conference (IHTC10), Vol. 6, pp. 67-72, Brighton, England.
- McClintock, F. A., 1951, The Design of Heat Exchangers for Minimum Irreversibility, ASME Paper No. 51-A-108, presented at the 1951 Annual Meeting of the ASME (1951).
- Mironova, V. A., Tsirlin, A. M., Kazakov, V. A., and Berry, R. S., 1994, Finite-Time Thermodynamics: Exergy and Optimization of Time-Constrained Processes, Journal of Applied Physics, 76 (2), pp. 629-636.
- Mohamed, H. A., 2006, Entropy Generation in Counter Flow Gas to Gas Heat Exchangers, ASME Journal of Heat Transfer, 128 (1), pp. 87-92.
- Muley, A. and Maglik, R. M., 1999, Performance Optimization of Plate Heat Exchangers with Chevron Plates, Proceedings of the 33rd National Heat Transfer Conference, August 15-17, 1999, Albuquerque, NM.

- Nafey, A. S., 2000, Maximum Entropy Generation of In-Series Connected Heat Exchangers, *International Journal of Energy Research* 24 (7), pp. 561-570.
- Naphon, P., 2006, Second Law Analysis on the Heat Transfer of the Horizontal Concentric Tube Heat Exchanger, *International Communications in Heat and Mass Transfer*, 33 (8), pp. 1029-1041.
- Natalini G., and Sciubba E., 1999, Minimization of the Local Rates of Entropy Production in the Design of Air-Cooled Gas Turbine Blades, *ASME Journal of Engineering Gas Turbine Power*, 121 (3), pp. 466-475.
- Nwachukwu, N. P., and Onyegegbu, S. O., 2009, Effect of Absorptive Coating of the Hot Fluid Passage of a Heat Exchanger Employing Exergy-Optimized Pin Fins in High Temperature Applications, *ASME Journal of Heat Transfer*, 131 (5), Article (054503).
- Ogulata, R. T., and Doba, F., 1998, Experiments and Entropy Generation Minimization Analysis of a Cross-Flow Heat Exchanger, *International Journal of Heat and Mass Transfer*, 41 (2), pp. 373-381.
- Ogulata, R. T., Doba, F., and Yilmaz, T., 1999, Second-Law and Experimental Analysis of a Cross-Flow Heat Exchanger, *Heat Transfer Engineering*, 20 (2), pp. 20-27.
- Ordóñez, J.C., and Bejan, A., 2000, Entropy Generation Minimization in Parallel-Plates Counterflow Heat Exchangers, *International Journal of Energy Research*, 24 (10), pp. 843-864.
- Paoletti, S., Rispoli, F., and Sciubba, E., 1989, Calculation of Exergetic Losses in Compact Heat Exchanger Passages, in Bajura R., Shapiro H. N., and Zaworski J. R. (Eds.), *ASME AES*, 10-2, pp. 21-29.
- Perez-Blanco H., 1984, Irreversibility in Heat Transfer Enhancement, in: Bejan A., and Reid R. L. (Eds.), *Second Law Aspects of Thermal Design*, Proceedings of 22nd National Heat Transfer, ASME, HTD, 33, pp. 19-26.
- Petrescu, S., 1994, Comments on the Optimal Spacing of Parallel Plates Cooled by Forced Convection, *International Journal of Heat and Mass Transfer*, 37 (8), pp. 1283.
- Pitchandi, K., and Natarajan, E., 2008, Entropy Generation in Periodic Regenerative Heat Exchanger Due to Finite Temperature Difference, *International Journal of Thermodynamics*, 11 (4), pp. 173-179.
- Poulidakos, D. and Bejan, A., 1982, Fin Geometry for Minimum Entropy Generation in Forced Flow, *ASME Journal of Heat Transfer*, 104 (4), pp. 616-623.
- Poulidakos, D., and Johnson, J. M., 1989, Second Law Analysis of Combined Heat and Mass Transfer Phenomena in External Flow, *Energy*, 14 (2), pp. 67-73.
- Rao, R. V., and Patel, V. K., 2010, Thermodynamic Optimization of Cross Flow Plate-Fin Heat Exchanger Using a Particle Swarm Optimization Algorithm, *International Journal of Thermal Sciences*, 49 (9), pp. 1712-1721.
- Rispoli F., and Sciubba E., 1990, Numerical Calculation of Local Irreversibilities in Compact Heat Exchangers, Workshop on Second Law of Thermodynamics, Erciyes U-TIBTD 27-30 August 1990, 8.1-8.12 Kayseri, Turkey.
- Ruan, D. -F., Yuan, X. -F., Li, Y. -R., and Wu, S. -Y., 2011, Entropy Generation Analysis of Parallel and Counter-Flow Three-Fluid Heat Exchangers with Three Thermal

- Communications, *Journal of Non-Equilibrium Thermodynamics*, 36 (2), pp. 141-154.
- Sahiti, N., Krasniqi, F., Fejzullahu, Xh., Bunjaku, J., and Muriqi, A., 2008, Entropy Generation Minimization of a Double-Pipe Pin Fin Heat Exchanger, *Applied Thermal Engineering*, 28 (17-18), pp. 2337-2344.
- San, J. -Y., 2010, Second-Law Performance of Heat Exchangers for Waste Heat Recovery, *Energy*, 35 (5), pp. 1936-1945.
- Şara, O. N., Yapici, S., Yilmaz, M., and Pekdermr, T., 2001, Second Law Analysis of Rectangular Channels with Square Pin-Fins, *International Communications in Heat and Mass Transfer*, 28 (5), pp. 617-630.
- Sarangi, S., and Chowdhury, K., 1982, On the Generation of Entropy in a Counterflow Heat Exchanger, *Cryogenics* 22 (2), pp. 63-65.
- Sciubba, E., 1996, A Minimum Entropy Generation Procedure for the Discrete Pseudo-Optimization of Finned-Tube Heat Exchangers, *Revue Generale de Thermique*, 35 (416), pp. 517-525.
- Sekulic, D. P., 1985-1986, Unequally Sized Passes in Two-Pass Crossflow Heat Exchangers: A Note on the Thermodynamic Approach to the Analysis, *Publications of the Faculty of Technical Sciences, University of Novi Sad, Yugoslavia*, 16.
- Sekulic, D. P., 1986, Entropy Generation in a Heat Exchanger, *Heat Transfer Engineering*, 7 (1-2), pp. 83-88.
- Sekulic, D. P., 1990, The Second Law Quality of Energy Transformation in a Heat Exchanger, *ASME Journal of Heat Transfer*, 112 (2), pp. 295-300.
- Sekulic D. P., and Baclic B. S., 1984, Enthalpy Exchange Irreversibility, *Publications of the Faculty of Technical Sciences, University of Novi Sad, Yugoslavia*.
- Sekulic, D. P., and Herman, C. V., 1986, One Approach to Irreversibility Minimization in Compact Crossflow Heat Exchanger Design, *International Communications in Heat and Mass Transfer*, 13 (1), pp. 23-32.
- Sekulic, D. P., and Milosevic, Z. S., 1988, Entropy Generation in Heat Exchanger Networks: The Component Balance Approach, *American Society of Mechanical Engineers, Advanced Energy Systems Division (Publication) AES* 6, pp. 49-55.
- Shah, R. K., and Skiepko, T. 2004, Entropy Generation Extrema and Their Relationship with Heat Exchanger Effectiveness - Number of Transfer Unit Behavior for Complex Flow Arrangements, *ASME Journal of Heat Transfer*, 126 (6), pp. 994-1002.
- Shapiro, A. H., 1953, *The Dynamics and Thermodynamics of Compressible Fluid Flow*, New York, Ronald.
- Shiba , T., and Bejan, A., 2001, Thermodynamic Optimization of Geometric Structure in the Counterflow Heat Exchanger for an Environmental Control System, *Energy*, 26 (5) pp. 493-511.
- Shuja, S. Z., and Zubair, S. M., 2011, Thermo-economic Considerations in the Design and Analysis of a Finned Heat Sink Array: The Effect of Material Cost, *International Journal of Exergy*, 9 (3), pp. 370-387.
- Sieniutycz, S., and Shiner, J. S., 1994, *Thermodynamics of Irreversible Processes and Its Relation to Chemical Engineering: Second Law Analyses and Finite Time*

- Thermodynamics, *Journal of Non-Equilibrium Thermodynamics*, 19 (4), pp. 303-348.
- Steinke, M., E., and Kandlikar, S., G., 2006, Single Phase Liquid Friction Factors in Microchannels, *International Journal of Thermal Sciences*, 45 (11), pp. 1073-1083.
- Strub, F., Castaing-Lasvignottes, J., Bédécarrats, J. P., Peuvrel, C., 2004, Application of the Second Law Analysis to a Heat Exchanger Working with Ethanol/Water Ice Slurry, *International Journal of Thermodynamics*, 7 (4), pp. 183-188.
- Su, Y., Deng, W., Jiang, F., and Shen, H., 2011, Second Law Optimization of Pin Fin Heat Exchangers with Lateral Ejection Holes, *Proceedings of International Conference on Computer Distributed Control and Intelligent Environmental Monitoring (CDCIEM2011)*, Article (5748046), pp. 1275-1278, Changsha, 19-20 February 2011.
- Su, Y., Luo, Z., and Cen, K., 1999, A Study on the Fins of Heat Exchangers from Optimization of Entropy Generation, *Huagong Xuebao/Journal of Chemical Industry and Engineering (China)*, 50 (1), pp. 118-124.
- Tagliafico, L. and Tanda, G., 1996, A Thermodynamic Method for the Comparison of Plate Fin Heat Exchanger Performance, *ASME Journal of Heat Transfer*, 118 (3), pp. 805-809.
- Tsujikawa, Y., Sawada, T., Morimoto, T., and Murata, K., 1986, Thermodynamic Optimization Method of Regenerator of Gas Turbine with Entropy Generation, *Journal of Heat Recovery Systems*, 6 (3), pp. 245-253.
- Vargas, J., and Bejan, A., 2001, Thermodynamic Optimization of Finned Crossflow Heat Exchangers for Aircraft Environmental Control Systems, *International Journal of Heat and Fluid Flow*, 22 (6), pp. 657-665.
- Vargas, J., Bejan, A., and Siems, D. L., 2001, Integrative Thermodynamic Optimization of the Crossflow Heat Exchanger for an Aircraft Environmental Control System, *ASME Journal of Heat Transfer*, 123 (4), pp. 760-770.
- Wang, Q. -W., Chen, G. -D., Xu, J., and Ji, Y. -P., 2010, Second-Law Thermodynamic Comparison and Maximal Velocity Ratio Design of Shell-and-Tube Heat Exchangers With Continuous Helical Baffles, *ASME Journal of Heat Transfer*, 132, 10, Article No. (101801).
- Wilson, E. E., 1915, A Basis for Rational Design of Heat Transfer Apparatus, *Trans. ASME*, 37, pp. 47.
- Witte, L. C., 1988, The Influence of Availability Costs on Optimal Heat Exchanger Design, *ASME Journal of Heat Transfer*, 110 (4A), pp. 830-835.
- Witte, L. C., and Shamsundar, N. A., 1983, A Thermodynamic Efficiency Concept for Heat Exchanger Devices, *ASME Journal of Engineering for Power*, 105 (1), pp. 199-203.
- Xiong, D., Li, Z., and Guo, Z., 1996, On Effectiveness and Entropy Generation in Heat Exchanger, *Journal of Thermal Science*, 5 (4), pp. 248-256.
- Xu, Z. M., Yang, S. R., and Chen, Z. Q., 1996, A Modified Entropy Generation Number for Heat Exchangers, *Journal of Thermal Science*, 5 (4), pp. 257-263.
- Yilmaz, M., Sara, O. N., and Karsli, S., 2001, Performance Evaluation Criteria for Heat Exchangers Based on Second Law Analysis, *Exergy-An International Journal*, 1 (4), pp.278-294.

- Yuan, P., and Kou, H.-S., 2001, Entropy Generation on a Three-Gas Crossflow Heat Exchanger with Longitudinal Wall Conduction, *International Communications in Heat and Mass Transfer* 28 (6), pp. 803-813.
- Yuan, P., and Kou, H.-S., 2003, Entropy Generation on a Crossflow Heat Exchanger Including Three Gas Streams with Different Arrangements and the Effect of Longitudinal Wall Conduction, *Numerical Heat Transfer; Part A: Applications*, 43 (6), pp. 619-638.
- Zhang, L., Yang, C., and Zhou, J., 2010, A Distributed Parameter Model and Its Application in Optimizing the Plate-Fin Heat Exchanger Based on the Minimum Entropy Generation, *International Journal of Thermal Sciences*, 49 (8), pp. 1427-1436.
- Zhou, J.-h., Yang, C.-x., and Zhang, L.-n., 2009, Minimizing the Entropy Generation Rate of the Plate-Finned Heat Sinks Using Computational Fluid Dynamics and Combined Optimization, *Applied Thermal Engineering*, 29 (8-9), pp. 1872-1879.
- Zubair, S. M., Kadaba, P. V., and Evans, R. B., 1987, Second-Law-Based Thermoeconomic Optimization of Two-Phase Heat Exchangers, *ASME Journal of Heat Transfer*, 109 (2), pp. 287-294. Also published as Zubair, S. M., Kadaba, P. V., and Evans, R. B., 1985, Design and Optimization of Two-Phase Heat Exchangers, *Two-Phase Heat Exchanger Symposium*, ed. Pearson, J. T. and Kitto, Jr., J. B., ASME, HTD, 44.

Analytical Solution of Dynamic Response of Heat Exchanger

D. Gvozdenac

*Faculty of Technical Sciences, Novi Sad
Serbia*

1. Introduction

Two-fluid heat exchangers are widely used in almost every energy process such as those in power plants, gas turbines, air-conditioning systems, numerous chemical plants and home appliances. Every change of steady state or starting of a plant causes changes in the system which can considerably affect not only the observed process but also the safety of the plant's operations. In all above cases, it is important to know the dynamic behavior of a heat exchanger in order to choose the most suitable design, controls and operations. The traditional design based on stationary approach has become inadequate and nowadays, more attention is devoted to the analysis of the heat exchanger's dynamic behavior and its design is adjusted to such conditions of work. Although the process control technology has made considerable headway, its practical application requires the knowledge of the dynamic behavior of both the plant's components and the plant as a whole.

Ever since Profos (Profos, 1943) showed the first dynamic model of a simple heat exchanger and Takahashi (Takahashi, 1951) published the first transfer functions for ordinary heat exchangers, there have been numerous studies of the heat exchanger's dynamic behavior. The historic overview of dynamic modeling is given in (Kays & London, 1984) and (Roetzel & Xuan, 1999) thus, the attention of this paper will be directed exclusively towards the review of some significant works in this area and works which this paper has been influenced by.

The paper (Liapis & McAvoy, 1981) defines the conditions for obtaining analytical solutions of transient phenomena in the class of problems associated with heat and mass transfers in counter flow fluid streams. Their solutions take into account forced flow and the dependence of transient coefficient on the fluid's flow and do not involve the effect of wall finite heat capacity. The exact solution of dynamic behavior of a parallel heat exchanger in which wall heat capacity is negligible in relation to the fluid capacity was shown in (Li, 1986). These solutions are valid for both finite and nonfinite flow velocities. The paper (Romie, 1985) shows responses of outlet fluid temperatures for the equation of a step fluid inlet temperature change in a counter flow heat exchanger. The responses are determined by means of a finite difference method and involve the wall effect. The exact analytical solution for transient phenomena of a parallel flow heat exchanger for unit step change of inlet temperature of one of the fluids is given in (Romie, 1986). Although this solution includes the wall effect, it is limited to heat exchangers with equal fluid velocities or heat exchangers

in which both fluids are gases. The paper (Gvozdenac, 1987) shows analytical solution for transient response of parallel and counter flow heat exchangers. However, these solutions are limited to the case in which heat capacities of both fluids are negligibly small in relation to the heat exchanger's separating wall capacity. Moreover, it is important to mention that papers (Romie, 1983), (Gvozdenac, 1986), (Spiga & Spiga, 1987) and (Spiga & Spiga, 1988) deal with two-dimensional problems of transition for cross flow heat exchangers with both fluids unmixed throughout. The last paper is the most general one and provides opportunities for calculating transient temperatures of wall temperatures and of both fluids by an analytical method for finite flow velocities and finite wall capacity. The paper (Gvozdenac, 1990) shows analytical solution of transient response of the parallel heat exchanger with finite heat capacity of the wall. The procedure presented in the above paper is also used for resolving dynamic response of the cross flow heat exchanger with the finite wall capacity (Gvozdenac, 1991).

A very important book is that of Roetzel W and Xuan Y (Roetzel & Xuan, 1999) which provides detailed analysis of all important aspects of the heat exchanger's dynamic behavior in general. It also gives detailed overview and analysis of literature.

This paper shows solutions for energy functions which describe convective heat transfer between the wall of a heat exchanger and fluid streams of constant velocities. The analysis refers to parallel, counter and cross flow heat exchangers. Initial fluids and wall temperatures are equal but at the starting moment, there is unit step change of inlet temperature of one of the fluids. The presented model is valid for finite fluid velocities and finite heat capacity of the wall. The mathematical model is comprised of three linear partial differential equations which are resolved by manifold Laplace transforms. To a certain extent, this paper presents a synthesis of the author's previous papers with some simplified and improved final solutions.

The availability of such analytical solutions enables engineers and designers a much better insight into the nature of heat transfers in parallel, counter and cross flow heat exchangers.

For the purpose of easier practical application of these solutions, the potential users are offered MS Excel program at the web address: www.peec.uns.ac.rs. This program is open and can be not only adjusted to special requirements but also modified.

2. Mathematical formulation

Regardless of seeming similarity of partial differential equations arising from mathematical modeling, this paper analyzes parallel, cross and counter flow heat exchangers separately. However, simplifying assumptions in the derivation of differential equations are the same and are as follows:

- a. Heat transfer characteristics and physical properties are independent of temperature, position and time;
- b. The fluid velocity is constant in each flow passage;
- c. Axial conduction is negligible in both fluids and the wall;
- d. Overall heat losses are negligible;
- e. The heat generation and viscous dissipation within the fluids are negligible;
- f. Fluids are assumed to be finite-velocity liquids or gases. This means that the fluid transit or dwell times are not small compared to the duration of transience.

By respecting above assumptions, the energy balance for parallel, counter and cross flow heat exchangers will be mathematically formulated.

2.1 Parallel flow

On the basis of simplified assumptions and by applying energy equations to both fluids and the wall, one can obtain three simultaneous partial differential equations in the coordinate system as shown in Fig. 1. It is obvious that both fluids flow in the same direction but on different sides of the heat exchanger's separating wall. Heat transfer areas and heat transfer coefficients from both sides are known. The length of the heat exchanger is L .

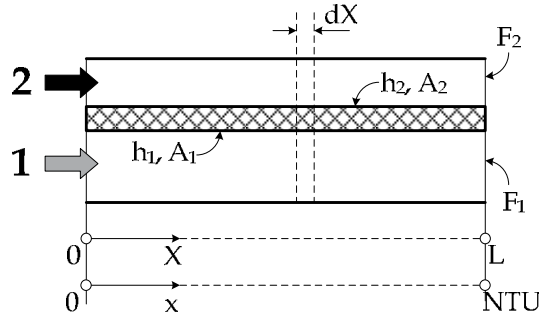


Fig. 1. Schematic Description of Parallel Flow Heat Exchanger.

Differential equations describing fluid-temperature fields in the heat exchanger core are statements of "micro" energy balances for an arbitrary differential control volume of that particular core. The following set of partial differential equations:

$$\begin{aligned}
 M_w \cdot c_w \cdot \frac{\partial T_w}{\partial t} &= (hA)_1 \cdot (T_1 - T_w) - (hA)_2 \cdot (T_w - T_1) \\
 \dot{m}_1 \cdot c_{p1} \cdot L \cdot \left(\frac{\partial T_1}{\partial X} + \frac{1}{U_1} \cdot \frac{\partial T_1}{\partial t} \right) &= (hA)_1 \cdot (T_w - T_1) \\
 \dot{m}_2 \cdot c_{p2} \cdot L \cdot \left(\frac{\partial T_2}{\partial X} + \frac{1}{U_2} \cdot \frac{\partial T_2}{\partial t} \right) &= (hA)_2 \cdot (T_w - T_2)
 \end{aligned} \tag{1}$$

represents the energy balance over the control volume shown in Fig. 1.

Due to simplified standard assumptions underlying the theory, the mathematical model is linear and tractable by available methods of calculus.

To define mathematical problem completely, inlet and initial conditions have to be prescribed:

$$\begin{aligned}
 T_1(0, t) &= \begin{cases} T_r & \text{for } t < 0 \\ T^* & \text{for } t \geq 0 \end{cases} \\
 T_2(0, t) &= T_r = \text{const.} \\
 T_1(X, 0) = T_w(X, 0) = T_2(X, 0) &= T_r = \text{const}
 \end{aligned} \tag{2}$$

These conditions assume that only fluid 1 inlet condition is perturbed. The step change of inlet temperature of fluid 1 is certainly the most important from physical point of view. Other inlet temperature changes can be analyzed using described mathematical model and procedures for their analytical solution.

In equations 1 and 2, the convention of index 1 referring to weaker fluid flow and index 2 to stronger fluid flow is introduced. Fluid undergoing higher temperature changes because of smaller value of the thermal capacity $W = \dot{m} \cdot c_p$ is called "weaker"? The other flow is then "stronger" and it is less changed in the heat exchanger. The product of mass flow rate and isobaric specific heat of fluid is the indicator of fluid's flow "strength" and represents its essential characteristic. Therefore, it is necessary to make strict distinction between weaker and stronger flow. Only the weaker fluid flow can change the state for maximum temperature difference. Therefore, $\dot{Q}_{\max} = (\dot{m} \cdot c_p)_{\min} \cdot |T_1' - T_2'|$. This is valid in steady state conditions although flow designation convention is also applicable to unsteady state analysis.

Generally, the heat exchanger's effectiveness is defined in the relation of actually exchanged heat and maximum possible one and it is the measure of thermodynamic quality of the device. In this way, the effectiveness of all heat exchangers can be a number taken from a closed interval $\varepsilon = [0, 1]$

Another convention is useful for further analysis. If weaker and stronger fluid flows are designated with indices 1 and 2, respectively, then standardized relation between heat capacities of fluids is:

$$\omega = \frac{W_1}{W_2} \quad (0 \leq \omega \leq 1) \quad (3)$$

The value $\omega \Rightarrow 0$ always designates that the stronger fluid flow tends to isothermal change in the heat exchanger since $(\dot{m} \cdot c_p)_2 \Rightarrow \infty$. With final \dot{Q} , implying $|T_2'' - T_2'| \Rightarrow 0$, this means that the flow 2 changes the phase (condensation or evaporation). On the contrary, $\omega = 1$ refers to well balanced flows, i.e. the temperatures from inlet to outlet change equally.

In order to define dimensionless temperatures, it is appropriate to choose reference temperature T_r and a characteristic temperature difference $T^* - T_r$ so that:

$$\theta_i(X, t) = \frac{T_i(X, t) - T_r}{T^* - T_r} \quad (i = 1, 2, w) \quad (4)$$

It is suitable that reference temperatures are minimum and maximum ones, i.e. T^* and T_r , respectively. If the weaker flow is designated with index 1 and if $T^* = T_1'$ and $T_r = T_2'$ then, the weaker flow enters the heat exchanger with $\theta_1' = 1$ and the stronger flow with $\theta_2' = 0$.

For the purpose of simplifying the mathematical model the dimensionless distance and dimensionless time are introduced:

$$x = \frac{X}{L} \cdot NTU, \quad z = \frac{t}{t^*} \quad (5)$$

The number of heat transfer units is:

$$NTU = \frac{(hA)_1 \cdot (hA)_2}{(hA)_1 + (hA)_2} \cdot \frac{1}{W_1} \quad (6)$$

and time parameter

$$t^* = \frac{c_w \cdot M_w}{(hA)_1 + (hA)_2} \quad (7)$$

Further, the relation for the product of heat transfer coefficient and heat transfer area of each fluid and the sum of these products is as follows:

$$K_1 = \frac{(hA)_1}{(hA)_1 + (hA)_2}, \quad K_2 = 1 - K_1 \quad (8)$$

Finally, complex dimensionless parameter is:

$$C_i = L \cdot \frac{W_i}{c_w \cdot M_w} \cdot \frac{1}{K_i \cdot U_i} \quad (i = 1, 2) \quad (9)$$

It is inversely proportional to the fluid speed in heat exchanger flow channels. The high fluid velocity with other unchanged values in the equation (9) means that $C_i \Rightarrow 0$ and that fluid dwell time in the heat exchanger is short. As the fluid velocity decreases, the value of parameters C_i increases and the time of fluid dwell time in the core of the heat exchanger is prolonged. Fluid velocity in heat exchangers is:

$$U_i = \frac{\dot{m}_i}{\rho_i \cdot F_i} \quad (\text{fluid velocity, } i = 1, 2) \quad (10)$$

Now, the system of equations (1) can be written in the following form :

$$\begin{aligned} \frac{\partial \theta_w}{\partial z} + \theta_w &= K_1 \cdot \theta_1 + K_2 \cdot \theta_2 \\ C_1 \cdot \frac{\partial \theta_1}{\partial z} + K_2 \cdot \frac{\partial \theta_1}{\partial x} &= \theta_w - \theta_1 \\ C_2 \cdot \frac{\partial \theta_2}{\partial z} + \frac{K_1}{\omega} \cdot \frac{\partial \theta_2}{\partial x} &= \theta_w - \theta_2 \end{aligned} \quad (11)$$

The initial and inlet conditions (Eqs. 2) become:

$$\begin{aligned} \theta_1(0, z) &= \begin{cases} 0 & \text{for } z < 0 \\ 1 & \text{for } z \geq 0 \end{cases} \\ \theta_2(0, z) &= 0 \\ \theta_1(x, 0) = \theta_w(x, 0) = \theta_2(x, 0) &= 0 \end{aligned} \quad (12)$$

The equation (11) and (12) define transient response of parallel flow heat exchanger with finite wall capacitance. Mathematical model is valid for the case when $W_1 \leq W_2$ and temperature of fluid 1 is perturbed (unit step change).

Outlet temperatures of both fluids in steady state ($z \rightarrow \infty$) are:

$$\begin{aligned}\theta_1''(NTU, \infty) &= 1 - \varepsilon \\ \theta_2''(NTU, \infty) &= \omega \cdot \varepsilon\end{aligned}\quad (13)$$

where ε is effectiveness of heat exchanger. Effectiveness of parallel heat exchanger is as follows:

$$\varepsilon = \frac{1 - \exp[-NTU(1 + \omega)]}{1 + \omega} \quad \text{for } 0 < \omega \leq 1 \quad (14)$$

For the case $\omega = 0$ the effectiveness is

$$\varepsilon = 1 - \exp(-NTU) \quad (15)$$

and is valid for all types of heat exchangers.

For the case when stronger fluid (fluid 2) is perturbed, the inlet condition of the mathematical problem is changed and is as follows:

$$\begin{aligned}\theta_1(0, z) &= 0 \\ \theta_2(0, z) &= \begin{cases} 0 & \text{for } z < 0 \\ 1 & \text{for } z \geq 0 \end{cases} \\ \theta_1(x, 0) = \theta_w(x, 0) = \theta_2(x, 0) &= 0\end{aligned}\quad (16)$$

In this case, outlet temperatures in the conditions of steady state are equal:

$$\begin{aligned}\theta_1''(NTU, \infty) &= \omega \cdot \varepsilon \\ \theta_2''(NTU, \infty) &= 1 - \varepsilon\end{aligned}\quad (17)$$

In this way, resolving of this mathematical problem for two inlet conditions includes all possible cases of fluid flow strength, i.e. $W_1 \leq W_2$ and $W_1 \geq W_2$. Only the case $W_1 \leq W_2$ is analyzed in this paper because of limited space. However, the presented procedure for resolving mathematical model for all types of heat exchangers gives opportunities to get easily to the solution in case when $W_1 \geq W_2$.

2.2 Counter flow

In the same way as in the case of parallel flow heat exchanger, it is possible to set up mathematical model of counter flow heat exchanger (Fig. 2). The essential difference between these two heat exchangers is in inlet conditions.

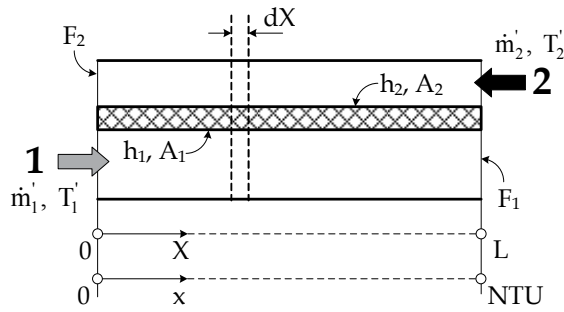


Fig. 2. Schematic Description of Counter Flow Heat Exchanger

Procedure similar to the above for parallel flow delivers the following mathematical formulation for the transient behavior of counter flow heat exchanger:

$$\begin{aligned} \frac{\partial \theta_w}{\partial z} + \theta_w &= K_1 \cdot \theta_1 + K_2 \cdot \theta_2 \\ C_1 \cdot \frac{\partial \theta_1}{\partial z} + K_2 \cdot \frac{\partial \theta_1}{\partial x} &= \theta_w - \theta_1 \\ C_2 \cdot \frac{\partial \theta_2}{\partial z} - \frac{K_1}{\omega} \cdot \frac{\partial \theta_2}{\partial x} &= \theta_w - \theta_2 \end{aligned} \quad (18)$$

The initial and inlet conditions are:

$$\begin{aligned} \theta_1(0, z) &= \begin{cases} 0 & \text{for } z < 0 \\ 1 & \text{for } z \geq 0 \end{cases} \\ \theta_2(NTU, z) &= 0 \\ \theta_1(x, 0) = \theta_w(x, 0) = \theta_2(x, 0) &= 0 \end{aligned} \quad (19)$$

If the system of equations (11) and (18) is compared, it can be observed that the difference is only in the sign before the second member on the right side of the third equation. If we compare equations (12) and (19) (inlet and initial conditions), the difference is only in the second equation. However, these seemingly small differences make substantial differences in the solution of the problem which will be shown later on.

Outlet temperatures of both fluids in steady state ($z \rightarrow \infty$) are as in the case of parallel flow heat exchanger but the effectiveness is in case of counter flow heat exchanger designed as follows:

$$\varepsilon = \frac{1 - \exp[-NTU(1 - \omega)]}{1 - \omega \cdot \exp[-NTU(1 - \omega)]} \quad \text{for } 0 \leq \omega < 1 \quad (20)$$

and

$$\varepsilon = \frac{NTU}{1 + NTU} \quad \text{for } \omega = 1 \quad (21)$$

When stronger fluid (fluid 2) is perturbed, the inlet condition of the mathematical problem is changed and is as follows:

$$\begin{aligned} \theta_1(0, z) &= 0 \\ \theta_2(NTU, z) &= \begin{cases} 0 & \text{for } z < 0 \\ 1 & \text{for } z \geq 0 \end{cases} \\ \theta_1(x, 0) = \theta_w(x, 0) = \theta_2(x, 0) &= 0 \end{aligned} \quad (22)$$

The problem formulated in this way is valid for $W_1 \leq W_2$. For the case $W_1 \geq W_2$, the problem is very similar and because of that it will not be elaborated in details.

2.3 Cross flow (both fluids unmixed)

The drawing of cross flow heat exchanger which is used for mathematical analysis is shown in Fig. 3. It contains the necessary system of designation and coordinates which will be used in this paper. The fluid 1 flows in the X direction and the fluid 2 in the Y direction. The fluid flows are not mixed perpendicularly to their flow.

Based on these assumptions and by applying energy equations to both fluids, three simultaneous partial differential equations can be obtained in the coordinate system as shown in Fig. 3.

$$\begin{aligned} M_w c_w \frac{\partial T_w}{\partial t} &= (h \cdot A)_1 (T_1 - T_w) - (h \cdot A)_2 (T_w - T_2) \\ m_1 c_{p1} X_o \left(\frac{\partial T_1}{\partial X} + \frac{1}{U_1} \frac{\partial T_1}{\partial t} \right) &= (h \cdot A)_1 (T_w - T_1) \\ m_2 c_{p2} Y_o \left(\frac{\partial T_2}{\partial Y} + \frac{1}{U_2} \frac{\partial T_2}{\partial t} \right) &= (h \cdot A)_2 (T_w - T_2) \end{aligned} \quad (23)$$

Independent variables in space and time (X, Y and t) vary from 0 to the length of heat exchangers X_o and Y_o , i.e from 0 to ∞ . By comparing the system of equations (1), it can be noticed that there is the presence of the space coordinate (Y) and the existence of two dimensions of heat exchangers (X_o and Y_o).

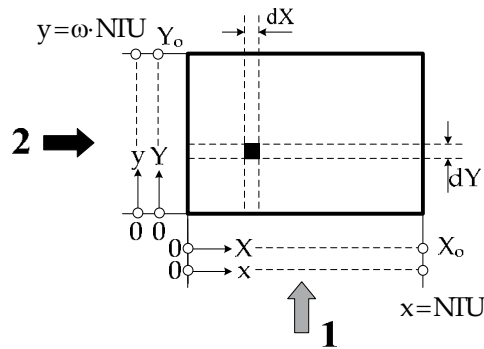


Fig. 3. Schematic Description of Cross Flow Heat Exchanger.

Initial and inlet conditions of analyzed problem are as follows:

$$T_1(0, Y, t) = \begin{cases} T & \text{for } t < 0 \\ T^* & \text{for } t > 0 \end{cases}$$

$$T_2(X, 0, t) = T = \text{const}$$

$$T_1(X, Y, 0) = T_w(X, Y, 0) = T_2(X, Y, 0) = T = \text{const} \quad (24)$$

By introducing new dimensionless variable:

$$x = \frac{X}{X_o} \cdot NTU, \quad x = \frac{Y}{Y_o} \cdot NTU, \quad z = \frac{t}{t^*} \quad (25)$$

the set of equations (23) is as follows:

$$\begin{aligned} \frac{\partial \theta_w}{\partial z} + \theta_w &= K_1 \cdot \theta_1 + K_2 \cdot \theta_2 \\ C_1 \cdot \frac{\partial \theta_1}{\partial z} + K_2 \cdot \frac{\partial \theta_1}{\partial x} &= \theta_w - \theta_1 \\ C_2 \cdot \frac{\partial \theta_2}{\partial z} + K_1 \cdot \frac{\partial \theta_2}{\partial y} &= \theta_w - \theta_2 \end{aligned} \quad (26)$$

and initial and inlet conditions (Eq. 24) as:

$$\theta_1(0, y, z) = \begin{cases} 0 & \text{for } z < 0 \\ 1 & \text{for } z > 0 \end{cases}$$

$$\theta_2(x, 0, z) = 0$$

$$\theta_1(x, y, 0) = \theta_w(x, y, 0) = \theta_2(x, y, 0) = 0 \quad (27)$$

Outlet temperatures of both fluids in steady state ($z \rightarrow \infty$) are defined by Eq. (13) but the effectiveness in the case of cross flow heat exchanger is defined as follows (Bačlić, 1978):

$$\begin{aligned} \varepsilon &= 1 - \exp[-(1 + \omega)NTU] \cdot \\ &\left[I_0(2 \cdot NTU \cdot \sqrt{\omega}) + \sqrt{\omega} \cdot I_1(2 \cdot NTU \cdot \sqrt{\omega}) - \frac{1 - \omega}{\omega} \sum_{n=2}^{\infty} \omega^{n/2} \cdot I_n(2 \cdot NTU \cdot \sqrt{\omega}) \right] \end{aligned} \quad (28)$$

and

$$\varepsilon = 1 - \exp[-2 \cdot NTU] \cdot [I_0(2 \cdot NTU) + I_1(2 \cdot NTU)] \quad \text{for } \omega = 1 \quad (29)$$

In Eqs. (28 and 29), the $I_n(\cdot)$ is modified Bessel function.

For the case when stronger fluid (fluid 2) is perturbed, the inlet condition of the mathematical problem is changed and it is as follows:

$$\begin{aligned}\theta_1(x,0,z) &= 0 \\ \theta_2(0,y,z) &= \begin{cases} 0 & \text{for } z < 0 \\ 1 & \text{for } z > 0 \end{cases} \\ \theta_1(x,y,0) = \theta_w(x,y,0) = \theta_2(x,y,0) &= 0\end{aligned}\quad (30)$$

As opposed to parallel and counter flow heat exchangers where outlet fluid temperatures are constant over the whole length of outlet edges, it is not the case for cross flow heat exchangers. Then, outlet temperature from the heat exchanger is obtained as mean temperature at the outlet edge of the heat exchanger.

Special cases of cross flow heat exchangers when one or both fluid flows are mixed throughout will not be elaborated in this paper.

In the Section that follows, defined mathematical problems for determining temperature fields and outlet temperatures will be resolved for three basic types: parallel, counter and cross flow heat exchangers.

3. General solution

The set of three partial differential equations for all types of heat exchanger are linear (Eqs. 11, 18 and 26). These systems can be solved by using multifold Laplace transform. In the case of parallel and counter flow heat exchangers, it is double-fold and in the case of cross flow it is three-fold Laplace transform.

3.1 Parallel flow

By applying this transform over the equations (11) and initial and inlet condition (Eq.16), the following algebraic equations are obtained:

$$\begin{aligned}\tilde{\theta}_w &= \frac{K_1 \cdot \tilde{\theta}_1 + K_2 \cdot \tilde{\theta}_2}{p+1} \\ \left(s + \frac{C_1 \cdot p + 1}{K_2}\right) \cdot \tilde{\theta}_1 &= \frac{1}{K_2} \cdot \tilde{\theta}_w + \frac{1}{p} \\ \left(s + \frac{\omega \cdot (C_2 \cdot p + 1)}{K_1}\right) \cdot \tilde{\theta}_2 &= \frac{\omega}{K_1} \cdot \tilde{\theta}_w\end{aligned}\quad (31)$$

From this set of equations, the outlet and wall temperatures are as follows:

$$\tilde{\theta}_w = \frac{\frac{K_1 \cdot K_2}{K_2 \cdot s + C_1 \cdot p + 1}}{p+1 - \frac{K_1}{K_2 \cdot s + C_1 \cdot p + 1} - \frac{K_2}{\frac{K_1}{\omega} \cdot s + C_1 \cdot p + 1}} \cdot \frac{1}{p}\quad (32)$$

$$\tilde{\theta}_1 = \frac{\tilde{\theta}_w}{K_2 \cdot s + C_1 \cdot p + 1} + \frac{K_2}{K_2 \cdot s + C_1 \cdot p + 1} \cdot \frac{1}{p} \quad (33)$$

$$\tilde{\theta}_2 = \frac{\tilde{\theta}_w}{\frac{K_1}{\omega} \cdot s + C_1 \cdot p + 1} \quad (34)$$

After performing some mathematical transformations and by using some well known relations:

$$\frac{1}{1+x} = \sum_{n=0}^{\infty} (-1)^n \cdot \frac{1}{x^{n+1}} ; \quad (a+b)^n = \sum_{m=0}^n \binom{n}{m} \cdot a^m \cdot b^{n-m} \quad (35)$$

the temperatures can be expressed in the following form which is convenient for developing the inverse Laplace transform:

$$\begin{aligned} \tilde{\theta}_w = & K_1 \cdot \sum_{n=0}^{\infty} \left(\frac{K_1}{K_2} \right)^{n+1} \cdot \frac{1}{p \cdot (p+1)^{n+1}} \cdot \frac{1}{\left(s + \frac{C_1}{K_2} \cdot p + \frac{1}{K_2} \right)^{n+1}} + \\ & K_1 \cdot \sum_{n=1}^{\infty} \sum_{m=0}^{n-1} \binom{n}{m} \cdot \left(\frac{K_1}{K_2} \right)^{m+1} \cdot \left(\frac{\omega \cdot K_2}{K_1} \right)^{n-m} \cdot \\ & \frac{1}{p \cdot (p+1)^{n+1}} \cdot \frac{1}{\left(s + \frac{C_1}{K_2} \cdot p + \frac{1}{K_2} \right)^{m+1}} \cdot \frac{1}{\left(s + \frac{\omega \cdot C_2}{K_1} \cdot p + \frac{\omega}{K_1} \right)^{n-m}} \end{aligned} \quad (36)$$

$$\begin{aligned} \tilde{\theta}_1 = & \frac{1}{p} \cdot \frac{1}{s + \frac{C_1}{K_1} \cdot p + \frac{1}{K_1}} + \sum_{n=0}^{\infty} \left(\frac{K_1}{K_2} \right)^{n+1} \cdot \frac{1}{p \cdot (p+1)^{n+1}} \cdot \frac{1}{\left(s + \frac{C_1}{K_2} \cdot p + \frac{1}{K_2} \right)^{n+2}} + \\ & \sum_{n=1}^{\infty} \sum_{m=0}^{n-1} \binom{n}{m} \cdot \left(\frac{K_1}{K_2} \right)^{m+1} \cdot \left(\frac{\omega \cdot K_2}{K_1} \right)^{n-m} \cdot \\ & \frac{1}{p \cdot (p+1)^{n+1}} \cdot \frac{1}{\left(s + \frac{C_1}{K_2} \cdot p + \frac{1}{K_2} \right)^{m+2}} \cdot \frac{1}{\left(s + \frac{\omega \cdot C_2}{K_1} \cdot p + \frac{\omega}{K_1} \right)^{n-m}} \end{aligned} \quad (37)$$

$$\begin{aligned} \tilde{\theta}_2 = & \sum_{n=0}^{\infty} \sum_{m=0}^n \binom{n}{m} \cdot \left(\frac{K_1}{K_2} \right)^{m+1} \cdot \left(\frac{\omega \cdot K_2}{K_1} \right)^{n-m+1} \cdot \\ & \frac{1}{p \cdot (p+1)^{n+1}} \cdot \frac{1}{\left(s + \frac{C_1}{K_2} \cdot p + \frac{1}{K_2} \right)^{m+1}} \cdot \frac{1}{\left(s + \frac{\omega \cdot C_2}{K_1} \cdot p + \frac{\omega}{K_1} \right)^{n-m+1}} \end{aligned} \quad (38)$$

From the techniques of Laplace transformation (convolution and translation theorems) and using the Laplace transforms of special functions $F_n(x, c)$ and $I_{n,m}(x, c, d)$, defined in the Appendix, one can obtain the inverse Laplace transformation of Eqs. 36-38, and the transient temperature distributions for the parallel flow heat exchanger:

$$\begin{aligned} \theta_w(x, z) = & K_2 \cdot \sum_{n=0}^{\infty} \left(\frac{K_1}{K_2} \right)^{n+1} \cdot F_{n+1} \left(x, \frac{1}{K_2} \right) \cdot I_{1,n+1} \left(z - \frac{C_1}{K_2} \cdot x, 0, -1 \right) + \\ & + K_2 \cdot \sum_{n=1}^{\infty} \sum_{m=0}^{n-1} \binom{n}{m} \cdot \left(\frac{K_1}{K_2} \right)^{m+1} \cdot \left(\frac{\omega \cdot K_2}{K_1} \right)^{n-m} \cdot \\ & \cdot \int_0^x F_{m+1} \left(x-u, \frac{1}{K_2} \right) \cdot F_{n-m} \left(u, \frac{\omega}{K_1} \right) \cdot I_{1,n+1} \left[z - \left(\frac{C_1}{K_2} (x-u) + \frac{\omega \cdot C_2}{K_1} \cdot u \right), 0, -1 \right] \cdot du \end{aligned} \quad (39)$$

$$\begin{aligned} \theta_1(x, z) = & \kappa \cdot \left(z - \frac{C_1}{K_2} \cdot x \right) \cdot F_1 \left(x, \frac{1}{K_2} \right) + \\ & + \sum_{n=0}^{\infty} \left(\frac{K_1}{K_2} \right)^{n+1} \cdot F_{n+2} \left(x, \frac{1}{K_2} \right) \cdot I_{1,n+1} \left(z - \frac{C_1}{K_2} \cdot x, 0, -1 \right) + \\ & + \sum_{n=1}^{\infty} \sum_{m=0}^{n-1} \binom{n}{m} \cdot \left(\frac{K_1}{K_2} \right)^{m+1} \cdot \left(\frac{\omega \cdot K_2}{K_1} \right)^{n-m} \cdot \\ & \cdot \int_0^x F_{m+2} \left(x-u, \frac{1}{K_2} \right) \cdot F_{n-m} \left(u, \frac{\omega}{K_1} \right) \cdot I_{1,n+1} \left[z - \left(\frac{C_1}{K_2} (x-u) + \frac{\omega \cdot C_2}{K_1} \cdot u \right), 0, -1 \right] \cdot du \end{aligned} \quad (40)$$

$$\begin{aligned} \theta_2(x, z) = & \sum_{n=0}^{\infty} \sum_{m=0}^n \binom{n}{m} \cdot \left(\frac{K_1}{K_2} \right)^{m+1} \cdot \left(\frac{\omega \cdot K_2}{K_1} \right)^{n-m+1} \cdot \\ & \cdot \int_0^x F_{m+1} \left(x-u, \frac{1}{K_2} \right) \cdot F_{n-m+1} \left(u, \frac{\omega}{K_1} \right) \cdot I_{1,n+1} \left[z - \left(\frac{C_1}{K_2} (x-u) + \frac{\omega \cdot C_2}{K_1} \cdot u \right), 0, -1 \right] \cdot du \end{aligned} \quad (41)$$

Outlet temperatures of both fluids are obtained for $x = \text{NTU}$.

In the practical use of solutions, the computation of integrals in this paper is done through collocation at nine Chebishev's points: 0.0000000000; ± 0.1679061842 ; ± 0.5287617831 ; ± 0.6010186554 ; ± 0.9115893077 , for the given integration interval.

Special case $\omega = 0$

In this case, $\theta_2(x, z) = 0$ resulting in reduced Eq. (31):

$$\tilde{\theta}_w = \frac{K_1}{p} \cdot \frac{1}{(p+1) \cdot \left(s + \frac{C_1}{K_2} \cdot p + \frac{1}{K_2} \right) - \frac{K_1}{K_2}} \quad (42)$$

After some mathematical manipulations, using already mentioned techniques, this equation can be transformed into:

$$\tilde{\theta}_w = K_2 \cdot \sum_{n=0}^{\infty} \left(\frac{K_1}{K_2} \right)^{n+1} \cdot \frac{1}{p \cdot (p+1)^{n+1} \cdot \left(s + \frac{C_1}{K_2} \cdot p + \frac{1}{K_2} \right)^{n+1}} \quad (43)$$

The inverse two-fold Laplace transform of Eq. 43 gives:

$$\theta_w(x, z) = K_2 \cdot \sum_{n=0}^{\infty} \left(\frac{K_1}{K_2} \right)^{n+1} \cdot F_{n+1} \left(x, \frac{1}{K_2} \right) \cdot I_{n+1,1} \left(z - \frac{C_1 \cdot x}{K_2}, 1, 1 \right) \quad (44)$$

and Eq. 32 gives:

$$\theta_1(x, z) = \kappa \left(z - \frac{C_1 \cdot x}{K_2} \right) \cdot F_1 \left(x, \frac{1}{K_2} \right) + \sum_{n=0}^{\infty} \left(\frac{K_1}{K_2} \right)^{n+1} \cdot F_{n+2} \left(x, \frac{1}{K_2} \right) \cdot I_{n+1,1} \left(z - \frac{C_1 \cdot x}{K_2}, 1, 1 \right) \quad (45)$$

This solution is valid for all types of heat exchangers with $\omega = 0$.

3.2 Counter flow

A very similar procedure can be applied for resolving the mathematical model of counter flow heat exchanger. The set of algebraic equations obtained after two-fold Laplace transform of Eqs. (18) and initial and inlet conditions (Eq (19)) is as follows:

$$(p+1) \cdot \tilde{\theta}_w = K_1 \cdot \tilde{\theta}_1 + K_2 \cdot \tilde{\theta}_2 \quad (46)$$

$$\left(s + \frac{C_1}{K_2} \cdot p + \frac{1}{K_2} \right) \cdot \tilde{\theta}_1 = \frac{1}{K_2} \cdot \tilde{\theta}_w + \frac{1}{p} \quad (47)$$

$$-\left(s - \frac{\omega \cdot C_2}{K_1} \cdot p - \frac{1}{K_1} \right) \cdot \tilde{\theta}_2 = \frac{\omega}{K_1} \cdot \tilde{\theta}_w - \tilde{\theta}_2(0, p) \quad (48)$$

The procedure will be explained in more details here since this case is much more complex than the previous one. By introducing designations:

$$\alpha(s, p) = K_2 \cdot s + C_1 \cdot p + 1 = K_2 \cdot \left(s + \frac{C_1}{K_2} \cdot p + \frac{1}{K_2} \right), \quad (49)$$

$$\beta(s, p) = -\frac{K_1}{\omega} \cdot s + C_2 \cdot p + 1 = -\frac{K_1}{\omega} \cdot \left(s - \frac{\omega \cdot C_2}{K_1} \cdot p - \frac{\omega}{K_1} \right), \quad (50)$$

$$A(s, p) = p + 1 - \frac{K_1}{\alpha(s, p)} - \frac{K_2}{\beta(s, p)}, \quad (51)$$

the both fluids and wall temperatures of the counter flow heat exchanger are as follows:

$$\tilde{\theta}_w = \frac{K_1 \cdot K_2}{p \cdot \alpha \cdot A} - \frac{K_1 \cdot K_2}{\omega \cdot \beta \cdot A} \cdot \tilde{\theta}_2(0, p) \quad (52)$$

$$\tilde{\theta}_1 = \frac{K_2}{p \cdot \alpha} + \frac{K_1 \cdot K_2}{p \cdot \alpha^2 \cdot A} - \frac{K_1 \cdot K_2}{\omega \cdot \alpha \cdot \beta \cdot A} \cdot \tilde{\theta}_2(0, p) \quad (53)$$

$$\tilde{\theta}_2 = \frac{K_1 \cdot K_2}{p \cdot \alpha \cdot \beta \cdot A} - \frac{K_1}{\omega \cdot \beta} \cdot \left(1 + \frac{K_2}{\beta \cdot A}\right) \cdot \tilde{\theta}_2(0, p) \quad (54)$$

It is very simple to prove that:

$$\frac{1}{A} = \sum_{n=0}^{\infty} \sum_{m=0}^n K_1^m \cdot K_2^{n-m} \cdot \binom{n}{m} \cdot \frac{1}{(p+1)^{n+1}} \cdot \frac{1}{\alpha^m \cdot \beta^{n-m}}, \quad (55)$$

and that inverse Laplace transformations of the functions $1/\alpha^{m+1}(s,p)$ and $1/\beta^{m+1}(s,p)$ ($m=1,2,3,\dots$) with respect to the complex parameter s are:

$$L_{s \rightarrow x}^{-1} \left\{ \frac{1}{\alpha^{m+1}} \right\} = \frac{1}{K_2^{m+1}} \cdot F_{m+1} \left(x, \frac{1}{K_2} \right) \cdot \exp \left(-\frac{C_1}{K_2} \cdot x \cdot p \right), \quad (56)$$

$$L_{s \rightarrow x}^{-1} \left\{ \frac{1}{\beta^{m+1}} \right\} = (-1)^{m+1} \cdot \left(\frac{\omega}{K_1} \right)^{m+1} \cdot F_{m+1} \left(x, -\frac{\omega}{K_1} \right) \cdot \exp \left(\frac{\omega \cdot C_2}{K_1} \cdot x \cdot p \right). \quad (57)$$

The essential problem in resolving dynamic behavior of the counter flow heat exchanger is in the use of other inlet conditions (Eq. 19).

If the Eq. 54 is collocated into $x=NTU$ then, INLET temperature of the fluid 2 is obtained which is according to given inlet conditions $\theta_2(NTU, z) = 0$, therefore:

$$L_{s \rightarrow NTU}^{-1} \left\{ \left(\frac{K_1}{\omega \cdot \beta} + \frac{K_1 \cdot K_2}{\omega \cdot \beta^2 \cdot A} \right) \cdot \tilde{\theta}_2(0, p) \right\} = L_{s \rightarrow NTU}^{-1} \left\{ \frac{K_1 \cdot K_2}{p \cdot \alpha \cdot \beta \cdot A} \right\} \quad (58)$$

This is Fredholm's integral equation of the second order. The problem is reduced to its solving.

The collocation method is used for solving this equation. Perhaps, it is the simplest one. The trial function is:

$$\theta_2(0, z) = \theta_2(0, \infty) \cdot \left[1 - \exp(-z) - \sum_{k=1}^{NCP} a_k \cdot \frac{z^k}{k!} \cdot \exp(-z) \right] \quad (59)$$

In equations (58) and further on, $\theta_2(0, \infty)$ is the steady-state fluid 2 outlet temperature for the counter flow heat exchanger. It can be calculated by using the second of Eq. 13 and effectiveness of counter flow heat exchanger (Eqs. 20 and 21). It follows that:

$$\tilde{\theta}_2(0, \infty) = \begin{cases} \frac{NTU}{1+NTU} & \text{for } \omega = 1 \\ \omega \cdot \frac{1 - \exp[-(1-\omega) \cdot NTU]}{1 - \omega \cdot \exp[-(1-\omega) \cdot NTU]} & \text{for } 0 \leq \omega < 1 \end{cases} \quad (60)$$

Laplace transform of trial function (Eq. 59) is:

$$\tilde{\theta}_2(0, p) = \theta_2(0, \infty) \cdot \left[\frac{1}{(p+1) \cdot p} - \sum_{k=1}^9 a_k \cdot \frac{1}{(p+1)^{k+1}} \right] \quad (61)$$

The trial function chosen in this way satisfies completely the equation (58) in points $z = 0$ and $z \rightarrow \infty$. Within the interval $0 < z < \infty$, it is necessary to determine collocation points and coefficients a_k ($k = 1, 2, 3, \dots, NCP$). Here, the NCP is the number of collocation points. The accuracy in which the outlet temperatures of fluid 2 versus time are determined depends directly on NCP. In this model of heat exchanger, there are many influential factors and determination of the number of collocation points for the given accuracy of outlet temperature is simplest through practical testing of the solution. For the heat exchanger's parameters appearing in practice, it can be said that NCP varying from 5 to 7 is sufficient for the accuracy of four significant figures and for $z \leq 15$.

Substituting the equation (61) in the equation (58) and collocating resulting equation in the NCP point, a set of linear algebraic equations is obtained and their solving generates unknown constants a_k . The set of algebraic solutions can also be written in the following form :

$$\sum_{k=1}^{NCP} a_k \cdot \Delta_k = \Delta_R \quad (62)$$

Substituting the equation (61) in (58) and using Eqs. (55), (56) and (57), it is obtained:

$$\begin{aligned} \Delta_k = \theta_2(0, \infty) \cdot \left\{ F_{k+1}(z(r), 1) - \sum_{n=0}^{\infty} (-1)^n \cdot \left(\frac{\omega \cdot K_2}{K_1} \right)^{n+1} \cdot F_{n+2}(NTU, 0) \cdot F_{n+k+2}(z(r), 1) - \right. \\ \left. - \sum_{n=1}^{\infty} \sum_{m=1}^n (-1)^{n-m} \cdot \left(\frac{K_1}{K_2} \right)^m \cdot \left(\frac{\omega \cdot K_2}{K_1} \right)^{n-m+1} \cdot \binom{n}{m} \cdot \int_0^{NTU} F_m \left(u, \frac{1}{K_2} \right) \cdot F_{n-m+2}(NTU - u, 0) \cdot \right. \\ \left. \cdot F_{n+k+2} \left[z(r) - \left(\frac{C_1}{K_2} + \frac{\omega \cdot C_2}{K_1} \right) \cdot u, 1 \right] \cdot \exp \left(-\frac{\omega}{K_1} \cdot u \right) \cdot du \right\} \quad (k, r = 1, 2, \dots, NCP) \end{aligned} \quad (63)$$

$$\begin{aligned} \Delta_R = \theta_2(0, \infty) \cdot \left\{ I_{1,1}(z(r), 1, 1) - \sum_{n=0}^{\infty} (-1)^n \cdot \left(\frac{\omega \cdot K_2}{K_1} \right)^{n+1} \cdot F_{n+2}(NTU, 0) \cdot I_{n+2,1}(z(r), 1, 1) - \right. \\ \left. - \sum_{n=1}^{\infty} \sum_{m=1}^n (-1)^{n-m} \cdot \left(\frac{K_1}{K_2} \right)^m \cdot \left(\frac{\omega \cdot K_2}{K_1} \right)^{n-m+1} \cdot \binom{n}{m} \cdot \int_0^{NTU} F_m \left(u, \frac{1}{K_2} \right) \cdot F_{n-m+2}(NTU - u, 0) \cdot \dots \right. \end{aligned}$$

$$\begin{aligned}
& \dots \cdot I_{n+2,1} \left[z(r) - \left(\frac{C_1}{K_2} + \frac{\omega \cdot C_2}{K_1} \right) \cdot u, 1, 1 \right] \cdot \exp \left(-\frac{\omega}{K_1} \cdot u \right) \cdot du - \\
& - \sum_{n=0}^{\infty} \sum_{m=0}^n (-1)^{n-m+1} \cdot \left(\frac{K_1}{K_2} \right)^{m+1} \cdot \left(\frac{\omega \cdot K_2}{K_1} \right)^{n-m+1} \cdot \binom{n}{m} \cdot \int_0^{NTU} F_{m+1} \left(u, \frac{1}{K_2} \right) \cdot F_{n-m+1}(NTU - u, 0) \cdot (64) \\
& \cdot I_{n+1,1} \left[z(r) - \left(\frac{C_1}{K_2} + \frac{\omega \cdot C_2}{K_1} \right) \cdot u, 1, 1 \right] \cdot \exp \left(-\frac{\omega}{K_1} \cdot u \right) \cdot du \}
\end{aligned}$$

The equations (63) and (64) define members in the set of algebraic equations (62). For determining constants a_k , it is possible to use any of the well known methods.

The temperature distribution of both fluids and the separating wall can be calculated by using Eqs. (52-54) and by substituting the Laplace transform of fluid 2 outlet temperature given by Eq. (59). Constants a_k are now known and are valid for all values of z within the close interval where the collocation is performed.

Temperatures of fluid and wall are as follows:

$$\begin{aligned}
\theta_1(x, z) = & \kappa \left(z - \frac{C_1}{K_2} \cdot x \right) \cdot F_1 \left(x, \frac{1}{K_2} \right) + \\
& \sum_{n=0}^{\infty} \left(\frac{K_1}{K_2} \right)^{n+1} \cdot F_{n+2} \left(x, \frac{1}{K_2} \right) \cdot I_{n+1,1} \left(z - \frac{C_1}{K_2} \cdot x, 1, 1 \right) + \\
& \sum_{n=1}^{\infty} \sum_{m=0}^{n-1} (-1)^{n-m} \cdot \left(\frac{K_1}{K_2} \right)^{m+1} \cdot \left(\frac{\omega \cdot K_2}{K_1} \right)^{n-m} \cdot \binom{n}{m} \cdot \\
& \int_0^x F_{m+2} \left(u, \frac{1}{K_2} \right) \cdot F_{n-m} \left(x - u, -\frac{\omega}{K_1} \right) \cdot I_{n+1,1} \left(z - \left[\frac{C_1}{K_2} \cdot u - \frac{\omega \cdot C_2}{K_1} \cdot (x - u) \right], 1, 1 \right) \cdot du - \quad (65) \\
& \frac{\theta_2(0, \infty)}{\omega} \cdot \sum_{n=0}^{\infty} \sum_{m=0}^n (-1)^{n-m+1} \cdot \left(\frac{K_1}{K_2} \right)^{m+1} \cdot \left(\frac{\omega \cdot K_2}{K_1} \right)^{n-m+1} \cdot \binom{n}{m} \cdot \\
& \int_0^x F_{m+1} \left(u, \frac{1}{K_2} \right) \cdot F_{n-m+1} \left(x - u, -\frac{\omega}{K_1} \right) \cdot I_{n+2,1} \left[z - \left(\frac{C_1}{K_2} \cdot u - \frac{\omega \cdot C_2}{K_1} \cdot (x - u) \right), 1, 1 \right] - \\
& \sum_{k=1}^9 a_k \cdot F_{n+k+2} \left[z - \left(\frac{C_1}{K_2} \cdot u - \frac{\omega \cdot C_2}{K_1} \cdot (x - u) \right), 1 \right] \cdot du
\end{aligned}$$

$$\begin{aligned}
\theta_w(x, z) = & K_2 \left\{ \sum_{n=0}^{\infty} \left(\frac{K_1}{K_2} \right)^{n+1} \cdot F_{n+1} \left(x, \frac{1}{K_2} \right) \cdot I_{n+1,1} \left(z - \frac{C_1}{K_2} \cdot x, 1, 1 \right) + \right. \\
& \sum_{n=1}^{\infty} \sum_{m=0}^{n-1} (-1)^{n-m} \cdot \left(\frac{K_1}{K_2} \right)^{m+1} \cdot \left(\frac{\omega \cdot K_2}{K_1} \right)^{n-m} \cdot \binom{n}{m} \cdot \\
& \left. \int_0^x F_{m+1} \left(u, \frac{1}{K_2} \right) \cdot F_{n-m} \left(x - u, -\frac{\omega}{K_1} \right) \cdot I_{n+1,1} \left(z - \left[\frac{C_1}{K_2} \cdot u - \frac{\omega \cdot C_2}{K_1} \cdot (x - u) \right], 1, 1 \right) \cdot du \right\} - \dots
\end{aligned}$$

$$\begin{aligned}
& \dots \frac{K_1}{\omega} \sum_{n=0}^{\infty} (-1)^{n+1} \cdot \left(\frac{\omega \cdot K_2}{K_1} \right)^{n+1} \cdot F_{n+1} \left(x, -\frac{\omega}{K_1} \right) \cdot \left[I_{n+2,1} \left(z + \frac{\omega \cdot C_2}{K_1} \cdot x, 1, 1 \right) - \right. \\
& \left. \sum_{k=1}^K a_k \cdot F_{n+k+2} \left(z + \frac{\omega \cdot C_2}{K_1} \cdot x, 1 \right) \right] + \frac{1}{\omega} \sum_{n=1}^{\infty} \sum_{m=1}^n (-1)^{n-m} \cdot \left(\frac{K_1}{K_2} \right)^{m+1} \cdot \left(\frac{\omega \cdot K_2}{K_1} \right)^{n-m+2} \cdot \binom{n}{m} \cdot \\
& \int_0^x F_m \left(u, \frac{1}{K_2} \right) \cdot F_{n-m+1} \left(x-u, -\frac{\omega}{K_1} \right) \cdot \left\{ I_{n+2,1} \left[z - \left(\frac{C_1}{K_2} \cdot u - \frac{\omega \cdot C_2}{K_1} \cdot (x-u) \right), 1, 1 \right] - \right. \\
& \left. \sum_{k=1}^K a_k \cdot F_{n+k+2} \left[z - \left(\frac{C_1}{K_2} \cdot u - \frac{\omega \cdot C_2}{K_1} \cdot (x-u) \right), 1 \right] \right\} \cdot du
\end{aligned} \tag{66}$$

$$\begin{aligned}
\theta_2(x, z) &= \sum_{n=0}^{\infty} \sum_{m=0}^n (-1)^{n-m+1} \cdot \left(\frac{K_1}{K_2} \right)^{m+1} \cdot \left(\frac{\omega \cdot K_2}{K_1} \right)^{n-m+1} \cdot \binom{n}{m} \cdot \\
& \int_0^x F_{m+1} \left(u, \frac{1}{K_2} \right) \cdot F_{n-m+1} \left(x-u, -\frac{\omega}{K_1} \right) \cdot I_{n+1,1} \left\{ z - \left[\frac{C_1}{K_2} \cdot u - \frac{\omega \cdot C_2}{K_1} \cdot (x-u) \right], 1, 1 \right\} \cdot du + \\
& \theta_2(0, \infty) \cdot F_1 \left(x, -\frac{\omega}{K_1} \right) \cdot \left[I_{1,1} \left(z + \frac{\omega \cdot C_2}{K_1} \cdot x, 1, 1 \right) - \sum_{k=1}^9 a_k \cdot F_{n+k+2} \left(z + \frac{\omega \cdot C_2}{K_1} \cdot x, 1 \right) \right] - \\
& \theta_2(0, \infty) \cdot \sum_{n=0}^{\infty} (-1)^n \cdot \left(\frac{\omega \cdot K_2}{K_1} \right)^{n+1} \cdot F_{n+2} \left(x, -\frac{\omega}{K_1} \right) \cdot \\
& \left[I_{n+2,1} \left(z + \frac{\omega \cdot C_2}{K_1} \cdot x, 1, 1 \right) - \sum_{k=1}^9 a_k \cdot F_{n+k+2} \left(z + \frac{\omega \cdot C_2}{K_1} \cdot x, 1 \right) \right] - \\
& \theta_2(0, \infty) \cdot \sum_{n=1}^{\infty} \sum_{m=1}^n (-1)^{n-m} \cdot \left(\frac{K_1}{K_2} \right)^m \cdot \left(\frac{\omega \cdot K_2}{K_1} \right)^{n-m+1} \cdot \binom{n}{m} \cdot \\
& \int_0^x F_m \left(u, \frac{1}{K_2} \right) \cdot F_{n-m+2} \left(x-u, -\frac{\omega}{K_1} \right) \cdot \left\{ I_{n+2,1} \left[z - \left(\frac{C_1}{K_2} \cdot u - \frac{\omega \cdot C_2}{K_1} \cdot (x-u) \right), 1, 1 \right] - \right. \\
& \left. \sum_{k=1}^9 a_k \cdot F_{n+k+2} \left[z - \left(\frac{C_1}{K_2} \cdot u - \frac{\omega \cdot C_2}{K_1} \cdot (x-u) \right), 1 \right] \right\} \cdot du
\end{aligned} \tag{67}$$

3.3 Cross flow

The equations (25) are linear per $\theta_1(x, y, z)$, $\theta_w(x, y, z)$, and $\theta_2(x, y, z)$. If three-fold Laplace transform of above equations is taken in relation to x , y and z with complex parameters s , q , and p , respectively, and if inlet and initial conditions are used (equation 15), a set of algebraic equations is generated :

$$(p+1) \cdot \tilde{\theta}_w = K_1 \cdot \tilde{\theta}_1 + K_2 \cdot \tilde{\theta}_2 \tag{68}$$

$$(K_2 \cdot s + C_1 \cdot p + 1) \cdot \tilde{\theta}_1 = \tilde{\theta}_w + \frac{K_2}{p \cdot q} \tag{69}$$

$$(K_1 \cdot q + C_2 \cdot p + 1) \cdot \tilde{\theta}_2 = \tilde{\theta}_w \quad (70)$$

Solving the set of algebraic set (equations (16)-(18)) is as follows:

$$\tilde{\theta}_w = \frac{\frac{K_1 \cdot K_2}{p \cdot q \cdot (K_2 \cdot s + C_1 \cdot p + 1)}}{p + 1 - \frac{K_1}{K_2 \cdot s + C_1 \cdot p + 1} - \frac{K_2}{K_1 \cdot q + C_2 \cdot p + 1}} \quad (71)$$

$$\tilde{\theta}_1 = \frac{\tilde{\theta}_w}{(K_2 \cdot s + C_1 \cdot p + 1)} + \frac{K_2}{p \cdot q \cdot (K_2 \cdot s + C_1 \cdot p + 1)} \quad (72)$$

$$\tilde{\theta}_2 = \frac{\tilde{\theta}_w}{(K_1 \cdot q + C_2 \cdot p + 1)} \quad (73)$$

After performing certain mathematical transformations as done in previous cases, the algebraic equation (71) can be expressed in the following form:

$$\tilde{\theta}_w = \sum_{n=0}^{\infty} \sum_{m=0}^n \binom{n}{m} \cdot \frac{K_1^{m+1} \cdot K_2^{n-m+1}}{p \cdot (p+1)^{n+1} \cdot (K_2 \cdot s + C_1 \cdot p + 1)^{m+1} \cdot q \cdot (K_1 \cdot q + C_2 \cdot p + 1)^{n-m}} \quad (74)$$

which is very suitable for inverse Laplace transforms by means of functions $F_n(x, c)$ and $I_{n,m}(x, c, d)$ defined in the Annex. However, for the case $n = m$ in the equation (74) and later on, the twofold sum will be separated into two (single and double) sums so that:

$$\begin{aligned} \tilde{\theta}_w = & \sum_{n=0}^{\infty} \frac{K_1^{n+1} \cdot K_2}{p \cdot (p+1)^{n+1} \cdot q \cdot (K_2 \cdot s + C_1 \cdot p + 1)^{n+1}} + \\ & \sum_{n=1}^{\infty} \sum_{m=0}^{n-1} \binom{n}{m} \cdot \frac{K_1^{m+1} \cdot K_2^{n-m+1}}{p \cdot (p+1)^{n+1} \cdot (K_2 \cdot s + C_1 \cdot p + 1)^{m+1} \cdot q \cdot (K_1 \cdot q + C_2 \cdot p + 1)^{n-m}} \end{aligned} \quad (75)$$

The insertion of the equation (74) in equations (72) and (73) generates the following algebraic equations:

$$\begin{aligned} \tilde{\theta}_1 = & \frac{K_2}{p \cdot q \cdot (K_2 \cdot s + C_1 \cdot p + 1)} + \sum_{n=0}^{\infty} \frac{K_1^{n+1} \cdot K_2}{p \cdot (p+1)^{n+1} \cdot q \cdot (K_2 \cdot s + C_1 \cdot p + 1)^{n+2}} + \\ & \sum_{n=1}^{\infty} \sum_{m=0}^{n-1} \binom{n}{m} \cdot \frac{K_1^{m+1} \cdot K_2^{n-m+1}}{p \cdot (p+1)^{n+1} \cdot (K_2 \cdot s + C_1 \cdot p + 1)^{m+2} \cdot q \cdot (K_1 \cdot q + C_2 \cdot p + 1)^{n-m}} \end{aligned} \quad (76)$$

$$\tilde{\theta}_2 = \sum_{n=0}^{\infty} \sum_{m=0}^n \binom{n}{m} \cdot \frac{K_1^{m+1} \cdot K_2^{n-m+1}}{p \cdot (p+1)^{n+1} \cdot (K_2 \cdot s + C_1 \cdot p + 1)^{m+1} \cdot q \cdot (K_1 \cdot q + C_2 \cdot p + 1)^{n-m+1}} \quad (77)$$

Now it is possible to get the inverse Laplace transform equation (75)-(77), so that:

$$\begin{aligned} \theta_w(x, y, z) = & \sum_{n=0}^{\infty} K_1^{n+1} \cdot F_{n+1} \left(\frac{x}{K_2}, 1 \right) \cdot I_{n+1,1} \left(z - C_1 \cdot \frac{x}{K_2}, 1, 1 \right) + \\ & \sum_{n=1}^{\infty} \sum_{m=0}^{n-1} \binom{n}{m} \cdot K_1^{m+1} \cdot K_2^{n-m} \cdot F_{m+1} \left(\frac{x}{K_2}, 1 \right) \cdot \\ & \int_0^{y/K_1} F_{n-m} \left(\frac{v}{K_1}, 1 \right) \cdot I_{n+1,1} \left(z - C_1 \cdot \frac{x}{K_2} - C_2 \cdot \frac{v}{K_1}, 1, 1 \right) \cdot \frac{dv}{K_1} \end{aligned} \quad (78)$$

$$\begin{aligned} \theta_1(x, y, z) = & \kappa \left(z - C_1 \cdot \frac{x}{K_2} \right) \cdot F_1 \left(\frac{x}{K_2}, 1 \right) + \\ & \sum_{n=0}^{\infty} K_1^{n+1} \cdot F_{n+2} \left(\frac{x}{K_2}, 1 \right) \cdot I_{n+1,1} \left(z - C_1 \cdot \frac{x}{K_2}, 1, 1 \right) + \\ & \sum_{n=1}^{\infty} \sum_{m=0}^{n-1} \binom{n}{m} \cdot K_1^{m+1} \cdot K_2^{n-m} \cdot F_{m+2} \left(\frac{x}{K_2}, 1 \right) \cdot \\ & \int_0^{y/K_1} F_{n-m} \left(\frac{v}{K_1}, 1 \right) \cdot I_{n+1,1} \left(z - C_1 \cdot \frac{x}{K_2} - C_2 \cdot \frac{v}{K_1}, 1, 1 \right) \cdot \frac{dv}{K_1} \end{aligned} \quad (79)$$

$$\begin{aligned} \theta_2(x, y, z) = & \sum_{n=0}^{\infty} \sum_{m=0}^n \binom{n}{m} \cdot K_1^{m+1} \cdot K_2^{n-m} \cdot F_{m+1} \left(\frac{x}{K_2}, 1 \right) \cdot \\ & \int_0^{y/K_1} F_{n-m+1} \left(\frac{v}{K_1}, 1 \right) \cdot I_{n+1,1} \left(z - C_1 \cdot \frac{x}{K_2} - C_2 \cdot \frac{v}{K_1}, 1, 1 \right) \cdot \frac{dv}{K_1} \end{aligned} \quad (80)$$

The equations (78)-(80) are analytical expressions for temperature fields of fluids 1 and 2 and separating wall of cross heat exchanger dependant on time. At the beginning, the inlet temperature of fluid 1 is instantly raised from 0 to 1, and flow velocities of both fluids are constant.

Outlet temperatures of both fluids are obtained by integrating temperatures along outlet edges of the heat exchanger. This is how outlet temperatures become equal;

$$\bar{\theta}_1''(z) = \frac{1}{b} \int_0^b \theta_1(a, y, z) \cdot dy \quad (81)$$

$$\bar{\theta}_2''(z) = \frac{1}{a} \int_0^a \theta_2(x, b, z) \cdot dx, \quad (82)$$

where $a = \text{NTU}$ and $b = \omega \cdot \text{NTU}$.

Substituting equations (79) and (80) in equations (81) and (82) generates accurate explicit expressions for mean outlet temperatures:

$$\begin{aligned}
\bar{\theta}_1''(z) = & \kappa \left(z - C_1 \frac{a}{K_2} \right) \cdot F_1 \left(\frac{a}{K_2}, 1 \right) + \\
& \sum_{n=0}^{\infty} K_1^{n+1} \cdot F_{n+2} \left(\frac{a}{K_2}, 1 \right) \cdot I_{n+1,1} \left(z - C_1 \cdot \frac{a}{K_2}, 1, 1 \right) + \\
& \frac{1}{b} \cdot \sum_{n=1}^{\infty} \sum_{m=0}^{n-1} \binom{n}{m} \cdot K_1^{m+2} \cdot K_2^{n-m} \cdot F_{m+2} \left(\frac{a}{K_2}, 1 \right) \cdot \\
& \int_0^{b/K_1} \frac{b-v}{K_1} \cdot F_{n-m} \left(\frac{v}{K_1}, 1 \right) \cdot I_{n+1,1} \left(z - C_1 \cdot \frac{a}{K_2} - C_2 \cdot \frac{v}{K_1}, 1, 1 \right) \cdot \frac{dv}{K_1}
\end{aligned} \tag{83}$$

$$\begin{aligned}
\bar{\theta}_2''(z) = & \frac{1}{a} \cdot \sum_{n=0}^{\infty} \sum_{m=0}^n \binom{n}{m} \cdot K_1^{m+1} \cdot K_2^{n-m} \cdot \\
& \int_0^{a/K_2} \int_0^{y/K_1} F_{m+1} \left(\frac{u}{K_2}, 1 \right) \cdot F_{n-m+1} \left(\frac{v}{K_1}, 1 \right) \cdot I_{n+1,1} \left(z - C_1 \cdot \frac{u}{K_2} - C_2 \cdot \frac{v}{K_1}, 1, 1 \right) \cdot \frac{du}{K_2} \frac{dv}{K_1}
\end{aligned} \tag{84}$$

Above solutions are also valid for the case of indefinite fluid velocities ($C_1 = C_2 = 0$).

4. Calculation results

The main purpose of this paper is to provide exact analytical solutions by which performances of parallel, counter and cross flow heat exchangers can be calculated and compared. Many parameters are involved in temperature distributions of both fluids and the wall and, therefore, it is not possible to present quantitative influences of all these parameters in this paper. However, there is enough space to give particular results showing main characteristics of solutions.

Programming of equations expressing temperature fields and outlet temperatures for considered types of heat exchangers can be very tiresome. Therefore, the website www.peec.uns.ac.rs presents programs in MS EXCEL for calculations. Programs can be modified and improved as required.

The example of a heat exchanger where $NTU = 1$, $\omega = 0.5$, $K_1 = 0.25$ ($K_2 = 1 - K_1 = 0.75$), $C_1 = 4.0$ and $C_2 = 0.5$ will be discussed below. The temperature distributions of both fluids and the wall of PARALLEL flow heat exchanger are plotted versus dimensionless heat exchanger length (distance x) for $z = 2$ and 4 in Figure 4.

The occurrence of heating up of separating wall and fluid 1 by fluid 2 is typical for parallel flow heat exchanger. This can happen at the beginning of a non-steady state process when the velocity of the fluid 2 flow is higher than the velocity of fluid 1. This will be explained somewhat later when comparing outlet temperatures for all three types of heat exchangers.

The Figure 5 shows temperature distribution for the COUNTER flow heat exchanger. The parameters of this heat exchanger are the same as for the parallel one. Differences of temperature distribution between parallel and counter flow heat exchangers are evident.

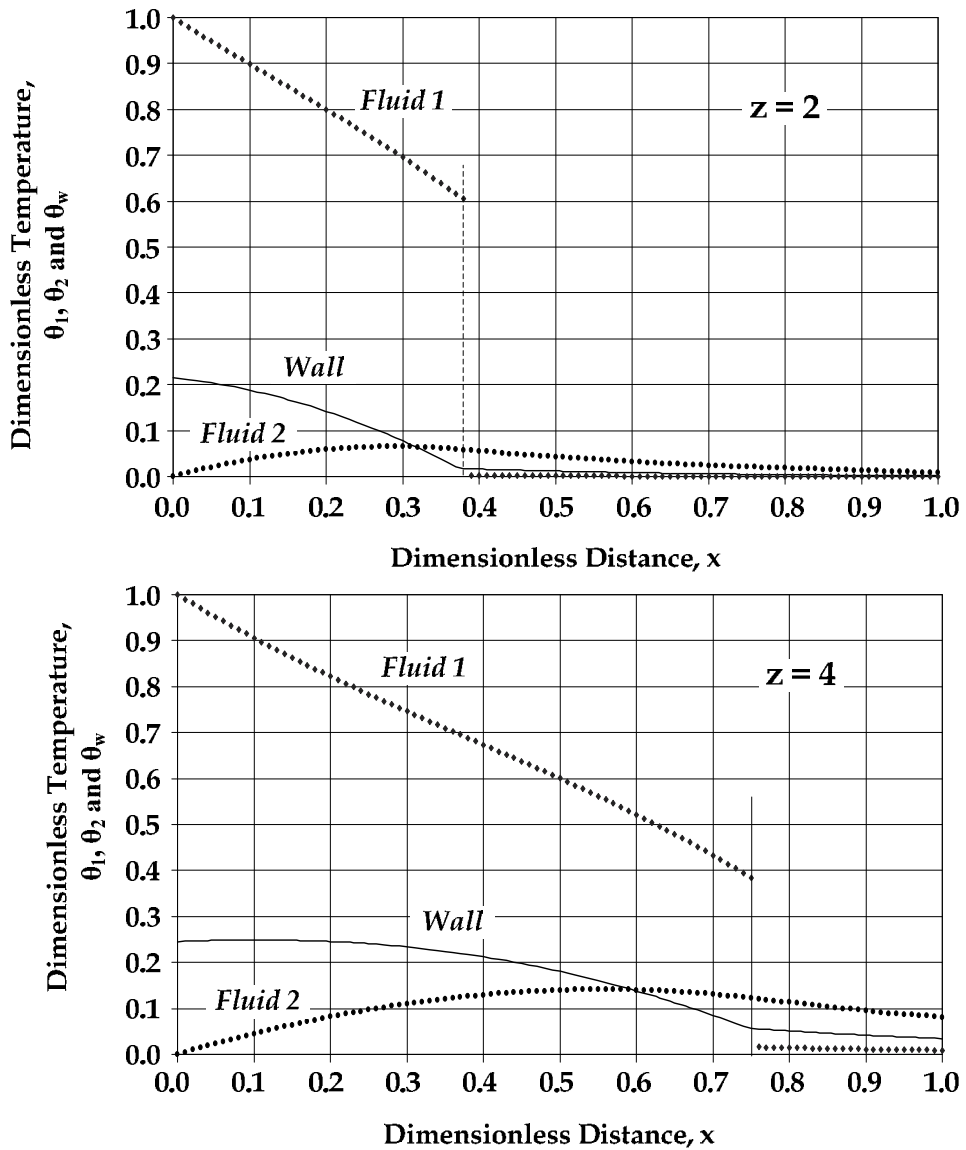


Fig. 4. Temperature Distribution of Both Fluids and the Wall of Parallel Flow Heat Exchanger for $z = 2$ and 4.

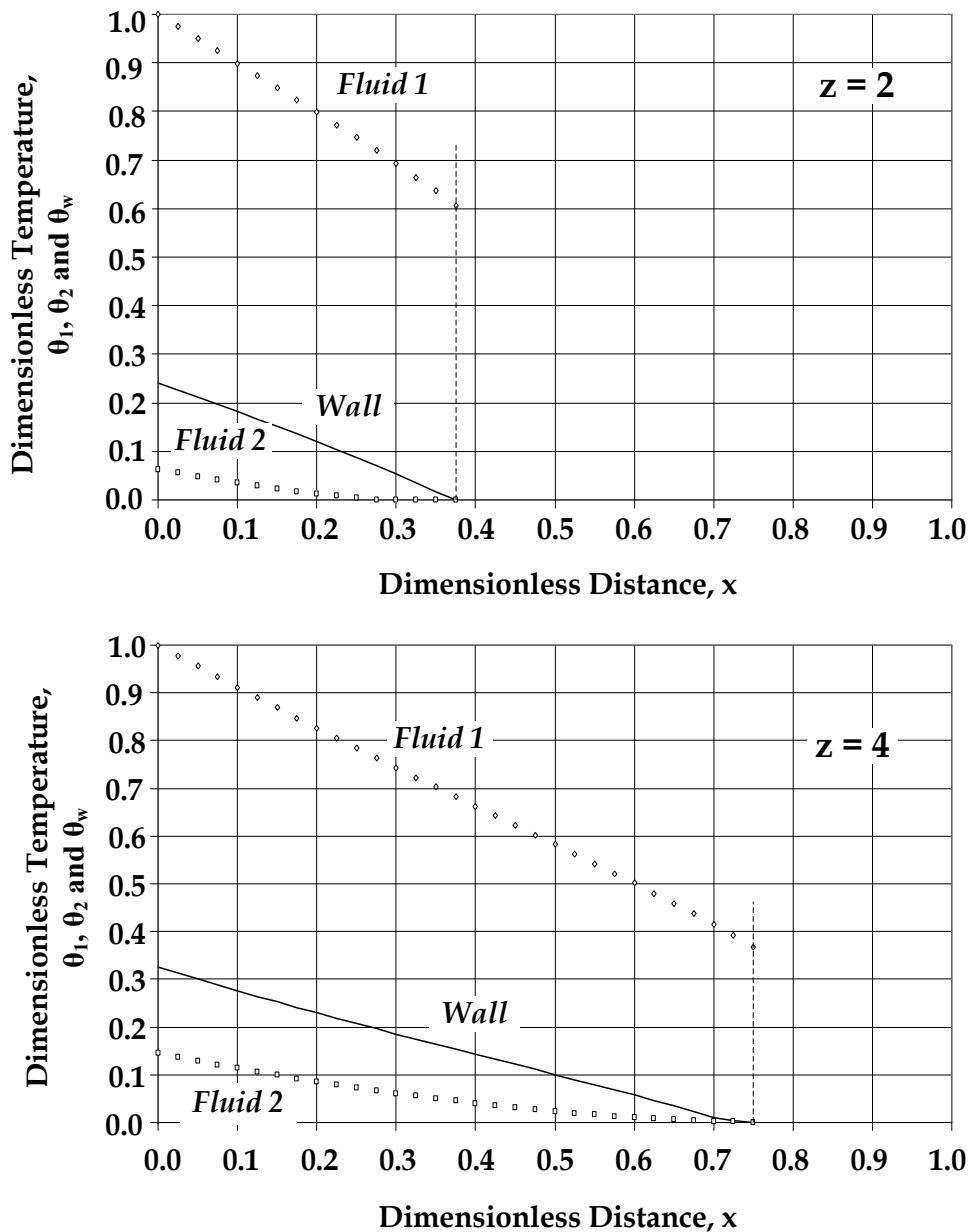


Fig. 5. Temperature Distribution of Both fluids and the Wall of Counter Flow Heat Exchanger for $z = 2$ and 4 .

As an example of the use of presented solutions for cross flow heat exchanger, temperature fields for both fluids and separating wall are given for the same case ($NTU = 1$, $\omega = 0.5$, $K_1 = 0.25$, $C_1 = 4$, and $C_2 = 0.5$). Temperature fields of both fluids and the wall are shown for dimensionless lengths of heat exchangers at dimensionless time $z = 6$ (Figure 6). At the time $z = 6$, the front of both fluids has left boundaries of the heat exchanger. Along the outlet

fluid edge, wall temperature has been significantly raised but wall temperature along the outlet edge of the fluid 1 is very modest. The perturbation of the fluid 1 has just left the outlet edge of the heat exchanger. For the fluid 2, the perturbation has moved far away from the outlet edge. Since the the perturbation front of the fluid 1 has just left the outlet edge of the heat exchanger, wall temperature at this edge are low. The same conclusion is also valid for fluid 2 temperature. However, it should be noted that the strength of the fluid 2 flow is two times higher that the strength of the fluid 1.

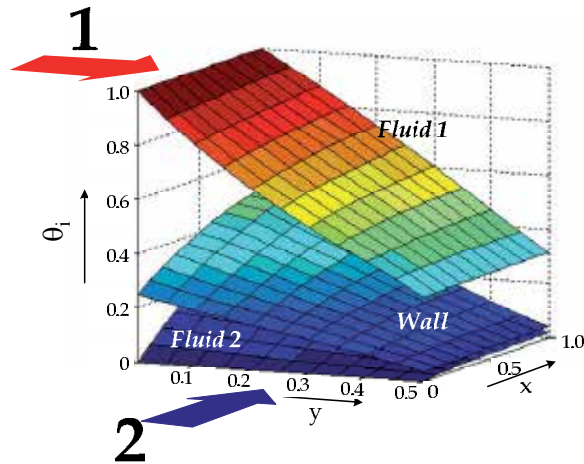


Fig. 6. Temperature Fields of Both Fluids and The wall of CROSS Flow Heat Exchanger for $z = 2$ and 4.

Fig. 7 shows outlet temperatures of both fluid flows for all three types of heat exchangers. The size of these three heat exchangers is $NTU = 1.0$ and $\omega = 0.5$. The characteristics of transient heat are also equal for all three types of heat exchangers and they are defined by $K_1 = 0.25$, i.e., $K_2 = 1 - K_1 = 0.75$. The velocity of fluid flow 1 ($C_1 = 4.0$, i.e., $U_1 \sim 1/C_1$) is less than the velocity of the flow 2 ($C_2 = 0.5$, i.e., $U_2 \sim 1/C_2$). This means that the fluid 1 flows longer through the flow channels than fluid 2. In the analyzed case, the ratio of fluid velocities is $U_1/U_2 = 0.04167$. For the fluid 2, the time from $z=0$ to 1 is necessary to pass the whole length of the heat exchanger at its side of the separating wall. The time $z = 5.33$ is required for the fluid 1.

The change curve of outlet temperature of fluid 2 is continuous for all three cases (Fig. 7). It is logical that the highest outlet temperature is achieved in the counter flow heat exchanger for which the effectiveness (steady-state) is also the highest for the same values of NTU and ω . It is followed by the cross flow and then by the parallel flow heat exchanger as the worst among the three. In all cases, the final outlet temperature ($z \rightarrow \infty$) is equal to $= 1 - \varepsilon(NTU, \omega, flow\ arrangement)$. Also, in transient regime, differences regarding the quality of exchangers are retained.

It is opposite for the fluid 1. The lowest temperature is obtained for the counter flow heat exchanger and the highest for the parallel one. Final outlet temperatures are equal

$= \omega \cdot \varepsilon(NTU, \omega, \text{flow arrangement})$. It is logical that the outlet temperature of the fluid 1 is a discontinued function. After the step unit increase of the temperature of the fluid 1 at $z = 0$, the temperature of the fluid 1 falls due to heating of the wall of the heat exchanger and then heating of the fluid 2. However, in the case of the parallel flow heat exchanger, in the beginning after perturbation, the outlet temperature of the fluid 1 grows even before the perturbation reaches the outlet of the exchanger. This means that at one time of the non-steady state part of the process, the fluid 2 heats up the flow of the fluid 1, as well as the wall instead of vice versa. Namely, ahead of the front, there is the fluid flow 2 heated up by the fluid flow 1. Since the velocity of the fluid flow 2 is higher than the velocity of the fluid flow 1 therefore, it heats up later non-perturbed part of the flow 1 which is ahead of the moving front of the perturbation. By all means, this indicates that before the occurrence of the perturbation all non-dimensionless temperatures are equal to zero (initial condition). After the time $z = 5.33$, the perturbation of the fluid 1 has reached the outlet edge of the exchanger which is registered by the step change of the outlet temperature. In case of the cross and counter flow heat exchangers, there is not heating up of the fluid flow 1 ahead of the perturbation front (Fig. 7). The fluid flow 1 cools down in the beginning by heating up the wall of the heat exchanger and the part of the fluid flow 2 in case of the cross flow heat exchanger and the whole fluid flow 1 in the case of counter flow but, it cannot happen that the fluid flow 2 gets ahead of the perturbation front and causes a reversal process of the heat transfer which is possible in case of the parallel flow heat exchanger.

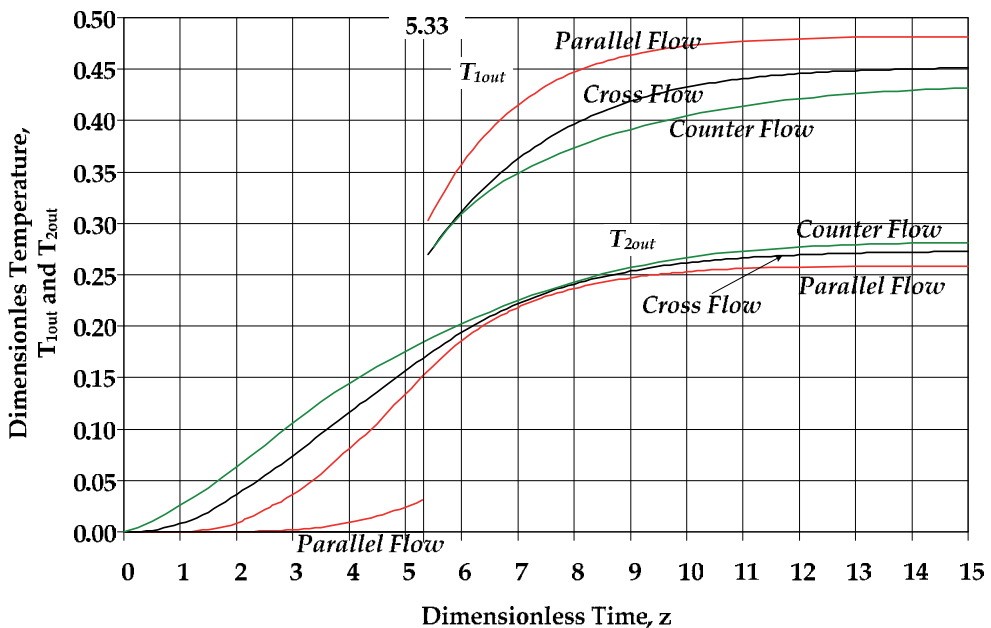


Fig. 7. Outlet Temperature of Both Fluids for Parallel, Counter and Cross Flow Heat Exchangers.

5. Conclusion

A method providing exact analytical solutions for transient response of parallel, counter and cross flow heat exchangers with finite wall capacitance is presented. Solutions are valid in the case where velocities are different or equal. These solutions procedure provides necessary basis for the study of parameters estimated, model discriminations and control of all analyzed heat exchangers.

Generally speaking, the analytical method is superior to numerical techniques because the final solution also preserves physical essence of the problem. Testing of solutions given in this paper indicates that they can be used in practice efficiently when designing and managing processes with heat exchangers.

6. Appendix

Functions $F_n(x, c)$ and $I_{n,m}(x, c, d)$ and their Laplace transforms are given as described below ($x \geq 0$, $-\infty < c, d < \infty$, and $n, m = 1, 2, 3, \dots$). For $x < 0$, both functions are equal to zero.

$$F_n(x, c) = \frac{x^{n-1}}{(n-1)!} \cdot \exp(-c \cdot x) \Leftrightarrow \frac{1}{(s+c)^n} \quad (\text{A.1})$$

$$I_{n,m}(x, c, d) = \sum_{j=1}^{\infty} \binom{m+j-1}{j} \cdot d^j \cdot F_{n+m+j}(x, c, d) \Leftrightarrow \frac{1}{(s+c)^n \cdot (s+c-d)^m} \quad (\text{A.2})$$

Some additional details about these functions can be found in an earlier paper (Gvozdenac, 1986).

7. Nomenclature

A_1, A_2	total heat transfer area on sides 1 and 2 of a heat exchanger, respectively, [m ²]
F_1, F_2	cross-section area of flow passages 1 and 2, respectively, [m ²]
c_p	isobaric specific heat of fluid, [J/(kg K)]
c_w	specific heat of core material, [J/(kg K)]
h	heat transfer coefficient between fluid and the heat exchanger wall, [W/(K m ²)]
M_w	mass of heat exchanger core, [kg]
\dot{m}	mass flow rate, [kg/s]
NTU	number of heat transfer units, [-] (Eq.)
T	temperature, [K]
t	time, [s]
W	thermal capacity rate of fluid, $= \dot{m} \cdot c_p$, [W/K]
W_{\min}	lesser of W_1 and W_2 , [W/K]
X, Y	distance from fluid entrances, [m]
U	fluid velocity, [m/s]
ρ	density, [kg/m ³]
κ	unit step function
θ	dimensionless temperature
x, y, z	dimensionless independent variables, (Eqs.)

Subscripts:

1	fluid 1
2	fluid 2
w	wall

8. Acknowledgment

This work was performed as a part of the research supported by Provincial Secretariat for Science and Technological Development of Autonomous Province of Vojvodina.

9. References

- Profos, P. (1943). *Die Behandlung von Regelproblemen vermittelt des Frequenzganges des Regelkreises*, Dissertation, Zurich, 1943
- Tahkahashi, Y. (1951). *Automatic control of heat exchanger*, Bull. JSME, 54, pp 426-431
- Kays, W. M. & London, A. L. (1984). *Compact heat exchangers* (3rd ed), New York, McGraw-Hill
- Liapis, A. I. & McAvoy, T. J. (1981). *Transient solutions for a class of hyperbolic counter-current distributed heat and mass transfer systems*, Trans. IChemE, 59, pp 89-94
- Li, Ch. H. (1986). *Exact transient solutions of parallel-current transfer processes*, ASME J. Heat Transfer, 108, pp 365-369
- Romie, F. E. (1985). *Transient response of counterflow heat exchanger*, ASME Journal of Heat Transfer, 106, pp 620-626
- Romie, F. E. (1986). *Transient response of the parallel-flow heat exchanger*, ASME J. Heat Transfer, 107, pp 727-730
- Gvozdenac, D. D. (1987). *Analytical solution of transient response of gas-to-gas parallel and counterflow heat exchangers*, ASME J. Heat Transfer, 109, pp 848-855
- Romie, E. E. (1983). *Transient response of gas-to-gas crossflow heat exchangers with neither gas mixed*, ASME J. Heat Transfer, 105, pp 563-570
- Gvozdenac, D. D. (1986). *Analytical solution of the transient response of gas-to-gas crossflow heat exchanger with both fluids unmixed*, ASME J. Heat Transfer, 108, pp 722-727
- Spiga, G. & Spiga, M. (1987). *Two-dimensional transient solutions for crossflow heat exchangers with neither gas mixed*, ASME J. Heat Transfer, 109, pp 281-286
- Spiga, M. & Spiga, G. (1988). *Transient temperature fields in crossflow heat exchangers with finite wall capacitance*, ASME J. Heat Transfer, 110, pp 49-53
- Gvozdenac, D. D. (1990). *Transient response of the parallel flow heat exchanger with finite wall capacitance*, Ing. Arch., 60, pp 481-490
- Gvozdenac, D. D. (1991). *Dynamic response of the crossflow heat exchanger with finite wall capacitance*, Wärme- und Stoffübertragung, 26, pp 207-212
- Roetzel, W. & Xuan, Y. (1999). *Dynamic Behavior of Heat Exchangers (Developments in Heat Transfer, Volume 3*, WITpress/Computational Mechanics Publications
- Bačlić, B. S. (1978). *A Simplified Formula for Cross-Flow Heat Exchanger Effectiveness*, ASME Journal of Heat Transfer, 100, pp 746-747

Self-Heat Recuperation: Theory and Applications

Yasuki Kansha¹, Akira Kishimoto¹,
Muhammad Aziz² and Atsushi Tsutsumi¹

¹*Collaborative Research Center for Energy Engineering, Institute of Industrial Science,
The University of Tokyo*

²*Advanced Energy Systems for Sustainability, Solution Research Laboratory
Tokyo Institute of Technology
Japan*

1. Introduction

Since the 1970s, energy saving has contributed to various elements of societies around the world for economic reasons. Recently, energy saving technology has attracted increased interest in many countries as a means to suppress global warming and to reduce the use of fossil fuels. The combustion of fossil fuels for heating produces a large amount of carbon dioxide (CO₂), which is the main contributor to global greenhouse gas effects (Eastop & Croft 1990, Kemp 2007). Thus, the reduction of energy consumption for heating is a very important issue. To date, to reduce energy consumption, heat recovery technology such as pinch technology, which exchanges heat between the hot and cold streams in a process, has been applied to thermal processes (Linnhoff et al. 1979, Cerda et al. 1983, Linnhoff et al. 1983, Linnhoff 1993, Linnhoff & Eastwood 1997, Ebrahim & Kawari 2000). A simple example of this technology is the application of a feed-effluent heat exchanger in thermal processes, wherein heat is exchanged between feed (cold) and effluent (hot) streams to recirculate the self-heat of the stream (Seider et al. 2004). To exchange the heat, an additional heat source may be required, depending on the available temperature difference between two streams for heat exchange. The additional heat may be provided by the combustion of fossil fuels, leading to exergy destruction during heat production (Som & Datta 2008). In addition, many energy saving technologies recently developed are only considered on the basis of the first law of thermodynamics, i.e. energy conservation. Hence, process design methods based on these technologies are distinguished by cascading heat utilization.

Simultaneously, many researchers have paid attention to the analysis of process exergy and irreversibility through consideration of the second law of thermodynamics. However, many of these investigations show only the calculation results of exergy analysis and the possibility of the energy savings of some processes, and few clearly describe methods for reducing the energy consumption of processes (Lampinen & Heillinen 1995, Chengqin et al 2002, Grubbström 2007). To reduce exergy reduction, a heat pump has been applied to thermal processes, in which the ambient heat or the process waste heat is generally pumped to heat the process stream by using working fluid compression. Although it is well-known that a heat pump can reduce energy consumption and exergy destruction in a process, the

heat load and capacity of the process stream are often different from those of the pumped heat. Thus, a normal heat pump still possibly causes large exergy destruction during heating. In heat recovery technologies, vapor recompression has been applied to evaporation, distillation, and drying, in which the vapor evaporated from the process is compressed to a higher pressure and then condensed, providing a heating effect. The condensation heat of the stream is recirculated as the vaporization heat in the process by using vapor recompression. However, many investigators have only focused on latent heat and few have paid attention to sensible heat. As a result, the total process heat cannot be recovered, indicating the potential for further energy savings in many cases. Recently, an energy recuperative integrated gasification power generation system has been proposed and a design method for the system developed (Kuchonthara & Tsutsumi 2003, Kuchonthara et al. 2005, Kuchonthara & Tsutsumi 2006). Kansha et al. have developed self-heat recuperation technology based on exergy recuperation (2009). The most important characteristics of this technology are that the entire process stream heat can be recirculated into a process designed by this technology based on exergy recuperation, leading to marked energy savings for the process.

In this chapter, an innovative self-heat recuperation technology, in which not only the latent heat but also the sensible heat of the process stream can be circulated without heat addition, and the theoretical analysis of this technology are introduced. Then, several industrial application case studies of this technology are presented and compared with their conventional counterparts.

2. Self-heat recuperation technology

Self-heat recuperation technology (Kansha et al. 2009) facilitates recirculation of not only latent heat but also sensible heat in a process, and helps to reduce the energy consumption of the process by using compressors and self-heat exchangers based on exergy recuperation. In this technology, i) a process unit is divided on the basis of functions to balance the heating and cooling loads by performing enthalpy and exergy analysis and ii) the cooling load is recuperated by compressors and exchanged with the heating load. As a result, the heat of the process stream is perfectly circulated without heat addition, and thus the energy consumption for the process can be greatly reduced. In this section, first, the theory of the self-heat recuperation technology and the design methodology for self-heat recuperative processes are introduced for a basic thermal process, and then self-heat recuperative processes applied to separation processes are introduced.

2.1 Self-heat recuperative thermal process

Exergy loss in conventional thermal processes such as a fired heater normally occurs during heat transfer between the reaction heat produced by fuel combustion and the heat of the process stream, leading to large energy consumption in the process. To reduce the energy consumption in the process through heat recovery, heating and cooling functions are generally integrated for heat exchange between feed and effluent to introduce heat circulation. A system in which such integration is adopted is called a self-heat exchange system. To maximize the self-heat exchange load, a heat circulation module for the heating and cooling functions of the process unit has been proposed, as shown in Figure 1 (Kansha et al. 2009).

Figure 1 (a) shows a thermal process for gas streams with heat circulation using self-heat recuperation technology. In this process, the feed stream is heated with a heat exchanger (1→2) from a standard temperature, T_1 , to a set temperature, T_2 . The effluent stream from the following process is pressurized with a compressor to recuperate the heat of the effluent stream (3→4) and the temperature of the stream exiting the compressor is raised to T_2 through adiabatic compression. Stream 4 is cooled with a heat exchanger for self-heat exchange (4→5). The effluent stream is then decompressed with an expander to recover part of the work of the compressor. This leads to perfect internal heat circulation through self-heat recuperation. The effluent stream is finally cooled to T_1 with a cooler (6→7). Note that the total heating duty is equal to the internal self-heat exchange load without any external heating load, as shown in Fig. 1 (b). Thus, the net energy required of this process is equal to the cooling duty in the cooler (6→7). To be exact, the heat capacity of the feed stream is not equal to that of the effluent stream. However, the effect of pressure to the heat capacity is small. Thus, two composite curves in Fig. 1 (b) seem to be in parallel. In addition, the exergy destruction occurs only during the heat transfer in the heat exchanger. The amount of this exergy destruction is illustrated by the gray area in Fig. 1 (b).

In the case of ideal adiabatic compression and expansion, the input work provided to the compressor performs a heat pumping role in which the effluent temperature can achieve perfect internal heat circulation without exergy destruction. Therefore, self-heat recuperation can dramatically reduce energy consumption. Figure 1 (c) shows a thermal process for vapor/liquid streams with heat circulation using the self-heat recuperation technology. In this process, the feed stream is heated with a heat exchanger (1→2) from a standard temperature, T_1 , to a set temperature, T_2 . The effluent stream from the subsequent process is pressurized by a compressor (3→4). The latent heat can then be exchanged between feed and effluent streams because the boiling temperature of the effluent stream is raised to T_b by compression. Thus, the effluent stream is cooled through the heat exchanger for self-heat exchange (4→5) while recuperating its heat. The effluent stream is then depressurized by a valve (5→6) and finally cooled to T_1 with a cooler (6→7). This leads to perfect internal heat circulation by self-heat recuperation, similar to the above gas stream case. Note that the total heating duty is equal to the internal self-heat exchange load without an external heating load, as shown in Fig. 1 (d). It is clear that the vapor and liquid sensible heat of the feed stream can be exchanged with the sensible heat of the corresponding effluent stream and the vaporization heat of the feed stream is exchanged with the condensation heat of the effluent stream. Similar to the thermal process for gas streams with heat circulation using self-heat recuperation technology mentioned above, the net energy required of this process is equal to the cooling duty in the cooler (6→7) and the exergy destruction occurs only during heat transfer in the heat exchanger and the amount of this exergy destruction is indicated by the gray area in Fig. 1 (d). As well as the gas stream, the effect of pressure to the heat capacity is small. Thus, two composite curves in Fig. 1 (b) are closed to be in parallel. As a result, the energy required by the heat circulation module is reduced to 1/22–1/2 of the original by the self-heat exchange system in gas streams and/or vapor/liquid streams.

To use the proposed self-heat recuperative thermal process in the reaction section of hydrodesulfurization in the petrochemical industry as an industrial application, Matsuda et al. (2010) reported that the advanced process requires 1/5 of the energy required of the

conventional process on the basis of enthalpy and examined the considerable reduction of the exergy destructions in this process. The other related industrial applications of the proposed self-heat recuperative thermal process are the preheating sections of the feed streams for reaction to satisfy the required physical conditions.

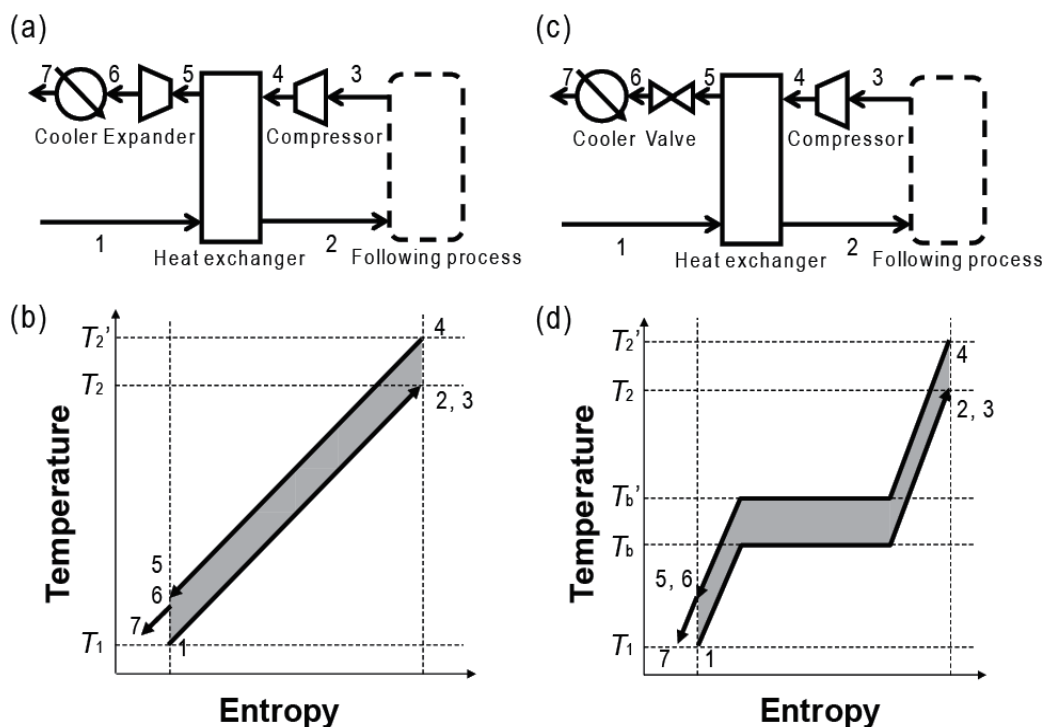


Fig. 1. Self-heat recuperative thermal process a) process flow of gas streams, b) temperature-entropy diagram of gas streams, c) process flow of vapor/liquid streams, d) temperature-entropy diagram of vapor/liquid streams.

2.2 Self-heat recuperative separation processes

Expanding the self-heat recuperative thermal process to separation processes (Kansha et al. 2010a), a system including not only the separation process itself but also the preheating/cooling section, can be divided on the basis of functions, namely the separation module and the heat circulation module, in which the heating and cooling loads are balanced, as shown in Fig. 2. To simplify the process for explanation, Fig. 2 shows a case that has one feed and two effluents. In this figure, the enthalpy of inlet stream (feed) is equal to the sum of the outlet streams (effluents) enthalpies in each module, giving an enthalpy

difference between inlet and outlet streams of zero. The cooling load in each module is then recuperated by compressors and exchanged with the heating load using self-heat recuperation technology. As a result, the heat of the process stream (self-heat) is perfectly circulated without heat addition in each module, resulting in perfect internal heat circulation over the entire separation process.

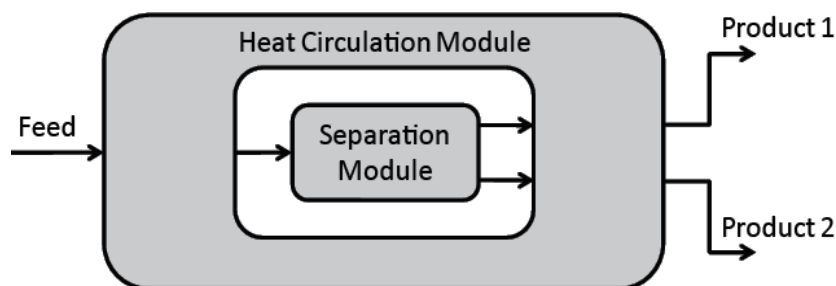


Fig. 2. Conceptual figure for self-heat recuperative separation processes.

2.2.1 Self-heat recuperative distillation process

Although distillation columns have been widely used in separation processes based on vapor/liquid equilibria in petroleum refineries and chemical plants, the distillation process consumes a massive amount of energy required for the latent heat of the phase change, resulting in the emission of a large amount of CO_2 . To prevent the emission of CO_2 through use of self-heat recuperation technology (Kansha et al. 2010b), a distillation process can be divided into two sections, namely the preheating and distillation sections, on the basis of functions that balance the heating and cooling load by performing enthalpy and exergy analysis, and the self-heat recuperation technology is applied to these two sections. In the preheating section, one of the streams from the distillation section is a vapor stream and the stream to the distillation section has a vapor-liquid phase that balances the enthalpy of the feed streams and that of the effluent streams in the section. In balancing the enthalpy of the feed and effluent streams in the heat circulation module, the enthalpy of the streams in the distillation module is automatically balanced. Thus, the reboiler duty is equal to the condenser duty of the distillation column. Therefore, the vapor and liquid sensible heat of the feed streams can be exchanged with the sensible heat of the corresponding effluent streams, and the vaporization heat can be exchanged with the condensation heat in each module.

Figure 3 (a) shows the structure of a self-heat recuperative distillation process consisting of two standardized modules, namely, the heat circulation module and the distillation module. Note that in each module, the sum of the enthalpy of the feed streams and that of the effluent streams are equal. The feed stream in this integrated process module is represented by stream 1. This stream is heated to its boiling point by the two streams independently recuperating heat from the distillate (12) and bottoms (13) by the heat exchanger (1→2). A distillation column separates the distillate (3) and bottoms (9) from stream 2. The distillate (3) is divided into two streams (4, 12). Stream 4 is compressed adiabatically by a compressor and cooled down by the heat exchanger (2). The pressure and temperature of stream 6 are adjusted by a valve and a cooler (6→7→8), and stream 8 is then fed into the distillation

column as a reflux stream. Simultaneously, the bottoms (9) is divided into two streams (10, 13). Stream 10 is heated by the heat exchanger and fed to the distillation column (10→11). Streams 12 and 13 are the effluent streams from the distillation module and return to the heat circulation module. In addition, the cooling duty of the cooler in the distillation module is equal to the compression work of the compressor in the distillation module because of the enthalpy balance in the distillation module.

The effluent stream (12) from the distillation module is compressed adiabatically by a compressor (12→14). Streams 13 and 14 are successively cooled by a heat exchanger. The pressure of stream 17 is adjusted to standard pressure by a valve (17→18), and the effluents are finally cooled to standard temperature by coolers (15→16, 18→19). The sum of the cooling duties of the coolers is equal to the compression work of the compressor in the heat circulation module. Streams 16 and 19 are the products.

Figure 3 (b) shows the temperature and heat diagram for the self-heat recuperative distillation process. In this figure, each number corresponds to the stream numbers in Fig. 3 (a), and T_{std} and T_b are the standard temperature and the boiling temperature of the feed stream, respectively. Both the sensible heat and the latent heat of the feed stream are subsequently exchanged with the sensible and latent heat of effluents in heat exchanger 1. The vaporization heat of the bottoms from the distillation column is exchanged with the condensation heat of the distillate from the distillation column in the distillation module. The heat of streams 4 and 12 is recuperated by the compressors and exchanged with the heat in the module. It can be seen that all the self-heat is exchanged. As a result, the exergy loss of the heat exchangers can be minimized and the energy required by the distillation process is reduced to 1/6-1/8 of that required by the conventional, heat-exchanged distillation process. To examine the energy required, the temperature difference of heat exchangers between cold and hot streams is an important parameter. In fact, to increase this, the heat transfer surface area can be decreased. To achieve industrial self-heat recuperative distillation processes, further investigation of the minimum temperature difference in the heat exchangers is required, especially the difference of the heat types of the streams in the heat exchanger (e.g. sensible heat and latent heat).

As industrial applications of this self-heat recuperative distillation processes, Kansha et al. (2010c) examined the energy saving efficiency of an integrated bioethanol distillation process using an azeotropic distillation method as compared with the conventional azeotropic distillation processes. In this paper, the energy required for the proposed integrated processes using self-heat recuperative distillation was only 1/8 of the conventional process, leading to a dramatic reduction in the production cost of bioethanol. They also applied it to the cryogenic air separation process and examined the energy required compared with the conventional cryogenic air separation for an industrial feasibility study (Kansha et al. 2011a). In that paper, the conventional cryogenic air separation was well integrated on the basis of the heat required to decrease the temperature to near -200 °C, especially, and they pointed out that a cryogenic air separation is a kind of multi-effect distillation column. However, there was potential for a 40% energy reduction by using self-heat recuperative distillation. Furthermore, the authors applied it to a well-known and recently developed energy saving distillation process, an internally heat integrated distillation column (HIDiC). In HIDiC, the distillation column can be divided into two sections (the rectification section and the stripping section) and the condensation heat is exchanged with the vaporization heat between these two sections using

the pressure difference. Designing this based on self-heat recuperation technology shows further energy saving (Kansha et al. 2011b). From these three industrial case studies, self-heat recuperation technology can be applied to recently developed heat recovery distillation processes such as heat integrated distillation processes, multi-effect distillation processes and HiDiC processes. Finally, to examine the feasibility of self-heat recuperation for industrial processes in the petrochemical industry, Matsuda et al. (2011) applied it using practical industrial data and modified the stream lines to enable practical processes and examined the energy required, exergy destruction and economical efficiency. From these studies, it can be concluded that the self-heat recuperative distillation process is very promising for saving energy.

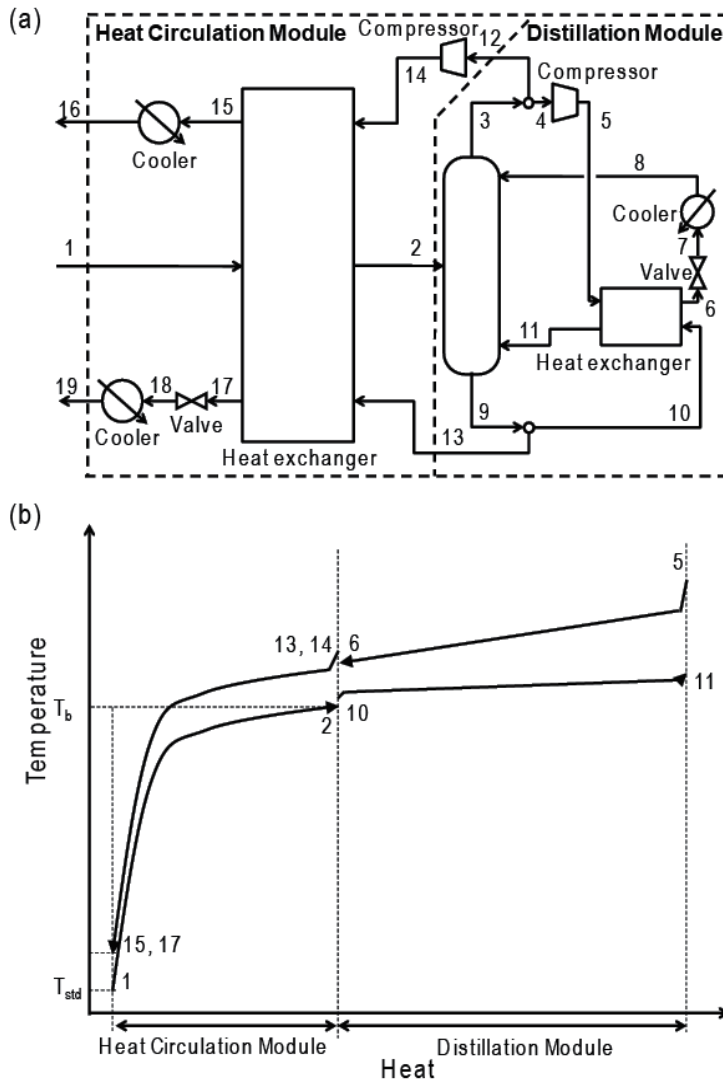


Fig. 3. Self-heat recuperative distillation process a) process flow diagram, b) temperature-heat diagram.

2.2.2 Self-heat recuperative drying process

Drying is usually conducted to reduce transportation costs by decreasing product weight and size, giving long-term storage stability and increasing the thermal efficiency in thermochemical conversion processes. Unfortunately, drying is one of the most energy intensive processes owing to the high latent heat of water evaporation. Theoretically, assuming an ambient temperature of 15 °C, the energy required for water evaporation ranges from 2.5 to 2.6 MJ per kg evaporated water, depending on the wet bulb temperature (Brammer & Bridgwater 1999). There are two important points regarding reduction of energy consumption during drying: (i) intensification of heat and mass transfer inside the dryer and (ii) efficient heat recovery and energy utilization (Strumillo et al. 2006). Concerning the latter, several methods have been developed to improve energy saving during drying, including heat recovery with and without flue gas recirculation, heat pumps, and pinch technology. However, these systems cannot effectively recover all the heat of the drying medium, the evaporated water, and the dried products.

To improve the energy efficiency in drying, Aziz et al. (2011a, 2011b) have recently developed a drying process based on self-heat recuperation technology. In this technology, the hot stream is heated by compression to provide a minimum temperature difference required for heat pairing and exchange with the cold stream and all of the self-heat of the process stream is recirculated based on exergy recuperation. As a result, all of the heat involved in drying can be recuperated and reused as a heat source for the subsequent drying process. This includes recuperation of sensible heat from the gas serving as the drying medium, both sensible and latent heat of the evaporated water and the sensible heat of the dried products. A process diagram for brown coal drying based on self-heat recuperation technology is shown in Fig. 4 (a). A fluidized bed dryer with an immersed heat exchanger is selected as the evaporator owing to its high heat transfer coefficient, excellent solid mixing, and uniform temperature distribution (Wan Daud, 2008, Law & Mujumdar 2009). Wet brown coal is fed and heated through a pre-heater (dryer 1a) to a given temperature. Subsequently, the main drying stage (water evaporation) is performed inside the fluidized bed dryer (dryer 2), where evaporation occurs. The immersed heat exchangers, which are filled by a compressed mixture of air and steam, are immersed inside the fluidized bed, providing the heat required for water removal. The exhausted mixture of air and steam is then compressed to achieve a higher exergy rate before it is circulated back and utilized as the heat source for evaporation (dryer 2) and pre-heating (dryer 1a, dryer 1b), in that order. In addition, the sensible heat of the hot, dried brown coal is recovered by the drying medium, to further reduce drying energy consumption (dryer 1c).

The heat exchange inside the fluidized bed dryer is considered to be co-current because the bed is well mixed and the minimum temperature approach depends on the outlet temperature of the hot streams (compressed air-steam mixture) and the temperature of the bed.

Figure 4 (b) shows a temperature-enthalpy diagram for the self-heat recuperative brown coal drying. Almost all of the heat is recovered, leading to a significant reduction in the total energy consumption. The largest amount of heat recuperation occurs in dryer 2, which involves the heat exchange between the condensation heat of the compressed air-steam mixture and the evaporation heat of the water in the brown coal. The heat curves of the hot

and cold streams, especially in dryer 2, are almost parallel owing to the efficient heat pairing within the dryer.

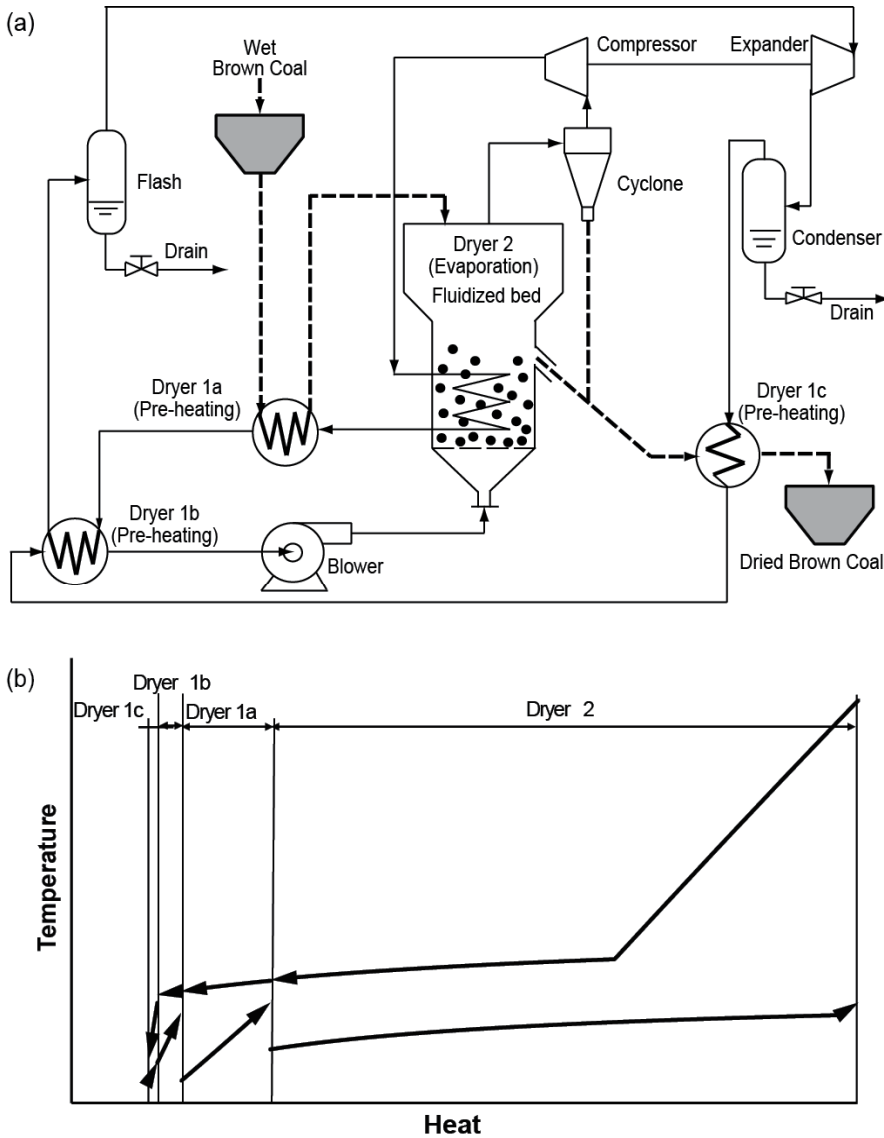


Fig. 4. Self-heat recuperative brown coal drying (a) process flow diagram, (b) temperature-heat diagram.

This drying process can reduce the total energy consumption to about 75% of that required for hot air drying using conventional heat recovery. Furthermore, as the heat required for water evaporation is provided by the condensation of the compressed air-steam mixture, the inlet air temperature is considerably lower, leading to safer operation due to reduced risk of fire or explosion.

In addition, the thermodynamic model of heat exchange inside the fluidized bed is shown in Fig. 5. The compressed air-steam mixture flows inside a heat transfer tube immersed in the fluidized bed dryer. Thus, in-tube condensation occurs and heat is transferred to the bed via the tube wall and is finally transferred from the bed to the brown coal particles.

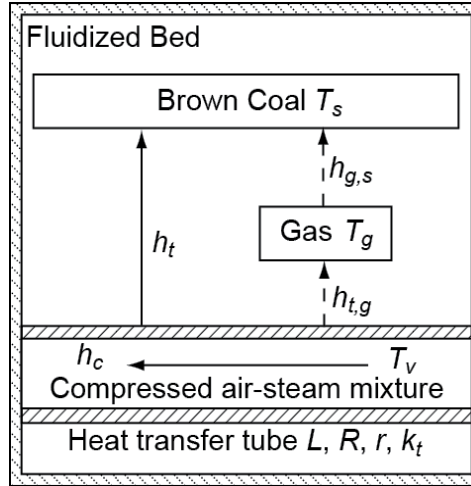


Fig. 5. Model of heat transfer inside the fluidized bed dryer.

The heat transfer rate from the compressed vapor inside the heat transfer tube to the drying sample in FBD, q_s , can be approximated as:

$$q_s = UA(T_v - T_s) \quad (1)$$

Also, because the heat exchange inside the fluidized bed dryer involves convection and conduction, the product of the overall heat transfer coefficient, U , and surface area, A , may be approximated by equation (2).

$$\frac{1}{UA} = \frac{1}{A_c \alpha_c} + \frac{\ln\left(\frac{R}{r}\right)}{2\pi L \lambda_t} + \frac{1}{\alpha_t A_t} \quad (2)$$

The first term of the right side of equation (2) represents the heat transfer resistance of vapor condensation inside the tube. A_c and α_c are the inner surface area of the tube and the heat transfer coefficient, respectively. The second term corresponds to the conductive heat transfer through the tube wall having the thermal conductivity, inner radius and outer radius of λ_t , r and R , respectively. Convective heat transfer from the outer tube surface to the brown coal particles inside the bed is expressed by the third term, in which the convective heat transfer coefficient and the outer surface area of the tube are α_t and A_t , respectively.

The heat transfer coefficient on a horizontal tube immersed inside the fluidized bed has been reported by Borodulya (1989, 1991):

$$Nu_t = 0.74 Ar^{0.1} \left(\frac{\rho_s}{\rho_g}\right)^{0.14} \left(\frac{C_s}{C_g}\right)^{0.24} (1-\varepsilon)^{2/3} + 0.46 Re Pr \frac{(1-\varepsilon)^{2/3}}{\varepsilon} \quad (3)$$

$$Nu_t = \frac{\alpha_t d_s}{\lambda_g} \quad (4)$$

The heat transfer coefficient of the condensing vapor is calculated using a general correlation proposed by Shah (1979):

$$\alpha_c = \frac{0.023 Re_1^{0.8} Pr_1^{0.4} \lambda_l}{2r} \left[(1-x)^{0.8} + \frac{3.8x^{0.76} (1-x)^{0.04}}{(p/p_{crit})^{0.38}} \right] \quad (5)$$

2.2.3 Self-heat recuperative CO₂ absorption process

Carbon capture and storage (CCS) has attracted significant attention in the past two decades to reduce greenhouse gas emissions and mitigate global warming. CCS consists of the separation of CO₂ from industrial and energy-related sources, transportation of CO₂ to a storage location and long-term isolation of CO₂ from the atmosphere (Rubin et al. 2005).

It is reported that the most significant stationary point sources of CO₂ are power generation processes. In fact, the amount of CO₂ emission from power generation processes comprises 40% of global CO₂ emissions (Rubin et al. 2005, Toftegaard, 2010). For power generation, there are three different types for CO₂ capture processes: post-combustion, pre-combustion and oxy-fuel combustion (Rubin et al. 2005). In this section, the CO₂ absorption process for post-combustion is used as a case study (Fig. 6).

Post-combustion capture in power plants is generally used for pulverized-coal-fired power plants. The CO₂ concentration in post-combustion is low compared with the other two CO₂ capture processes: around 10% (wet base). The CO₂ capture is generally performed through chemical absorption with monoethanolamine (MEA).

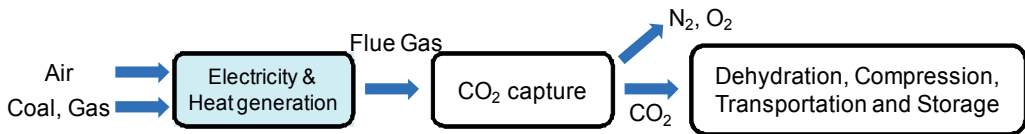


Fig. 6. Post-combustion capture.

Figure 7 shows a diagram of the conventional CO₂ absorption process, which consists of an absorber, a heat exchanger (HX) for heat recovery and a stripper (regenerator) with a reboiler. The flue gas and a 'lean CO₂ concentration' amine solution (lean amine) are fed into the absorber, and CO₂ gas is absorbed into the lean amine. This amine solution containing absorbed CO₂ is called the 'rich CO₂ concentration' amine solution (rich amine). Exhaust gases are discharged from the top of the absorber. The rich amine is fed into the stripper through the HX and then lean amine is regenerated and the CO₂ gas is stripped by heating in the reboiler of the stripper. In the conventional absorption process using MEA, the heat (4.1 GJ/t-CO₂) is supplied by the reboiler in the stripper. The ratio of this heat for regeneration and vaporization is 1:1. From Fig. 7, it can be understood that a part of sensible heat is recovered from lean amine using the HX. However, the heat of vaporization cannot be recovered from heat of steam condensation for stripping in the reboiler because of the

temperature difference between the condenser and the reboiler. Thus, CO₂ capture is the most costly and high energy consumption process of power generation, leading to higher CO₂ emissions. In fact, it is reported that this process drops the net efficiency of the power plant by about 10% (Damen 2006, Davison 2007).

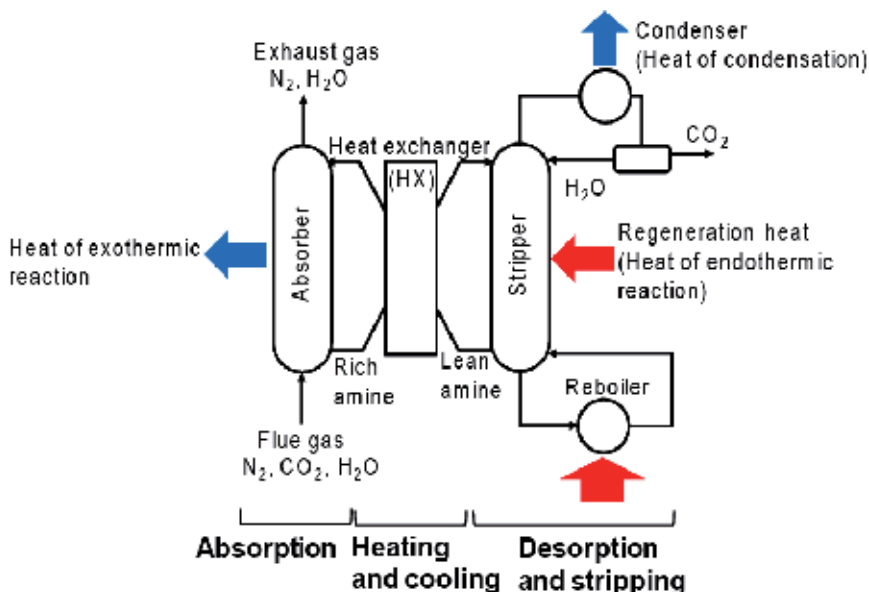


Fig. 7. Conventional CO₂ absorption process.

If all process heat (sensible heat, latent and reaction heat) can be recirculated into the process, the energy required for CO₂ capture can be greatly reduced. To achieve perfect internal heat circulation, a self-heat recuperation technology was applied to the CO₂ absorption process and a self-heat recuperative CO₂ absorption process was proposed, as shown in Fig. 8 (a) (Kishimoto et al. 2011). In this process, the aforementioned self-heat recuperative distillation module in 2.2.1 can be applied to the stripping section (A) in Fig. 8 (a). A mixture of CO₂ and steam is discharged from the top of stripper and compressed adiabatically by a compressor to recuperate the steam condensation heat. This recuperated heat is exchanged with the heat of vaporization for stripping in the reboiler, leading to a reduction in the energy consumption for stripping.

In the section B in Fig. 8 (a), the aforementioned heat circulation module in 2.2.1 can be applied, and furthermore the heat of the exothermic reaction generated at low temperature in the absorber is transported and reused as reaction heat for solution regeneration at high temperature using a reaction heat transformer (RHT). This RHT is a type of closed-cycle compression system with a volatile fluid as the working fluid and consists of an evaporator to receive heat from the heat of exothermic reaction in the absorber, a compressor with driving energy, a condenser to supply heat to the stripper as heat of the endothermic reaction, and an expansion valve. The heat of the exothermic absorption reaction at the evaporator in the absorber is transported to the endothermic desorption reaction in the condenser of the stripper by the RHT. Therefore, both the heat of the exothermic absorption reaction in the absorber and the heat of steam condensation from the condenser in the

stripper are recuperated and reused as the reaction heat for solution regeneration and the vaporization heat for CO₂ stripping in the reboiler of the stripper.

As a result, the proposed self-heat recuperative CO₂ absorption process can recirculate the entire process heat into the process and reduce the total energy consumption to about 1/3 of the conventional process.

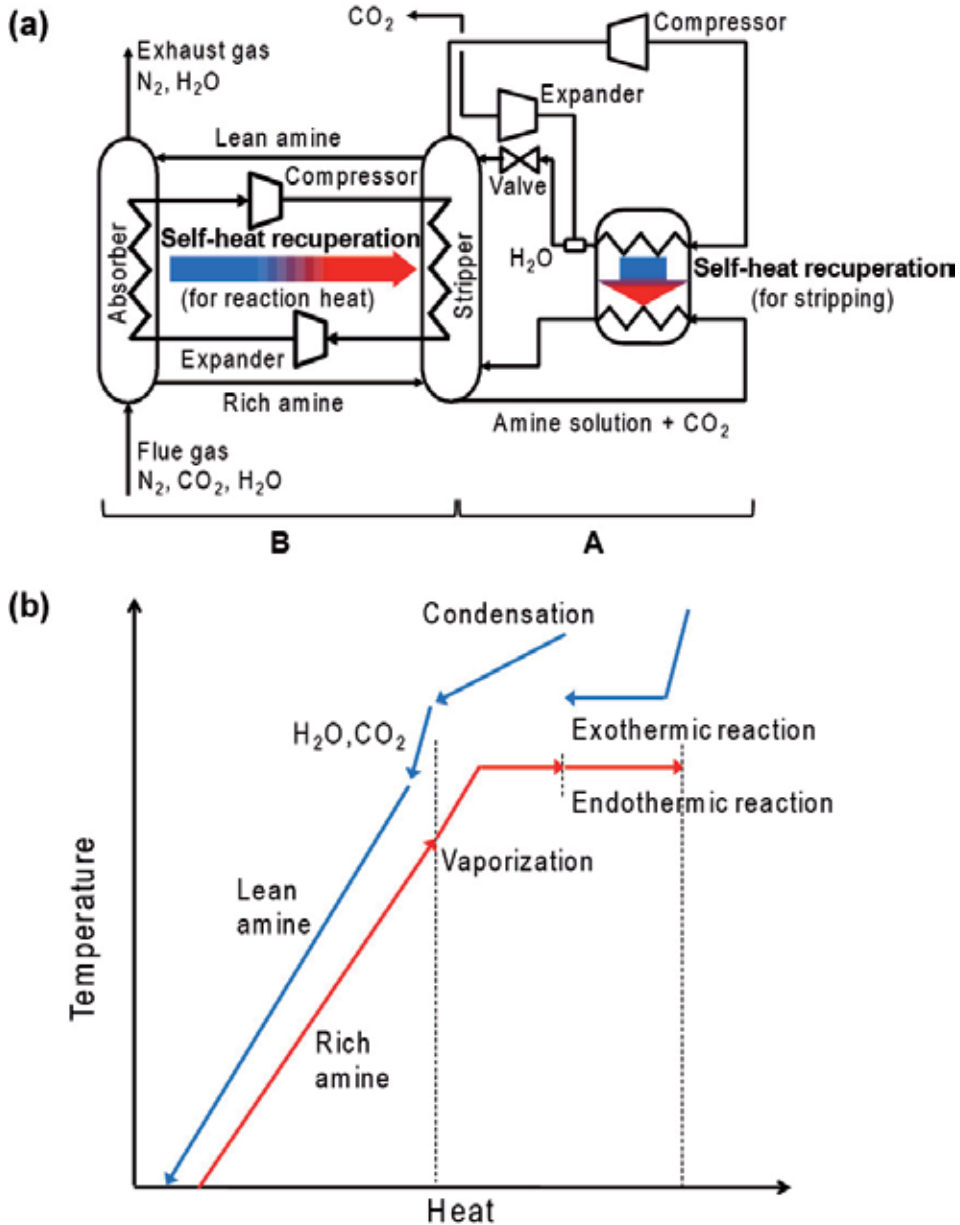


Fig. 8. Self-heat recuperative CO₂ absorption process, (a) process flow diagram, (b) temperature-heat diagram.

3. Conclusion

In this chapter, a newly developed self-heat recuperation technology, in which not only the latent heat but also the sensible heat of the process stream can be circulated without heat addition, and the theoretical analysis of this technology were introduced. Several industrial application case studies of the technology were then presented and compared with their conventional counterparts. Although these processes require the power to circulate the process self heat instead of fuel for the furnace heater, a large amount of the energy required can be eliminated. Furthermore, to integrate the proposed self-heat recuperative processes with power generation plants, some amount of the power required can be generated from surplus fuel and energy, leading to achievement to co-production of products and power. Finally, this self-heat recuperation technology is a very promising technology for suppressing global warming and reducing the use of fossil fuels.

4. Nomenclature

A	Surface area (m^2)
Ar	Archimedes number (dimensionless)
C	specific heat capacity ($\text{J kg}^{-1} \text{K}^{-1}$)
d	diameter (m)
h	heat transfer coefficient ($\text{W m}^{-2} \text{K}^{-1}$)
k	thermal conductivity ($\text{W m}^{-1} \text{K}^{-1}$)
L	tube length (m)
Nu	Nusselt number (dimensionless)
p	pressure (kPa)
Pr	Prandtl number (dimensionless)
R	outer diameter (m)
Re	Reynolds number (dimensionless)
r	inner diameter (m)
q	heat transfer rate (W)
T	temperature (K)
U	overall heat transfer ($\text{W m}^{-2} \text{K}^{-1}$)
x	vapor quality (dimensionless)

Greek letters

α	heat transfer coefficient ($\text{W m}^{-2} \text{K}^{-1}$)
ε	void fraction (dimensionless)
λ	thermal conductivity ($\text{W m}^{-1} \text{K}^{-1}$)
ρ	density (kg m^{-3})

Subscripts

b	boiling point
c	condensation
crit	critical
g	gas

l	liquid
s	particle sample
std	standard condition
t	heat transfer tube
v	vapor

5. References

- Aziz, M.; Fushimi, C.; Kansha, Y.; Mochidzuki, K.; Kaneko, S.; Tsutsumi, A.; Matsumoto, K.; Hashimoto, T.; Kawamoto, N.; Oura, K.; Yokohama, K.; Yamaguchi, Y. & Kinoshita, M. (2011). Innovative Energy-Efficient Biomass Drying Based on Self-Heat Recuperation Technology. *Chemical Engineering and Technology*, Vol.34, No.7, pp. 1095-1103, ISSN 1521-4125
- Aziz, M.; Kansha, Y. & Tsutsumi, A. (2011). Self Heat Recuperative Fluidized Bed Drying of Brown Coal. *Chemical Engineering and Processing: Process Intensification*, Vol.50, No.9, pp. 944-951, ISSN 0255-2701
- Borodulya, V.A.; Teplitsky, Y.S.; Sorokin, A.P.; Matsnev, V.V.; Markevich, I.I. & Kovenskii, V.I. (1989). External Heat Transfer in Polydispersed Fluidized Beds at Elevated Temperatures. *Journal of Engineering Physics and Thermophysics*, Vol.56, No.5, (May 1989), pp. 541-546, ISSN 1062-0125
- Borodulya, V.A.; Teplitsky, Y.S.; Sorokin, A.P.; Markevich, I.I.; Hassan, A.F. & Yeryomenko, T.P. (1991). Heat Transfer between a Surface and a Fluidized Bed: Consideration of Pressure and Temperature Effects. *International Journal of Heat and Mass Transfer*, Vol.34, No.1, pp. 47-53, ISSN 0017-9310
- Brammer, J.G. & Bridgwater, A.D. (1999). Drying Technologies for an Integrated Gasification Bio-Energy Plant. *Renewable and Sustainable Energy Reviews*, Vol.3, No.4, pp. 243-289, ISSN 1364-0321
- Eastop, T.D. & Croft, D.R. (1990). *Energy Efficiency for Engineers and Technologists*, Longman Scientific & Technical, ISBN 0-582-03184-2, London, UK
- Ebrahim, M. & Kawari, A. (2000). Pinch Technology: An Efficient Tool for Chemical-Plant and Capital-Cost Saving, *Applied Energy*, Vol. 65, No. 1-4, pp. 45-49 ISSN 0306-2619
- Cerda, J.; Westerberg, A. W.; Mason, D. & Linnhoff, B. (1983) Minimum Utility Usage in Heat Exchanger Network Synthesis, *Chemical Engineering Science*, Vol. 38, No. 3, pp. 371-387, ISSN 0009-2509
- Chengqin, R.; Nianping, L. & Guangfa, T. (2002). Principle of Exergy Analysis in HVAC and Evaluation of Evaporative Cooling Schemes, *Building and Environment*, No. 37, No. 11, pp. 1045-1055, ISSN 0360-1323
- Damen, K.; Troost, V.M.; Faaij, A. & Turkenburg, W. (2006). A Comparison of Electricity and Hydrogen Production Systems with CO₂ Capture and Storage. Part A: Review and Selection of Promising Conversion and Capture Technologies, *Progress in Energy and Combustion Science*, Vol. 32, No. 6, pp. 215-246, ISSN 0360-1285

- Davison, J. (2007) Performance and Costs of Power Plants with Capture and Storage of CO₂. *Energy*, Vol. 32, No. 7, pp.1163-1176, ISSN 0360-5442.
- Grubbström, R. W. (2007). An Attempt to Introduce Dynamics into Generalized Exergy Consideration, *Applied Energy*, Vol. 84, No. 7-8, pp. 701-718, ISSN 0306-2619
- Rubin, E.; Myer, L. & de Coninck, H., (2005). Technical Summary, In Carbon Dioxide Capture And Storage:, Metz, B., Davidson, O.; de Coninck, H.; Loos, M. & Meyer, L., (Ed.), 17-50, Cambridge University Press, ISBN 13 978-0-521-68551-1, New York, USA
- Kansha, Y.; Tsuru, N.; Sato, K.; Fushimi, C. & Tsutsumi, A. (2009). Self-Heat Recuperation Technology for Energy Saving in Chemical Processes, *Industrial and Engineering Chemistry Research*, Vol. 48, No. 16, pp.7682-7686, ISSN 0888-5885
- Kansha, Y.; Tsuru, N.; Fushimi, C.; Shimogawara, K. & Tsutsumi, A. (2010a). An Innovative Modularity of Heat Circulation for Fractional Distillation, *Chemical Engineering Science*, Vol. 65, No.1, pp.330-334, ISSN 0009-2509
- Kansha, Y.; Tsuru, N.; Fushimi, C. & Tsutsumi, A. (2010b). Integrated Process Module for Distillation Processes Based on Self-Heat Recuperation Technology, *Journal of Chemical Engineering of Japan*, Vol. 43, No. 6, pp. 502-507, ISSN 0021-9592
- Kansha, Y.; Tsuru, N.; Fushimi, C. & Tsutsumi, A. (2010c). New Design Methodology Based on Self-Heat Recuperation for Production by Azeotropic Distillation, *Energy & Fuels*, Vol. 24, No. 11, pp. 6099-6102, ISSN 0887-0624
- Kansha, Y.; Kishimoto, A.; Nakagawa, T. & Tsutsumi, A (2011a). A Novel Cryogenic Air Separation Process Based on Self-Heat Recuperation, *Separation and Purification Technology*, Vol. 77, No. 3, pp. 389-396, ISSN 1383-5866
- Kansha, Y.; Kishimoto, A. & Tsutsumi, A (2011b). Process Design Methodology for High-Energy Saving HiDiC Based on Self-Heat Recuperation, *Asia-Pacific Journal of Chemical Engineering*, Vol. 6, No. 3, pp. 320-326, ISSN 1932-2143
- Kemp, I.C. (2007). *Pinch Analysis and Process Integration A User Guide on Process Integration for the Efficient Use of Energy 2nd Ed.*, Elsevier, ISBN 13 978-0-75068-260-2, Oxford, UK
- Kishimoto, A.; Kansha, Y.; Fushimi, C. & Tsutsumi, A. (2011). Exergy Recuperative CO₂ Gas Separation in Post-Combustion Capture, *Industrial and Engineering Chemistry Research*, Vol. 50, No. 17, pp. 10128-10135, ISSN 0888-5885
- Kuchonthara, P. & Tsutsumi, A. (2003). Energy-Recuperative Biomass Integrated Gasification Power Generation System, *Journal of Chemical Engineering, Japan*, Vol. 36, No. 7, pp. 846-851, ISSN 0021-9592
- Kuchonthara, P.; Bhattacharya, S. & Tsutsumi, A. (2005). Combination of Thermochemical Recuperative Coal Gasification Cycle and Fuel Cell for Power Generation, *Fuel*, Vol. 84, No. 7-8, pp. 1019-1021, ISSN 0016-2361
- Kuchonthara, P. & Tsutsumi, A. (2006). Energy-Recuperative Coal-Integrated Gasification/Gas Turbine Power Generation System, *Journal of Chemical Engineering, Japan*, Vol. 39, No. 5, pp. 545-552. ISSN 0021-9592

- Lampinen, M. J. & Heillinen, M. A. (1995). Exergy Analysis for Stationary Flow Systems with Several Heat Exchange Temperatures, *International Journal of Energy Research*, Vol. 19, No. 5, pp. 407-418, ISSN 1099-114X
- Law, C. & Mujumdar, A.S. (2009). Fluidize Bed Dryers, In: *Handbook of Industrial Drying*, A.S. Mujumdar, (Ed.), 173-202, CRC Press, ISBN 978-157-4446-68-5, Florida, USA
- Linnhoff, B.; Mason, D.R. & Wardle, I. (1979). Understanding Heat Exchanger Networks, *Computers & Chemical Engineering*, Vol. 3, No. 1-4, pp. 295-302, ISSN 0098-1354
- Linnhoff, B. & Hindmarsh, E. (1983). The Pinch Design Method for Heat Exchanger Networks, *Chemical Engineering Science*, Vol. 38, No. 5, pp. 745-763. ISSN 0009-2509
- Linnhoff, B. (1993) Pinch Analysis-A State-of-the-Art Overview, *Chemical Engineering Research & Design*, Vol. 71, No. A5, pp. 503-522, ISSN 0263-8762
- Linnhoff, B. & Eastwood, A.R. (1997). Overall Site Optimization by Pinch Technology. *Chemical Engineering Research & Design*, Vol. 75, pp. S138-S144, ISSN 0263-8762
- Matsuda, K.; Kawazuishi, K.; Hirochi, Y.; Sato, R.; Kansha, Y.; Fushimi, C.; Shikatani, Y.; Kunikiyo, H. & Tsutsumi, A. (2010). Advanced Energy Saving in the Reaction Section of the Hydro-Desulfurization Process with Self-Heat Recuperation Technology, *Applied Thermal Engineering*, Vol. 30, No. 16, pp. 2300-2305, ISSN 1359-4311
- Matsuda, K.; Kawazuishi, K.; Kansha, Y.; Fushimi, C.; Nagao, M.; Kunikiyo, H.; Masuda, F. & Tsutsumi, A. (2011). Advanced Energy Saving in Distillation Process with Self-Heat Recuperation Technology, *Energy*, Vol. 36, No. 8, pp. 4640-4645, ISSN 0360-5442
- Riemer, P. W. F. & Ormerod, W.G. (1995). International Perspectives and the Results of Carbon Dioxide Capture Disposal and Utilization Studies, *Energy Conversion and Management*, Vol. 36, No. 6-9, pp. 813-818, ISSN 0196-8904
- Seider, W.D.; Seader, J.D. & Lewin D.R. (2004). *Product & Process Design Principles Synthesis, Analysis, and Evaluation 2nd Ed.*, John Wiley & Sons, ISBN 0-471-45247-5, New York, USA
- Shah, M.M. (1979). A General Correlation for Heat Transfer during Film Condensation inside Pipes. *International Journal of Heat and Mass Transfer*, Vol.22, No.4, pp. 547-556, ISSN 0017-9310
- Som, S. K. & Datta, A. (2008). Thermodynamic Irreversibilities and Exergy Balance in Combustion Processes, *Progress in Energy Combustion Science*, Vol. 34, No. 3, pp. 351-376, ISSN 0360-1285
- Strumillo, C.; Jones, P.L. & Zylla, R. (2009). Energy Aspects in Drying, In: *Handbook of Industrial Drying*, A.S. Mujumdar, (Ed.), 1075-1101, CRC Press, ISBN 978-157-4446-68-5, Florida, USA
- Toftegaard, MB.; Brix, J.; Jensen, P.A.; Glarborg, P. & Jensen, A.D. (2010). Oxy-Fuel Combustion of Solid Fuels, *Progress in Energy and Combustion Science*, Vol. 36, No. 5, pp. 581-625, ISSN 0360-1285

Wan Daud, W.R. (2008). Fluidized Bed Dryers-Recent Advances. *Advanced Powder Technology*, Vol.19, No.5, pp. 403-418, ISSN 0921-8831

Development of High Efficiency Two-Phase Thermosyphons for Heat Recovery

Ignacio Carvajal-Mariscal, Florencio Sanchez-Silva and Georgiy Polupan
*National Polytechnic Institute of Mexico
Mexico*

1. Introduction

Due to high fuel prices, it has become necessary to investigate new methods for saving and more efficient use of energy, emphasizing the use of energy remaining in the waste gases of combustion equipment. For this reason, in the last five decades there has been an important technological development in heat transfer equipment, to promote changes in configuration and applying heat transfer systems with high effectiveness. One example is the use of two-phase thermosyphons (Azada et al., 1985; Faghri, 1995; Gershuni et al., 2004; Noie, 2005; Peterson, 1994; Reay, 1981).

A two-phase thermosyphon is a device that is used for heat transfer; this process occurs inside it as a cycle of evaporation and condensation of a working fluid (Faghri, 1995; Peterson, 1994). This device is easily constructed, has no moving parts inside and works individually. The two-phase thermosyphon consists of: condensation, evaporation and adiabatic zones (Figure 1). Operation starts when heat is supplied to the evaporator zone, so a portion of the fluid evaporates, taking the latent heat of evaporation inside the tube up to the condenser section. In this last section, vapor condenses and transfers its latent heat of condensation to the surroundings. The condensate runs down as a film on the inner wall of the tube with the aid of gravity.

There have been conducted several investigations in the field of thermosyphon design and development. The authors of reference (Park et al., 2002) studied the heat transfer characteristics depending on the amount of working fluid and when the operation limits occur. The two-phase element was made of copper and as working fluid FC-72 (C14 F14) was used. The thermosyphon was subjected to a heat supply in the range of 50-600 W and with 10-70% load rate. For the convection coefficients in the condenser and in the evaporator, the authors used the theory of Nusselt and Roshenow respectively. They found that the operation limits manifest in different forms depending on the loading rate of the fluid. For small loading rates ($\Psi = 10\%$) the drying limit occurs in the evaporator, while for high loading rates ($\Psi = 50\%$) is the flooding limit that appears. In the first case, evaporator temperature increases from the evaporator bottom; in the second case the evaporator temperature increases at the top of the evaporator. These conclusions were made by observing the temperature distribution along the thermosyphon. Moreover, (Zuo & Faghri, 2002) conducted an analytical and experimental research on the thermodynamic behavior of the working fluid in a thermosyphon and a heat pipe, using a temperature-entropy diagram.

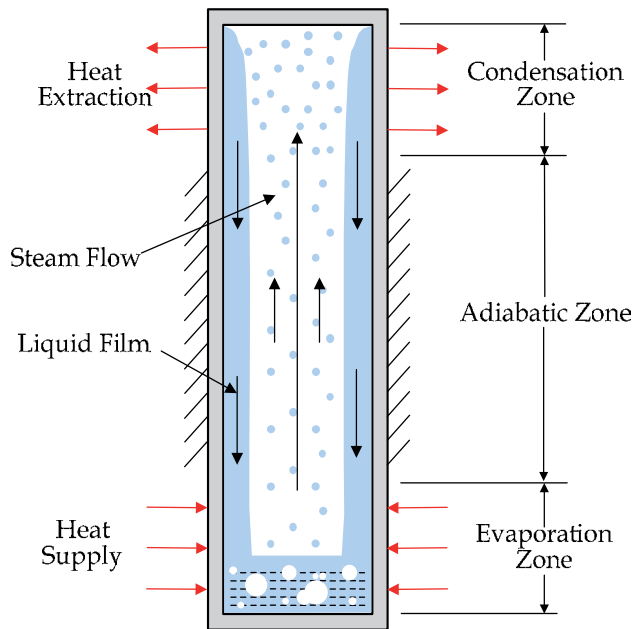


Fig. 1. Two-phase thermosyphon.

The authors divide the thermodynamic processes in 2 categories: 1) heat transfer by conduction through the tube wall and 2) heat and mass transfer, by convection inside the two-phase thermosyphon. (Noie, 2005) presented in his work an experimental study of a thermosyphon (980 mm of length and an internal diameter of 25 mm) made of copper and smooth inside, using distilled water as a working fluid. The goal of the study was to obtain the thermal characteristics of the thermosyphon (temperature distribution in the outer wall and all along the tube, boiling heat transfer coefficient and the maximum heat transfer rate), varying 3 parameters: heat supply ($100 < Q < 900$ W), loading rate ($30\% \leq \Psi \leq 90\%$) and length of the evaporator (varying the length of electrical resistance).

From above mentioned, it follows that in order to design high efficiency heat recovery equipment based on two-phase thermosyphons, there should be solved first the main issues inherent to their manufacture: loading rate, maximum heat transfer rate, and compatibility between material of container and the working fluid. In order to address these issues, an analytical-experimental investigation has been carried out in the Thermal Engineering and Applied Hydraulics Laboratory, for the last four years. Following are presented the results of this investigation.

2. Design and manufacture

The design and manufacture of a thermosyphon is a complex process because there should be considered several parameters such as length, shape, weight and volume of the device, heat load, transport distance, ratio of lengths between evaporator and condenser, acceptable temperature gradients, temperature range of operation, amount of working fluid, service life and safety. Of course, the working fluid thermophysical properties and the manufacturing material properties should be taken into account as key variables.

Because there are no standards in the public domain for the manufacture and design of two-phase thermosyphons is necessary to develop the methodologies to design them. Following are described three methodologies for the calculation of key parameters used in the design and manufacture of two-phase thermosyphons. For the development of these methodologies water was considered as the working fluid.

The first parameter to calculate is the relation between the lengths of the zones of evaporation and condensation, and the total length of the thermosyphon. From this relation it can be obtained the total length of the thermosyphon for certain heat recovery equipment.

For security reasons, one of the most important parameters to be calculated is the working pressure of thermosyphon under different operation conditions and for distinct amounts of working fluid in the thermosyphon. These working pressures of the internal fluid are: the pressure when the device is off, i.e., when the thermosyphon is at room temperature, this is when the device is in non-operating conditions (transportation, storage, etc.), and the operating pressure.

The third parameter is the evaporation rate of the working fluid in the process of loading the thermosyphon. This process is directly related to the procedure of loading the working fluid to the thermosyphon, which was implemented in this research.

2.1 Relations between the lengths of the areas of air and gases and the total length of the thermosyphon

Heat recovery equipment based on two phase thermosyphons consists of an outer envelope with thermosyphons grouped inside. According to the principle of operation of the thermosyphons (evaporation/condensation of a working fluid) heat is transferred from the evaporator, located at the bottom where the combustion hot gases flow, to the condenser, located at the top, where the fluid to be heated circulates. Thus, the hot gases flowing through the evaporation zone, transferring the heat from that zone to the condensation zone through the thermosyphons. On the other hand, the gases to be heated, for example air, flow in the opposite direction through the condensation zone absorbing the heat dissipated by the thermosyphons.

It can be considered that the efficiency of the thermosyphon is 95%, that is, 95% of heat of combustion gases is transferred into the condensation zone for heating the air. The energy balance for steady state conditions may be expressed as:

$$\dot{m}_a c_{pa} (T_{a,out} - T_{a,in}) = \dot{m}_g c_{pg} (T_{g,in} - T_{g,out}) \quad (1)$$

Applying the continuity equation gives the expression (2).

$$\rho_a A_a v_a c_{pa} (T_{a,out} - T_{a,in}) = \rho_g A_g v_g c_{pg} (T_{g,in} - T_{g,out}) \quad (2)$$

In addition, the area for the passage of air, A_a , is defined as the product of the length of the thermosyphon condensation zone, l_c , by the width of the passage of air, a :

$$A_a = l_c a \quad (3)$$

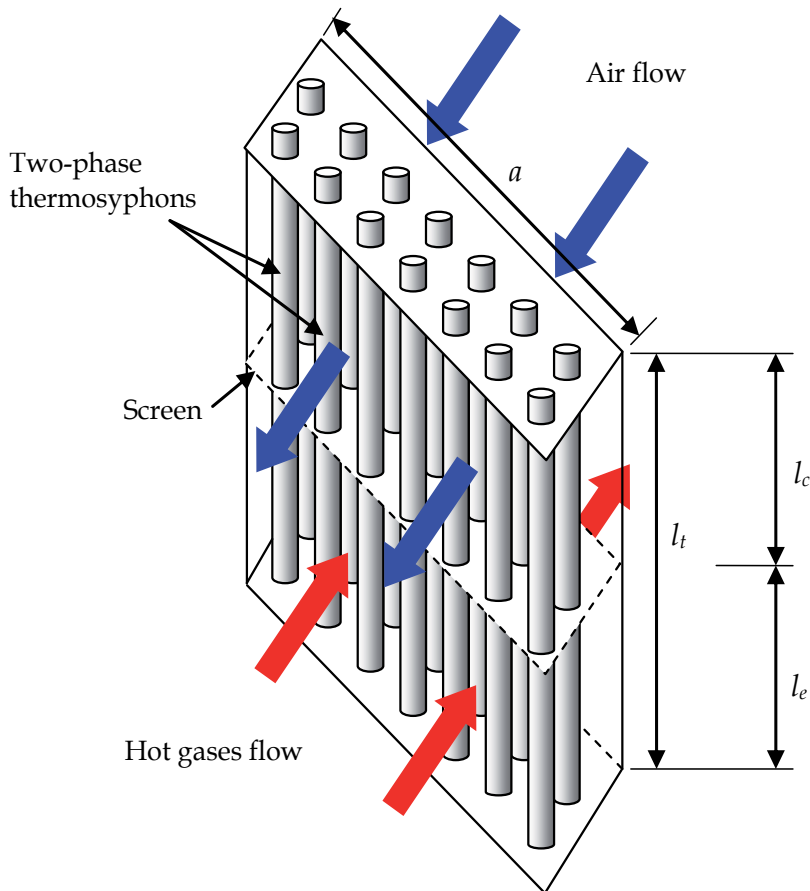


Fig. 2. Gas-gas type heat transfer equipment. Total, evaporation zone and condensation zone characteristic lengths are shown.

Similarly, for the passage of hot gases

$$A_g = l_e a \quad (4)$$

Because the adiabatic zone is negligible, the total length of the thermosyphon is the sum of the lengths of the evaporation and condensation zones (5),

$$l_t = l_c + l_e \quad (5)$$

This methodology considers that the velocities of hot gases and air are equal and that the thermosyphon has an efficiency of 95%. In addition, the width of the passage of air is equal to the width of the passage of hot gases, which is the width of the air preheater, a . Taking these considerations into account and substituting equations (3) and (4) in equation (2) gives the expression (6)

$$\rho_a l_c c_{pa} (T_{a,out} - T_{a,in}) = 0.95 \rho_g l_e c_{pg} (T_{g,in} - T_{g,out}) \quad (6)$$

To determine one of the design parameters sought, which is the ratio between the length of the condensation zone and the total length of the thermosyphon, equations (5) and (6) are resolved simultaneously and following equation (7) is obtained.

$$\frac{l_c}{l_t} = \frac{0.95 \rho_g c_{pg} (T_{g,in} - T_{g,out})}{0.95 \rho_g c_{pg} (T_{g,in} - T_{g,out}) + \rho_a c_{pa} (T_{a,out} - T_{a,in})} \quad (7)$$

Knowing this, from equation (5) is obtained the relation between the length of the evaporation zone and the total length of the thermosyphon (8).

$$\frac{l_e}{l_t} = 1 - \frac{l_c}{l_t} \quad (8)$$

However, the equations developed above, consider only the energy and mass balances, this analysis could lead to violations of the second law of thermodynamics. To be sure that the results do not violate this law, the mathematical models to calculate the entropy production in the system are used. Just for recalling that the total entropy change must be greater than or equal to zero.

If the air is considered as an ideal gas and the isobaric heating process is reversible, then the entropy change of air is expressed as follows:

$$\Delta \dot{S}_a = \dot{m}_a c_{pa} \ln \left(\frac{T_{a,out}}{T_{a,in}} \right) \quad (9)$$

Similarly for combustion gases the entropy change is expressed as follows:

$$\Delta \dot{S}_g = \dot{m}_g c_{pg} \ln \left(\frac{T_{g,out}}{T_{g,in}} \right) \quad (10)$$

The expression to calculate the total entropy change of the system is as follows:

$$\Delta \dot{S}_{sys} = \Delta \dot{S}_g + \Delta \dot{S}_a \quad (11)$$

As an example, a parametric analysis to study the relationship of the lengths of the zones of evaporation and condensation with respect to the total length of the thermosyphon was carried out. The outlet temperatures of both air and combustion gases were varied. The air inlet temperature is assumed to be 25 °C and the combustion gases of 250 °C. The

investigated interval of the air outlet temperature is 35 °C to 105 °C. If temperature difference between the entrance and outlet of both air and gas are equal to 70 °C,

$$T_{a,out} - T_{a,in} = T_{g,in} - T_{g,out} = 70 \text{ °C} \quad (12)$$

so at the exit of the air preheater, outlet temperatures of air and hot gases are equal to $T_{a,out} = 95 \text{ °C}$ and $T_{g,out} = 180 \text{ °C}$. This requires that the ratios of the lengths of the zones must be 42% of l_t , as shown in Figure 3, and l_e must be 58% of the total length of the thermosyphon according to the equations (7) and (8).

2.2 Operating pressure

To determine the pressure during operation and non-operation of the thermosyphons, there were considered the loading ratios, and ambient temperature and pressure at which was done the loading process of the thermosyphon. The loading ratio is determined by

$$\Psi = V_f / V_t \quad (13)$$

After choosing the values of loading ratios, it can be obtained the working fluid volume; in this case is water, and therefore it may also be known the mass, m_f , of water that fills the thermosyphon. After the loading process of the thermosyphon, this mass of water, m_f , will fill the total internal volume of the thermosyphon, V_t , as steam and liquid, so the specific volume of water can be determined by the expression (14)

$$v_f = V_t / m_f \quad (14)$$

Upon completion of loading process of the thermosyphon, it is then sealed and exposed again to ambient temperature, therefore, the internal pressure drops to the design parameter called the non-operating pressure. From the tables of thermodynamic properties of water (Incropera & Dewitt, 2006) the value of the non-operating pressure is determined with the values of ambient temperature, T_{amb} , and the specific volume, v_f .

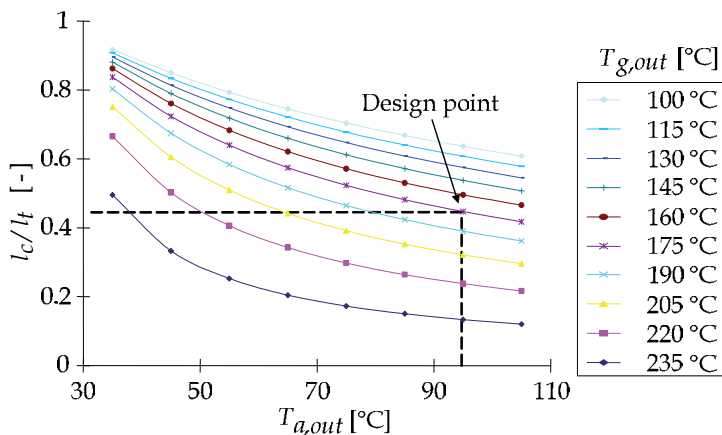


Fig. 3. Length of the condensation zone and total length versus the outlet air temperature, for different outlet temperatures of gases.

The operating pressure of the thermosyphon is also found in the tables of thermodynamic properties of water (Incropera & Dewitt, 2006), the specific volume of water was calculated with the equation (14), v_f , and operating temperature.

To calculate the operating pressure of the thermosyphon a parametric analysis was performed, where the variable parameter is the loading ratio. The interval of studied loading ratio is 5% to 45%. The geometric characteristics of the thermosyphon were taken as follows: length of 1 m and a diameter of 2.54 cm. The temperature of 20 °C and a pressure of 1 bar were the ambient conditions. It was considered that the maximum operating temperature of the thermosyphon is 250 °C.

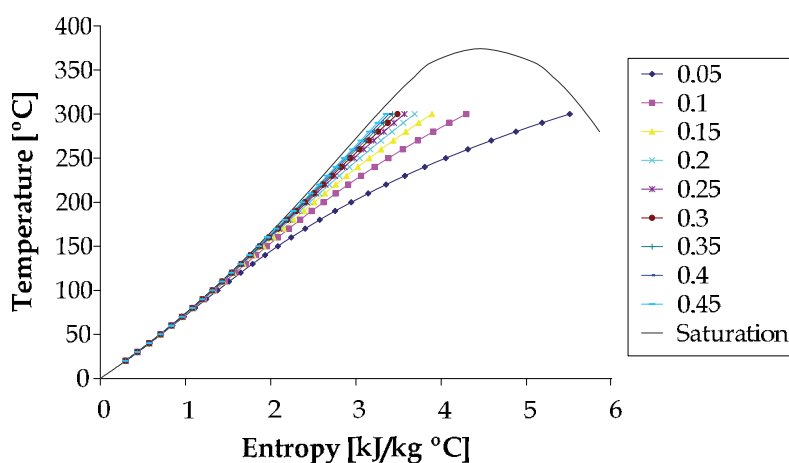


Fig. 4. T-s diagram of isochoric operation of the thermosyphon for different loading ratios.

Figure 4 shows in a T-s diagram the isochoric process that takes place in the thermosyphon for different loading ratios, from 5% to 45%.

As an example applying the described method a loading ratio of 10% is given, and the value of the specific volume of water that was obtained using equation (14) is 0.0100177 m³/kg. Therefore by exposing the thermosyphon at room temperature of 20 °C, after the loading process, the non-operating pressure is equal to 0.0233 bar. Table 1 shows the thermodynamic properties of water inside the thermosyphon. On the other hand, by bringing the thermosyphon to the operating temperature for an isochoric process, an operating pressure equal to 39.7 bar is achieved. Table 1 shows the properties for the operating temperature of 250 °C and the specific volume of 0.0100177 m³/kg.

T (°C)	p (bar)	v (m ³ /kg)	H kJ/kg	s kJ/kg °C	x (-)	u kJ/kg	c kJ/kg °C
20	0.0233	0.010017	84.21	0.297	0.00015	84.83	5.8805
250	39.7	0.010017	1393.1	3.38	0.1794	1353.3	238.0

Table 1. Properties of the working fluid, water, for 10% loading ratio and non-operating conditions.

2.3 Evaporation rate

In the loading procedure developed in this research it is required that part of the working fluid evaporates filling all the internal volume of the device and forcing the non condensable gases to leave from the upper end of the thermosyphon. Thus, in this process a small amount of water escapes, so the initial water mass must be bigger than the desired final mass inside the thermosyphon. Therefore, it is important to determine the time of evaporation of the desired amount of initial fluid. This methodology proposes to know this time by the rate of evaporation or mass flow rate of evaporation from a free water surface (Incropera & Dewitt, 2006), defined by the following equation

$$\dot{m}_{eva} = \bar{h}_m A_{eva} (\rho_{v,satop} - \phi \rho_{v,satam}) \quad (15)$$

In the tables of saturated water vapor (Incropera & Dewitt, 2006), it was obtained the saturation density corresponding to room temperature, $\rho_{v,satam}$, and the saturation density corresponding to the temperature of the fluid during the loading process, $\rho_{v,satop}$.

The area of evaporation surface, A_{eva} , can be obtained from the following expression

$$A_{eva} = \pi d_{int}^2 / 4 \quad (16)$$

To calculate the mass transfer coefficient (\bar{h}_m) it was used the analogy of heat and mass transfer (Incropera & Dewitt, 2006)

$$\bar{h}_m = \bar{h}_a / (\rho_a c_{pa}) (D_{a,w} / \alpha_a)^{2/3} \quad (17)$$

The binary diffusion coefficient is calculated using the following relation

$$D = D_0 (p_0 / p) (T / T_0)^{3/2} \quad (18)$$

To calculate the average coefficient of free convection it was used the definition of Nusselt number, equation (19) (Incropera & Dewitt, 2006)

$$\bar{h}_a = k_a \text{Nu} / L_{eva} \quad (19)$$

Where the Nusselt number is given by equation (20) for Rayleigh numbers, $\text{Ra} \leq 109$ (Incropera & Dewitt, 2006)

$$\text{Nu} = 0.68 + \frac{0.67 \text{Ra}^{1/4}}{\left[1 + (0.492 / \text{Pr})^{9/16}\right]^{4/6}} \quad (20)$$

Where the Rayleigh number is defined by equation (21) (Incropera & Dewitt, 2006)

$$\text{Ra} = \text{Gr} \times \text{Pr} \quad (21)$$

Where the Grashof number, Gr , which is the ratio between buoyancy forces and viscous, is defined by the expression (21) (Incropera & Dewitt, 2006)

$$Gr = g\beta_a T_p L_{eva}^3 / \nu_a^2 \quad (22)$$

From the tables of properties of air, it is possible to get all the properties required to find the values of the parameters above mentioned using the average air temperature, T_p (23). This average temperature is obtained from room temperature, T_{amb} , and temperature of the thermosyphon during the loading process, T_{op} .

$$T_p = \frac{(T_{amb} + T_{op})}{2} \quad (23)$$

The developed methodology allows the calculation of the evaporation rate to analytically study the behavior of the flow of water evaporation as a function of ambient conditions that occur at the time of the loading process of the thermosyphon.

A parametric analysis was made with the same geometric conditions that the above described analysis, it is considered a thermosyphon with a length of 0.9 m and an inner diameter of 2.15 cm. The ambient conditions were taken as 20 °C and a pressure of 1 atm. The temperature of the thermosyphon during the filling process, T_{op} , which takes place during the loading process is 100 °C. The characteristic length of evaporation, L_{eva} is equal to the area divided by the perimeter of the orifice where the steam escapes from the thermosyphon during the filling process.

Figure 5 shows the evaporation mass flow as a function of the temperature for different relative humidity, ranging from 40% to 90%.

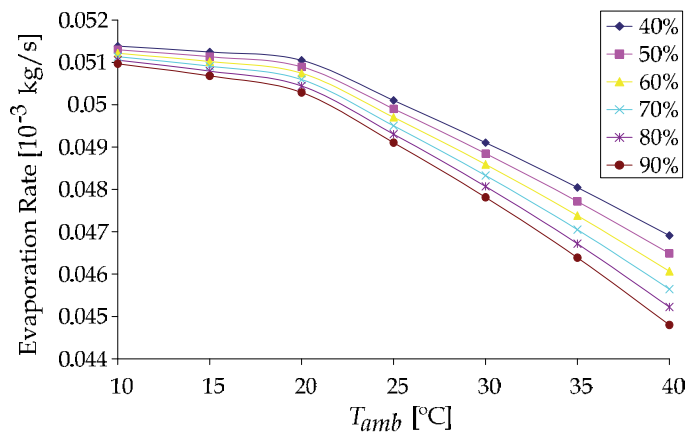


Fig. 5. Evaporation mass flow as a function of the ambient temperature and relative humidity.

2.4 Control of corrosion in the thermosyphons

The use of steel and water as a building material and working fluid, respectively, is very attractive in the design of the thermosyphon due to its low cost and high heat transmission (Terdtoon et al. 2001). However, it is well known that the ferrous material is chemically incompatible with water, and a manifestation of this incompatibility is the appearance of

rust. To avoid this effect, there have been used a series of corrosion-inhibiting additives that are added to water, among which is hydrazine hydrate.

For application in thermosyphon tubes, hydrazine hydrate has the following characteristics:

- It is dosed at a ratio close to 1:1 for the concentration of dissolved oxygen in water.
- In the form of hydrazine hydrate is considerably reduced the toxicity of pure hydrazine.
- Generates no solid waste.
- Pressure and temperature of degradation are higher than those to be taken when operating the thermosyphon in heat recovery processes of medium temperature (up to 300 °C).
- Acts as a passivator by forming a protective layer.

Hydrazine interacts with the iron oxide to form magnetic iron oxide Fe_3O_4 (magnetite), which is of black color and usually forms in water or steam when there is a deficiency of oxygen and on a layer of Fe_2O_3 (hematite). This film or barrier that adheres to the metal surface prevents the transport of reactive species of water, or the transport of products outside of this interface, i.e., prevents the flow of electricity. Therefore, the metal-water system is not oxidized or reduced, so the addition of hydrazine can slow and sometimes halt the destruction of the steel.

The addition of hydrazine hydrate to thermosyphon working fluid may have some effect on the heat transfer of the device. Therefore, it was determined experimentally the influence of the amount of hydrazine hydrate on the thermal performance of a thermosyphon. The results of this research are presented in (Carvajal-Mariscal et al., 2011) and it was found that the minimum concentration of hydrazine hydrate, which is necessary to reduce the effects of corrosion, but little changes the thermal performance of the thermosyphon is 50 mg/L.

2.5 Manufacture of the two-phase thermosyphon

The two-phase thermosyphons used in this investigation were made with A179 carbon steel tubes, with 900 mm long, 25.4 mm external diameter and 21.5 mm inner diameter. According to the calculations using the methodology above mentioned and corrected to standard sizes, was established that the length of the condensation zone should be 40% of the length of the thermosyphon, and the other 60% is the evaporation zone. Because it was chosen the length of the thermosyphon equal to 90 cm, so the evaporation zone has a length of 0.55 m and the length of the condenser is 0.35 m.

Generally, the thermosyphons are built with a lid of the container of the same material at the bottom which is welded to the container. At the top is also welded a cap, which has a concentric orifice where is welded an appendix, which is used to enter the working fluid, and also serves to facilitate the sealing. However, the thermosyphons used in this study were constructed with the following additions: The lower end is fitted with a coupling to use a tapered cap of 3/8 of diameter and with a PTN thread. At the top is installed a needle valve.

Coupling was implemented at the bottom because its diameter allowed the cleaning and loading of the working fluid, the conical cap was chosen to avoid leaks of the working fluid during the testing. The needle type valve was implemented for quick and easy sealing of the

thermosyphons. This avoids the use of a complex procedure that could cause leakage or contamination inside the thermosyphon.

It was also determined that the material of which has to be built the core of the thermosyphon is A-179 carbon steel. This type of material is commercial steel used in the manufacture of heat exchangers and boilers. In order to check if the wall thickness is adequate, i.e., if the tube will withstand the maximal operating pressures, it was used the equation (24)

$$t = \frac{p_i r_{ext}}{\zeta E + 0.4 p_i} = \frac{(40 \text{ bar})(0.0127 \text{ m})}{[(1800 \text{ bar})0.85 + 0.4(40 \text{ bar})]} = 0.341 \text{ mm} \quad (24)$$

It was obtained a minimum thickness of 0.341 mm, which is less than the thickness of the commercial tube (1.953 mm) used in the thermosyphons, so it is guaranteed to use it only to the pressures and temperatures planned in this investigation, without the risk of an accident.

The chosen working fluid is distilled water. Distilled water was chosen because of its easy availability, is not dangerous and its thermodynamic and physical properties are well known, also allows the use of the thermosyphon in the range of 5 °C to 250 °C.

Table 2 presents the specifications of the thermosyphon designed and implemented in this investigation.

Total length	900 mm.
Evaporator length	525 mm.
Adiabatic zone length	25 mm
Condenser length	350 mm.
Inside diameter of the container	21.5mm
Outside diameter of the container	25.4 mm
Outer diameter of aluminum tube	27 mm
Fin diameter	53.9 mm
Material of the container	Carbon Steel A-179.
Material of the outer tube and fins	Extruded aluminum
Working fluid	Distilled water
Maximum operating pressure	40 bar
Maximum operating temperature	250 °C

Table 2. Specifications of the two-phase thermosyphons.

3. Experimental investigation

The aim of experimental research is to understand the performance of a thermosyphon when varying the following parameters: amount of working fluid, heat supply and cooling air speed. To achieve this there were designed two experimental facilities for loading the working fluid and for testing the efficiency of two-phase thermosyphon.

3.1 Installation for loading of working fluid

Figure 6 shows an outline of the facility for loading working fluid. It consists of an array of 2 resistors of the band type with an electrical power of 250 W each. The supply of electricity to the resistance was provided by a voltage variable autotransformer of 1.4 kW and power was calculated from data obtained by a voltmeter and an ammeter, both digital.

Before starting the loading procedure of fluid inside the thermosyphon, the tube was cleaned with soapy water and rinse with distilled water followed by methyl alcohol and finally dried by applying heat. After that the process of loading fluid began.

First to fill the thermosyphons with the required filling rate, it must be known how quickly the fluid evaporates in the loading process. To carry out this process a known mass of water was introduced, then the evaporator section was heated and some time was allowed to evaporate this water mass.

In this research seven tests of loading were performed at different times. The testing time was measured when the steam started to leave the thermosyphon from the needle valve installed on the top, until closing the valve. After valve was closed and the device was cooled off, the working fluid was removed to check how much fluid was ejected from thermosyphon during the loading process.

The loading process consisted of heating for some time the thermosyphon filled with a little more than the desired amount of fluid. This in order to evaporate the difference, and so fill all the volume with water vapor, so that it forces the non-condensable gases to escape through the needle valve installed on the top of the thermosyphon, along with water vapor excess. Knowing the rate of evaporation of the fluid, the loading process time depends on the amount of fluid is desired to leave inside the thermosyphon.

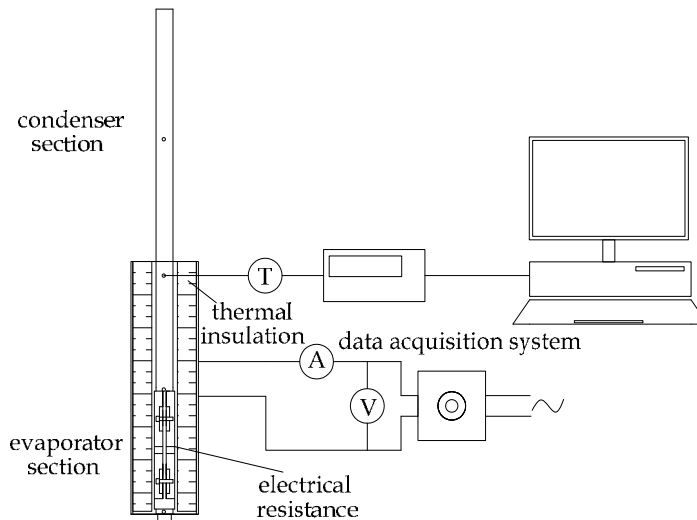


Fig. 6. Outline of the facility for loading working fluid.

To check the amount of fluid evacuated during the loading time, the steam was captured and taken through a condenser to a container where the mass ejected can be measured by a

scale. The electrical resistances arrangement of the evaporator was isolated with mineral wool and a stainless steel shell, in order to minimize heat losses.

With this method of loading the inner volume of the thermosyphon fills only with working fluid as vapor or liquid. This ensures that there are no non-condensable gases accumulated in it. The time that takes to perform this procedure depends on the excess fluid that has to be removed, in that way that at the end of the procedure only the desired amount of working fluid stays in the thermosyphon.

3.2 Testing facility for thermosyphon performance

Figure 7 shows a schematic of the experimental setup. It consists of a thermosyphon installed in a wind tunnel. On the section of the evaporator are placed, three electrical resistances of 250 W and 110 V AC. The power source is the same as in the previous installation.

Heat is removed from condenser section by a flow of cooling air. The test section is located on the suction side of the tunnel; the air is forced by an axial ventilator with a 1.12 kW motor. To measure the air temperatures at the inlet and outlet of the test section type "K" thermocouples were used. Moreover, seven K-type thermocouples were placed on the outer surface of the tube in order to measure the temperature distribution along the thermosyphon. The record of these temperatures was achieved by a Cole Parmer data acquisition system.

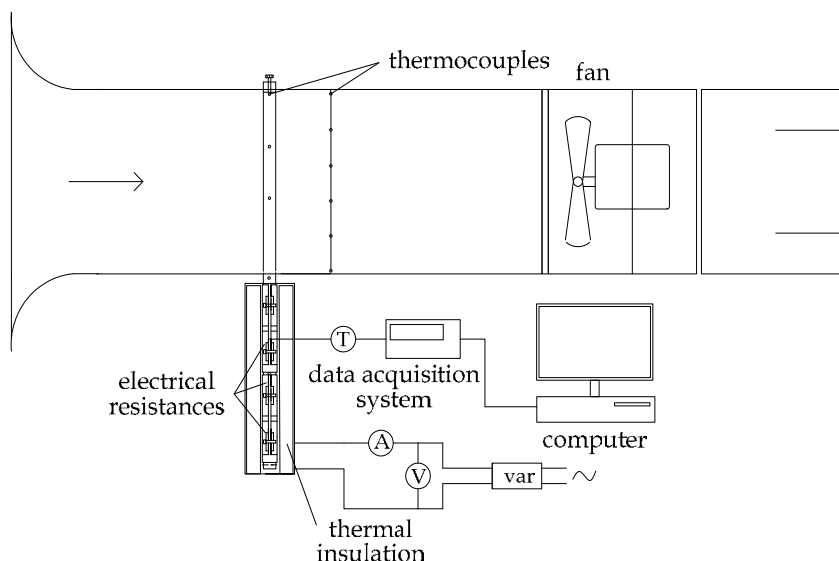


Fig. 7. Schematic of the experimental setup for thermosyphon performance testing.

Thermocouples were placed from the bottom of the evaporator in the positions of 5, 18, 35.5, 52, 65, 76.5 and 88 cm. These thermocouples were attached firmly to the surface and small sections of the fins were removed to provide a better placement.

The supply of heat to the evaporator section is calculated using the following relationship:

$$Q_{sup} = \frac{U^2}{R} = UI \quad (25)$$

On the other hand, the heat dissipated by the condenser is obtained by the following relationship:

$$Q_{ext} = \dot{m}_a c_{pa} (T_{out} - T_{in}) \quad (26)$$

The experimental tests consisted of the systematic variation of the supply of heat flow to the evaporator, keeping constant the amount of working fluid, the electric motor speed and the length of heating. Once the temperatures are stable throughout the thermosyphon this is considered a test point. Thus the data of temperature distribution and the heat dissipated is obtained for a loading volume of working fluid. Table 3 shows the parameters that were varied for these tests.

Loading rates (Ψ)	10%, 15%, 20%, 25%, 30%
Heat supply	800 W < Q < 2000 W
Mass flow of cooling air	0.175, 0.247, 0.380 kg/s

Table 3. Test parameters.

4. Results and discussion

4.1 Thermosyphon behavior during loading of the working fluid

Figure 8 shows the time and mass of water leaved in thermosyphon after the loading tests applying 272 W to evaporate the fluid. By applying a least squares method to approximate the data it was obtained an evaporation rate equal to 3.2683 g/min. Figure 8 shows the line fitted to the data obtained experimentally, which has a negative slope. Table 4 presents the values of standard deviation in the final internal mass measurement and uncertainties in the estimated value of the interceptor and the value of the evaporation rate, calculated by the least squares method.

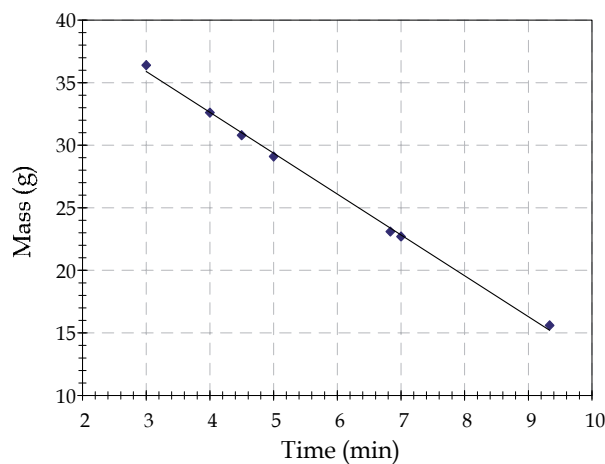


Fig. 8. Final internal mass experimental values approximation to a line.

\dot{m}_{eva}	-3.26829	[g/min]
b	45.72	[g]
σy	0.32	[g]
$\delta \dot{m}_{eva}$	0.06	[g/min]
δb	0.35	[g]

Table 4. Evaporation rate \dot{m}_{eva} , intercept b , standard deviation σy and uncertainties in the estimated values of the evaporation rate $\delta \dot{m}_{eva}$ and intercept δb .

4.2 Temperature distribution on the outer surface of the thermosyphon tube

To study the temperature distribution along the thermosyphon, temperatures were recorded simultaneously at three points in the evaporator section, at one point in the adiabatic section and three more points in the condenser.

Figure 9 shows the temperature variation over time during the loading process. An applied power of 242 W and an ambient temperature of 20 °C were the test conditions. It was obtained a loading rate of 20% with a fluid excess of 5%. During the loading process may be present operation limits of the thermosyphon because this loading process is similar to the operation of a semi-open thermosyphon (Zhu et al., 2004).

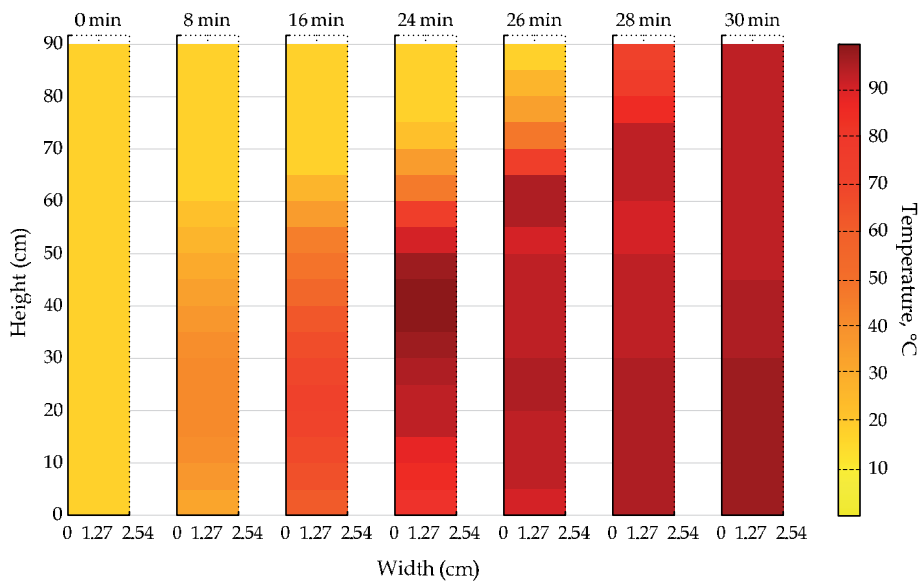


Fig. 9. Temperature rise versus time along the thermosyphon during loading.

4.3 Transported heat, efficiency and isothermal behavior

The data shown below were obtained in tests of thermosyphons loaded with five different rates. After the tests, from each thermosyphon was extracted and measured the amount of water contained in them in order to determine their loading rate. The obtained loading rates were: 28.82%, 24.81%, 18.91%, 15.06% and 10.17%.

From the results of this experiment can be extracted the heat transport capacity, efficiency and the temperature profile along the thermosyphons. Due to the restriction in the scope of this chapter there are presented below only the results for a cooling air mass flow of (0.38 kg/s).

Figure 10 shows the heat transported by the thermosyphons, loaded with different percentages of working fluid, with respect to operating temperature (thermocouple installed on adiabatic zone, T_{ad}). As shown in Figure 10, the thermosyphon with a load of 18.91% show the greatest amount of heat extracted in comparison to the rest of the thermosyphons. Therefore, it can be concluded that the thermosyphon loaded with this amount of fluid is the one that had a higher heat transfer for this flow of cooling air. On the other hand, the thermosyphons loaded with 28.82% and 10.17%, are the thermosyphons which have the lowest amounts of heat extracted.

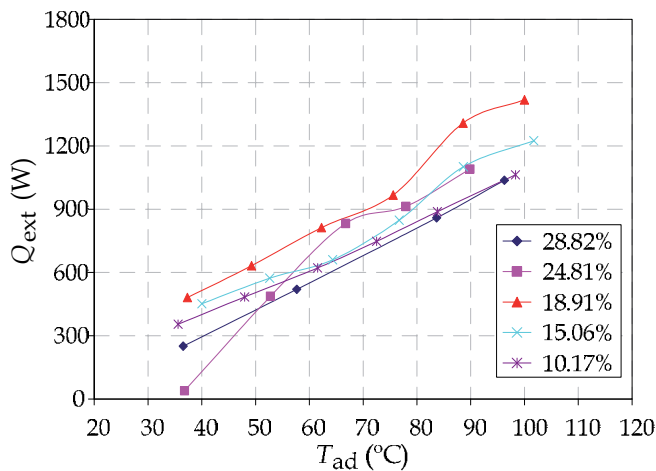


Fig. 10. Transported heat versus the operating temperature (cooling air flow: 0.38 kg/s).

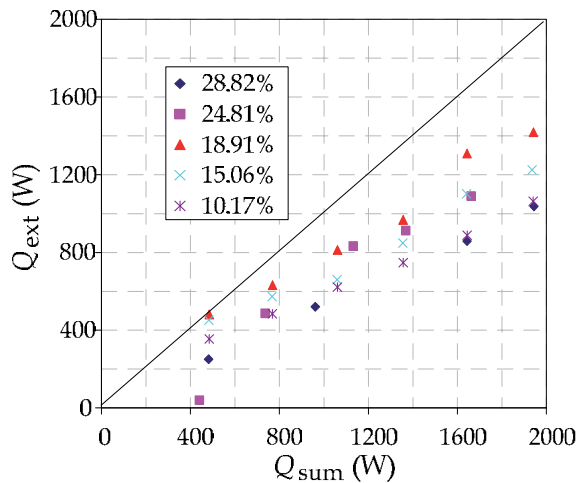


Fig. 11. Transported heat versus supplied heat (cooling air flow: 0.38 kg/s).

In Figure 11 it can be seen that as the heat flow supplied into the evaporation area increases, the ability to transfer heat of the thermosyphons decreases. Also, it can be seen in this plot that the thermosyphon loaded with 18.91% is the one that has a greater capacity to transport heat.

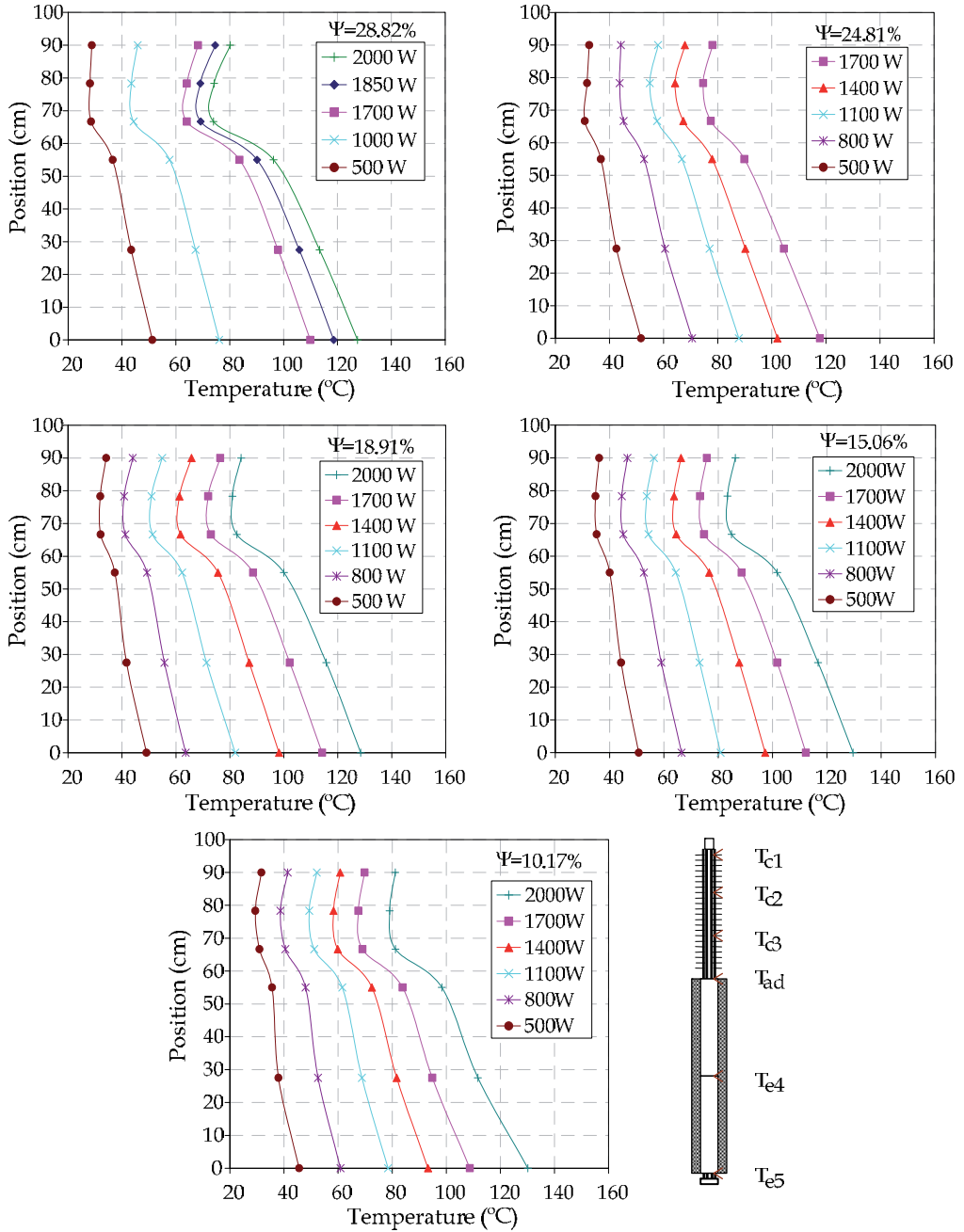


Fig. 12. Temperature profiles versus amounts of delivered heat (cooling air flow: 0.38 kg/s).

Figure 12 shows the temperature profiles along the thermosyphons for different loading rates. In the plots of Figure 12 it can be seen that profiles with higher temperatures are of the thermosyphons loaded with rates of 24.81%, 18.91% and 15.06%. This means that these thermosyphons reached higher temperatures, compared to the other two thermosyphons, under the same conditions of heat supply and cooling air flow. Moreover, these plots show that the lowest average temperature differences between condenser and evaporator are presented in the thermosyphon loaded with 10.17% in the range of heat input of 500 W to 800 W.

Also, it can be noted that for this thermosyphon it was presented a relative increase of temperature at the bottom of the evaporator for each value of the heat supplied, specifically for the heat supply 2000 W, this indicates the start of drying in the area of evaporation.

In the plots of Figure 12 it can be observed that at the top of the condenser (thermocouple T_{c1}) there is a higher temperature than in the middle of the condensation zone (low thermocouple T_{c2}). For this flow of cooling air, the rate of heat extraction is higher compared to the steam generation in the evaporator, so in this region drying occurs causing a rapid condensation on the top of the thermosyphon.

5. Conclusion

The methodologies for the calculation of three key parameters implemented in the design and manufacture of two-phase thermosyphons were developed. These key parameters are: the relationship of the lengths of evaporation and condensation zones, the operational pressure values and the evaporation rate of the working fluid during the filling process. The developed methodologies were applied in the design and manufacture of several two-phase thermosyphons. Distilled water was used as working fluid and hydrazine hydrate was added to it as corrosion inhibitor.

Two experimental installations were designed and constructed. One was used to load the thermosyphons, without using a vacuum pump, eliminating the non-condensing gases; the other one is a wind tunnel modified to test the performance of the thermosyphons using electrical resistances as heat source. A series of experiments to investigate the effect of parameters as heat power supply, amount of working fluid and speed of cooling air, on the performance of two-phase thermosyphons were carried out. In each experimental test, the temperature distribution along the external surface of thermosyphons, the heat power supply and the dissipated heat power by the device as well were registered. The results showed that the thermosyphons work isothermally with efficiencies around 90% for a working fluid loading of 20% of the internal volume of the thermosyphon.

The results of these investigations can be used to design and construct high efficiency two-phase thermosyphons for heat recovery from waste gas with a temperature up to 250 °C.

6. Acknowledgment

The authors wish to express their thanks to CONACyT, COFAA and National Polytechnic Institute of Mexico for their support of this work.

7. Nomenclature

A – area, [m²];
 a – width of the gas-gas heat exchanger, [m];
 c_p – heat capacity at constant pressure, [J/kg K];
 d – diameter, [m];
 D – binary diffusion coefficient, [m²/s];
 E – modulus of elasticity, [Pa];
 Gr – Grashof number;
 g – gravitational force, [m/s²];
 H – specific enthalpy, [kJ/kg];
 \bar{h} – convective heat transfer coefficient, [W/m² K];
 \bar{h}_m – mass transfer coefficient, [m/s];
 I – electric current, [A];
 k – thermal conductivity, [W/m K];
 L_{eva} – characteristic length of evaporation, [m];
 l – length, [m];
 \dot{m} – mass flow, [kg/s];
 m – mass, [kg];
 Nu – Nusselt number;
 Pr – Prandtl number;
 p – pressure, [Pa];
 \dot{Q} – heat flow, [W];
 R – electric resistance, [Ω];
 Ra – Rayleigh number;
 r – radius, [m];
 ζ – stress, [N/m²];
 S – entropy, [kJ/°C];
 s – specific entropy, [kJ/kg °C];
 T – temperature, [°C, K];
 t – wall thickness of container, [m];
 U – voltage, [V];
 u – specific internal energy, [kJ/kg];
 V – volumen, [m³];
 v – velocity, [m/s];
 x – quality;
 Ψ – loading rate;
 α – thermal diffusivity, [m²/s];
 β – volumetric thermal expansion coefficient, [K⁻¹];
 ν – kinematic viscosity, [m²/s];
 ρ – density, [kg/m³].
 v – specific volume, [kg/m³];
 ϕ – relative humidity;
 Subscripts:
 0 – normal conditions;
 a – air;

eva – evaporation;
ext – external;
f – working fluid;
g – hot gases;
int – internal;
t – total;
w – water.

8. References

- Azada, E., Mohammadiha, F., & Moztarzadeh, F. (1985). Thermal performance of heat pipe heat recovery system. *Journal of Heat Recovery Systems*, Vol. 5, No. 6, pp. 561-570, ISSN 0890-4332.
- Carvajal-Mariscal, I., Sanchez-Silva, F., Polupan, G., & Quinto-Diez, P. Additive amount influence on the thermal performance of a two-phase thermosyphon (IMECE2011-64177). *Proceedings of the ASME 2011 International Mechanical Engineering Congress & Exposition*, Denver Colorado, November 2011.
- Faghri, A. (1995). *Heat pipe science and technology*, Taylor & Francis, ISBN 978-1560323839, New York USA.
- Gershuni, A., Nishchik A., Pysmennyy Ye., Polupan G., Sanchez-Silva F., & Carvajal-Mariscal I. (2004). Heat exchangers of the gas-gas type based on finned heat pipes. *International Journal of Heat Exchangers*, Vol. 5, No. 2, pp. 347-358, ISSN 1524-5608.
- Incropera, P. F., & Dewitt, P. D. (2006). *Introduction to Heat Transfer*, 5th edition, Prentice Hall, ISBN 978-0471457275.
- Noie, S.H. (2005). Heat transfer characteristics of a two-phase closed thermosyphons. *Applied Thermal Engineering*, Vol. 25, No. 4, pp. 495-506, ISSN 1359-4311.
- Park, J., Kang, K., & Kim, J. (2002). Heat transfer characteristics of a two-phase closed thermosyphon to the fill charge ratio. *International Journal of Heat and Mass Transfer*, Vol. 45, No. 23, pp. 4655-4661, ISSN 0017-9310.
- Peterson, G.P. (1994). *An introduction to heat pipe modeling, testing, and applications*, John Wiley & Sons, Inc., ISBN 978-0471305125, New York USA.
- Reay, D.A. (1981). A review of gas-gas heat recovery systems. *Journal of Heat Recovery Systems*, Vol. 1, No. 1, pp. 3-41, ISSN 0890-4332.
- Terdtoon, P., Charoensawan, P., & Chaitep, S. (2001). Corrosion of tubes used in thermosyphon heat exchanger for waste heat recovery system: A case of internal Surface. *Heat Transfer Engineering*, Vol. 22, No. 4, pp. 18-27, ISSN 0145-7632.
- Zhu, H., Wang, J., Zhang, Q., & Tu, C. (2004). Experimental study on transient behavior of semi-open two-phase thermosyphon. *Journal of Zhejiang University SCIENCE A*, Vol. 5, No. 12, pp. 1565-1569, ISSN 1673-565X.
- Zuo, Z. J., & Faghri, A. (1998). A network thermodynamic analysis of the heat pipe. *International Journal of Heat and Mass Transfer*, Vol. 41, No. 11, pp. 1473-1484, ISSN 0017-9310.

Impact of a Medium Flow Maldistribution on a Cross-Flow Heat Exchanger Performance

Tomasz Bury
Silesian University of Technology
Poland

1. Introduction

1.1 Characteristics of the problem

The plate exchangers (with the mixed current) and the finned cross-flow heat exchangers, which core has the form of a bunch of pipes with flat plate ribs, have the most important meaning among the currently applied heat exchangers with extended surface. These heat exchangers are usually used for heat transfer between a liquid flowing inside the tubes and a gaseous medium flowing outside the tubes, on the ribs side. Small size, low weight and a high efficiency determine the strong position of such devices. Compact ribbed heat exchangers are commonly used in thermal technique, refrigeration, air-conditioning and automotive industry.

A typical thermodynamic analysis of a cross-flow heat exchanger is usually aimed in determination of the heat transfer surface for the desired design and its capacity. There are several simplifying assumptions made during such calculations, for example neglecting of the heat losses to the environment, uniform flow of media through the exchanger, heat transfer coefficients determined for the average temperatures. These assumptions are fulfilled very rarely in reality and of course it affects the analytical results to some degree.

The subject of this work is evaluation of the impact of a non-uniform flow of media (or flow maldistribution) on very popular finned cross-flow heat exchangers performance. The reasons for such maldistribution occurring in an exchanger include the layout of the exchanger with respect to other components in the system, effects of manufacturing tolerances, the design of the flow circuits in the exchanger and the design of the inlet and outlet headers. In some instances, the maldistribution could also be induced due to temperature effects. These factors become even more critical when the exchangers are applied in compact designs which involve a tortuous flow path for both the fluid streams. This situation may lead to some losses in the total heat flow rates transferred in the heat exchanger and affects its thermal efficiency. There is therefore the obvious question: to what extent inequality of media flows worsens effects of the heat exchanger?

One of the most important parameters describing such heat exchangers is the heat transfer coefficient on the gas side. Usually, this coefficient is determined as an average value for the whole heat transfer surface. This is of course another simplification. Beside of these simplifying assumptions, a variety of constructions being applied causes significant

problems with determination of this coefficient. The problem is additionally complicated by a non-uniform flow of a gas. This flow maldistribution induces also some non-uniform distribution of the heat transfer coefficient. So, another important question is how this situation influences the thermodynamic analysis where the average value of this parameter is applied usually?

1.2 Review of previous studies

The question of a non-uniform flow of media through heat exchangers is not a new problem. It is the subject of investigations for many years. Results, especially taken from older works, are sometimes very unambiguous.

The first one investigation referred to the heat exchangers with unequal flow of agents was performed at the Institute of Thermal Technology of the Silesian University of Technology (ITT SUT) for gaseous mediums and they had only computational form (Hanuszkiewicz-Drapala, 1996). Investigations of the gas-liquid type cross-flow heat exchanger have been conducted at the ITT SUT since a few years to evaluate an influence of a non-uniform gas inlet on the exchanger functioning (Piątek, 2003). A range and form of the air inflow non-uniformity have been determined on the special testing station - see Fig.1 in the next section. Configuration of the measuring system of the test station allows determining the air velocity and temperature distribution at the heat exchanger inlet and outlet. This test station, in its original arrangement, allowed only for "cold" experiments, it means without presence of the hot medium. Thus, the influence of the measured non-uniformity has been assessed by means of numerical simulations performed by the computer code called HEWES - worked out for thermal analyses of the considered heat exchanger. R. Piątek in his work (Piątek, 2003) concludes that the maldistribution of the air inlet to the investigated car cooler may significantly influence the effectiveness of the heat exchanger.

An unique feature of the investigations realized at the ITT SUT is experimental consideration of the air flow non-uniformity. Similar heat exchangers have been investigated by D. Taler with co-workers (Taler, 2002; Taler and Cebula, 2004) by means of physical experiments and numerical simulations too. Very good compliance of experimental and numerical results has been achieved, but the problem of the non-uniform agents flow is neglected and this fact simplified experimental measurements.

Many researches considering the problem of the non-uniform flow of media have been realized only numerically. Authors of (Ranganayakulu et al., 1997) have simulated the plate fin heat exchanger using the finite elements method and found out that the influence of the non-uniformity of the liquid flow may have significant meaning in some work regimes. A very significant drop of the heat exchanger efficiency has been also observed by authors of (Andreovich and Clarke, 2003). The opposite results have obtained authors of (Nair et al., 1998) and (Lee and Oh, 2004). Numerical simulations realized for a rotary heat exchanger in the first work and optimization procedure presented in the second one have not shown significant dependence on the agents flow non-uniformity.

There are many works, both experimental and numerical, considering only the flow maldistribution impact on hydraulic efficiency of heat exchangers. Anjun with his co-workers investigated the influence of headers configuration on the non-uniformity range (Anjun et al., 2003). The numerical results presented in (Wen and Li, 2004) indicate that the

improved header configuration can effectively improve the performance of a fin-and-tube type heat exchanger. An experimentally determined flow maldistribution for a plate fin-and-tube heat exchanger has been also described in (Hoffmann-Vocke et al., 2009), but the authors have not considered its impact on the heat exchanger thermal efficiency. This group of authors has presented in (Hoffmann-Vocke et al., 2011) even more detailed, but still only hydraulic analysis of the considered heat exchanger.

Experimental analyses considering maldistributions of the agents flow through the heat exchangers and dealing with thermodynamic effects are rare. A. Mueller in (Mueller, 1987) concludes about major significance of flow maldistributions for heat exchangers performance. Based on the study of gross flow maldistribution in an experimental electrical heater the paper (Lalot et al., 1999) presents the effect of flow non-uniformity on the performance of heat exchangers. The original fluid distribution is applied to heat exchangers (condensers, counterflow and cross-flow heat exchangers), and it is shown that gross flow maldistribution leads to a loss of effectiveness of about 7% for condensers and counterflow heat exchangers, and up to 25% for cross-flow exchangers. Similar effects have been observed by the authors of (Luo et al., 2001) indicate that the non-uniformity influences the efficiency of the heat exchangers to a large extent. Berryman and Russell have studied flow maldistribution across tube bundles in air-cooled heat exchangers (Berryman and Russel, 1987). Their experimental results have detected thermal degradation up to 4%, which is much less than in previously cited works. The authors of (Meyer and Kröger, 1998) concluded about minor – up to 5% - effects of this phenomenon also.

Another group of investigations deals with evaporators and condensers, applied in air-conditioning and refrigeration. The effects of maldistribution in fin-tube heat exchangers, which takes place on the air-side through the fin passages as well as on the liquid side in the tube circuits, have been investigated by several researchers, for example (Fagan, 1980; Chwalowski et al. 1989; Lee and Domanski, 1997; Aganda et al. 2000). The findings of these works have indicated dependence of the degradation on the mean and standard deviation of the flow maldistribution profile.

A very complex research has been realized by teams from Indian Institute of Technology – Madras and Lund University of Technology. These works concern plate-type heat exchangers. The numerical model of a one-pass plate heat exchanger has been elaborated first for hydraulic analyses of a flow maldistribution impact (Shrihari et al., 2005) and next it was arranged for multi-pass units (Shrihari and Das, 2008). An experimental investigation has been also carried out to find the flow and the pressure difference across the port to channel in plate heat exchangers (Rao et al., 2006). More recently this research team realized thermal analysis also. The single-blow transient test technique based on axial dispersion model was proposed for the determination of both heat transfer coefficient and axial dispersion coefficient in plate heat exchangers. The experimental analysis presented in (Shaji and Das, 2010) deals with the effect of flow maldistribution on the transient temperature response for U-type plate heat exchangers. The experiments are carried out with uniform and non-uniform flow distributions for various flow rates and two different numbers of plates.

According to (Li-Zhi, 2009) the inlet and outlet duct geometry in an air to air compact heat exchanger is always irregular. Such duct placements usually lead to a non-uniform flow distribution on core surface. The author used a CFD model to predict the flow distribution

and next calculated the heat exchange effectiveness and the thermal performance deterioration factor with finite difference scheme. Experiments were performed to validate the flow distribution and heat transfer model. The results indicate that when the channel pitch is below 2.0 mm, the flow distribution is quite homogeneous and the thermal deterioration due to flow maldistribution can be neglected. However, when the channel pitch is larger than 2 mm, the maldistribution is quite large and a 10–20% thermal deterioration factor could be found.

This literature review of the selected positions shows, as already mentioned, that the problem of the non-uniform fluid inflow to the heat exchangers has been the subject of many computational and experimental investigations, but the results obtained are unambiguous in terms of thermal performance. Many investigations are limited to the hydraulic analysis only and they deal with liquid-liquid type heat exchangers. Most researchers are consistent in finding that the non-uniformity of the flow significantly strikes the hydraulic efficiency of heat exchangers. Thermal analyses refer first of all to the heat exchanger effectiveness, but they are not very numerous. It is lack of complete investigations of the finned cross-flow heat exchangers of the gas-liquid type with unequal inflow of the agents, especially of unequal inflow of the gas.

1.3 Aim and scope of presented studies

The degradation effects of flow maldistribution on the performance of a heat exchanger are well-known. Not only does the thermal performance decrease but the fluid pressure drop across the exchanger core also increases simultaneously. Analyzing the results of (Piątek, 2003) the obvious question has appeared: how reliable are these results? The HEWES code validation procedure has to be carried out in order to answer this question. It became possible after modernization of the experimental rig and installation of the hot water supply module. In (Bury et al., 2007b) there have been presented the only initial results obtained by use of the modified testing station, and the results of initial and detailed validation and sensitivity analysis have been presented in (Bury et al., 2008a) and (Bury et al., 2008b). Significant differences have been recorded between experimental and numerical data after the initial validation of the model. Minor changes have been put into the code and the validation procedure was then repeated with usage of the infra-red thermography measurements results also. The last stage of the research was the sensitivity analysis. This analysis has shown that the heat transfer coefficient from ribbed surfaces to a gas may be a reason for recorded discrepancies between numerical and experimental results. An additional testing station, in the lab-scale, has been designed and constructed in order to check the numerical procedure responsible for determination of the heat transfer coefficient from the ribs to the gas. The papers (Bury et al., 2009a; Bury and Składzień, 2010) and recently also (Składzień and Bury, 2011) present results of this analysis.

Applying the validated version of the HEWES code and modified testing station the analysis of the above mentioned car cooler has been repeated and the results allowed to sustain the conclusions withdrawn by Piątek – the air inflow maldistribution may significantly affect the heat exchanger performance (Bury et al., 2009b).

The following questions have emerged after analysis the experience gained so far:

- are own results consistent with data published by other authors stating an important meaning of the flow maldistribution (considering the range of observed heat exchanger efficiency drop)?
- are these results repeatable?

The whole analytical procedure (experiments and numerical simulations) has been performed for three cross flow heat exchangers with different ribbing structure in order to answer these questions. The experimental and numerical procedures are presented in this chapter, as well as the most important results and conclusions.

2. Experimental investigations

2.1 Test station

The test station consists of two main modules: the air supply module (see Fig. 1) and the hot water supply module (Fig. 2). The air supply module originally was a special testing station constructed during realization of the project (Piątek, 2003) for determination of a form and scope of the air inflow non-uniformity.

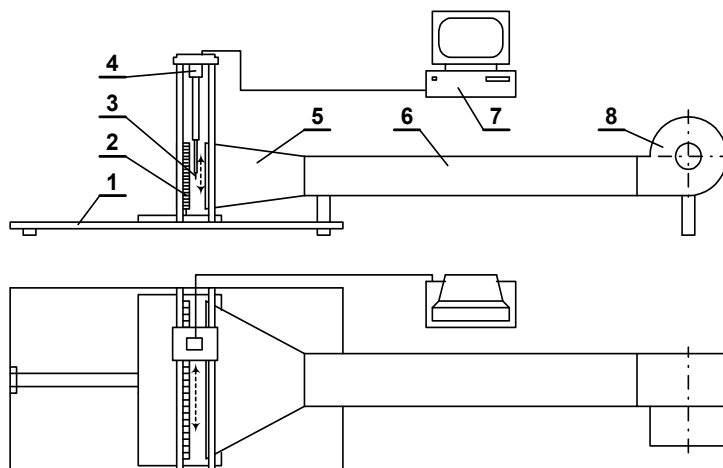


Fig. 1. Test station - the air supply module (1 - support plate, 2 - heat exchanger, 3 - thermoanemometric sensor, 4 - measuring probe, 5 - diffuser, 6 - channel, 7 - control computer, 8 - fan).

The air is supplied by the radial fan of the maximum capacity of 6900 m³/h. The fan capacity can be controlled by the throttling valve installed before the fan. Then the air flows through the 1.7 m long channel (rectangular cross-section 190x240 mm). The channel ends with the filter section. Usually this section is empty and only during special tests filters having the form of wire nets or perforated metal sheets are used. Actually, filter is not a good word describing the purpose of these elements - they are installed in order to make the air flow more uniform. The diffuser dimensions have been fit to the first examined heat exchanger: they are 280x490 mm.

The main element of the measuring system is the VIT-type thermoanemometric sensor installed onto the measuring probe which shifting is controlled by a computer. It allows

determining velocity and temperature fields of the air at the exchanger's inlet and outlet. The measuring probe moves in a slit cut out in the upper wall of the diffuser. The slit is seal up with a soft insulating foam. Unfortunately, such a solution is the reason of some air leakage. As the thermoanmenometric sensor is a very fragile instrument its contact with walls and other structures should be prevented. There are 20 mm wide margins left on the all sides and the probe movement plane is placed 25 mm in front of the heat exchanger's inlet cross-section. Signals from the sensor are gathered by the FMC 921 control card and send to the computer where they are analysed.

The original testing station has been modified and the hot water supply module was installed. Water is heated up to the desired temperature (up to 95°C) by the electric heater. The water circulation is forced by the pump and its flow rate can be regulated by the control valve. The flow rate is measured by the rotameter and the K-type thermocouples (NiCr-NiAl) measure its temperature at the inlet and outlet of the heat exchanger.

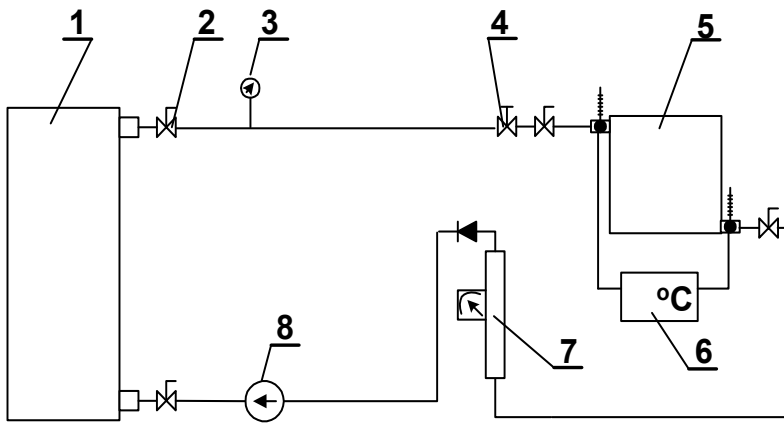


Fig. 2. Test station - the hot water supply module (1 - electric heater, 2 - cut-out valve, 3 - manometer, 4 - control valve, 5 - heat exchanger, 6 - temperature measuring system, 7 - flow meter, 8 - pump).

The measuring system allows for acquisition of the following parameters at the moment: total air volumetric flow, the water mass flow rate, inlet and outlet water temperature, distribution of the air velocity and temperature at the inlet and outlet of the heat exchanger.

2.2 Procedures of measurements and experimental data analysis

The air temperature and velocity distributions measurement need the measuring task to be defined in the form of an input file for the program controlling the measuring probe's work. The trajectory of the probe's shifting is determined by location of measuring nodes. There are two ways for realizing the measurements: applying the spiral-type measuring mesh or the regular-type mesh. These two types of measuring meshes are shown in Fig. 3. The first one is usual while determining the form and scope of the air inlet non-uniformity. Data obtained by use of the regular mesh are more convenient for the complete thermodynamic analysis. Such mesh divides the whole measuring cross-section into identical rectangles and the measuring nodes are located in the middle of each rectangle.

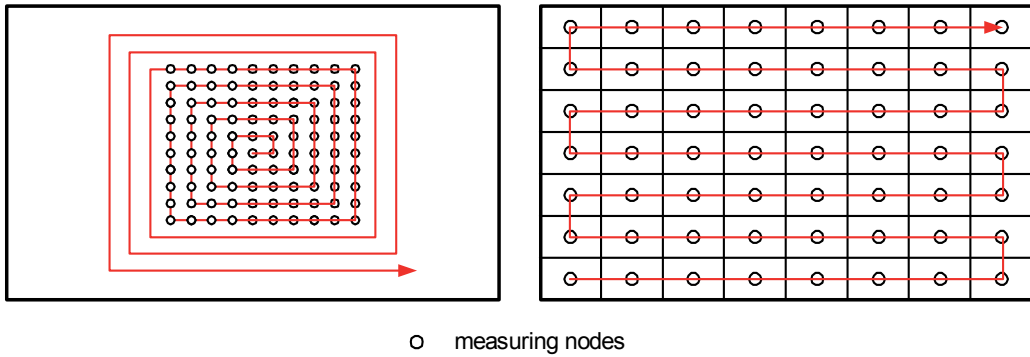


Fig. 3. The idea of the spiral-type (left) and regular-type measuring meshes and trajectories of the measuring probe movement.

The time constant of the measurement and the number of measurements realized in each node should be entered in the file. The data are acquired with the maximum frequency allowed by the hardware (CPU clock). So, assuming a 100 Hz frequency and 0.5 s time constant there would be 50 samples obtained for the given measuring node. The results are analysed online and the output file contains the average values with their standard deviations for each measuring node, considering both velocity and temperature of the air.

A higher resolution of the results (velocity and temperature distributions) can be achieved by making the measuring meshes more dense. Definition of the measuring mesh needs some optimization between resolution of results and time of measurement, and the aim of measurement as well as the heat exchanger structure should be also taken into account.

A regular measuring mesh of 196 nodes has been used for measurements realized in this work. The measuring program has been started after the steady state conditions were achieved.

Three parameters are assumed as independent and may be set by a researcher: the air and water flow rates and the inlet water temperature.

The cooler heat capacity has been determined as the heat flow rate transferred in the exchanger computed from the air and the water side. Obvious relationships describing the medium enthalpy decrease (increase) have been used:

$$\dot{Q}_a = \dot{V}_a \cdot \rho_a \cdot c_{pa} \cdot (t_{a,out} - t_{a,in}) \quad (1)$$

$$\dot{Q}_w = \dot{V}_w \cdot \rho_w \cdot c_{pw} \cdot (t_{w,in} - t_{w,out}) \quad (2)$$

The air density has been calculated using the ideal gas law for the absolute pressure and the air average temperature at the inlet to the exchanger. The density of water has been assumed according to thermodynamic tables for the outlet temperature.

The water enthalpy drop has been used for calculations of the heat flow rates because of more accurate measurement of the water flow.

2.3 Analysed heat exchanger types

The investigations accomplished in this work deal with the ribbed cross-flow heat exchangers of the gas-liquid type. There were three water coolers investigated during realization of this work (see Fig. 4):

HE-1 - typical car cooler (Skoda Favorit 135L) with the core having the form of 2 rows pipe bundle (15 cylindrical pipes ribbed with the plate fins in each row, 380 fins on each pipe); aluminium,

HE-2 - the cross-flow heat exchanger made by GEA Heat Exchangers Company with the core made of 10 rows of elliptical pipes ribbed with the plate fins (175 on each pipe); steel,

HE-3 - the cross-flow heat exchanger made by GEA Heat Exchangers Company with the core having the form of 2 rows pipe bundle (81 fins on each pipe in the first row and 140 fins on each pipe in the second row); steel.

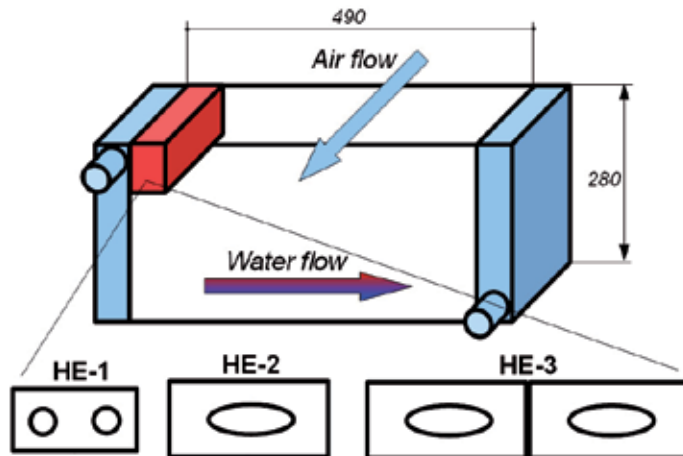


Fig. 4. General sketch of the heat exchangers under consideration and the recurrent elements of three versions of the heat exchangers

2.4 Selected experimental results

There were six measuring series carried out for each of the heat exchangers under consideration. The distributions of the air velocity and temperature are one of the most interesting results that may be achieved on the described testing station. These distributions are very important because they allow evaluating the air inflow maldistribution range and form. Sample distributions obtained for the HE-1 heat exchanger are shown in Figs. 5 and 6. These results have been obtained with the total air flow rate of $1.556 \text{ m}^3/\text{s}$, the water flow rate of $4.5 \cdot 10^{-4} \text{ m}^3/\text{s}$ and the water temperature set on the boiler in 50°C .

The form and scope of the air inlet non-uniformity depend on the fan capacity, as shown in Fig. 7. This observation, recorded in (Piątek, 2003) and (Bury et al., 2007a) has been confirmed during actual tests and, moreover, some dependence on the heat exchanger has been also noticed. So, it would be better to say that these parameters depend on the piping and ribbing structures in this certain case.

An attempt for systemizing this non-uniformity has been undertaken in (Malinowski, 2008). The numerical analysis has proved that the reason of the observed air inflow maldistribution is the radial fan. Unfortunately, attempts to describe the measured inequality by using mathematical functions have failed. For this reason, data on the non-uniformity are included in the calculations in tabulated form using rows. This extends the calculation time slightly, but on the other hand allows for accurate recognition of this phenomenon.

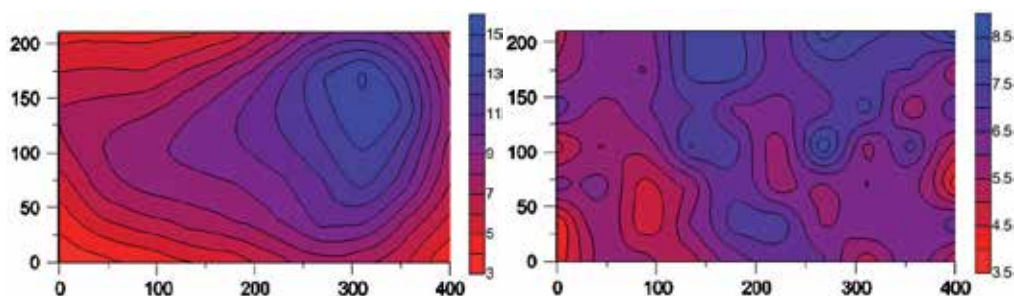


Fig. 5. Distribution of the air velocity at the inlet (left) and outlet (right) cross-sectional flow area (210mm x 400mm) of HE-1/1 measurement, m/s.

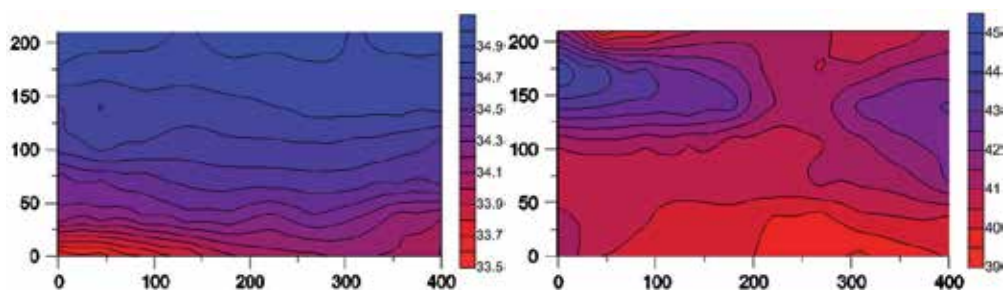


Fig. 6. Distribution of the air temperature at the inlet (left) and outlet (right) cross-sectional flow area (210mm x 400mm) of HE-1/1 measurement, °C.

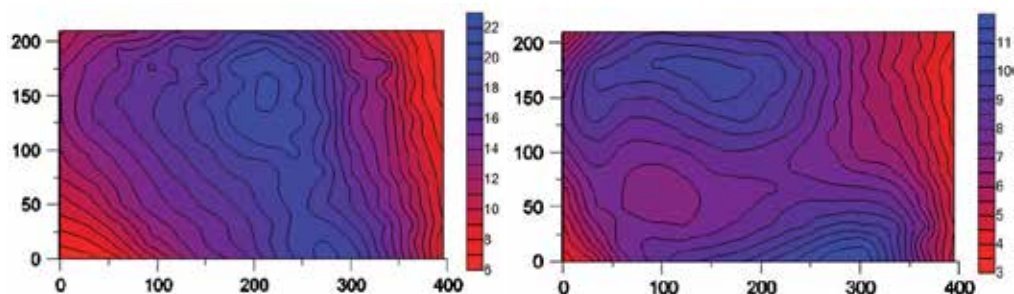


Fig. 7. Distribution of the air velocity at the inlet cross-sectional flow area (210mm x 400mm) of HE-2/1 measurement (left - without throttling) and of HE-3/4 measurement (right - maximum throttling), m/s.

Presented in Figs. 5-7 distributions of velocity and temperature of the air were drawn as viewed from the outlet of the heat exchanger.

Measurement No.	\dot{V}_a m ³ /s	\dot{V}_w m ³ /s	$t_B^{(1)}$ °C	$t_{w,in}$ °C	$t_{w,out}$ °C	\dot{Q}_w kW
HE-1/1	1.556	4.5 · 10 ⁻⁴	50	49.8	43.9	11.03
HE-1/2	1.556	4.5 · 10 ⁻⁴	70	68.9	56.7	22.61
HE-1/3	1.556	4.5 · 10 ⁻⁴	90	86.4	67.9	34.08
HE-1/4	1.083	4.5 · 10 ⁻⁴	50	49.7	44.5	9.72
HE-1/5	1.083	4.5 · 10 ⁻⁴	70	69.2	58.7	19.42
HE-1/6	1.083	4.5 · 10 ⁻⁴	90	88.0	72.2	29.11
HE-2/1	2.04	4.5 · 10 ⁻⁴	50	48.2	42.8	10.07
HE-2/2	2.04	4.5 · 10 ⁻⁴	70	69.6	62.0	14.08
HE-2/3	2.04	4.5 · 10 ⁻⁴	90	90.2	79.5	19.58
HE-2/4	1.063	4.5 · 10 ⁻⁴	50	48.0	45.6	4.48
HE-2/5	1.074	4.5 · 10 ⁻⁴	70	68.5	62.0	12.04
HE-2/6	2.033	4.5 · 10 ⁻⁴	90	89.8	79.0	19.76
HE-3/1	1.876	4.5 · 10 ⁻⁴	50	49.3	42.7	12.39
HE-3/2	1.876	4.5 · 10 ⁻⁴	70	69.1	59.8	17.31
HE-3/3	1.877	4.5 · 10 ⁻⁴	90	87.8	74.6	24.08
HE-3/4	1.052	4.5 · 10 ⁻⁴	50	50.1	47.1	5.51
HE-3/5	1.052	4.5 · 10 ⁻⁴	70	69.6	61.6	14.81
HE-3/6	1.877	4.5 · 10 ⁻⁴	90	88.7	75.4	24.30

⁽¹⁾: the temperature set at the electric boiler outlet

Table 1. Results of measurements.

The results of the measurements for the three considered heat exchangers are summarized in Table 1. All the measurements have been repeated for three times in order to verify repeatability of results. Presented in the last column heat flow rates, of course, refer to the conditions of non-uniform air flow. In order to determine the impact of this inequality on the efficiency of considered heat exchangers in the next stage the computational analysis was carried out. The measured inlet media parameters were used as input for calculations.

3. Computational analyses

3.1 Mathematical model of the heat exchanger

The mathematical model of the considered heat exchanger has been worked out taking into account the following simplifying assumptions (only most important):

- steady state conditions,
- one-dimensional media flow,
- radiation is neglected,
- heat losses are neglected,
- heat flow is normal to a boundary,
- real rib is replaced with a round or a plate-elliptic rib of the same surface.

It has been also assumed that the air inflow is non-uniform and the water inflow may be non-uniform. An influence of temperature on thermal properties of the agents has been taken into account too.

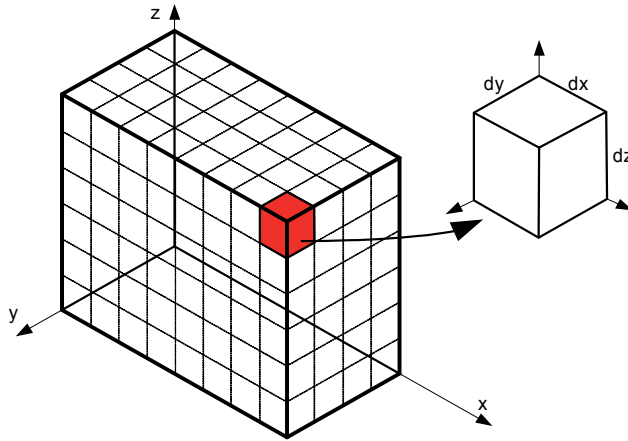


Fig. 8. Model heat exchanger and the recurrent fragment.

The analysed real cross-flow heat exchanger has been replaced with a model rectangular heat exchanger. The model was then divided into elementary fragments (Fig. 8). Each fragment represents a recurrent element of the real heat exchanger - a single tube with the rib (Piątek, 2003).

The energy balance equations for each fragment constitute the mathematical basis of the model. Assuming that the water flows along the X axis and the air flows along the Y axis the energy balance for a recurrent fragment may be written as follow:

$$d\dot{Q} = -\dot{m}_w c_{pw} \frac{\partial T_w}{\partial x} dydz = \dot{m}_a c_{pa} \frac{\partial T_a}{\partial y} dx dz = h_a (T_m - T_a) dA \quad (3)$$

where h_a is an average heat transfer coefficient on the gas side for all the ribbed surface and T_m is the average temperature of rib and pipe surface.

The inlet temperatures of the mediums are known so the following boundary conditions may be used:

$$T_w(0, y, z) = T_{w,in} \quad T_a(x, 0, z) = T_{a,in} \quad (4)$$

The mass flow rates of the fluids are described by the following formulas:

$$d\dot{m}_w = \frac{g_w \cdot \dot{m}_w}{Y_{\max} Z_{\max}} dy dz \quad (5)$$

$$d\dot{m}_a = \frac{g_a \cdot \dot{m}_a}{X_{\max} Z_{\max}} dx dz \quad (6)$$

The inequality factors g_w and g_a are defined as follows:

$$g_w = \frac{w_w}{w_{w,m}} \quad (7)$$

$$g_a = \frac{w_a}{w_{a,m}} \quad (8)$$

The subscript m in relationships (7) and (8) means the average velocity of the medium. Information about the non-uniform flow of the air is put into the model on the basis of measurements. A non-uniform water inlet to the exchanger may be set arbitrary by a function or on the basis of numerical simulations (Bury et al., 2007a).

The control volume method based model of heat transfer for the recurrent fragment of the heat exchanger has been worked out to calculate the average temperature of the ribs and tube outer surface. The detailed description of the model and equations can be found in (Piątek, 2003).

The parameters calculated with the model of the recurrent fragment are: outlet and average temperature of the water flowing in the pipe, average temperature of the air, average temperature of the rib and the pipe surface, average values of the heat transfer coefficients at the gas side and the heat flux transported in the recurrent fragment. The heat transfer coefficient from the hot water to the pipe has been computed from Colburn's formula (Welty et al., 2008):

$$Nu = 0.023 \cdot Re^{0.8} \cdot Pr^{1/3} \quad (9)$$

The heat transfer coefficient on the gas side may be determined on the way of the numerical simulations for a numerical model of the recurrent fragment of the considered heat exchanger (see subsection 3.2.2 and Bury and Składzień, 2006) or may be computed from one of available Nusselt number correlations.

The calculation procedure for the whole exchanger model is iterative and it is repeated for all the recurrent fragments of the considered heat exchanger. First, the air temperature increase in the analysed fragment is assumed. Next, the heat transfer coefficients for the water and the gas sides are calculated as well as the rib and pipe surface average temperature. The heat flux transported in the recurrent fragment is then computed and the accuracy criterion is checked. If the criterion is satisfied the procedure is realized for the next fragment. If the criterion is not fulfilled the described procedure is then repeated for the given recurrent fragment till the demanded accuracy is achieved.

The validation procedure was performed by means of comparison of the experimental and numerical results. The total heat flux transported in the heat exchanger is the main compared parameter and it is the basis for evaluation of the code. Significant differences have been recorded between experimental and numerical data after the initial validation of the model (Bury et al., 2008a). Minor changes have been put into the code and the validation procedure was then repeated with usage of the infra-red thermography measurements results also. The last stage of the research was the sensitivity analysis (Bury et al., 2008b). This analysis has shown that the heat transfer coefficient from ribbed surfaces to the gas may be the reason for recorded discrepancies between numerical and experimental results.

3.2 Heat transfer coefficient on the gas side

3.2.1 Application of Nusselt number correlations

A traditional analysis of the convective heat transfer for simple cases is based on the similarity theory and application of the dimension analysis. It is very difficult to find an

analytical solution for real cases and extensive measurements are necessary. A statistic analysis of the experimental results allows formulating an empirical correlation. A large number of such relationships have been worked so far. It should be however mentioned here that their application is limited to the heat exchangers of the same or very similar constructions to the experimental units. A review of available correlations allowed choosing those applicable for the heat exchangers under consideration. Six formulas have been investigated (Kays and London, 1998; Welty et al., 2008):

- Kays and London correlation:

$$Nu = \frac{0.011 \cdot Re^{-0.418} \cdot \dot{m}_{a,max} \cdot c_p \left(\frac{D_h}{k_a} \right)}{Pr^{2/3}} \quad (10)$$

- Berman correlation:

$$Nu = 0.3375 \cdot Re^{0.633} \quad (11)$$

- Brigs and Young correlation:

$$Nu = 0.134 \cdot Re^{0.681} \cdot Pr^{0.333} \left(\frac{s}{l} \right)^{0.2} \left(\frac{s}{\delta} \right)^{0.1131} \quad (12)$$

- Norris and Spofford correlation:

$$Nu = 1.0 \cdot Re^{1/2} \cdot Pr^{1/3} \quad (13)$$

- Paikert correlation:

$$Nu = 0.26 \cdot Re^{0.6} \cdot Pr^{0.333} \left(\frac{A_0}{A_e} \right)^{0.6} \left(\frac{A}{A_{G0}} \right)^{-0.15} \quad (14)$$

where

$$\left(\frac{A_0}{A_e} \right) = \frac{s_{tp}(s + \delta)}{(s_{tp} - d) \cdot s + (s_{tp} - d - 2 \cdot l) \cdot \delta}, \quad \left(\frac{A}{A_{G0}} \right) = 1 + \frac{2 \cdot l \cdot (l + d + \delta)}{d \cdot (s + \delta)}$$

- Schmidt correlation:

$$Nu = 0.3 \cdot Re^{0.625} \cdot Pr^{0.333} \left(\frac{A_{r+p}}{A_p} \right)^{-0.375} \quad (15)$$

The relationships shown above have been used to calculate the heat transfer coefficient for the air velocity ranging from 2 to 20 m/s and for the air temperatures equal to 10°C, 20°C or 30°C. The range of the air parameters has been established based on the experiments.

Figure 9 illustrates how big the discrepancy of the heat transfer coefficient is obtained depending on the choice of Nusselt number relationship. The use of different empirical correlations does not lead to conclusive results, but difficult to find criteria for selecting the

correct equation for the present case (range of Reynolds numbers and the equivalent diameter of the pipes are not sufficient criteria). The Kays and London correlations (presented for the specific geometry of the heat exchanger core) seem to be the most accurately determined according to empirical findings. But it is hard to tell what the impact of differences in the geometric parameters of the heat exchangers cores used in the study is.

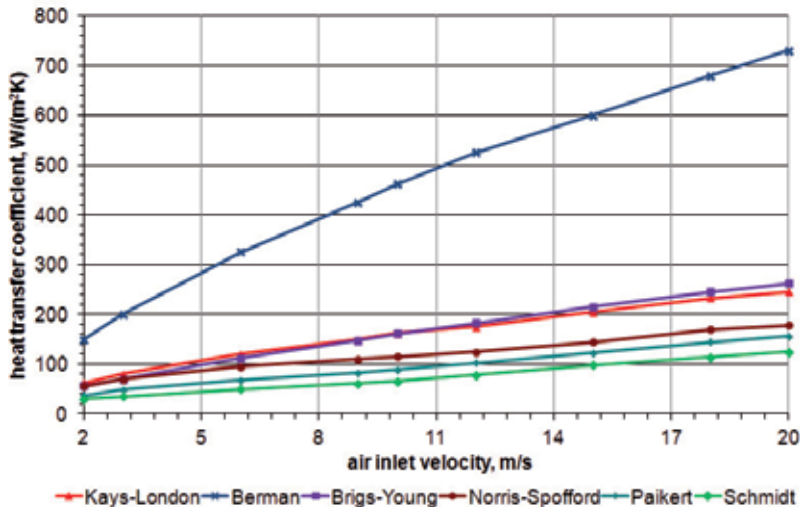


Fig. 9. Comparison of results obtained by different Nusselt number correlations for HE-1 heat exchanger.

3.2.2 Numerical simulations using CFD software

Two geometrical models have been made for numerical computations: the recurrent element of the considered heat exchangers and the recurrent segment – see Fig. 10. Geometries and numerical grids have been created using Gambit pre-processor.

The models of the recurrent segments of the radiators are related to the measurement series which results were described earlier. Each model consists of one or two rows of pipes and there are ten ribs in each row. The reason for the creation of these two numerical models is to test whether the simplification of real geometries affect the results.

The testing computations have shown that for considered models non-structured meshes are useless in most cases – the calculations were not converged or gave non-physical results. So for the fundamental computations for the recurrent element the structured meshes of 170 to 250 thousands cells for single recurrent element have been chosen.

The Reynolds Stress Model of turbulence has been chosen for the fundamental computations. The standard $k-\epsilon$ and the realizable $k-\epsilon$ models have been also tested, but some problems appeared during the calculations at low velocities of the air.

The Fluent CFD software has been applied for simulations. It has been assumed that the air inlet is parallel to the X axis of the models. Except the inlet and the outlet surfaces all of the remaining planes have been assumed as the symmetry planes. First the testing computations have been performed to choose the proper numerical grid and the turbulence

model. These computations have been realized for the air inlet temperatures of 10°C, 20°C or 30°C, and the velocity ranging from 2 m/s to 20 m/s. The water temperature has been assumed equal to 90°C, and the heat transfer coefficient inside the pipes has been calculated from the Colburn relationship.

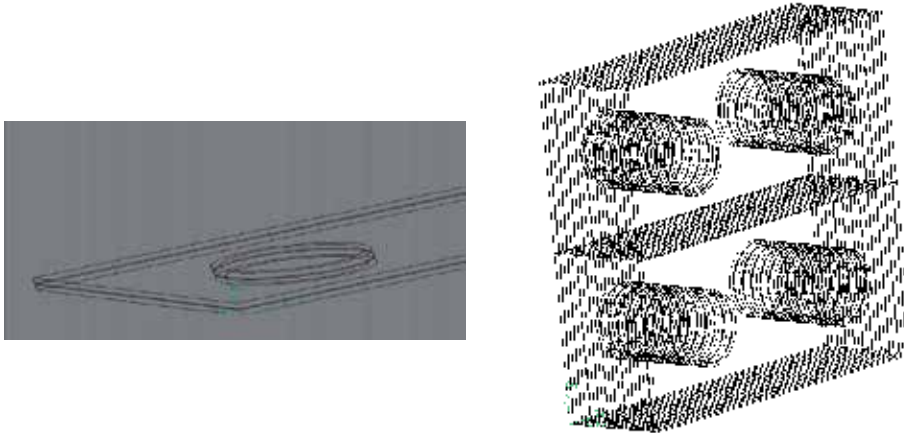


Fig. 10. The recurrent element (left) and the recurrent fragment (right) of the heat exchanger HE-1.

The averaged value of the heat transfer coefficient at the air side has been calculated based on the known fields of temperature for the rib surface and the pipe surface as well as the average temperature of the air and the transferred heat flux – see (Bury and Składzień, 2006) for details. The results for the HE-1 exchanger obtained by using the recurrent element model are presented in Fig. 11.

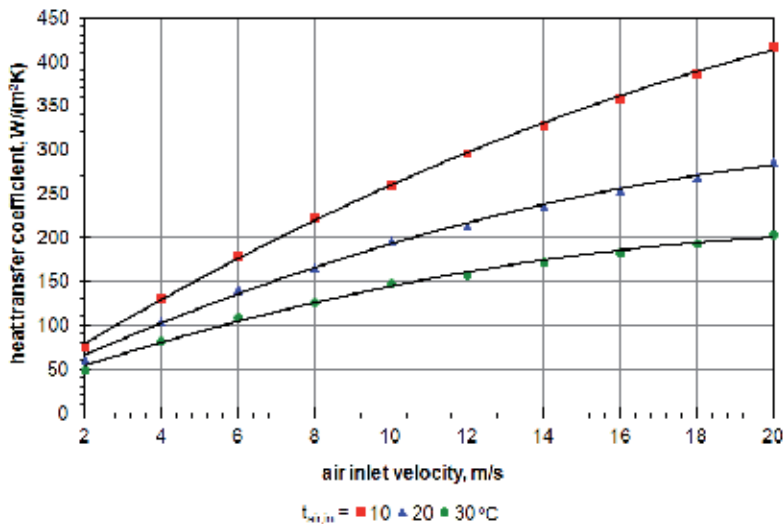


Fig. 11. Heat transfer coefficient versus the air inlet velocity – HE-1 exchanger, recurrent element model.

The comparison of results for the recurrent element and recurrent segment is shown in Fig. 12. One may observe that the values of the air heat transfer coefficient obtained from the segment model are higher than the results from the element model. The initial difference reaches almost 22 per cent and it decreases down to 6 per cent along with the rising velocity of the air. The more significant difference for the lower velocities may be an effect of a non-fully developed turbulence. Using the recurrent fragment model allows for more accurate mapping of the real object, but also increases the computation time almost ten times.

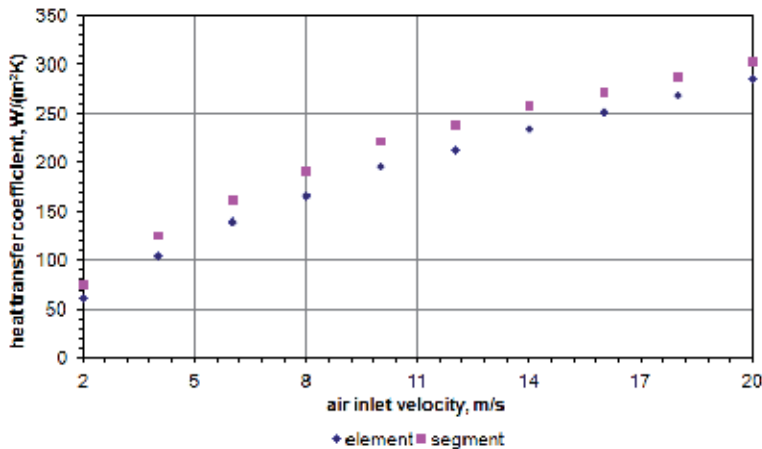


Fig. 12. Heat transfer coefficient versus the air inlet velocity – comparison of results for the recurrent element and segment of HE-1 exchanger.

3.2.3 Validation of the numerical procedure for the heat transfer coefficient determination

A simple comparison of heat transfer coefficient values presented in subsections 3.2.1 and 3.2.2 allows to see large differences, both between the empirical correlations and numerical models. Computational results, however, appear to coincide with the results obtained using the Kays-London correlations, which were previously considered to be the most accurate. Numerical approach is very convenient for the considered problem: it allows both to reproduce the accurate geometry of the recurrent element of the actual heat exchanger, as well as to take account of the non-uniform air flow. However, requires detailed plausibility study.

An enlarged special model of a fragment of the heat exchanger HE-1 has been built in order to check the numerical procedure responsible for determination of the heat transfer coefficient from the ribs to the gas.

The model consists of four plate ribs with respective pipe sections. Two electric heaters simulate the hot water flow inside the pipes. This model is placed in a flow channel with an observation window and it is cooled by the forced air flow (see Fig. 13). The air flow rate and temperatures at the inlet and outlet are measured. The infra-red thermography technique is used for measurement of the temperature field on the surface of the first rib. Several thermocouples are also installed for measuring the temperature on the other ribs surfaces.

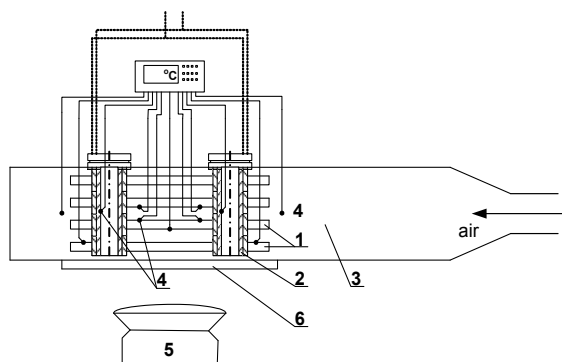


Fig. 13. Simplified sketch of the test station (1 - ribs and pipe models, 2 - electric heaters, 3 - flow channel, 4 - thermocouples, 5 - infra-red camera, 6 - speculum).

Two parameters have been set as independent during experiments: the temperature of the pipe internal wall and the air flow rates. Following parameters have been recorded during measurements:

- the air volumetric flow rate,
- the air temperature at the inlet and outlet of the ribs section $t_{a,in}$ and $t_{a,out}$,
- electric power consumed by the heaters N_{h} ,
- the electric heater surface temperature t_{h1} and t_{h2} (assumed after as the pipe inner surface temperature),
- temperatures on the ribs surfaces in the measuring points (seven measuring points have been marked as L1, L2, L3, M, R1, R2 and R3),
- temperature distribution on the surface of the first rib.

There have been 25 measurements realized within the framework of this project. These experiments have been divided into five measuring series differing with the set temperature of the electric heaters (from 50 to 90 degrees Celsius with ten degree step). The range of the independent parameters changes has been chosen to obtain flow conditions (Reynolds' number) similar to those from the main testing station. Selected results of experiments are presented in Table 2. Sample temperature distribution measured during experiment MS-2 is presented in Fig. 14.

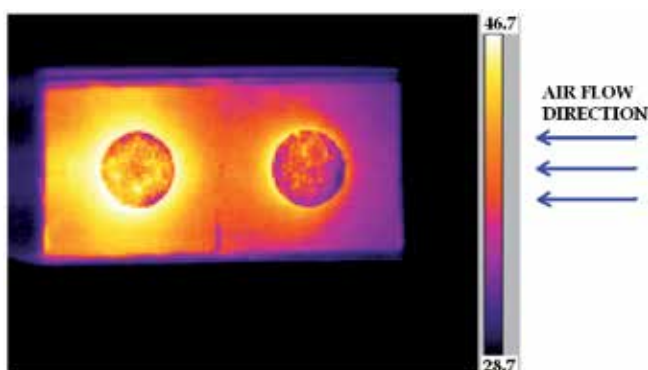


Fig. 14. Sample infrared thermographic picture of the first rib surface - experiment MS-2.

Meas. No.	\dot{V}_a	t_{h1}	t_{h2}	N_h	$t_{a,in}$	$t_{a,out}$	t_{L1}	t_{L2}	t_{L3}	t_M	t_{R1}	t_{R2}	t_{R3}
	m ³ /s	°C	°C	W	°C	°C	°C	°C	°C	°C	°C	°C	°C
MS-1	$7.03 \cdot 10^{-3}$	49.5	50.2	116.5	24.0	37.5	45.3	40.0	49.4	42.3	37.3	38.0	37.9
MS-5	$12.47 \cdot 10^{-3}$	49.7	50.4	137.1	22.9	31.1	38.6	33.8	43.2	38.9	31.2	31.4	31.6
MS-6	$7.00 \cdot 10^{-3}$	59.6	60.5	143.3	24.1	40.1	46.0	41.9	53.6	46.5	39.2	38.3	37.8
MS-10	$12.47 \cdot 10^{-3}$	60.1	60.7	152.5	23.4	33.1	41.7	35.9	43.7	40.9	33.1	31.0	31.8
MS-11	$7.03 \cdot 10^{-3}$	69.6	70.7	159.6	24.2	41.9	50.1	46.3	55.2	48.7	38.2	38.2	42.3
MS-15	$12.47 \cdot 10^{-3}$	69.9	71.1	173.4	23.7	34.4	42.9	40.3	45.3	43.1	36.9	33.8	34.5
MS-16	$7.00 \cdot 10^{-3}$	79.5	80.6	179.1	24.0	44.5	52.0	45.6	56.8	48.5	41.9	41.2	42.2
MS-20	$12.50 \cdot 10^{-3}$	79.2	80.0	189.2	24.2	36.2	45.3	39.4	47.7	45.1	35.8	33.9	36.2
MS-21	$7.03 \cdot 10^{-3}$	93.7	90.4	192.0	23.9	44.8	56.1	48.3	60.1	52.4	41.8	39.7	42.1
MS-25	$12.53 \cdot 10^{-3}$	89.7	90.6	215.8	24.5	38.3	46.5	39.1	48.3	42.4	35.2	32.8	35.3

Table 2. Selected results of measurements.

All experiments described above have been next simulated using numerical model of the laboratory stand. The same assumptions as used during creation of the models described in subsection 3.2.2 have been applied. The numerical model of the system under consideration is a part of the laboratory stand and contains the flow channel with the ribs section. The geometry of the model has been created using Gambit preprocessor and it is shown in Fig. 15 as well as the boundary conditions types. All remaining boundary conditions have been set as coupled and isolated walls for external surfaces of the model. The numerical model contains near 560 thousands of tetrahedral cells.

All performed simulations have been realized using the measured air flow rate and the electric heaters surfaces temperature as the boundary conditions. A part of simulations also considered thermal radiation. The surface to surface model of this phenomena implemented into the Fluent has been applied.

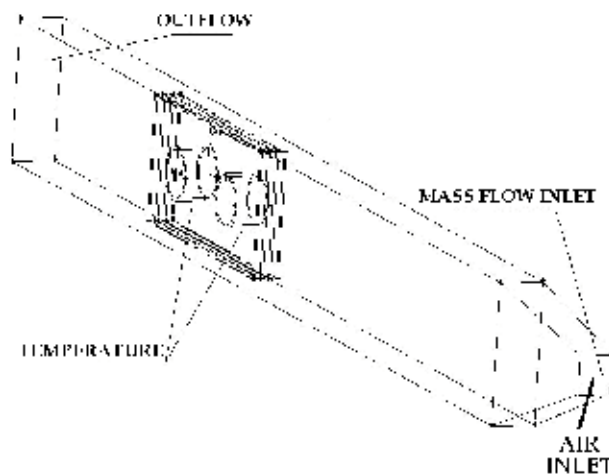


Fig. 15. Geometry of the numerical model of the test rig and boundary conditions types.

Selected results of simulations of the MS-1 experiment are presented in Fig. 16. The CFD analysis gives the possibility to view fields of the most important parameters in different cross sections of the object under consideration. The air velocity distribution is shown in Fig. 16 on left. The cross section plane is parallel to the flow direction and it crosses the second rib. One may note that the air inflow to the ribs section is quite well unified.

The most interesting numerical results are the temperature distributions on the first rib surface (see Fig. 16 on right), as well as the experimental results. These distributions may be next compared with the infra-red thermography measurements.

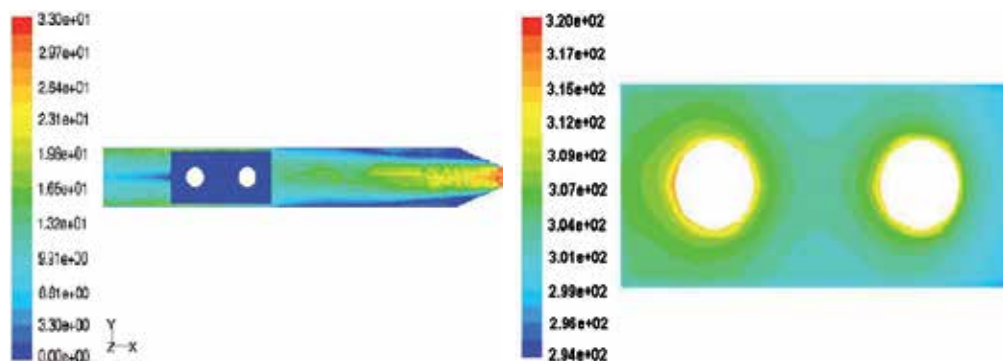


Fig. 16. The air velocity contours (left - m/s) and temperature distribution on the first rib surface (right - K) for the MS-1 experiment.

The main goal of the analysis is to evaluate the numerical CFD model used for computations of the heat transfer coefficient at the gas side of the considered heat exchanger. A simple comparison of measured and computed temperatures for two analyzed experiments is presented in Table 3. The first three thermocouples are placed on the first rib visible surface and are also used for calibration of the infra-red camera. The calculated surface temperature values are a little bit underestimated, as well as the air outlet temperature. The last parameter is computed as the area weighted average value for the cross section placed 2 cm next to the ribs section.

The most interesting is comparison of the temperature field for the first rib surface (see Fig. 17). Due to different color scales a direct comparison is somewhat difficult but one can see that similarity of temperature distributions is quite good, both quantitatively and qualitatively.

		$t_{L1}, ^\circ\text{C}$	$t_{L2}, ^\circ\text{C}$	$t_{L3}, ^\circ\text{C}$	$t_M, ^\circ\text{C}$	$t_{R1}, ^\circ\text{C}$	$t_{R2}, ^\circ\text{C}$	$t_{R3}, ^\circ\text{C}$	$t_{a,out}, ^\circ\text{C}$
MS-4	Measurement	40.4	41.5	34.5	43.9	39.8	40.6	33.9	33.4
	Simulation	40.1	40.9	33.8	43.5	39.4	39.9	33.3	32.9
MS-22	Measurement	56.2	57.7	48.0	61.1	55.4	56.5	47.2	42.9
	Simulation	55.5	56.2	47.1	60.5	54.6	55.1	46.3	41.3

Table 3. Comparison of experimental and numerical data for the rib temperature – sample results.

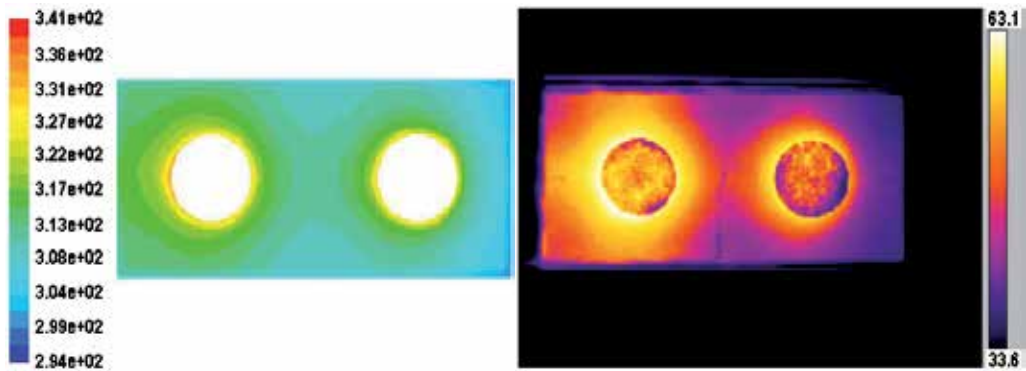


Fig. 17. Calculated (left, K) and measured (right, °C) temperature field of the first rib surface for experiment MS-4 – air flow direction same as in Fig. 14.

The next step in the analysis was the computation and comparison of the total heat flow rates transported from the ribbed surface to the flowing air. The results for measuring series MS-1 to MS-5 and MS-21 to MS-25 are presented in Table 4. The total heat flow rates has been calculated twice based on the air enthalpy rise:

- considering the measured values of the volumetric air flow and its temperature measured at the inlet and outlet of the ribs section (\dot{Q}_{air} in Table 4),
- taking into account the computed values of the mentioned parameters (\dot{Q}_{Fluent} in Table 4).

Measurement No.	N_h, W	\dot{Q}_{air}, W	$\dot{Q}_{\text{Fluent}}, W$	$\delta \dot{Q}_{\text{air}}, \%$	$\delta \dot{Q}_{\text{Fluent}}, \%$
MS-1	116.5	111.8	104.5	4.03	10.30
MS-2	122.6	117.2	109.9	4.40	10.36
MS-3	128.0	119.0	111.7	7.03	12.73
MS-4	132.4	117.2	109.9	11.48	16.99
MS-5	137.1	120.9	113.6	11.82	17.14
MS-21	192.0	173.1	165.8	9.84	13.65
MS-22	196.5	186.2	178.9	5.24	8.96
MS-23	200.5	190.7	183.4	4.89	8.53
MS-24	207.0	200.0	192.7	3.38	6.91
MS-25	215.8	203.3	196.0	5.79	9.18

Table 4. Comparison of experimental and computational data – heat flow rates.

The relative differences ($\delta \dot{Q}$) between experimental and numerical results have been calculated. The heat flow rates calculated based on the measured values, as it can be seen, is lower than the measured values of the electric power of the heaters. The obvious reason of this situation is the heat losses through the rear wall of the flow channel. The differences between experimental and computational heat flow rates calculated as the CFD results reach up to 18% for some cases, but the average difference is somewhat over 10%.

In the paper (Bury et al., 2009a) authors concluded that neglecting of thermal radiation phenomena may be a reason of discrepancies between numerical and experimental results. An additional set of simulations has been initiated taking into account thermal radiation. The results however have shown almost no differences in comparison to these shown in Table 4. This situation could be an effect of assuming dry air flow through the ribs section. This gas contains mostly two-atom particles and it is almost optically inactive regarding the thermal radiation.

According to the results of analyses it may be noted that the CFD based numerical model portrays the physical phenomena with satisfying accuracy. Probable reasons of recorded discrepancies are some simplifications in the numerical model geometry as well as neglecting the heat losses to the environment.

3.3 Results of numerical simulations

The analyses presented in subsection 3.2 allowed to withdrawn following conclusions:

- application of available correlations for Nusselt number leads to a wide deviation of the heat transfer coefficient values; it is difficult to define the characteristic dimension in some cases; even application of Kays-London approach (assumed as the most accurate) does not assure reliable results,
- the numerical models of recurrent element and recurrent segment of considered heat exchangers give the heat transfer coefficient results within the range determined by investigated correlations for Nusselt number; the results obtained by using the recurrent element and recurrent segment differ, especially at low velocities; application of the recurrent segment model seems to be more correct but it needs a lot of computing time; such approach allows for detailed representation of real geometries in numerical model.

Measurement No.	\dot{Q}_{num} , kW	\dot{Q}_{ex} , kW	$\delta\dot{Q}$, %
HE-1/1	12.78	11.03	15.9
HE-1/2	26.44	22.61	16.9
HE-1/3	39.96	34.08	17.3
HE-1/4	11.11	9.72	14.3
HE-1/5	22.44	19.42	15.6
HE-1/6	33.48	29.11	15.0
HE-2/1	11.59	10.07	15.1
HE-2/2	16.24	14.08	15.4
HE-2/3	22.75	19.58	16.2
HE-2/4	5.10	4.48	13.9
HE-2/5	13.76	12.04	14.3
HE-2/6	22.68	19.76	14.8
HE-3/1	14.27	12.39	15.2
HE-3/2	20.02	17.31	15.6
HE-3/3	28.10	24.08	16.7
HE-3/4	6.28	5.51	14.0
HE-3/5	17.00	14.81	14.8
HE-3/6	28.14	24.30	15.8

Table 5. Selected computational results.

Considering the abovementioned facts it was decided to apply the CFD approach with the recurrent elements models for determination of the heat transfer coefficient from ribbed surfaces to the flowing air during the numerical simulations.

Simulations were aimed in determination of the non-uniform air inlet impact on the heat exchangers efficiency and have been realized using the described earlier model and the computer code HEWES. All these simulation have been performed applying the uniform air inflow to the exchanger. The uniform mass flow rate of the air has been derived assuming that the total mass flow rate of the air spreads equally on the all measuring fields. The selected results of computations are gathered in Table 5 and, as expected, they shown quite significant improvement of the efficiency of the heat exchanger. The efficiency growth raises with increasing the air flow rate and water inlet temperature.

The numbers in the last column of Table 5 give an average value of 15%. This should be considered as significant deterioration of the cross-flow heat exchanger thermal efficiency due to the medium flow maldistribution. Moreover, these results obtained for three units with different ribbing structure are similar. So, it seems that the air inlet non-uniformity affects the performance of the heat exchangers under consideration to the same extent.

4. Conclusions

The experiments performed for three considered cross-flow heat exchangers have shown that the air inflow non-uniformity range may be significant and its form depends on the air volumetric flow rate in the considered configuration. The experimental data allowed for determination of the total heat flow rates transported between the agents in the heat exchangers.

The computational results, as it was expected, have shown significant decrease in the heat flow rates comparing with the exchanger with fully uniform air inflow. The average deterioration factor is about 15%. Two aspects should be taken into account while evaluating the numbers from Table 5: the measurements errors and the accuracy of the code HEWES. Taking into account accuracy of the measuring instruments the maximum measurements error has been determined to be of $\pm 4\%$. The uncertainty of numerical results has been assessed during the validation of the code - see (Bury et al., 2008a; Bury et al., 2008b) for more details - and the differences between numerical and experimental results may reach almost 11%. These two numbers and the fact that the numerical results are always underestimated allow to conclude that the air inlet maldistribution has significant impact on a cross-flow heat exchanger performance.

Following final conclusions and remarks can be pointed for summarizing this study:

- experimental and numerical analyses accomplished within the framework of investigations confirmed the earlier observations about significant meaning of media flow maldistribution for cross-flow heat exchanger thermal performance,
- results concerning the increase of the efficiency due to uniformization of flow obtained in this work remain in the range achieved by the other researchers,
- application of CFD tools for computational analyses of heat exchangers may be useful and reliable but models should be thoroughly validated first; further validation of the numerical models described in subsection 3.2.2 is planned in the nearest future for models of ribs referring to HE-2 and HE-3 heat exchangers.

The author realizes that the combination of experimental tests and numerical simulations to assess the impact of inequality for the work of the heat exchangers may be the subject of some criticism. The best solution would be to do all the analysis by means of measurements. However, to obtain a homogeneous air flow on the described testing rig, while maintaining the appropriate parameters, it is impossible due to technical limitations. Some attempts to implement this idea has been taken in (Bury et al., 2009b), and although it failed to get the full homogeneity of the flow, it was noted the positive effects.

5. Acknowledgment

This investigation was supported by the Polish Ministry of Science and Higher Education under the project No. N N512 458836. Technical support of the GEA Heat Exchangers Company is also acknowledged.

6. Nomenclature

c_p	- specific heat capacity at constant pressure, J/(kg K)	\dot{Q}	- heat flow rate, W
d	- heat exchanger pipe diameter, m	Re	- Reynolds number
D_h	- hydraulic diameter, m	s	- distance between ribs, m
h	- heat transfer coefficient, W/(m ² K)	S	- surface area, m ²
k	- thermal conductivity, W/(m K)	s_{tp}	- transverse distance between pipes, m
l	- height of a rib, m	t, T	- temperature, °C, K
\dot{m}	- mass flow rate, kg/s	\dot{V}	- volumetric flow rate, m ³ /s
Nu	- Nusselt number	δ	- thickness of a rib, m
Pr	- Prandtl number	ρ	- mass density, kg/m ³

Subscripts

a	- air	p	- refer to pipes without ribs
in	- inlet	r	- refer to ribbed surface
max	- maximum value	w	- water
out	- outlet		

7. References

- Aganda, A.A.; Coney, J.E.R.; Farrant, P.E.; Sheppard, C.G.W. & Wongwuttanasatian, T. (2000). A Comparison of the Predicted and Experimental Heat Transfer Performance of a Finned Tube Evaporator. *Applied Thermal Engineering*, Vol. 20, No. 6, (June 2000), pp. 499-513, ISSN 1359-4311
- Andreovich, M. & Clarke, R. (2003). Simple Modeling of Flow Maldistribution in Plate-Fin Exchangers, *Proceedings of the 21st IIR International Congress of Refrigeration*, Paper ICR0639, Washington DC, USA, August 17-22, 2003
- Anjun, J.; Rui, Z. & Sangkwon J. (2003). Experimental Investigation of Header Configuration on Flow Maldistribution in Plate-Fin Heat Exchanger. *Applied Thermal Engineering*, Vol. 23, No. 10, (July 2003), pp. 1235-1246, ISSN 1359-4311
- Berryman, R.J. & Russell, C.M.B. (1987). The Effect of Maldistribution of Air Flow on Aircooled Heat Exchanger Performance, In: *Maldistribution of Flow and Its Effect on*

- Heat Exchanger Performance*, J.B. Kitto & J.M. Robertson (Eds.), pp. 19-23., ASME Htd, Vol. 75, ISBN 978-9991621319 (June 1987)
- Bury, T. & Składzień, J., (2006). The Experimental and the Numerical Analysis of a Ribbed Heat Exchanger With an Unequal Inlet of the Air, *Proceedings of the 11th International Symposium on Heat Transfer and Renewable Sources of Energy*, pp. 419-426, Międzyzdroje, Poland, September 13-16, 2006
- Bury, T.; Składzień, J. & Piątek, R. (2007a). Experimental and Numerical Hydraulic Analysis of the Water Chiller With Unequal Inlet of the Agents, *Proceedings of the 13th Symposium of Heat and Mass Transfer*, pp. 297-304, Darłówko, Poland, September 3-6, 2007
- Bury, T., Kruczek, T. & Składzień, J. (2007b). Experimental Investigations of the Effectiveness of Functioning of the Cross-Flow Water Cooler With Unequal Flow of the Agents, *Proceedings of the 1st Conference on Contemporary Power Engineering Technology*, pp. 23-34, Kraków, Poland
- Bury, T.; Piątek, R. & Składzień, J. (2008a). Experimental Validation of The Numerical Thermal Model Of The Cross-Flow Heat Exchanger With Unequal Agent Flow. *Proceedings of the 21st International Conference on Efficiency, Cost, Optimization, Simulation and Environmental Impact of Energy Systems - ECOS 2008*, pp. 329-336, Kraków - Gliwice, Poland, June 24-27, 2008
- Bury, T.; Składzień, J. & Piątek, R. (2008b). Validation and Sensitivity Analysis of the Mathematical Model of a Cross-Flow Heat Exchanger with Non-Uniform Flow of Agents. *Systems - Journal of Transdisciplinary Systems Science*, Vol. 13, special issue 1/2, (November 2008), pp. , ISSN 1427-275X
- Bury, T.; Składzień J. & Sachajdak, A. (2009a). Experimental Validation of the Numerical Model of the Heat Transfer Coefficient Calculation for a Cross Flow Heat Exchangers. *Proceedings of the 7th World Conference on Experimental Heat Transfer, Fluid Mechanics and Thermodynamics*, on CD, Kraków, Poland, June 28 - July 3, 2009
- Bury, T.; Składzień, J. & Hanuszkiewicz-Drapała, M. (2009b). Experimental and Numerical Analyses of a Non-Uniform Agents Flow Impact on a Finned Cross-Flow Heat Exchanger Effectiveness. *Proceedings of the 22nd International Conference on Efficiency, Cost, Optimization, Simulation and Environmental Impact of Energy Systems - ECOS 2009*, on CD, Foz do Iguacu, Parana, Brasil, August 31 - September 3, 2009
- Bury, T. & Składzień, J. (2010). Verification of the CFD Model of the Heat Transfer Model on a Rib Surface. *Proceedings of the 13th International Symposium on Heat Transfer and Renewable Sources of Energy*, pp. 285-292, Szczecin - Międzyzdroje, Poland, September 9-12, 2010
- Chwalowski, M.; Didion, D.A. & Domanski, P.A. (1989). Verification of Evaporator Computer Models and Analysis of Performance of an Evaporator Coil. *ASHRAE Transactions*, Vol. 95, No. 2, (1989), pp. 1229-1236, ISSN 0001-2505
- Fagan, T.J. (1980). The Effects of Air Flow Maldistributions on Air-to-Refrigerant Heat Exchanger Performance. *ASHRAE Transactions*, Vol. 86, No. 2, (1980), pp. 699-713, ISSN 0001-2505
- Hanuszkiewicz-Drapała, M. (1996). *Thermodynamic Analysis of a Cross-Flow Heat Exchanger with Non-uniform Flow of Agents*, PhD Thesis, Institute of Thermal Technology, Silesian University of Technology, Gliwice, Poland (in Polish)

- Hoffmann-Vocke, J.; Neale, J. & Walmsley, M. (2009). Flow Profiles on the Fin Side of a Plate Fin-And-Tube Heat Exchanger Experiencing Gross Flow Maldistribution, *Proceedings of 7th World Conference on Experimental Heat Transfer, Fluid Mechanics and Thermodynamics*, on CD, Kraków, Poland, June 28 - July 3, 2009
- Hoffmann-Vocke, J.; Neale, J. & Walmsley, M. (2011). The Effect of Inlet Conditions on the Air Side Hydraulic Resistance and Flow Maldistribution in Industrial Air Heaters. *International Journal of Heat and Fluid Flow*, Vol. 32, No. 4, (August 2011), pp. 834-845, ISSN 0142-727X.
- Kays; W.M. & London, A.L. (1998). *Compact Heat Exchangers*, 3rd Revised Edition, Krieger Publishing Company, EAN 9781575240602, Malabar, Florida, USA
- Lalot, S.; Florent, P.; Lang, S.K. & Bergles, A.E. (1999). Flow Maldistribution in Heat Exchangers. *Applied Thermal Engineering*, Vol. 19, No. 8, (August 1999), pp. 847-863, ISSN 1359-4311
- Lee, J. & Domanski, P.A. (1997). Impact of Air and Refrigerant Maldistributions on the Performance of Finned-Tube Evaporators With R-22 and R-407C, Final Report, ARTI MCLR Project Number 665-54500, (July 1997), Arlington, USA
- Lee, K.-S. & Oh S.-J. (2004). Optimal Shape of the Multi-Passage Branching System in a Single-Phase Parallel-Flow Heat Exchanger. *International Journal of Refrigeration*, Vol. 27, No. 1, (January 2004), pp. 82-88, ISSN 0140-7007
- Luo, X.; Roetzel, W. & Lüdersen, U. (2001). The Single-Blow Transient Technique Considering Longitudinal Core Conduction and Fluid Dispersion. *International Journal of Heat and Mass Transfer*, Vol. 44, No. 1, (January 2001), pp. 121-129, ISSN 0017-9310
- Malinowski, Ł. (2008). Experimental and Numerical Analysis of a Non-Uniform Air Inflow to a Cross-Flow Heat Exchanger. MSc Thesis, Institute of Thermal Technology, Silesian University of Technology, Gliwice, Poland (in Polish)
- Meyer, C.J. & Kröger, D.G. (1998). Plenum Chamber Flow Losses in Forced Draught Air-Cooled Heat Exchangers. *Applied Thermal Engineering*, Vol. 18, No. 9-10, (September 1998), pp. 875-893, ISSN 1359-4311
- Mueller, A.C. (1987). Effects of Some Types of Maldistribution on the Performance of Heat Exchanger. *Heat Transfer Engineering*, Vol. 8, No. 2, (1987), pp. 75-86, ISSN 0145-7632
- Nair, S.; Verma, S. & Dhingra, S.C. (1998). Rotary Heat Exchanger Performance With Axial Heat Dispersion. *International Journal of Heat and Mass Transfer*, Vol. 41, No. 18, (September 1998), pp. 2857-2864, ISSN 0017-9310
- Piątek, R. (2003). *Thermal Analysis of Plate Fin and Tube Heat Exchanger With Unequal Inlet of Media*, PhD Thesis, Institute of Thermal Technology, Silesian University of Technology, Gliwice, Poland (in Polish)
- Ranganayakulu, Ch.; Seetharamu, K.N. & Sreevatsan, K.V. (1996). The Effects of Inlet Fluid Flow Nonuniformity on Thermal Performance and Pressure Drops in Crossflow Plate-Fin Compact Heat Exchangers. *International Journal of Heat and Mass Transfer*, Vol. 40, No. 1, (October 1996), pp. 27-38, ISSN 0017-9310
- Rao, B. P.; Sunden, B. & Das S. K. (2006). An Experimental Investigation of the Port Flow Maldistribution in Small and Large Plate Package Heat Exchangers. *Applied Thermal Engineering*, Vol. 26, No. 16, (November 2006), pp. 1919-1926, ISSN 1359-4311
- Shaji, K. & Das S. K. (2010). The Effect of Flow Maldistribution on the Evaluation of Axial Dispersion and Thermal Performance During the Single-Blow Testing of Plate Heat

- Exchangers. *International Journal of Heat and Mass Transfer*, Vol. 53, No. 7-8, (March 2010), pp. 1591-1602, ISSN 0017-9310
- Składzień, J. & Bury T. (2011). Application of Infra-Red Thermography for Validation of the Heat Transport Model on a Rib Surface. *Proceedings of the 6th International Conference on Transport Phenomena in Multiphase Systems*, pp. , Ryn, Poland, June 28 - July 2, 2011
- Srihari, N. & Das S. K. (2008). Transient Response of Multi-Pass Plate Heat Exchangers Considering the Effect of Flow Maldistribution. *Chemical Engineering and Processing: Process Intensification*, Vol. 47, No. 4, (April 2008), pp. 695-707, ISSN 0255-2701
- Srihari, N.; Rao, B.P.; Sundén, B. & Das S. K. (2005). Transient Response of Plate Heat Exchangers Considering Effect of Flow Maldistribution. *International Journal of Heat and Mass Transfer*, Vol. 48, No. 15, (July 2005), pp. 3231-3243, ISSN 0017-9310
- Taler, D. & Cebula, A. (2004). Numerical Modeling of the Heat Transfer in the Lamel Type Heat Exchangers, *Proceedings of the 12th Symposium on Heat and Mass Transfer*, Vol. 2, pp. 827-836, Kraków, Poland, June 15-18, 2004
- Taler, D. (2002). Theoretical and Experimental Analysis of Heat Exchangers With Extended Surfaces. Polish Academy of Sciences, *Papers of the Scientific Commission of Automotive Industry*, Vol. 25, No. 3, Kraków, Poland
- Welty, J.; Wicks, C.E.; Rorrer, G.L. & Wilson, R.E. (2008). *Fundamentals of Momentum, Heat and Mass Transfer*, John Wiley & Sons, 5th Edition, ISBN 978-0-470-12868-8, New York, USA
- Wen, J. & Li, Y. (2004). Study of Flow Distribution and Its Improvement on the Header of Plate-Fin Heat Exchanger. *Cryogenics*, Vol. 44, No. 11, (November 2004), pp. 823-831, ISSN 0255-2701
- Zhang, L.-Z. (2009). Flow Maldistribution and Thermal Performance Deterioration in a Cross-Flow Air to Air Heat Exchanger With Plate-Fin Cores. *International Journal of Heat and Mass Transfer*, Vol. 52, No. 19-20, (September 2009), pp. 4500-4509, ISSN 0017-9310

Control of LNG Pyrolysis and Application to Regenerative Cooling Rocket Engine

R. Minato, K. Higashino, M. Sugioka and Y. Sasayama
Muroran Institute of Technology
Japan

1. Introduction

Rocket propellant has various requirements, such as higher specific impulse (Isp), large density, non-toxic, storability, operational reliability and easy handling. In addition, large heat capacity of the fuel is also desirable. A regenerative cooling system is often adopted to cool a combustion chamber because of high combustion temperature (about 3000K), and high heat transfer rates from combustion gas. In the regenerative cooling system, the combustion chamber is a kind of a heat exchanger and fuel of a rocket engine is used as a coolant. The fuel heated in regenerative cooling passage is injected into the combustion chamber and burned. Heat loss from combustion gas to chamber wall is absorbed into the heat capacity of fuel and utilize them to propulsive work again. (regeneration).

Unfortunately, no propellant can satisfy all of those requirements. The requirements of higher Isp and larger thrust trade off each other. For example, Liquid hydrogen (LH₂) has high Isp and "clean" propellant. In addition, hydrogen has large heat capacity, and thus, is favorable coolant for regenerative cooling. However, the molecular weight of hydrogen is the lowest among the all of chemical compounds, thus, it is difficult to obtain larger thrust by using LH₂. For those reasons, LH₂ is suitable for an upper staged rocket engine, rather than an booster staged one. Another disadvantage of LH₂ is difficulty to handle because it is cryogenic fluid (20K at tank) and easy to leak from the tank.

The hydrocarbon fuels have been also widely used for rocket propulsion because they have advantages of non-toxic, lower cost, higher density and easier handling. RP-1 is the typical kerosene fuel for rocket propulsion, which was used for F-1 engine of Saturn 5. Kerosene can produce larger thrust than LH₂, although it has a drawback of lower Isp. Therefore, kerosene fuel is suitable for a booster staged rocket engine. If kerosene fuel would be employed to the regenerative cooling system, the combustion chamber has fuel flow passage within its wall. The regenerative cooling combustion chamber plays role of heat exchanger. The temperature of fuel increases to begin the thermal decomposition and cause soot formation in the regenerative cooling fuel passage. The soot in the fuel passage can clog the fuel flow and deteriorate the heat transfer from a chamber wall to fuel. Thus, the rocket engine designers must pay attention to coking of hydrocarbon fuel.

Liquefied Natural Gas (LNG) is one of the hydrocarbon fuel and its main component is CH₄. The volumetric fraction of CH₄ typically ranges from 85% to 95%. The rest of them are ethane

and propane. The average molecular weight of LNG is about 16 g/mol, which is larger than hydrogen but much less than kerosene. Thus, the Isp of LNG propellant is greater than Kerosene. LNG can be stored in a tank at 110K and easier to handle than LH₂, though LNG is cryogenic fluid. However, the application of LNG propellant has not been realized so far. For the booster stage rocket, kerosene can produce greater thrust than LNG. For the upper stage, the Isp of LH₂ is superior to LNG.

Recently, LNG is reconsidered as the propellant for an interplanetary transfer vehicle or an booster rocket engine due to its low cost and easy handling (Brown, C.D. 2004 and Crocker, A. M. 1998). In such engine, the regenerative cooling system and a turbopump are necessary to improve its propulsive performance. As well as kerosene fuel, LNG pyrolysis can be also occurred in high temperature condition, which means that coking problem arise in the regenerative cooling with LNG. Few databases are available about LNG pyrolysis, because LNG propellant has not been utilized in the rocket engine until now. Therefore, such databases must be prepared for a successful development of this engine. For the turbopump, it feeds the propellant to combustion chamber with high pressure and is operated by various cycles, for example, gas generator cycle, staged combustion cycle and expander cycle. In the expander cycled rocket engine, turbopump is driven by the high temperature propellant gas. The propellant cooled the combustion chamber and receive the heat. The higher temperature and the lower molecular weight propellant is, the larger turbine power can be obtained. Therefore, the expander cycle have usually employ the LH₂, however, LNG also has the feasibility for the expander cycled turbopump(Brown, C.D. 2004 and Crocker, A. M. 1998). the efficient heat exchange in cooling passage is one of the most important factors to establish the expander cycled rocket engines. It is necessary to control the LNG pyrolysis in the high temperature environment.

For successful development of LNG rocket engine with regenerative cooling, the fundamental characteristics of LNG pyrolysis must be cleared. The present study focused on 1) the temperature to begin CH₄ pyrolysis, 2) the catalytic effect of combustion chamber materials, 3) the effects of addition of propane to CH₄. At same time, numerical analyses are conducted to simulate CH₄ and CH₄-propane mixture. Secondary, the authors proposed coking inhibition methods and experimentally evaluate it.

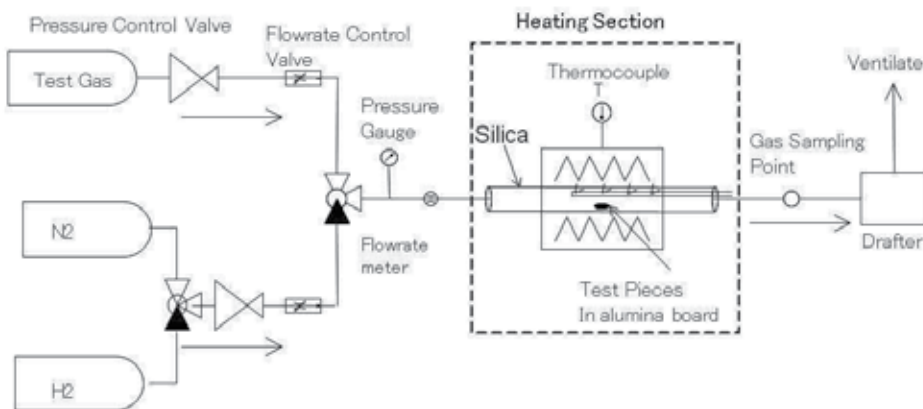


Fig. 1. Schematic of Test Apparatus.

Temperature	°C	500, 700, 800 for Constant Temperature Heating	
		From 500 to 850 for Ascendant Heating	
Pressure	(MPa A)	0.20	
Flowrate	(ml/min)	20.0	
Test Duration		60 min for Constant temperature heating	
		40 min from 500 to 850 °C	
Test piece materials		Inconel 718, Inconel 600, A286	
Constituents of test piece materials		Inconel 718	Ni: 53.5%, Cr : 19%, Fe: 18%
		Inconel 600	Ni: 78%, Cr : 15%, Fe: 7%
		A286	Ni: 25%, Cr : 15%, Fe: 54.9%

Table 1. Test Conditions of CH₄ Heating Test.

2. Fundamental study on coking characteristics of LNG rocket engine chamber

2.1 Experimental study of CH₄ pyrolysis and catalytic effects of chamber material

To make clear the fundamental characteristics of methane pyrolysis, the authors conducted the experimental investigation. In the present section, we introduced the experimental results by Higashino, K. et. al. (Higashino, K. et. al. 2009A) The test apparatus shown in the Figure 1 is employed. The CH₄ gas (99.99% of purity) is supplied from the test gas bottle to silica glass tube, where is heated by the electronic furnace. The nitrogen gas can be also fed to gas flow passage to purge the CH₄ gas. The flowrates of those gases are controlled by using flowrate control valves and pressure control valves. To investigate its catalytic effects on pyrolysis reaction, 10 pieces of combustion chamber materials (10mm length x 5mm width x 0.5mm thickness) are placed into the alumina board, which are located in this tube. The materials of those test pieces are Inconel 718, Inconel 600 and A286. The formers of two are Nickel based alloy and have mechanical strength under high temperature condition. They were utilized for combustion chamber material, however, Nickel has the catalytic effects to accelerate the thermal decomposition of CH₄. On the other hand, A286 is Iron based alloy, but contains Ni of 25%. The details of test conditions and properties of those materials are summarized in Table.1. Prior to the test, the oxide film on the surface of the test pieces was hydrogenated at 500 °C because it can hamper accurate evaluation of the catalytic effects. The gas sampling point is located in the downstream of the heating section, where the test gas is sampled to investigate its chemical composition. The test gas was ventilated after diluting with the air at draft.

Two types of heating methods are employed, constant temperature heating and ascendant heating. In ascendant heating, temperature of the electronic furnace increases with time linearly. The existence of pyrolysis can be found by analyzing the sampled gas by using gas chromatograph with thermal conductivity detector. During the heating tests, gas sampling is conducted in every 5 minutes. The volume of the sampled gas is about 0.5 ml per one time. The progression of CH₄ pyrolysis is evaluated by the CH₄ conversion rate (%) as expressed in equation (1)

$$Conversion\ Rate = \left[1 - \frac{(A_{CH_4}/\lambda_{CH_4})}{(A_{CH_4}/\lambda_{CH_4}) + (A_{H_2}/\lambda_{H_2})} \right] \times 100 \tag{1}$$

where A and λ indicate the area shown in the gas chromatograph results and thermal conductivity, respectively. The subscripts of CH_4 and H_2 indicate CH_4 and hydrogen, respectively. For the gas chromatograph with thermal conductivity detector, volumetric fractions of chemical species can be A divided by λ .

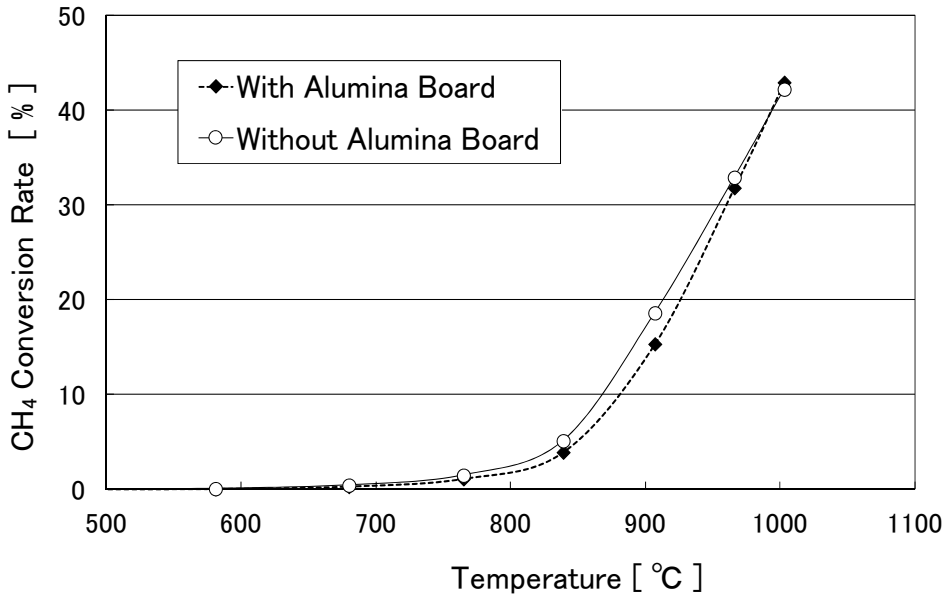
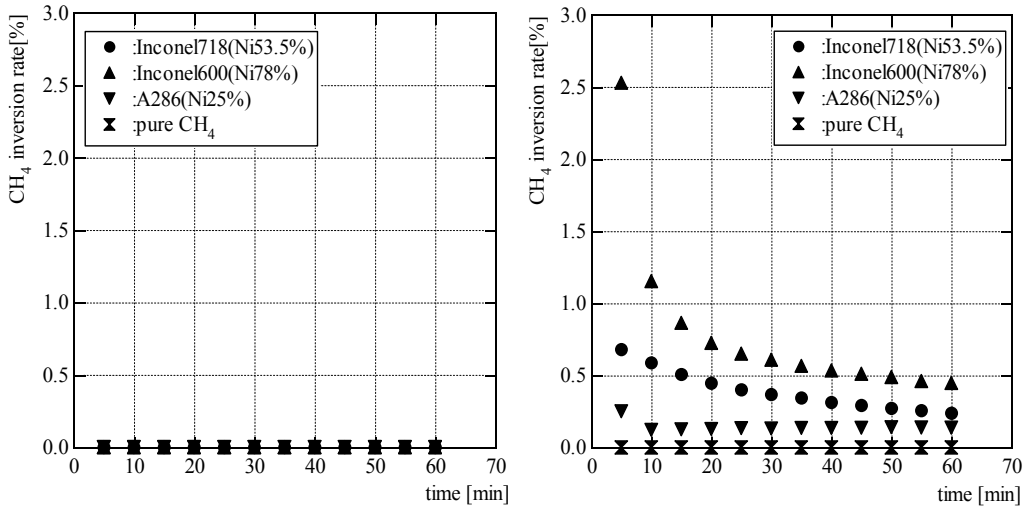


Fig. 2. Effects of Alumina Board on Methane and Propane Pyrolysis.



(a) Constant temperature heating at 500 °C (b) Constant temperature heating at 700 °C

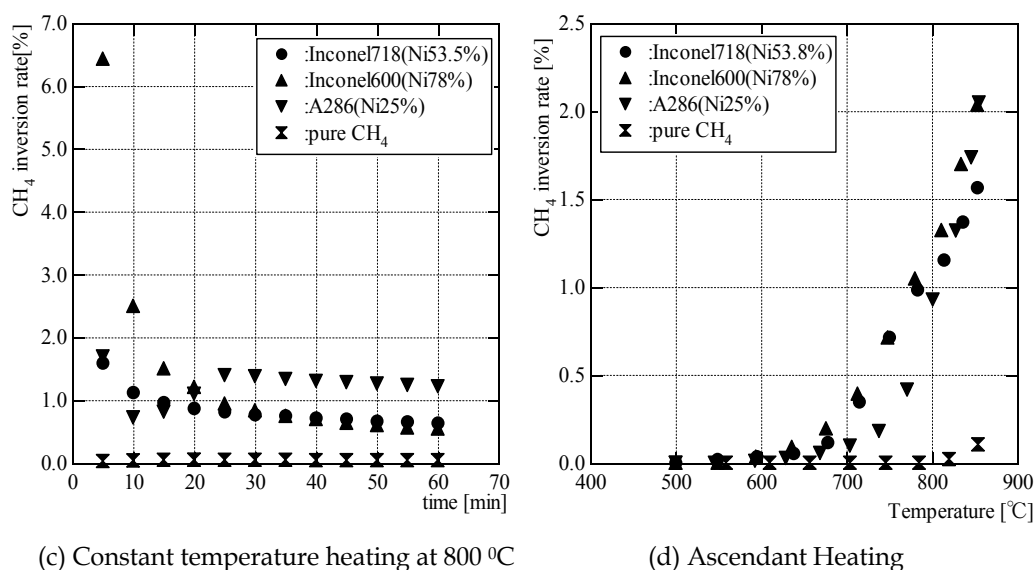


Fig. 3. CH₄ Conversion Rate for pure CH₄ Gas heating tests.

Before the present tests, it must be evaluated whether the alumina board has any catalytic effects. If this alumina board has the catalytic effects on CH₄ or C₃H₈ decomposition, it is very difficult to evaluate the accurate catalytic effect quantitatively. Figure 2 shows that time histories of methane conversion rates with pseudo LNG of 1 vol% C₃H₈ for ascendant heating tests. The pseudo LNG mean the gas mixture of CH₄ and C₃H₈. In the heating tube, there is no INCONEL 600 piece, but the test conditions with and without alumina board are conducted. CH₄ conversions on those two conditions are compared each other. Those two CH₄ conversion rate have no differences and it is clear that the present alumina board has no catalytic effect on the CH₄ and C₃H₈ pyrolysis.

Figure 3 shows the results of pure CH₄ gas heating test. Fig.3 (a), (b) and (c) are the results of constant temperature heating test at 500 °C, 700 °C and 800 °C, respectively. As shown Fig.3(a), CH₄ conversion rate are always equal to 0 at 500 °C as shown in Fig.3(a). This means CH₄ pyrolysis did not occurred at this temperature. However, CH₄ pyrolysis is admitted at 700 °C if any test pieces are placed in CH₄ gas and CH₄ conversion rate are greater in order of Inconel 600, Inconel 718 and A286 condition. The progression of CH₄ pyrolysis is proportional to the amounts of Ni in alloys, because Ni contents are 78%, 53.5% and 25% for Inconel 600, Inconel 718 and A286, respectively. This result indicates that Ni has the catalytic effect to promote this reaction. CH₄ conversion rate decrease with time for all of test pieces conditions. It is considered that the carbon deposits have adhered on the surface of test pieces and inhibit the catalytic effects. At 800 °C, the time histories of CH₄ conversion rate are very different from those at 700 °C, especially for A286 condition. For A286 condition, CH₄ conversion rate is decreased until 10 minutes, however, it turned to increase after that. A286 contains more Iron than Inconel 718 and Inconel 600. The carbon deposit on the A286 surface combined with Iron, if CH₄ pyrolysis proceeded. The carbon and Iron are combined to produce Iron carbide, which also has the catalytic effects. It is considered that it causes the tendency of A286 condition in Fig.2(c). The results of the ascendant temperature

heating test are shown in Fig.3(d). CH_4 pyrolysis begins at about 800 °C for no-test piece condition, while it does at 650 °C if any test pieces are placed in CH_4 .

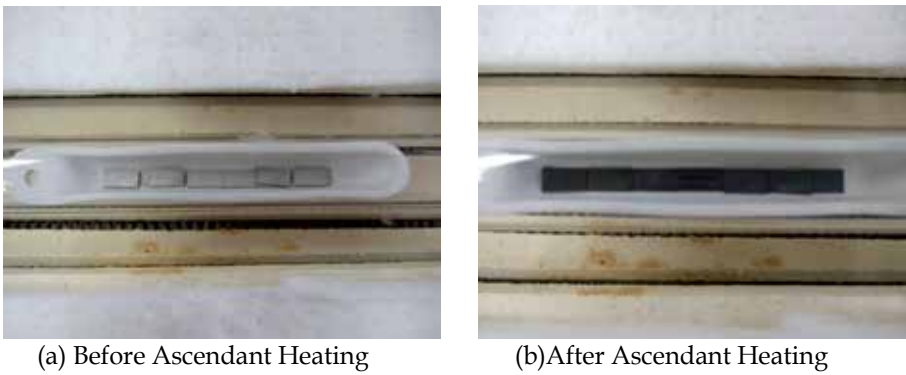


Fig. 4. Photographs of the Inconel 718 Test Pieces Before and After Ascendant Heating test

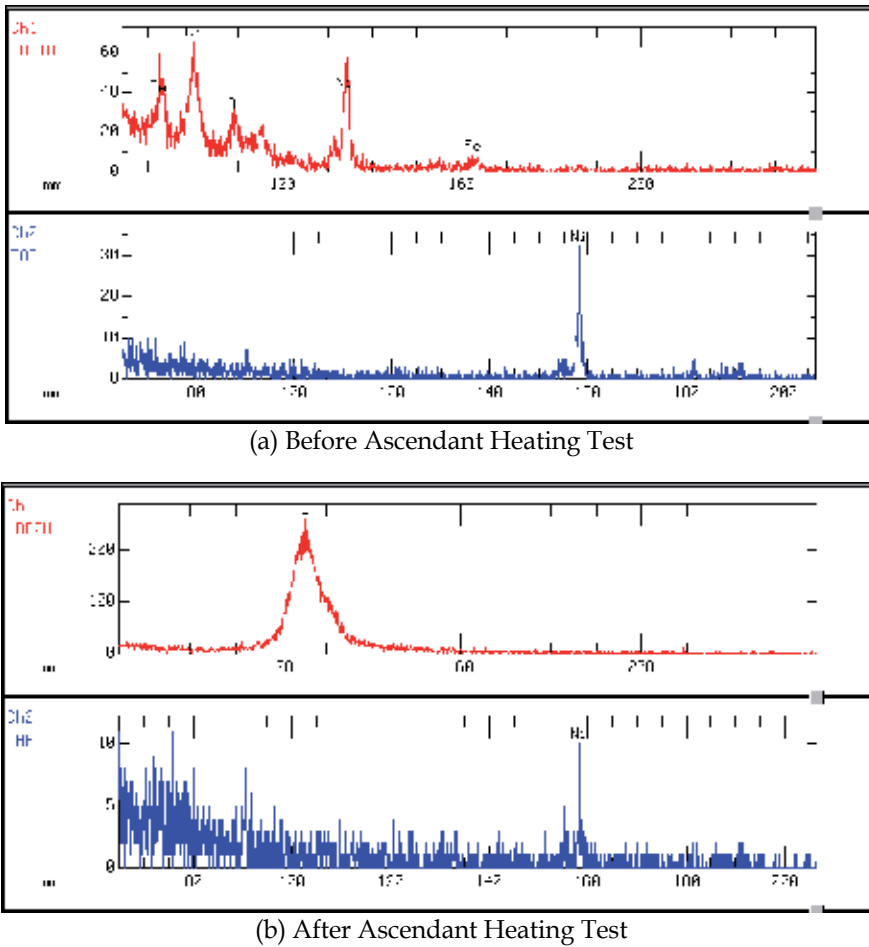


Fig. 5. Results of MPMA Analysis for test pieces in Ascendant Heating test.

Test Condition		Thickness of Carbon deposit films (μm)		
		Inconel 600	Inconel 718	A286
Constant temperature heating Test	700 $^{\circ}\text{C}$	2.0	—	—
	800 $^{\circ}\text{C}$	3.5	4.0	6.0
Ascendant Heating Test	up to 850 $^{\circ}\text{C}$	3.0	—	—

Table 2. Thicknesses of Carbon Deposit Films on the Surface of Test Pieces.

Figure 4 shows the photographs of Inconel 718 test pieces employed for the ascendant heating test. It is clearly observed that carbon deposit on the surface of the test pieces. EPMA analysis is conducted to investigate the chemical constituents of those depositions. Figure 5 shows the results of MPMA analysis for ascendant heating test. These results also indicate that carbon deposits on the surface of the test piece after this test. MPMA can evaluate the thickness of the carbon deposit film on the test piece surfaces, which are indicated in Table 2. In the case of Inconel 600, which has the maximum Ni constituent among these 3 materials, the carbon deposit films are measured in the constant temperature heating test (700 and 800 $^{\circ}\text{C}$) and the ascendant heating condition. The thickness of the carbon deposit film is 3.0 μm at constant temperature heating condition of 800 $^{\circ}\text{C}$. However, that of A286 is 6.0 μm and the thickest among those 3 materials at same heating condition. Measuring the mass difference of test pieces before and after test, the total mass of carbon deposit is amount to 3.7mg which is equivalent to CH_4 of 4.933mg. The total mass of CH_4 gas fed on can be evaluated as 1.603 g from equation (2).

$$\dot{m}_{\text{CH}_4} = \frac{PQt}{(\hat{R}/M_{\text{CH}_4})T} \quad (2)$$

where P , Q , \hat{R} and M_{CH_4} are pressure(=0.2MPa), volume flowrate(=20ml/min), Universal gas constant and molecular weight of CH_4 . T and t are the temperature and test period. The ratio of thermal decomposed CH_4 to total amount of supplied CH_4 is 0.308 %.

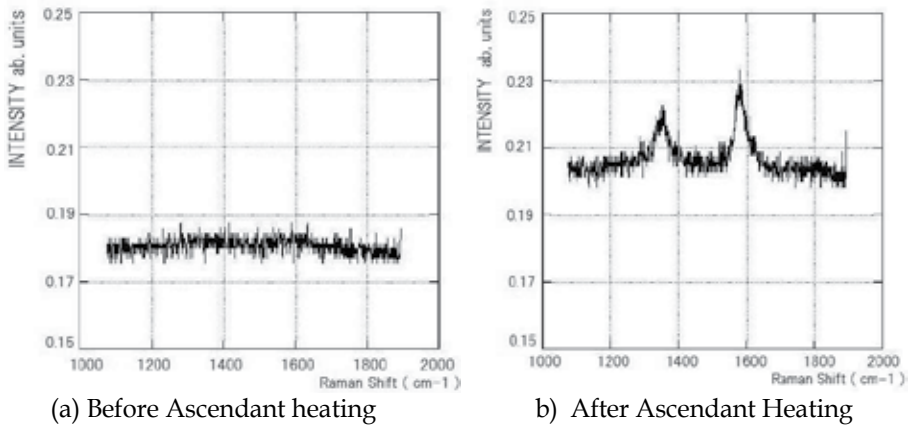


Fig. 6. Results of Raman Analysis of Inconel 718 for Ascendant Heating Test.

The crystal structures of carbon deposits on the test piece surface are investigated by Raman analysis. Figure 6 shows the results of Raman analysis of Inconel 718 test pieces before and after the ascendant heating test. The two peaks are appeared in the test pieces after heating and the right peak is more distinguished than the left one, which means the pyrolytic carbon is deposited [Yoshikawa, S. 1991]. If the left peak would be higher than the right one, amorphous carbon is deposited, in contrast. For other materials in ascendant heating condition, Raman analysis of Inconel 600 shows the same tendencies with Inconel 718, however, that of A286 indicates that the amorphous carbon was deposited. In the constant temperature heating conditions for those 3 materials, pyrolytic carbon is deposited in lower temperature heating and amorphous carbon in higher temperature. The amorphous carbons are appeared in higher than 700 °C for Inconel 718 and A286 and 800 °C for Inconel 600. The pyrolytic carbon is easier to peel off from the metallic surface than the amorphous carbon, thus, pyrolytic carbon must be careful for the design of a regenerative cooling engine. It is considered that the crystal of the pyrolytic carbon has a strong combination with a metal.

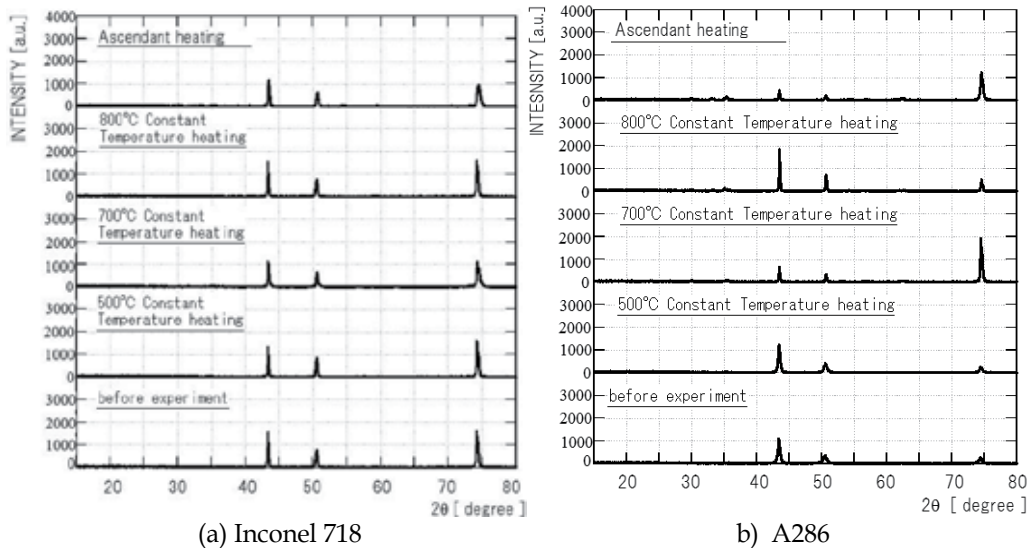


Fig. 7. Results of XRD Analysis of Inconel 718 and A286.

The XRD analysis is also employed for these test pieces. XRD analyses can make clear the internal crystal structure of these metallic materials and prevail that the peaks for Inconel 718 do not change after heating test as shown in Figure 7. Those for Inconel 600 also do not change, however for A286, the peaks of XRD analysis are changed after the ascendant heating. This means that the Iron carbide is produced on the surface of A286 test pieces.

2.2 CH₄ – C₃H₈ mixture pyrolysis and catalytic effects

The main constituent of LNG is CH₄ and the others are C₂H₆, C₃H₈ and larger hydrocarbon molecule. Non-hydrocarbon constituents are N₂ or H₂S. The higher purity of CH₄ is, the more favourable propellant is. LNG from Alaska or Canada have higher purity of CH₄, however, those from South East Asia have 10 to 15 vol. % of C₂H₆ and C₃H₈, which may be used for a rocket propellant because of cost. C₃H₈ is known to be decomposed easier than

CH_4 and radical species like H atom, CH_3 and C_2H_5 are produced. The radical species can attack to CH_4 and promote its pyrolysis. The effects of those radical species are significant even if mole fraction of C_3H_8 is a few percent.

The chemical compositions of LNG are varied from the production area. Thus, in the present section, LNG is modelled by CH_4 and C_3H_8 mixture, which is call as pseudo-LNG in the present study. The details of test conditions are listed in Table 3. The test pieces materials are selected as Inconel 600, Haetelloy -X, SMC, OFMC and OMC. Hastelloy-X is one of the Ni-based alloy, as well as Inconel 600. SMC, OFMC and OMC are Copper based Alloys and included in the test pieces materials. Copper has high heat conductivity, thus, is also used for combustion chamber material. Test apparatus is same one shown in Fig.1. The results in this section are referred from Higashino, K. (Higashino, K. et. al 2009B)

To investigate the effects of C_3H_8 addition of CH_4 , the ascendant heating test is conducted for pseudo-LNG, whose volumetric fraction of C_3H_8 is 1.0 %. In these tests, the catalytic effects are also experimentally evaluated. C_3H_8 molecules begin to decompose as well as CH_4 , if test gas would be heated. The test gas is sampled and the volumetric fractions of the remained C_3H_8 are measured by the gas chromatograph. Figure 8 shows the C_3H_8 residual ratios, which means the ratio of the remained and the initial volumetric fractions of C_3H_8 . If there is no test piece, C_3H_8 begin to decrease at 527°C (800 K), which is about 300°C lower than pure CH_4 pyrolysis without test piece.

Temperature ($^\circ\text{C}$)	Isothermal	627, 727, 827
	Ascendant	From Room temperature to 1273
Pressure (MPaA)		From 0.14 to 0.20
Flowrate (ml/min)		20
Material of Test Pieces		SMC, OMC, Inconel 600, Hastelloy-X
Test Piece configuration		10mm L X 10mm W X 1 or 2 mm T
Test Duration	Isothermal	4800 sec
	Ascendant	15000 sec (max)
Volumetric Fraction of C_3H_8		1 , 3, 5 percent
Constituents of test piece materials	SMC	Cu: 99.13% Zr :0.8% Cr :0.7%
	OFMC	Cu: 99.99%
	OMC	Cu: 99.12% Zr :0.1% Cr :0.7%
	Inconel 600	Ni: 78% Cr : 15% Fe: 7%
	Hastelloy-X	Ni: 47% Cr : 22 % Fe: 19%

Table 3. List of Test Condition of Pseudo-LNG Heating Test.

If the test pieces of Inconel 600 or Hastelloy-X are employed, C_3H_8 residual ratios begin to decrease at 377°C . Thus, these materials have the catalytic effects to promote the C_3H_8 pyrolysis. On the other hand, tendency of C_3H_8 residual ratio with SMC test pieces are

almost same as that without test pieces. SMC does not have the catalytic effects. If the temperature is more than 727 °C, C_3H_8 residual ratios are less than 100 ppm, and too low to be detected by gas chromatograph.

The thicknesses of the carbon film on the test piece surface are measured by using the electron microscope and its results are shown in Figure 9. The heating condition of Fig.9 is the constant temperature heating of 727 °C. The thicknesses of the carbon film on SMC and OMC are less than 10 μm . On the other hands, the thicknesses of the carbon film on Inconel 600 and Hastelloy-X enlarge if the volumetric fraction of C_3H_8 is greater than 3.0 percent. Especially for Inconel 600, the thicknesses of the carbon film grows up to 442.3 μm at 5.0 volumetric percent of C_3H_8 , while it is 2.4 μm and 38.5 μm at 1.0 and 3.0 vol.% of C_3H_8 , respectively.

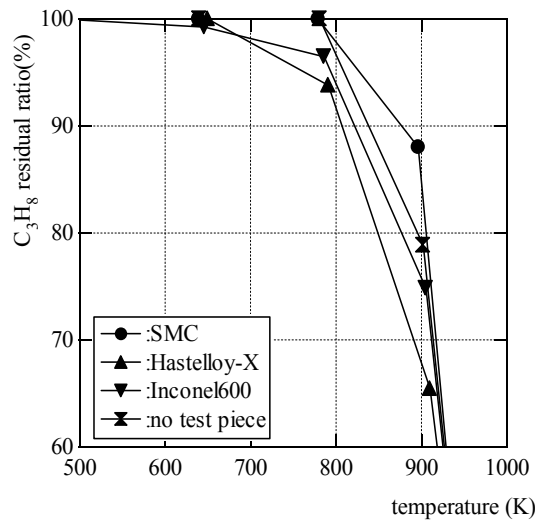


Fig. 8. C_3H_8 residual ratio of Pseudo LNG with C_3H_8 1.0 vol.% at the ascendant heating.

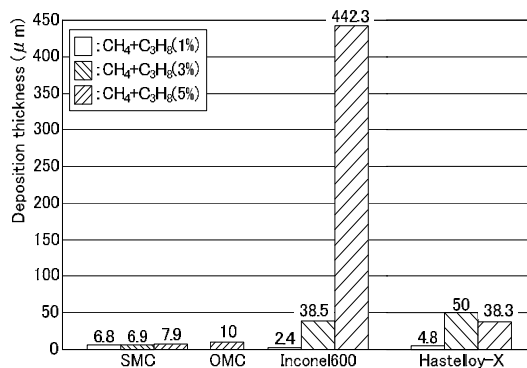


Fig. 9. Thickness of Carbon Films on Test Pieces for Constant temperature heating of 727 °C.

For Inconel 600 with C_3H_8 5.0 vol.%, the amounts of carbon deposited on the test pieces are measured by the electronic balance and evaluated as 78.2 mg. As well as equation (2) for pure CH_4 , the total mass of pseudo LNG can be calculated as 2.324g by equation (3).

$$\dot{m}_{supply} = \frac{PQt}{\left(\hat{R}/[0.95M_{CH_4} + 0.05M_{C_3H_8}]\right)T} \quad (3)$$

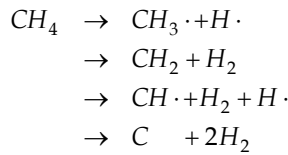
where those notations are same as equation(2), but the subscripts means the chemical species. The mass fraction of carbon atoms in pseudo LNG with C₃H₈ 5.0 vol.% is given as equation (4).

$$\frac{\dot{m}_{C\ atom}}{\dot{m}_{supply}} = \frac{0.95M_C + 0.05 \times 3 \times M_C}{0.95M_{CH_4} + 0.05M_{C_3H_8}} \quad (4)$$

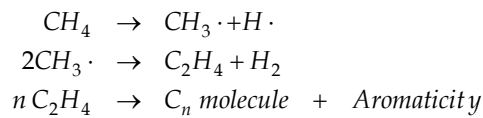
The mass of carbon atom in supplied pseudo LNG is calculated as 1.768 g and, then, the ratio of thermal decomposed gas to total supplied gas are about 4.4 %. In the previous section, the ratio of the decomposed CH₄ gas to total supplied gas are only 0.308 % at the constant temperature heating of 800 °C. This temperature is higher than the present test; however, higher ratio of pseudo LNG gas is thermally decomposed. The addition of C₃H₈ is very effective to promote the pyrolysis of CH₄ and C₃H₈.

2.3 Analytical model of CH₄ and C₃H₈ pyrolysis

The experimental results described in the previous section are theoretically investigated in the present section. The reaction model of CH₄ pyrolysis are considered as described by Ichikawa [Ichikawa 2001].

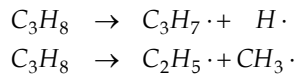


However, if the catalytic effects are considerable, larger hydrocarbon molecules are produced.



where n is higher than 3 in C_n molecule.

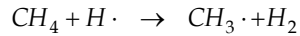
On the other hand, if C₃H₈ is involved in the CH₄ pyrolysis, the reactions of CH₄ and C₃H₈ pyrolysis proceed as follow. C₃H₈ pyrolysis begins via the following reactions.



Those reactions can occur at the lower temperature than CH₄ pyrolysis. C₂H₅ radicals decompose further and produce H atom and C₂H₄.



H atom can attack to CH_4 to decompose it.



This reaction proceeds much faster than CH_4 solo pyrolysis. Thus, the addition of C_3H_8 to CH_4 can promote the CH_4 pyrolysis. Various reaction models have been proposed to simulate combustion of lighter hydrocarbon molecules like CH_4 , C_2H_4 , C_2H_6 and C_3H_8 . Among them, GRI-Mech Ver.3.0 is one of the most widely employed model (Smith, G. P.). The authors developed the numerical code to simulate those experimental results by using the GRI-Mech. Ver.3.0.

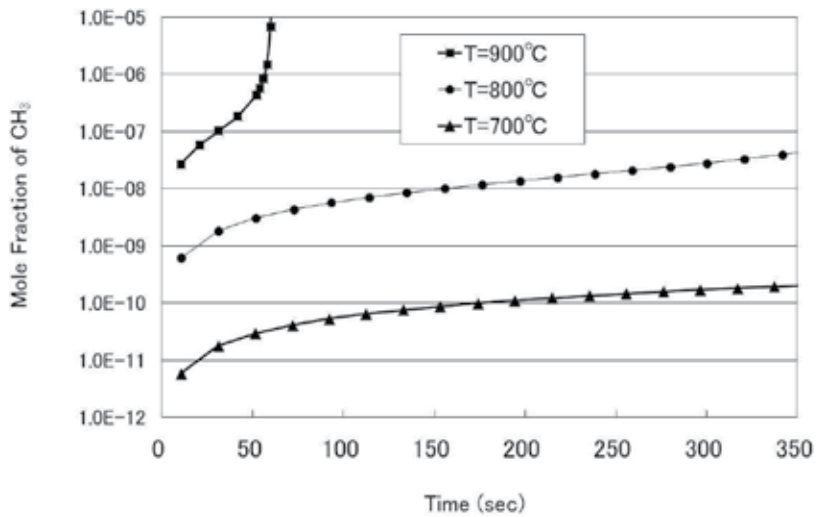


Fig. 10. Time History of CH_3 mole fraction for Constant temperature heating of pure CH_4 gas.

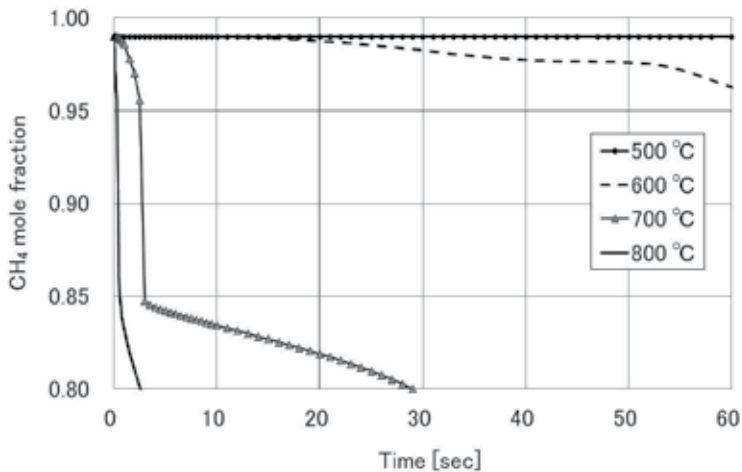


Fig. 11. Time History of CH_4 mole fraction for constant temperature heating of pseudo LNG with C_3H_8 1.0 vol.%.

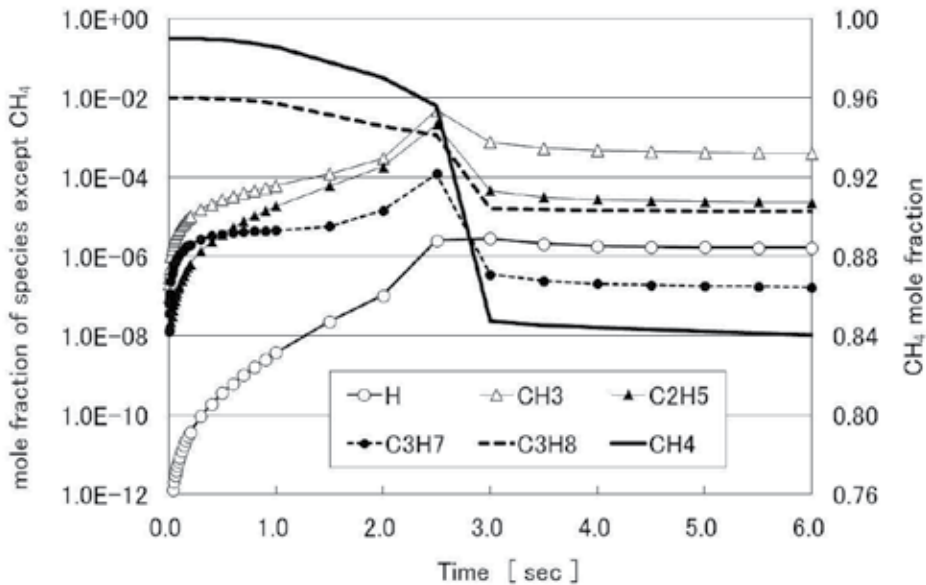


Fig. 12. Time Histories of Principal Chemical Species Mole Fraction for C_3H_8 1.0 vol.% and 700 °C.

Figure 10 shows the numerical results of the time histories of CH_3 radical for constant temperature heating of CH_4 . The mole fraction of CH_3 is rapidly increased at 900 °C, while they remain to low values less than 800 °C. This figure indicates that the CH_4 pyrolysis begins at temperature between 800 and 900 °C, which agrees with the experimental data shown in Figure 3(d). Figure 11 shows the time histories of mole fractions of CH_4 for pseudo LNG with C_3H_8 1.0 vol.% and indicates the simulation of the experimental results in Fig. 8. The mole fraction of CH_4 for 700 °C is instantaneously decreased, thus this numerical result is also agreed with the experimental data. Figure 12 shows the time histories of mole fraction of the principal chemical species for pseudo LNG with C_3H_8 1.0 vol.% and 700 °C. The mole fraction of CH_4 is rapidly decreased at 2.5 sec. At the same time, the radical species, such as H atom, CH_3 and C_2H_5 reach to maximum values. As described previously, those radical species are involved in CH_4 pyrolysis. Especially, C_2H_5 and C_3H_7 are the products of C_3H_8 pyrolysis and precursors of CH_3 and H atom. C_2H_5 and C_3H_7 play an important role in promoting CH_4 pyrolysis. After 3.0 sec, the mole fractions of those species are constant and reach to equilibrium.

3. Coking inhibition by graphite coating

3.1 Experimental evaluation of graphite coating for coking inhibition

In the previous section, it is indicated that CH_4 or CH_4 and C_3H_8 gas mixture (pseudo LNG) can be decomposed under high temperature conditions and carbon deposits. This coking phenomenon can be accelerated by the catalytic effects of combustion chamber material. Thus, thermal design of regenerative cooling passage will be difficult because fuel temperature must be kept lower to prevent coking at there. However, if some inert materials would lay on the metallic surface, those catalytic effects might be prevented. Thus, the

authors present to coat the graphite layer on the metallic surface for the purpose of preventing of coking. Graphite is a kind of the carbon materials and chemically inert. Therefore, graphite layer on the metallic surface is considered to confine the catalytic effect. With those test pieces, the heating tests are conducted for CH₄, pseudo LNG and N₂+C₃H₈ gas mixture.

The experimental apparatus is same with the previous sections. The conditions of the graphite coating tests are listed as Table 4.

Test Gas (vol %)	CH ₄ more than 99.9%
	CH ₄ 95% + C ₃ H ₈ 5% (Pseudo LNG)
	CH ₄ 99% + C ₃ H ₈ 1% (Pseudo LNG)
	N ₂ 95% + C ₃ H ₈ 5%
Test Pieces	Inconel 600 (Ni 73.58%, Cr 16.18%, Fe 9.16%)
	Activated Carbon
	Amorphous Carbon
	Graphite
Heating Condition	Isothermal Heating with 627°C, 700°C, 800°C
	Ascendant Heating from Room Temp. to 1000°C
Heating Time	60 min at Isothermal Heating
	120 min for Ascendant Heating
Flowrate of test gas	20 ml /min
Pressure	0.14 ~ 0.20 MPa
Coating Conditions	n-Hexane Coating : test pieces are located in n-hexane vapor for 60 min with 800°C. Then, they are located in N ₂ gas for 60min with 800°C.
	Graphite Coating : Graphite powder are mixed with ethanol and Surface of INCONEL 600 are coverd with them. They are located in N ₂ gas for 60 min with 800°C

Table 4. Test Conditions for Graphite Coating Tests.

To evaluate the C₃H₈ pyrolysis, C₃H₈ conversion rate is introduced in equation (5) as well as CH₄ conversion rate.

$$\text{Conversion Rate} = \left[1 - \frac{(A_{C_3H_8}/\lambda_{C_3H_8})}{(A_{C_3H_8}/\lambda_{C_3H_8}) + (A_{H_2}/\lambda_{H_2})} \right] \times 100 \quad (5)$$

The definition of equation (5) is same as equation (1), except subscript of C₃H₈.

If the carbon deposited in a regenerative cooling passage would have chemical activation, like as amorphous or activated carbon, these might be able to accelerate the thermal decomposition of CH₄ and C₃H₈ because those carbon deposit will play role of catalysis.

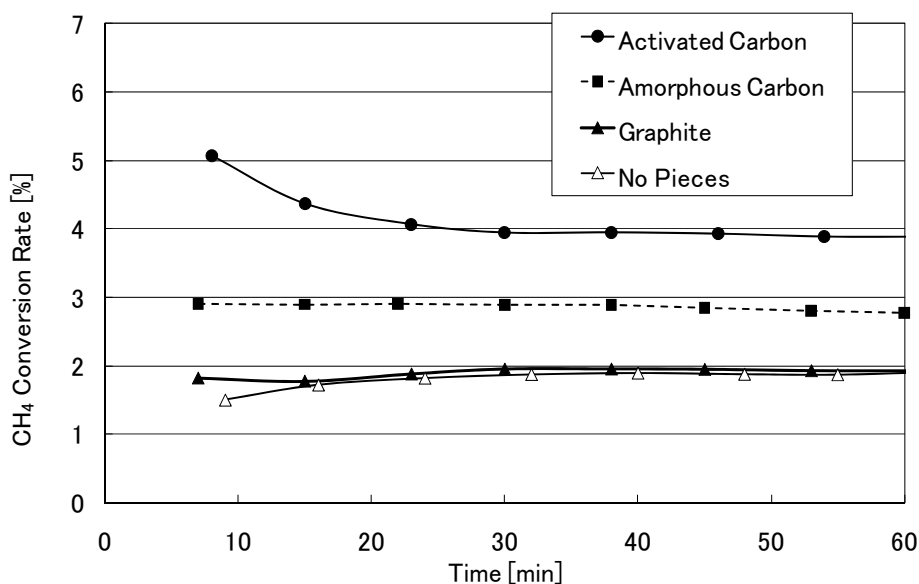


Fig. 13. CH₄ conversion rate of pseudo LNG with C₃H₈ 5.0 vol.% for constant temperature heating of 700 °C.

In the present section, the authors investigate the catalytic effects of carbon compounds such as, graphite, amorphous and activated carbon. Figure 13 indicates time histories of the CH₄ conversion rate in 700 °C constant temperature heating tests. The test gas is the pseudo LNG gas with C₃H₈ 5.0 vol.%. Activated carbon, amorphous carbon and graphite are used for test pieces to investigate their catalytic effects. It is indicated that activated and amorphous carbon have the catalytic effects to thermal decomposition for this gas. On the other hand, graphite does not have them. This reason is considered that graphite would have been chemically inert. The results in Fig.13 indicate that graphite is chemically inert for LNG thermal decomposition. Based on these results, inhibition effects of graphite coating on the surface of INCONEL 600 test pieces are experimentally evaluated. For comparison, conditions of n-hexane coating, no coating and no test pieces conditions (Only alumina board is located.) are also investigated. Figure 14 show the CH₄ conversion rates in ascendant heating test for those four carbon coating conditions. Ten test pieces are used for one heating test. From Fig.14(a), CH₄ begins to decompose at 600 to 700 °C. As described in the previous section, it begins to decompose at 800 or 900 °C with no catalytic conditions. Addition of C₃H₈ can reduce the CH₄ decomposition temperature. C₃H₈ can be decomposed at lower temperature than CH₄, and radical species caused by C₃H₈ pyrolysis can attack to CH₄, resulting of reduction of thermal decomposition temperature. In Fig.14(a) and (b), pyrolysis inhibition by graphite coating is apparent. Conversion rates for graphite coating condition increase more moderate than even those for no piece condition. Although, this reason is not clear, it is no doubt that graphite coating is effective to inhibit the catalytic effect of INCONEL 600. Moreover, these inhibitions are more effective for the decomposition of C₃H₈ than that of CH₄. This fact is more meaningful for the practical application of LNG rocket engine because most of LNG gas contains a few percent of C₃H₈. LNG highly purified by CH₄ is very costly.

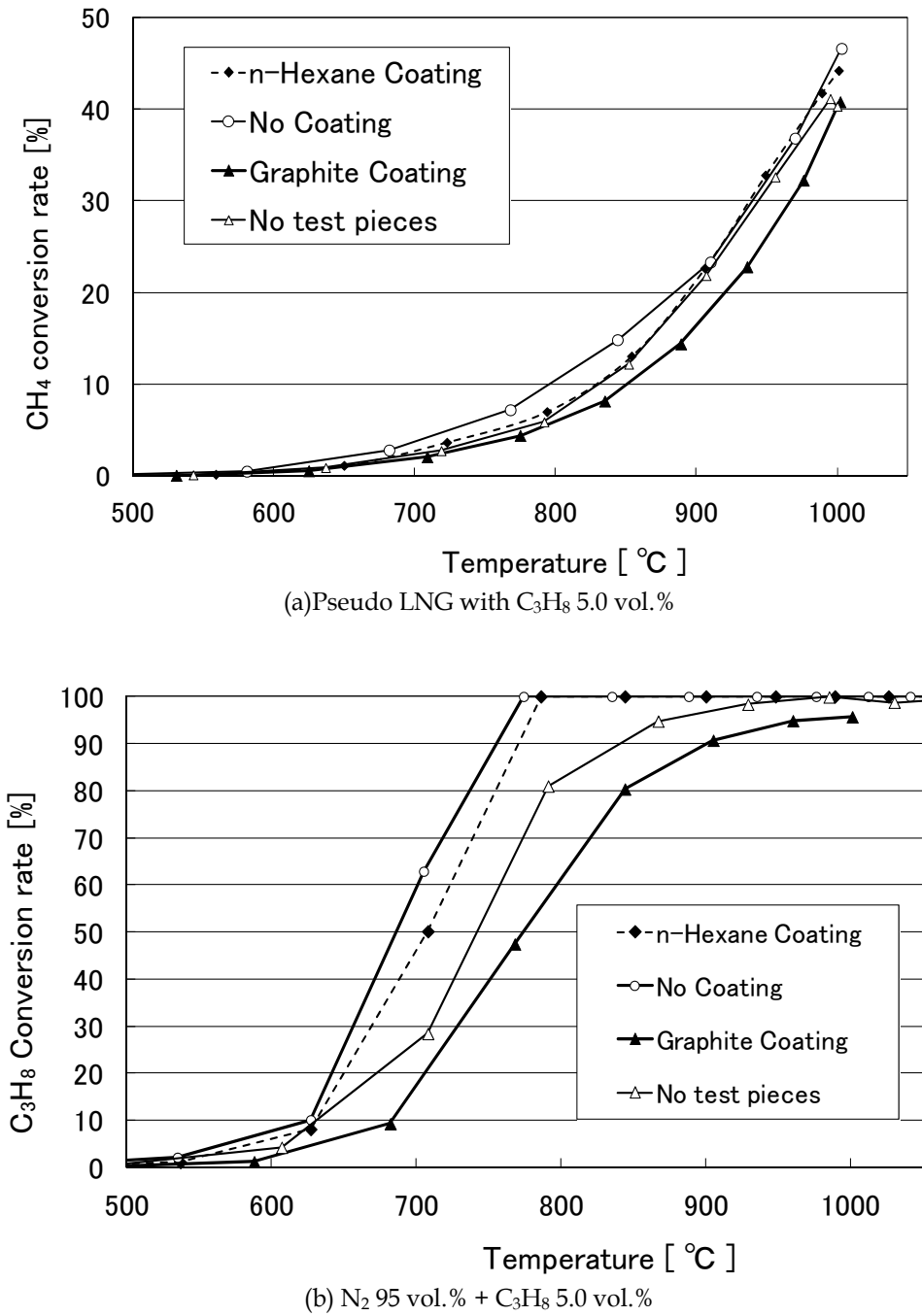


Fig. 14. The Effects of Carbon Coating for Ascendant Heating.

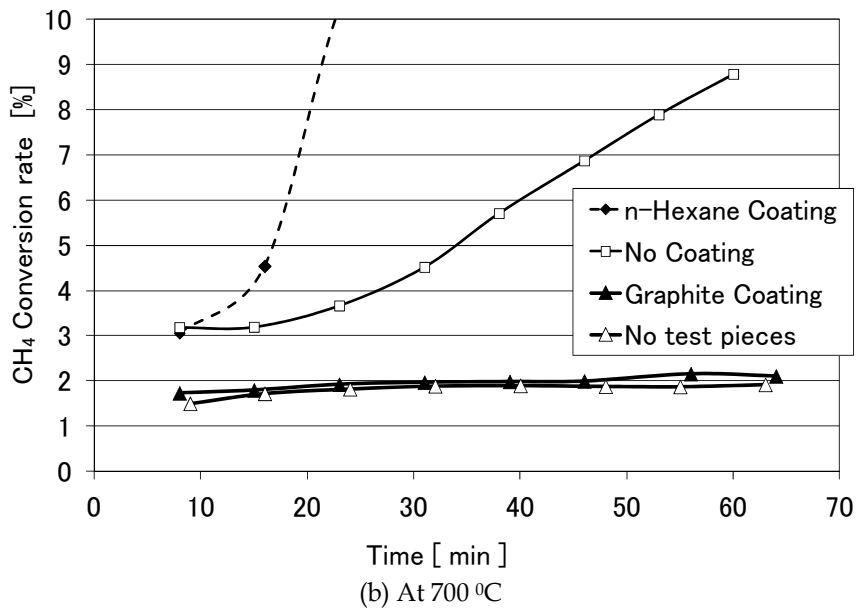
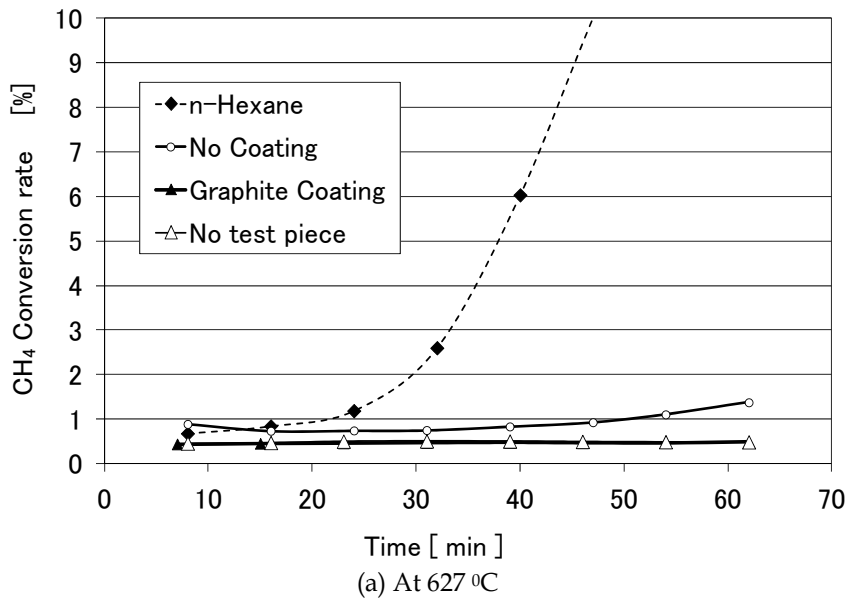


Fig. 15. The Effects of Carbon Coating on CH_4 pyrolysis for Constant temperature heating.

On the other hand, n-hexane coating can accelerate CH_4 or C_3H_8 pyrolysis more than no coating test pieces. This means the carbon in n-hexane coating have chemical activation.

For the practical LNG rocket engine, fuel temperature at the exit of regenerative cooling passage may be lower than the pyrolysis initiation temperature. However, it is necessary to grasp this temperature because high temperature turbine driven gas can obtain the turbine

power. In addition, catalyses are generally effective to accelerate pyrolysis around this temperature range. Therefore, constant temperature heating tests at 627, 700 and 800 °C are conducted for pseudo LNG gas with 5 vol % C_3H_8 and Figure 15(a) to (c) show the time histories of those CH_4 conversion rates. Five test pieces are employed for one heating test. For 627 °C and 700 °C heating test, CH_4 conversion rates for graphite coating condition are much lower than those for n-hexane and No coating conditions and are same level with those for no test piece condition. For 800 °C heating test, no difference appeared in CH_4 conversion rates among those 4 conditions and catalytic effect is not observed. At 800 °C, the decomposition rates of CH_4 or C_3H_8 may mainly depend on temperature rather than catalytic effect. The results in Fig.15(a) to (c) remarkably show the inhibition effect of graphite coating for LNG gas pyrolysis.

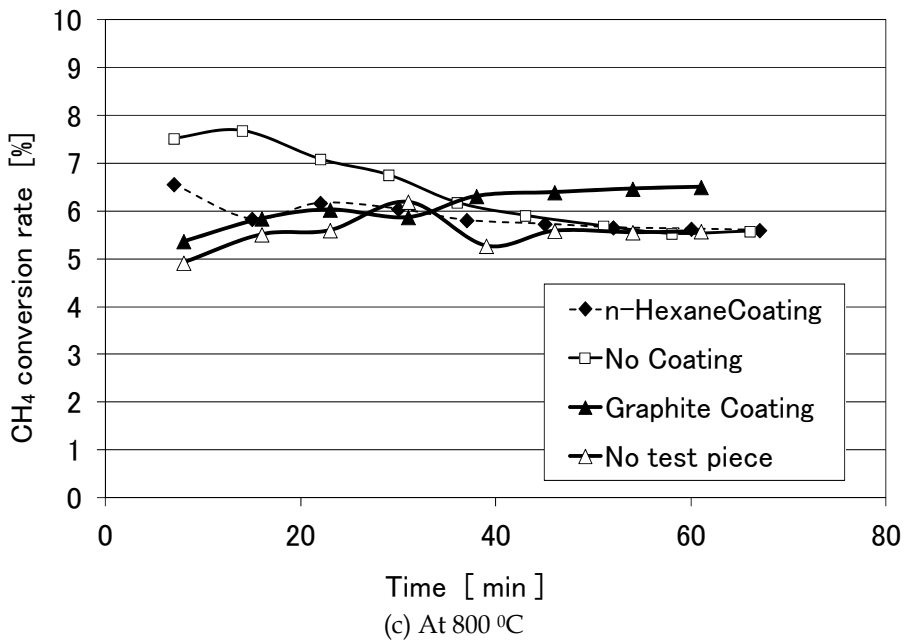


Fig. 15. (cont.) The Effects of Carbon Coating on CH_4 pyrolysis for Constant temperature heating.

It is remarkable that CH_4 conversion rates for n-hexane coating and no coating conditions increase more rapidly at 627 and 700 °C than at 800 °C. In general, catalysis used in cracking of hydrocarbon become to deactivate with time passing because cokes deposit on its surface and reduce the catalytic effects. This reason is considered that for less than 700 °C heating, carbon deposited at test pieces is similar compound to amorphous or activated carbon. They are chemically activated and play role of catalysis. Thus, the types of the deposits on the test pieces after constant temperature heating tests are analyzed by Raman spectroscopy. Figure 16(a) and (b) show the reference peaks of graphite and activated carbon, respectively. Raman spectroscopy of graphite has a peak at 1350 cm^{-1} and that of activated carbon has two peaks at 1300 and 1570 cm^{-1} . Peak at 1300 cm^{-1} is higher than 1570 cm^{-1} .

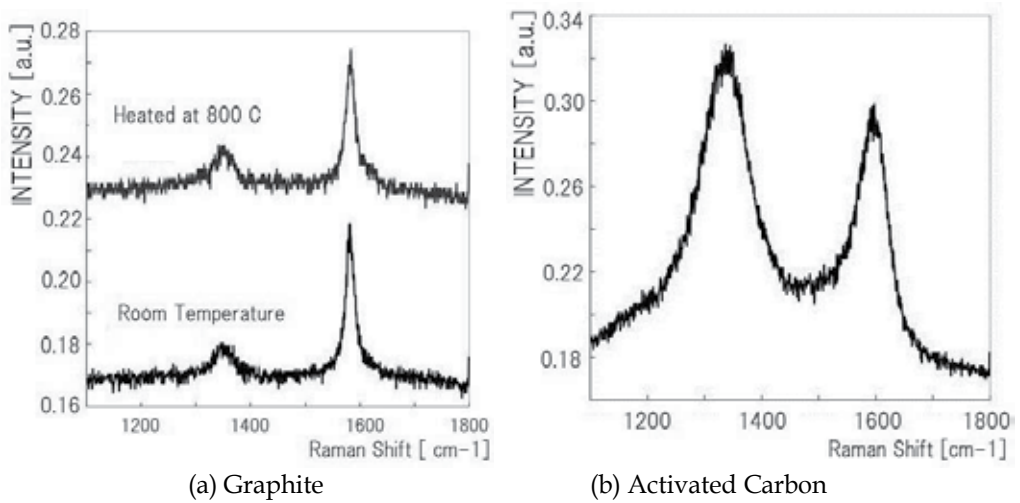


Fig. 16. Reference Peaks of Carbon Compounds of Raman Spectroscopy.

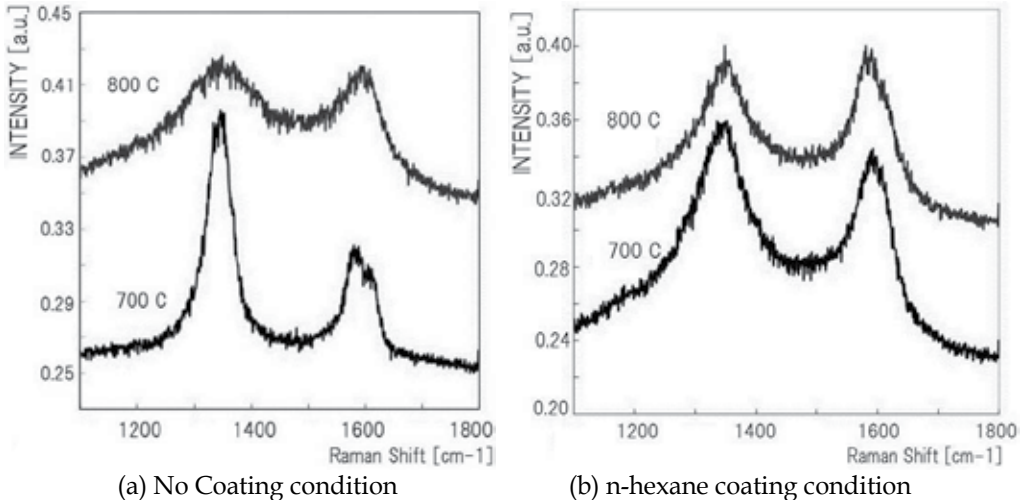


Fig. 17. Raman spectroscopy peaks of deposits on the test pieces after constant temperature heating test.

Figure 17 shows the Raman spectroscopy peaks of the deposits on the test pieces after constant temperature heating test. Those pieces are used in No coating and n-hexane coating conditions. For both two conditions at constant temperature heating 700 °C, the peaks at 1350 cm^{-1} is higher than 1570 cm^{-1} . On the other hand, at constant temperature heating of 800 °C, peaks at 1350 cm^{-1} are close to that at 1570 cm^{-1} . The results in Fig.17 indicate the deposit at 700 °C is similar to activated carbon and has catalytic effects. They are considered to accelerate the pyrolysis of CH_4 or C_3H_8 . However, deposits at 800 °C differ from those at 700 °C and are less activated. For practical application to rocket engine designing, heating 700 °C at regenerative cooling passage should be avoided without graphite coating. For heating of LNG at this temperature, coke begins to deposit within fuel passages and promote the thermal decomposition by itself. However, graphite coating is effective to inhibit the coking

deposit for such heating conditions. Figure 15 indicate the graphite coating can inhibit coking to thermal decomposition in those temperature ranges.

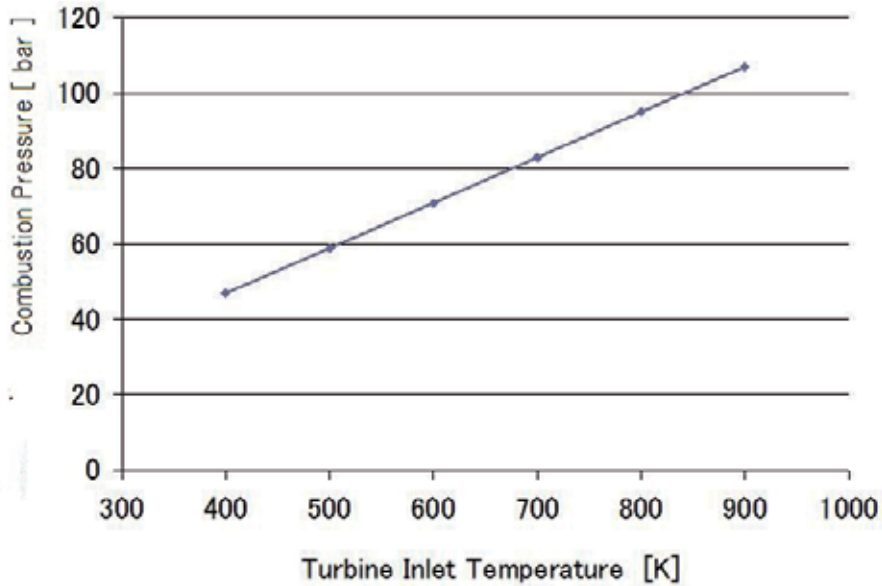


Fig. 18. Effect of TIT on chamber pressure for Expander Cycled Rocket Engine.

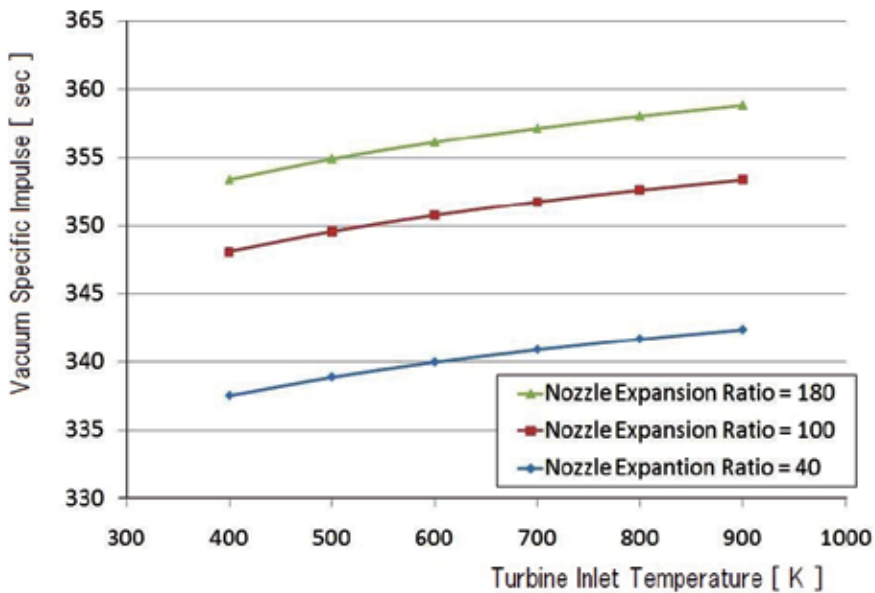


Fig. 19. Effect of TIT on Vacuum Isp for Expander Cycled Rocket Engine.

3.2 Application of graphite coating to expander cycle rocket engine

The graphite coating has the possibility to improve an expander cycle rocket engine performance because temperature at an exit of regenerative cooling passage can be higher. That leads to increase the turbine power. Simple analysis of turbopump is considered in the present study. The specification of turbopump and rocket engine are considered as Table.2. The specification of turbopump and rocket engine are same as those studied by Schuff (2006). 90 percent of LNG fuel is used to drive the turbopump and the rest of them are bypassed.

The combustion chamber pressure, P_c , can be given by the power balance and pressure loss at fuel passage. although the detailed analysis is still necessary. Figure 18 show the combustion chamber pressure, P_c , versus Turbine Inlet Temperature (TIT). TIT is considered to be equal to the maximum allowable temperature at the exit of regenerative cooling passage.

The effects of TIT on P_c and vacuum Isp are indicated in Figure 18 and 19, respectively. Vacuum Isp is evaluated with chemical frozen flow in a nozzle and calculated by computational code by Gordon and Mcbride [6]. The higher TIT is, the greater vacuum Isp can be obtained, however, improvement of vacuum Isp is not so great. For example, in the case of nozzle expansion of 40, only 4 sec of vacuum Isp increment (from 337.5 sec to 342.4 sec) can be expected when TIT would be varied from 400 K to 900 K. However, combustion pressure can be increased to about twice as shown in Fig.18.

Therefore, practical application of graphite coating may be useful to minimize the combustion chamber size, rather than the improvement of Isp. In such cases, the size of combustion chamber will be depended on heat exchange between fuel and combustor. In our future study, more detailed and practical estimation should be conducted on heat transfer analysis and turbopump specification.

4. Conclusion

In the present chapter, the experimental and numerical studies on fundamental chemical phenomena of CH_4 and LNG pyrolysis are conducted. CH_4 pyrolysis is promoted by the catalytic effects of chamber material and the addition of C_3H_8 . CH_4 pyrolysis can begin at temperature of 800 to 900 °C, however, the catalytic effect of combustion chamber materials can reduce the temperature which CH_4 pyrolysis begins by 200 °C. In addition, the addition of C_3H_8 can promote the coking on the test pieces, especially it is apparent if the volumetric fraction of C_3H_8 is more than 3.0 %. The numerical simulation can predict the experimental results of CH_4 and C_3H_8 pyrolysis.

Based on those experimental results, the effective coking inhibition method by graphite coating for LNG rocket engine can be developed and confine pyrolysis temperature up to 700 °C. INCONEL 600 with the graphite coating did not have their catalytic effect on LNG pyrolysis absolutely.

If this method can be applied to expander cycle rocket engine, the improvement of vacuum Isp can be achieved from 338.6 to 342.5 sec when the nozzle expansion ratio is 40. However, it is expected that the size of combustion chamber may be dramatically reduced. In the next phase, more detailed investigations for heat transfer in regenerative cooling passage and

turbopump must be done for practical application of the graphite coating on the expander cycle LNG rocket engine.

5. Nomenclature

A_i	Area indicated in the results of Gas Chromatograph for species i
\dot{m}_{carbon}	Mass flow rate of carbon contained in supplied test gas [kg/sec]
\dot{m}_{supply}	Mass flow rate of supplied test gas [kg/sec]
M_i	Molecular weight of species i [kg/kmol]
P	Pressure [Pa]
Q	Volumetric flow rate of gas [m ³ /sec]
\hat{R}	Universal gas constant (= 8.3143 [J/(mol K)])
t	Time [sec]
T	Temperature [K]
λ_i	Heat transfer rate of species i [J/(m K)]

6. References

- Brown, C. D. (2004). Conceptual Investigation for a CH₄-Fueled Expander Rocket Engine, *AIAA Paper 2004-4210*.
- Crocker, A. M. and Peery, S. D. (1998) System Sensitivity Studies of a LOX/CH₄ Expander Cycle Rocket Engine, *AIAA Paper-1998-3674*
- Higashino, K. et. al (2009A) : Fundamental Study on Coking Characteristics of LNG Rocket Engines, *Journal of the Japan Society for Aeronautical and Space Sciences*, Vol.57, No.664, pp.210-216. (in Japanese)
- Higashino, K. et. al (2009B) : Fundamental Study on Sulfur Attack and Coking of LNG Rocket Engines, *Journal of the Japan Society for Aeronautical and Space Sciences*, Vol.57, No.670, pp.445-452. (in Japanese)
- Ichikawa, M. (2001). *Advanced Technologies for the use of Natural Gas : The Frontier of Research and Development*, 660-661, NTC Inc. ISBN4-900830-76-3, Tokyo, Japan (in Japanese)
- Schuff, R. et. al. (2006). Integrated Modeling & Analysis for a LOX/CH₄ Expander Cycle Engine Focusing on Regenerative Cooling Jacket Design, *AIAA Paper 2006-4534*
- Smith, G. P. et. al. : http://www.me.berkeley.edu/gri_mech/
- Yoshikawa, S. (1981). Evaluation of Diamond Film by Raman Spectrophotometer *Zairyokagaku*, Vol.28 pp.133-138 (1991). (in Japanese)

Numerical Analysis of the Structural Stability of Heat Exchangers – The FEM Approach

Agnieszka A. Chudzik

*Technical University of Lodz/Department of Machine Dynamics
Poland*

1. Introduction

A demand for improved computational methods of complex systems used in modern structures has been followed by development of theory and analysis in the field of stability of shell structures. Nonlinear problems, in which, for instance, shape imperfections, complex loads, nonelastic properties of the material used in the structure are accounted for, are of deep interest. Thanks to an advance in computer technology and numerical methods, a possibility to conduct more precise analysis which corresponds better to actual structures of mathematical models arises. In the linear and nonlinear analysis of structures, stability occupies a special place. To test the load carrying capacity of the structure, the phenomena that occur during a stability loss and after it should be recognized. An application of thin-wall elements results in advantages such as light weight, a possibility to carry high loads, thermo-insulating properties, etc. Here, analysis and recognition of transfer phases since an appearance of plastic strains up to a complete reduction of the load carrying capacity is essential. A demand for such complex analysis that includes stability and leads to more actual evaluation of the structure safety has been observed in many disciplines of technology, e.g., in designing of ships, airplanes, pressure chemical apparatus, in modern construction industry and in power and heat generation. Heat exchangers that are widely applied in, e.g., power and heat generation, operate under very high temperatures. The principal elements of these devices are perforated walls – perforated plates in which heating cartridge pipes are fixed. The number of pipes, i.e., of holes in the plate, is very high and these holes are separated from one another by a thin bridge. The issue of differences in temperatures in individual parts of the heat exchanger and in various media that flow in the device is a source of considerable design difficulties. Heat exchangers usually operate under pressure or in vacuum. Independently of the fact that not only the knowledge of material strength properties is needed for computations of heat exchangers, there are legal regulations that standardize the calculations of the devices operating under pressure. They define the way the basic parts are calculated, providing thus hints concerning the structure of the devices under control. A decrease in the safety factor due to stability, i.e., a rapprochement to the real state of stress up to the critical one, is the way the modern engineering structures can be characterized by. Therefore, the calculations of stability, stiffness of thin-walled structural elements are becoming more and more important nowadays in designing and performance of many devices. A heat exchange is a common phenomenon in technology and nature – it occurs when there are differences in

temperatures. A trial to determine the conditions under which a stability loss will occur in the elements of the heat exchanger that are most exposed to this threat is presented in this paper.

2. Formulation of the problem

Heat exchangers have versatile industrial applications. They are widely used in the food and chemical industry and in energy and power generation, etc. The heat exchanger very often stops to be used as a separate device, designed solely for the heat exchange and its role is connected with other tasks as well. In such a case, the heat exchanger is a part of a facility used for some technological processes. A versatility of applications of heat exchangers is followed by a high diversity in their designs. Various conditions of the process and properties of the substances heated up or cooled, condensed or evaporated result in a necessity to select the material strength properties and the design itself in a proper way. The analysis of an effect of the perforated plate on structural elements of the heat exchanger is an important issue in designing and operation of these devices Hobler (1986), Horak (2005). Working temperatures of the media flowing in the heat exchanger have a decisive impact on the design. In the initial phase of designing, the designer is interested in values of applied temperatures and differences in temperatures between individual elements of the device. The magnitude of the applied temperatures decides about the selection of materials used in the designed structure (due to their strength properties). With an increase in the temperature, "volume" of the materials applied for elements of the heat exchanger increases. The dimensions of a jacket, perforated plates, heating cartridge pipes, bottoms, as well as any other part of the heat exchanger are subject to alternations. This phenomenon is referred to as heat dilatation. Differences in temperatures of the media working in the heat exchanger cause various heat dilatations, for instance, pipes elongate in a different way than the jacket does, a diameter of the perforated bottom changes differently than the outer wall, etc. Heat dilatations are the most cumbersome problem for the designer of heat exchangers as they can cause considerable stresses in the material that can lead to plastic strains or even a failure of the device. The jacket attains the temperature close to the temperature of the flowing medium with which it comes into contact, pipes have a different temperature outside and inside. A difference in these temperatures, as well as in pressure of the flowing media that results from the task the heat exchanger is to fulfill can be considerable. In strength calculations, the designer considers the creep strength limit or the creep limit. They both are time functions. Design difficulties very often arise when a difference in working temperatures in various parts of the heat exchanger is accounted for. Significant changes in strength characteristics of the material occur along with alternations in its temperature, namely: an increase in temperature makes the material more plastic, the tensile strength R_m and the immediate yield point R_e become lower. Strength tests have shown that at higher temperatures, the duration of stress affects strongly the strength and the yield point. Then, the plastic strain of the element depends on: stress, time and temperature. The designer decides thus what material to choose for the elements of the structure to postpone possible plastic strains or a structural failure beyond the predicted operating life. The issues related to computations of circular-symmetrical disks are very important problems in the theory of elasticity and plasticity. Many researchers have investigated also the problem of assembly of pipes in holes of the perforated bottom Ryś (2003). The problem of strength and tightness of such a connection gives rise to serious difficulties to heat exchanger manufacturers.

Numerous studies quote results of the analysis of mathematical models. These studies include, however, significant simplifications as regards actual operating conditions, shapes of the calculated elements, the manufacturing technology of connections, and the behavior of materials under operating conditions. Analytical methods consist in a separation of the fragment from the perforated plate among the surrounding heating pipes, assuming the boundary conditions for the operation of the cut circular plate and applying the pressure. The elastic behavior of the background (pipes) is usually not accounted for, the plate edge is treated as fixed (or other boundary conditions), which is very far from the reality. These engineering simplifications of assumptions result in considerable differences between values of actual stresses and those obtained experimentally. Calculations made with the FEM can be the way the majority of the above-mentioned factors are accounted for Chudzik (2002,2008).

2.1 Aim of the investigations

Differences in the temperatures heat exchangers operate in can result in a remarkable difference in heat displacements. These displacements can give rise to high stresses and strains in parts of heat exchanger such as pipes, jackets and bottoms. An increase in stresses and strains is especially dangerous in case of a failure. It can lead to loads that can result in a stability loss of the perforated bottom together with heating cartridge pipes. A stability loss of the pipe does not have to be followed by damage, but the effects it will cause in the structure depend on the kind and the nature of buckling. A deflection or a shortening of the pipe axis (global stability) that can result in exceeding inconsiderably the critical force may lead to a rapid increase in stresses. When the pipe in the complex structure is buckled, it loses its stability, which can lead to a stability loss of the whole structure. In thin-walled pipes, a new phenomenon has occurred, i.e., local stability. As opposed to global stability, it consists in the fact that the cross-section of the pipe deforms and the rod axis remains straight. Critical stresses under the local stability loss are calculated on the basis of the theory of plates and shells. Analytical calculations of the above-mentioned phenomena give rise to some difficulties. The FEM enables an accurate reproduction of the structure, as well as of the manufacturing technology and the assembly of the heat exchanger. Thus, the calculations of the heat exchanger as regards its stability loss can be carried out. A one-cycle heat exchanger working as a water heater is chosen for our analysis. The perforated bottom of these heat exchangers is an expensive and difficult to manufacture element and, therefore, it is economically justified to decrease its mass. That is why the FEM calculations aimed at a more accurate analysis whose results could affect possible alternations in the heat exchanger design, e.g., through a decrease in the perforated bottom thickness, have been conducted. The calculations are a continuation of the investigations carried out formerly (Chudzik, 2002; 2008).

3. Stability – a literature survey

First studies devoted to stability loss issues were already published more than seven decades ago Zielnica (2001) and they dealt with elastic-plastic shells. An intensive development has been observed since 1955, when Gerard (1956), Lee (1961,1962), Grigoluk (1957) and other researchers published their works. For instance, Sewell (1972), Hutchinson (1972,1973) proposed the methods and the results of solutions to problems of elastic-plastic

stability of structures made of pipes, plates and shells, Nowak and Życzkowski (1963) are responsible for a survey of shell structures. Iiuzyn (1944) developed the fundamentals of the stability theory of thin-walled shells made of an incompressible material with arbitrary characteristics of reinforcement beyond the elastic limit. Zielnica (1969), Bijlaard (1950), Murphy and Lee (1971), Gellin (1979), Hardig (1978), Sobel and Newmann (1982) – these are the researchers who blazed a trail in the analysis of shell stability to follow as they dealt with:

- determination of bifurcation loads (eigenvalues) in the linear range under the membrane precritical state of stresses,
- determination of bifurcation points on nonlinear paths or critical loads under geometrical nonlinearities in the precritical state, accounting for bending effects before the stability loss and determination of nonlinear equilibrium paths including imperfections (shape imperfections),
- application of the FEM method to determine nonlinear paths of the subcritical equilibrium.

In 1947 Shanley presented a new concept of the stability loss in rods, referred to as buckling under increasing load. The stability investigations of the jointly supported rod under compression showed that the rod was subject to buckling and the axial force compressing the rod grew simultaneously after it reached the critical load. Shanley's concept of buckling under critical load enabled to simplify the stability equations as in that case the limit that separates the active process zone from the deloading zone does not have to be established.

In the uniaxial state of stresses (rod systems), the stability analysis can be based on the actual material characteristics obtained from, e.g., the uniaxial elongation test.

In the biaxial state of stresses (shells, plates), the knowledge of material characteristics is not enough as in the case discussed above. To determine the dependence between components of the tensor of the stress and strain state beyond the elastic limit, one should go into detail in the theory of plasticity. Nowadays there are numerous publications devoted to this issue. The majority of them include solutions to comparatively simple models exposed to a stability loss. If the literature survey were to be further discussed here, it could take a form a separate book. The author's task was, however, to conduct a numerical analysis of the more complex device such as the heat exchanger is. A demand for such calculations result from a lack of studies presenting the calculation methods, numerical computations, results of the calculations of, e.g., more complex experimental structures as regards their stability loss. Experimental investigations to compare the results would be very expensive. The results of the experiment will be followed by the need to lead the device to a failure. A mathematical analysis of such a device also gives rise to many difficulties to researchers due to complexity of the problem and the device.

3.1 Stability of load carrying elements of the structure

The behavior of load carrying elements of the structure under increasing loads can be divided into a few phases of their operation, namely: linear in the precritical state, postbuckling elastic under considerable deflections, postcritical elastic-plastic and a failure.

The first three phases are of fundamental importance to designers. In order to determine boundaries between these phases, the following should be known: the critical load, the load at which first plastic deformations occur and the limit load understood as the maximum load after which the damage of the structure will start.

Phase I, the prebuckling phase, occurs when the behavior of the element is described with the classical linear theory. A solution (analytical or numerical) to this problem does not give rise to serious difficulties. Phase II is characterized by high deflections. Due to this fact, the problem becomes geometrically nonlinear whereas physically it is still linear, and its solution allows one to analyze the behavior of the structure until the limit of proportionality is attained. Different modes of buckling can occur in this phase: local and global. An appearance and development of plasticized regions are characteristic of phase III. An analysis and knowledge of the structure in this phase is very useful and needed in the designing process as the load of the structure attains the maximal value in this phase. The determination of the value of this load, referred to as the limit load carrying capacity, requires a physical and geometrical solution to the nonlinear problem of stability. A full analysis in the elastic-plastic range consists in taking into account numerous phenomena that occur in real structures (initial imperfections, interactions of different modes of buckling, the “shear lag” phenomenon, etc.). Despite such a complex issue, many problems related to, e.g., plates subject to simple loads, rectangular plates under uniform compression, have already been solved and the results are supported by the corresponding experimental investigations. However, there is a large group of structures subject to complex loads, whose structure is more sophisticated and for which the determination of the limit load carrying capacity via solution to the stability problem under high deflections in the elastic-plastic range is very complicated even if up-to-date computational numerical methods are employed. Therefore, modern engineering structures during the designing process are based on theories of elasticity on the assumption of high deflections which allow for determination of the load at which plasticization of the structure begins. This state is referred to as the limit state and it is treated as a sort of failure criterion that allows one to design a safe structure although sometimes not an economically favorable one Królak et al (1990).

4. The model under investigation

The calculations were made for a one-cycle heat exchanger, Fig. 1, whose model has been developed on the basis of the technical documentation of the Py-100-020 decarbonized water heater.

The elements that were taken into account in the 3D model of the heat exchanger are as follows: perforated plates (1), bottoms (2), a jacket (3), heating cartridge pipes (8), heating cartridge gaskets (10) shown in Fig.1. Perforated plates are fixed to bottoms with screw fasteners (9). Connector pipes (6) and (7) supply and take off the steam. Detail B shows dimensions of the hole in the perforated bottom before rolling out and a view of the pipe-perforated bottom connection after rolling out. The perforated plates have a hexagonal system of holes that make perforations. The materials used in the structure are listed in Table 1.

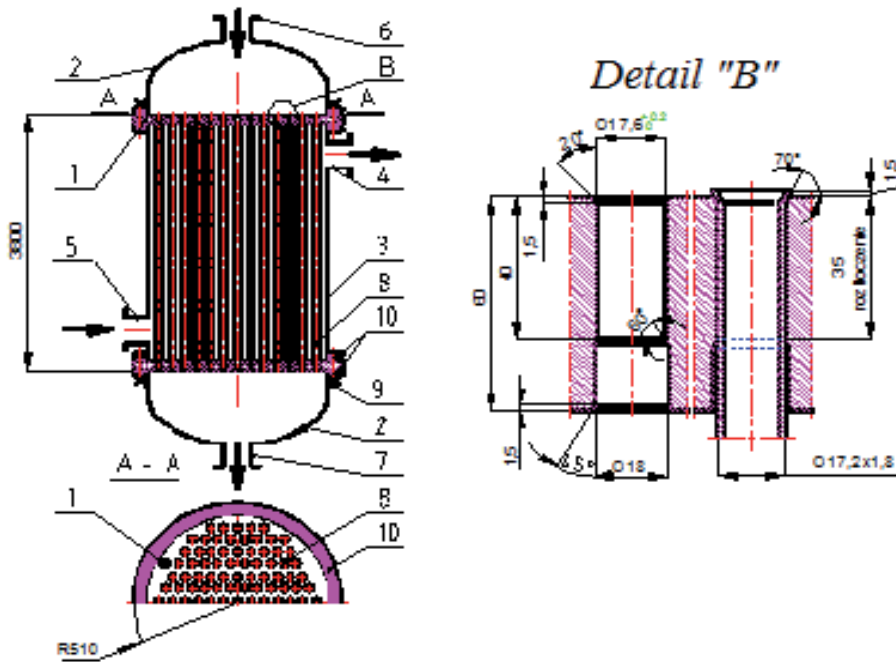


Fig. 1. Schematic view of the heat exchanger.

	I- K10 PN-74/H-74252 boiler pipe	St41K PN-75/H-92123 boiler sheet	St 36K PN-75/H-92123 boiler sheet
yield point	$R_e = 235 \text{ MPa}$	$R_e = 255 \text{ MPa}$	$R_e = 196 \text{ MPa}$
tensile strength	$R_m = 345 \div 440 \text{ MPa}$	$R_m = 400 \div 490 \text{ MPa}$	-
Young's modulus	$E = 2 \cdot 10^5 \text{ MPa}$	$E = 2 \cdot 10^5 \text{ MPa}$	$E = 2 \cdot 10^5 \text{ MPa}$
consolidation factor	$\lambda = 0.99$	$\lambda = 0.99$	$\lambda = 0.99$
Poisson's ratio	$\nu = 0.3$	$\nu = 0.3$	$\nu = 0.3$
friction coefficient	$\mu = 0.23$	-	-

Table 1. Strength properties of the materials used in the structure

5. Numerical calculations

The numerical calculations were conducted for the case when the water inflow and the outflow of were closed, whereas the steam was still supplied to the heat exchanger. The data presented in Table 2 were assumed in the calculations on the basis of the technical documentation:

Parameters	Steam chamber
Pressure	$p_0=1.17$ MPa
Temperature	$T_0=523$ K

Table 2. Parameters of the heat exchanger operation.

For the strength analysis in the elastic-plastic range, stresses σ versus strains ϵ at the maximum operating temperature were used as the basic model of the material the perforated plate and the heating cartridge pipes were made of. A physical model of the St41K steel is presented in Fig. 2, whereas the physical model of the I-K10 steel is shown in Fig. 3. In the calculations, the material consolidation factor $\lambda=0.99$ was assumed, according to Table 1.

The pressure acting on the gasket was calculated on the basis of the required value of the initial stress of screws in the bottom-gasket-perforated bottom-gasket-jacket connection given in the technical documentation.

A shell-solid model (Fig. 4) was built for the numerical calculations. The calculations were conducted for the plate thickness decreased by approx. 15% up to 50 mm and by 50% up to 30 mm, the remaining dimensions were unaltered. The numerical model was divided into elements of the SOLID 45 type (perforated bottoms) and Shell 43 (heating cartridge pipes and the jacket). The numerical calculations were conducted to calculate initial stresses and strains occurring in the heat exchanger with respect to a stability loss, whereas the thickness of perforated bottoms was altered. The calculations were carried out for the emergency state.

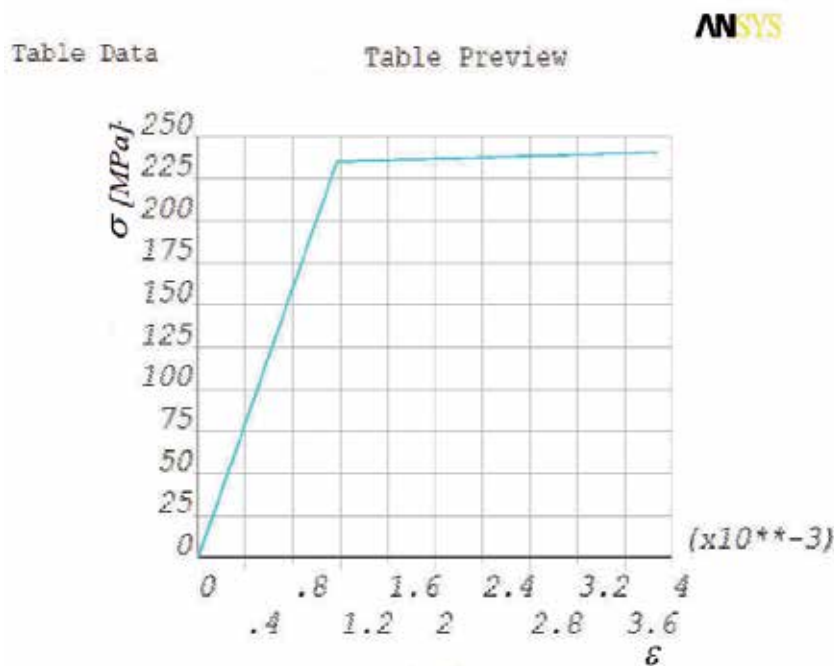


Fig. 2. Physical model of the St 41K steel. (perforated bottom plate).

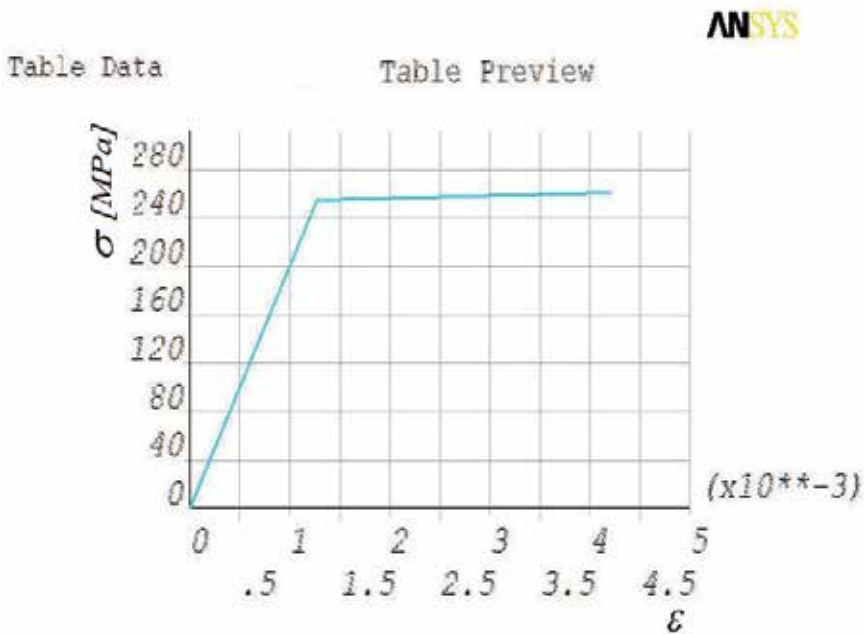


Fig. 3. Physical model of the I-K10 steel (heating cartridge pipes).

The mathematical model of the numerical code is described by the following equations from numerical program ANSYS

$$\{\epsilon^{pi}\} = [B]\{u\} - \{\epsilon^{th}\} \text{ - strain} \quad (1)$$

$$\{\sigma\} = [D]\{\epsilon^{el}\} \text{ - stresses} \quad (2)$$

$$\sigma_e = \left[\frac{3}{2} \{S\}^T [T] \{S\} \right]^{\frac{1}{2}} \text{ - equivalent stress} \quad (3)$$

the flow rule determines the direction of plastic straining

$$\{d\epsilon^{pl}\} = \lambda \left\{ \frac{\delta Q}{\delta \sigma} \right\} \quad (4)$$

where:

- $\{\epsilon^{pi}\}$ strains that cause stresses
- $[B]$ strain-displacement matrix evaluated at integration point
- $\{u\}$ nodal displacement vector
- $\{\epsilon^{th}\}$ thermal strain vector
- $\{\sigma\}$ stress vector
- $[D]$ elasticity matrix

σ_e equivalent stress
 $\{S\}$ deviatoric stress
 λ plastic multiplier (which determines the amount of plastic straining)
 Q function of stress termed potential (which determines the direction of plastic straining)

The following boundary conditions were assumed in the calculations: the rear perforated plate $U_x=U_y=U_z=0$, the front perforated plate $U_x=U_y=0$. Such boundary conditions were assumed on the circumference of both plates (Fig.4).

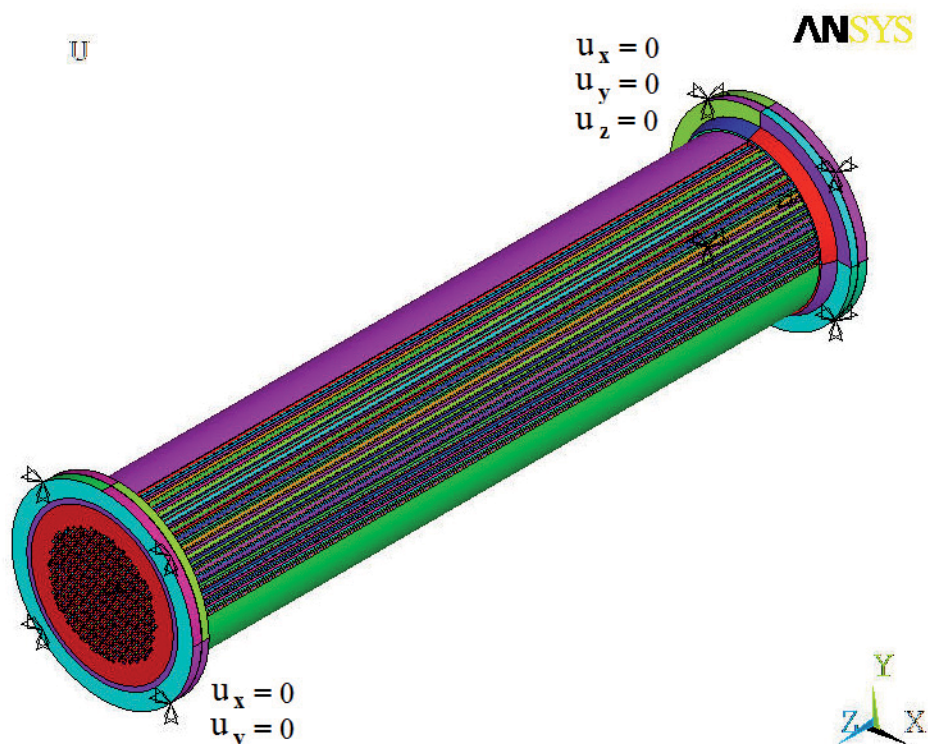


Fig. 4. Numerical model of the heat exchanger under investigation.

5.1 Results

In heat exchangers, the analysis of a complex influence of perforated bottoms on the jacket connected to them, as well as a distribution of stresses in the jacket, pipes and perforated bottoms is essential. The substitutive stress that decides basically about strains occurring in steel structures was calculated according to the Huber-Misses hypothesis. The calculations of the heat exchanger were conducted on the assumption of high strains in the structural elements.

The Finite Element Method - ANSYS 12.0 - was used for the numerical calculations. The results of the numerical calculations have been presented in the form of maps of stresses and strains. The results shown in Figs. 5-12 concern the heat exchanger in which the thickness of

the perforated plate was decreased up to 50mm, whereas Figs.13-20 depict the results for the plate thickness equal to 30mm.

The ANSYS code used in the calculations shows the results in the form of maps for stresses or strains, respectively. The maps are colored. Individual colors correspond to specific numerical values (see the legend). While analyzing Figs. 5 and 6, we have observed that the maximum stresses $\sigma_{\max}=198\text{MPa}$ and the maximum strains $\varepsilon_{\max}=(0.56-0.72)\text{mm}$ occur in the jacket collar and they are marked in red. Figure 7 presents strains in the heating cartridge pipes. It was expected that highest strains would occur in the central part along the pipe length. The numerical calculations confirmed the earlier assumptions of $U_{\max}=0.21\text{mm}$. The pipes in this region show a tendency to deflection along the geometrical axis of the heat exchanger.

A detailed discussion of the results shown in Figs. 5-20 is to be found in the section entitled “Analysis of the results”.

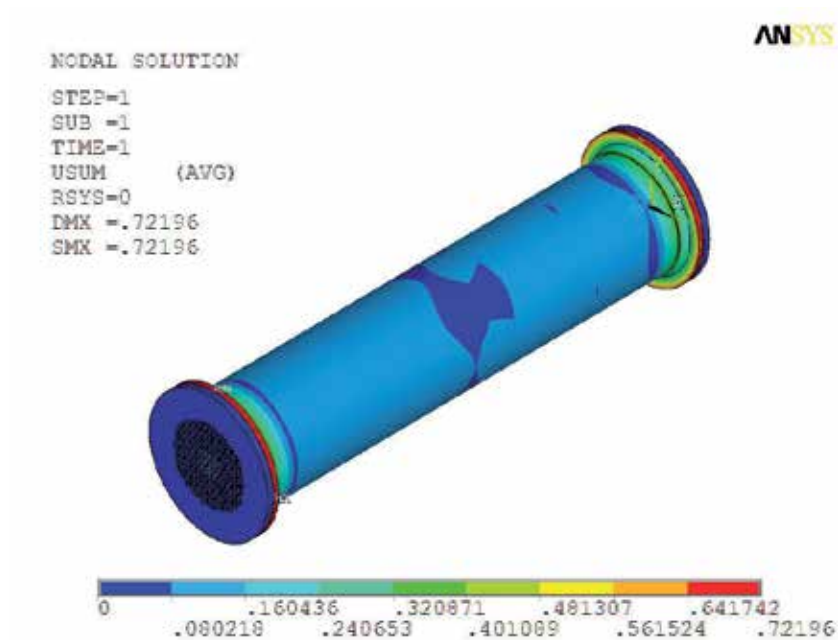


Fig. 5. Total strains in the heat exchanger [mm] – case 1.

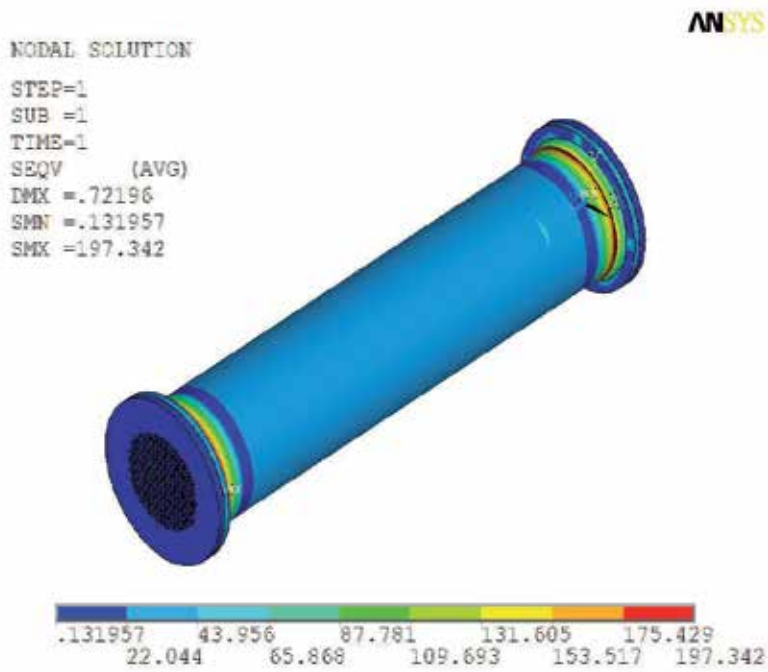


Fig. 6. Distribution of reduced stresses in the heat exchanger [MPa] – case1.

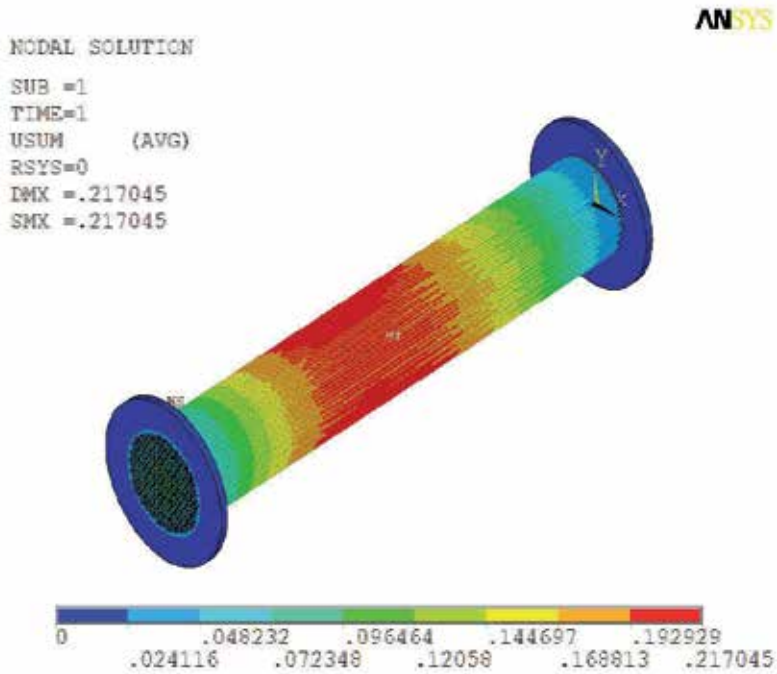


Fig. 7. Total strains in pipes and perforated bottoms [mm] – case 1.

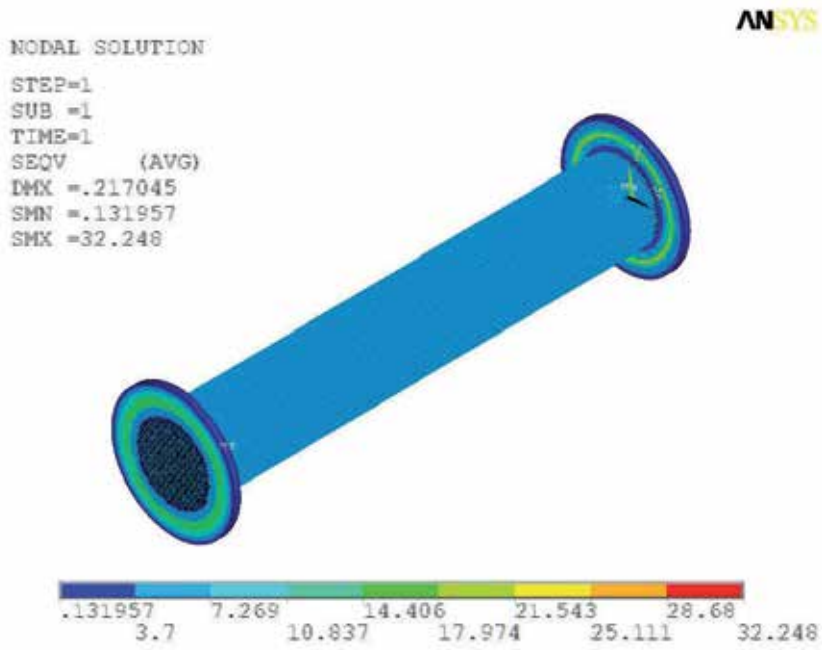


Fig. 8. Distribution of reduced stresses in pipes and perforated bottoms [MPa] - case 1.

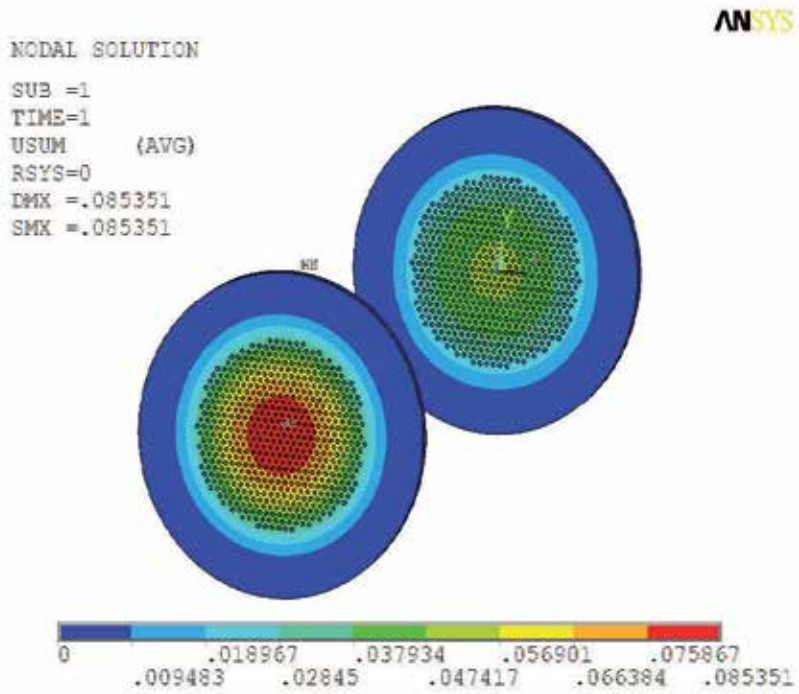


Fig. 9. Total strains in perforated bottoms [mm] - case 1.

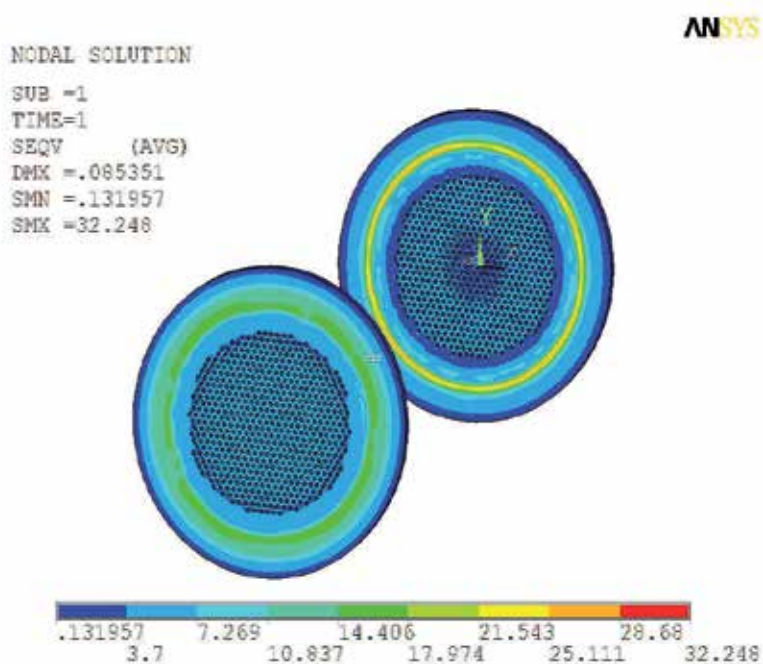


Fig. 10. Distribution of reduced stresses in perforated bottoms [MPa] – case 1.

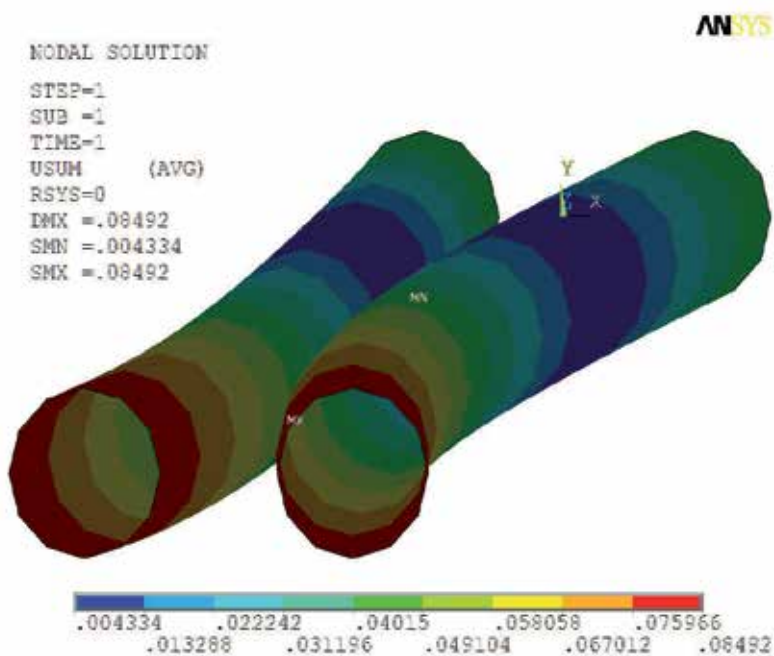


Fig. 11. Total strains in pipes mounted in the center of the perforated plate; magnified deformation of pipes [mm] – case 1.

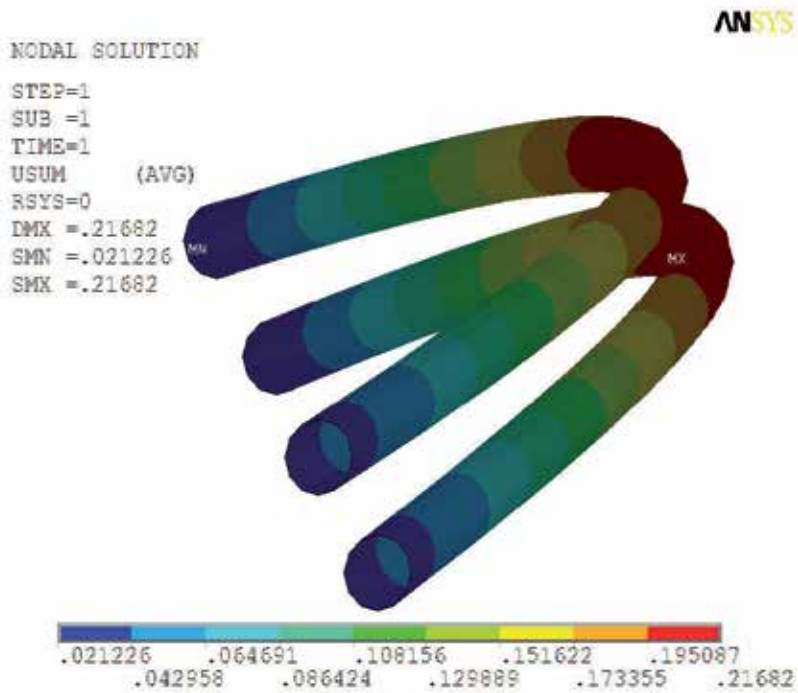


Fig. 12. Total strains in pipes subject to the maximal strain; magnified deformation of pipes [mm] – case 1.

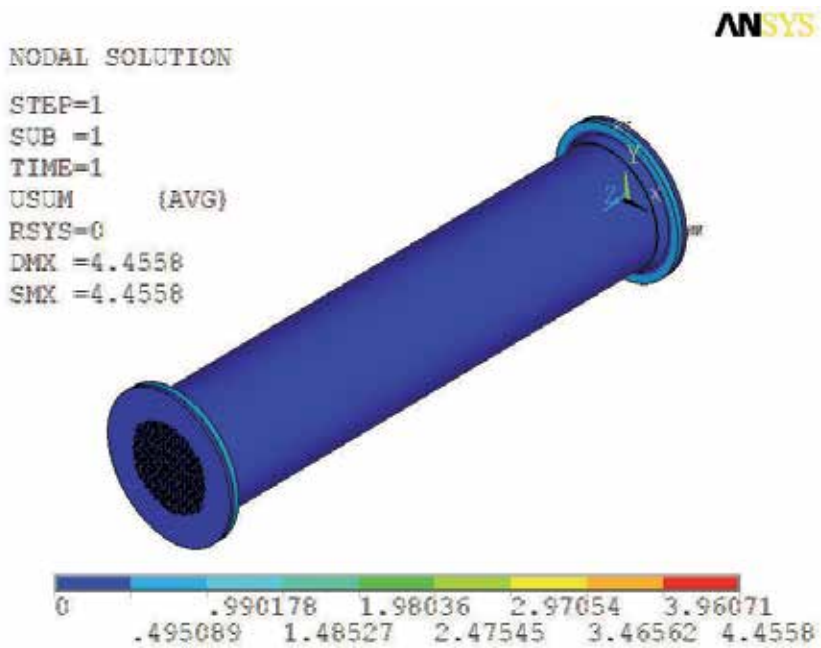


Fig. 13. Total strains in the heat exchanger [mm] – case 2.

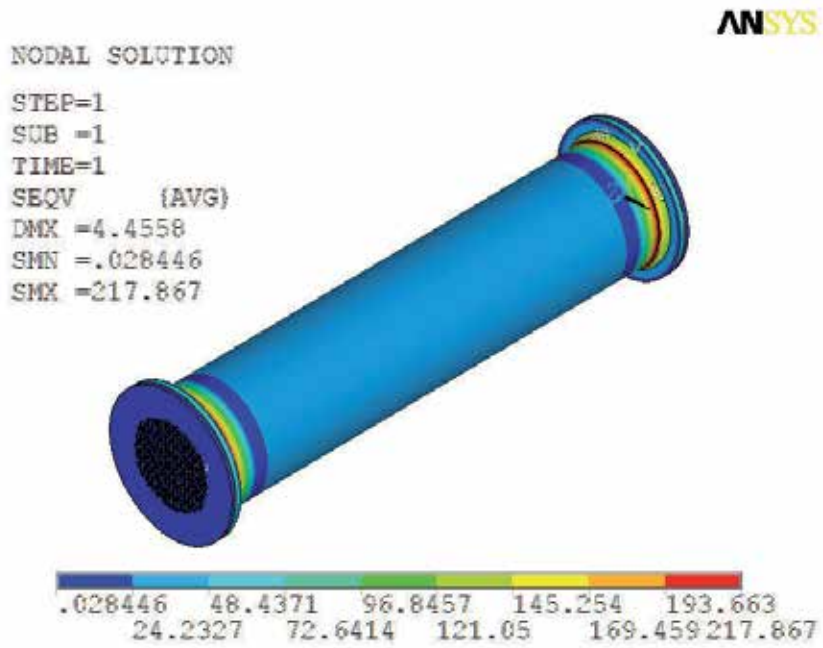


Fig. 14. Distribution of reduced stresses in the heat exchanger [MPa] – case 2.

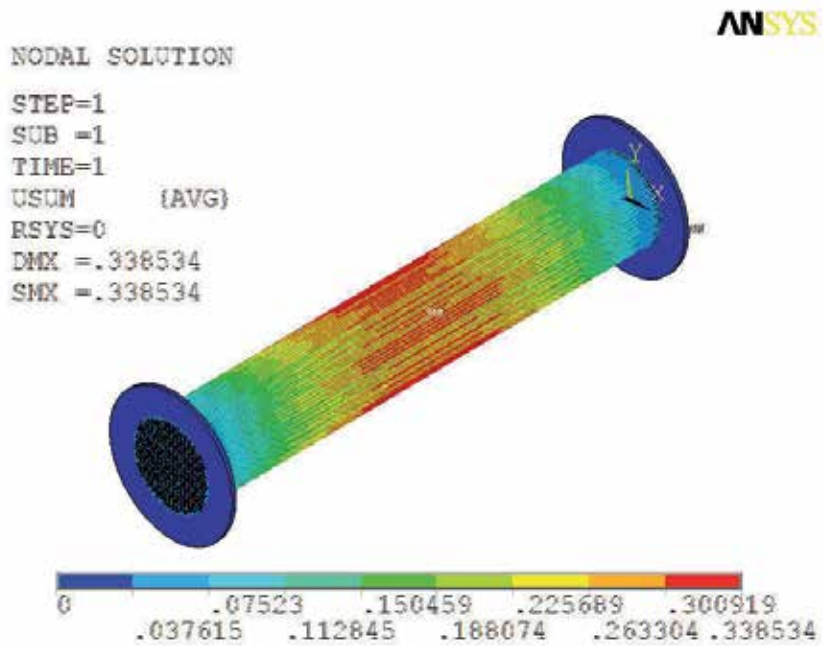


Fig. 15. Total strains in pipes and perforated bottoms [mm] – case 2.

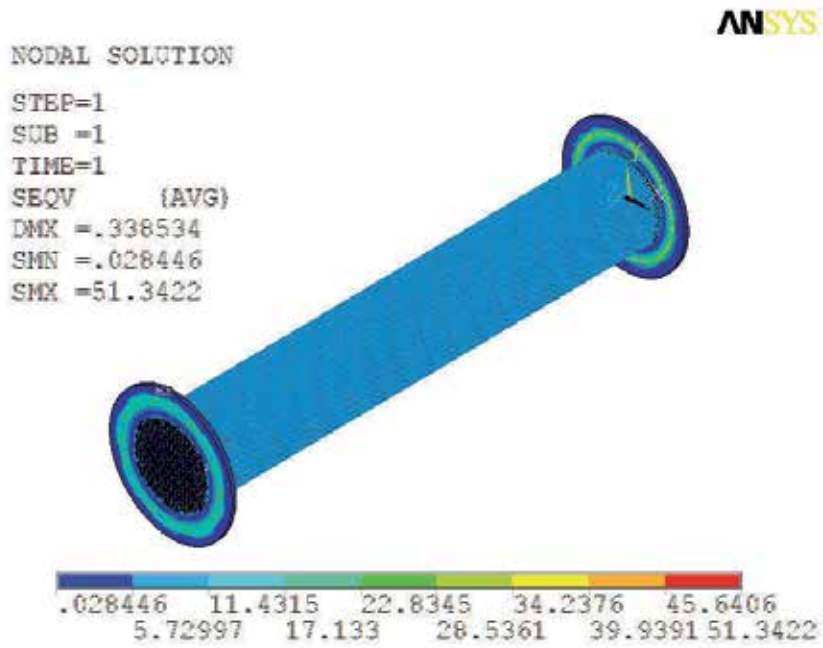


Fig. 16. Distribution of reduced stresses in pipes and perforated bottoms [MPa] – case 2.

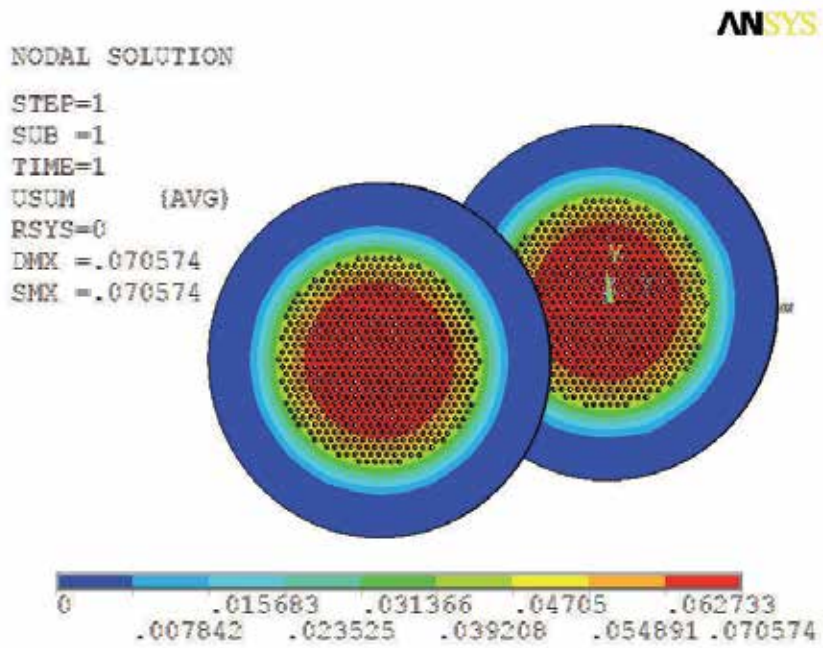


Fig. 17. Total strains in perforated bottoms [mm] – case 2.

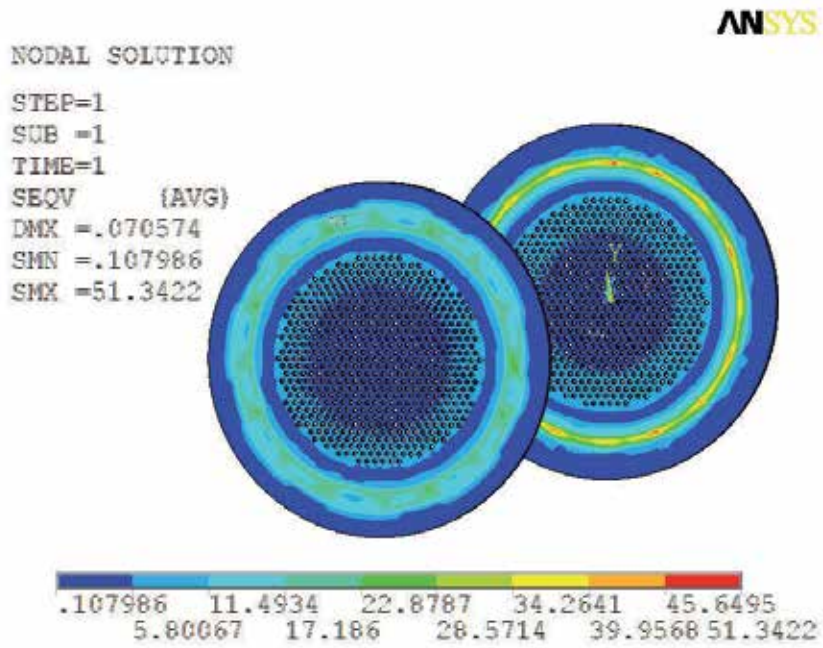


Fig. 18. Distributions of reduced stresses in perforated bottoms [MPa] – case 2.

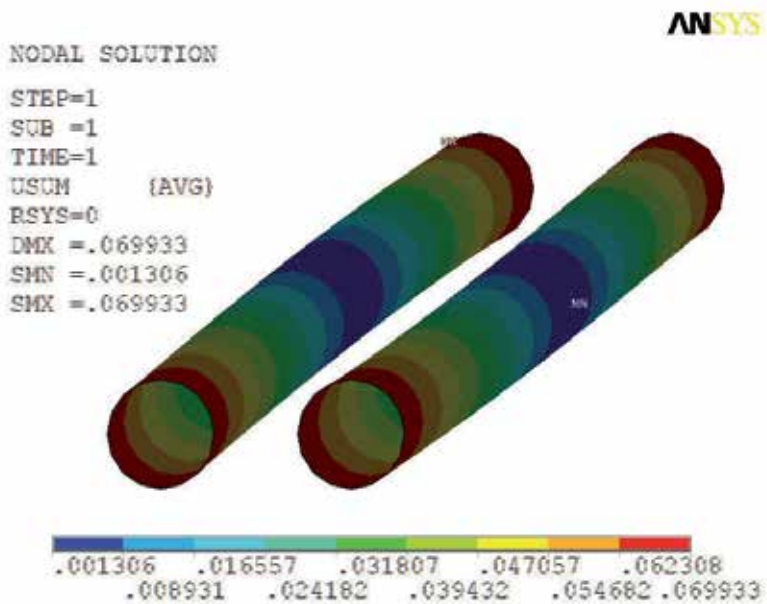


Fig. 19. Total strains in pipes mounted in the center of the perforated plate; magnified deformation of pipes [mm] – case 2.

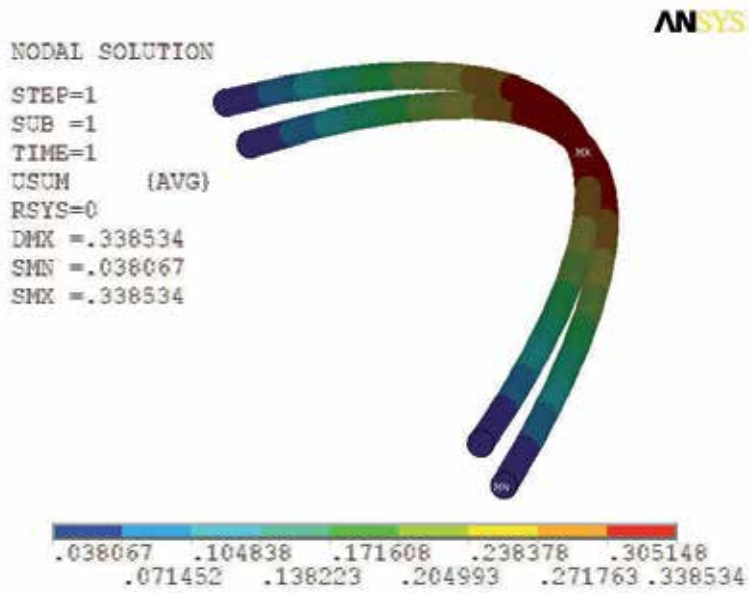


Fig. 20. Total strains in pipes subject to the maximal strain; magnified deformation of pipes [mm] – case 2.

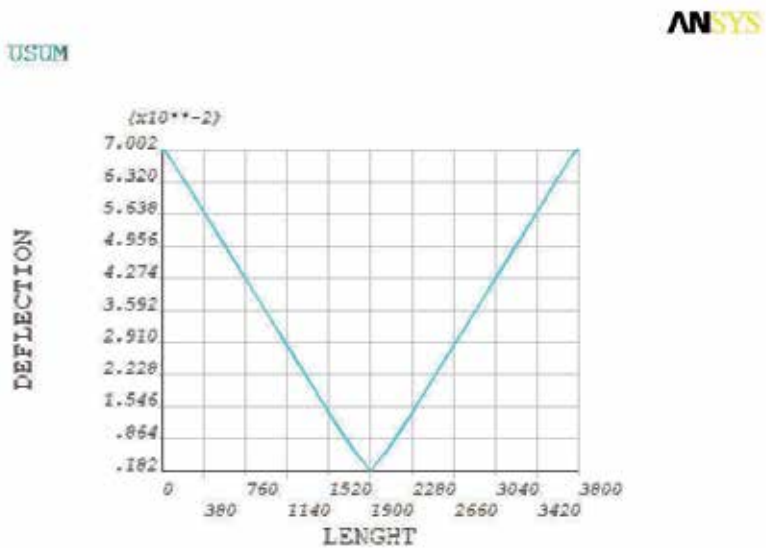


Fig. 21. Strain path in the pipe along its length [mm] - an example (the pipe is mounted in the position closest to the geometrical axis of the heat exchanger).

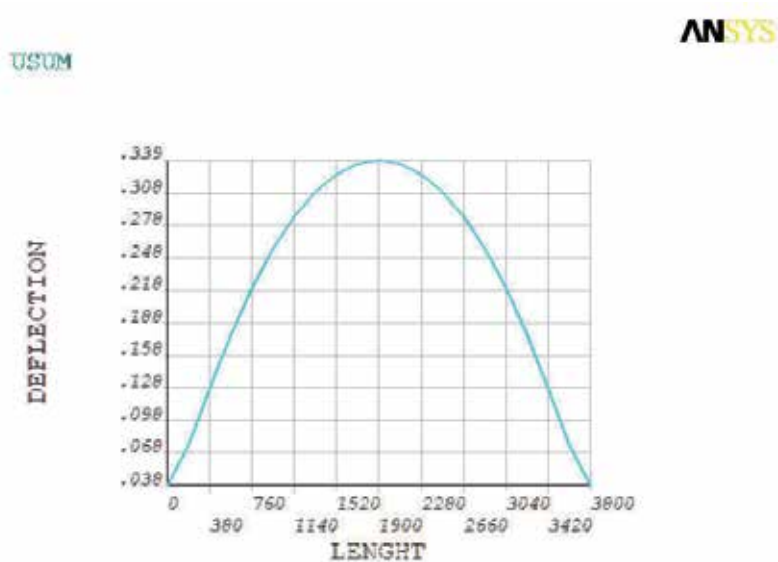


Fig. 22. Strain path in the pipe along its length [mm] – an example (the pipe is mounted in the position farthest from the geometrical axis of the heat exchanger).

6. Analysis of the results

A shell-solid model of the heat exchanger - a water heater - was subjected to the numerical calculations. The author's task was to conduct a possibly full analysis of stresses and strains occurring in structural elements of the heat exchanger, especially under extreme conditions that appear during, e.g., emergency operation. The calculations were carried out for altered thickness of the plate (in the first case by 15%, in the second one by 50%). This change was dictated by economic reasons. On the basis of the calculation results and the analysis of distributions of stresses and strains, one can conclude that the perforated bottom (the perforated plate) is not the place where stresses concentrate. In the first case, the reduced stresses in the bottom were equal to approx. 30 MPa (Fig.10), and in the second case they increased to approx. 50 MPa (Fig.18). The analysis of local zones of stresses in the whole heat exchanger has allowed us to find out that the maximal stresses in both cases appeared in the connections between the collar with the jacket and they were equal to, respectively, 198MPa, and in the second case they increased by approx. 10%. As opposed to the values of stresses, the total strains differ considerably. The maximal strains occurring in the heat exchanger were of the magnitude of 0.07 mm in the first case (Fig.5), whereas in the second case they increased up to 4.45 mm (Fig.13). Some exemplary maps of strains in the selected pipes mounted, correspondingly:

1. in the central part of the perforated plate (Fig. 11 and Fig.19),
2. in the outer part of the perforated plate, in the place where the maximal deflection is anticipated (Fig.12 and Fig. 20) have been presented in the paper.

The analysis of the calculation results has shown that the pipes mounted in the outer part are subject to higher deformations than the pipes mounted inside the central part of the plate that are subject more to elongation than to deflection.

In the general case, a stability loss of the elastic structure is a nonlinear problem that can be investigated with the iterative or incremental analysis of large displacements. This issue was dealt with by Arygyris (1977). With respect to the critical value of load, an influence of geometrical nonlinearity remains insignificant in numerous cases. When it is exceeded, a radical change in the configuration that corresponds to the equilibrium state occurs. If we are interested in the value P_{kr} and the postcritical state, it is enough to apply an elastic analysis. The task is not so easy in the heat exchanger under investigation. The structure of the device is complex and loaded with pressures that follow from the operation, therefore the FEM calculations were proposed. The investigations of the deformation nature of the heat exchanger and the analysis of strains and displacements are very important tasks which would allow designers to evaluate the correctness of the structure in order to avoid considerable differences in displacements, e.g., through a change in the connection of the perforated bottom with the jacket or an application of a pipe compensation, etc.

The conducted here analysis of strains in individual structural elements of the heat exchanger allows researchers to foresee the places of stress concentration. Thus, respective changes can be introduced in order to decrease a number of failures of the structure.

7. Conclusions

The investigations of the heat exchanger have allowed us to formulate the following conclusions:

- structural elements of the heat exchanger (perforated plates, a jacket) do not exhibit geometrical modes of buckling;
- perforated plates, a jacket and heating cartridge pipes do not show local plasticization zones either;
- pipes fixed farthest from the geometrical axis of the heat exchanger are subject to highest displacements, deflections; the dependence of displacements and the pipe length is of a nonlinear character (Fig.21);
- displacements of the pipes situated close to the geometrical axis of the heat exchanger are significantly lower; the dependence of displacements along the pipe length is linear (Fig. 22);
- the highest value of stresses was observed in the connection region of the jacket with the collar (Fig.6 and Fig.14),
- perforated plates, an integral part of the heat exchanger, are not the place where stresses concentrate, and the stresses that occur in them are considerably lower than the maximal stresses occurring in pipes and the jacket.

The further analysis enables the following conclusions:

- pipes most distant from the geometrical axis of the heat exchanger are most prone to a stability loss,

- a concentration of stresses occurs in the region where the jacket is connected to the collar,
- there is a possibility to decrease further the thickness of perforated plates of the heat exchanger.

The analysis of the obtained results has allowed us to observe the places that are most prone to a stability loss, where a concentration of stresses occurs and to determine possible alternations in the thickness of perforated plates (which would be justified economically).

8. References

- Achtelik H., Gasiak G., Grzelak J. (2005). *Strain and load carrying capacity of perforated plates under axial – symmetrical load*, Oficyna Wydawnicza, Opole, Poland [in Polish]
User's Guide ANSYS 12
- Bijlaard P.P. (1950). *On the plastic buckling of plates*, J. Aeron. Sci., Vol.17
- Chudzik A.A. (2002). *Analysis of the state of stress in perforated plates of heat exchangers, including effects of elastic and plastic zones*, PhD Dissertation [in Polish]
- Chudzik A.A. (2008). *Preliminary analysis of inelastic buckling of the heat exchangers*, Journal Of Theoretical and Applied Mechanics, Warsaw [in Polish]
- Concession documentation of the Py-100-020 decarbonized water heater* [in Polish]
- Gellin S. (1979). *Effect of an axisymmetric imperfection on the plastic buckling of an axially compressed cylindrical shell*, J. Appl. Mech., Vol. 46
- Gerarad G. (1956). *Compressive and torsional buckling of thin-wall cylinders in the yield region*, NACA Techn. Note, No.3276
- Grigoluk E.I. (1957). *O vypucivonii tonkich oblocek za predelom uprugosti*, Izv. AN SSSR, Otd. Tech. N., 10
- Grigoluk E.I. (1957). *Cisto plasticeskaja proteja ustojcivosti tonkich oblocek*, Prikl. Matem. i mech., 21, No 6
- Harding J.E., (1978). *The elastic-plastic analysis of imperfect cylinders*, Proc. Ins. Civ. Eng, Part 2
- Hobler T. (1986), *Heat Transfer and Heat Exchangers*, Wydawnictwo Naukowo-Techniczne, Warsaw [in Polish]
- Horak J., Lord G.J., Peletier M.A. (2005), *Cylinder buckling: the mountain pass as an organizing center*, *arXiv:math. AP/0507 263*, 1
- Hutchinson J.W. (1972). *On the postbuckling behaviour of imperfection-sensitive structures in the plastic range*, J Appl. Mech., Vol.39
- Hutchinson J.W. (1973). *Imperfection sensitivity in the plastic range*, J. Mech. Phys.Solids, Vol 21
- Iljussin A.A. (1944). *Ustojcivost plastinok I oblocek za predelom uprugosti*, Prikl. matem. i mech., 8, No. 5
- Lee L.H.N. (1961). *Inelastic buckling of cylindrical shells under axial compression and internal pressure*, Developments in Mechanics, 1
- Lee L.H.N. (1962). *Inelastic buckling of initially imperfect cylindrical shells subject to axial compression*, J. Aerospace Sci., Vol.29, No.1
- Lee L.H.N. (1962). *Inelastic buckling of cylindrical shells under axial compression and internal pressure*, w: Proc.4thU.S. Nat. Congr. Appl. Mech., Berkley, Calif.
- Murphy L. M., Lee L.H.N. (1971). *Inelastic buckling process of axially compressed cylindrical shells subject to edge constrains*, Int. J. Solids Struct., 7,8

- Nowak Z., Życzkowski M. (1963). *Survey of the latest studies on shell stability*, Mechanika teoretyczna stosowana, 1,2 [in Polish]
- Sobel L.H., Newman S.Z. (1982). *Plastic buckling of cylindrical shells under axial compression*, J. Press. Ves. Tech., 102
- Królak M. et. al. (1990). *Postcritical states and the limit load carrying capacity of flat-walled grinders*, Państwowe Wydawnictwo Naukowe, ISBN 83-01-10377-9, Warsaw [in Polish]
- Sewell M.J. (1972). *A survey of plastic buckling*, in: *Stability*, H. Leipholz, University of Waterloo Press, Ontario
- Ryś J.(2003).*Methodology of calculation of stresses in the perforated walls of heat exchangers*,Inżynieria I aparatura chemiczna, Nr 6/2003 [in Polish]
- Zielnica J. (1969). *Stabilty loss in the thin-walled shell rolled out beyond the elastic limit*, Zeszyty Naukowe Politechniki Poznańskiej, Mechanika 63,9 [in Polish]

Part 2

Micro-Channels and Compact Heat Exchangers

Microchannel Simulation

Mohammad Hassan Saidi, Omid Asgari and Hadis Hemati
Sharif University of Technology
Iran

1. Introduction

In the current state of fast developing electronic equipment, having high speeds and at the same time high heat generation rates, researchers are trying to find an effective microcooling method. The main problem in the cooling of microdevices is their high heat generation rate in a limited space. In this way, much research has been conducted on the analysis of different novel microcooling methods such as microheat pipes, microjet impingements, microcapillary pumped loops, microelectrohydrodynamic coolers, and microchannel heat sinks. Among the different microcooling devices the microchannel heat sink has been of special consideration due to its capabilities such as high capacity of heat removal. In principle, microchannels can be machined at the back of a substrate of electronic chips and, therefore, can reduce the internal (contact) thermal resistance of the heat sink practically to zero. The cooling rates in such microchannel heat exchangers should increase significantly due to a decrease in the convective resistance to heat transport caused by a drastic reduction in the thickness of thermal boundary layers.

The overall excellent potential capacity of such a heat sink for heat dissipation is based on the large heat transfer surface-to-volume ratio of the microchannel heat exchangers. The use of microchannel heat sink was first introduced by Tuckerman and Pease in 1981 [1]. Their research was based on an experiment where they showed that high heat rates of 790 W/cm^2 could be removed by microchannel heat sinks.

Currently, research in the field of microchannels is going on in three aspects of experimental methods [2,3,4], numerical methods [5,6,7,8], and analytical methods [9,10,11,12]. It is well known that the cross-sectional shape of a channel can have significant affect on the fluid flow and heat transfer characteristics in microchannels. Peng and Peterson [13] performed experimental investigations of the pressure drop and convective heat transfer for water flowing in rectangular microchannels, and found that the cross-sectional aspect ratio had significant influence on the flow friction and convective heat transfer in both laminar and turbulent flows. Kawano et al. [14] provided experimental data on the friction and heat transfer in rectangular, silicon based microchannel heat sinks, and more recently Wu and Cheng [15,16] conducted a series of experiments to measure the friction factor and convective heat transfer in smooth silicon microchannels of trapezoidal cross-section. The experimental methods has its own values and the new developments in the micromachining techniques help the researchers to perform precise experiments, but because of its high cost it fails to be commonly applied.

There has been much effort to analytically model the microchannel heat sink. Knight et al. [9] used empirical correlations to evaluate the performance of a microchannel heat sink. Koh and Colony [17] first modeled microstructures as a porous medium using Darcy's law. Later on Tien and Kuo [18] developed a model for heat transfer in microchannels using the modified Darcy equation and the two-equation model. Another method to model the microchannel heat sink analytically is to use the fin and plate theory. In this way, the solid walls are assumed to be as fins that are connected to the base plate. Applying this assumption, the thermal resistance and other thermal characteristics of the system could be derived using the fin and plate heat transfer relations. Because of limiting and less accuracy of the analytical approach in some phenomena, e.g. conjugate heat transfer the numerical method is being used vastly to simulate the performance of microchannels like other fields of heat transfer.

Webb and Zhang [19] claim that the accepted single-phase flow correlations adequately predict their experimental data for round and rectangular tubes with hydraulic diameter of the order of 1 mm. Wesberg et al. [8] solved a two-dimensional conjugate heat transfer problem for microchannel heat sinks to obtain detailed spatial distributions of the temperature of the heat sink cross-section along the length of the channels. Fedorov and Viskanta [6] developed a three dimensional model to investigate the conjugate heat transfer in a microchannel heat sink with the same channel geometry used in the experimental work done by Kawano et al. [14]. This simulation showed that the average channel wall temperature along the flow direction was nearly uniform except in the region close to the channel inlet, where very large temperature gradients were observed. Qu and Mudawar [5] conducted a three-dimensional fluid flow and heat transfer analysis for a rectangular microchannel heat sink with a geometry similar to that of Kawano et al. [14] using a numerical method similar to that proposed by both Kawano et al. [14] and Fedorov and Viskanta [6]. This model considered the hydrodynamic and thermal developing flow along the channel and found that the Reynolds number will influence the length of the developing flow region. It was also found that the highest temperature is typically encountered at the heated base surface of the heat sink immediately adjacent to the channel outlet and that the temperature rise along the flow direction in the solid and fluid regions can both be approximated as linear.

In this study the SIMPLE pressure correction approach has been chosen. For simplicity the equations are solved in a segregated manner. An effective multigrid solver is developed for pressure correction equation. Methods for calculating cell-face velocities are studied. Convection and diffusion terms are modeled using upwind and the central difference stencil, respectively. The variables are located in the cell-centred collocated grid. The general coordinates are described using the pure control volume approach with vector notations. In the method developed herein, the velocity field is first solved and then the mean velocity derived. The thermophysical properties are chosen at a reference temperature (an estimated averaged liquid bulk temperature) determined from the energy balance and then a new final velocity field and temperature distribution for the microchannel is defined. A numerical model with fully developed flow is presented and used to analyze the heat transfer in a microchannel heat sink for low Re numbers. The numerical model is based upon a three dimensional conjugate heat transfer approach (3D fluid flow and 3D heat transfer). Computations were performed for different total pressure drops in the channel. The system of three-dimensional Navier-Stokes equations for conservation of mass, momentum, and energy based on the continuum flow assumption is used as a mathematical model of the process.

2. Analysis

2.1 Problem description

The micro-heat sink modeled in this investigation consists of a 10 mm long silicon substrate with a silicon cover. The rectangular microchannels have a width of 57 μm and a depth of 180 μm . The hydraulic diameter of microchannel under development is about 86.58 μm and is expected to decrease to 10 μm . This yields a typical Knudsen number for water as a coolant to be between 3.5×10^{-5} and 3.5×10^{-4} which lies in the continuous flow regime ($Kn < 10^{-3}$) [20]. Hence, the conservation equations based on the continuum model (Navier-Stokes equations of motion) can still be used to describe the transport processes.

A schematic of the rectangular microchannel heat sink is shown in Figure 1 where a unit of cell consisting of one channel was selected because of the symmetry of the structure. The unit cell of the heat sink can be represented by an asymmetric rectangular channel with the cross-sectional dimensions as shown in Table 1. The channel geometry is similar to that employed in the experimental work of Kawano et al. [14] and in the numerical investigations of Qu and Mudawar [5] and Fedorov and Viskanta [6]. It is assumed that the heat flux input at the bottom of the heat sink is uniform.

2.2 Model equations and boundary conditions

Consider a steady 3D flow in a silicon microchannel heat sink with heating from below and with adiabatic conditions at the other boundaries, as showed in Figure 1. There are some assumptions in this numerical simulation, e.g. the transport processes are considered to be steady-state and three-dimensional, the flow is incompressible and laminar, thermal radiation is neglected, the thermophysical properties are temperature dependent. Under the stated assumptions, the governing equations and related boundary conditions for a fully developed 3D flow heat transfer are given as [21],

- Continuity equation

$$\frac{\partial}{\partial x}(\rho u) + \frac{\partial}{\partial y}(\rho v) + \frac{\partial}{\partial z}(\rho w) = 0 \quad (1)$$

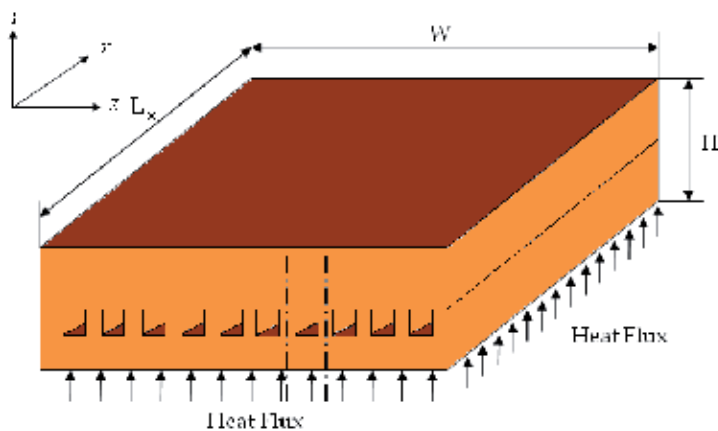


Fig. 1. Part I

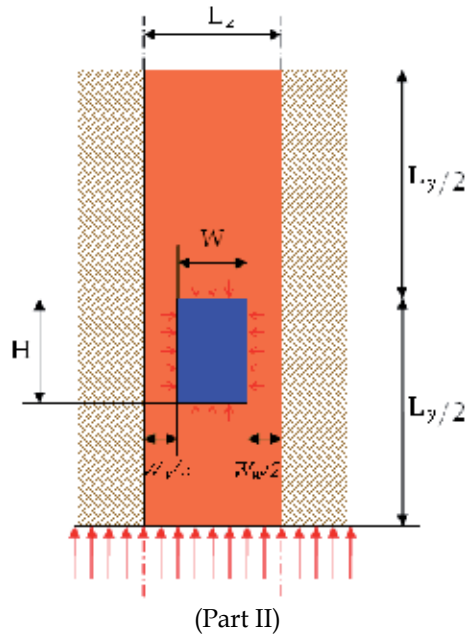


Fig. 1. Schematic of a rectangle microchannel heat sink and the unit of cell.

H μm	L_x μm	L_z μm	L_y μm	D_h μm	W_w μm	W μm
180	10	100	900	86.58	43	57

Table 1. Geometric dimensions of the unit cell.

- Momentum equations

$$\begin{aligned} & \frac{\partial}{\partial x}(\rho u^2) + \frac{\partial}{\partial y}(\rho uv) + \frac{\partial}{\partial z}(\rho uw) \\ &= -\frac{\partial P}{\partial x} + \frac{\partial}{\partial x}\left(\mu \frac{\partial u}{\partial x}\right) + \frac{\partial}{\partial y}\left(\mu \frac{\partial u}{\partial y}\right) + \frac{\partial}{\partial z}\left(\mu \frac{\partial u}{\partial z}\right) \end{aligned} \tag{2}$$

$$\begin{aligned} & \frac{\partial}{\partial x}(\rho uv) + \frac{\partial}{\partial y}(\rho v^2) + \frac{\partial}{\partial z}(\rho vw) \\ &= -\frac{\partial P}{\partial y} + \frac{\partial}{\partial x}\left(\mu \frac{\partial v}{\partial x}\right) + \frac{\partial}{\partial y}\left(\mu \frac{\partial v}{\partial y}\right) + \frac{\partial}{\partial z}\left(\mu \frac{\partial v}{\partial z}\right) \end{aligned} \tag{3}$$

$$\begin{aligned} & \frac{\partial}{\partial x}(\rho wu) + \frac{\partial}{\partial y}(\rho wv) + \frac{\partial}{\partial z}(\rho w^2) \\ &= -\frac{\partial P}{\partial z} + \frac{\partial}{\partial x}\left(\mu \frac{\partial w}{\partial x}\right) + \frac{\partial}{\partial y}\left(\mu \frac{\partial w}{\partial y}\right) + \frac{\partial}{\partial z}\left(\mu \frac{\partial w}{\partial z}\right) \end{aligned} \tag{4}$$

- Energy equation

$$\begin{aligned} & \frac{\partial}{\partial x}(c_p \rho u T) + \frac{\partial}{\partial y}(c_p \rho v T) + \frac{\partial}{\partial z}(c_p \rho w T) \\ & = \frac{\partial}{\partial x}\left(k \frac{\partial T}{\partial x}\right) + \frac{\partial}{\partial y}\left(k \frac{\partial T}{\partial y}\right) + \frac{\partial}{\partial z}\left(k \frac{\partial T}{\partial z}\right) \end{aligned} \quad (5)$$

where u , v , w , p , ρ , μ , T , k and c_p are the velocity in x -direction, y -direction, z -direction, pressure, density, dynamic viscosity, temperature, thermal conductivity and specific heat at constant pressure respectively. The hydrodynamic boundary conditions are as follow:

at the inner wall surface (no slip)

$$u = 0, \quad v = 0, \quad w = 0 \quad (6)$$

at the inlet of channel

$$x = 0, \quad p_f = p_{in}, \quad u = 1 \frac{m}{s}, \quad v = 0, \quad w = 0 \quad (7)$$

at the outlet of channel

$$x = L_x, \quad p_f = p_{out}(1atm), \quad v = 0, \quad w = 0 \quad (8)$$

the heat conduction in the solid section is,

$$\frac{\partial}{\partial x}\left(k \frac{\partial T}{\partial x}\right)_s + \frac{\partial}{\partial y}\left(k \frac{\partial T}{\partial y}\right)_s + \frac{\partial}{\partial z}\left(k \frac{\partial T}{\partial z}\right)_s = 0 \quad (9)$$

the thermal boundary conditions can be stated as:

$$0 \leq x \leq L_x, y = 0, 0 \leq z \leq L_z \Rightarrow -k_s \frac{\partial T_s}{\partial y} = q_s \quad (10)$$

$$0 \leq x \leq L_x, y = L_y, 0 \leq z \leq L_z \Rightarrow -k_s \frac{\partial T_s}{\partial y} = 0 \quad (11)$$

$$\begin{aligned} x = 0 \left\{ \begin{array}{l} (L_y / 2 - H) \leq y \leq L_y / 2 \\ W_w / 2 \leq z \leq (W_w / 2 + W) \end{array} \right. & \Rightarrow T_f = T_{in} \\ \text{else} & \Rightarrow -k_s \frac{\partial T_s}{\partial x} = 0 \end{aligned} \quad (12)$$

$$\begin{aligned} x = L_x \left\{ \begin{array}{l} (L_y / 2 - H) \leq y \leq L_y / 2 \\ W_w / 2 \leq z \leq (W_w / 2 + W) \end{array} \right. & \Rightarrow -k_f \frac{\partial T_f}{\partial x} = 0 \\ \text{else} & \Rightarrow -k_s \frac{\partial T_s}{\partial x} = 0 \end{aligned} \quad (13)$$

$$0 \leq x \leq L_x, 0 \leq y \leq L_y, z = 0 \Rightarrow -k_s \frac{\partial T_s}{\partial z} = 0 \quad (14)$$

$$0 \leq x \leq L_x, 0 \leq y \leq L_y, z = L_z \Rightarrow -k_s \frac{\partial T_s}{\partial z} = 0 \quad (15)$$

at the inner wall surface,

$$-k_s \left(\frac{\partial T_s(x, y, z)}{\partial n} \Big|_{\Gamma} \right) = -k_f \left(\frac{\partial T_f(x, y, z)}{\partial n} \Big|_{\Gamma} \right) \quad (16)$$

$$T_{s,\Gamma} = T_{f,\Gamma}$$

where, Equation (10) gives the uniform heat flux boundary condition at the bottom wall of the substrate. Equations (11)–(15) assumes no heat loss from the solid to the environment at the boundary except at $x = 0$ for the fluid, where $T_f = T_{in}$. It should be noted that in reality, heat losses from the heat sink to the environment should be considered by conduction and convection at the inlet and outlet and at the top surface of the heat sink. Heat transfer in the unit cell is a conjugate one combining heat conduction in the solid and convection to the cooling fluid. The two heat transfer modes are coupled by continuities of temperature and heat flux at the interface between the solid and fluid, which are expressed by Equation (16). Γ denotes the perimeter of the inner wall of the channel. Equations (1), (2), (3), (4) and (5) form a closed system from which the flow properties u , v , w , p and T can be solved as a function of space and time. But, in this study only steady-state flows will be calculated.

2.3 Calculation of incompressible flows

Simultaneous numerical calculation of Equations (1), (2), (3), (4) and (5) is computationally complex. Therefore, the equations are solved one after another, i.e. in a segregated manner. The basic structure of Equations (2), (3), (4) and (5) is similar to each other, containing an unsteady term, convection, diffusion and possibly source terms, and they are often called convection-diffusion equations. The flow properties u , v , w and T are solved from Equations (2), (3), (4) and (5) respectively. Therefore, the continuity Equation (1) is to be modified for pressure or pressure-like quantity. The first stage is to derive a convection-diffusion equation to finite form. In this study the control volume approach is utilized. The process is to be studied by the aid of a general convection-diffusion equation for quantity Φ ,

$$\begin{aligned} & \frac{\partial}{\partial x}(\rho u \phi) + \frac{\partial}{\partial y}(\rho v \phi) + \frac{\partial}{\partial z}(\rho w \phi) \\ & = \frac{\partial}{\partial x} \left(\alpha \frac{\partial \phi}{\partial x} \right) + \frac{\partial}{\partial y} \left(\alpha \frac{\partial \phi}{\partial y} \right) + \frac{\partial}{\partial z} \left(\alpha \frac{\partial \phi}{\partial z} \right) + S \end{aligned} \quad (17)$$

where α is diffusion coefficient and the source term S could contain, for instance, pressure gradient and/or body force, etc. Next, Equation (17) is integrated over the control volume $V_{i,j,k}$. After the rearrangements the integrated equation can be obtained in the form,

$$\begin{aligned} F_{i+1/2,j,k} - F_{i-1/2,j,k} + F_{i,j+1/2,k} - \\ F_{i,j-1/2,k} + F_{i,j,k+1/2} - F_{i,j,k-1/2} = S_{i,j,k} \end{aligned} \quad (18)$$

$$F_{i-1/2,j,k} = \left[A \left(\rho u \phi - \alpha \frac{\partial \phi}{\partial x} \right) \right]_{i-1/2,j,k} \quad (19)$$

where A is a surface area of a face of the cell. From the physical point of view, the convection transfers the information downstream. Therefore, the approximation of convection terms must be weighted to the up-stream-side. The simplest stencil is the first-order upwind (FOU),

$$\phi_{i-1/2,j,k} = \phi_{i-1,j,k} + O(\Delta x); \quad u_{i-1/2,j,k} > 0 \quad (20)$$

$$\phi_{i-1/2,j,k} = \phi_{i,j,k} + O(\Delta x); \quad u_{i-1/2,j,k} < 0 \quad (21)$$

The diffusion terms of Equation (19) are approximated by using the central difference scheme,

$$\left[\frac{\partial \phi}{\partial x} \right]_{i+1/2,j,k} = \frac{\phi_{i+1,j,k} - \phi_{i,j,k}}{\Delta x} + O(\Delta x^2) \quad (22)$$

where the grid is assumed to be uniform. Also the pressure gradient terms of the momentum equations are approximated by using central differencing. After the integration over the control volume $V_{i,j,k}$ they are obtained in the form

$$\int_{V_{i,j,k}} \frac{\partial p}{\partial x} d\Omega = (pA)_{i+1/2,j,k} - (pA)_{i-1/2,j,k} \quad (23)$$

where central difference schemes like,

$$p_{i+1/2,j,k} = 0.5(p_{i,j,k} + p_{i+1,j,k}) + O(\Delta x^2) \quad (24)$$

are applied.

To close the partial differential equation system (1), (2), (3), (4) and (5) for a certain problem, the boundary conditions must be specified. In the present solver, the boundary conditions are handled by using ghost cells, which are illustrated in Figures (2) and (3), the principal idea is to use the ghost cell values to give the fixed boundary value at the boundary of the domain, i.e. the ghost cell values are extrapolated from the face and domain values. Thus, the Dirichlet and Neumann conditions are given in the form

$$\phi_{2,j,k} = 2\phi_{face} - \phi_{3,j,k} \quad (25)$$

$$\phi_{2,j,k} = \phi_{3,j,k} - \Delta x \left. \frac{\partial \phi}{\partial x} \right|_{face} \quad (26)$$

respectively.

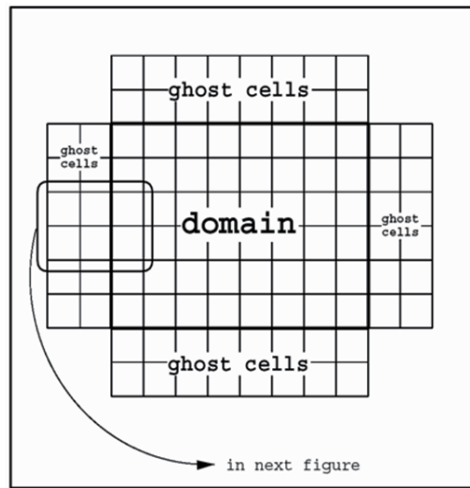


Fig. 2. Ghost cells around the domain.

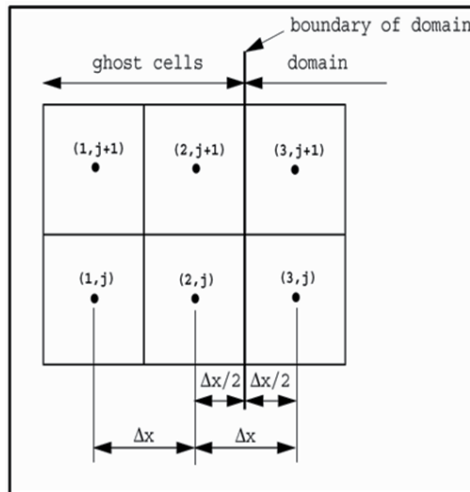


Fig. 3. The notations of the ghost cells.

2.4 Treatment of pressure in incompressible Navier-Stokes equations

The spatial oscillations occur when central differencing is applied to both the continuity equation and the pressure gradient term in the momentum equations. The momentum equations at the even-numbered nodes depend only on pressures at odd-numbered nodes, and vice versa. The same holds for the continuity equation. This situation permits two different pressure fields to co-exist, which is known as checkerboard pressure field.

Nowadays, the staggered grid arrangement is no more necessary. The remarkable turn toward the collocated grid arrangement was the study presented by Rhie and Chow [22]. In the collocated grid arrangement all variables use the same grid and interpolation is needed. As it was mentioned, the collocated grid arrangement causes problems when central

differencing is applied to cell-face velocities, Rhie and Chow [21] presented a method for avoiding the usage of the staggered grid arrangement. In this method central differencing has been applied to the pressure gradient and cell-face pressure, while the Rhie & Chow interpolation has been applied to the cell-face velocity as follow,

$$u_{i-1/2,j,k} = \frac{1}{2} \left(u_{i-1,j,k} - u_{i,j,k} \right) - \frac{1}{2} \left(\frac{V_{i-1,j,k}}{a_{i-1,j,k}} + \frac{V_{i,j,k}}{a_{i,j,k}} \right) \times \frac{\partial p}{\partial x} \Big|_{i-1/2,j,k} + \frac{1}{2} \left(\frac{V_{i-1,j,k}}{a_{i-1,j,k}} \frac{\partial p}{\partial x} \Big|_{i-1,j,k} + \frac{V_{i,j,k}}{a_{i,j,k}} \frac{\partial p}{\partial x} \Big|_{i,j,k} \right) \tag{27}$$

2.5 Pressure correction equation and multigrid technique

The current research indicates that the AC-MG acceleration technique is highly efficient, reliable and robust, which makes it feasible for CPU-intensive computations, such as pressure Correction equations. When compared to the discretized momentum equations, the pressure Poisson equations tend to be very stiff and ill-conditioned, i.e. $a_p \equiv \sum_{nb} a_{nb}$ because of these reasons, solving the pressure Poisson equation is usually the CPU bottle-neck for the incompressible N-S equation system and AC-MG technique is required. With this acceleration technique the residuals of the large-scale algebraic equation system are guaranteed to be continuously driven down to the level of the computer machine round-off error and warrants strong conservations of mass and momentum satisfied over all the control volumes. In this cell centered multigrid algorithm both restriction and prolongation operators are based on piecewise constant interpolation.

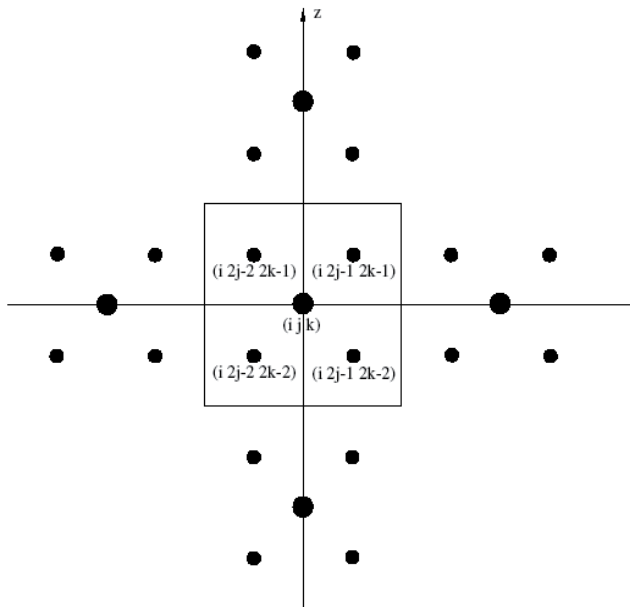


Fig. 4. Schematic of a cell-centered two-level multigrid configuration.

The additive-correction multigrid scheme described in [23] is used for the two cross-streamwise directions (y and z). The cell-centred two-level multigrid configuration is sketched in Figure 4, in which the grid point (i, j, k) on the coarse level is surrounded by four grid points on the fine level in the y and z directions, namely $(i, 2j-2, 2k-2)$, $(i, 2j-2, 2k-1)$, $(i, 2j-1, 2k-2)$ and $(i, 2j-1, 2k-1)$. The variables on the coarse and fine levels are denoted by superscripts c and f , respectively, in the following equations. Based on the idea introduced in [23], the following algebraic equation system can be used to determine the correction for the fine grid level:

$$\begin{aligned} a_{p(i,j,k)}^c \phi_{i,j,k}^c &= a_{e(i,j,k)}^c \phi_{i+1,j,k}^c + a_{w(i,j,k)}^c \phi_{i-1,j,k}^c \\ &+ a_n^c(i,j,k) \phi_{i,j+1,k}^c + a_s^c(i,j,k) \phi_{i,j-1,k}^c \\ &+ a_t^c(i,j,k) \phi_{i,j,k+1}^c + a_b^c(i,j,k) \phi_{i,j,k-1}^c + S_{C_{i,j,k}}^c \end{aligned} \quad (28)$$

where the coefficients on the coarse grid are calculated from the following restriction formulae:

$$\begin{aligned} a_{e(i,j,k)}^c &= a_{e(i,2j-2,2k-2)}^f + a_{e(i,2j-2,2k-1)}^f \\ &+ a_{e(i,2j-1,2k-2)}^f + a_{e(i,2j-1,2k-1)}^f \end{aligned} \quad (29)$$

$$\begin{aligned} a_{w(i,j,k)}^c &= a_{w(i,2j-2,2k-2)}^f + a_{w(i,2j-2,2k-1)}^f \\ &+ a_{w(i,2j-1,2k-2)}^f + a_{w(i,2j-1,2k-1)}^f \end{aligned} \quad (30)$$

$$a_n^c(i,j,k) = a_n^f(i,2j-1,2k-2) + a_n^f(i,2j-1,2k-1) \quad (31)$$

$$a_s^c(i,j,k) = a_s^f(i,2j-2,2k-2) + a_s^f(i,2j-2,2k-1) \quad (32)$$

$$a_t^c(i,j,k) = a_t^f(i,2j-2,2k-1) + a_t^f(i,2j-1,2k-1) \quad (33)$$

$$a_b^c(i,j,k) = a_b^f(i,2j-2,2k-2) + a_b^f(i,2j-1,2k-2) \quad (34)$$

$$\begin{aligned} a_p^c(i,j,k) &= a_p^f(i,2j-2,2k-2) + a_p^f(i,2j-2,2k-1) \\ &+ a_p^f(i,2j-1,2k-2) + a_p^f(i,2j-1,2k-1) \\ &- a_s^f(i,2j-1,2k-2) + a_s^f(i,2j-1,2k-1) \\ &- a_n^f(i,2j-2,2k-2) + a_n^f(i,2j-2,2k-1) \\ &- a_b^f(i,2j-2,2k-1) + a_b^f(i,2j-1,2k-1) \\ &- a_t^f(i,2j-2,2k-2) + a_t^f(i,2j-1,2k-2) \end{aligned} \quad (35)$$

$$Sc_{i,j,k}^c = r_{i,2j-2,2k-2}^f + r_{i,2j-2,2k-1}^f + r_{i,2j-1,2k-2}^f + r_{i,2j-1,2k-1}^f \quad (36)$$

the residuals on the fine grid level $r_{i,j,k}^f$ are calculated from the current iterative values of $\hat{\phi}_{i,j,k}^f$ using the following relation:

$$\begin{aligned} r_{i,j,k}^f = & -a_{p(i,j,k)}^f \hat{\phi}_{i,j,k}^f + a_{e(i,j,k)}^f \hat{\phi}_{i+1,j,k}^f \\ & + a_{n(i,j,k)}^f \hat{\phi}_{i,j+1,k}^f + a_{t(i,j,k)}^f \hat{\phi}_{i,j,k+1}^f \\ & + a_{w(i,j,k)}^f \hat{\phi}_{i-1,j,k}^f + a_{s(i,j,k)}^f \hat{\phi}_{i,j-1,k}^f \\ & + a_{b(i,j,k)}^f \hat{\phi}_{i,j,k-1}^f + Sc_{i,j,k}^f \end{aligned} \quad (37)$$

A typical two-level multigrid iterative algorithm consists of restriction, relaxation on the coarse grid and prolongation. After a number of relaxation sweeps, such as TDMA sweeps, on the fine grid level, the residuals are calculated using Equation (37) and are restricted to the coarse grid using Equations (29-36). The restricted residuals are then used as the source terms in Equation (28) and relaxation sweeps are used to solve Equation (28) on the coarse level. The solutions to Equation (28) are then utilized as the corrections to be prolonged back to the fine grid using the following relations to update the current iterative solution of $\hat{\phi}_{i,j,k}^f$,

$$\begin{aligned} \hat{\phi}_{i,2j-2,2k-2}^f &= \hat{\phi}_{i,2j-2,2k-2}^f + \phi_{i,j,k}^c \\ \hat{\phi}_{i,2j-2,2k-1}^f &= \hat{\phi}_{i,2j-2,2k-1}^f + \phi_{i,j,k}^c \\ \hat{\phi}_{i,2j-1,2k-2}^f &= \hat{\phi}_{i,2j-1,2k-2}^f + \phi_{i,j,k}^c \\ \hat{\phi}_{i,2j-1,2k-1}^f &= \hat{\phi}_{i,2j-1,2k-1}^f + \phi_{i,j,k}^c \end{aligned} \quad (38)$$

Equation (38) provides the prolongation formulation in the AC multigrid calculation. Obviously, the restriction (Equations (29-36)) and prolongation (Equation (38)) are second-order accuracy in space and no extra interpolations are needed. The AC-MG solution procedure contains two parts. The first part consists of a subroutine of TDMA sweeps, which is controlled by the residual convergence rate. A flowchart of the TDMA solver is depicted in Figure 5. If the total residual before iteration n on the current mesh is $R^n = \sum_{i,j,k} r_{i,j,k}^n$ and the residual after iteration n is R^{n+1} , then another TDMA sweeping iteration is performed if the residual convergence rate satisfies $R^{n+1} \geq f \cdot R^n$ where the value for f is usually set to 0.5 [23]. If the convergence rate is lower than 0.5, i.e. $R^{n+1}/R^n > f$, a correction on the coarser grid is required, which invokes the second part of the AC-MG solution procedure. A schematic figure of the three-level AC-MG solution procedure will be shown in Figure 6.

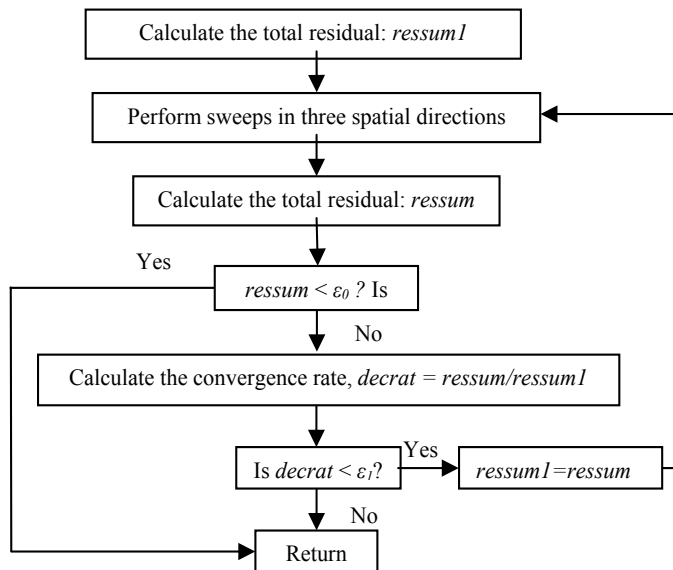


Fig. 5. Flowchart of the TDMA solver controlled by the residual convergence rate.

In order to check the sensitivity of the numerical results to mesh size, three different grid systems were tested. They consisted of $18 \times 42 \times 16$, $30 \times 82 \times 30$ and $50 \times 162 \times 58$ nodes in the x , y , and z directions, respectively. The results from the last two grid systems were very close to each other and local temperature differences were less than 0.1%. Since less computational time and computer memory were needed for the second grid system, it was employed in the final simulation.

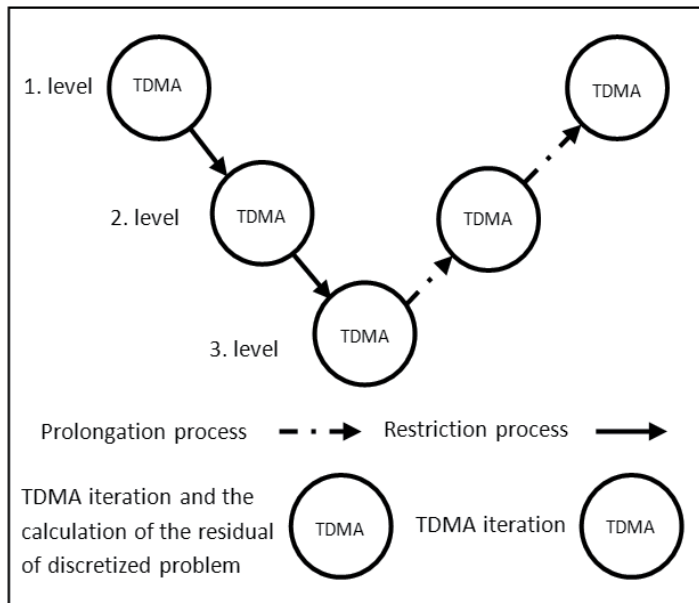


Fig. 6. A schematic of the three-level AC-MG solution procedure.

The total grid number is 73,800 ($N_x \times N_y \times N_z$ is $30 \times 82 \times 30$) for the domain. This type of a fine grid mesh for the y and z directions was chosen in order to properly resolve the velocity and viscous shear layers, and to more accurately define the conjugate heat transfer at the surface of the channel, thereby improving the temperature resolution. Furthermore, comparison with standard theoretical or numerical results indicates that the finer the mesh size the higher the numerical accuracy. The reasons for the comparative coarse discretization for the x -direction are: (i) with the exception of the inlet region, the temperature gradients are small compared to the gradients occurring in other directions; and (ii) The CPU time as well as the memory storage required increases dramatically as the number of grid nodes is increased.

3. Validation of the code

3.1 Velocity field

The velocity field can be determined analytically using a more direct approach. As illustrated in Figure 7, the following relations represent the reasonable results for this type of problem by Shah and London [24],

$$u = -\frac{16c_1 a^2}{\pi^3} \sum_{n=1,3,\dots}^{\infty} \frac{1}{n^3} (-1)^{(n-1)/2} \times \left[1 - \frac{\cosh(n\pi y / 2a)}{\cosh(n\pi b / 2a)} \right] \cos\left(\frac{n\pi z}{2a}\right) \tag{39}$$

$$u_m = -\frac{c_1 a^2}{3} \left[1 - \frac{192}{\pi^5} \left(\frac{a}{b}\right) \sum_{n=1,3,\dots}^{\infty} \frac{1}{n^5} \tanh\left(\frac{n\pi b}{2a}\right) \right] \tag{40}$$

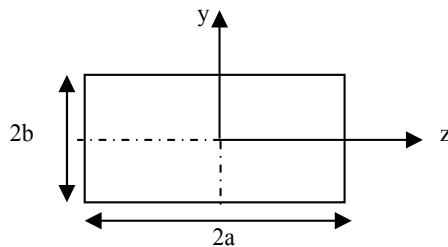


Fig. 7. A schematic of the rectangular channel.

This velocity profile is in excellent agreement with the experimental results. Since Equation (39) involves considerable computational complexity, a simple approximation in the following form for the aspect ratio $\alpha^* \leq 0.5$ is proposed [24],

$$\frac{u}{u_{\max}} = \left[1 - \left(\frac{y}{b}\right)^n \right] \left[1 - \left(\frac{z}{a}\right)^m \right] \tag{41}$$

where m and n are derived from below relations,

$$m = 1.7 + 0.5(\alpha^*)^{-1.4} \quad (42)$$

$$n = \begin{cases} 2 & \text{for } \alpha^* \leq 1/3 \\ 2 + 0.3(\alpha^* - 1/3) & \text{for } \alpha^* \geq 1/3 \end{cases} \quad (43)$$

The integration of Equation (41) over the duct cross section yields,

$$\frac{u}{u_m} = \left(\frac{m+1}{m}\right) \left(\frac{n+1}{n}\right) \left[1 - \left(\frac{y}{b}\right)^n\right] \left[1 - \left(\frac{z}{a}\right)^m\right] \quad (44)$$

$$\frac{u_{\max}}{u_m} = \left(\frac{m+1}{m}\right) \left(\frac{n+1}{n}\right) \quad (45)$$

With fRe of Equation (46), u_m for the rectangular ducts can be expressed in a closed form as,

$$fRe_{D_h} = 24(1 - 1.3553\alpha^* + 1.9467\alpha^{*2} - 1.7012\alpha^{*3} + 0.9564\alpha^{*4} - 0.2537\alpha^{*5}) \quad (46)$$

$$u_m = -\frac{8c_1a^2}{fRe_{D_h} \left[1 + (a/b)^2\right]} \quad (47)$$

where

$$c_1 = \frac{dp/dx}{\mu} = \frac{\Delta p/L_x}{\mu} \quad (48)$$

Substituting Equations (46) and (48) into Equation (47), the mean velocity for a given pressure drop, u_m can be obtained. Then, using the resulting value for u_m and Equations (42-44), the approximate analytical velocity distribution in the microchannel as shown in Figure 8 can be obtained. The numerically determined velocity profile developed here is illustrated in Figure 9. Comparison of the analytical and numerical results indicates that while the numerical code exactly represents the general trend of the results, there is some disparity between the analytical and numerical results. The small difference of the velocity profile between Figures 8 and 9 is due to the approximations in the analytical solution described in Equations (41) and (44). But clearly, as evidenced by the magnitude of the mean velocities and the Reynolds numbers obtained from the different methods, the agreement between the two methods is quite good and provides sufficient evidence for validation of the numerical method. In this comparison, the thermophysical properties of water were chosen at a temperature of 293 K (20°C). Because the thermophysical properties are temperature dependent, especially the liquid viscosity, the velocity and the Reynolds numbers are different under the same pressure drop conditions. This issue will be discussed in more detail later.

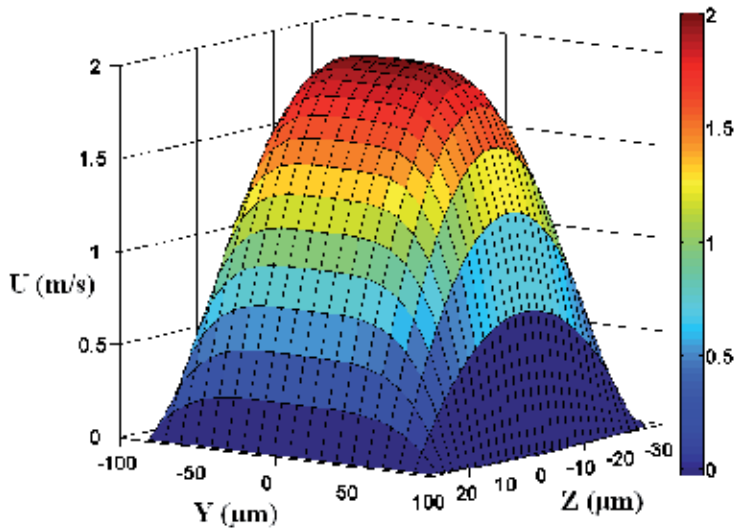


Fig. 8. Velocity field in channel from the approximate analytical expression Equation (44), $\Delta p=50 \text{ kPa}$, $Re=92.68$, $T_{reference}=20^\circ\text{C}$, $u_m=1.0779 \text{ m/s}$.

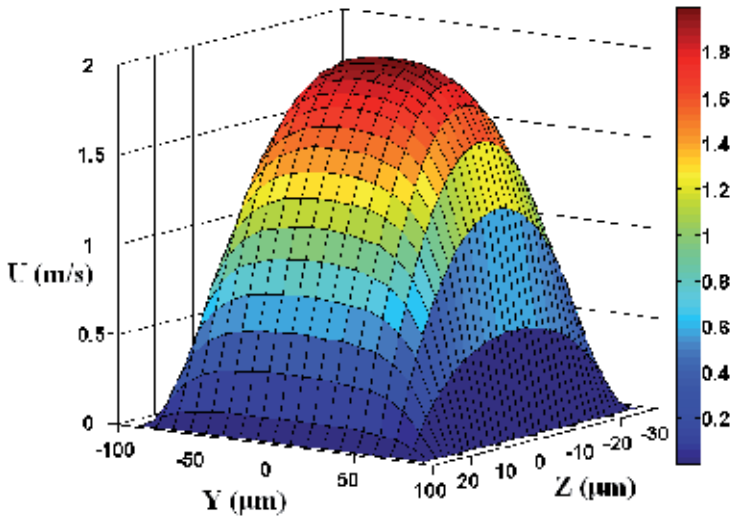


Fig. 9. Velocity field in channel from the numerical calculation, $\Delta p=50 \text{ kPa}$, $Re=92.383$, $T_{reference}=20^\circ\text{C}$, $u_m=1.1032 \text{ m/s}$, $u_{max}=1.997 \text{ m/s}$.

Figure 10 compares the analytical friction coefficient as determined from Equation (46) with the numerical results obtained using the following procedure, should be noted that, $f_{Darcy}=4f$. The mass flow rate is calculated from the velocity as,

$$\dot{m} = \sum \sum \rho_f \cdot u(i = \text{constant}, j, k) \Delta y \Delta z \tag{49}$$

and then, the mean velocity is obtained as

$$u_m = \frac{\dot{m}}{\rho_f A} = \frac{\dot{m}}{\rho_f HW} \quad (50)$$

then using Equation (51), the friction factor can be determined as Equation (52),

$$\Delta p = f \frac{4L_x}{D_h} \frac{\rho_f u_m^2}{2} \quad (51)$$

$$f_{Darcy} Re_{D_h} = 2 \frac{\Delta p D_h^2}{u_m L_x \mu_f} \quad (52)$$

In References [25-27], the friction coefficient, $f_{Darcy} Re$, is determined numerically for different duct cross-sections. For the rectangular channel with an aspect ratio (height to width) of 3-1 ($H:W$), which approximates the geometry used here, $180\mu\text{m} \times 57\mu\text{m}$, the Darcy friction factor-Reynolds number product, $f_{Darcy} Re$, is 69. The agreement between the numerical calculations here and the calculations obtained by others [25-27] represents that the numerical code developed here is quite accurate for the fully developed laminar flow.

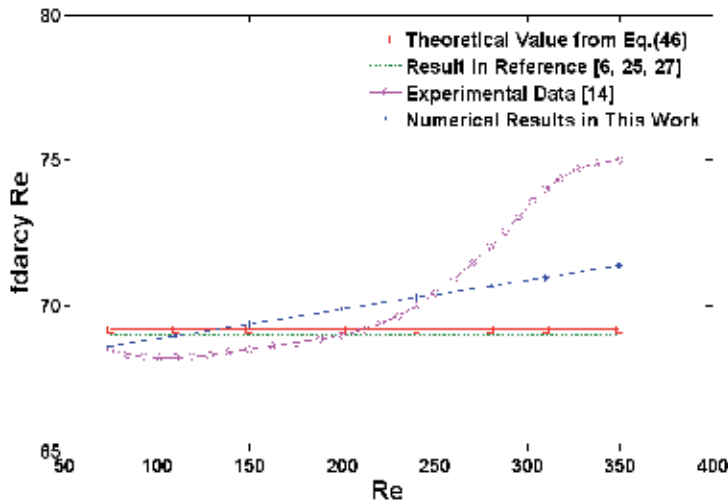


Fig. 10. Comparison among the numerical calculations, the analytical and the experimental data for the friction coefficient.

The length required for the formation of a fully developed laminar profile in a microchannel can be estimated by the following analytical relation [26] that is developed for a round tube,

$$\frac{L_e}{D_h} = 0.0575 Re_{D_h} \quad (53)$$

For a hydraulic diameter of $D_h = 86.58 \mu\text{m}$ and for $Re = 160$ the entrance length is $796.5 \mu\text{m}$. In References [25-27], it is noted that the shape of the entrance is very important, with much

shorter entrance lengths occurring for square-edged entrances than for rounded ones. Thus, because the flow entrance length may be less than 5% of the total length for a rectangular channel heat sink, the assumption of fully developed laminar flow over the entire length of the microchannel is acceptable for the heat transfer analysis, particularly in cases such as this where the Reynolds number is less than 200 (or low mass flow rates).

3.2 Heat transfer

The code was first validated for one dimensional heat conduction by comparing the results with a 1D analytical solution of heat conduction with a specified boundary condition [25]. The agreement was quite good and indicated very good correlation between the numerical results and the 1D analytical solution, Secondly, using conservation of energy, it can be shown that the maximum possible temperature rise between the fluid inlet and outlet can be expressed as:

$$\Delta T_{f,con} = \frac{q_s \cdot A_s}{\dot{m} \cdot c_p} \quad (54)$$

In addition, the average temperature rise between the inlet and outlet of the channel can be determined from the numerical analysis as follow,

$$\begin{aligned} \Delta T_{f,ave} &= \bar{T}_f(x=L_x) - \bar{T}_f(x=0) \\ &= \frac{\left\{ \sum \sum \rho_f \cdot u \cdot c_p \cdot T \cdot \Delta y \Delta z \right\}_{i=outlet,j,k}}{\dot{m} \cdot c_p} \\ &\quad - \frac{\left\{ \sum \sum \rho_f \cdot u \cdot c_p \cdot T \cdot \Delta y \Delta z \right\}_{i=inlet,j,k}}{\dot{m} \cdot c_p} \end{aligned} \quad (55)$$

In this work, three different cases ($q_s=90 \text{ W/cm}^2$, $\Delta p=50, 15$ and 6 kPa) were investigated. Comparison of the results in Table 2, indicates that the difference between $\Delta T_{f,ave}$ and $\Delta T_{f,con}$ is small. This issue also is illustrated in Figure 11. Differences of this magnitude can be attributed to (i) Equation (54) is the maximum possible temperature rise in the bulk liquid from the energy balance; (ii) the mesh size is not as fine as required (infinitesimal), hence the accuracy of the statistical result from Equation (55) is limited.

$\Delta p(\text{kPa})$	50	15	6
Re	162.68	85.60	47.32
$\Delta T_{f,con} (\text{°C})$	14.62	36.82	78.57
$\Delta T_{f,ave} (\text{°C})$	12.79	35.10	77.16

Table 2. Comparison between $\Delta T_{f,ave}$ and $\Delta T_{f,con}$ for $\Delta p=50, 15$ and 6 kPa , $q_w=90 \text{ W/cm}^2$.

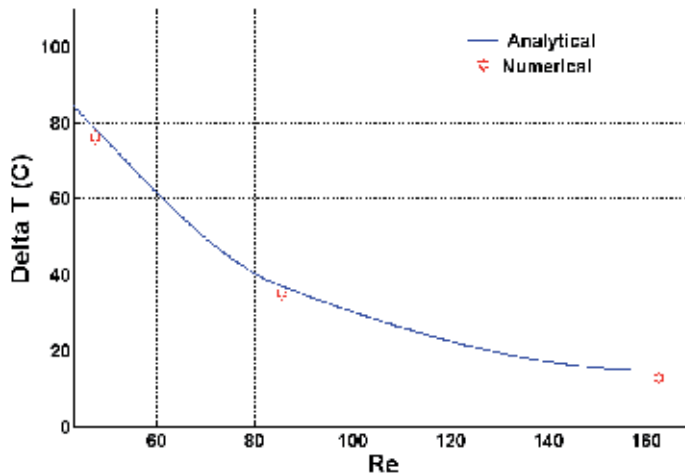


Fig. 11. Comparison between the numerical and analytical results for temperature differences upon the Reynolds number.

4. Results and discussion

The following four subsections are devoted to the local temperature distributions, the average and bulk characteristics, the local heat flux distributions and the Convergence Performance for the Pressure Correction Equations in microchannel heat sinks.

4.1 Local temperature distributions

Figure 12 shows a velocity field in a microchannel at $\Delta p=50 \text{ kPa}$. As discussed previously, the thermophysical properties of the water are based upon the estimated liquid bulk temperature. As can be seen by comparison with the results shown in Figure 9, for the same pressure drop along the channel, the thermal properties, velocity profile, mean velocity and Reynolds number are all mainly different.

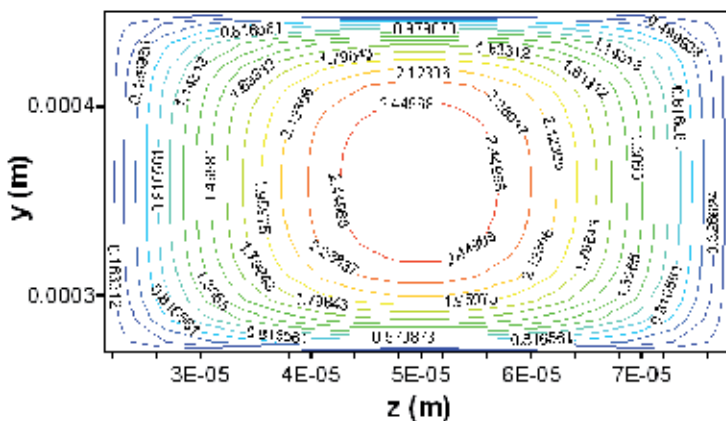


Fig. 12. X- component velocity field from the numerical calculation, $\Delta p=50 \text{ kPa}$, $Re=162.68$, $T_{\text{reference}}=32^\circ\text{C}$, $u_m=1.44 \text{ m/s}$, $u_{\text{max}}=2.61 \text{ m/s}$.

As shown, a variation in the reference temperature, $T_{reference}$ from 20 to 32°C, changes the mean velocity from 1.1032 to 1.44 m/s, and results in a corresponding change in the Reynolds number from 95.38 to 162.68. The numerical results for the temperature distribution in the heat sinks are shown in Figures 13, 14, 15, 16 and 17 for different locations along the channel. Figures 13, 14 and 15 show the local cross-sectional temperature distribution in the y - z plane at $x=0$, $x=Lx/2$ and $x=Lx$, respectively. As shown in Figure 13, the temperature of the liquid at the inlet is initially uniform (at 20°C). The temperature profiles shown in Figures 14 and 15 are identical in shape due to the assumption of hydrodynamic fully developed flow, but the magnitudes of the temperature are different.

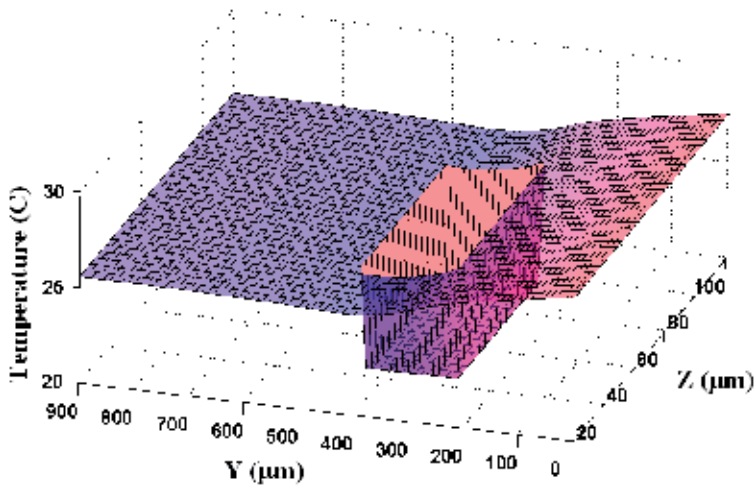


Fig. 13. Local temperature distribution in y - z plane at $x=0$, ($\Delta p=50$ kPa, $Re=162.68$, $T_{reference}=32^\circ\text{C}$, $u_m=1.44$ m/s).

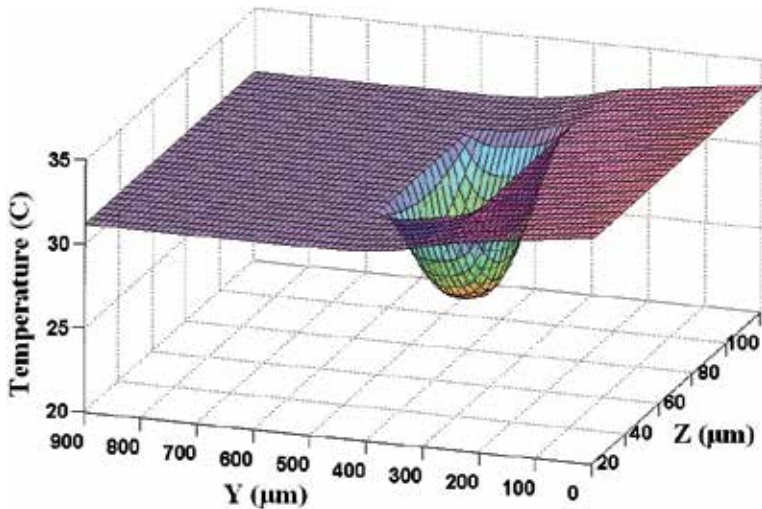


Fig. 14. Local temperature distribution in y - z plane at $x=L/2$, ($\Delta p=50$ kPa, $Re=162.68$, $T_{reference}=32^\circ\text{C}$, $u_m=1.44$ m/s).

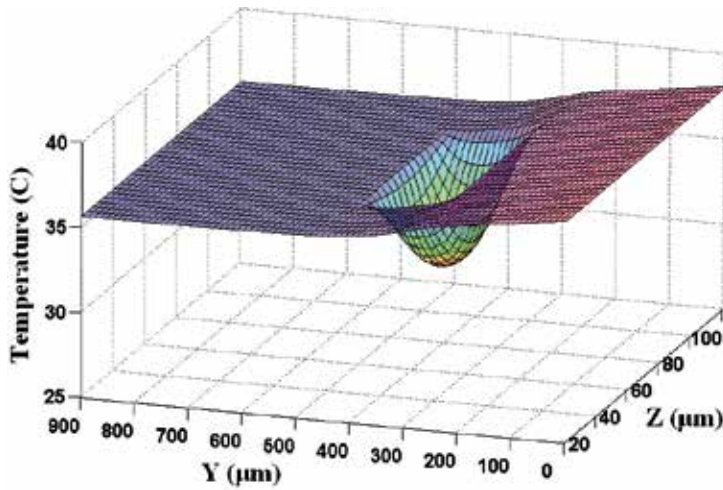


Fig. 15. Local temperature distribution in y - z plane at $x = L_x$, ($\Delta p = 50 \text{ kPa}$, $Re = 162.68$, $T_{reference} = 32^\circ\text{C}$, $u_m = 1.44 \text{ m/s}$).

Figure 16 shows the temperature contours in the heat sink at the outlet of the channel and Figure 17 shows the local temperatures inside the channel. It is noted in Figure 17 that the temperature is highest at the channel corner. This is due to the low velocity of the flow and the resulting high concentration of heat flux. From these calculations it is apparent that there is a 2–3°C temperature difference between the bottom wall of the substrate and the bottom surface of the channel.

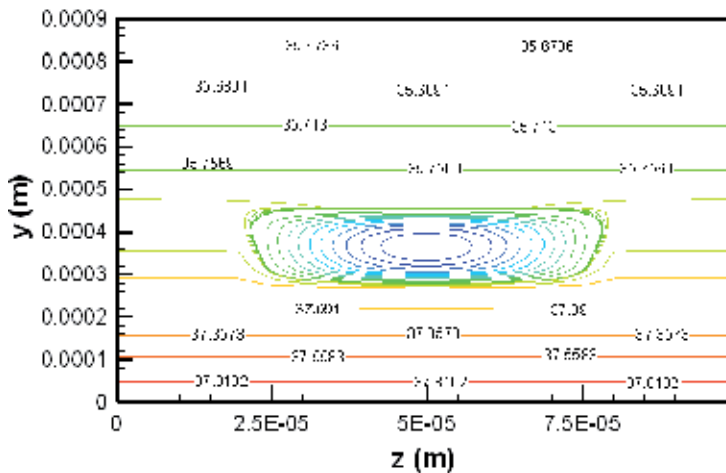


Fig. 16. Contour of temperature in the heat sink at the cross-section of the outlet of the channel ($\Delta p = 50 \text{ kPa}$, $Re = 162.68$, $T_{reference} = 32^\circ\text{C}$, $u_m = 1.44 \text{ m/s}$).

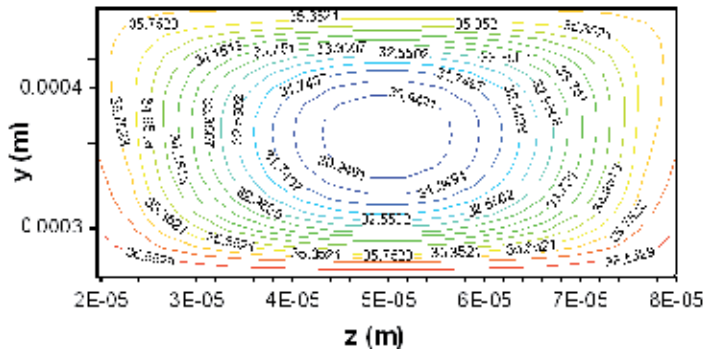


Fig. 17. Contour of local temperature inside the channel at the cross-section of the outlet of the channel ($\Delta p=50\text{ kPa}$, $Re=162.68$, $T_{reference}=32^\circ\text{C}$, $u_m=1.44\text{ m/s}$).

The temperature distribution can be showed obviously in Figures 18, 19 and 20, which indicate the local temperature distribution in the x - y plane at $z=L_z/2$ for the three cases with $q_s=90\text{ W/cm}^2$, at $\Delta p=50, 15$ and 6 kPa , respectively.

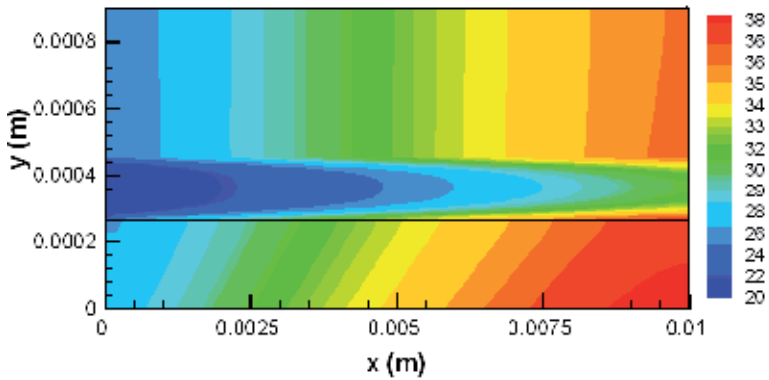


Fig. 18. Local temperature distribution in x - y plane at $z=L_z/2$ ($\Delta p=50\text{ kPa}$, $Re=162.68$, $T_{reference}=32^\circ\text{C}$, $u_m=1.44\text{ m/s}$).

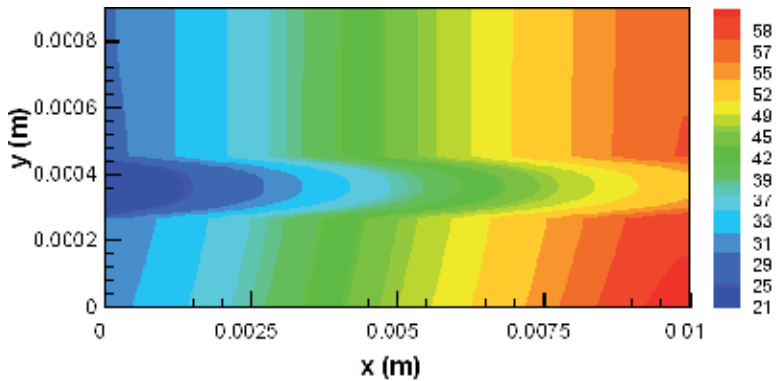


Fig. 19. Local temperature distribution in x - y plane at $z=L_z/2$ ($\Delta p=15\text{ kPa}$, $Re=85.60$, $T_{reference}=48^\circ\text{C}$, $u_m=0.57\text{ m/s}$).

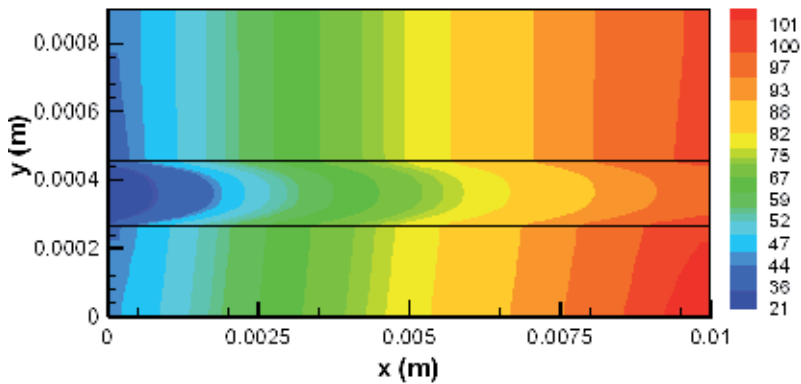


Fig. 20. Local temperature distribution in x - y plane at $z=L_z/2$ ($\Delta p=6$ kPa, $Re=47.32$, $T_{\text{reference}}=57^\circ\text{C}$, $u_m=0.271$ m/s).

The water flow is clearly specified in these Figures, which when combined with Figures 13, 14, 15, yield detailed information about the temperature distribution in the micro-heat sink. The temperature at the outlet for the case of $\Delta p=6$ kPa is higher than 100°C where boiling may occur. Therefore, the numerical solution for single-phase flow may not be valid there. The temperature increases along the longitudinal x -direction over the channel inner walls. There are very slight changes in the temperature gradient in the x -direction at the channel bottom wall, Figure 21, and the channel top wall, Figure 22.

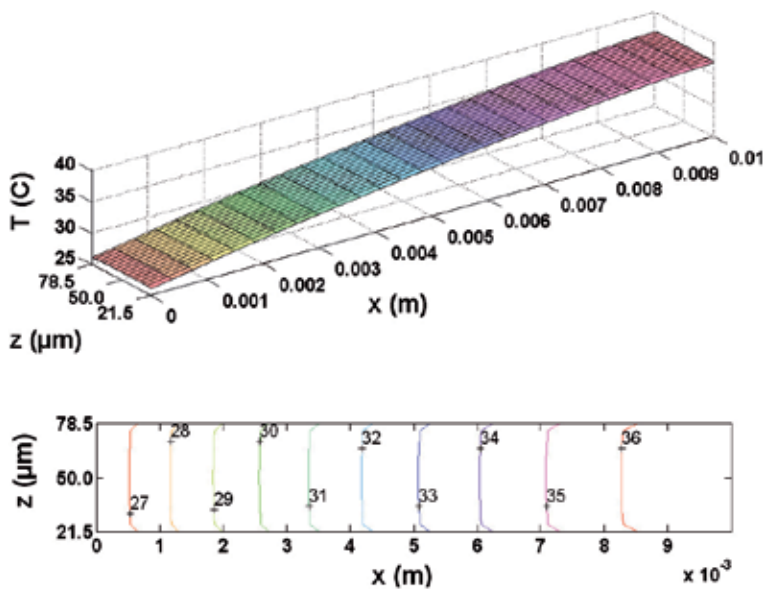


Fig. 21. Numerical predictions of local temperature distribution in the unit cell bottom wall.

In fact, a linear temperature rise can be regarded as a good approximation for both planes. The temperature along the transverse z -direction is virtually constant for all the x - z planes just discussed.

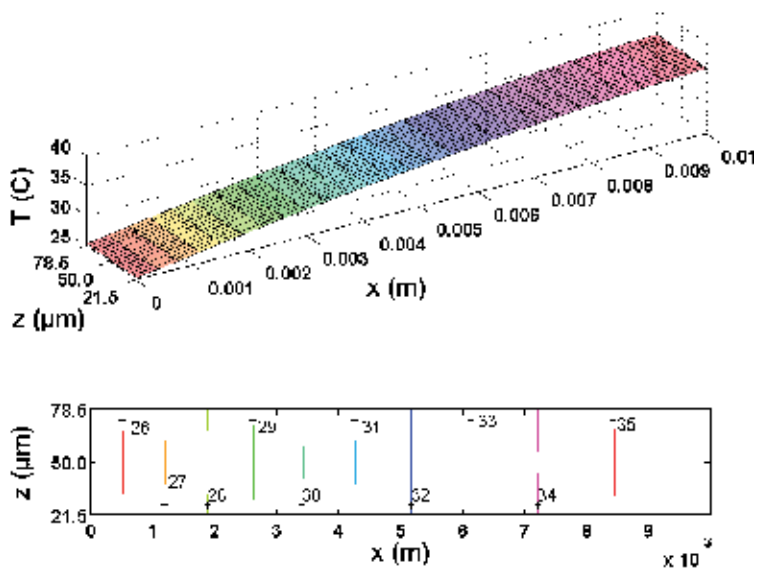


Fig. 22. Numerical predictions of local temperature distribution in the unit cell top wall.

The temperatures of the side walls vary noticeably in the transverse y -direction. As expected, the temperature decreases from the unit cell bottom wall to the unit cell top wall. Figure 23 shows higher temperatures for small y values close to the channel bottom wall.

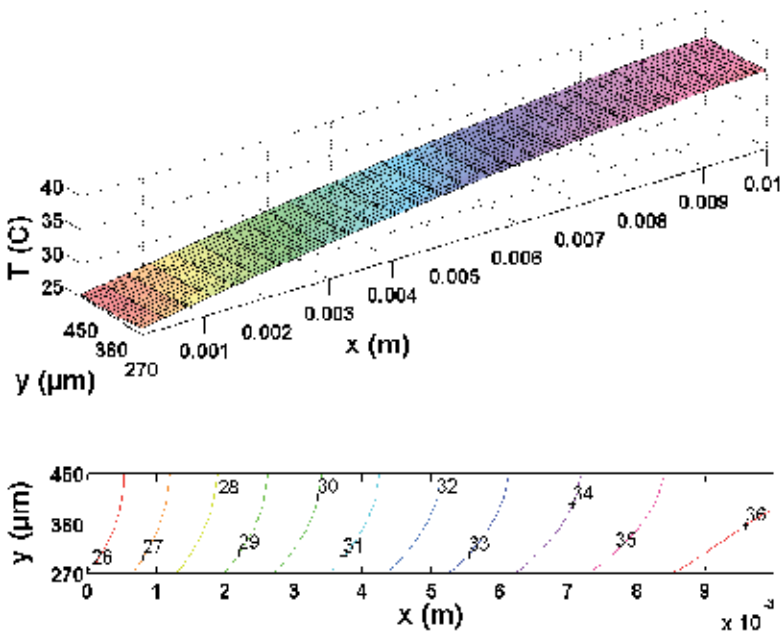


Fig. 23. Numerical predictions of local temperature distribution in the unit cell side walls.

4.2 Average and bulk characteristics

In order to evaluate the local (averaged on the channel circumference) heat transfer characteristics along the flow direction, the convective heat transfer coefficient and Nusselt number, must be defined. The longitudinal convective heat transfer coefficient is defined as

$$\bar{h}_x = \frac{\bar{q}_{s,\Gamma}(x)}{\Delta\bar{T}(x)} \quad (56)$$

and the averaged longitudinal Nusselt number as

$$\overline{Nu}_x = \frac{\bar{h}_x \cdot D_h}{k_f} \quad (57)$$

The averaged longitudinal local heat flux along the perimeter of the inner wall of the channel in Equation (56) is defined as,

$$\begin{aligned} \bar{q}_{s,\Gamma}(x) &= -k_s \left(\frac{\partial T_s(x,y,z)}{\partial n} \right) \Big|_{\Gamma} \\ &= -k_f \left(\frac{\partial T_f(x,y,z)}{\partial n} \right) \Big|_{\Gamma} \end{aligned} \quad (58)$$

and the longitudinal mean temperature difference in Equation (56) is defined as,

$$\Delta\bar{T}(x) = \bar{T}_{s,\Gamma}(x) - \bar{T}_f(x) \quad (59)$$

$$\bar{T}_{s,\Gamma}(x) = \frac{\sum_{\Gamma} T_{s,\Gamma}(i,j,k)}{N_{\Gamma}} \quad (60)$$

$$\bar{T}_f(x) = \frac{\left\{ \sum \sum \rho_f \cdot u \cdot c_p \cdot T \cdot \Delta y \Delta z \right\}_{i=\text{constant},j,k}}{\dot{m} \cdot c_p} \quad (61)$$

where N_{Γ} is the total number of nodes along the perimeter of the inner wall (here $N_{\Gamma} = 2 \times 16 + 2 \times 16$). The averaged longitudinal inner wall temperature $\bar{T}_{s,\Gamma}$ and the averaged local heat flux $\bar{q}_{s,\Gamma}$ are mathematically averaged along the perimeter of the inner wall, and the longitudinal bulk liquid temperature \bar{T}_f is averaged according to energy conservation. With Equations (56)–(59), the longitudinal heat transfer coefficient variation and the longitudinal Nusselt number variation for these three cases can be determined and are shown in Figures 24 and 25, respectively.

From these two Figures it can be concluded that the variations of the heat transfer coefficient and the Nusselt number along the flow direction is quite small for this type of microchannel heat sink after the thermal entrance lengths. Comparisons between the average Nusselt number for the different heat flux and same Reynolds number are shown in Figure 26.

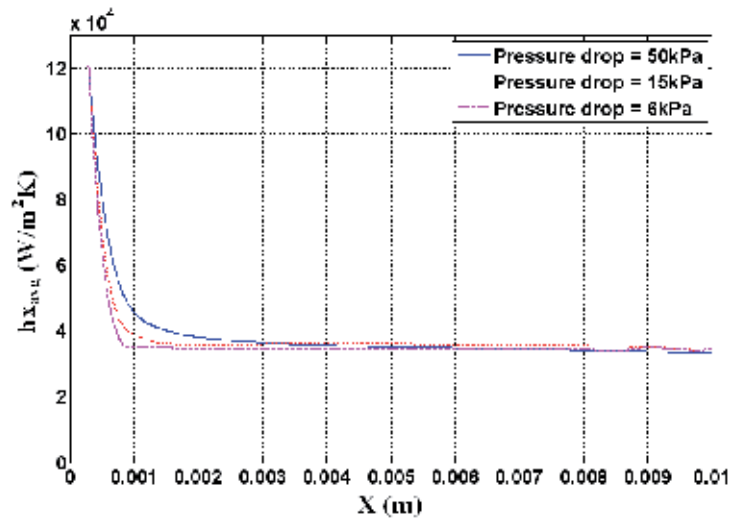


Fig. 24. Distribution of heat transfer coefficient along the channel at specified pressure drop.

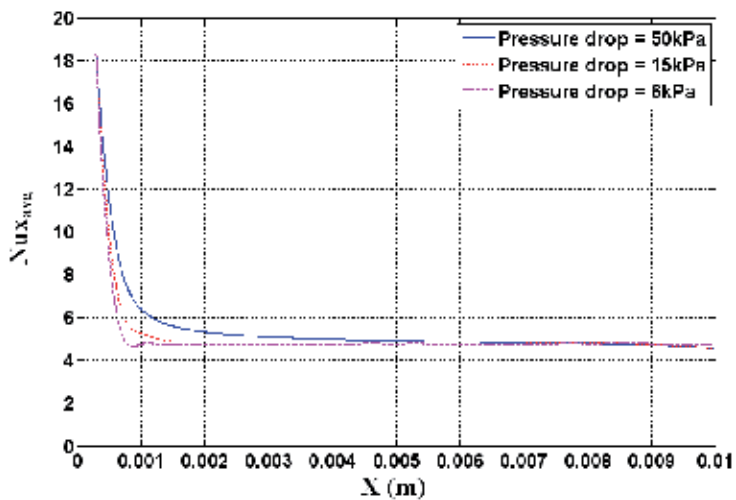


Fig. 25. Nusselt number variation along the channel at specified pressure drop.

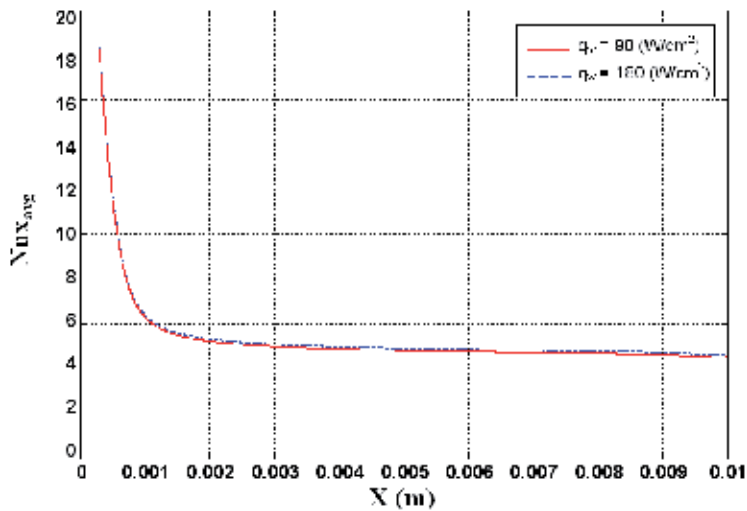


Fig. 26. Comparisons between the average Nusselt numbers.

These two trends are identical; this is because the Nusselt number for laminar flow is determined solely by the channel geometry and the local flow conditions.

Figure 27 shows the fluid bulk temperature and the average temperatures of the top, bottom and side channel walls, as the functions of the longitudinal distance x , for $\Delta p = 50 \text{ kPa}$. The fluid bulk temperature increases quasi-linearly along the x -direction, and it almost reaches the wall temperature at the exit of the microchannel. Overall, the average temperatures of side walls are slightly larger than top wall and smaller than bottom wall, because the convective resistance is much smaller for the close space between the side walls. While, in Figure 28 that is $\Delta p = 6 \text{ kPa}$, due to low liquid velocity and low convective heat transfer, temperature difference will be increased between the solid and liquid, especially in the inlet region of the channel.

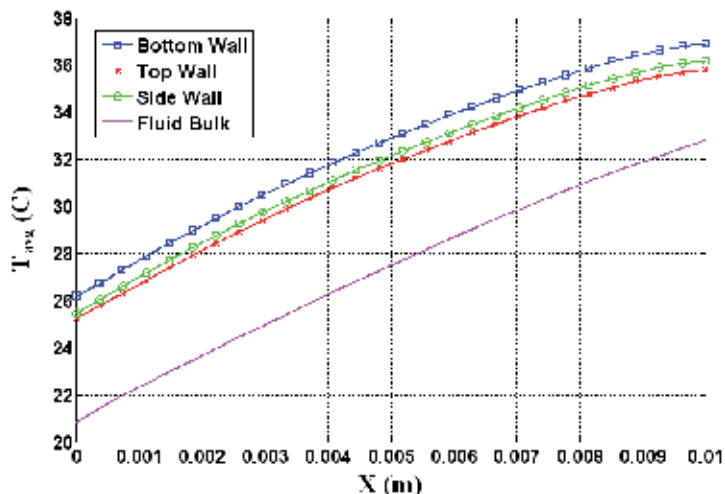


Fig. 27. Mean temperature variations along the channel at the top, bottom and side walls and in bulk liquid for $\Delta p = 50 \text{ kPa}$.

Large temperature gradients near the inlet region are mainly to induce significant thermal stresses and, therefore, must be carefully considered in the practical sink design in order to avoid the mechanical failure. The quasi-linear trend is not validated for the low Reynolds numbers as be shown in Figure 28. In Figure 28 a large portion of heat is conducted into the front part of the heat sink due to the low liquid velocity, and so the temperature gradient between the top and bottom walls is much small and approaching to the zero value.

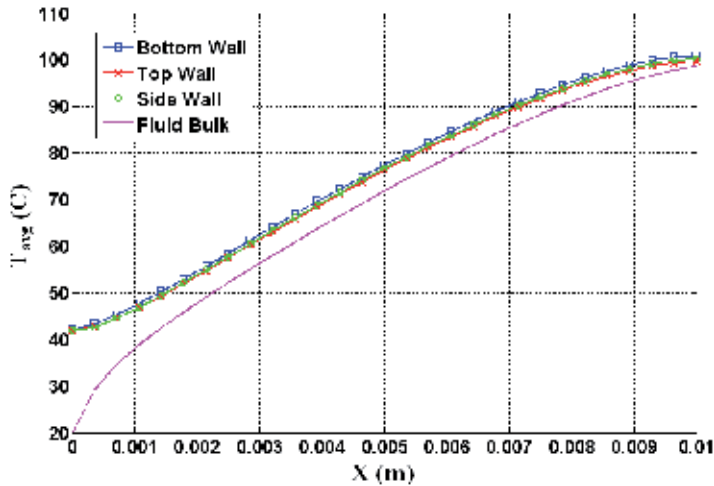


Fig. 28. Mean temperature variations along the channel at the top, bottom and side walls and in bulk liquid for $\Delta p = 6 \text{ kPa}$.

As the flow develops and the boundary layers grow in the longitudinal direction, the average heat transfer coefficients (Figure 29) gradually decrease in magnitude. The heat transfer coefficients are expected and, indeed, are larger at the side walls than at the top and bottom walls.

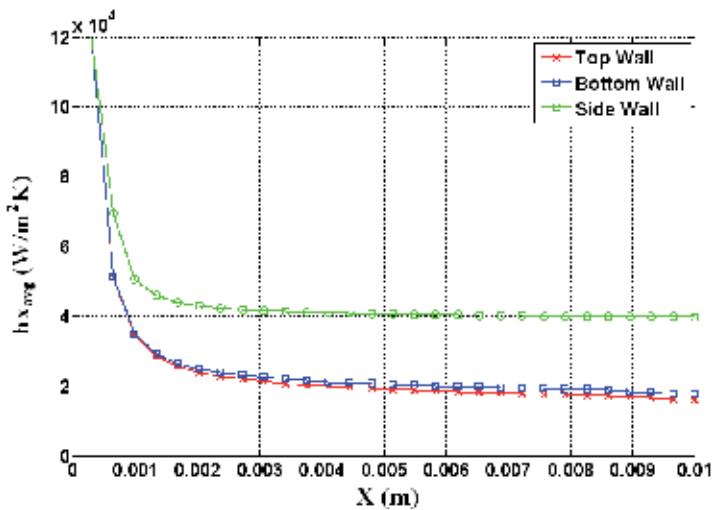


Fig. 29. Average heat transfer coefficient distributions along the channel.

4.3 Local heat flux distribution

Figs 30, 31 and 32 illustrate the heat flux distribution along the channel walls for $\Delta p=50 \text{ kPa}$, $Re=162.68$, $T_{reference}=32^\circ\text{C}$, $u_m=1.44 \text{ m/s}$. For all the channel walls, higher heat fluxes are encountered near the channel inlet. This is attributed to the thin thermal boundary layer in the developing region. The heat fluxes vary around the channel periphery, approaching zero in the corners where the flow is weak for a rectangular channel. Figure 32 shows the heat flux along the channel side walls is higher than along the channel top and bottom walls (almost two orders of magnitude larger than those at the top and bottom walls) due to the short distance between the channel side walls and the large velocity gradient present. The local heat fluxes at both the bottom and top walls (Figures 30 and 31, respectively) show significant variation in the transverse z -direction, unlike the fluxes at the side walls (Figure 32), which are nearly uniform everywhere but in the inlet and corner regions.

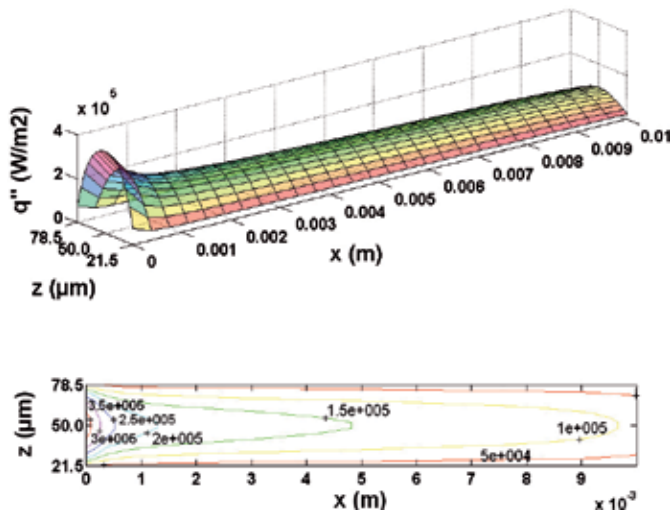


Fig. 30. Numerical predictions of local heat flux distribution for the channel bottom wall.

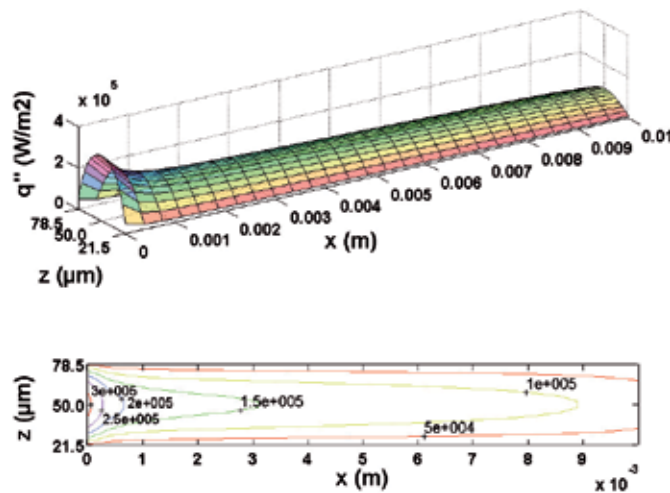


Fig. 31. Numerical predictions of local heat flux distribution for the channel top wall.

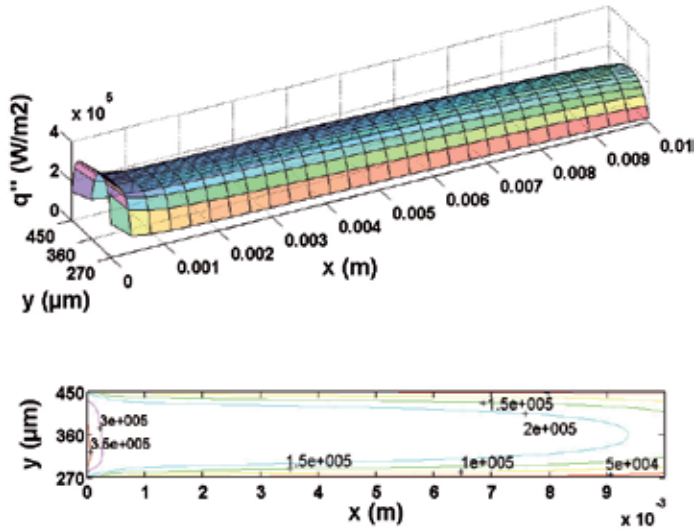


Fig. 32. Numerical predictions of local heat flux distribution for the channel side walls.

4.4 Convergence performance for the pressure correction equations

For the microchannel heat sink model, illustrated in Figure 1, the total number of control volumes in the heat sink and inside the channel were set to $N_x \times N_y \times N_z = 30 \times 82 \times 30$ and $N_x \times N_y \times N_z = 30 \times 16 \times 16$ in the three spatial directions, respectively. The multigrid scheme, as discussed in the previous section, was implemented in the two cross-streamwise directions, which consisted of four grid levels from the finest grid ($30 \times 16 \times 16$) to the coarsest grid ($30 \times 2 \times 2$). The multigrid behavior followed the typical V-cycle pattern. The entire residual convergence history with the AC-MG algorithm is depicted in Figure 33.

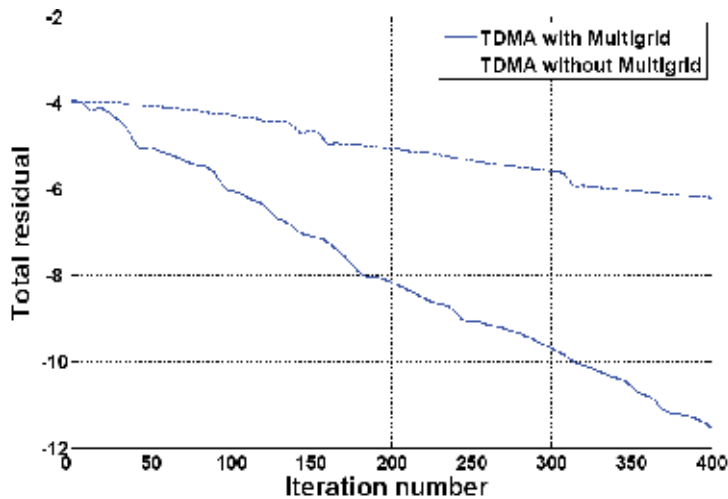


Fig. 33. Residual convergence history of the pressure Poisson equation.

The results are compared with the solution procedure that used only the TDMA solver without a multigrid correction. The TDMA solver with the AC-MG algorithm was capable of efficiently driving the residual down to the level of the computer machine round-off error within 400 AC-MG cycles. The residual was driven down by about twelve orders of magnitude.

5. Conclusion

A three-dimensional mathematical model, developed using incompressible laminar Navier-Stokes equations of motion, is capable of predicting correctly the flow and conjugate heat transfer in the microchannel heat sink. The microchannel heat sink model consists of a 10 mm long silicon substrate, with rectangular microchannels, 57 μm wide and 180 μm deep, fabricated along the entire length. A finite volume numerical code with a multigrid technique, based on additive correction multigrid (AC-MG) scheme, that is a high-performance solver, was developed to solve the steady incompressible laminar Navier-Stokes (N-S) equations, over a collocated Cartesian grid arrangement. Higher Reynolds numbers are beneficial at reducing both the water outlet temperature and the temperatures within the heat sink, also at the expense of greater pressure drop. By the magnitude of the mean velocities and the Reynolds numbers obtained from the analytical and numerical methods, the agreement between the two methods is quite good and provides sufficient evidence for validation of the numerical method. The variations of the heat transfer coefficient and the Nusselt number along the flow direction is quite small for this type of microchannel heat sink after the thermal entrance lengths. The heat flux along the channel side walls is higher than along the channel top and bottom walls (almost two orders of magnitude larger than those at the top and bottom walls) due to the short distance between the channel side walls and the large velocity gradient present. The temperature is highest at the channel corner; this is due to the low velocity of the flow and the resulting high concentration of heat flux. The results indicate that the thermophysical properties of the liquid can significantly influence both the flow and heat transfer in the microchannel heat sink. The bulk liquid temperature is shown to vary in a quasi-linear form along the flow direction for high fluid flow rates, but not for low flow rates (low Reynolds number).

6. References

- [1] D.B. Tuckerman, R.F. Pease, "High-Performance Heat Sinking for VLSI, " *IEEE Electronic Devices Letters EDL-2* (1981) 126-129.
- [2] S.P. Jang, S. Kim, K.W. Paik, 2003, "Experimental Investigation of Thermal Characteristics for a Microchannel Heat Sink Subject to an Impinging Jet, Using a Micro Thermal Sensor Array," *Sens. Actuators, A*, 105, pp. 211- 224.
- [3] Y. Chen, S. Kang, W. Tuh, and T. Hsiao, 2004, "Experimental Investigation of Fluid Flow and Heat Transfer in Microchannels," *Tamkang Journal of Science and Engineering*, 7(1), pp. 11-16.
- [4] H.Y. Wu, P. Cheng, "An Experimental Study of Convective Heat Transfer in Silicon Microchannels with Different Surface Conditions," *Int. J. Heat Mass Transfer* 46 (14) (2003) 2547- 2556.
- [5] W. Qu, I. Mudawar, "Analysis of Three-Dimensional Heat Transfer in Microchannel Heat Sinks," *Int. J. Heat Mass Transfer* 45 (2002) 3973-3985.

- [6] A.G. Fedorov, R. Viskanta, "Three-dimensional Conjugate Heat Transfer in the Microchannel Heat Sink for Electronic Packaging," *Int. J. Heat Mass Transfer* 43 (3) (2000) 399-415.
- [7] Fedorov, R. Viskanta, "A Numerical Simulation of Conjugate Heat Transfer in an Electronic Package Formed by Embedded Discrete Heat Sources in Contact with a Porous Heat Sink," *ASME Journal of Electronic Packaging* 119 (1997) 8-16.
- [8] Weisberg, H.H. Bau, J.N. Zemel, "Analysis of Microchannels for Integrated Cooling," *Int. J. Heat Mass Transfer* 35 (1992) 2465-2474.
- [9] R.W. Knight, J.S. Goodling, D.J. Hall, "Optimal Thermal Design of Forced Convection Heat Sinks-Analytical," *ASME J. Electron Packaging*, No.113, pp.313-321, 1991.
- [10] R.W. Keyes, "Heat Transfer in Forced Convection through Fins," *IEEE Trans. Electron Dev.* ED-31 (1984) 1218-1221.
- [11] Bejan, A.M. Morega, "Optimal Arrays of Pin Fins and Plate Fins in Laminar Forced Convection," *ASME J. Heat Transfer* 115 (1993) 75-81.
- [12] D.Y. Lee, K. Vafai, "Comparative Analysis of Jet Impingement and Microchannel Cooling for High Heat Flux Applications," *Int. J. Heat Mass Transfer* 42 (1999) 1555-1568.
- [13] X.F. Peng, G.P. Peterson, "Convective Heat Transfer and Flow Friction for Water Flow in Microchannel Structures," *Int. J. Heat Mass Transfer* 39 (12) (1996) 2599-2608.
- [14] K. Kawano, K. Minakami, H. Iwasaki, M. Ishizuka, "Development of Micro Channels Heat Exchanging," in: R.A. Nelson Jr., L.W. Swanson, M.V.A. Bianchi, C. Camci (Eds.), *Application of Heat Transfer in Equipment, Systems, and Education*, HTD-Vol. 361-3/PID-Vol. 3, ASME, New York, 1998, pp. 173-180.
- [15] H.Y. Wu, P. Cheng, "Friction Factors in Smooth Trapezoidal Silicon Microchannels with Different Aspect Ratios," *Int. J. Heat Mass Transfer* 46 (14) (2003) 2519-2525.
- [16] P. Cheng, C.T. Hsu, A. Choudhury, "Forced Convection in the Entrance Region on a Packed Channel with Asymmetric Heating," *ASME Journal of Heat Transfer* 110 (1988) 946-954.
- [17] J.C.Y Koh, R. Colony, 1986, "Heat Transfer of Micro Structures for Integrated Circuits," *Int. Commun. Heat Mass Transfer*, 13, pp. 89-98.
- [18] C.L Tien, S.M. Kuo, 1987, "Analysis of Forced Convection in Microstructures for Electronic Systems Cooling," *Proc. Int. Symp. Cooling Technology for Electronic Equipment*, Honolulu, HI, August 31-September 2, pp. 217-226.
- [19] R.L. Webb, M. Zhang, "Heat Transfer and Friction in Small Diameter Channels," *Microscale Thermophysical Engineering* 2 (1998) 189-202.
- [20] E. Eckert, R. Drake, "Analysis of Heat and Mass Transfer," McGraw-Hill, New York, 1972.
- [21] J. Ferziger, M. Peric, "Computational Methods for Fluid Dynamics," Berlin: Springer-Verlag, 1996. ISBN 3-540-59434-5.
- [22] C.M. Rhie, W.L. Chow, "Numerical Study of the Turbulent Flow Past an Airfoil with Trailing Edge Separation," *AIAA Journal*, Vol. 21, November 1983, pp. 1525-1532.
- [23] B.R. Hutchinson, G.D. Raithby, "A Multigrid Method Based on the Additive Correction Strategy," *Numer. Heat Transfer* 9 (1986)511-537.
- [24] R.K. Shah, A.L. London, "Laminar Flow Forced Convection in Ducts," Academic Press, NY, 1978, pp. 78-283.

- [25] Bejan, "Convection Heat Transfer," first ed., John Wiley & Sons, New York, 1984.
- [26] S. Kakac, Y. Yener, "Convective Heat Transfer," second ed., CRC Press, Begell House, Boca Raton, 1995.
- [27] A.F. Mills, "Heat Transfer," second ed., Prentice Hall, Upper Saddle River, 1999.

Compact Heat Exchange Reformer Used for High Temperature Fuel Cell Systems

Huisheng Zhang, Shilie Weng and Ming Su
*Shanghai Jiao Tong University
China*

1. Introduction

High temperature fuel cell systems are an attractive emerging technology for stationary power generation, especially for the distributed generation [1]. Today, there are mainly two types of high temperature fuel cell systems, including the molten carbonate fuel cell (MCFC) and solid oxide fuel cell (SOFC), which are generally operated at high temperatures ranging from 823K to 1273K. Several advantages of this setup are listed in the references [2]. The main advantages of both fuel cells are related to what could be done with the waste heat and how they can be used to reform fuels, provide heat, and drive engines. Therefore, high temperature fuel cell systems can never be simply considered as fuel cells; instead, they must always be thought of as an integral part of a complete fuel processing and heat generating system [2].

Steam reforming is a well-established industrial fuel process for producing hydrogen or synthetic gas from natural gas, other hydrocarbon fuels, and alcohols [3]. In the high temperature fuel cell systems, the pre-reformer is usually needed for fuel processing. Due to the high endothermic reaction, a great amount of heat must be provided from the outside, such as waste heat from the fuel cell, catalyst combustion, etc.

High temperature heat exchangers are widely used in the high temperature fuel cell/gas turbine system, closed cycle gas turbine system, high temperature gas cooled reactors, and other thermal power systems. It is an effective method of improving the whole system efficiency [4]. Compact heat exchangers are generally characterized by extended surfaces with large surface area/volume ratios that are often configured in either plate-fin or tube-fin arrangements [5]. In a plate-fin exchanger, many augmented surface types are used: plain-fins, wavy fins, offset strip fins, perforated fins, pin fins, and louvered fins. Offset strip fins, which have a high degree of surface compactness and feasible manufacturing, are very widely applied.

In general, the high temperature heat exchanger is used to preheat the air or fuel, while the pre-reformer is used to produce hydrogen rich fuel from methane or other hydrocarbons. Fig. 1 shows one of the fuel cell systems, which consists of a direct internal reforming solid oxide fuel cell (DIR-SOFC), a high temperature heat exchanger (HTHE), a low temperature heat exchanger (LTHE), a pre-reformer, a gas turbine, a generator, etc. In order to simplify the system, reduce the cost, and improve the fuel cell system's efficiency, it is suggested that

a compact heat exchange reformer replace the heat exchanger and the pre-reformer. The new fuel cell system is illustrated in Fig. 2. The offset strip fin heat exchanger and pre-reformer are combined into the heat exchange reformer. In this device with the counter-flow type, the high temperature waste gas from the fuel cell flows in the hot passage, and the fuel flows in the cold passage. In particular, the Ni catalyst is coated on the fuel passage surface [6, 7]. When the fuel flows along the passage, the endothermic steam reforming reaction will take place using the heat transferring from the hot side.

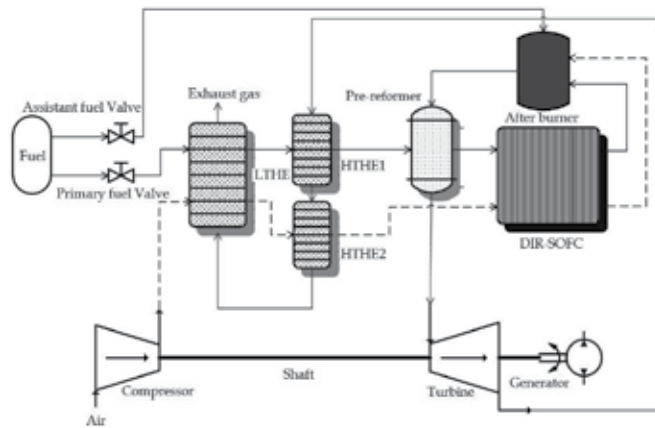


Fig. 1. Schematic view of the traditional SOFC/GT hybrid system.

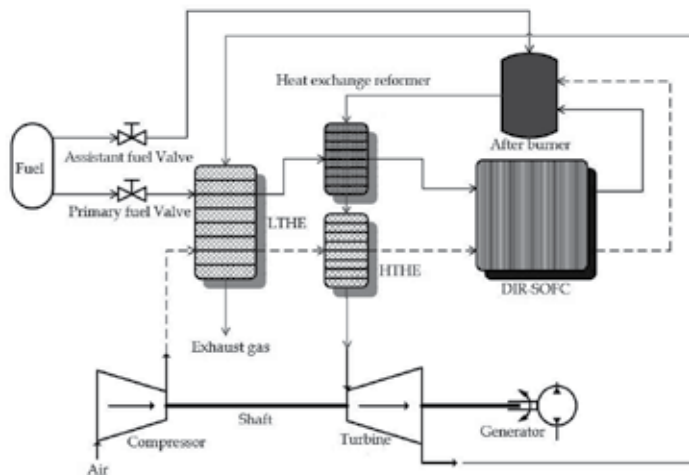


Fig. 2. Schematic view of the SOFC/GT hybrid system with novel concept heat exchange reformer.

Several kinds of compact heat exchange reformers have been investigated and designed in the past. In 2001, Kawasaki Heavy Industries in Japan developed a plate-fin heat-exchange reformer with highly dispersed catalyst [8]. A planar micro-channel concept was proposed by Pacific Northwest National Laboratories (PNNL), but this kind of micro-channel device is oriented toward the low to medium power range (20-500W) for man-portable applications

[9, 10]. A novel micro fuel processor for PEMFCs with heat generation by catalytic combustion was developed and characterized in South Korea [11-13].

All these previous works were mainly developed based on experiments, but the steady state and dynamic performance simulations have not been investigated in detail. The heat supplied for the methane steam reforming reaction has different sources, such as catalytic combustion [11, 12] and auto-thermal methane reforming reactions [10]. The purposes are mainly for the portable devices [9, 10] or the low temperature fuel cells [11-13]. Here, the waste heat from the high temperature fuel cell systems will be used as the heat resource in the compact heat exchange reformer for the steam reforming reaction.

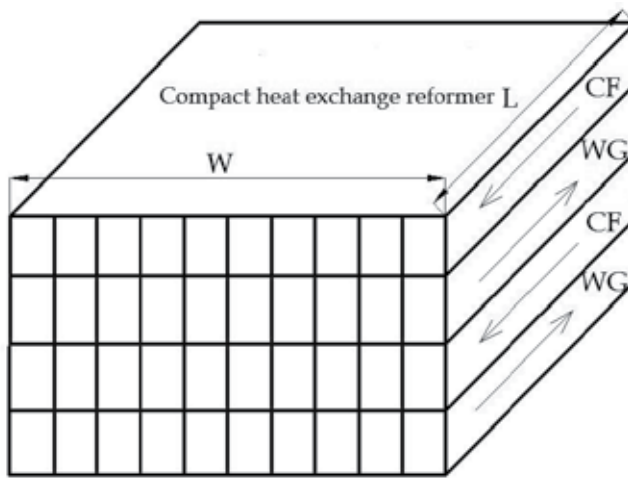
This chapter aims to: design a compact heat exchange reformer for the high temperature fuel cell systems; develop a real time simulation model using the volume-resistance characteristic modeling technique; study the steady state distribution characteristics by considering local fluid properties such as pressure, velocity, density, heat capacity, thermal conductivity, dynamic viscosity, etc; discuss some factors that will affect the performance of the reformer during steady state operation under the same operating condition; and finally, investigate dynamic behavior under different input parameters including step-change conditions.

2. Description of heat exchange reformer

2.1 Configuration

The configuration of the heat exchange reformer is similar to the compact heat exchanger. The only difference is that the catalyst is coated in the cold passage to make steam reforming reactions take place.

As shown in Fig. 3, the configuration of the offset strip fin heat exchanger is adopted here. The fin surface is broken into a number of smaller sections. Generally, each type of fin is characterized by its width X , height Y , thickness t , and length of the offset strip fin l . The detailed configuration can also be found in other references for the heat exchanger [14-18].



(a)

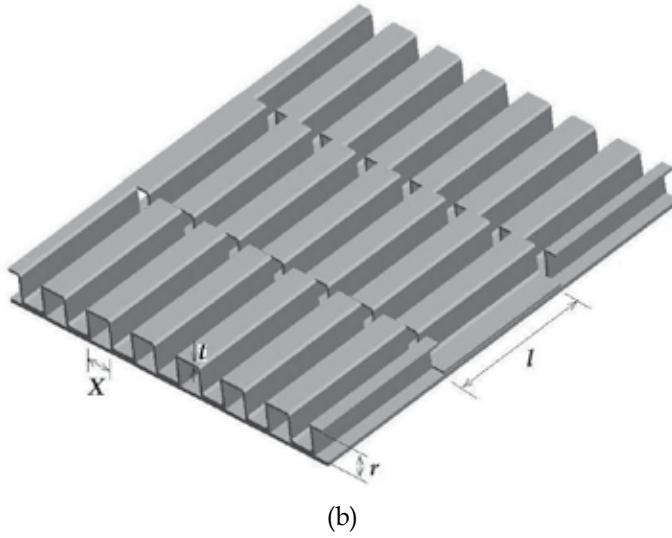


Fig. 3. Flow (a) and fin structure (b) diagram of heat exchange reformer.

Taking the hot passage as an example, the calculations for individual geometry variables are listed as following:

$$\text{Passage number: } n_h = W / (X_h + t_h) \quad (1)$$

$$\text{Offset strip number: } n_{hl} = L / l_h \quad (2)$$

$$\text{Cross area of flow passage: } A_h = n_h X_h Y_h \quad (3)$$

$$\text{Heat transfer surface of flow passage: } S_h = 2n_h (X_h + Y_h) L + n_{hl} n_h (X_h + Y_h + t_h) t_h \quad (4)$$

$$\text{Wet perimeter: } U_h = 4S_h / L \quad (5)$$

$$\text{Hydraulic diameter: } D_h = 4A_h / U_h \quad (6)$$

2.2 Passage fin efficiency

The passage fin efficiency η_0 is given by Rosehnow et al. [18] as

$$\eta_0 = 1 - \frac{S_f}{S} (1 - \eta_f) \quad (7)$$

where the secondary heat transfer area of a stream S_f for the hot passage equals S_h . The total area of the heat exchanger S is calculated by the sum of the primary heat transfer surface and the secondary heat transfer area of a stream.

According to Rosehnow et al. [15, 18], the fin efficiency for the offset strip fin with a rectangular section can be approximated by:

$$\eta_{i,h} = \frac{\tanh(m_h k_h)}{m_h k_h} \quad (8)$$

where,

$$m_h = \sqrt{\frac{\alpha_h U_h}{\lambda_h f_h}}, k_h = Y_h/2 - t_h.$$

Finally, the fin efficiency can be simplified by:

$$\eta_{0,h} = 1 - \frac{Y_h}{X_h + Y_h} (1 - \eta_{i,h}) \quad (9)$$

The fin efficiency is mainly influenced by the material, configuration of the fin, and the heat transfer coefficient between the fin and the flow.

2.3 Pressure loss

The frictional pressure loss across an offset strip fin passage and at any associated entry, exit, and turning loss [15], can be expressed by:

$$\Delta P = 4f \left(\frac{L}{D_h} \right) \left(\frac{G_m^2}{2\rho} \right) + K \left(\frac{G_m^2}{2\rho} \right) \quad (10)$$

where, $G_m = \rho u$.

Here, turning losses are neglected, so the pressure loss per unit length can be expressed by:

$$\frac{\Delta P}{L} = \frac{U}{A} \left(\frac{1}{2} f \rho u^2 \right) \quad (11)$$

Let the friction resistance $\sigma = \frac{1}{2} f \rho u^2$,

Then,

$$\frac{dP}{dx} = \frac{U\sigma}{A} \quad (12)$$

The fanning friction factor f has been developed by many authors. Basing on the data of Kays & London [14], Manglik & Bergles [17] recommend:

$$f = 9.6243 \text{Re}^{-0.7422} \alpha^{-0.1856} \delta^{0.3053} \gamma^{-0.2659} \\ \times \left[1 + 7.669 \times 10^{-8} \text{Re}^{4.429} \alpha^{0.920} \delta^{3.767} \gamma^{0.236} \right]^{0.1} \quad (13)$$

2.4 Heat transfer coefficient

Generally, the heat transfer coefficient α is related to the Colburn factor [15, 17, 18] and is expressed as:

$$\alpha = JG_m c_p \text{Pr}^{-2/3} \quad (14)$$

where the Colburn factor $J = St \text{Pr}^{2/3}$ and the Prandtl number $\text{Pr} = \mu c_p / \lambda$.

The correlation developed by Manglik & Bergles [17] from the data of Kays & London [14] reads:

$$J = 0.6522 \text{Re}^{-0.5403} \alpha^{-0.1541} \delta^{0.1499} \gamma^{-0.0678} \times \left[1 + 5.269 \times 10^{-5} \text{Re}^{1.340} \alpha^{0.504} \delta^{0.456} \gamma^{-1.055} \right]^{0.1} \quad (15)$$

2.5 Steam reforming

In the cold fuel passage, the steam reforming reaction (I), water gas shift reaction (II), and CO_2 direct reforming reactions of methane (III) are carried out over a Ni catalyst coat on the passage surface at sufficiently high temperatures, typically above 773K.

Kinetic rate equations for the reactions (I-III) are adopted from Xu and Froment [19]. The three kinetic rate equations are listed in Table 1 as well.

(I)	$\text{CH}_4 + \text{H}_2\text{O} \Leftrightarrow \text{CO} + 3\text{H}_2$	$R_{(I)} = \frac{k_1}{p_{\text{H}_2}^{2.5}} \left(p_{\text{CH}_4} p_{\text{H}_2\text{O}} - \frac{p_{\text{H}_2}^3 p_{\text{CO}}}{K_{e1}} \right) * \frac{1}{\text{DEN}^2}$	(16)
(II)	$\text{CO} + \text{H}_2\text{O} \Leftrightarrow \text{CO}_2 + \text{H}_2$	$R_{(II)} = \frac{k_2}{p_{\text{H}_2}} \left(p_{\text{CO}} p_{\text{H}_2\text{O}} - \frac{p_{\text{H}_2} p_{\text{CO}_2}}{K_{e2}} \right) * \frac{1}{\text{DEN}^2}$	(17)
(III)	$\text{CH}_4 + 2\text{H}_2\text{O} \Leftrightarrow \text{CO}_2 + 4\text{H}_2$	$R_{(III)} = \frac{k_3}{p_{\text{H}_2}^{3.5}} \left(p_{\text{CH}_4} p_{\text{H}_2\text{O}}^2 - \frac{p_{\text{H}_2}^4 p_{\text{CO}_2}}{K_{e3}} \right) * \frac{1}{\text{DEN}^2}$	(18)

Table 1. Reaction and its rate in the heat exchange reformer (Xu and Froment, [19]).

The enthalpy changes of chemical reactions are calculated according to Smit et.al [20].

$$\Delta H_{(I)} = \Delta H_{(I)}^0 - 16373.61 + R(7.951T_c - 4.354e - 3T_c^2 + 0.7213e - 6T_c^3 - 0.097e5/T_c) \quad (19)$$

$$\Delta H_{(II)} = \Delta H_{(II)}^0 - 7756.56 + R(1.86T_c - 0.27e - 3T_c^2 + 1.164e5/T_c) \quad (20)$$

$$\Delta H_{(III)} = \Delta H_{(III)}^0 - 26125.07 + R(10.657T_c - 4.624e - 3T_c^2 + 0.7213e - 6T_c^3 + 1.067e5/T_c) \quad (21)$$

3. Mathematic model of heat exchange reformer

To simplify the complexity of the mathematical model, some assumptions [4, 21] adopted in the theoretic analysis are presented as follows:

1. The heat exchange reformer is adiabatic to the surrounding;

2. The viscosity dissipation effects are neglected;
3. The parameters are considered to be uniform over a cross-section, one dimensional flow along the passage, without inside circumfluence;
4. For the horizontal fluid, the effect of height change can be omitted.

In the cold fuel passage, the chemical species are CH_4 , H_2 , CO , CO_2 , and H_2O . Species mass balances in the cold fuel passage are considered.

$$\frac{\partial C_{c,i}}{\partial t} = -u_c \frac{\partial C_{c,i}}{\partial x} + \sum_{k \in \{(I),(II),(III)\}} v_{i,k} R_k \frac{1}{Y_c} \quad i \in \{\text{CH}_4, \text{H}_2, \text{CO}, \text{CO}_2, \text{H}_2\text{O}\} \quad (22)$$

The mass, momentum, and energy conservation equations for the hot passage and cold passage are established in Table 2 and Table 3, respectively. In the hot passage, the heat transfer to the solid structure is considered. Due to the very thin catalyst coat, the enthalpy changes of the reactions (I-III) are also considered in the cold passage, in addition to the heat transferred from the solid structure.

Mass conservation equation

$$\frac{\partial \rho_h}{\partial t} = -\frac{\partial(\rho_h u_h)}{\partial x} \quad (23)$$

Momentum conservation equation

$$\frac{\partial(\rho_h u_h)}{\partial t} = -\frac{\partial(\rho_h u_h^2)}{\partial x} - \frac{\partial P_h}{\partial x} - \frac{U_h \sigma_h}{A_h} \quad (24)$$

Energy conservation equation

$$\frac{\partial T_h}{\partial t} = -u_h \frac{\partial T_h}{\partial x} - \frac{S_h \alpha_h \eta_{0,h}}{\rho_h C p_h A_h L} (T_h - T_w) \quad (25)$$

Table 2. Hot passage dynamic mathematical model.

Mass conservation equation

$$\frac{\partial \rho_c}{\partial t} = \frac{\partial(\rho_c u_c)}{\partial x} \quad (26)$$

Momentum conservation equation

$$\frac{\partial(\rho_c u_c)}{\partial t} = \frac{\partial(\rho_c u_c^2)}{\partial x} + \frac{\partial P_c}{\partial x} - \frac{U_c \sigma_c}{A_c} \quad (27)$$

Energy conservation equation

$$\frac{\partial T_c}{\partial t} = u_c \frac{\partial T_c}{\partial x} - \frac{S_c \alpha_c \eta_{0,c}}{\rho_c C p_c A_c L} (T_c - T_w) + \frac{1}{\rho_c C p_c Y_c} \sum_{k \in \{(I),(II),(III)\}} (-\Delta H)_k R_k \quad (28)$$

Table 3. Cold passage dynamic mathematical model.

For the solid structures, such as the fins and the separators, the temperature is considered to be uniform at the same cross-section. The energy conservation equation is written as:

$$\frac{\partial T_w}{\partial t} = K \frac{\partial^2 T_w}{\partial x^2} + \frac{\alpha_h S_h \eta_{0,h}}{M_w C p_w} (T_w - T_h) + \frac{\alpha_c S_c \eta_{0,c}}{M_w C p_w} (T_w - T_c) \quad (29)$$

The heat conductivity coefficient is $K = L\lambda_w A_w / M_w C p_w$, the cross area of solid structure is $A_w = 2Wt + n_h(X_h + Y_h + t_h)t_h + n_c(X_c + Y_c + t_c)t_c$, and the mass is $M_w = \rho_w A_w L$.

The control equations of the heat exchange reformer are strongly coupled. In addition to the partial differential equations presented above, two perfect state equations $P=f(\rho, T)$ for the hot and cold passages are also needed in order to compose a close equation set.

4. Simulation modelling and conditions

4.1 Volume-resistance characteristic model

In general, nonlinear partial differential equations are treated numerically. However, stability is one crucial factor when using a difference algorithm. In addition, the time step for the difference algorithm is usually very short, so the numerical process is very time consuming [4].

In order to avoid the coupled iteration between the flow rate and pressure, the volume-resistance characteristic modeling technique [4, 22] is introduced into the heat exchange reformer. This modeling technique is based on the lumped-distributed parameter method, which can obtain a set of ordinary differential equations from partial differential equations.

The volume-resistance characteristic model is listed in Table 4 in detail.

Hot passage

$$\frac{dP_{h,1}}{dt} = \frac{RT_{h,1}}{M_h A_h} \frac{G_{h,1} - G_{h,2}}{dx} \quad (30)$$

$$\frac{dG_{h,2}}{dt} = A_h \frac{P_{h,1} - P_{h,2}}{dx} - U_h \sigma_{h,2} \quad (31)$$

$$\frac{dT_{h,2}}{dt} = -\frac{G_{h,2}}{A_h \rho_{h,2}} \frac{T_{h,1} - T_{h,2}}{dx} - \frac{S_h \alpha_{h,2}}{\rho_{h,2} C p_{h,2} A_h L} (T_{h,2} - T_{w,2}) \quad (32)$$

Cold passage

$$\frac{dC_{c,i,2}}{dt} = -\frac{u_{c,2} C_{c,i,2} - u_{c,1} C_{c,i,1}}{dx} + \sum_{k \in \{(I),(II),(III)\}} v_{i,k} R_{k,2} \frac{1}{Y_c} \quad i \in \{\text{CH}_4, \text{H}_2, \text{CO}, \text{CO}_2, \text{H}_2\text{O}\} \quad (33)$$

$$\frac{dP_{c,2}}{dt} = \frac{RT_{c,2}}{M_c A_c} \frac{G_{c,2} - G_{c,1}}{dx} \quad (34)$$

$$\frac{dG_{c,1}}{dt} = A_c \frac{P_{c,2} - P_{c,1}}{dx} - U_c \sigma_{c,1} \quad (35)$$

$$\frac{dT_{c,1}}{dt} = \frac{G_{c,1}}{A_c \rho_{c,1}} \frac{T_{c,1} - T_{c,2}}{dx} - \frac{S_c \alpha_{c,1}}{\rho_{c,1} C p_{c,1} A_c L} (T_{c,1} - T_{w,1}) + \frac{1}{\rho_{c,1} C p_{c,1} Y_c} \sum_{k \in \{(I),(II),(III)\}} (-\Delta H)_{k,1} R_{k,1} \quad (36)$$

Solid structure

$$\frac{dT_{w,2}}{dt} = K_x \frac{T_{w,3} - 2T_{w,2} + T_{w,1}}{(dx)^2} - \frac{\alpha_{h,2} S_h}{M_w C p_w} (T_{h,2} - T_{w,2}) - \frac{\alpha_{c,2} S_c}{M_w C p_w} (T_{c,2} - T_{w,2}) \quad (37)$$

Table 4. Heat exchange reformer volume-resistance characteristic model.

4.2 Simulation conditions

In addition to the configuration and geometry parameters of the heat exchange reformer, as shown in Table 5, and fluid properties calculated at the local position, some boundary conditions were also required to carry out the simulation. These included inlet flow rate, fluid composition, and the inlet temperature and outlet pressure of both the hot and cold streams (Table 6).

System geometry parameters	
Length	1 m
Width	0.5 m
Height	0.532 m
Hot passage	
Width	4.5E-3 m
Height	6.5E-3 m
Offset strip fin length	0.05m
Fin thickness	3.0E-3 m
Cold passage	
Width	4.5E-3 m
Height	5.0E-3 m
Offset strip fin length	0.05m
Fin thickness	5.0E-3 m
Separator	
Thickness	1.0E-3 m
Solid structure properties (SiC ceramic [27-29])	
Density	3100 kgm ⁻³
Heat capacity	0.640 kJkg ⁻¹ K ⁻¹
Thermal conductivity	0.080 kJm ⁻¹ s ⁻¹ K ⁻¹
Catalyst properties	
thickness	5.0E-5 m
Density	2355 kgm ⁻³
Catalyst reduced activity	0.003

Table 5. Geometry and properties parameters of heat exchange reformer.

Simulation conditions	
Cold fuel	
Inlet mass flow rate (kgs ⁻¹)	0.06
Inlet temperature (K)	898
Fluid molar fraction	0.25CH ₄ ,0.75H ₂ O (STC=3:1)
Outlet pressure (Pa)	1.0E+5
Hot waste gas	
Inlet mass flow rate (kgs ⁻¹)	0.4
Inlet temperature (K)	1200
Fluid molar fraction	0.1CO ₂ ,0.2H ₂ O,0.1O ₂ ,0.6N ₂
Outlet pressure (Pa)	1.0E+5

Table 6. Key simulation parameters under the basic condition.

At the same time, some simplifying conditions are used to solve the equations; for example, the heat flux of both the solid structure at inlet and outlet are considered to be zero. As a result, contrasted to the centre difference algorithm in the middle of the solid structure, the difference algorithms for both the front and end modules are treated independently.

5. Results and discussions

In this section, due to the high cost of the complicated experiments, only simulation studies are employed on a counter-flow type heat exchange reformer. Section 5.1 provides the distributed characteristics of some important parameters, such as fuel species, temperature, and fluid properties (pressure, density, velocity, heat capacity, thermal conductivity and dynamic viscosity), under steady state conditions. Section 5.2 compares and analyzes the results under different input parameter conditions, such as steam to carbon ratio, catalyst reduced activity, and operating outlet pressure. In Section 5.3, the dynamic behaviours of the compact heat exchanger reformer are investigated.

5.1 Steady state result analysis

For the rated condition, some related parameters are presented in Table 6, such as inlet temperature, mass flow rate, molar fraction, and outlet pressure.

Fig. 4 presents the fuel molar fraction along the heat exchange reformer length. The flow direction in the fuel channel is from 1.0 to 0 in the figures, so all the parameters in the fuel channel should be understood to proceed from 1.0 to 0. At the cold fuel passage inlet, the fluid only contains methane and water. The steam reforming reaction takes place on the surface of the catalyst along the flow direction. Therefore, the methane is gradually consumed. The methane and water concentration decreases along the flow direction. The concentration of produced hydrogen gradually increases. The methane steam reforming reaction has two simultaneous effects. The carbon monoxide molar fraction increases and the carbon dioxide molar fraction increases along the flow direction. At the exit, the flow composition is 4.24% of CH₄, 45.35% of H₂, 10.00% of CO, 3.84% of CO₂, and 36.57% of H₂O.

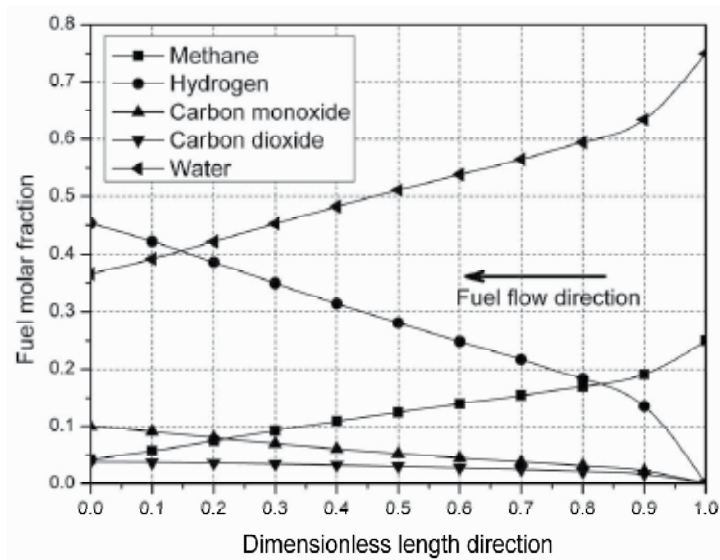


Fig. 4. Fuel molar fraction along the heat exchange reformer length.

The temperature profiles of the cold stream, hot stream, and solid structure along the heat exchange reformer length are presented in Fig. 5. Because of the high endothermic methane reforming reaction, the cold fuel temperature decreases a little at the entrance. Then, the cold fuel temperature increases along its flow direction due to the heat transfer from hot gas. The temperatures of the hot gas stream and the solid structure decrease along the heat exchange reformer length. It should be noted that the temperature curve is just the line between measured points, so it can't indicate the trend at both ends.

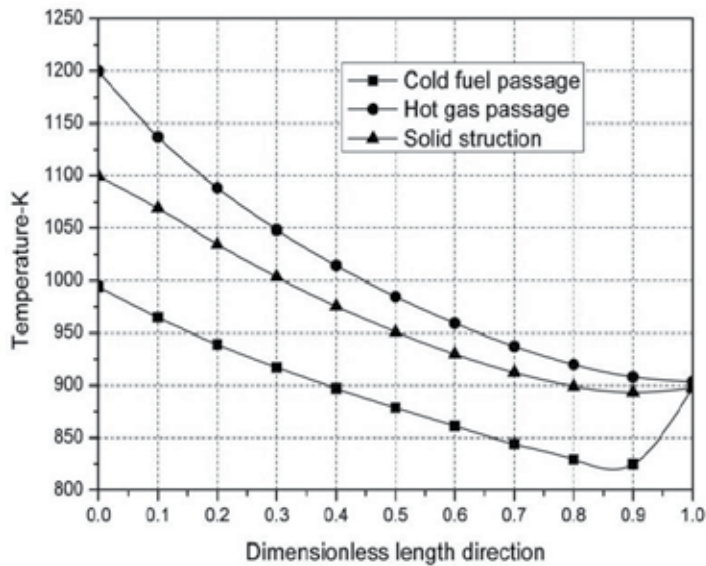


Fig. 5. Temperature distribution along the heat exchange reformer length.

The pressure profiles in the cold fuel and hot gas passages are illustrated in Fig. 6. Owing to the friction of the passage, the pressure loss is about 0.08% in the cold fuel passage, and about 4.23% in the hot gas passage. The primary reason that the pressure loss is greater in the hot gas passage is that the mass flow rate in the hot gas passage is larger than that in the cold passage. Of course, the geometrical configuration is a key factor as well.

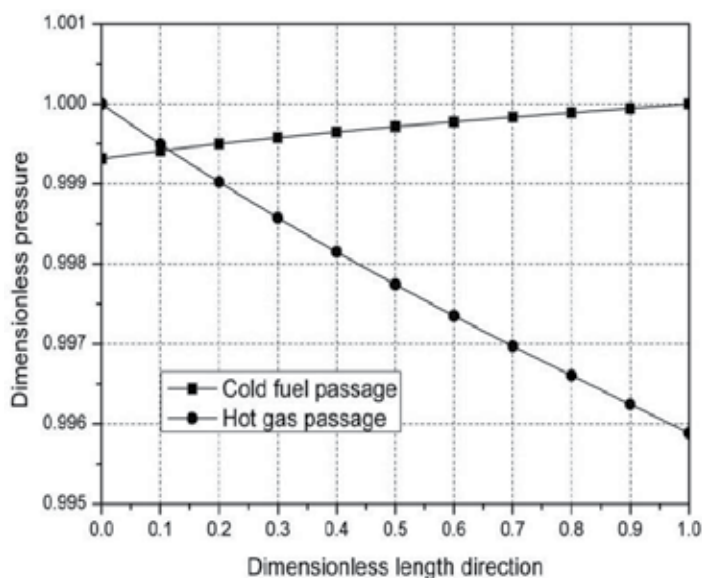


Fig. 6. Pressure distribution along the heat exchange reformer length.

The dimensionless fluid properties (such as: density, velocity, heat capacity, thermal conductivity, and dynamic viscosity) of the cold fuel and hot gas along the heat exchange reformer are illustrated in Fig. 7 and Fig. 8, respectively. The dimensionless properties are defined as the ratio of local values and corresponding inlet values, which can be calculated by the inlet conditions in the methods depicted in the reference [23]. Examples of this include situations where: the density is based on the gas state equation; the velocity is calculated by the mass flow rate, density and the channel cross area; the heat capacity of the multi-component gas mixture is related to the single component heat capacity and the corresponding molar fraction; the dynamic viscosity of the multi-component gas mixture is based on the Reichenberg's expression; the thermal conductivity of multi-component gas mixtures is based on Wassiljewa's expression and the Mason & Saxena modification.

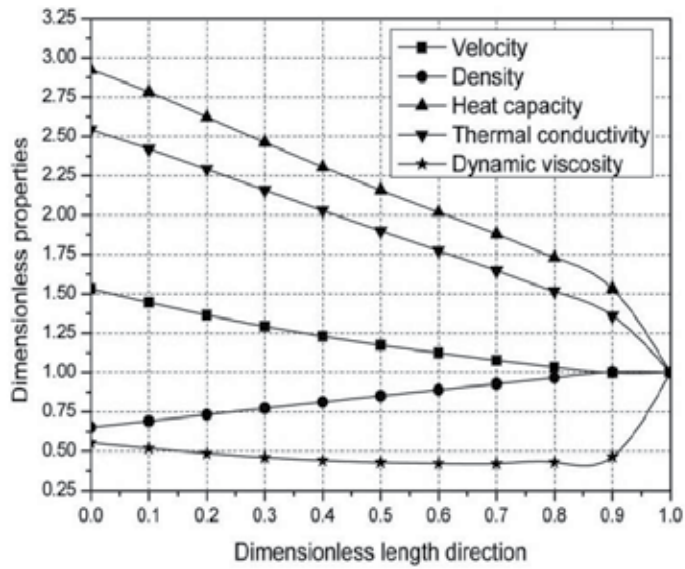


Fig. 7. Cold fuel properties along the heat exchange reformer length.

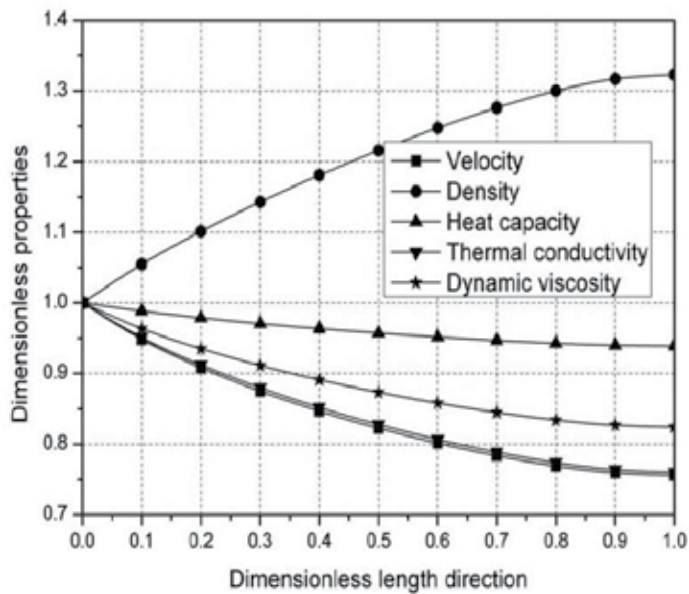


Fig. 8. Hot gas properties along the heat exchange reformer length.

The density is related to the pressure and the temperature, which are decided by the gas state equation $P = \rho RT$. In the cold fuel passage, the temperature increases and the pressure decreases, so the density decreases along the flow direction while, in the hot gas passage, both the pressure and the temperature decrease. The ratio of pressure and temperature along the passage is increased, so the density of the hot gas increases along the flow direction.

Two primary factors that affect the velocity are the mass flow rate and the density. Here, the mass flow rate is constant, and the velocity is mainly determined by the density. That is to say, the velocity increases in the cold fuel passage and decreases in the hot gas passage, following the trend of the density.

Specific heat capacity, thermal conductivity, and dynamic viscosity are primarily influenced by the temperature and the gas composition. This has been discussed by Todd and Young [24] and Lijin WANG [22] for high temperature SOFCs.

5.2 Analysis of the influence of some parameters

In this section, some key parameters that affect the heat exchange reformer performance are investigated, such as the steam to carbon ratio (STC), catalyst reduced activity (CRA), and passage operating pressure.

5.2.1 Steam to carbon ratio

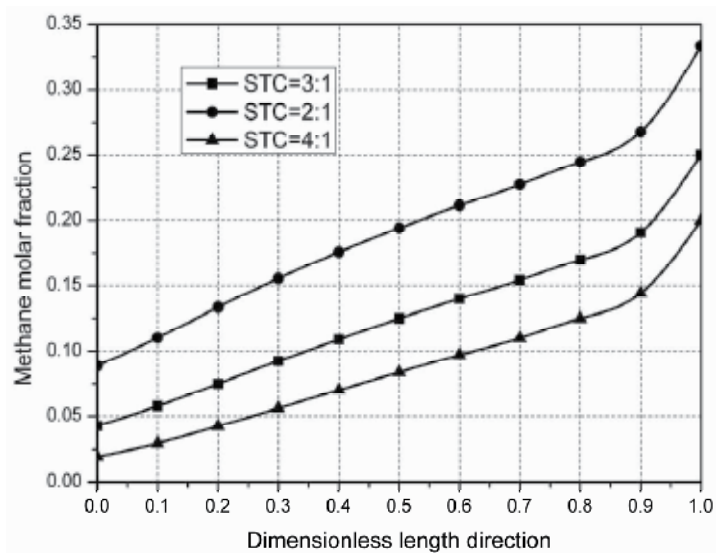
In general, the STC must be greater than 2.0 to avoid carbon coking in the fuel lines, reformer, and fuel cell stack [25]. The effect of different STCs on the heat exchange reformer is presented in Fig. 9 and Fig. 10.

Fig. 9 presents effect of STC on the methane and hydrogen distribution along the heat exchange reformer. In the internal reforming high temperature fuel cell, the endothermic reforming reaction will cause a great temperature gradient, which could decrease the life of the fuel cell stack due to excessive thermal stress. Therefore, too much remaining methane would be no good for the steady operation of the high temperature fuel cell. With the STC changing from 2:1 to 4:1, less methane remains at the exit (Fig. 9 (a)), while the hydrogen molar fraction at the exit is almost the same as at the entrance (Fig. 9 (b)). Therefore, a suitable and acceptable STC is essential for the internal reformation of high temperature fuel cells.

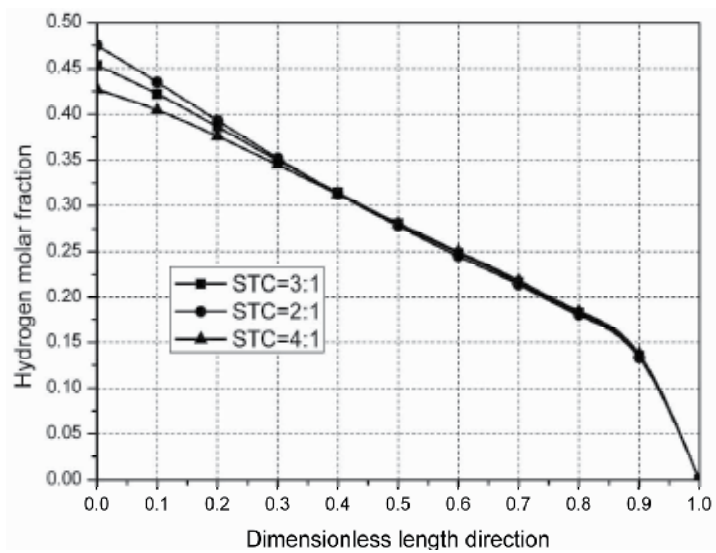
The temperature distribution of cold fuel and hot gas is illustrated in Fig. 10. When the STC changes from 2:1 to 4:1, less methane is provided at the inlet, and less heat is needed for the steam reforming reaction. Meanwhile, a higher STC will result in a higher rate of the exothermic water gas-shift reaction, so the temperature curves of both the cold and hot stream are higher.

5.2.2 Catalyst reduced activity

The CRA is defined as the ratio between the activity of the catalyst in use and that of a conventional Ni catalyst (Xu and Froment, [19]) at typical feed conditions (temperature, pressure, and composition) [26]. The CRA is the key factor in determining the reforming reaction rate. For the rated case, the CRA is defined as 0.003 [7] in Table 5. Fig. 11 and Fig. 12 present the effect of the CRA on the performance of the heat exchange reformer.

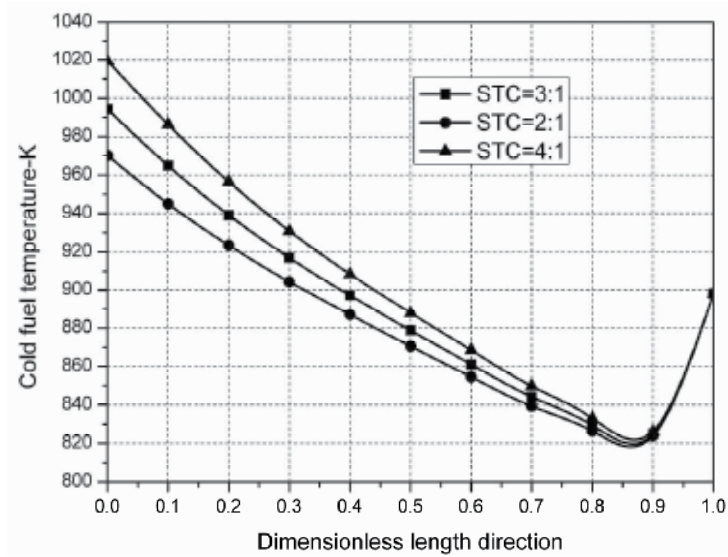


(a)

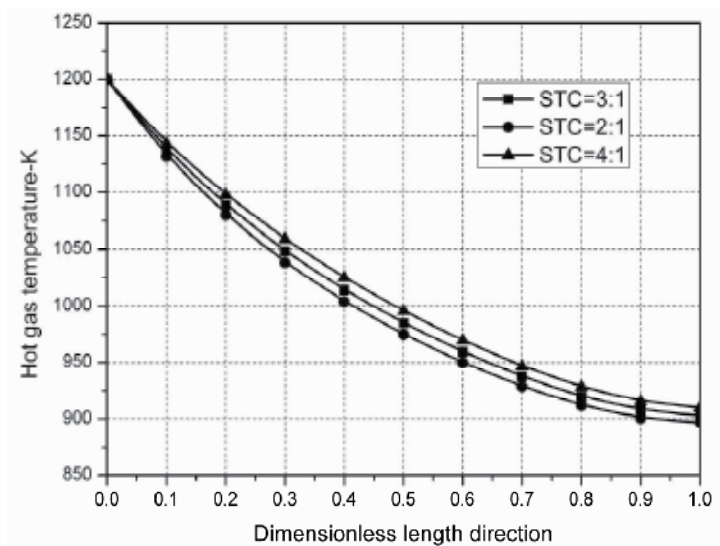


(b)

Fig. 9. STC effect on the methane (a) and hydrogen (b) molar fraction distributions.



(a)



(b)

Fig. 10. STC effect on the cold fuel (a) and hot gas (b) temperature distributions.

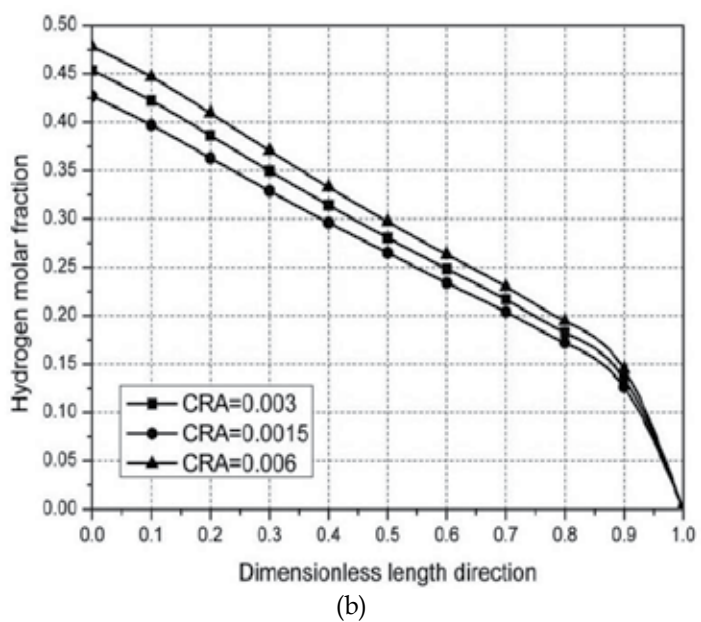
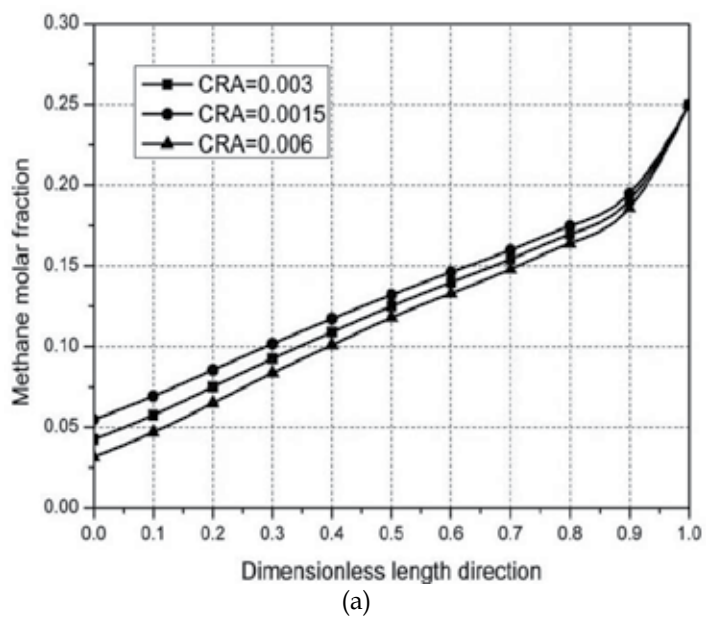
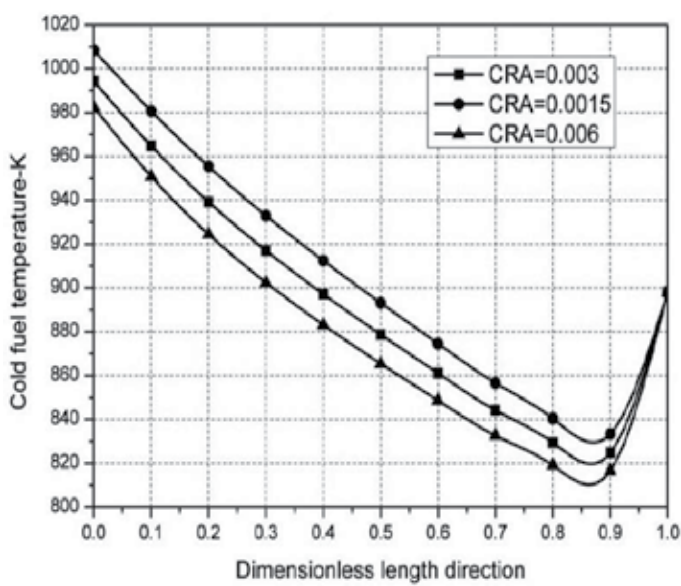
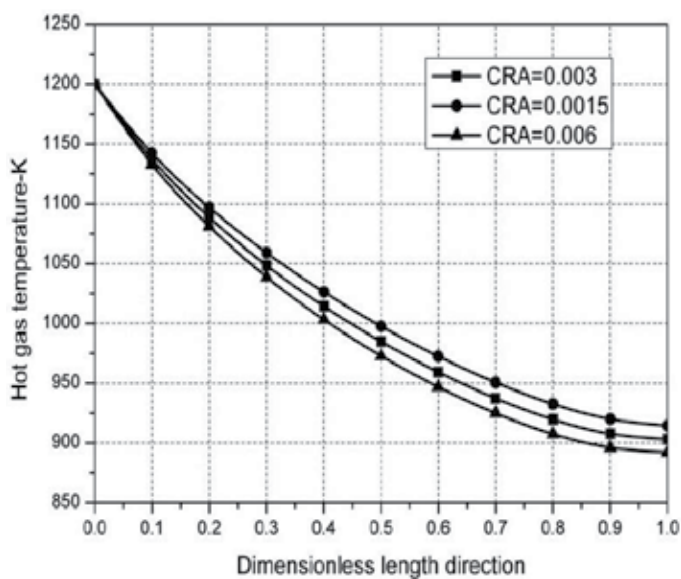


Fig. 11. CRA effect on the methane (a) and hydrogen (b) molar fraction distributions.



(a)



(b)

Fig. 12. CRA effect on the cold fuel (a) and hot gas (b) temperature distributions.

The influence on the methane and hydrogen molar fraction distribution along the heat exchange reformer is shown in Fig. 11. When the CRA changes from 0.0015 to 0.006, the rate of the methane reforming reaction increases, so more methane is consumed (Fig. 11 (a)) and more hydrogen is produced (Fig. 11 (b)). More heat is needed to satisfy the requirements of the high endothermic reaction, so the temperature curves of both the cold and hot stream are lower (Fig. 12).

5.2.3 Passage operating pressure

The passage pressure often changes with the operation condition, even during malfunctions or damage. The effect of the cold passage outlet pressure on the heat exchange reformer is investigated in this section and illustrated in Fig. 13 and Fig. 14.

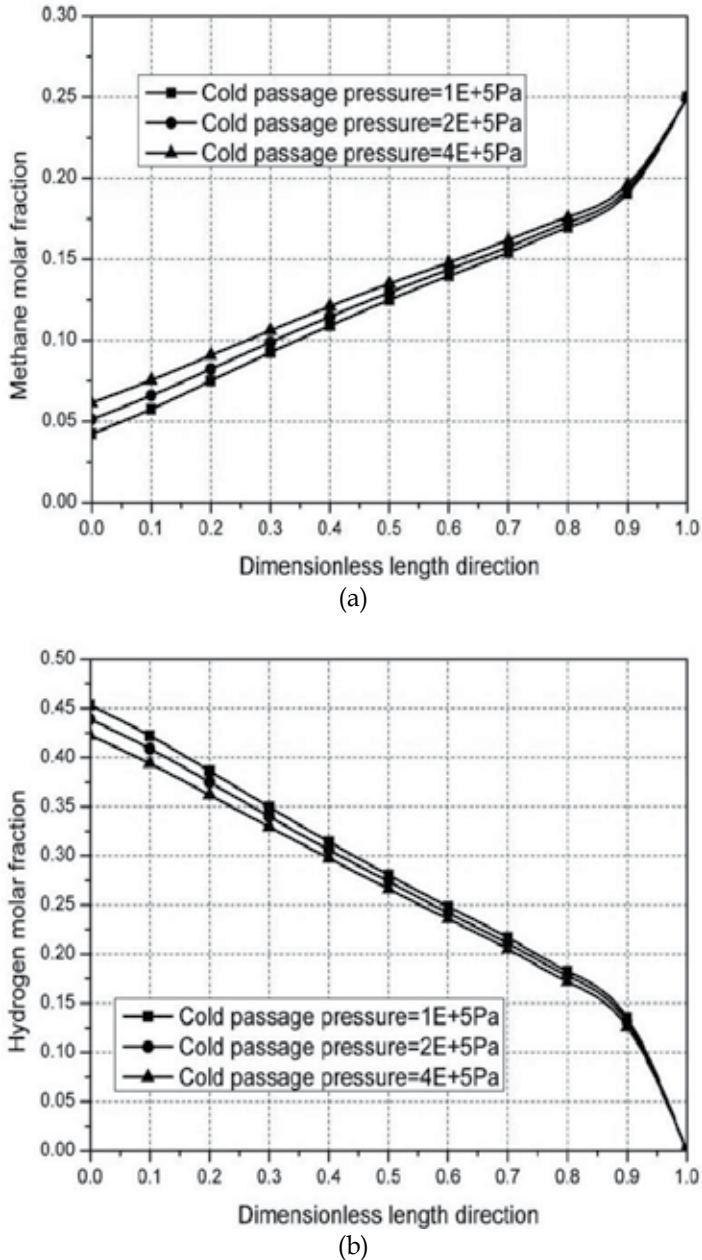
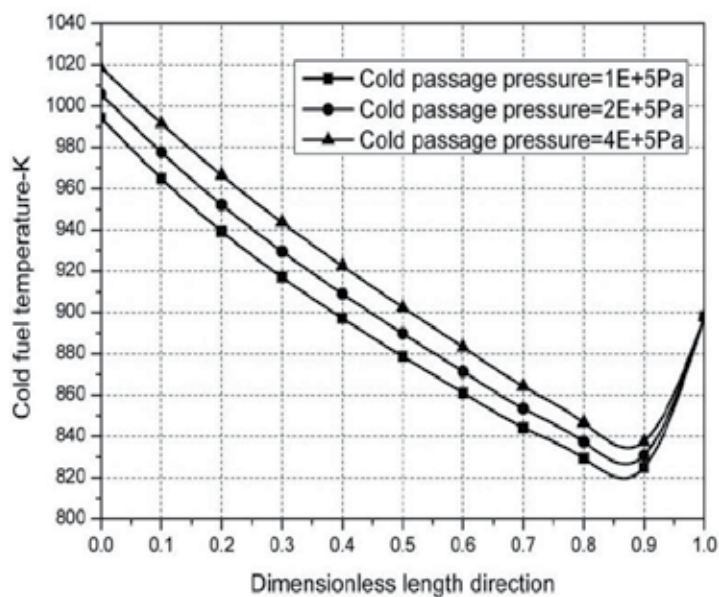
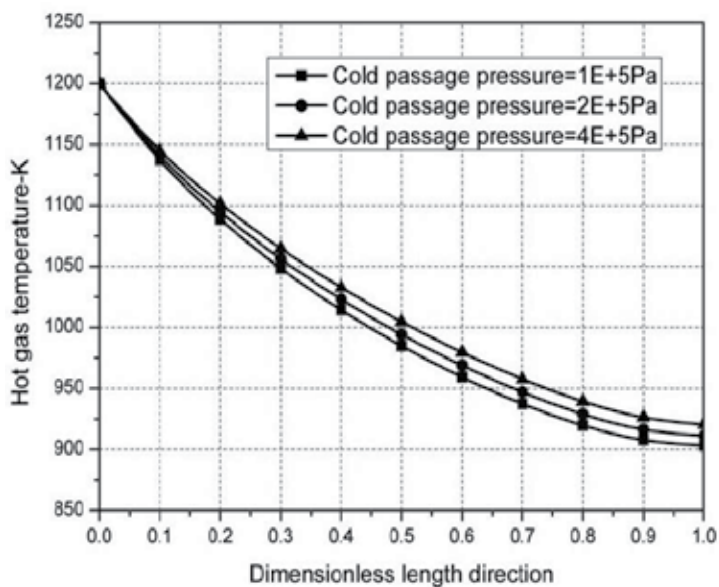


Fig. 13. Cold passage outlet pressure effect on the methane (a) and hydrogen (b) molar fraction distributions.



(a)



(b)

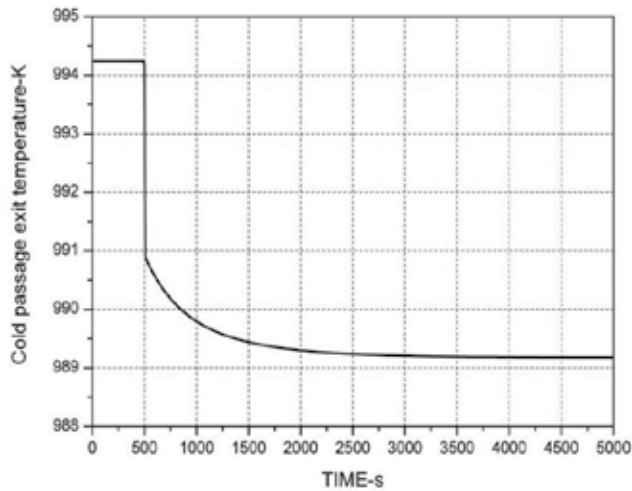
Fig. 14. Cold passage outlet pressure effect on the cold fuel (a) and hot gas (b) temperature distributions.

The cold passage outlet pressure has little influence on the heat exchange reformer performance. When the passage pressure is elevated from 1E+5Pa to 4E+5Pa, less methane is consumed, less hydrogen is produced (Fig. 13), and less heat is needed for the methane steam reforming reaction, so the cold fuel and hot gas temperatures are higher (Fig. 14).

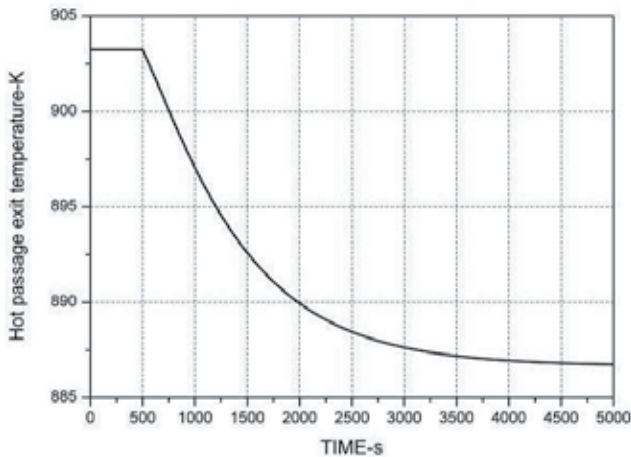
5.3 Dynamic simulation result

In this section, the transient behaviours of the compact heat exchange reformer are investigated. Several step-change input parameters (such as inlet mass flow rate and inlet temperature of both the cold and hot stream) are imposed when the device has been operated for 500s.

Fig. 15 illustrates the dynamic response of the temperatures at the cold and hot passage exits, when the cold fuel mass flow rate has a step increase of 10%. The cold passage exit temperature has a sudden decrease at the initial period due to the step input. Then, because of the great thermal inertia of the solid structure, the temperature decreases gradually. Therefore, the temperature at the cold passage exit decreases. Owing to a greater cold fuel mass flow rate, more heat is provided from the hot side, so the temperature at the hot passage exit has a gradual decrease.



(a)



(b)

Fig. 15. Dynamic response of the temperatures at the Cold (a) and hot (b) passage exits when cold fuel mass flow rate up by 10%.

Fig. 16 shows the dynamic effect on methane, hydrogen, and the water molar fraction distribution when the cold fuel mass flow rate has a step increase of 10%. The methane and water molar fraction increase a little, while the hydrogen decreases a little. It can be shown that the molar fraction has a little change when the cold fuel inlet mass flow rate changes.

Fig. 17 presents the dynamic response of the cold fuel and hot gas temperatures when the hot gas inlet temperature decreases to 1100K from 1200K. The temperature at the cold passage exit is influenced by the thermal capacity of the solid structure, and decreases gradually. Owing to the decrease of the inlet temperature, the temperature at the hot gas passage exit also undergoes a decrease (Fig. 17 (b)). When the temperature of the cold stream decreases, the rate of the steam reforming reaction will be slower. Therefore, less fuel is reformed, which can be shown from the methane molar fraction distribution in Fig. 18 (a); less hydrogen is produced (Fig. 18 (b)) and more water remains (Fig. 18 (c)).

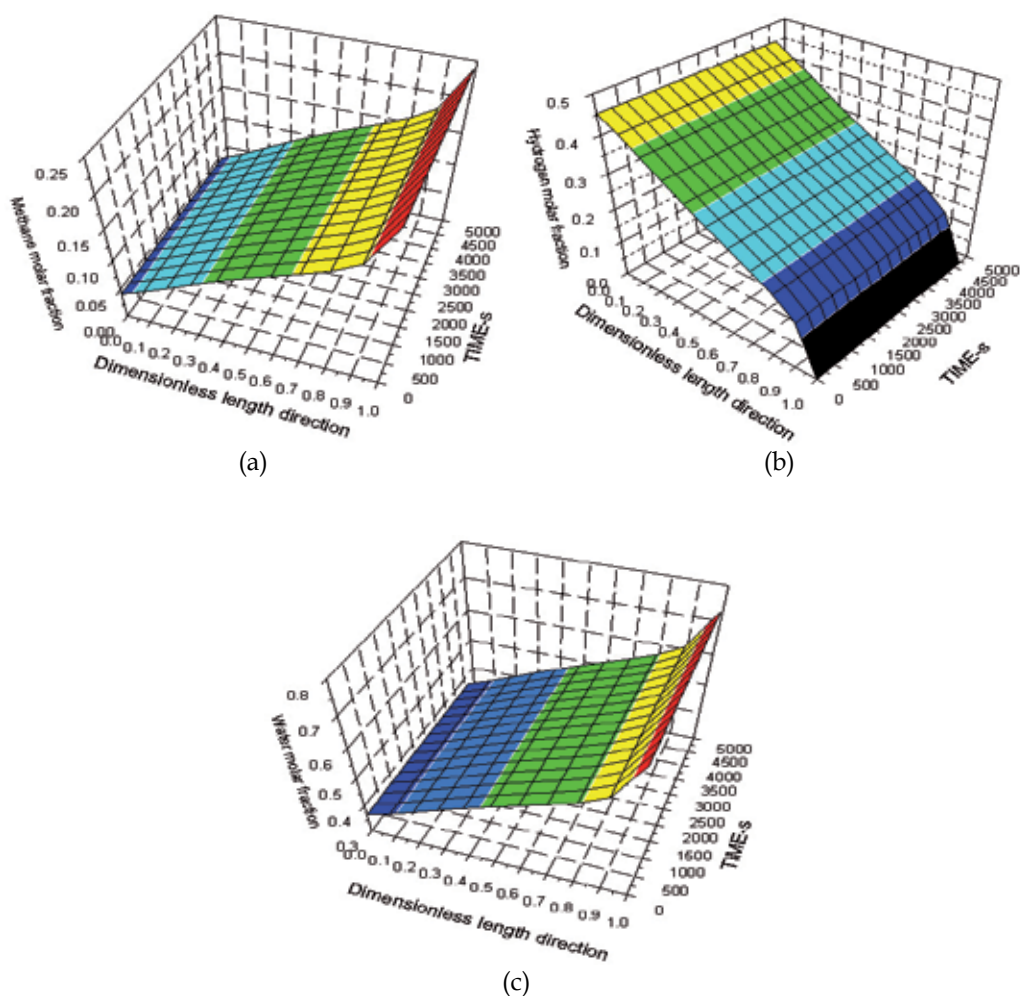
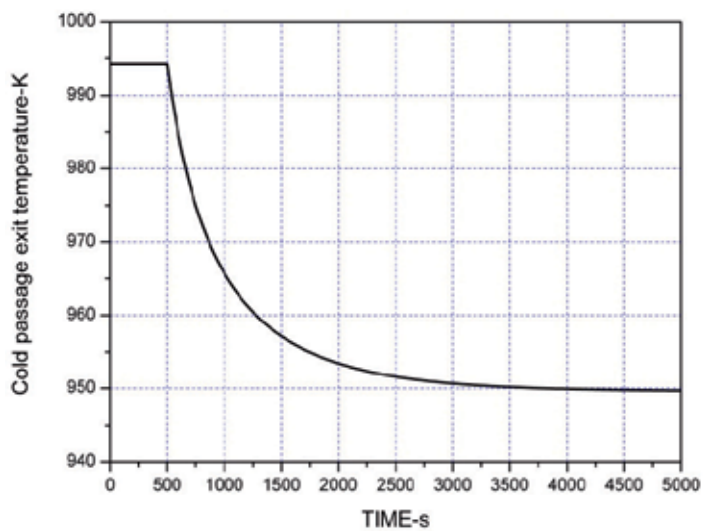
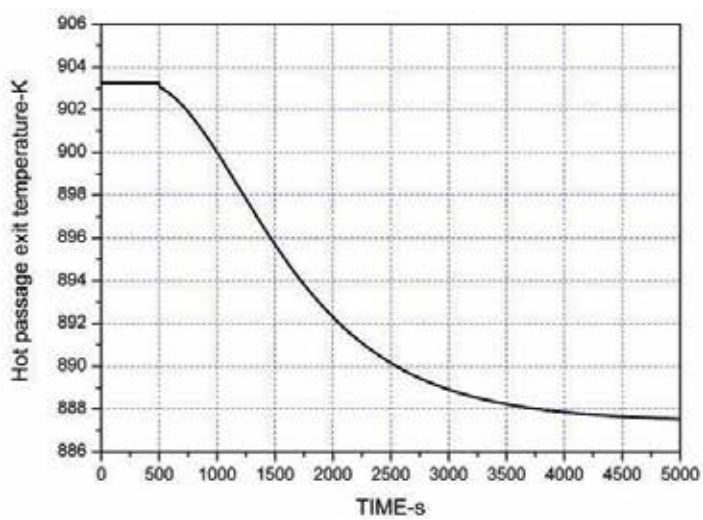


Fig. 16. Dynamic response of methane (a), hydrogen (b) and water (c) distributions when cold fuel mass flow rate up by 10%.

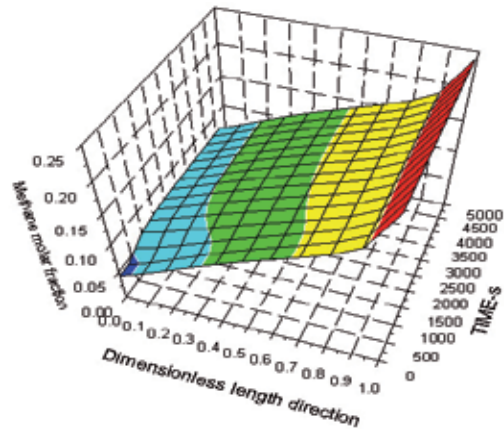


(a)

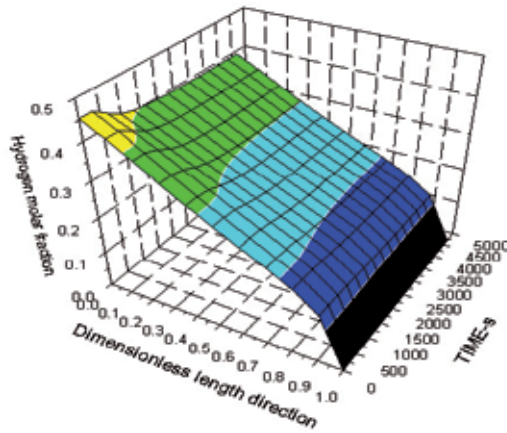


(b)

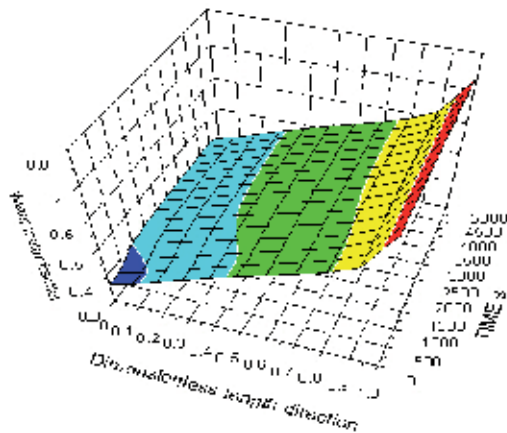
Fig. 17. Dynamic response of the temperatures at the cold (a) and hot (b) passage exits when the hot inlet temperature down to 1100K.



(a)



(b)



(c)

Fig. 18. Dynamic response of methane (a), hydrogen (b) and water (c) distributions when the hot inlet temperature down to 1100K.

Based on all the dynamic performance figures from Fig. 15 to Fig. 18, the inertial delay time of this kind of heat exchange reformer is about 3000s. Such a substantial thermal inertia can seriously influence the whole fuel cell hybrid system transient performance and the design of the control system.

6. Conclusions

A compact heat exchange reformer for high temperature fuel cell systems is presented in this paper. Based on the volume-resistance characteristic modeling technique, the distributed-lumped parameter method, and the modular modeling idea, a simulation model that is suited for quick and real time simulations is completed. The model can predict the key distribution characteristic parameters and the influence of some factors, such as the steam to carbon ratio, catalyst reduced activity, and passage pressure. The dynamic results indicate that this kind of heat exchange reformer has a great thermal inertia.

Both the model and modeling method will be useful and valuable for other heat exchange reformer designs and optimization; it can also provide a reference for the design of the control system in the future.

7. Acknowledgement

Financial support from the National Natural Science Foundation of China (NSFC) under the contract no. 50676061 and Shanghai Key Research Program from Science and Technology Committee of Shanghai Municipal under the contract No. 09DZ1200701 and 09DZ1200702 is gratefully acknowledged

8. Nomenclature

A	area (m^2)
C	molar concentration ($molm^{-3}$)
C_p	specific heat capacity ($kJkg^{-1}K^{-1}$)
D_h	hydraulic diameter (m)
DEN	parameter used in Table 1
f	fanning friction factor
G	mass flow rate (kgs^{-1})
G_m	mass velocity ($kgm^{-2}s^{-1}$)
J	Colburn factor
K	parameter used in Table 1
k	parameters used in Table 1, or geometry parameter used in formula (8) (m)
L	heat exchanger length (m)
l	offset strip fin length (m)
M	molecular weight ($kgmol^{-1}$)
n	number
p	partial pressure of component i in the cold fuel passage (Pa)
P	pressure (Pa)
Pr	Prandtl number
R	gas constant ($Jmol^{-1}K^{-1}$)
Re	Reynolds number

S	passage heat transfer surface (m)
St	Stanton number
T	temperature (K)
t	fin or plate thickness (m), time (s)
U	wet perimeter (m)
u	velocity (ms^{-1})
W	whole heat exchanger width (m)
X	passage width (m)
Y	passage height (m)

Greek letters

α	convective heat transfer coefficient ($\text{kJm}^{-1}\text{s}^{-1}\text{K}^{-1}$) or dimensionless geometry parameter used in formula (13) and (15)
δ	dimensionless geometry parameter used in formula (13) and (15)
γ	dimensionless geometry parameter used in formula (13) and (15)
ρ	density (kgm^{-3})
η	fin efficiency
σ	friction resistance
μ	dynamic viscosity (Pa.s)
λ	thermal conductivity ($\text{kJm}^{-1}\text{s}^{-1}\text{K}^{-1}$)
$\Delta H, \Delta H^0$	enthalpy change and enthalpy change at the standard state (kJmol^{-1})
ΔP	pressure loss (Pa)

Subscripts

c	cold side
f	fin
h	hot side
i	fuel component
w	solid fin structure
(I)	steam reforming reaction
(II)	gas shifting reaction
(III)	CO_2 direct reforming reaction

9. References

- [1] EG&G Technical Services Inc, M. (2004). *Fuel Cell Handbook* (seventh edition), U. S. Department of Energy Office of Fossil Energy National Energy Technology Laboratory. New York, USA.
- [2] Larminie, J. & Dicks, A., M. (2003). *Fuel Cell Systems Explained* (Second edition), John Wiley & Sons Ltd, England.
- [3] Dicks, A.L., J. (1998). Advances in catalysts for internal reforming in high temperature fuel cells, *Journal of Power Sources*, 71(1998) pp.111-122.
- [4] Zhang, H.S.; Weng, S.L. & Su M. (2005). Dynamic modeling and simulation of distributed parameter heat exchanger, *Proceedings of ASME TURBO EXPO 2005-68293*, Nevada, USA, June 14-17, 2005.

- [5] Shah, R. K. & Webb, R. L., M. (1983). *Compact and enhanced heat exchangers, Heat Exchangers: Theory and Practice*, Hemisphere, Washington, DC.
- [6] Zanfir, M. & Gavriilidis, A., J.(2003). Catalytic combustion assisted methane steam reforming in a catalytic plate reactor, *Chemical Engineering Science*, 58(2003) pp. 3947-3960.
- [7] Lim, L.T.; Chadwich, D. & Kershenbaum, L., J.(2005). Achieving autothermal operation in internally reformed solid oxide fuel cells: Simulation studies, *Ind. Eng. Chem. Res.* 44 (2005) pp. 9609-9618.
- [8] Plate-fin heat-exchange reformer with highly dispersed catalyst, *Fuel Cells Bulletin*, 4(37) (2001) 16
- [9] Wegeng, R.S.; Pederson, L.R.; TeGrotenhuis, W.E. & Whyatt, G.A., Compact fuel processors for fuel cell powered automobiles based on microchannel technology. *Fuel Cells Bulletin*, 3(28) (2001) 8-13.
- [10] Patil, A.S.; Dubois, T.G.; Sifer, N. & Bostic, E., J. (2004). Portable fuel cell systems for America's army: technology transition to the field, *Journal of Power Sources* 136(2004) pp. 220-225.
- [11] Tonkovich, A.Y.; Perry, S.; Wang, Y.; Qiu, D.; LaPlante, T. & Rogers, W.A., J. (2004). Microchannel process technology for compact methane steam reforming. *Chemical Engineering Science* 59(2004) pp. 4819-4824.
- [12] Ryi, S.K.; Park, J.S.; Choi, S.H.; Cho, S.H. & Kim, S.H., J. (2005). Novel micro fuel processor for PEMFCs with heat generation by catalytic combustion. *Chemical Engineering Journal* 113(2005) pp. 47-53.
- [13] Park, G.G.; Yim, S.D.; Yoon, Y.G.; Lee, W.Y.; Kim, C.S.; Seo, D.J. & Eguchi, K., J. (2005). Hydrogen production with integrated microchannel fuel processor for portable fuel cell systems. *Journal of Power Sources* 145(2005) pp. 702-706.
- [14] Kays, W.M. & London, A.L., M. (1984). *Compact Heat Exchangers*, McGraw Hill, New York, Third Edition, 1984.
- [15] ALPEMA, (2000) *The standards of the brazed Aluminum plate-fin heat exchanger manufactures' association*, Second Edition, 2000
- [16] Hachemi, A., J. (1999). Experimental study of thermal performance of offset rectangular plate fin absorber-plates, *Renewable Energy* 17 (1999) pp.371-384.
- [17] Manglik, R.M. & Bergles, A.E., J. (1995). Heat Transfer and Pressure Drop Correlations for the Rectangular Offset Strip Fin Compact Heat Exchanger, *Experimental Thermal and Fluid Science* 10 (1995) pp.171-180.
- [18] Rosehnow, W.M., M. (1985). *Handbook of heat transfer applications*, 2nded, USA: McGraw-Hill; 1985.
- [19] Xu, J. & Froment, G.F., J. (1989). Methane steam reforming, methanation and water gas shift: I Intrinsic kinetics, *AIChE* 35 (1989) pp.3929-3940
- [20] Smith, J.M.; Van Ness, H.C. et.al, M. (2005). *Introduction to Chemical Engineering Thermodynamics 7th edition*, McGraw-Hill, New York, 2005, pp.140-141.
- [21] Luo, X.; Guan, X. et.al, J. (2003). Dynamic behavior of one-dimensional flow multistream heat exchangers and their networks, *Int. J. Heat Mass Transfer* 46 (2003) 705-715.
- [22] Wang, L.J.; Zhang, H.S. & Weng, S.L., J. (2008). Modeling and simulation of solid oxide fuel cell based on the volume-resistance characteristic modeling technique, *Journal of Power Sources* 177(2008) pp.579-589.

- [23] Poling, B.E., Prausnitz, J.M. et.al, M. (2000). *The Properties of Liquids & Gases*, 5th Edition, McGraw-Hill, New York, 2000.
- [24] Todd, B. & Young, J.B., J. (2002). Thermodynamic and transport properties of gases for use in solid oxide fuel cell modeling, *Journal of Power Sources* 110 (2002) pp.186-200.
- [25] Mueller, F.; Jabbari, F.; Gaynor, R. & Jacob, B., J. (2007). Novel solid oxide fuel cell system controller for rapid load following, *Journal of Power Sources* 172 (2007) pp.308-323.
- [26] Aguiar, P.; Chadwick, D. & Kershenbaum, L., J. (2004). Effect of methane slippage on an indirect internal reforming solid oxide fuel cell, *Chemical Engineering Science* 59(2004) pp.87-97.
- [27] Steen, M. & Ranzani, L., J. (2000). Potential of SiC as a heat exchanger material in combined cycle plant, *Ceramics International*, 26(2000) 849-854.
- [28] Yasar, I., J. (2004). Finite element model for thermal analysis of ceramic heat exchanger tube under axial non-uniform convective heat transfer coefficient, *Materials and Design* 25(2004) 479-482.
- [29] Akiyoshi, M.; Takagi, I.; Yano, T.; Akasaka, N. & Tachi, Y., J. (2006). Thermal conductivity of ceramics during irradiation, *Fusion Engineering and Design* 81 (2006) 321-325.

Single-Phase Heat Transfer and Fluid Flow Phenomena of Microchannel Heat Exchangers

Thanhtrung Dang¹, Jyh-tong Teng², Jiann-cherng Chu², Tingting Xu³,
Suyi Huang³, Shiping Jin³ and Jieqing Zheng⁴

¹*Department of Heat and Refrigeration Technology, Hochiminh City University of
Technical Education, Hochiminh City,*

²*Department of Mechanical Engineering, Chung Yuan Christian University, Chung-Li,*

³*School of Energy and Power Engineering, Huazhong
University of Science and Technology, Wuhan,*

⁴*College of Mechanical Engineering, Jimei University, Xiamen, Fujian,*

¹*Vietnam*

²*Taiwan*

^{3,4}*P. R. China*

1. Introduction

In recent years, microfabrication technologies have been utilized in the fields of process engineering using microchannel devices as heat exchangers. The microchannel heat transfer means is of importance to the areas of small and confined spaces, high heat flux devices for cooling electronic components, or other cooling applications in thermal and chemical engineering. Increasing the heat transfer rate and decreasing characteristic dimension of a heat exchanger are key design requirements, and a micro heat exchanger satisfies these needs.

A review of micro heat exchanger related issues such as flow behaviors, fabrication methods, and practical applications was done by Bowman and Maynes [1]. The review firstly introduced the experimental and numerical investigations of channel flow. Subsequently, Friction and heat transfer measurements of gas flow and liquid flow were discussed in the paper. The paper indicated that the transition Reynolds number is a function of surface roughness and channel geometry. Moreover, in the paper, the heat exchanger designs - including their comparison and optimization - were also reviewed. Furthermore, several fabrication methods including micromachining, chemical etching, laser machining, electroplating, and lamination, were discussed.

Review of the experimental results concerning single-phase convective heat transfer in microchannels was presented by Morini [2], with additional review of the results obtained for friction factor, laminar-to-turbulent transition, and Nusselt number in channels having hydraulic diameters less than 1 mm. Dang [3] and Dang et al. [4] presented the fluid flow

and heat transfer characteristics for rectangular-shaped microchannel heat exchangers, both numerically and experimentally. Effects of flow arrangement on the performance index (expressed as the ratio of the heat transfer rate to the pressure drop) of a microchannel heat exchanger were evaluated. In addition, influences of configurations on the performance index of microchannel heat exchangers were presented.

Brandner et al. [5] described microstructure heat exchangers and their applications in laboratory and industry. In their paper, several micro heat exchangers were introduced, including polymer microchannel heat exchanger with aluminum separation foil, electrically powered lab-scale microchannel evaporator, ceramic counter-flow microstructure heat exchanger, etc. An analysis of effectiveness and pressure drop in micro cross-flow heat exchanger was presented by Kang and Tseng [6]. For each effectiveness, the heat transfer rate and pressure drop as a function of average temperature were obtained. The results indicated that pressure drop was reduced with a rising average temperature. Using silicon or copper as the materials for the microchannel heat exchangers, the difference in heat transfer rates between these two types of heat exchangers was found to be minimal. This was due to the fact that the substrate thicknesses between the hot and the cold channels were very thin; as a result, their thermal conductivity resistances were very small. Henning et al. [7] made three devices – the “standard” channel device with straight layout and a hydraulic diameter of 153 μm , the “short” channel with straight layout and a hydraulic diameter of 149 μm , and the “wavy” channel with wavy layout and a hydraulic diameter of 125 μm . Their experimental results indicated that the standard channel device was the best choice for heating at moderate and high flow rates.

The crossflow microstructure heat exchanger made of stainless steel W316L was studied by Brandner [8]. It was observed that heat transfer in a microstructure heat exchanger was enhanced by using staggered microcolumn array heat exchangers which were designed to operate in the transition or turbulent flow regime. Results obtained from experiments and from modeling of an integrated preferential oxidation-heat exchanger (ProxHeatex) microdevice were presented by Delsman et al. [9]. The ProxHeatex consisted of two heat exchangers and a cooled reactor, as shown in Fig. 1. Those researchers also improved a new version of a ProxHeatex from an earlier prototype [10]. Heat recovery efficiency of the ProxHeatex device was found to be a function of the reformed gas flow rate. The overall heat recovery of the device varies between 73% and 95%, with the higher values corresponding to higher flow rates and higher oxygen excess.

Shen and Gau [11] presented a paper dealing with design and fabrication of sensors and heaters for the study of micro-jet impingement cooling. The local Nusselt number distribution along the wall, Nu_x , was found to be a function of Z/B ratio, where Z is nozzle-to-wall distance and B is the slot width. A heat exchanger for power electronic components was studied by Gillot et al. [12]. The prototype was composed of four elementary modules. Each module was composed of two IGBT (Insulated Gate Bipolar Transistor) chips directly brazed onto a piece of copper where rectangular channels were machined. The thermal resistance of the chips was calculated using 3D finite element simulation tool (FLUX 3D). Numerical and experimental values of the metal temperature at five testing locations were in good agreement, with the maximum percentage error being 1.7%. The pressure drop observed to be increased with a rising flow rate. The heat spread effect was observed to be a function of the heat transfer coefficient.

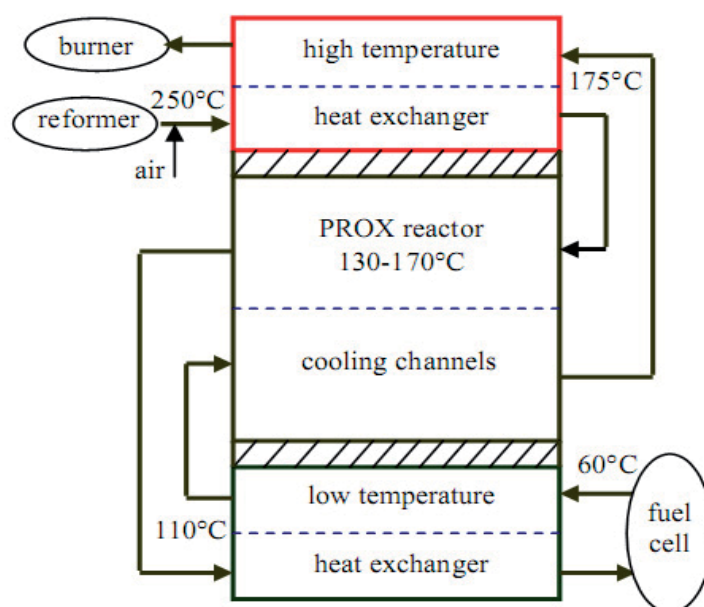


Fig. 1. Schematic of the integrated preferential oxidation-heat exchanger [3,4,9,10].

Ceramic microstructure devices in the forms of counter-flow and cross-flow microchannel heat exchangers were manufactured by Alm et al. [13] and used in thermal and chemical process engineering. The peak experimental heat transfer coefficient for the cross-flow heat exchanger was observed to reach $22 \text{ kW}/(\text{m}^2\text{K})$. Hallmark et al. [14] presented an experimental investigation on the heat transfer response of plastic microcapillary films (MCF). Thermal power removed by the MCF heat exchanger was shown to be a function of input electrical power for an increasing flow rate of the MCF. Jiang et al. [15] investigated fluid flow and forced convection heat transfer in microchannel heat exchanger (MCHE). The transition from laminar to turbulent flow in the microchannel heat exchanger was observed to occur at $Re \approx 600$. A new method of fabrication of heat transfer surfaces with micro-structured profile was presented by Schulz et al. [16]. By the ion track etching combined with metal electro-plating method, arrays of copper whiskers with high aspect ratio were produced on surfaces of heat transfer tubes. At the same temperature, the structured tube had higher heat flux or heat transfer coefficient value than that of the smooth one. Lee et al. [17] studied a polymer type micro-heat exchanger applicable to 272 BGA multi-chip module (MCM) and selected polydimethylsiloxane (PDMS) as the package material. The design was evaluated numerically using the Fluent CFD simulation tool. Results obtained from both the experiment and the simulation for each fabricated heat exchanger were compared; difference of temperature distribution in chip was less than 2°C . Surface temperature of the chip was found to be a function of pressure drop, the temperature decreased with a rising of the pressure drop for all the conditions being tested.

Wei [18] fabricated a stacked microchannel heat sink using microfabrication techniques. Experiments were conducted to study the thermal performance of stacked microchannel structure, and overall thermal resistance was determined to be less than $0.1 \text{ K}/\text{W}$ for both counter-flow and parallel-flow configurations. In the study, the numerical simulations were

References	Material/ Shape	Working fluid	Flow rate	Heat transfer	Pressure drop	Comments
Brandner [5]	Polymer	Water	m: 10-400 kg/h	q: 0.2-1.1 W/cm ²	0-0.4 MPa	
Kang [6]	Silicon/ Rect	Water	m: 0.0643-0.07 kg/s	Q: 2,690-2,925 W	0.16-0.28 MPa (Hot side)	Given the same effectiveness
			m: 0.1746-0.0026 kg/s	Q: 500-7,300 W	0.22-0.44 MPa (Cold side)	Given the same temperature
	Copper/ Rect	Water	m: 0.0663-0.724 kg/s	Q: 2,780-3,030 W	10-400 kPa (Hot side)	Given the same effectiveness
			m: 0.1803-0.0027 kg/s	Q: 500-7,500 W	10-900 kPa (Cold side)	Given the same temperature
Henning [7]	Metal	Water	m: 64 kg/h	Q: 3,000 W	None	Electrical power up to 3 kW with effectiveness ~ 0.95
Brandner [8]	Stainless steel/ Rect	Water	m: 0-400 kg/h	Q: 0-8,500 W	0-6.2x10 ⁵ Pa	For hydraulic diameter of 70 μm
			m: 0-300 kg/h	Q: 0-12,000 W	None	For staggered microcolumns
Delsman [9,10]	Stainless steel/ Rect	Methanol, water	V: 2.5-6 SLM	Heat recovery efficiency of the ProHeatex: 73-95%		
Shen [11]	Silicon/ Rect	Air	None	$\overline{Nu} = 0.045 \text{Re} \left(\frac{Z}{L} \right)^{0.4}$	None	For the case before jet breakdown
				$\overline{Nu} = 0.052 \text{Re} \left(\frac{Z}{L} \right)^{-0.5}$	None	For the case after jet breakdown
Gillot [12]	Copper/ Rect	Water with 40% glycol	V: 130-280 ml/s	R: 100-110 K/kW	50-200 kPa	
Alm [13]	Ceramic	Water	m: 10-140 kg/h	h: 7-22 kW/m ² K (For crossflow HE)	20-450 kPa (For counterflow HE)	
Hallmark [14]	Plastic	Water	V: 30 or 60 or 120 mL/min	h: 125-230 W/m ² K	None	
Jiang [15]	Copper/ Rect	Water	m: 0.0093-0.34 kg/s	K _v : 11-38.5 MW/m ³ K	3.3-90 kPa	
Schulz [16]	Copper/ tube	Water	V: 4 L/m	q: 1,000-17,000 W/m ²	None	Overheat from 4-16 °C
Lee [17]	PDMS/ Rect	Water	None	Q: 0-14 W	0-10 kPa	The top chip's temperature was 125 °C

References	Material/Shape	Working fluid	Flow rate	Heat transfer	Pressure drop	Comments
Wei [18]	Silicon/Rect	Water	V: 1.4×10^{-6} – 5.8×10^{-6} m ³ /s	R: 0.24×10^{-4} – 0.12×10^{-4} °Cm ² /W	$p = f(V)$	for several channels
Hasan [19]	Silicon	Water	Re = 50	$\varepsilon = f(Kr)$	7.8 kPa	For rectangular channel
Dang [21-31]	Silicon/Trapezoidal	Water	m: 0.0579–0.1158 g/s	q: 12 – 13.6 W/cm ²	None	
	Aluminum/Rect	Water	m: 0.1859–0.3625 g/s	q: 6.5 – 8.2 W/cm ²	500-1400 Pa	With the mass flow rate of the hot side of 0.1667 g/s
	Aluminum/Rect	Water	m: 0.2043–0.401g/s	q: 14.3 – 17.8 W/cm ² ξ : 13.9-21.7 W/kPa		With the mass flow rate of the hot side of 0.2321 g/s

(Note: Rect- Rectangular, Q-heat transfer rate, q -heat flux, R-thermal resistance, h-heat transfer coefficient, K_v -volumetric heat transfer coefficient, \overline{Nu} -average Nusselt number, SLM-standard liter per minute, m-mass flow rate, V-volume flow rate, PDMS- polydimethylsiloxane, Z- nozzle-to-wall distance, L- distance from nozzle to the breakdown point of the jet, HE-heat exchanger), Kr-thermal conductivity ratio, and ξ - performance index)

Table 1. Summary of the microchannel heat exchangers with single phase flow [3,4].

also done by using Fluent CFD package. Hasan et al. [19] evaluated the effect of the size and shape of channels for a counter-flow microchannel heat exchanger by using Fluent CFD numerical simulation. The effect of various channels showed that the circular shape achieved the best overall performance, with the second being the square channels. Results obtained from the numerical analyses and the experimental data of [18, 19] were in good agreement with the maximum error being 5.1% and the maximum difference in wall temperature being 1.7 K. Ameel et al. [20] presented an overview of the miniaturization technologies and their applications to energy systems. Based on the MEMS (microelectromechanical systems) technologies, the processes (including silicon-based micromachining, deep X-ray lithography, and the micro mechanical machining) were discussed in the context of applications to fluid flow, heat transfer, and energy systems.

A study on the simulations of a trapezoidal shaped micro heat exchanger was presented by Dang et al. [21]. Using the geometric dimensions and the flow condition associated with this micro heat exchanger, a heat flux of 13.6 W/cm² was determined by the numerical method. The effects of flow arrangement on the heat transfer behaviors of a microchannel heat exchanger were presented by Dang et al. [22-25]. For all cases done in these studies, the heat flux obtained from the counter-flow arrangement was observed to be always higher than that obtained from the parallel-flow: the value obtained from the counter-flow was evaluated to be 1.1 to 1.2 times of that obtained from the parallel-flow. The authors also presented an experimental study of the effects of gravity on the behaviors of heat transfer and pressure drop of a microchannel heat exchanger. The results showed that for microchannel heat exchangers, the influence of gravity on the pressure drop and heat transfer behaviors was negligibly small [26, 27].

Dang and Teng [28, 29] studied the effects of the configuration (such as substrate thickness, cross-sectional area, and inlet/outlet location) on the behaviors of heat transfer and fluid flow of the microchannel heat exchangers. It was found that the actual heat transfer rate was observed to vary insignificantly with the substrate thickness in the range from 1.2 to 2 mm. Moreover, a comparison of the pressure drop and heat transfer behaviors between the microchannel and minichannel heat exchangers was done by Dang et al. [30]. Furthermore, numerical simulations of the microchannel heat exchangers using solver with the capability of dealing with steady-state and time-dependent conditions were carried out [31]. Numerical studies of the behaviors of the microchannel heat exchangers with 3D single-phase fluid flow and heat transfer in [22-26, 28-31] were done by using the COMSOL Multiphysics software, version 3.5. The algorithm of this software was based on the finite element method. The results obtained from the simulation were in good agreement with those obtained from the experiments, with the maximum percentage error being less than 9%.

To summarize, Table 1 listed the heat transfer and fluid flow behaviors for single phase microchannel heat exchangers [3, 4]. The heat exchangers were manufactured by different materials with a variety of shapes. Water was the most frequently used working fluid. The heat transfer coefficient and pressure drop were observed to be functions of the mass flow rate. The staggered microcolumn array and the micro-structured surface were found to enhance heat transfer rate in the micro heat exchangers. Because that the substrate thickness (between the hot and the cold channels) of micro heat exchangers was very thin, so the differences between the heat transfer rates obtained from these heat exchangers were negligibly small for several materials used in the studies.

From the above literatures, it is important to better understand the behaviors of heat transfer and pressure drop of the fluid through the microchannel heat exchangers in order to improve their design and optimize their performance. For the present study, single phase heat transfer and fluid flow phenomena obtained from experiments and numerical simulations for rectangular-shaped microchannel heat exchangers were investigated. In the following sections, five heat exchangers with different geometrical configurations will be discussed.

2. Experimental method

2.1 Experimental setup

Three major parts are used in the experimental system: the test section (the microchannel heat exchangers), syringe system, and overall testing loop, as shown in Fig. 2, with four microchannel heat exchangers being tested. The heat transfer process of these devices is carried out between two liquids which are hot water and cold water; the hot and cold fluids are flowing in the opposite directions.

Fig. 3 shows the dimensions of the test sections. The material used for the substrate of heat exchangers is aluminum, with thermal conductivity of 237 W/(mK), density of 2,700 kg/m³, and specific heat at constant pressure of 904 J/(kgK). For each microchannel heat exchanger, the top side for the hot water has 10 microchannels and the bottom side for the cold water also has 10 microchannels. The length of each microchannel is 32 mm. Microchannels have rectangular cross-section with the width and the depth being W_c and D_c , respectively.

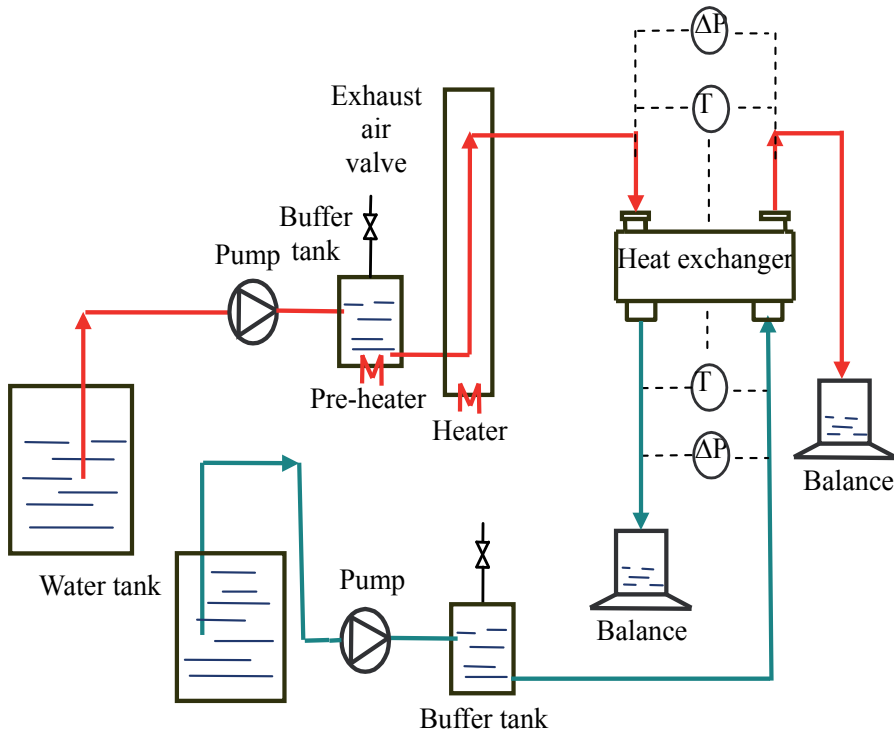
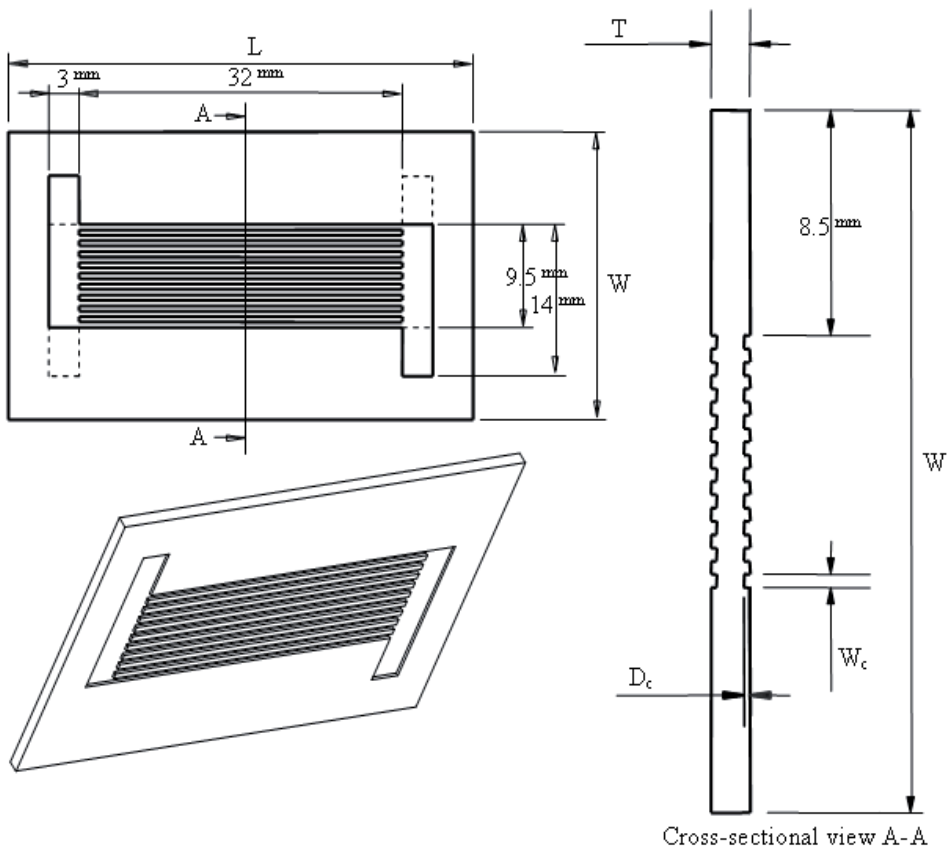


Fig. 2. Schematic of the test loop for the heat exchangers [3, 22-31].

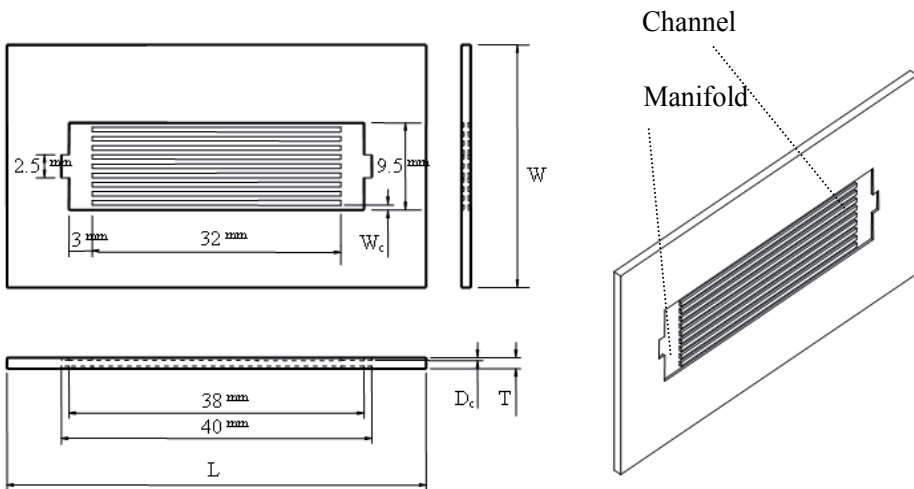
In a microchannel heat exchanger, all channels are connected by manifolds for the inlet and outlet of hot water and for those of cold water, respectively. The manifolds of the heat exchangers are of the same cross-sections: having a rectangular shape with a width of 3 mm and a depth of 300 μm . Figs. 3a and 3b show the dimensions of the S-types and I-type, respectively, with three S-types and one I-type being designed and manufactured and their dimensions listed in Table 2. Fig. 4 shows the photos of the microchannel heat exchangers with S-type and I-type manifolds. These test sections were manufactured by precision micromachining [20]. Each inlet hole or outlet hole of the heat exchangers has a cross-sectional area of 9 mm². The four sides of the heat exchanger were thermally insulated by the glass wool with a thickness of 5 mm. To seal the microchannels, two layers of PMMA (polymethyl methacrylate) were bonded on the top and bottom sides of the substrate by UV (ultraviolet) light process, as shown in Fig. 4. The physical properties of the PMMA and the glass wool are listed in Table 3 [32].

No.	Type	Dimensions of the substrate (mm)			Dimensions of the channel (μm)	
		L	W	T	W_c	D_c
T1	S- Type (Microchannel)	46	26.5	1.2	500	300
T2	S- Type (Microchannel)	46	26.5	2	500	300
T3	S- Type (Microchannel)	46	26.5	1.2	500	180
T4	I- Type (Microchannel)	54	26.5	2	500	300

Table 2. Geometric parameters of the microchannel heat exchangers [3, 25].



a) S-type



b) I-type

Fig. 3. Dimensions of the test samples.

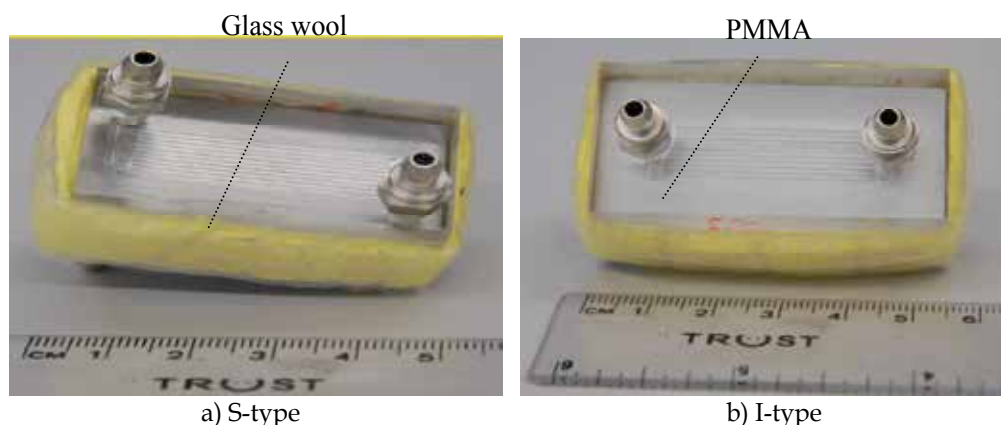


Fig. 4. Photos of the microchannel heat exchangers being tests.

Material	Density kg/m^3	Thermal conductivity W/(mK)
PMMA	1420	0.19
Glass wool	154	0.051

Table 3. Physical properties of the PMMA and the glass wool [32].

Experimental data for the microchannel heat exchanger were obtained under the constant room temperature of 25 – 26 °C. DI water (deionized water) was used as the working fluid. Each inlet or outlet of the heat exchanger has a set of two thermocouples to record the temperature values, and there are eight thermocouples in total. At each side, a differential pressure transducer was used to measure the pressure drop. To assess the accuracy of measurements presented in this work, the uncertainty values for measured parameters are listed in Table 4. In addition, the uncertainties on the dimensions of microchannel evaluated by using a scanning laser made by Mitaka/Ryokosha model NH-3. The uncertainties of the scanning laser were estimated to be $\pm 0.03 \mu\text{m}$. Equipments used for the experiments are listed as follows [3, 22-31]:

1. Thermocouples, T-type
2. Pump, Model PU-2087, made by Jasco
3. Pump, VSP-1200, made by Tokyo Rikakikai
4. Heater, Model AXW-8, made by Medilab
5. Differential pressure transducer, Model PMP4110, made by Duck
6. Micro electronic balance, Model TE-214S, made by Sartorius.

Parameter	Uncertainty
Temperature	$\pm 0.1 \text{ } ^\circ\text{C}$
Pressure	$\pm 0.025\% \text{ FS}$
Mass flow rate	$\pm 0.0015 \text{ g}$
Channel height	$\pm 7 \mu\text{m}$
Channel width	$\pm 10 \mu\text{m}$
Channel length	$\pm 70 \mu\text{m}$

Table 4. Uncertainty data for measured parameters.

2.2 Analysis of data

In the following analyses, five assumptions were made:

- The fluid flow is laminar
- The fluid flow is incompressible and continuum
- Heat transfer is steady
- Radiation heat transfer is negligible
- Four heat exchangers were designed and fabricated by a precision micromachining process; as a result of this manufacturing process, roughness of microchannels was of the same order.

For the experiments carried out in this study, the effects of various parameters on the heat transfer and fluid flow – such as heat flux, effectiveness, pressure drop, and performance index – of the heat exchangers are discussed as follows.

The maximum heat transfer rate, Q_{max} , is evaluated by

$$Q_{max} = (mc)_{\min} (T_{h,i} - T_{c,i}) \quad (1)$$

The heat transfer rate of the heat exchanger, Q , is calculated by

$$Q_c = m_c c_c (T_{c,o} - T_{c,i}) \quad (2)$$

The effectiveness (NTU method) is determined by

$$\varepsilon = \frac{Q_c}{Q_{max}} \quad (3)$$

Heat flux is calculated by

$$q = \frac{Q_c}{A} = \frac{m_c c_c (T_{c,o} - T_{c,i})}{nL_c W_c} \quad (4)$$

or

$$q = k \Delta T_{lm} = \frac{\Delta T_{lm}}{\Sigma R} \quad (5)$$

The overall thermal resistance ΣR is determined by

$$\Sigma R = R_{cond} + R_{conv} \quad (6)$$

The log mean temperature difference is calculated by

$$\Delta T_{lm} = \frac{\Delta T_{\max} - \Delta T_{\min}}{\ln \frac{\Delta T_{\max}}{\Delta T_{\min}}} \quad (7)$$

where m is mass flow rate (subscripts h and c stand for the hot side and cold side, respectively), n is number of microchannels, c is specific heat, $T_{h,i}$, $T_{h,o}$, $T_{c,i}$ and $T_{c,o}$ are inlet

and outlet temperatures of the hot and cold side, respectively, q is heat flux, A is heat transfer area, k is overall heat transfer coefficient, $R_{cond} = \delta / \lambda$ is conductive thermal resistance, $R_{conv} = 1 / h_h + 1 / h_c$ is convective thermal resistance, h_h and h_c are the convective heat transfer coefficients of the hot side and the cold side, respectively, δ is thickness of heat transfer, λ is thermal conductivity, and ΔT_{lm} is the log mean temperature difference.

The Reynolds number is calculated by:

$$\text{Re} = \frac{\rho w D_h}{\mu} = \frac{2m}{\mu(W_c + D_c)} \quad (8)$$

The pressure drop due to friction is determined by [33,34]:

$$\Delta p = 2f \rho w^2 \frac{L}{D_h} = 2f \text{Re} \frac{L}{D_h^2} w \mu \quad (9)$$

where $D_h = 4A_c / P$ is the hydraulic diameter, w is velocity in the z -direction, μ is dynamic viscosity, ρ is density, A_c is cross-sectional area, P is wetted perimeter, L is channel length, and f is Fanning friction factor.

The total pressure drop of the heat exchanger is given by

$$\Delta p_t = \Delta p_h + \Delta p_c \quad (10)$$

where Δp_h and Δp_c are pressure drops of hot and cold sides, respectively.

The performance index, ξ , is determined by [19, 25]

$$\xi = \frac{Q_c}{\Delta p_t} = \frac{m_c c_c (T_{c,o} - T_{c,i})}{\Delta p_h + \Delta p_c} \quad (11)$$

The experimental uncertainties were estimated, following the method described by Holman [35]; the final expressions for uncertainties were given as follows:

$$\frac{U_q}{q} = \left[\left(\frac{\partial m_c}{m_c} \right)^2 + \left(\frac{\partial c_c}{c_c} \right)^2 + \left(\frac{\partial T_{c,o} + \partial T_{c,i}}{T_{c,o} + T_{c,i}} \right)^2 + \left(\frac{\partial W_c}{W_c} \right)^2 + \left(\frac{\partial L_c}{L_c} \right)^2 \right]^{1/2} \quad (12)$$

$$\frac{U_k}{k} = \left[\left(\frac{\partial m_c}{m_c} \right)^2 + \left(\frac{\partial c_c}{c_c} \right)^2 + \left(\frac{\partial T_{c,o} + \partial T_{c,i}}{T_{c,o} + T_{c,i}} \right)^2 + \left(\frac{\partial W_c}{W_c} \right)^2 + \left(\frac{\partial L_c}{L_c} \right)^2 + \left(\frac{\partial T_{h,i}}{T_{h,i}} \right)^2 + \left(\frac{\partial T_{h,o}}{T_{h,o}} \right)^2 + \left(\frac{\partial T_{c,i}}{T_{c,i}} \right)^2 + \left(\frac{\partial T_{c,o}}{T_{c,o}} \right)^2 \right]^{1/2} \quad (13)$$

$$\frac{U_{\text{Re}}}{\text{Re}} = \left[\left(\frac{\partial m}{m} \right)^2 + \left(\frac{\partial \rho}{\rho} \right)^2 + \left(\frac{\partial \mu}{\mu} \right)^2 + \left(\frac{\partial W_c}{W_c} \right)^2 + \left(\frac{\partial D_c}{D_c} \right)^2 \right]^{1/2} \quad (14)$$

$$\frac{U_{\varepsilon}}{\varepsilon} = \left[\left(\frac{\partial m_c}{m_c} \right)^2 + \left(\frac{\partial c_c}{c_c} \right)^2 + \left(\frac{\partial m}{m} \right)^2 + \left(\frac{\partial c}{c} \right)^2 + \left(\frac{\partial T_{c,o} + \partial T_{c,i}}{T_{c,o} + T_{c,i}} \right)^2 + \left(\frac{\partial T_{h,i} + \partial T_{c,i}}{T_{h,i} + T_{c,i}} \right)^2 \right]^{1/2} \quad (15)$$

$$\frac{U_{\xi}}{\xi} = \left[\left(\frac{\partial m_c}{m_c} \right)^2 + \left(\frac{\partial c_c}{c_c} \right)^2 + \left(\frac{\partial T_{c,o} + \partial T_{c,i}}{T_{c,o} + T_{c,i}} \right)^2 + \left(\frac{\partial \Delta p_h}{\Delta p_h} \right)^2 + \left(\frac{\partial \Delta p_c}{\Delta p_c} \right)^2 \right]^{1/2} \quad (16)$$

By using the estimated errors of parameters listed in Table 3, the maximum experimental uncertainties in determining q , k , Re , ε , and ξ were 2.1%, 2.2%, 3.1%, 0.9%, and 3.3%, respectively, for all cases being studied.

3. Numerical simulation

Numerical study of the behavior of the microchannel heat exchanger with 3D single-phase fluid flow and heat transfer was done by using the COMSOL Multiphysics software, version 3.5. The algorithm of this software was based on the finite element method. For the COMSOL package, the generalized minimal residual (GMRES) method was used to solve for the model used in this study; the GMRES method was an iterative method for general linear systems. At every step, the method performed minimization of the residual vector in a Krylov subspace [32], and the Arnoldi iteration was used to find this residual vector. To improve the convergence of the iterative solver used by the GMRES method, the Incomplete LU (lower-upper) pre-conditioner was selected for nonsymmetric systems, where LU is a matrix which was the product of a lower triangular matrix and an upper triangular matrix. For the study, water was used as the working fluid. With the mass flow rate of water from 0.1667 to 0.8540 g/s, the Reynolds number was lower than 400 and the working fluid in the microchannels of the heat exchanger was under laminar flow condition [2]. No internal heat generation was specified, resulting in $Q_i = 0$. The finite elements in the grid meshes were partitioned to be triangular, as shown in Fig. 5. The maximum element size scaling factor was 1.9, with element growth rate of 1.7, mesh curvature factor of 0.8, and mesh curvature cut-off of 0.05. In Fig. 4, the schematic meshing of the heat exchanger consists of 26,151 mesh elements, the number of degrees of freedom is 76,411, and a relative tolerance is 10^{-6} .

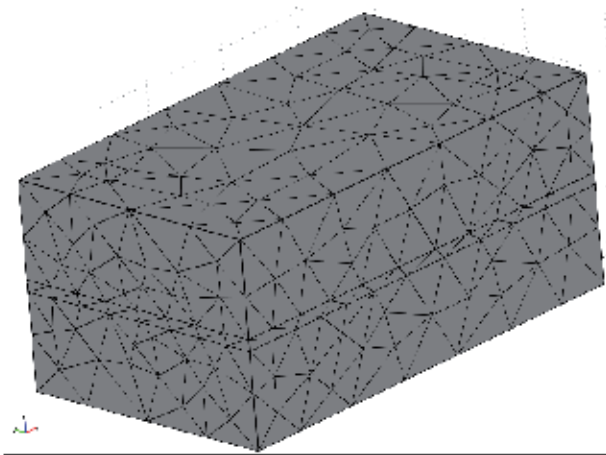


Fig. 5. Grid mesh diagram of the microchannel heat exchanger.

4. Results

4.1 Effects of fluid properties

For the effects of fluid properties on heat transfer and fluid flow behaviors, the microchannel heat exchanger T1 was tested; the results were shown more in detail by Dang et al. [26]. The parameters of heat exchangers are listed in Table 2.

Flow rate and inlet temperature being constant for the cold side

For experiments carried out in the study, the inlet temperature and mass flow rate of the cold side were fixed at 26.5 °C and 0.1773 g/s, respectively. For the hot side, an inlet temperature was fixed at 52 °C and the mass flow rates were varying from 0.1841 to 0.3239 g/s. The thermal boundary conditions of the top and bottom walls of the heat exchanger were assumed to be constant heat flux. The convective heat transfer coefficient between the wall and the ambient used for this solver was 10 W/(m²K), with the ambient temperature and air velocity of 26 °C and 0.2 m/s, respectively. The temperature profile of the microchannel heat exchanger is shown in Fig. 6 for a mass flow rate of 0.2556 g/s at the hot side.

At a constant inlet temperature of 52 °C at the hot side, for the case with both mass flow rate and temperature constant at the inlet of cold side, a relationship between the outlet temperatures (for both the hot side and cold side) and the mass flow rate of the hot side is shown in Fig. 7a. The outlet temperatures increase as the mass flow rate of the hot side increases. Because that the heat exchanger under study is the one with counter-flow, the outlet temperature of the cold side is higher than that obtained at the hot side [22-24]. A comparison between the numerical and experimental results is also shown in Fig. 7a. Fig 7a shows the outlet temperatures as a function of the mass flow rate of the hot side, and the results obtained from the simulation are in good agreement with those obtained from the experiments. The maximum difference of the outlet temperatures is 0.8 °C and the maximum percentage error is 2%.

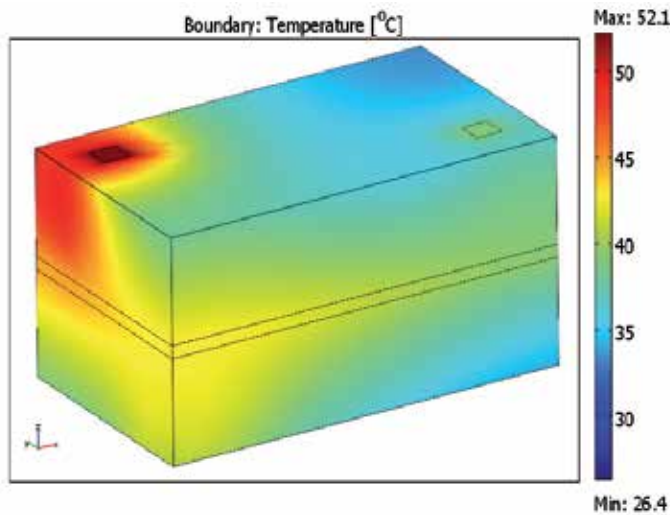


Fig. 6. The temperature profile of the microchannel heat exchanger.

At the condition stated above, the heat transfer rates of the hot side and cold side increase with rising mass flow rate of the hot side, as shown in Fig. 7b. The maximum difference of the heat transfer rate between the numerical results and experimental data is 1.08 W and the maximum percentage error is 7.3%. However, it is observed that the heat transfer rate for the hot side increases at a higher slope than that for the cold side as the mass flow rate increases. It is also observed that the actual effectiveness for the microchannel heat exchanger decreases with rising mass flow rate of the hot side, as shown in Fig. 7c. This means that the heat loss increases with rising flow rate of the hot side. Fig. 7c shows a relation of effectivenesses (actual effectiveness and NTU effectiveness) as a function of the mass flow rate of the hot side.

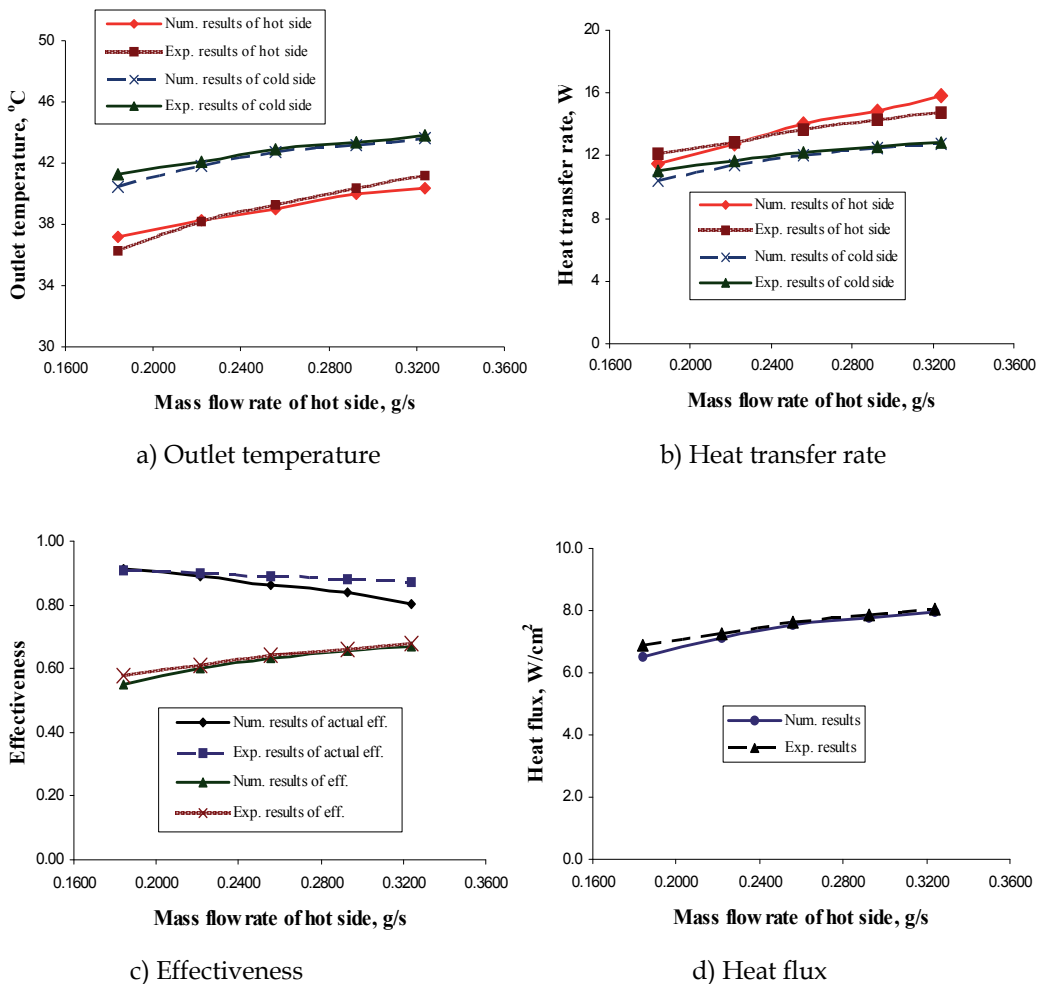


Fig. 7. A comparison between numerical and experimental results at constant inlet temperature and mass flow rate for the cold side.

Because that the inlet temperatures of both sides are fixed at constant values and that the heat capacity rate $(mc)_{min}$ is fixed, the maximum heat transfer Q_{max} is fixed at a constant

value, as shown in Eq. (6). When the mass flow rate of the hot side is increased, the heat transfer rate Q of the heat exchanger increases also. As a result, heat transfer obtained from the effectiveness increases with a rising the mass flow rate at the hot side. The trends of effectiveness and actual effectiveness are observed to be in the opposite directions, as shown in Fig. 7c.

The results obtained from numerical simulation and from experimental data for the actual effectiveness and for the effectiveness are compared also. Fig. 7c indicates that at various mass flow rates of the hot side, the heat transfer results obtained from the actual effectivenesses are higher than those obtained from the effectivenesses. The maximum difference of the effectivenesses between the two occurs at high mass flow rate of the hot side, with the maximum difference of 0.7 and the maximum percentage error of 8.7 %. This difference may be due to errors in the experiments or mesh generation in the numerical simulations. It is noted that experimental results of effectiveness obtained from this study are higher than those obtained from Kang and Tseng [6].

Again, at the condition stated above, the heat flux of the microchannel heat exchanger increases from 5.8 to 8.0 W/cm² with a rising the mass flow rate of the hot side ranging from 0.1841 to 0.3239 g/s, as shown in Fig. 7d. A comparison between the numerical and experimental results for the heat flux at various mass flow rates of the hot side is shown in Fig. 7d. Since the heat flux obtained from the simulation is only slightly higher than that obtained from the experiment, the results obtained from the simulation are judged to be in good agreement with those obtained from the experiments. The maximum difference of heat fluxes is 0.40 W/cm²; it occurs at low mass flow rate of the hot side, and the maximum percentage error is 7.2%. This difference may be due to errors in the experiments or mesh generation in the numerical simulations also. The heat flux obtained from this study is higher than that obtained from [5]; the latter has the heat flux increasing from 0.2 to 1.1 W/cm² and the mass flow rate increasing from 2.7 to 111.1 g/s. However, due to the variation in presenting data, it is difficult to make a complete comparison between the results obtained from the present study and those obtained from [5] and [7].

To summarize, for this case with the results presented in Figs. 7a-7d, the trends for actual effectiveness and effectiveness indicate that as the mass flow rate of hot side goes up, the former goes down while the latter goes up; this is an important effect observed for the microchannel heat exchanger used in the study.

Flow rate and inlet temperature being constant for the hot side

For this case, the inlet temperature and mass flow rate of the hot side were fixed at 52 °C and 0.1667 g/s, respectively. For the cold side, an inlet temperature was fixed at 26.5 °C and the mass flow rates were varying from 0.1859 to 0.3625 g/s. Fig. 8a shows a relationship between the outlet temperatures (for both the hot side and cold side) and the mass flow rates of the cold side at the condition stated above. Contrary to the category of cases of constant mass flow rate and inlet temperature for the cold side, the outlet temperatures decrease as the mass flow rate of the cold side increases. A comparison between the results obtained from numerical simulation and experimental data for the outlet temperatures of both the hot side and the cold side is shown in Fig. 8a. The maximum difference between the two results is 0.4 °C, occurring at low mass flow rate of cold side, with the maximum percentage error of 1.2%.

It is observed that with a rising the mass flow rate of the cold side, the outlet temperatures decrease, as shown in Fig. 8a; however, for the same flow rate condition, both the heat transfer rates of the hot side and cold side increase. As the mass flow rate of the cold side increases, the heat transfer rate for the cold side increases at a slightly higher rate than that for the hot side. It is also observed that the actual effectiveness for the microchannel heat exchanger increases with a rising the mass flow rate of the cold side, as shown in Fig. 8b. The results obtained from the effectiveness (NTU method) are lower than those obtained from the actual effectiveness, as shown in Fig. 8.b. Hence, a conclusion can be drawn for the heat exchanger under study: at constant inlet temperature and mass flow rate of the hot side, it is more effective to use the heat exchanger with high mass flow rate of cold side. However, leakage of liquid out of the microchannel heat exchanger can occur when the mass flow rate of the cold side increases above 0.854 g/s, as a result of the excessive pressure exerted on the system under study.

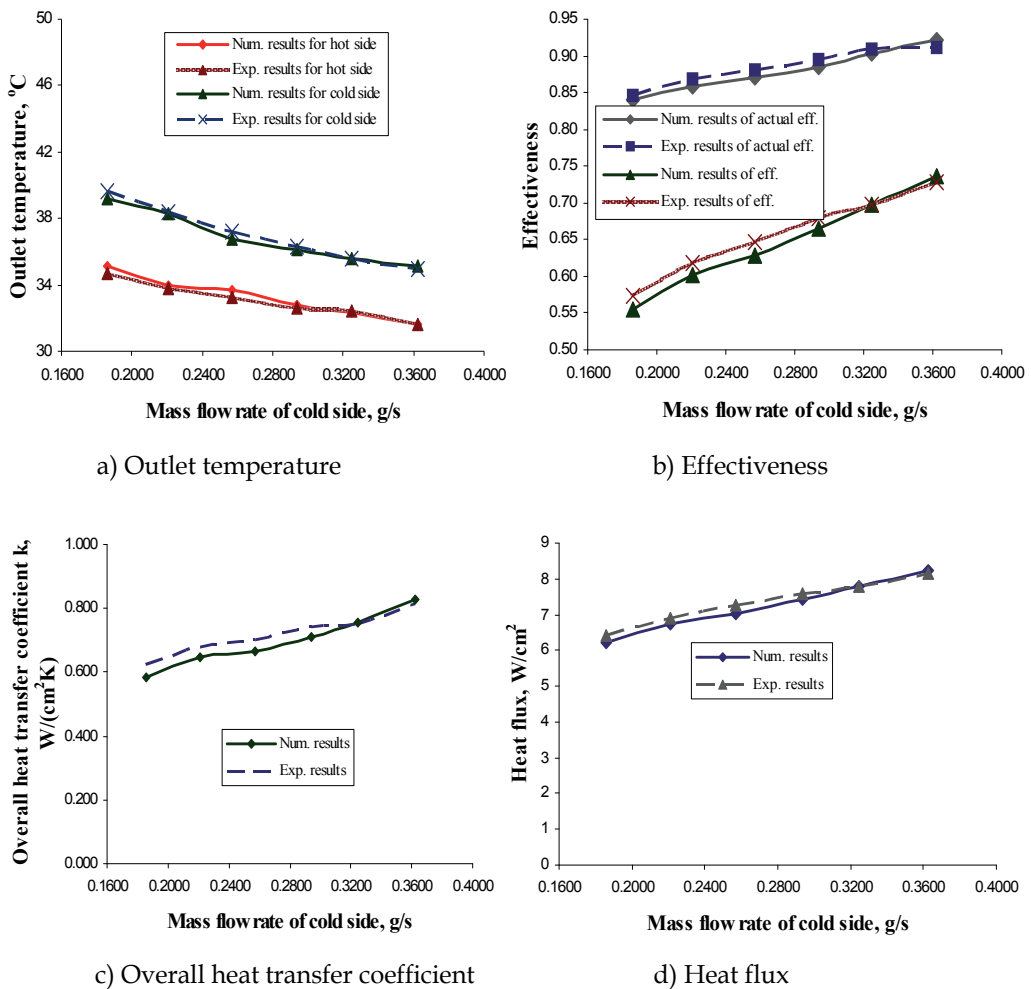


Fig. 8. Comparison between numerical and experimental results at constant inlet temperature and mass flow rate for the hot side.

At the condition stated above, the overall heat transfer coefficient k of the heat exchanger increases from 0.625 to 0.815 W/(cm²K) with the mass flow rate of cold side rising from 0.1859 to 0.3625 g/s, as shown in Fig. 8c. At a hydraulic diameter of 375 μ m, Kandlikar et al. [44] gave $k = 0.85$ W/(cm²K), compared to $k = 0.815$ W/(cm²K) obtained in this study. Thus, the two results are in good agreement. For this case, the change in the log mean temperature difference is small: it reduces from 10.7 to 10.0 °C with the mass flow rate of cold side rising from 0.1859 to 0.3625 g/s. The heat flux increases from 6.2 to 8.2 W/cm² with the mass flow rate of cold side rising from 0.1859 to 0.3625 g/s, as shown in Fig. 8d. Thus, the heat flux affected by the log mean temperature difference is less than that by the overall heat transfer coefficient (7.0% versus 30.4% on a percentage basis). Comparisons between the results obtained from numerical simulation and experimental data for the outlet temperature, the effectiveness, the overall heat transfer coefficient, and the heat flux at various mass flow rates of the cold side are shown in Figs. 8a-8d, respectively, with the maximum percentage error being less than 7.2%.

Fluid behaviors

The boundary conditions of the two outlets of the hot side and the cold side are at the atmospheric pressure. Fig. 9 shows the velocity field along channels of the microchannel heat exchanger. The streamlines of water pass from the microchannels to the manifold. At the edge between channels and manifold, the streamlines appear to be curved in shape. The velocity field at the outlet of the manifold is parabolic which is consistent with that predicted by the laminar flow theory for fluid in a channel.

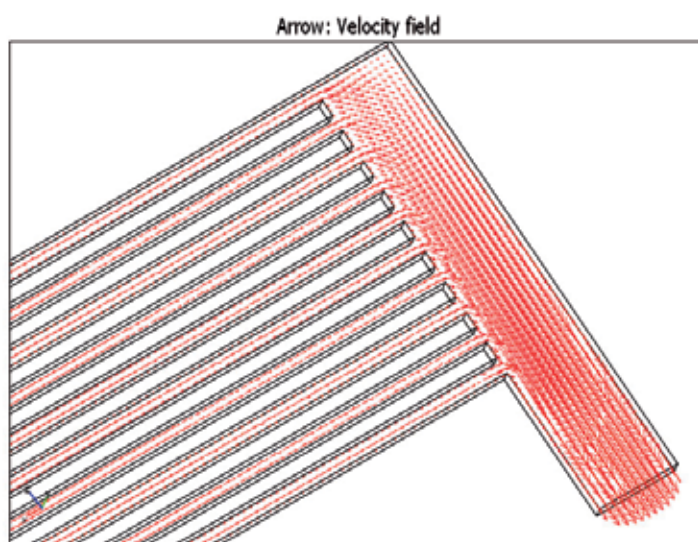


Fig. 9. The velocity field along channels of the microchannel heat exchanger.

Fig. 10 shows the pressure distribution in channels of the hot side at the mass flow rate of 0.2321 g/s and the inlet temperature of 45 °C. The pressure decreases gradually from the first channel to the last one, with the first channel being the nearest one to the entrance of the inlet of the manifold [25, 26].

For microchannel heat exchanger used in this study, at an inlet temperature of 25 °C, the pressure drop increases from 889 to 4,411 Pa, with the mass flow rate rising from 0.1812 to 0.8540 g/s. In addition, the pressure drop decreases as the inlet temperature increases, since as the inlet temperature increases, the dynamic viscosity decreases. Because that the Poiseuille number ($Po = f Re$) depends only on the geometry of the microchannel, the pressure drop decreases with a rising inlet temperature of water. This conclusion is in agreement with [6]. Fig. 11 shows the pressure drop obtained experimentally as a function of the inlet water temperature for various mass flow rates. At a mass flow rate of 0.4972 g/s, the pressure drop decreases from 2,437 to 1,776 Pa, with the inlet temperature rising from 25 °C to 52 °C.

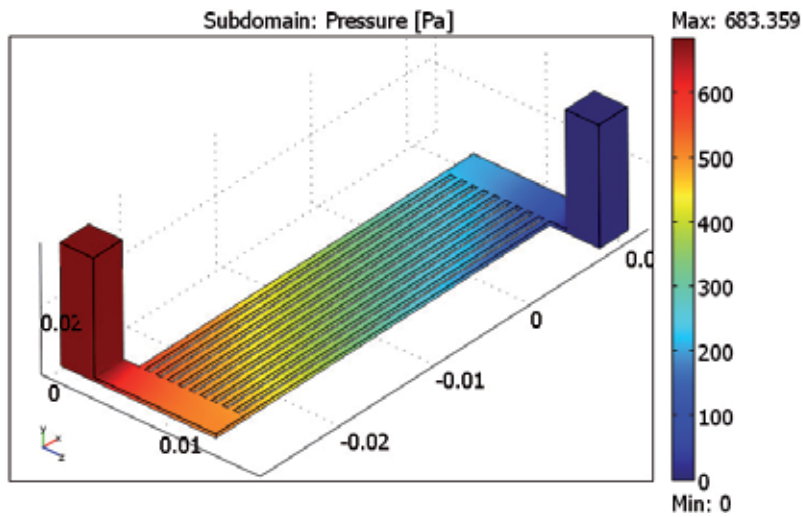


Fig. 10. Pressure distribution of the hot side of the heat exchanger.

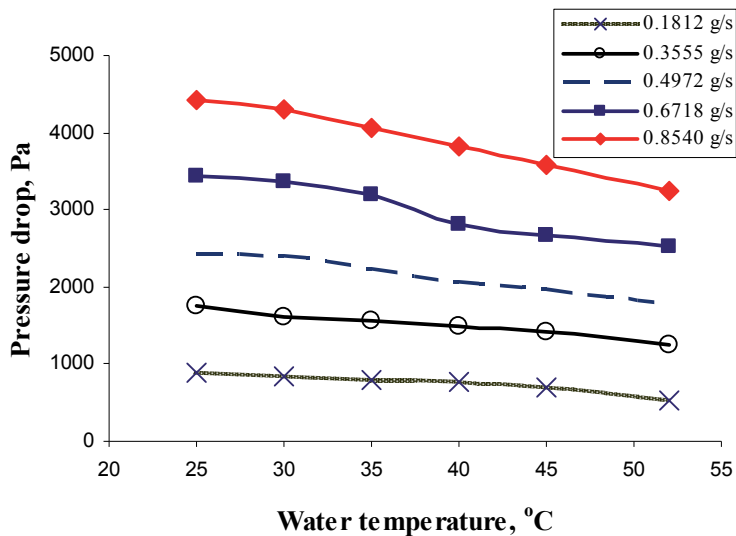


Fig. 11. Pressure drop as a function of the inlet water temperature for various mass flow rates.

Fig. 12 shows a comparison between numerical and experimental results for the pressure drops and the mass flow rates at various inlet water temperatures. As shown in the figure, the pressure drop decreases as the inlet water temperature increases. The maximum difference between the two results obtained is 131 Pa, with a maximum percentage error of 7.8%.

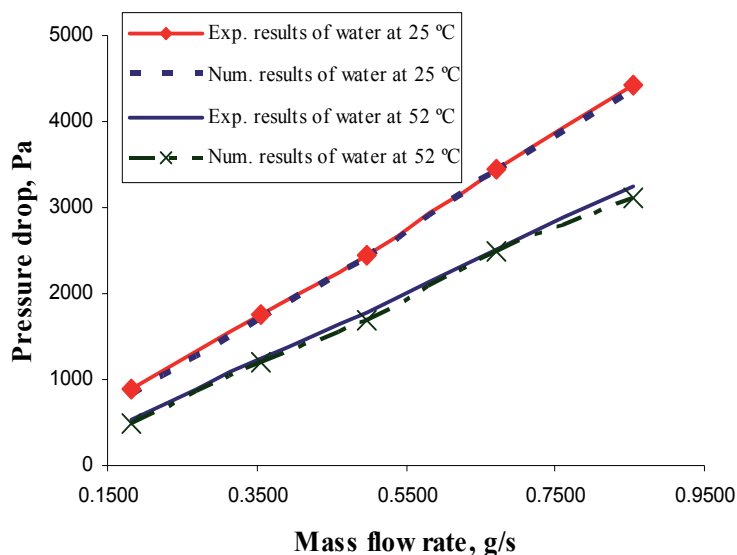


Fig. 12. Comparison between numerical and experimental results for the pressure drop and the flow rate at various inlet water temperatures.

Under various conditions for all cases studied up to now, the maximum percentage errors between the results obtained from numerical simulations and those from experimental data are found to be less than 9% and are in good agreement.

4.2 Effects of flow arrangements

For this section, single-phase heat transfer and fluid flow phenomena obtained from experimental data and numerical simulations for the microchannel heat exchanger T1 were investigated. Two cases of flow arrangements will be discussed for the heat exchanger under investigation: (1) the counter-flow arrangement and (2) the parallel-flow arrangement. The dimensions of this microchannel heat exchanger are shown in Fig 3 and its geometric parameters are listed in Table 2. The conditions of the numerical simulation and experimental data are indicated in more detail in [3, 22-25].

For the experiments carried out in this section, the inlet temperature and the mass flow rate of the cold side were fixed at 22.5 °C and 0.2043 g/s, respectively. For the hot side, the mass flow rate was fixed at 0.2321 g/s and the inlet temperatures were varying from 45 to 70 °C (Dang et al. [26]). The thermal boundary conditions of the top and bottom walls of the heat exchanger are assumed to be constant heat flux. The temperature profile of the microchannel heat exchanger is shown in Fig. 13 for the inlet temperature of 45 °C at the hot

side. Fig. 13a and Fig. 13b show the temperature profiles for the cases with counter-flow and parallel-flow at the conditions specified above.

The 3D temperature profiles of the microchannel heat exchanger were shown in more detail in [24-26] also. Profiles of the temperature gradients shown in Fig. 14 indicate the temperature gradients from heat exchanger's cold region towards its hot region, with Fig. 14a being the counter-flow and Fig. 14b being the parallel-flow. Distribution of the temperature gradients varies along the channel length of the heat exchanger with counter-flow and parallel-flow configurations. In the middle of the heat exchanger with counter-flow arrangement, the temperature gradients are in fishbone shapes. However, the temperature gradients are in the perpendicular direction towards the substrate of the heat exchanger with parallel-flow arrangement.

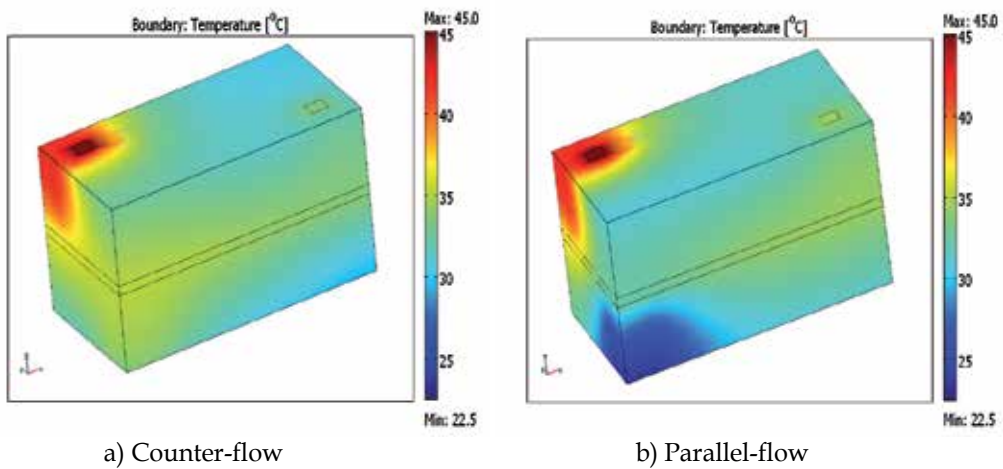


Fig. 13. Temperature profiles of the microchannel heat exchanger.

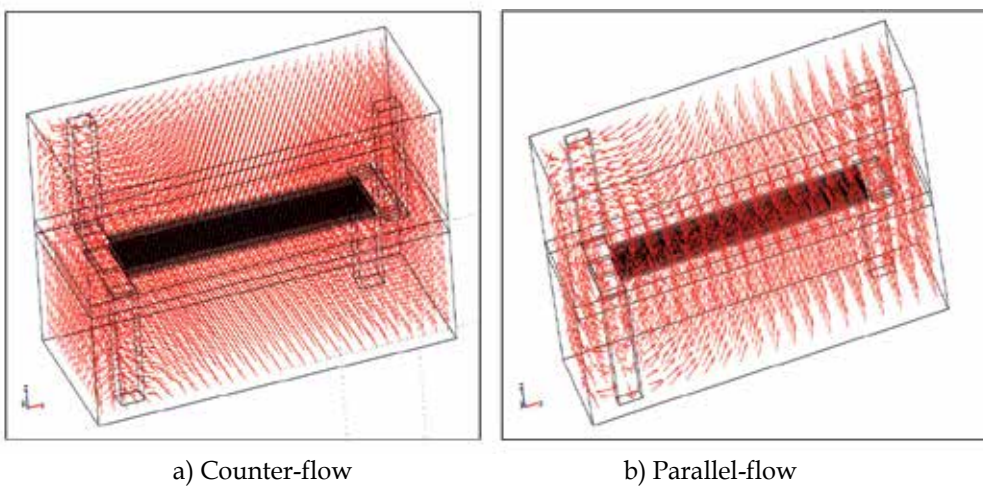


Fig. 14. The profiles of temperature gradients of the microchannel heat exchanger.

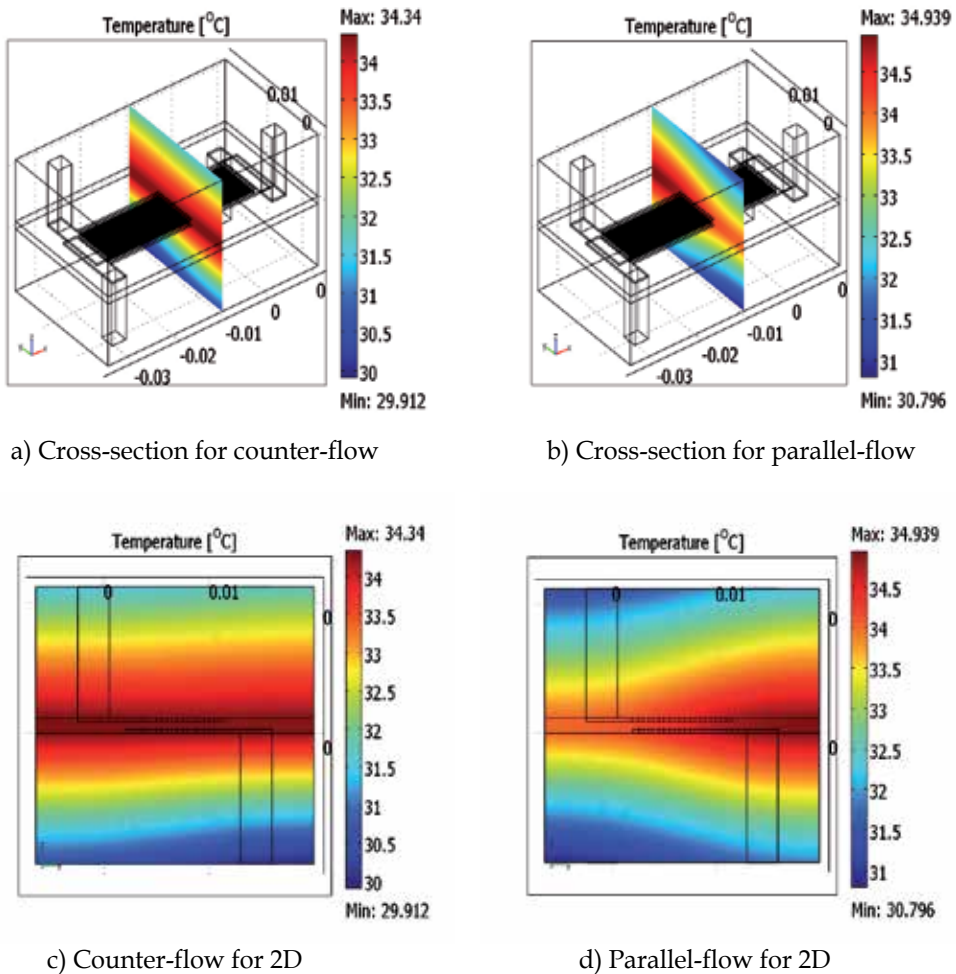


Fig. 15. Temperature profiles of a cross-section of the microchannel heat exchanger.

The temperature profiles of the microchannel heat exchanger are shown in Fig. 15 for the inlet temperature of 45 °C at the hot side at the cross-section through three points: (-0.01, 0.02, -0.02), (-0.01, 0.02, 0.00), and (-0.01, 0, 0.00). Fig. 15a and Fig. 15b show the temperature profiles of the cross-section in the microchannel heat exchanger for the cases with counter-flow and parallel-flow at the conditions specified above. At this cross-section, it is observed that the temperature profiles varying along the distance measured from the substrate for counter-flow arrangement are more evenly distributed (as shown in Fig. 15c) than those for parallel-flow arrangement with the hot temperature region skewed to the right-side of the microchannel, as shown in Fig. 15d.

As a result, the range of temperature gradient obtained from counter-flow arrangement is smaller than that obtained from parallel-flow one. For the counter-flow one, the temperature gradients obtained numerically ranging from 50.3 to 529.1 K/m, as shown in Fig. 16a. However, the range is from 16.6 to 574 K/m for parallel-flow one, as shown in Fig. 16b. The

profiles of the temperature gradients in 3D and in these three planes (x-y, y-z, and z-x planes) for the whole subdomains of the heat exchanger were shown in more detail in [24-26].

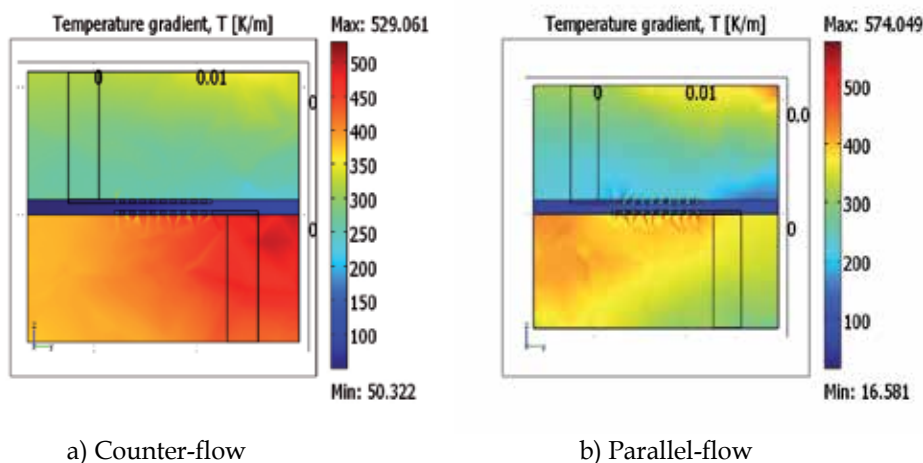


Fig. 16. Profiles of 2D temperature gradients of the microchannel heat exchanger.

Under the condition stated above, the inlet temperature and the mass flow rate of the cold side were fixed at 22.5 °C and 0.2043 g/s, respectively. For the hot side, the mass flow rate was fixed at 0.2321 g/s and the inlet temperatures were varying from 45 to 70 °C [22-25]. A relationship of the experimental results between the counter-flow and the parallel-flow cases is shown in Fig. 17.

For the counter-flow case, the outlet temperature at the cold side is higher than that obtained at the hot side (see Fig. 17a). However, for the parallel-flow case, the outlet temperature at the cold side is lower than that obtained at the hot side. As a result, the heat transfer rate obtained from the counter-flow arrangement is higher than that obtained from the parallel-flow arrangement of the microchannel heat exchanger, as shown in Fig. 17b. It is noted that to compute the heat transfer rates for an adiabatic heat exchanger, these rates were based on those of the cold side. Fig. 17c shows the comparison of pressure drops of both cases for the counter- and parallel-flow arrangements. It is observed that the pressure drop obtained from the hot side is higher than that obtained from the cold side; this is consistent with the fact that the mass flow rate of the hot side is also higher than that of the cold side. It is also observed that the pressure drop obtained from the counter-flow arrangement is the same as that obtained from parallel-flow one. As a result, the performance index obtained from the counter-flow arrangement is higher than that obtained from the parallel-flow one: the value obtained from the counter-flow is 1.192 to 1.2 times of that obtained from the parallel-flow, as shown in Fig. 17d.

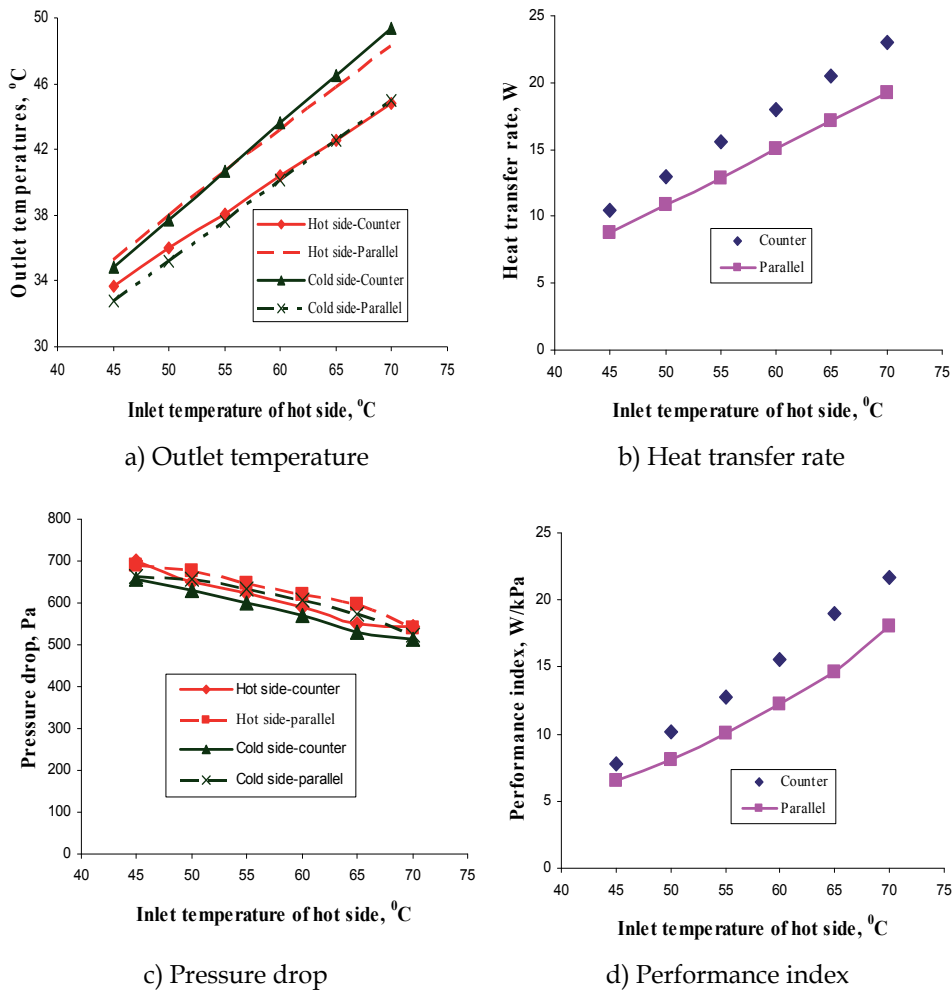


Fig. 17. Comparison of the experimental results between the counter-flow and parallel-flow.

When the inlet temperature of the hot side is increased, the heat transfer rate Q of the heat exchanger increases also. As a result, the heat transfer result obtained from the effectiveness (NTU method) increases with rising inlet temperature at the hot side, as shown in Fig. 18a. The figure shows a comparison between numerical and experimental results of the effectiveness (NTU method) for the microchannel heat exchanger with counter-flow arrangement. The maximum difference of the effectiveness is 0.009; it occurs at low inlet temperature of the hot side, and the maximum percentage error is 1.6%. Fig. 18b shows the comparison of the performance indexes between the numerical and experimental results for the case with counter-flow arrangement. Since the performance index obtained from the simulation is in the vicinity of that obtained from the experiment, the results obtained from the simulation are judged to be in good agreement with those obtained from the experiments. The maximum difference of the performance index is 0.413 W/kPa; it occurs at low inlet temperature of the hot side for the counter-flow arrangement, and the maximum percentage error is 5.3%.

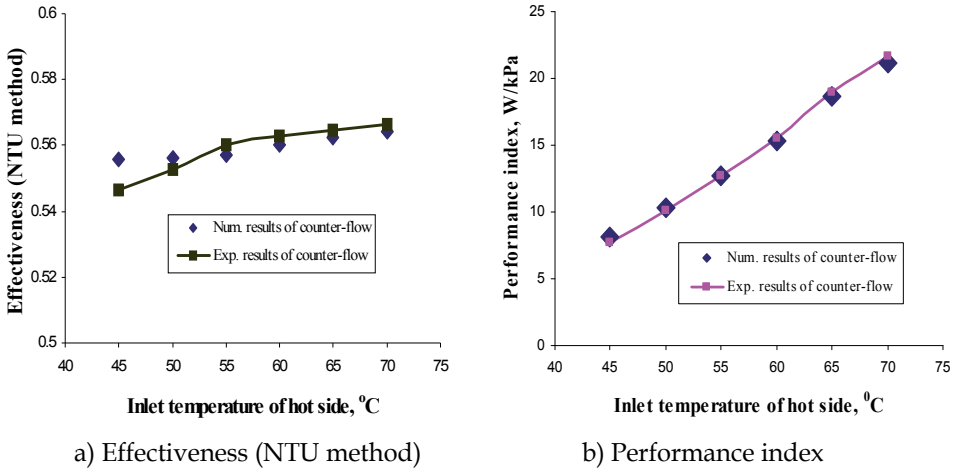


Fig. 18. Comparison between numerical and experimental results.

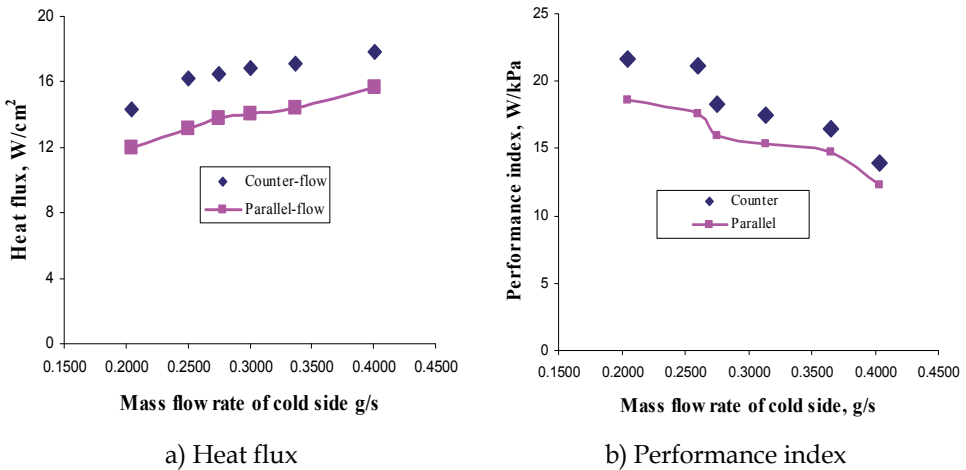


Fig. 19. Comparison of the experimental results with a rising mass flow rate of the cold side.

Under another experimental condition, for the experiments done in this study, the inlet temperature and the mass flow rate of the hot side were fixed at 70 °C and 0.2321 g/s, respectively. For the cold side, the inlet temperature was fixed at 22.5 °C and the mass flow rates were varying from 0.2043 to 0.401 g/s. The outlet temperatures are a function of the mass flow rate at the cold side, as shown in more detail in [22-25]. Contrary to the case of varying inlet temperature of the hot side, the outlet temperatures decrease as the mass flow rate of the cold side increases. For the counter-flow case, the outlet temperature of the cold side is higher than or equal to that obtained at the hot side. However, for the parallel-flow case, the outlet temperature at the cold side is lower than that obtained at the hot side. As a result, for the microchannel heat exchanger, the heat flux obtained from the counter-flow arrangement is higher than that obtained from the parallel-flow arrangement, as shown in Fig. 19a. The heat flux of 17.81×10^4 W/m² (or 17.81 W/cm²) was achieved for water from the

hot side of the device having the inlet temperature of 70 °C and mass flow rate of 0.2321 g/s and for water from the cold side having the inlet temperature of 22.5 °C and mass flow rate of 0.401 g/s.

Fig. 19b shows the comparison of the performance indexes between the counter- and parallel-flow arrangements. The performance index obtained from the counter-flow arrangement is higher than that obtained from the parallel-flow one: the value obtained from the counter-flow is 1.13 to 1.17 times of that obtained from the parallel-flow. The performance index of 21.69 W/kPa was achieved for water from the hot side of the device having the inlet temperature of 70 °C and the mass flow rate of 0.2321 g/s and for water from the cold side having the inlet temperature of 22.5 °C and the mass flow rate of 0.401 g/s.

4.3 Effects of geometrical configurations

In order to study the effects of geometrical configurations on the performance of the heat exchangers, all experimental conditions for the four microchannel heat exchangers were kept the same, more detail in [28,29]. Throughout the section, two cases of testing were discussed: the first one for increasing the inlet temperature of the hot side and the second for increasing the mass flow rate of the cold side. Further details of these cases are as follows:

1. Case No. 1 is for the case of increasing the inlet temperature of the hot side: the inlet temperature and the mass flow rate of the cold side were fixed at 22.5 °C and 0.2135 g/s, respectively; at the hot side, the mass flow rates was fixed at 0.2308 g/s and the inlet temperature were varying from 45 to 70 °C.
2. Case No. 2 is for the case of increasing the mass flow rate of the cold side: the inlet temperature and the mass flow rate of the hot side were fixed at 70 °C and 0.2308 g/s, respectively; at the cold side, the inlet temperature was fixed at 22.5 °C and the mass flow rates were varying from 0.2135 to 0.401 g/s.

The flow parameters for these two cases are summarized in Table 5.

Case	Flow conditions	
	Variable parameters	Fixed parameters
1	$T_{h,i} = 45 \div 70 \text{ } ^\circ\text{C}$	$m_h = 0.2308 \text{ g/s}$ $m_c = 0.2135 \text{ g/s}$ $T_{c,i} = 22.5 \text{ } ^\circ\text{C}$
2	$m_c = 0.2135 \div 0.401 \text{ g/s}$	$m_h = 0.2308 \text{ g/s}$ $T_{h,i} = 70 \text{ } ^\circ\text{C}$ $T_{c,i} = 22.5 \text{ } ^\circ\text{C}$

Table 5. Flow parameters for the cases under study.

The effects of substrate thicknesses

For the effects of substrate thicknesses, the two microchannel heat exchangers (T1 and T2) were tested. These two heat exchangers have the same dimensions of the channel and the manifolds with the same means (that is, the S-type, as shown in Fig. 3a)) for connecting the channels to the manifolds; however, the two heat exchangers under study have different substrate thicknesses. Detailed parameters of the heat exchangers (T1 and T2) are listed in Table 2.

Fig. 20 shows the effects of the substrate thickness with rising inlet temperature of the hot side. The heat flux is a function of the inlet temperature of hot side; the heat flux increases with rising inlet temperature of the hot side, as shown in Fig. 20a. For the substrate thicknesses of 1.2 (Heat Exchanger T1) and 2 mm (Heat Exchanger T2), the heat fluxes of T1 are 1.024 to 1.046 times of those obtained from T2. Besides, it was found that the heat transfer rate obtained from the present study (23 W) is slightly higher than that obtained from García-Hernando et al. [36] (22 W) (At Reynolds number of 400, the present study used the overall channel size with 9.5 mm in width and 32 mm in length (304 mm² in area), compared with that of 20 mm in width and 16 mm in length (320 mm² in area) for García-Hernando et al. [36]). It was also found for the present study that the heat transfer rate increases with rising inlet temperature of the hot side. As a result, the effectiveness – defined as the ratio of heat transfer rate to the maximum heat transfer rate, expressed by Eq. (3) – increases with rising inlet temperature of the hot side, as shown in Fig. 20b. Because that the configuration of the heat exchangers and the mass flow rates of water at the hot and cold sides are fixed and the variation of temperature of water at both side is minimal, so the convective heat transfer term is essentially fixed. Further, it is found that the conductive heat transfer term does not affect strongly the overall heat transfer coefficient of the heat exchangers. It is concluded that the results shown in Figs. 20a and 20b indicate that the substrate thickness affects negligibly the parameters associated with the heat transfer process of the heat exchangers with the substrate thicknesses of 1.2 and 2 mm.

For the present study, the results obtained from the experimental data showed the pressure drop as a function of the inlet temperature of the hot side. For both heat exchangers (T1 and T2), the mass flow rate of the hot side is higher than those of the cold side, so the pressure drop obtained from the hot side is higher than that obtained from the cold side, as shown in Fig. 20c. Fig. 20c illustrates that pressure drop of T2 is not the same as that of T1, due to the fact that the roughness of channels in T2 could be higher than that of channels in T1. However, the maximum difference of pressure drops between T1 and T2 is less than 10 %.

Fig. 20d shows that the performance of the heat exchangers increase with the rising of inlet temperature of the hot side; the performance obtained from T1 is higher than that obtained from T2. The performance index of 21.67 W/kPa was achieved for water from the hot side of Heat Exchanger T1 having the inlet temperature of 70 °C and mass flow rate of 0.2308 g/s and water from the cold side having the inlet temperature of 22.5 °C and mass flow rate of 0.2135 g/s.

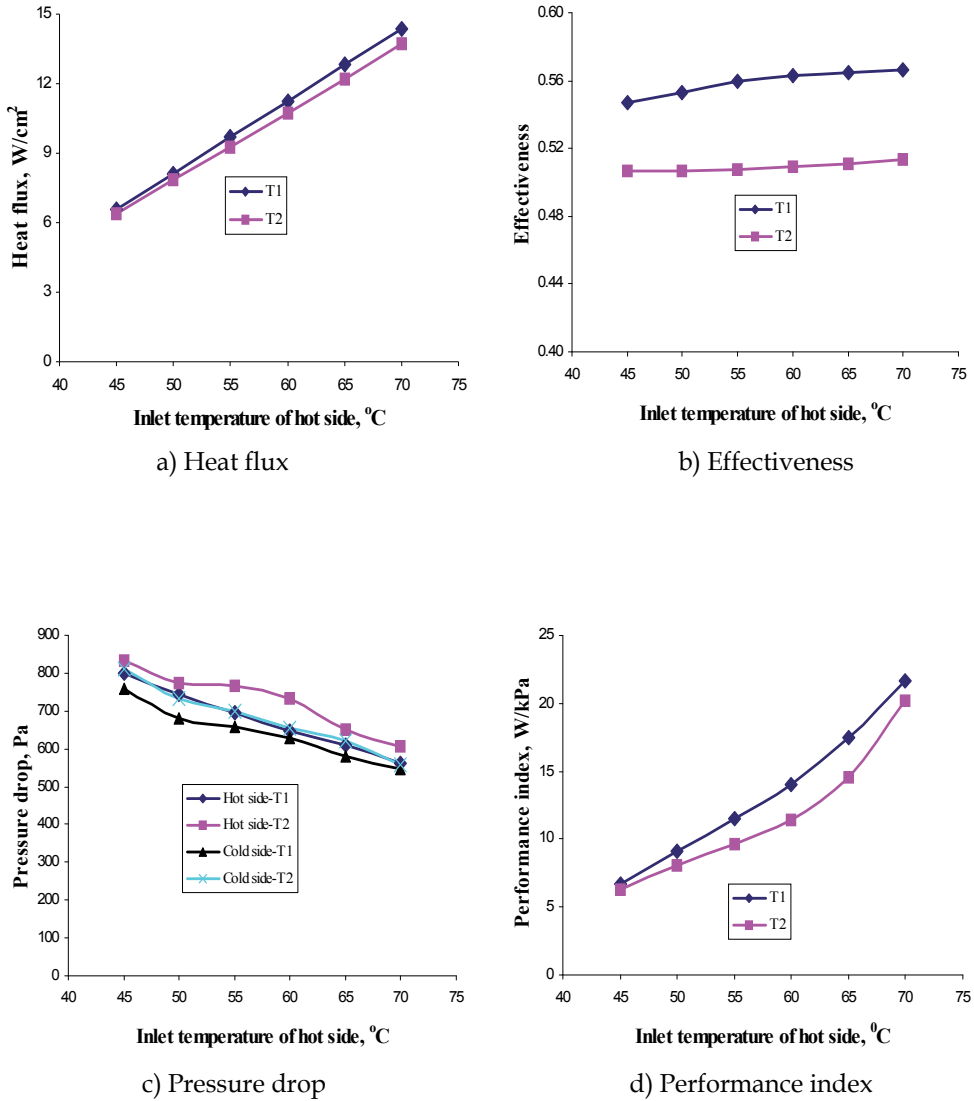


Fig. 20. Effects of the substrate thickness with a rising inlet temperature of hot side.

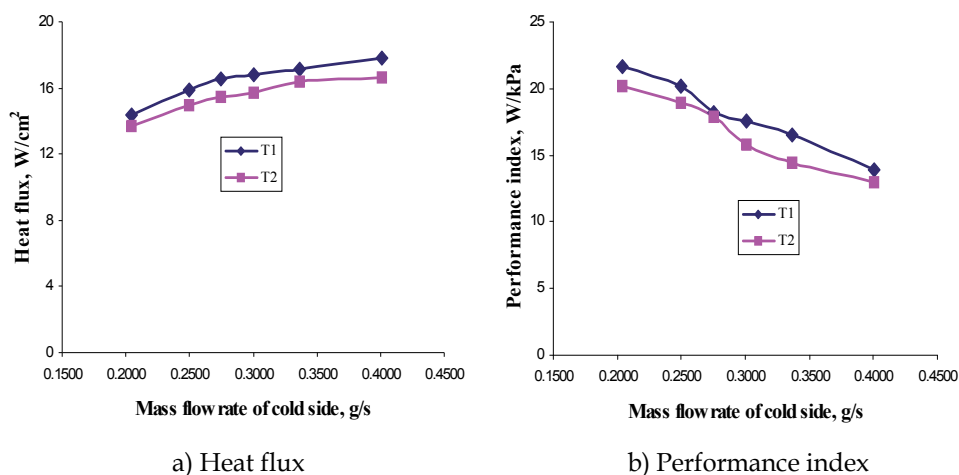


Fig. 21. Effects of the substrate thickness with a rising mass flow rate of cold side.

For the case of increasing the mass flow rate of the cold side (Case 2 was developed to study the effects of substrate thickness at various mass flow rates of the cold side), the heat fluxes of the heat exchangers increase with rising mass flow rate of the cold side, as shown in Fig. 21. Fig. 21 shows the effects of the substrate thickness with rising mass flow rate of the cold side. For this case, the heat flux obtained from T1 is also higher than that obtained from T2, as shown in Fig. 21a. When the mass flow rate of the cold side increases, the pressure drop of the cold side also increases; when the mass flow rate of the cold side increases, the average temperature of the hot side decreases, resulting in an increase of the pressure drop of the hot side. Besides, it was observed from the experimental data that the pressure drops increase at a higher slope than those for the effectiveness. It is noted that the performance index decreases with the rising mass flow rate of the cold side, as shown in Fig. 21b; however, the performance index obtained from the T1 is higher than that obtained from T2.

The effects of cross-sectional areas

For the evaluation of the effects of cross-sectional areas on the fluid and heat transfer of the microchannel heat exchangers, two cases were investigated: (1) Case 1 for the study of the effects of cross-sectional area for the heat exchanger at various inlet temperatures of the hot side and (2) Case 2 for the study of the effects of cross-sectional area for the heat exchanger at various mass flow rates of the cold side. Two microchannel heat exchangers T1 and T3 are tested for the effects of magnitude of cross-sectional area on the behaviors of heat transfer and fluid flow. These two microchannel heat exchangers have the same physical configurations for their substrates, manifolds, and lengths of channels. However, only the cross-sectional areas of microchannels are different. The microchannels of T1 have a rectangular cross-section with width of 500 μm and depth of 300 μm ; the microchannel of T3, width of 500 μm and depth of 180 μm . These dimensions are listed in Table 2.

For Case 1, Fig. 22 shows the effects of the cross-sectional areas on the behaviors of heat flux, effectiveness, pressure drop, and performance index for T1 and T3 with the inlet temperatures of the hot side ranging from 45 to 70 $^{\circ}\text{C}$. The heat fluxes of the heat exchangers increase with

the inlet temperature of the hot side increasing, as shown in Fig. 6a. It is observed that the heat transfer rates obtained from T3 are higher than those obtained from T1, leading to the fact that heat fluxes obtained from T3 are higher than those obtained from T1. The results obtained from the present study are in good agreement with those obtained from [37]. Foli et al. [37] indicated that under the constant mass flow rate condition, the higher the heat flux, the lower the aspect ratio (defined as the ratio of the microchannel height to its width). Under the same condition, the mass flow rates are fixed for two cases T1 and T3 used in this study. The conductive thermal resistance of T1 was found to be lower than that of T3. However, the convective thermal resistance of T1 was found to be higher than that of T3. The heat fluxes obtained from Fig. 22a show that the effect of the convective thermal resistance on the overall thermal resistance (appeared in Eqs. (5) and (6)) of the microchannel heat exchangers is more significantly than that of the conductive thermal resistance.

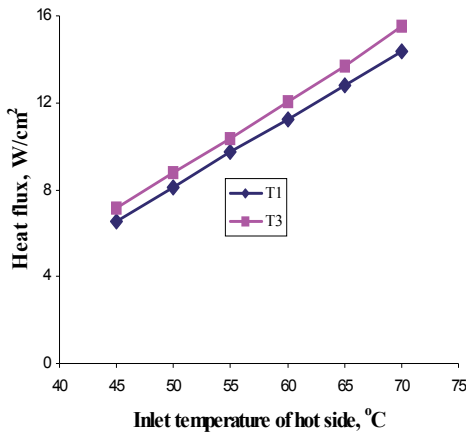
The effectiveness obtained from T3 is higher than that obtained from T1, as shown in Fig. 22b. However, because that the hydraulic diameter of channel in T3 is smaller than that of channel in T1, this results in the velocity in the channel of T3 to be higher than that of T1, leading to a higher pressure drop in T3 than that in T1, as shown in Fig. 22c. It was found that the pressure drop of T3 is 2 times higher than that of T1, while the effectiveness of T3 is 1.04 times higher than that of T1. As a result, the performance index (defined as the ratio of the heat transfer rate to the pressure drop in the heat exchanger) obtained from T1 is higher than that obtained from T3, as shown in Fig. 22d.

For Case 2, Fig. 23 shows the effects of the cross-sectional area on the behaviors of heat flux and performance index for T1 and T3 with the mass flow rates of the cold side ranging from 0.2135 to 0.401 g/s. It was found that the heat fluxes of T3 are higher than those of T1, as shown in Fig. 23a. For microchannel heat exchanger T3, a heat flux of 18.7 W/cm^2 (or overall average heat transfer coefficient of $8,500 \text{ W/m}^2\text{K}$) was achieved for water from the hot side having a fixed inlet temperature of $70 \text{ }^\circ\text{C}$ and a fixed mass flow rate of 0.2308 g/s and for water from the cold side having a fixed inlet temperature of $22.5 \text{ }^\circ\text{C}$ and a mass flow rate of 0.401 g/s . It was also found that the pressure drop of T3 is higher than that of T1; the curve of the pressure drop is at a higher slope than that of the heat flux; as a result, the performance index of T1 is higher than that of T3, as shown in Fig. 23b.

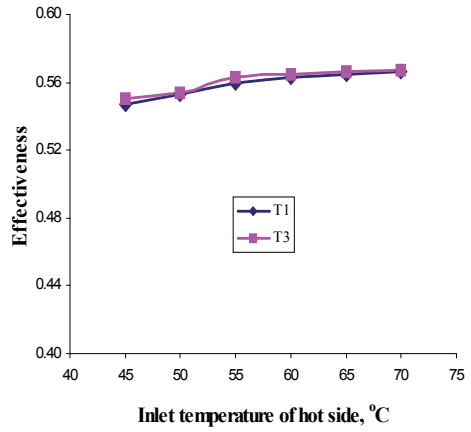
From Figs. 20-23 obtained in this study, it indicates that for the microchannel heat exchangers being investigated, the effect of the hydraulic diameter on the performance index is more pronounced than that of the substrate thickness. In addition, it demonstrates that the lower the hydraulic diameter, the higher the heat flux and the pressure drop.

The effects of inlet/outlet location

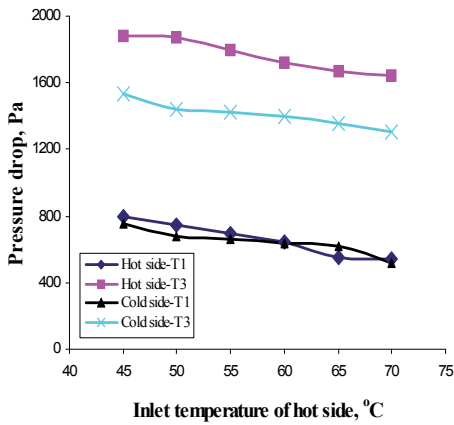
Again, in Dang [3] and Dang and Teng [25], two cases were investigated: (1) Case 1 for the study of the effects of inlet/out location for the heat exchanger at various inlet temperatures of the hot side and (2) Case 2 for the study of the effects of inlet/out location for the heat exchanger at various mass flow rates of the cold side. The inlet/outlet locations affect significantly the behaviors of heat transfer and fluid flow of the microchannel heat exchangers. The two microchannel heat exchangers T2 and T4 were tested for this case. These two heat exchangers have the same dimensions of the channel and manifold; however, as shown in Fig. 3, the configuration of manifold together with the channel for T2 is the S-type and that for T4 is the I-type. Parameters of the heat exchangers are listed in more detail in Table 2.



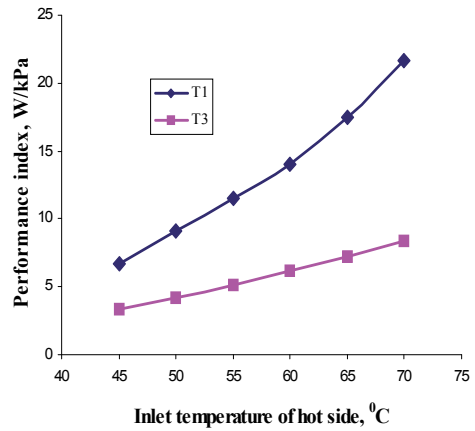
a) Heat flux



b) Effectiveness



c) Pressure drop



d) Performance index

Fig. 22. Effects of the cross-sectional area with a rising inlet temperature of hot side.

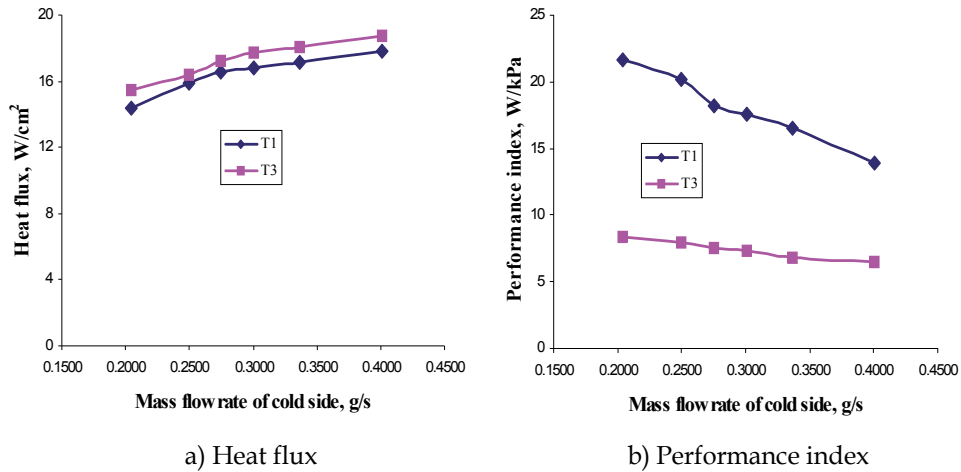
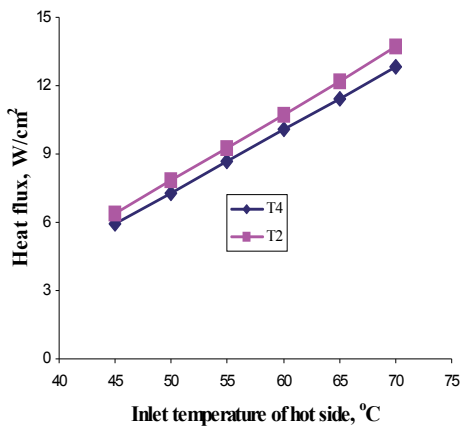


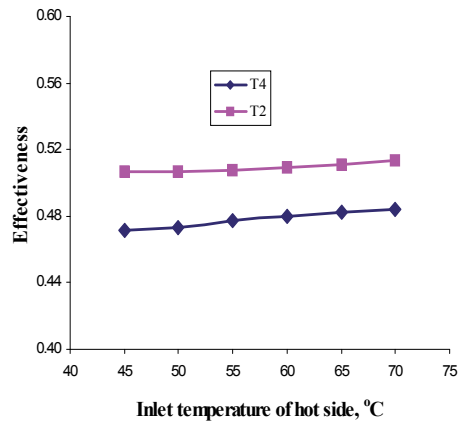
Fig. 23. Effects of the cross-sectional area with a rising mass flow rate of cold side.

For Case 1, Fig. 24 shows the effects of the inlet/outlet location on the behaviors of heat flux, effectiveness, pressure drop, and performance index for heat exchangers T2 and T4 with the inlet temperatures of the hot side ranging from 45 to 70 °C. In these two heat exchangers, the effects of maldistribution by the manifolds are important for heat transfer and pressure drop. The distance of flow path for the fluid moving from the entrance to the exit for the S-type microchannel heat exchanger is longer than that for the I-type, leading to the fact that the heat flux of T2 is higher than that of T4, as shown in Fig. 24a; as a result, the effectiveness of T2 is also higher than that of T4, as shown in Fig. 24b. However, it is also due to the fact that the distance the fluid moves from the entrance to the exit for the S-type is longer than that obtained with the I-type, so the pressure drop obtained from T2 is higher than that obtained from T4 for the same mass flow rate through the two heat exchangers being investigated, as shown in Fig. 24c. Fig. 24d shows the performance index of the heat exchangers as a function of the inlet temperature of the hot side. The performance index obtained from T4 is higher than that obtained from T2.

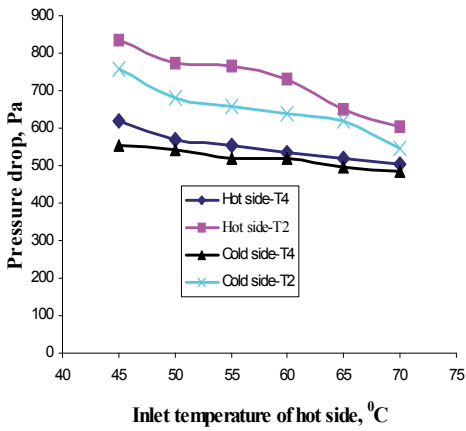
For Case 2, Fig. 25 shows the effects of the cross-sectional area on the behaviors of heat flux and performance index for the heat exchangers T2 and T4 with the mass flow rates of the cold side ranging from 0.2135 to 0.401 g/s. It was found that the heat fluxes obtained from T2 are higher than those from T4, as shown in Fig. 25a. However, when the mass flow rates of the cold side increase, the pressure drops increase also, leading to the fact that the pressure drop of T4 is lower than that of T2. It was also found that the performance index of T4 is higher than T2, as shown in Fig. 25b.



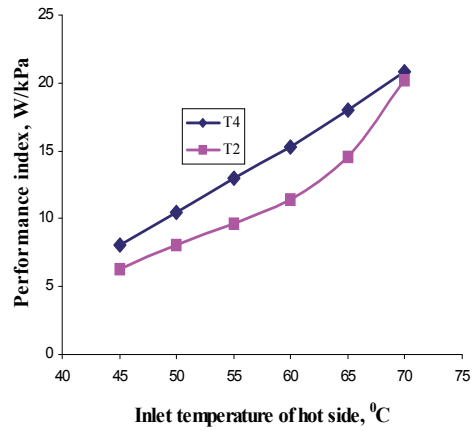
a) Heat flux



b) Effectiveness



c) Pressure drop



d) Performance index

Fig. 24. Effects of the inlet/outlet location with a rising inlet temperature of hot side.

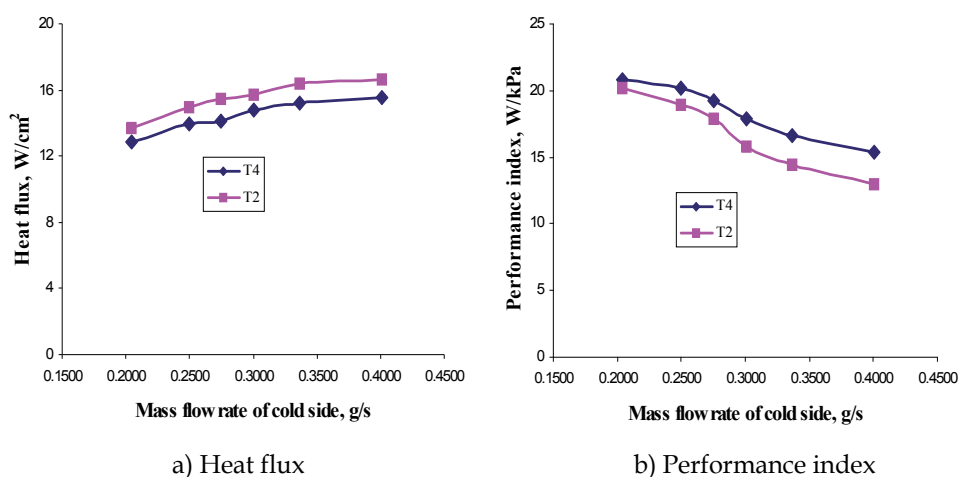


Fig. 25. Effects of the inlet/outlet location with a rising mass flow rate of cold side.

In summary, Figs. 20-25 indicate that the highest heat flux achievable for all cases studied is the microchannel heat exchanger T3. However, the performance index of T3 is lowest among all cases being investigated. It is observed that the heat flux and pressure drop obtained from the S-type manifold together with the channels are higher than that from the I-type. However, the performances indexes of both types of heat exchangers are essentially the same. For all cases studied, the microchannel heat exchanger T1 yields the highest performance index, with T4 being the second best. From the experimental data shown in Figs. 20-25, the overall average heat transfer coefficients of the heat exchangers with a value of 8,500 W/(m²K) which was evaluated in this study are in good agreement with the overall heat transfer coefficient obtained in Kandlikar et al. [34] for microchannels with the same hydraulic diameter; however, the overall average heat transfer coefficient obtained from the present study is higher than that (~5,100 W/(m²K)) obtained in García-Hernando et al. [36] due to the difference in design.

4.4 Effects of gravity

An experimental study of the effects of gravity on the fluid in microchannel heat exchangers was carried out in the study to find out how does the gravity affect the behaviors of heat transfer and pressure drop for the microchannel heat exchangers? For the experimental system, the inlet temperature and the mass flow rate of the hot side were fixed at 70 °C and 0.2308 g/s, respectively; at the cold side, the inlet temperature was fixed at 22.5 °C and the mass flow rates were varying from 0.2135 to 0.401 g/s. In this study, influence of gravity was determined by two cases: one with horizontal channels, the other with vertical channels. For vertical channels, the hot water is flowing upward which is against the gravitational field, while the cold water is flowing downward which is in the same direction as the gravitational field [26,27]. Two microchannel heat exchangers T1 and T3 were tested: these two microchannel heat exchangers have the same physical configurations for their substrates, manifolds, and lengths of channels; only the cross-sectional areas of microchannels are different. The microchannels of T1 have a rectangular cross-section with width of 500 μm and depth of 300 μm; the microchannel of T3, width of 500 μm and depth of 180 μm. Parameters of the heat exchangers (T1 and T3) are listed in more detail in Table 2.

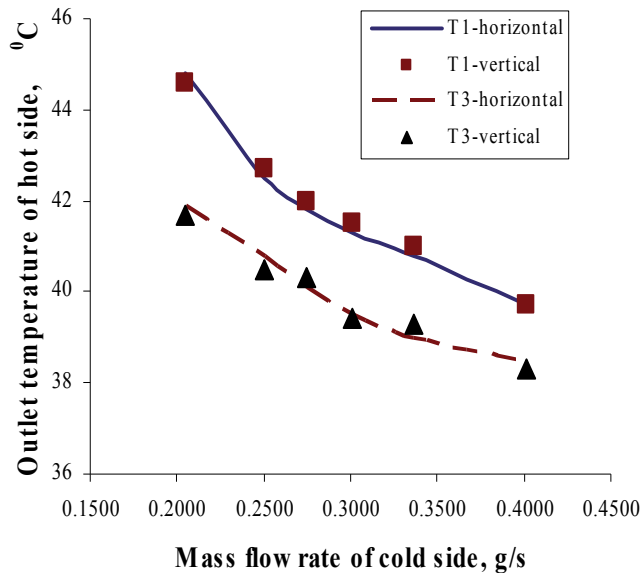


Fig. 26. Comparison of outlet temperatures of hot side.

Fig. 26 shows a comparison of at specified mass flow rate of the cold side the difference between outlet temperature of hot side obtained from a horizontal channel (either T1 or T3) and that from the vertical one (the corresponding T1 or T3) is negligibly small. A comparison of the outlet temperatures of cold side of two microchannel heat exchangers is shown in Fig. 27. The outlet temperatures (for both the hot and the cold sides) are functions of the mass flow rate of cold side; the outlet temperatures decrease as the mass flow rate of the cold side increases.

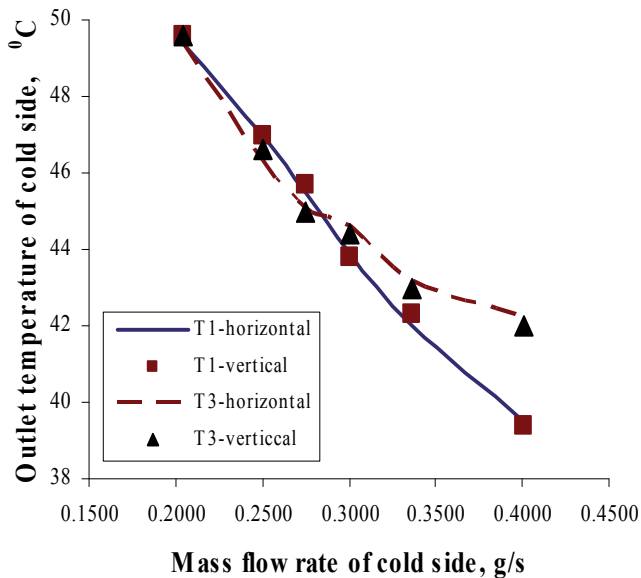


Fig. 27. Comparison of outlet temperatures of cold side.

The outlet temperatures of hot side obtained from T1 is higher than those obtained from T3; however, the outlet temperatures of cold side obtained from T1 is lower than those obtained from T3. As a result, the heat transfer rate obtained from T3 is higher than that obtained from T1, as shown in Fig. 28. The results obtained from the present study are in good agreement with those obtained from [37]. Foli et al. [37] indicated that under the constant mass flow rate condition, the higher the heat flux, the lower the aspect ratio (defined as the ratio of the microchannel height to its width).

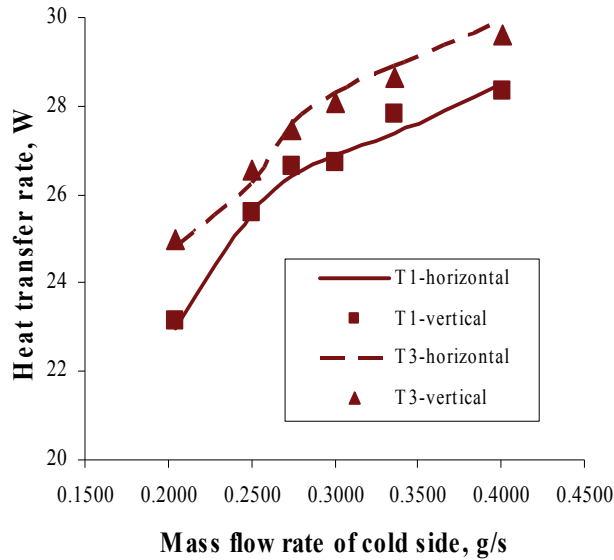


Fig. 28. Comparison of heat transfer rates.

It is shown from Fig. 28 that at specified mass flow rate of the cold side the difference between the heat transfer rate obtained from a horizontal channel (either T1 or T3) and that from the vertical one (the corresponding T1 or T3) is negligibly small. The heat transfer rate of the heat exchangers is a function of the mass flow rate of cold side: it increases from 24.8 to 29.92 W with the mass flow rate of cold side rising from 0.2043 to 0.401 g/s (for the heat exchanger T3).

Because that the hydraulic diameter of channel in T3 is smaller than that of channel in T1, this results in the velocity in the channel of T3 to be higher than that of T1, leading to a higher total pressure drop in T3 than that in T1, as shown in Fig. 29. Besides, the figure shows that the total pressure drop is a function of Reynolds number of cold side; the total pressure drop increases as rising the Re number of cold side.

Experimental results for effects of gravity on the behavior of pressure drop for the microchannel heat exchanger are also shown in Fig. 29. It is observed that the change of pressure drop between the two cases (horizontal channels and vertical channels) is negligibly small; the maximum change in pressure is 7.2% for a pressure drop from 1060 to 2044 Pa.

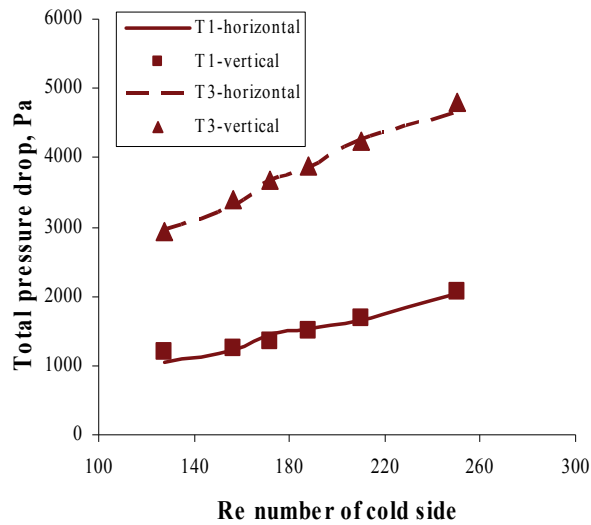


Fig. 29. Comparison of total pressure drops.

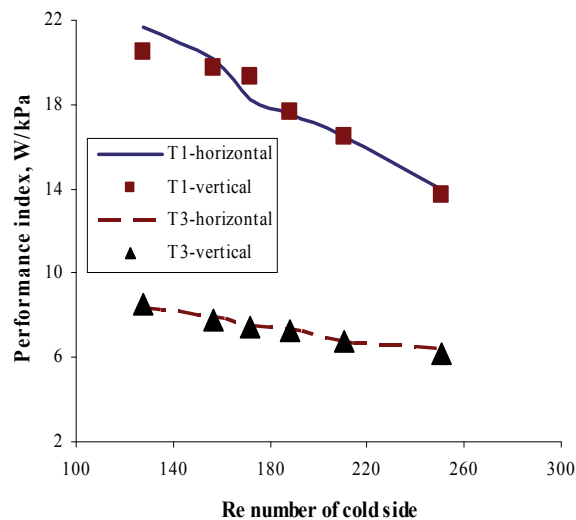


Fig. 30. Comparison of performance indices.

It was found that the pressure drop of T3 is 2 times higher than that of T1, while the heat transfer rate of T3 is 1.06 times higher than that of T1. As a result, the performance index (defined as the ratio of the heat transfer rate to the pressure drop in the heat exchanger) obtained from T1 is higher than that obtained from T3, as shown in Fig. 30. For heat exchanger T1, a performance index of 21.68 W/kPa was achieved for water from the hot side having an inlet temperature of 70 °C and a mass flow rate of 0.2308 g/s and for water from the cold side having an inlet temperature of 22.5 °C and mass flow rate of 0.2135 g/s. It is also observed that the change of performance between the two cases (horizontal channels and vertical channels) is negligibly small; the maximum change in performance is 5.5%, out of a performance index from 13.69 to 21.68 W/kPa.

In summary, it is concluded that for both heat transfer and pressure drop behaviors, the impact of gravity on the fluid flowing through the microchannel heat exchange can be ignored as indicated in [3,26,27,33,34].

5. Conclusion

In this study, for the cases with both inlet temperature and mass flow rate constant at the cold side of the device, the trends for the results obtained from the actual effectiveness method and those obtained from the effectiveness (ϵ -NTU) method are in the opposite directions as the mass flow rate of the hot side increases. However, for the cases with constant inlet temperature and mass flow rate at the hot side of the device, the trends for the results obtained from both methods for evaluating effectiveness are in the same directions.

With all cases done in the study, the performance index obtained from the counterflow is always higher than that obtained from the parallel-flow. As a result, the microchannel heat exchanger with counter-flow should be selected to use for every case (except few special cases).

In the study, it indicates that the substrate thickness affects negligibly the parameters associated with the heat transfer process of the heat exchangers with the substrate thicknesses of 1.2 and 2 mm. The effect of the hydraulic diameter (cross-sectional area) on the performance index is more pronounced than that of the substrate thickness. In addition, it demonstrates that the lower the hydraulic diameter, the higher the heat flux and the pressure drop. Regarding the effects of inlet/outlet locations, for two types (I-type and S-type) of the microchannel heat exchangers, the heat flux and pressure drop obtained from the S-type are higher than those from the I-type, even though the performance indexes of both heat exchangers are essentially the same.

The impact of gravity on the fluid flowing through the microchannel heat exchanger was found to be small, with the maximum difference between the results of horizontal and vertical channels being less than 8%. In addition, in this study, good agreements were achieved between the results obtained from the present study and the results obtained from the literatures.

In the study, good agreements were achieved for the behaviors of heat transfer and fluid flow between the results obtained from numerical simulations and those obtained from experimental data for fluid flowing in the counter-flow microchannel heat exchanger used, with the maximum percentage difference between the two results of less than 9%.

This chapter summarized the work performed and the results obtained both in the fluid flow and heat transfer done by TFAAG over the last several years. The authors would like to express their deep appreciation for the financial supports obtained from National Science Council, the Republic of China in Taiwan (Grant Nos. NSC93-2212-E-033-012, NSC94-2212-E-033-017, NSC95-2212-E-033-066, NSC96-2212-E-033-039, NSC97-2212-E-033-050, NSC99-2212-E-033-025, and NSC 100-2221-E-033-065) and Chung Yuan Christian University (Grant No. CYCU-98-CR-ME).

6. Nomenclature

A_c	cross-sectional area, m ²
D_h	hydraulic diameter, m
f	friction factor

h	heat transfer coefficient, W/m ² K
k	overall heat transfer coefficient, W/m ² K
K _r	thermal conductivity ratio
K _v	volumetric heat transfer coefficient, W/m ³ K
L	length of channel, m
	distance from the nozzle to the breakdown point of the jet, m
m	mass flow rate, kg/s
n	number of tubes
NTU	Number of Transfer Unit
Nu	Nusselt number
\overline{Nu}	average Nusselt number
p	pressure, Pa
P	wetted perimeter, m
Q	heat transfer rate, W
q	heat flux, W/m ²
R	thermal resistance, m ² K/W
Re	Reynolds number
T	temperature, K
T _d	mean temperature, K
V	volume flow rate, m ³ /s
Z	nozzle-to-wall distance, m

Greek symbols

μ	dynamic viscosity, Ns/m ²
ρ	density, kg/m ³
λ	thermal conductivity, W/m K
ω	velocity, m/s
ε	effectiveness
ξ	performance index, W/kPa
φ	liquid fill ratio
ΔT	different temperature, K
Δp	pressure drop, Pa

7. References

- [1] W.J. Bowman and D. Maynes (2001): A review of micro-heat exchanger flow physics, fabrication methods and application, Proceedings of ASME IMECE 2001, New York, USA, Nov 11-16, HTD-24280, pp. 385-407
- [2] G.L. Morini (2004): Single-phase convective heat transfer in microchannels: a review of experimental results, *Int. J. of Thermal Sciences*, Vol. 43, 631-651
- [3] T.T. Dang (2010): A study on the heat transfer and fluid flow phenomena of microchannel heat exchanger, Ph.D. thesis, Chung Yuan Christian University, Chung-Li, Taiwan
- [4] T.T. Dang, J.T. Teng, and J.C. Chu, Pressure drop and heat transfer characteristics of microchannel heat exchangers: A review of numerical simulation and experimental data (Accepted for Publication), *International Journal of Microscale and Nanoscale Thermal and Fluid Transport Phenomena*, 2011

- [5] J.J. Brandner, L. Bohn, T. Henning, U. Schygulla and K. Schubert (2006): Microstructure heat exchanger applications in laboratory and industry, Proceedings of ICNMM2006, Limerick, Ireland, June 19-21, ICNMM2006-96017, pp. 1233-1243
- [6] S.W. Kang and S.C. Tseng (2007): Analysis of effectiveness and pressure drop in micro cross-flow heat exchanger, *Applied Thermal Engineering*, Vol. 27, 877-885
- [7] T. Henning, J.J. Brandner and K. Schubert (2004): Characterisation of electrically powered micro-heat exchangers, *Chemical Engineering Journal*, Vol. 101, 339-345
- [8] J.J. Brandner, E. Anurjew, L. Bohn, E. Hansjosten, T. Henning, U. Schygulla, A. Wenka, and K. Schubert (2006): Concepts and realization of microstructure heat exchangers for enhanced heat transfer, *Experimental Thermal and Fluid Science*, Vol. 30, 801-809
- [9] E. R. Delsman, M. H. J. M. de Croon, G. J. Kramer, P. D. Cobden, Ch. Hofmann, V. Cominos and J. C. Schouten (2004): Experiments and modelling of an integrated preferential oxidation-heat exchanger microdevice, *Chemical Engineering Journal*, Vol. 101, 123-131
- [10] E.R. Delsman, M.H.J.M.D Croon, A. Pierik, G.J. Kramer, P.D. Cobden, Ch. Hofmann, V. Cominos and J.C. Schouten (2004): Design and operation of a preferential oxidation microdevice for a portable fuel processor, *Chemical Engineering Science*, Vol. 59, 4795-4802
- [11] C. H. Shen and C. Gau (2004): Heat exchanger fabrication with arrays of sensors and heaters with its micro-scale impingement cooling process analysis and measurements, *Sensors and Actuators A: Physical*, Vol. 114, 154-162
- [12] C. Gillot, A. Bricard and C. Schaeffer (2000): Single and two-phase heat exchangers for power electronic components, *Int. J. of Thermal Sciences*, Vol. 39, 826-832
- [13] B. Alm, U. Imke, R. Knitter, U. chygulla and S. Zimmermann (2008): Testing and simulation of ceramic micro heat exchangers, *Chemical Engineering Journal*, Vol. 135, S179-S184
- [14] B. Hallmark, C.H. Hornung, D. Broady, C. Price-Kuehne and M.R. Mackley (2008): The application of plastic microcapillary films for fast transient micro-heat exchange, *Int. J. Heat Mass Transfer*, Vol. 51, 5344-5358
- [15] P.X. Jiang, M.H. Fan, G.S. Si and Z.P. Ren (2001): Thermal-hydraulic performance of small scale micro-channel and porous-media heat-exchangers, *Int. J. Heat Mass Transfer*, Vol. 44, 1039-1051
- [16] Schulz, G.N. Akapiev, V.V. Shirkova, H. Rösler and S.N. Dmitriev (2005): A new method of fabrication of heat transfer surfaces with micro-structured profile, *Nuclear Instruments and Methods in Physics Research Section B: Beam Interactions with Materials and Atoms*, Vol. 236, 254-258
- [17] H. Lee, Y. Jeong, J. Shin, J. Baek, M. Kang and K. Chun (2004): Package embedded heat exchanger for stacked multi-chip module, *Sensors and Actuators A: Physical*, Vol. 114, 204-211
- [18] X. Wei (2004): Stacked microchannel heat sinks for liquid cooling of microelectronics devices, Ph.D. thesis, Academic Faculty, Georgia Institute of Technology
- [19] M.I. Hasan, A.A. Rageb, M. Yaghoubi, and H. Homayoni (2009): Influence of channel geometry on the performance of a counter flow microchannel heat exchanger, *Int. J. Thermal Sciences*, Vol. 48, 1607-1618
- [20] T.A. Ameel, R.O. Warrington, R.S. Wegeng and M.K. Drost (1997): Miniaturization technologies applied to energy systems, *Energy Conversion and Management*, Vol. 38, 969-982
- [21] T.T. Dang, Y.J. Chang and J.T. Teng (2009): A study on the simulations of a trapezoidal shaped micro heat exchanger, *Journal of Advanced Engineering*, Vol. 4, 397-402

- [22] T.T. Dang, J.T. Teng and J.C. Chu (2010): Effect of flow arrangement on the heat transfer behaviors of a microchannel heat exchanger, Proceedings of the International MultiConference of Engineers and Computer Scientists 2010 (IMECS2010), Hongkong, pp. 2209-2214 (Best student paper award)
- [23] T.T. Dang, J.T. Teng and J.C. Chu (2010): Effect of flow arrangement on the heat transfer behaviors of a microchannel heat exchanger, Lecture Notes in Engineering and Computer Science, Vol. 2182, 2209-2214
- [24] T.T. Dang and J.T. Teng (2010): Numerical and experimental studies of the impact of flow arrangement on the behavior of heat transfer of a microchannel heat exchanger, *IAENG International Journal of Applied Mathematics*, Vol. 40, 207-213
- [25] T.T. Dang and J.T. Teng (2010): Influence of flow arrangement on the performance for an aluminium microchannel heat exchanger, *IAENG Transactions on Engineering Technologies Volume 5, the American Institute of Physics (AIP)*, Vol. 1285, 576-590
- [26] T. Dang, J.T. Teng, and J.C. Chu (2010): A study on the simulation and experiment of a microchannel counter-flow heat exchanger, *Applied Thermal Engineering*, Vol. 30, 2163-2172
- [27] T.T. Dang, J.T. Teng, and J.C. Chu, Influence of Gravity on the Performance Index of Microchannel Heat Exchangers – Experimental Investigations, World Congress on Engineering (WCE 2011), London, U.K., pp. 2094-2099
- [28] T.T. Dang and J.T. Teng (2010): Effect of the substrate thickness of counter-flow microchannel heat exchanger on the heat transfer behaviors, Proceedings of the International Symposium on Computer, Communication, Control and Automation 2010 (3CA2010), Taiwan, pp. 17-20
- [29] T. Dang and J.T. Teng (2011): The effects of configurations on the performance of microchannel counter-flow heat exchangers-An experimental study, *Applied Thermal Engineering*, Vol. 31, 3946-3955
- [30] T.T. Dang and J.T. Teng (2011): Comparison on the heat transfer and pressure drop of the microchannel and minichannel heat exchangers, *Heat and Mass Transfer*, Vol. 47, 1311-1322
- [31] T.T. Dang and J.T. Teng (2010): Numerical simulation of a microchannel heat exchanger using steady-state and time-dependent solvers, ASME 2010 International Mechanical Engineering Congress & Exposition (IMECE2010), Vancouver, Canada, pp. 1-10
- [32] COMSOL Multiphysics version 3.5 – Documentation, 2008
- [33] L.M. Jiji, Heat Convection, Second edition, Springer, Verlag Berlin Heidelberg, 2009
- [34] S.G. Kandlikar, S. Garimella, D. Li, S. Colin, and M.R. King, Heat Transfer and Fluid Flow in Minichannels and Microchannels, Elsevier Pte Ltd, Singapore, 2006.
- [35] J.P. Holman, Experimental methods for engineers, McGraw-Hill, New York, 1984
- [36] N. García-Hernando, A. Acosta-Iborra, U. Ruiz-Rivas and M. Izquierdo, Experimental investigation of fluid flow and heat transfer in a single-phase liquid flow micro-heat exchanger, *International Journal of Heat and Mass Transfer* 52 (23-24) (2009) 5433-5446
- [37] K. Foli, T. Okabe, M. Olhofer, Y. Jin, and B. Sendhoff, Optimization of micro heat exchanger: CFD, analytical approach and multi-objective evolutionary algorithms, *International Journal of Heat and Mass Transfer* 49 (5-6) (2006) 1090-1099.

Heat Exchangers for Thermoelectric Devices

David Astrain and Álvaro Martínez
Public University of Navarre
Spain

1. Introduction

Heat exchangers play an important role in the performance of thermal machines, namely, electric power generators, engines and refrigerators. Regarding thermoelectrics, this influence is even higher, owing to the difficulty of transferring heat from the small surface area of a typical thermoelectric module to a bigger one. Particularly, in the hot face of an average 40 mm x 40 mm Peltier module, the heat flux readily yields 40600 W/m². The thermoelectric effects, namely, Joule, Seebeck, Peltier and Thomson, describe the interaction between thermal and electric fields, and are well known since the XIX century (Rowe, 2006).

German physicist Thomas J. Seebeck discovered in 1821 that an electric circuit composed of two dissimilar conductors A and B connected electrically in series and exposed to a thermal gradient induces an electric current -or an electromotive force (E_{AB}) if the circuit is opened- which depends on the materials and the temperature difference between junctions (ΔT). This phenomenon is called **Seebeck effect**, characterized by the *Seebeck coefficient* α .

$$\alpha_{AB} = \frac{\Delta E_{AB}}{\Delta T} = \alpha_A - \alpha_B \quad (1)$$

Likewise, in 1834, French physicist Jean Peltier discovered that if an electrical current (I) is applied across the electric circuit composed of two dissimilar conductors, the inverse effect takes place, that is, heating occurs at one junction whereas cooling occurs at the other. This phenomenon is called **Peltier effect**, described by the *Peltier coefficient* π .

$$\dot{Q}_P = \pm I \pi_{AB} = \pm IT (\alpha_B - \alpha_A) \quad (2)$$

In 1851, William Thomson stated the *Thomson effect*, which indicates that a homogeneous material exposed to thermal and electrical gradients absorbs or generates heat. Moreover, he described the relation between Seebeck and Peltier effects, given by *Thomson coefficient* τ .

$$\tau_A - \tau_B = -T \frac{\partial \alpha_A}{\partial T} + T \frac{\partial \alpha_B}{\partial T} = T \frac{\partial}{\partial T} (\alpha_B - \alpha_A) \quad (3)$$

The possibility of using thermoelectric devices to produce electric power was raised by John W. Strutt in 1885. Subsequently, between 1909 and 1911, Edmund Altenkirch proved that thermoelectric materials must feature high Seebeck coefficient (α), high electrical conductivity (σ) and low thermal conductivity (λ), in order for the material to retain heat in

the junctions and minimize losses due to Joule effect. These three parameters were combined to form the Figure of merit ($Z = \alpha^2 \sigma / \lambda$), key parameter in the characterization of thermoelectric materials. By then, further developments had been rejected because of the low efficiencies attained, and it was not until the application of semiconductor materials to thermoelectric devices by Abram F. Ioffe in 1957, that thermoelectric technology contemplated its major breakthrough. Since that moment, scientific efforts focused on increasing the Figure of merit via new thermoelectric materials.

Although the thermoelectric effects were discovered almost two centuries ago, the application of thermoelectric technology to either heating or cooling (Peltier effect), and electric power generation (Seebeck effect) was not relevant until the fifties of the last century, when this technology was successfully used for military and aerospace purposes. The application to other fields was then rejected because of the high price of thermoelectric materials, but now has become a reality. In this regard, some in-depth reviews on the state of the art of thermoelectric technology can be found in the literature (Goldsmid, 1964, 1986, 1995; Riffat & Xiaoli, 2003). Nowadays, the successful development of thermoelectrics for civil purposes depends mainly on two aspects: thermoelectric materials development and heat exchangers thermal design. Whereas the first one intends to increase the Figure of merit and efficiency of the devices via new thermoelectric materials, the second one focuses on enhancing the heat transfer via improving the heat exchangers.

Thermoelectric technology presents significant advantages with respect to common devices used for refrigeration or electric power generation, since thermoelectric devices have no moving parts (no compressor, turbine, etc. must be installed), which makes them virtually noiseless and increases their lifespan to a great extent. Furthermore, thermoelectric devices are easily and accurately controlled. All these advantages, along with the fact that the prices of Peltier modules are constantly decreasing, boosted the development of highly interesting thermoelectric applications, competing nowadays in the civil market with good prospects for the future (Bell, 2008; Chang et al., 2009; Chein & Huang, 2004; Gordon et al., 2002; Hongxia & Lingai, 2007; Khattab & El Shenawy, 2006; Martínez et al., 2010; Min & Rowe, 1999, 2006; Omer et al., 2001; Riffat et al., 2006; Vian et al., 2002; Vian & Astrain, 2009a, 2009b; Yang & Stabler, 2009; Yodovard et al., 2001). Regarding the last comment, it is common knowledge that efficiency of thermoelectric devices represents the key point to bear in mind, in order for these prospects to become reality.

A proper analysis of thermoelectric applications requires detailed studies on heat transfer between the thermoelectric modules, the heat source and the heat sink. In this sense, wrong selection of either the dissipation method (natural or forced convection, thermosyphons, etc.) or the refrigerant (air, water, eutectic fluids, etc.) leads to poor heat transfer and finally to low efficiencies. Although published improvements on heat transfer processes for other fields of knowledge are very common in scientific literature, thermoelectric developers have not been able to use all this information and apply it to the thermoelectric field, though this fact is being corrected nowadays. Thus, several studies have come out recently which address the application of different dissipation techniques to thermoelectric modules (Astrain et al., 2003, 2005, 2010; Knight et al., 1991; Omer et al., 2001; Ritzer & Lau, 1994, 2000; Rowe et al., 1995; Stockholm & Stockholm, 1992; Vian & Astrain, 2008, 2009a).

This chapter shows in the first place the influence of heat exchangers on the performance of both thermoelectric generation and thermoelectric refrigeration devices. Then, there are

presented different types of heat exchangers specifically designed for dissipating high heat fluxes from the cold and the hot side of thermoelectric devices. After that, the chapter studies the improvement in the efficiency of thermoelectric devices achieved with these heat exchangers. Finally, the concept of thermoelectric self-refrigeration is introduced; this application uses thermoelectric technology for the refrigeration and temperature control of a device, without electricity consumption.

2. Influence of heat exchangers on thermoelectric devices

A thermoelectric pair can be used to generate electric power, since Seebeck effect indicates that if the junctions of two thermoelectric legs type “p” and “n” are exposed to different temperatures, an electric current is induced. On the other hand, if an external electric source supplies power to the thermoelectric pair, Peltier effect states that one junction absorbs heat whereas the other one generates heat, so that the thermoelectric pair performs like a thermal machine that receives electric work, removes heat from a cold reservoir and emits heat to a hot reservoir. There are in the market different types of Peltier modules, composed of several thermoelectric pairs connected electrically in series and thermally in parallel. Figure 1 shows an average thermoelectric module working as refrigerator. In order to improve the heat transfer both in the hot and the cold side, a heat exchanger must be installed at either side of the Peltier module to increase the heat transfer area.

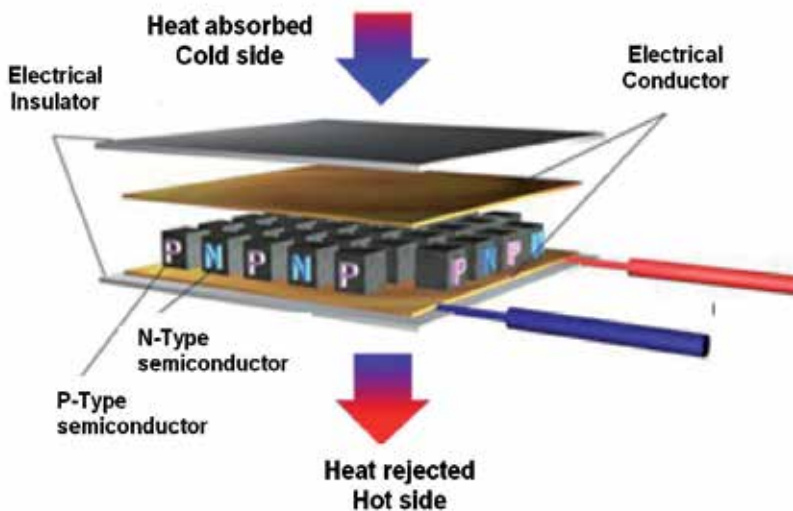


Fig. 1. Sketch of a Peltier module working as refrigerator.

The Peltier module is a small device that emits –or absorbs– large amounts of heat, so that the heat density or heat flux is significantly high. The face of a Peltier module is so small that increasing the heat transfer surface area of the heat exchanger (finned dissipator and cold plate in Figure 2) is virtually useless, since the effectiveness of the heat exchanger

decreases as more heat transfer surface area is added. This makes difficult to attain proper heat transfer. Therefore, efficiencies of thermoelectric modules and thermoelectric devices in general, designed for either generation or refrigeration purposes, depend to a great extent on the thermal resistances of the heat exchangers installed at either side of the modules.

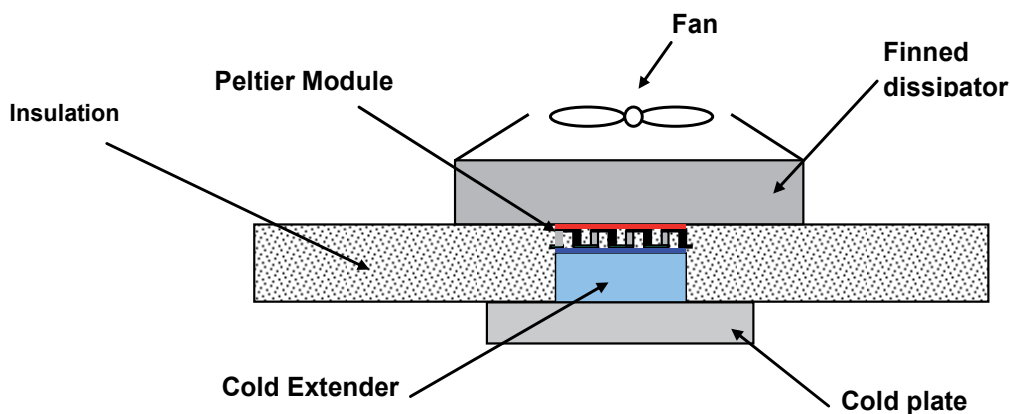


Fig. 2. Thermoelectric device.

Several computational models have been developed (Stockholm & Stockholm, 1992; Astrain et al., 2005, 2010; Crane & Bell, 2006; Crane et al., 2009) to study the whole thermoelectric system, including the heat exchangers. These models serve as study and design tools for both thermoelectric refrigeration and generation devices.

2.1 Development and validation of a computational model for thermoelectric systems

The computational model described in this section is an example that serves to assess the influence of the thermal resistances of the heat exchangers on the performance of thermoelectric devices. This model (Astrain et al., 2010) solves the non-linear system composed of thermoelectric and heat transfer equations, using the implicit finite-differences method. When used to simulate thermoelectric generation devices, the model requires the following inputs: geometric data, material properties, number and type of thermoelectric modules, thermal resistances of the heat exchangers, ambient temperature and energy introduced into the system. Then, the model outputs are: efficiency, voltage, electric current, electric power generated, temperatures and heat fluxes, all of them time-dependent. On the other hand, when the model simulates thermoelectric refrigeration devices, the inputs must be: geometric data, material properties, number and type of thermoelectric modules, thermal resistances of the heat exchangers, ambient temperature and voltage supplied to the modules. Then, the model provides temperatures and heat fluxes, coefficient of performance (COP), electric current and electric power consumed, again all of them time-dependent.

The model solves the one-dimensional thermal conduction equation in transitory state, being ρ density, c_p specific heat under constant pressure, t time, and \dot{q} heat flux generated.

$$\rho c_p \frac{\partial T}{\partial t} = k \left(\frac{\partial^2 T}{\partial x^2} \right) + \dot{q} \quad (4)$$

Firstly, the system must be discretized, that is, reduced into a set of representative nodes, as can be seen in Figure 3 for a thermoelectric generation system. Then, after using the first and second derivatives in finite differences (Özisik, 1994), the one-dimensional thermal conduction equation in transitory state is transformed into the finite differences form, applied to a node "i".

$$\frac{C_i}{\delta\tau} (T'_i - T_i) = \frac{T'_{i-1} - T'_i}{R_{i-1,i}} + \frac{T'_{i+1} - T'_i}{R_{i,i+1}} + \dot{Q}_i \quad (5)$$

The thermal resistance between nodes "i" and "i+1", as well as the thermal capacity of node "i" are expressed by the following equations, being $L_{i,i+1}$, A_i and V_i respectively the distance, cross section and volume between two connected nodes. Thermal resistances and capacities of commercial thermoelectric modules can be found in the scientific literature (Astrain et al., 2005, 2010; Min & Rowe, 2006). Thermal contact resistances between the components of the thermoelectric system can be found in the literature (Ritzer & Lau, 1994). The thermal resistances of the heat exchangers are parameters of study; therefore they are model inputs.

$$R_{i,i+1} = \frac{L_{i,i+1}}{k_i A_i} \quad (6)$$

$$C_i = V_i \rho_i c_p \quad (7)$$

The generated (or absorbed) heat flux in node "i" is represented by the last member on the right of the equation (5), and its value is given by the Peltier, Joule and Thomson effects.

Regarding thermoelectric generation, one can obtain the voltage and the electric power generated by a thermoelectric module with the following expressions, where m stands for the ratio of the electrical load resistance to the electrical resistance of the module, and N represents the number of thermoelectric pairs of the module.

$$\Delta V = \left(\frac{m}{1+m} \right) 2N \left((\alpha_h T_h - \alpha_c T_c) - \tau (T_h - T_c) \right) \quad (8)$$

$$P = \Delta VI \quad (9)$$

Regarding thermoelectric refrigeration, the thermal resistance of the insulating chamber of a thermoelectric refrigerator is provided by the following expressions, where S and e represents the surface area and thickness of the chamber, whereas U stands for the global heat transfer coefficient. The convection coefficients inside and outside the chamber (h_{in} , h_{out})

are calculated with equation (12), which is an experimental expression of the convection coefficient in a plane plate that considers laminar flow and dismisses viscosity dissipation (Parmelee & Huebscher, 1947).

$$R_{ins} = \frac{1}{US} \tag{10}$$

$$U = \frac{1}{1/h_{in} + e/k + 1/h_{out}} \tag{11}$$

$$\begin{aligned} Nu_L &= 0.664 \cdot Pr^{1/3} \cdot Re_L^{1/2} \\ 0.6 \leq Pr \leq 50, Re < Re_{x,c} &\approx 5 \cdot 10^5 \end{aligned} \tag{12}$$

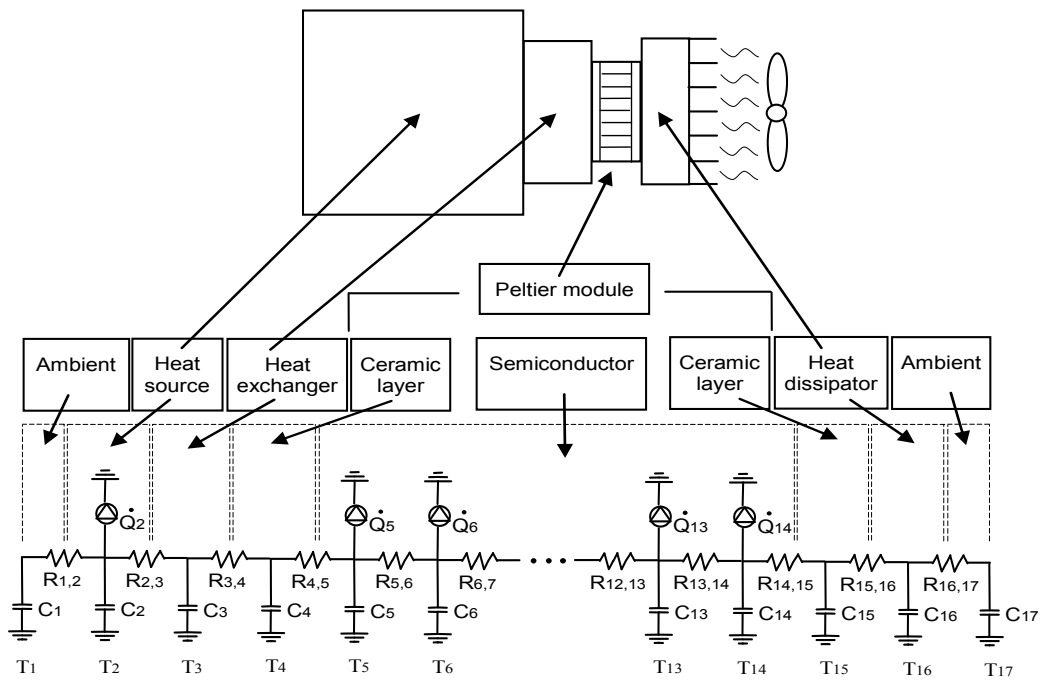


Fig. 3. Sketch and discretization of a thermoelectric generator.

The experimental validation proved that this computational model predicts the experimental values of the output parameters with errors always lower than 10%. Therefore, this model is an appropriate tool to study and present the significant influence that the heat exchangers have on the performance of both thermoelectric refrigerators and generators.

2.2 Influence of heat exchangers on the performance of thermoelectric refrigerators

Different values of thermal resistances of the heat exchangers at either side of the thermoelectric module are introduced in the computational model in order to study their influence on the performance of a thermoelectric refrigerator. Moreover, resulting model

simulations were complemented with experimental tests conducted with a prototype thermoelectric refrigerator supplied with 12 V, and different configurations of heat exchangers. A controllable fan was installed over the heat exchanger outside the refrigerator (consisting of a finned dissipator), which allows the control of the air flowing through the fins of this heat exchanger and, therefore, its thermal resistance. Inside the refrigerator, the studied configurations of heat exchanger were: flat plate (no fins) without fan, finned dissipator without fan, finned dissipator with a fan supplied with 3 V (0.5 W).

Table 1 shows experimental and simulated temperatures inside the refrigerator (T_{int}) and at either side of the Peltier module (T_{hp} and T_{cp}), as well as the temperature difference between the inside and the ambient ($T_{amb}-T_{int}$). The model predicts temperatures accurately, and the maximum error in temperature differences reaches 1.2 K. What is more, the study highlights the significant influence of the thermal resistances of the heat exchangers on the performance of thermoelectric refrigerators; particularly, the temperature difference between the inside of the refrigerator and the ambient increases by more than 40% when configuration 4 is used instead of configuration 2.

Configuration	Test characteristics	Temperature (K)	Model	Prototype
1	Outside: Finned dissipator, fan supplied with 12 V.	T_{int}	278.9	277.7
		T_{hp}	311.2	308.4
		T_{cp}	263.3	261.6
	Inside: Flat plate, no fan.	$(T_{amb}-T_{int})$	17.8	19
2	Outside: Finned dissipator, fan supplied with 4 V.	T_{int}	280.6	279.8
		T_{hp}	316.2	312.1
		T_{cp}	265.2	264
	Inside: Flat plate, no fan.	$(T_{amb}-T_{int})$	16.1	16.9
3	Outside: Finned dissipator, fan supplied with 12 V.	T_{int}	278.5	277.3
		T_{hp}	312.6	309.4
		T_{cp}	265.3	264.2
	Inside: Finned dissipator, no fan.	$(T_{amb}-T_{int})$	18.1	19.3
4	Outside: Finned dissipator, fan supplied with 12 V.	T_{int}	273.7	272.7
		T_{hp}	311.4	308.8
		T_{cp}	266.6	266
	Inside: Finned dissipator, fan supplied with 3 V.	$(T_{amb}-T_{int})$	22.9	23.9

Table 1. Experimental and simulated results for 12 V of supplied voltage to the Peltier module, ambient temperature 296.6 K and 60% of relative humidity.

2.3 Influence of heat exchangers on the performance of thermoelectric generators

A methodology similar to that used for thermoelectric refrigerators was applied to study the influence of the thermal resistances of the heat exchangers at either side of the thermoelectric modules on the electric power generated by a thermoelectric generator. Figure 4 shows the electric power as a function of both thermal resistances, where one can observe the significant increase in the electric power that occurs when decreasing the thermal resistances of both heat exchangers. As an example, if both thermal resistances improved from 0.5 to 0.4 K/W, the electric power generated would increase by 20 %. On average, a decrease by 10 % in both thermal resistances entails an increase in the electric power by around 8 %. This serves to illustrate the importance of the design of heat exchangers in thermoelectric generation applications.

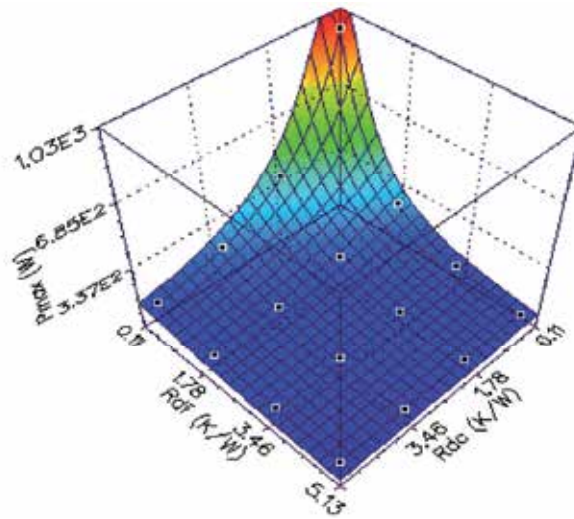


Fig. 4. Electric power generated (P_{max}) versus thermal resistance of the hot side heat exchanger (R_{dc}) and thermal resistance of the cold side heat exchanger (R_{df}).

3. Heat exchangers analysis

Once we have demonstrated the enormous importance that thermal resistances of heat exchangers have on the performance of thermoelectric devices, it is of high interest to show the most significant designs of heat exchangers applied to thermoelectrics.

3.1 Finned dissipator

This type of heat exchanger represents the most used heat dissipation system in thermoelectric refrigeration, essentially because of its low manufacturing cost. However, this is not the best option whatsoever. Major problems of this design relate to constriction thermal resistances (Lee et al., 1995), which are inherent to the small surface areas of Peltier modules. This fact entails that a significant surface area of the dissipator is useless, as can be seen at the top of Figure 5.

Some works (Astrain & Vian, 2005) have already addressed the optimization of a finned dissipator for the hot end of a Peltier module. The optimization parameters were: position of the module, position and type of fan, thickness of the dissipator base, and height of the fins. The most outstanding conclusions were:

- When the fan is placed at one end of the dissipator so that the air crosses the dissipator from one side to the other, the optimal position of the module is not the exact centre but a bit closer to the fan. Moreover, this fact gains significance as the air flow increases.
- If an axial fan is installed over the dissipator, the thermal resistance decreases by 5.5 % with respect to the previous case.
- Increasing the base thickness of the dissipator leads to a decrease in the thermal resistance without affecting the pressure losses. Specifically, if this parameter increases from 8 mm to 16 mm, the thermal resistance decreases by 13.2 %. However, this fact also leads to heavier and more expensive dissipators.

- Increasing the height of the fins is also beneficial from both a thermal and hydrodynamic point of view. Specifically, if this parameter rises from 40 mm to 60 mm in a dissipator with an axial fan over it, the thermal resistance reduces by 10.4 %.

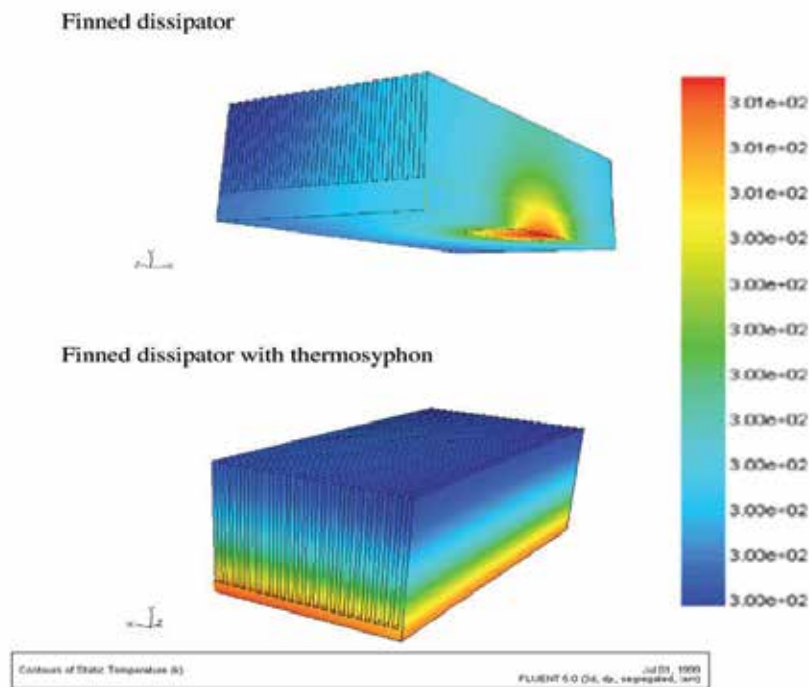


Fig. 5. Temperature distribution in a finned dissipator, with and without thermosyphon.

Finally, this work presents a prototype thermoelectric refrigerator that served to experimentally prove that the COP improves by 10 % if the thermal resistance of the heat exchanger installed at the hot side of the Peltier modules decreases by 13 %.

In conclusion, this work makes evident the important role that holds the thermal resistance of the heat exchangers in the efficiency of a thermoelectric refrigeration device. Likewise, it also indicates that the thermal resistance of a finned dissipator is too high despite the optimization process. This fact indicates that it is absolutely necessary to design new types of heat exchangers in order to reduce even more the thermal resistance and increase the efficiency of thermoelectric devices. In this line of work, there have been developed the phase-change thermosyphons, described in the following section.

3.2 Thermosyphon for the hot end of a Peltier module

A thermosyphon is a hermetically sealed container in the shape of a straight prism, enclosing a fluid. The Peltier module is attached to the bottom of the rear surface, so that the heat flux produced by the module is transmitted to the fluid, which begins to boil. Vapour produced in the process rises up to the top of the thermosyphon by natural convection. Likewise, the cold reservoir (usually the ambient) is connected to the front surface of the thermosyphon, where several fins are installed. Thus, when the vapour touches this cold

surface, it cools down, then condensates and finally gravity makes it go down to the bottom of the thermosyphon. As a result, the fluid forms a cycle completely closed and self-sufficient. Figure 6 describes the process.

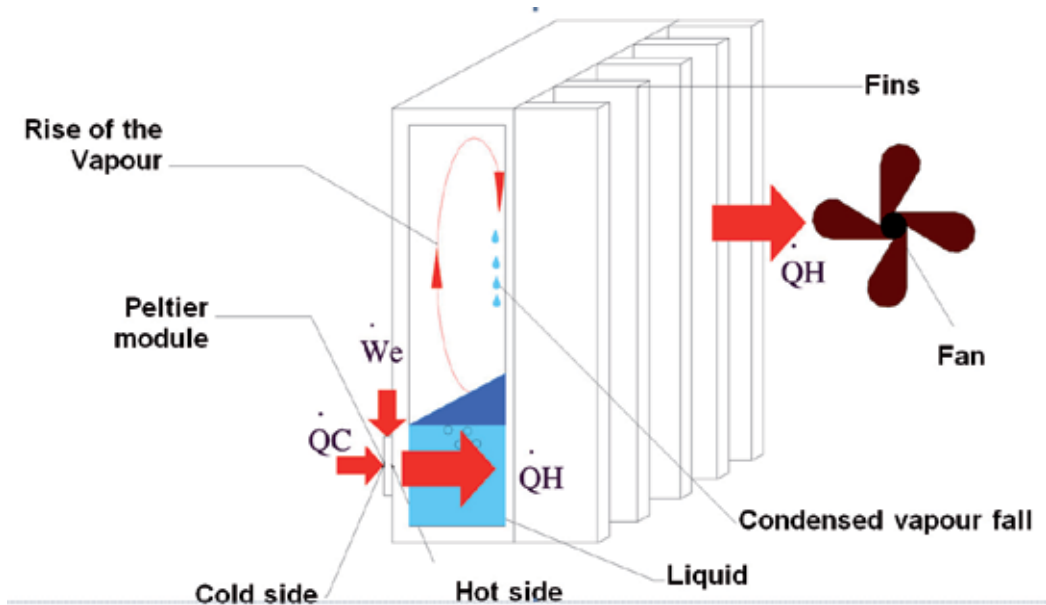


Fig. 6. Phase-change thermosyphon for the hot end of a Peltier module.

The heat flux emitted by the module (\dot{Q}_c) is uniformly distributed along the base area of the finned dissipator, as can be seen at the bottom of Figure 5, thus increasing significantly the efficiency of the system. Likewise, the heat flux produced by the condensation process (\dot{Q}_h) is transferred to the ambient. A fan enhances the heat transfer.

Figure 7 presents experimental values of thermal resistances of a prototype thermosyphon (called TSF) attached to a commercial 40 mm x 40 mm Peltier module, for different ambient temperatures, along with the thermal resistance of a similar-in-weight commercial dissipator (Astrain et al., 2003). It can be seen that the thermal resistance of this TSF decreases as the ambient temperature increases, owing to the fact that the boiling and condensation coefficients improve with temperature. This thermosyphon attains a thermal resistance ranging from 0.125 °C/W for 20 °C of ambient temperature to 0.079 °C/W for ambient temperature 35 °C. This leads to an improvement in the dissipation by 23.8 % at 20 °C, and 51.4 % at 35 °C of ambient temperature, with respect to the values obtained with a similar commercial dissipator. This heat exchanger was installed in a prototype thermoelectric refrigerator and the COP increased by 21.3 % for ambient temperature 19 °C, and 36.5 % for ambient temperature 30 °C.

As indicated before, the major advantage of thermoelectric technology with respect to vapour compression refrigeration lies on the reduction in the number of moving parts, since no compressor needs to be installed. However, the thermosyphon TSF does need a fan. Further designs present optimized thermosyphons that require no fans at all, thus removing all the moving parts, such as the Bosch-Siemens patented thermosyphon called TSV (Astrain

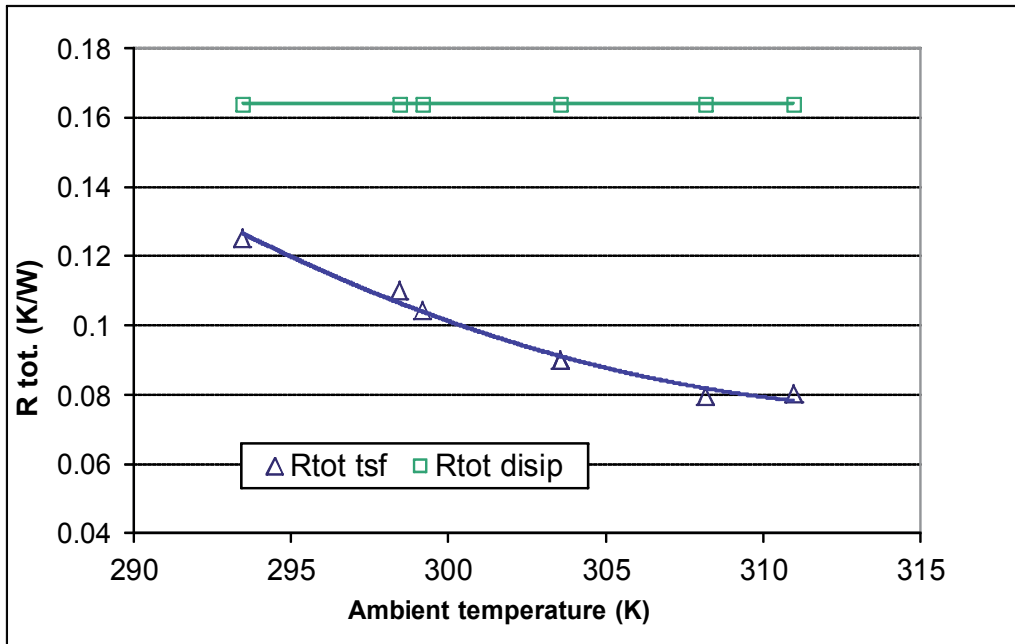


Fig. 7. Thermal resistance of a real thermosyphon and a similar finned dissipator versus ambient temperature.

et al., 2006a). Figure 10 shows a sketch of a thermoelectric device that incorporates a cylindrical TSV for the hot side of the Peltier module. Its basic concept is similar to that behind the TSF, so that a deposit for the liquid and a condensation zone must be included in the design. The latter represents the major difference with respect to the TSF, since it must be cylindrical now, thus increasing the heat transfer surface area, which makes TSV work properly with natural convection. Experimental values of TSV's thermal resistances are showed in Figure 8, where they are compared with those obtained with a TSF for both natural and forced convection.

3.3 Thermosyphon and capillarity lift for the cold end of a Peltier module

At the cold side of a Peltier module, the problem remains similar to that at the hot side, though in this case the heat flux is not emitted but absorbed by the module, and the objective is to improve the heat transfer between the thermoelectric module and the refrigeration chamber of a thermoelectric refrigerator.

Like in the previous case, the most used heat exchanger is a finned dissipator due to its low cost. However, new designs combining thermosyphon and capillarity lift technologies have been proposed, such as the Bosch-Siemens patented thermosyphon TMP (Astrain et al., 2006b), which improves significantly the thermal resistance of this heat exchanger. The TMP is installed in the refrigerator so that one face is attached to the cold end of the module, and the opposite face is inside the refrigeration chamber. This thermosyphon increases the heat transfer surface area from the small surface of the Peltier module to the significantly bigger surface area of a finned dissipator, taking advantage of the high heat transfer inherent to

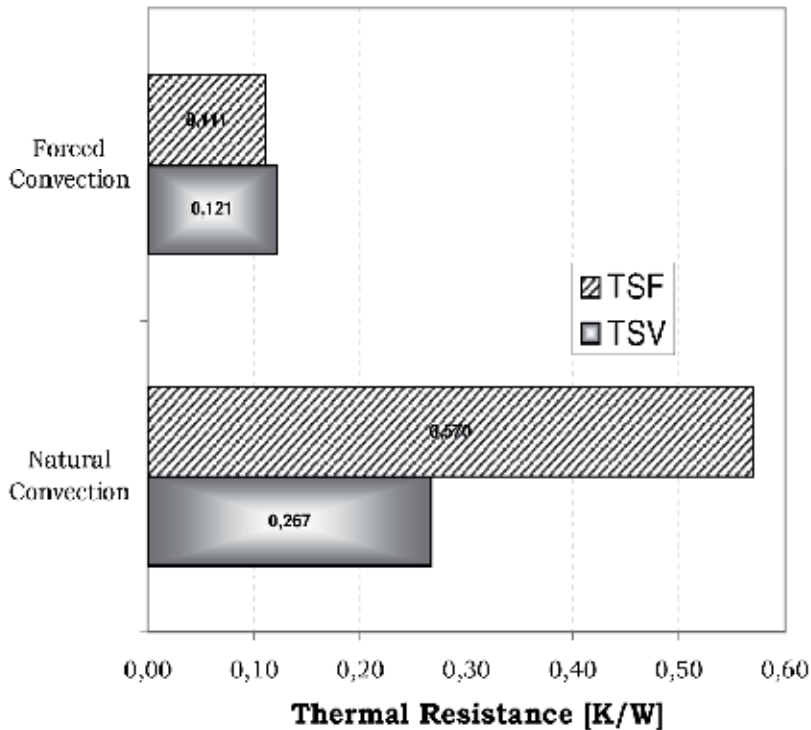


Fig. 8. Thermal resistances of TSF and TSV for natural and forced convection.

phase-change processes, capillarity lift through porous materials and gravity pulling down condensed liquids.

As can be seen in Figure 9, the TMP basically consists of a watertight compartment and a porous layer attached to one of its inner faces. When heat is absorbed from the refrigerated chamber, the liquid evaporates and transfers this heat to the cold end of the Peltier module. The porous layer makes the fluid at the bottom of the TMP ascend by capillarity, surmounting gravity, thus making use of all the surface area of the TMP for the evaporation process. Vapour formed ascends by natural convection, condenses near the cold face of the Peltier module and goes down as liquid pulled by gravity, thus forming a completely closed and self-sufficient cycle.

Subsequently, this TMP was incorporated into a prototype of thermoelectric refrigerator, which served to assess the improvement attained with respect to a similar thermoelectric refrigerator including a finned dissipator for the cold side of the Peltier modules (Vian & Astrain, 2009b). The TMP had a thermal resistance of 0.323 K/W when a small fan with 0.75 W of electric power consumption was installed in the refrigeration compartment. In the same conditions, a finned dissipator similar in size to the TMP provided a significantly higher thermal resistance of 0.513 K/W. Likewise, it was experimentally proved that the COP of the thermoelectric refrigerator endowed with a TMP increases by 32 % with respect to the COP of this refrigerator but including a finned dissipator at the cold side of the Peltier module.

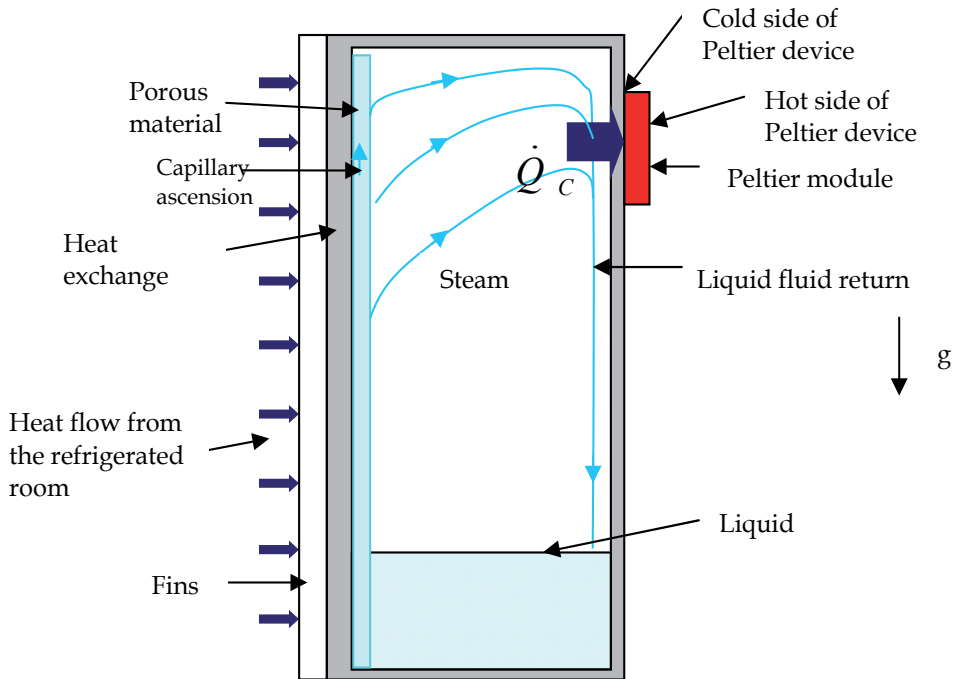


Fig. 9. Performance of the TMP.

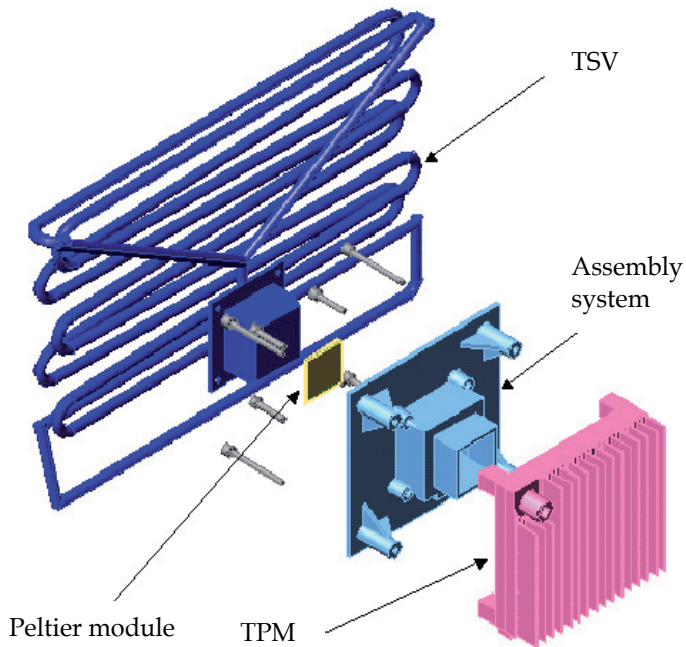


Fig. 10. Thermoelectric device with the heat exchangers TSV and TPM.

Figure 10 shows the sketch of a prototype thermoelectric refrigerator including the two types of thermosyphon explained along this section, for either end of the Peltier module.

Likewise, Figure 11 provides two photographs of this prototype, indicating the cited heat exchangers (TSV and TMP) in a thermoelectric refrigerator, the COP increased by 66% with respect to that obtained with a similar thermoelectric refrigerator endowed with finned dissipators (Vian & Astrain 2009b).

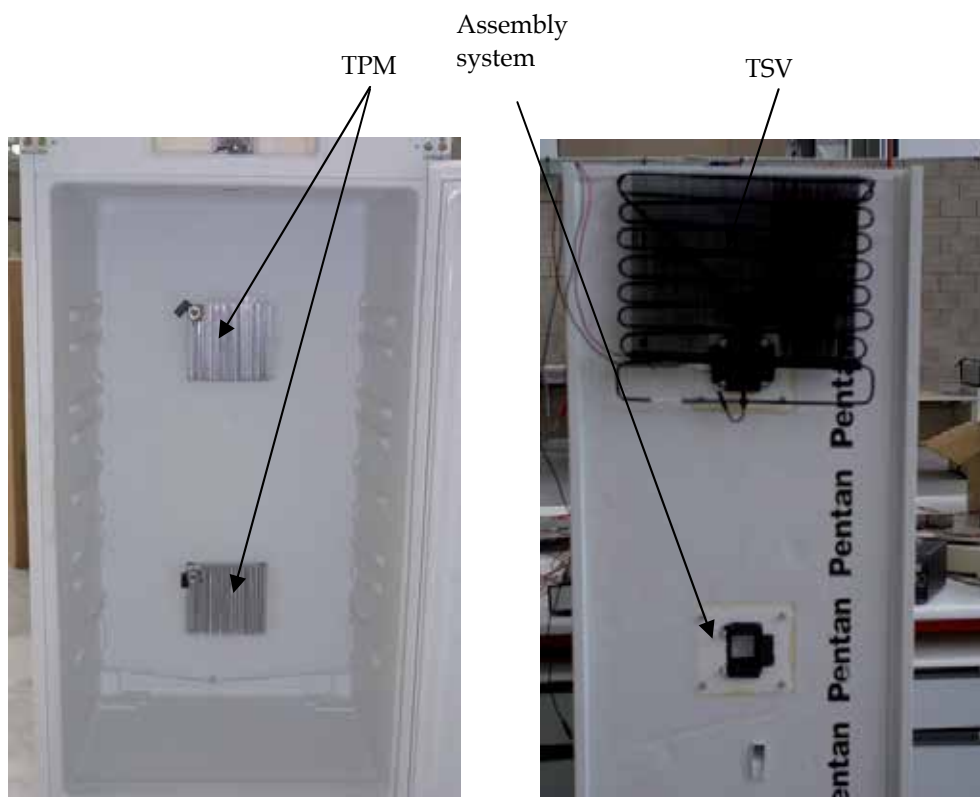


Fig. 11. Photographs of the prototype with heat exchangers TPM and TSV.

4. Thermoelectric self-cooling of devices (TSC)

Recently, a new thermoelectric application has come out (Martinez et al., 2011), which allows the self-cooling of any device that generates a certain amount of heat, such as electrical power converters, transformers, control systems, etc. As can be seen in Figure 12, the Peltier module in this application works as an electric power generator, since it harnesses the thermal gradient between the heat source (device that generates a certain amount of heat and must be cooled) and the ambient to produce electric power, which in turn is used to operate a fan and attain forced convection over a dissipator, thus improving the cooling of the device without electricity consumption. At the same time, the hot side of the module absorbs heat by Peltier effect, which reinforces the cooling process of the device. This work describes the design and experimental study of a prototype of TSC composed of:

- Two thin film heating resistors with dimensions 80 mm × 80 mm × 0.5 mm, each one capable of providing 150 W at 200 °C, connected in series to a controllable DC power source. These elements serve to generate a controllable and measurable heat flux, and represent the heat source that must be cooled.
- A 220 mm × 160 mm × 32 mm aluminium plate composed of two pieces screwed to each other, the bottom one endowed with two similar cavities, wherein the heating resistors are installed.
- Four Peltier modules Kryotherm TGM-287-1.0-1.5, with dimensions 40 mm × 40 mm × 3.8 mm, and capable of working at 225 °C.
- An aluminium finned dissipator composed of a square base plate, with side length 155 mm and height 12 mm, and 23 fins with dimensions 155 mm × 23 mm × 1.5 mm.
- One rectangular aluminium prism is installed between the modules and the dissipator in order to separate the device from the dissipator and avoid thermal bridges between them, which would decrease the efficiency of the system. This element is 55 mm long and has a squared base area with side length 80 mm.
- A DC fan type SUNON KDE1208PTS1-6, and a wind tunnel over the dissipator.

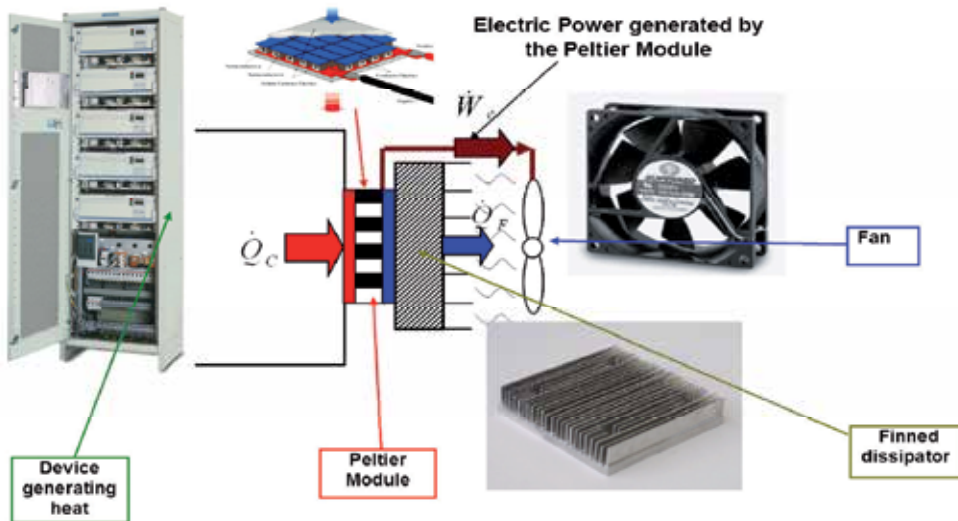


Fig. 12. Sketch of a thermoelectric self-cooling system.

This prototype served to conduct several experimental tests in order to study the thermal resistance between the heat source and the ambient, and compare it to that obtained when only the dissipator was mounted over the heat source (no modules, no fan), and finally compare it to the thermal resistance between the heat source and the ambient when no cooling system was mounted. Figure 13 shows the comparison between these three thermal resistances as functions of the heat flux generated by the heating resistors. As expected, the highest thermal resistance is achieved when no cooling system is attached to the device. More interesting is the fact that the TSC system always outperforms the dissipator alone, especially when the heat flux generated by the device exceeds 130 W. For lower values of heat flux, the electric power generated by the Peltier modules does not suffice to operate the fan. However for heat fluxes higher than 130 W, the electric power generated by the

modules makes the fan rotate and, therefore, provides forced convection over the dissipator, which improves the heat transfer efficiency and decreases the thermal resistance between the heat source and the ambient by 30 % without electricity consumption.

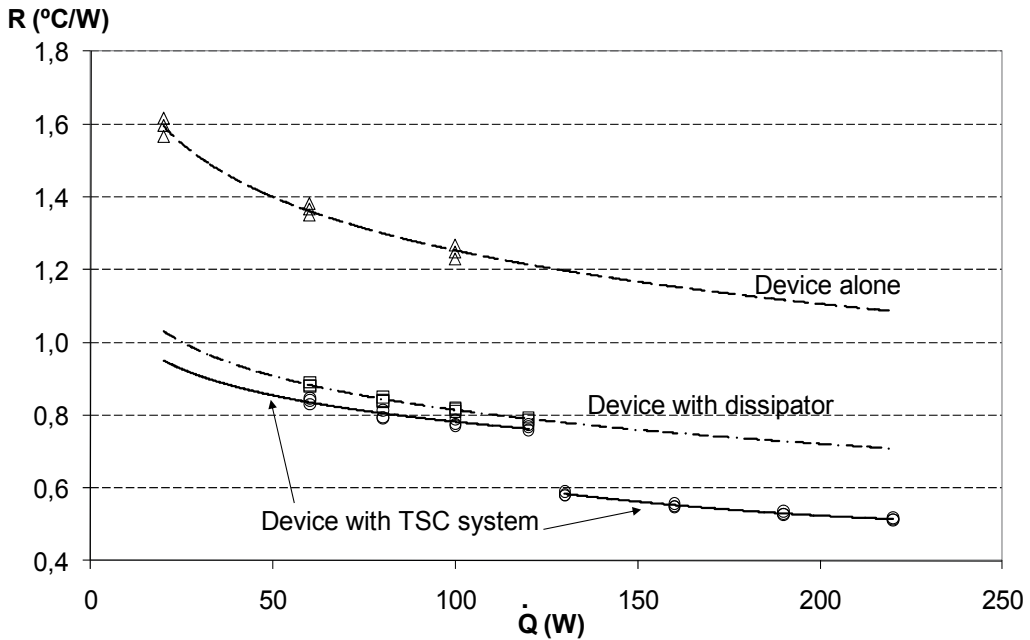


Fig. 13. Thermal resistances between heat source and ambient versus heat flux generated.

5. Conclusions

Thermoelectric technology has evolved significantly in the last decade, fundamentally due to the improvement of thermoelectric materials, which boosted the commercialization of novel applications in the civil market. However, efficiencies of thermoelectric devices that provide heating, cooling and generation of electric power are still low. In this sense, the scientific community considers essential the optimization of heat exchangers that must be mounted at either end of the Peltier modules.

This chapter has shown the major influence of the heat exchangers on the efficiency of thermoelectric devices, and indicates that this efficiency rises as the thermal resistances of both heat exchangers decreases. Particularly, for thermoelectric generators, a decrease by 10 % in both thermal resistances leads to an average increase in the electric power generated by around 8 %.

The optimization of finned dissipators used in thermoelectric refrigerators allows the reduction of their thermal resistances, which in turn increases the COP of these

thermoelectric devices. However, finned dissipators do not represent the most efficient heat exchangers, since constriction thermal resistances restrict, to a great extent, the global thermal resistance of the dissipator.

Two different heat exchangers are presented, one for the hot side and the other for the cold side of the Peltier modules. On one hand, the TSF (phase-change thermosyphon) reduces the thermal resistance between the hot side of the module and the ambient by 51 %, which means an increase in the COP of thermoelectric refrigerators by 36.5 %. Subsequently, this TSF was improved and a thermosyphon with natural convection (TSV) came out, thus eliminating all moving parts. On the other hand, for the cold side of the Peltier modules, the described TMP joins thermosyphon and capillarity lift technologies and improves by 37 % the thermal resistance of a similar-in-size finned dissipator. Finally, a prototype that included the developed thermosyphons TSV and TMP showed an improvement on the COP by 66 % with respect to that attained with a similar prototype but including finned dissipators.

In the last part of the chapter, the novel concept of thermoelectric self cooling has been introduced, which can be applied to any device that generates a certain amount of heat, such as electrical power converters, transformers and control systems. When the thermoelectric self cooling system is installed, the thermal resistance between the heat source and the environment decreases by up to 30 % without electricity consumption.

6. References

- Astrain, D.; Vian, J. G. & Domínguez, M. (2003). Increase of COP in the Thermoelectric Refrigeration by the Optimization of Heat Dissipation. *Applied Thermal Engineering*, Vol.23, No.17, (December 2003), pp. 2183-2200, ISSN 1359-4311
- Astrain, D. & Vian, J. G. (2005). Study and Optimization of the Heat Dissipator of a Thermoelectric Refrigerator. *Journal of Enhanced Heat Transfer*, Vol.12, No.2, (April 2005), pp. 159-170, ISSN 1065-5131
- Astrain, D.; Vian, J. G. & Albizua, J. (2005). Computational Model for Refrigerators based on Peltier Effect Application. *Applied Thermal Engineering*, Vol.25, No.17, (December 2005), pp. 3149-3162, ISSN 1359-4311
- Astrain, D.; Lamuela, J. M.; García, S. & Vian, J. G. (2006a). Kältegerät und Peltier-Kühlvorrichtung dafür, 2006, WO2006010539, BOSCH-SIEMENS, Germany. *INTERNATIONAL PATENT*: F25B21/02; F25B21/02. EUROPEAN: F25B21/02
- Astrain, D.; Lamuela, J. M.; García, S. & Vian, J.G. (2006b). Thermosiphon, 2006, WO2006010541, BOSCH-SIEMENS, Germany. *INTERNATIONAL PATENT*: (IPC1-7): F28D15/04 EUROPEAN: F28D15/04B;H01L35/30.
- Astrain, D.; Vian, J. G.; Martínez, A. & Rodríguez, A. (2010). Study of the Influence of Heat Exchangers' Thermal Resistances on a Thermoelectric Generation System. *Energy*, Vol.35, No.2, (February 2010), pp. 602-610, ISSN 0360-5442
- Bell, L. E. (2008). Cooling, Heating, Generating Power, and Recovering Waste Heat with Thermoelectric Systems. *Science*, Vol.321, No.5895, (September 2008), pp. 1457-1461, ISSN 1095-9203

- Crane, D. T. & Bell, L. E. (2006). Progress towards Maximizing the Performance of a Thermoelectric Power Generator. *Proceedings of the 25th International Conference on Thermoelectrics* (2006), pp. 11-16, ISBN 1-4244-0811-3, Vienna, Austria, August 6-10 2006
- Crane, D. T.; Kossakovski, D. & Bell, L. E. (2009). Modelling the Building Blocks of a 10% Efficient Segmented Thermoelectric Power Generator. *Journal of Electronic Materials*, Vol.38, No.7, (July 2009), pp. 1382-1386, ISSN 0361-5235
- Chang, Y.; Chang, C.; Ke, M. & Chen, S. (2009). Thermoelectric Air-cooling Module for Electronic Devices. *Applied Thermal Engineering*, Vol.29, No.13, (September 2009), pp. 2731-2737, ISSN 1359-4311
- Chein, R. & Huang, G. (2004). Thermoelectric Cooler Application in Electronic Cooling. *Applied Thermal Engineering*, Vol.24, No. 14-15, (October 2004), pp. 2207-2217, ISSN 1359-4311
- Goldsmid, H. J. (1964). *Thermoelectric Refrigeration*, Plenum Press, New York, NY, USA
- Goldsmid, H. J. (1986). *Electronic Refrigeration*, Pion, ISBN 0-8508-6119-5, London, UK
- Goldsmid, H. J. (1995) Conversion Efficiency and Figure-of-Merit, In: *Handbook of Thermoelectrics*, D. M. Rowe, pp. 19-40, CRC Press, ISBN 0-8493-0146-7, New York, NY, USA
- Gordon, J. M.; Ng, K. C.; Chua, H. T. & Chakraborty, A. (2002). The Electro-adsorption Chiller: a Miniaturized Cooling Cycle with Applications to Micro-electronics. *International Journal of Refrigeration*, Vol.25, No.8, (December 2002), pp. 1025-1033, ISSN 0140-7007
- Hongxia, X. & Lingai, L. (2007). Development and Applications of Solar-based Thermoelectric Technologies. *Renewable and Sustainable Energy Reviews*, Vol.11, No.5, (June 2007), pp. 923-936, ISSN 1364-0321
- Khattab, N. M. & El Shenawy, E. T. (2006). Optimal Operation of Thermoelectric Cooler Driven by Solar Thermoelectric Generator. *Energy Conversion and Management*, Vol.47, No.4, (March 2006), pp. 407-426, ISSN: 0196-8904
- Knight, R. W.; Gooding, R. W. & Hall, D. J. (1991). Optimal Thermal Design of Forced Convection Heat sinks-analytical, *Journal of Electronic Packaging* Vol.113, No.3, (September 1991), pp. 313-321 ISSN 1043-7398
- Martínez, A.; Vian, J. G.; Astrain, D.; Rodríguez, A. & Berrio, I. (2010). Optimization of the Heat Exchangers of a Thermoelectric Generation System. *Journal of Electronic Materials*, Vol.39, No.9 (September 2010), pp. 1463-1468, ISSN 0361-5235
- Martínez, A.; Astrain, D. & Rodríguez, A. (2011). Experimental and Analytical Study on Thermoelectric Self-cooling of Devices. *Energy*, Vol.36, No.8 (August 2011) pp. 5250-5260, ISSN 0360-5442
- Min, G. & Rowe D. M. (1999). Cooling Performance of Integrated Thermoelectric Microcooler. *Solid State Electronics*, Vol.43, No.5, (May 1999), pp. 923-929, ISSN 0038-1101
- Min, G. & Rowe, D. M. (2006). Experimental Evaluation of Prototype Thermoelectric Domestic-refrigerators. *Applied Energy*, Vol.83, No.2, (February 2006), pp. 133-152, ISSN 0306-2619

- Omer, S. A.; Riffat, S. B. & Ma, X. (2001). Experimental Investigation of a Thermoelectric Refrigeration System employing a Phase-change Material Integrated with Thermal Diode (Thermosyphons). *Applied Thermal Engineering*, Vol.21, No.12 (August 2001), pp. 1265-1271 ISSN 1359-4311
- Özisik, M. N. (1994). *Finite Difference Methods in Heat Transfer*, CRC Press, ISBN 0-8493-2491-2, Boca Raton, FL, USA
- Lee, S.; Song, S.; Au, V. & Moran, K. P. (1995). Constriction/Spreading Resistance Model for Electronics Packaging, *Proceedings of the 4th ASME/JSME Thermal Engineering Conference* (1995), Vol.4, pp. 199-206, ISBN 0-7918-1301-0, Lahaina, Maui, Hawaii, March 19-24 1995
- Parmelee, G. V. & Huebscher, R. G. (1947). Heat Transfer by Forced Convection Along a Smooth Flat Surface, *Heat Piping Air Conditioning Engineer*, Vol.19, No.8, (December 1947), pp. 115-122, ISSN 1527-4055
- Riffat, S. B. & Xiaoli, M. (2003). Thermoelectrics: a Review of Present and Potential Applications. *Applied Thermal Engineering*, Vol.23, No.8, (June 2003), pp. 913-935, ISSN 1359-4311
- Riffat, S. B.; Xiaoli, M. & Wilson, R. (2006). Performance Simulation and Experimental Testing of a Novel Thermoelectric Heat-pump System. *Applied Thermal Engineering*, Vol.26, No.5-6, (April 2006), pp. 494-501, ISSN 1359-4311
- Ritzer, T. M. & Lau, P. G. (1994). Economic Optimization of Heat Sink Design, *Proceedings of the 13th International Conference on Thermoelectrics* (1994), pp. 177-180, ISSN 0094-243X, Kansas City, Missouri, USA, August 30-September 1 1994
- Ritzer, T. M. & Lau, P. G. (2000). The Effect of Fan Orientation on Heat Sink Performance. *Proceedings of the 19th International Conference on Thermoelectrics* (2000), pp. 333-335, Cardiff, UK, August 22-24 2000
- Rowe, D. M.; Williams, S. G. K. & Min, G. (1995). The Effect of Heat Exchanger and Interface Materials on the Performance of a Hot-Water Thermoelectric Generating System. *Proceedings of the 2nd European Workshop on Thermoelectrics* (1995), pp. 98-102, Nancy, France, November 7-8 1995
- Rowe, D. M. (2006). *Thermoelectrics Handbook: Macro to Nano*. CRC Press, ISBN 0-8493-2264-2, Boca Raton, FL, USA
- Stockholm, J. G. & Stockholm, D. W. (1992). Thermoelectric Modelling of a Cooling Module with Heat Exchangers. *Proceedings of the 12th International Conference on Thermoelectrics* (1992), pp. 140-146, Austin, TX, USA, October 7-9 1992
- Vian, J. G.; Astrain, D. & Domínguez, M. (2002). Numerical Modelling and Design of a Thermoelectric Dehumidifier. *Applied Thermal Engineering*, Vol.22, No.6, (March 2002), pp. 407-422, ISSN 1359-4311
- Vian, J. G. & Astrain, D. (2008). Development of a Heat Exchanger for the Cold Side of a Thermoelectric Module. *Applied Thermal Engineering*, Vol.28, No.11-12, (August 2008), pp. 1514-1521, ISSN 1359-4311
- Vian, J. G. & Astrain, D. (2009a). Development of a Thermoelectric Refrigerator with Two-phase Thermosyphons and Capillary Lift. *Applied Thermal Engineering*, Vol.29, No.10, (July 2009), pp. 1935-1940, ISSN 1359-4311

- Vian, J. G. & Astrain, D. (2009b). Development of a Hybrid Refrigerator Combining Thermoelectricity and Vapour-compression Technologies. *Applied Thermal Engineering*, Vol.29, No.16 (November 2009), pp. 3319-3327, ISSN 1359-4311
- Yang, J. & Stabler, F. R. (2009). Automotive Applications of Thermoelectric Materials. *Journal of Electronic Materials*, Vol.38, No.7, (July 2009) pp. 1245-1251, ISSN 0361-5235
- Yodovard, P.; Khedari, J. & Hirunlabh, J. (2001). The Potential of Waste Heat Thermoelectric Power Generation from Diesel Cycle and Gas Turbine Cogeneration Plants. *Energy Source*, Vol.23, No.3 (January 2001), pp. 213-224, ISSN 0090-8312

Part 3

Helical Coils and Finned Surfaces

Helically Coiled Heat Exchangers

J. S. Jayakumar

*Professor, Dept. of Mechanical Engineering,
Amrita Vishwa Vidyapeetham,
Amrita School of Engineering, Amritapuri, Kollam,
India*

1. Introduction

It has been widely reported in literature that heat transfer rates in helical coils are higher as compared to those in straight tubes. Due to the compact structure and high heat transfer coefficient, helical coil heat exchangers find extensive use in industrial applications such as power generation, nuclear industry, process plants, heat recovery systems, refrigeration, food industry, etc. (Abdulla 1994; Bai et al. 1999; Futagami and Aoyama 1988; Jensen and Bergles 1981; Patankar et al. 1974; Xin et al., 1996). Heat exchanger with helical coils is used for residual heat removal systems in islanded or barge mounted nuclear reactor systems, wherein nuclear energy is utilised for desalination of seawater (Manna et al., 1998). The performance of the residual heat removal system, which uses a helically coiled heat exchanger, for various process parameters was investigated by Jayakumar and Grover (1997). The work had been extended to find out the stability of operation of such a system when the barge on which it is mounted is moving (Jayakumar, 1999; Jayakumar et al., 2002).

1.1 Terminology of helically coiled pipes

Fig. 1 gives the schematic of the helical coil. The pipe has an inner diameter $2r$. The coil diameter is represented by $2R_C$ (measured between the centres of the pipes). The distance between two adjacent turns, called pitch is H . The coil diameter is also called as pitch circle diameter (PCD). The ratio of pipe diameter to coil diameter (r/R_C) is called curvature ratio, δ . The ratio of pitch to developed length of one turn ($H/2\pi R_C$) is termed non-dimensional pitch, λ . Consider the projection of the coil on a plane passing through the axis of the coil. The angle, which projection of one turn of the coil makes with a plane perpendicular to the axis, is called the helix angle, α . Consider any cross section of the pipe created by a plane passing through the coil axis. The side of pipe wall nearest to the coil axis is termed inner side of the coil and the farthest side is termed as outer side of the coil. Similar to Reynolds number for flow in pipes, Dean number is used to characterise the flow in a helical pipe.

1.2 Review of single-phase flow and heat transfer

Heat transfer and flow through a curved tube is comprehensively first reviewed by Berger et al. (1983) and subsequently by Shah and Joshi (1987). The latest review of flow and heat transfer characteristics is provided by Naphon & Wongwises (2006). The characteristics of

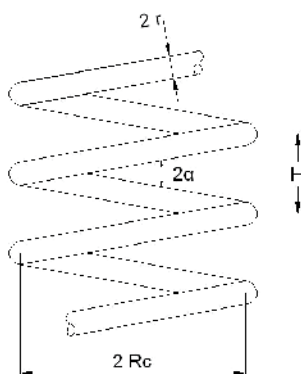


Fig. 1. Basic geometry of a helical pipe.

flow, pressure drop and heat transfer have been reported by many investigators. The heat transfer enhancement in helical coil systems is reported by Prabhanjan et al. (2004), Berger et al. (1983), Janssen & Hoogendoorn (1978) and Ruthven (1971). Condensing heat transfer and pressure drop of refrigerant R 134A in helicoidal (helical double pipe heat exchanger) is experimentally investigated by Kang et al. (2000). The effect of torsion on the flow in a helical tube of circular cross-section is experimentally investigated by Yamamoto et al. (1995) for a range of Reynolds numbers from about 500 to 20000. Study of fluid flow through curved tubes are of interest to the medical community since many arteries are curved (Zabielski, & Mestel, 1998a; Zabielski, & Mestel, 1998b).

1.2.1 Laminar-turbulent transition

The curved shape of the tube causes the flowing fluid to experience centrifugal force. The extent of centrifugal force experienced depends on the local axial velocity of the fluid particle and the radius of curvature of the coil. The fluid particles flowing at the core of the pipe have higher velocities than those flowing near to the pipe wall. Thus the fluid particles flowing close to the tube wall experience a lower centrifugal force than the fluid particles flowing in the tube core. This causes the fluid from the core region to be pushed towards the outer wall (away from the coil axis). This stream bifurcates at the wall and drives the fluid towards the inner wall along the tube periphery, causing generation of counter-rotating vortices called secondary flows. The secondary flows produce additional transport of the fluid over the cross section of the pipe. This additional convective transport increases both the heat transfer and the pressure drop when compared to that in a straight tube.

It has been found that the effect of coil curvature is to suppress turbulent fluctuations arising in the flowing fluid and smoothing the emergence of turbulence. Thus it increases the value of the Reynolds number required to attain a fully turbulent flow, as compared to that of a straight pipe. The above effect of turbulent fluctuations suppression enhances as the curvature ratio increases. Torsion, on the other hand, is found to destabilize the flow, reducing the Reynolds number at which turbulence emerges. It may impart a Reynolds number for transition to turbulent, close to or even lower than the ones characteristic of straight pipe flow. The above destabilizing effect first increases, as torsion increases, reaches a maximum and then decreases with further increase in torsion. Due to the interaction

between turbulence emergence and curvature effects, the same Reynolds number flow may present an equal or even a lower hydraulic resistance in a curved channel than it does in a straight one. Apparently, the reducing effect of curvature on friction, due to the smoothing of turbulence emergence, equals, or even overcomes, the increasing effect due to the secondary flow. But in practical applications, due to layout and economic considerations, the value of torsion is never reaches an effect of destabilization of flow and hence reduction in value of critical Reynolds number.

Another important phenomena observed in helical tubes is the relaminarization. The fluid flow, which was originally turbulent, changes to laminar while flowing inside a helical pipe. This has been experimentally demonstrated by Sreenivasan and Strykowski (1983). The experiment was conducted using a pipe of diameter 19.1 mm wound to form a coil of 90 mm. In the experiment, dye streak introduced at two locations, viz., into the straight section upstream of the coil and into the fourth turn of the coil. It has been observed that the dye introduced in the straight section diffuses rapidly, indicating that the flow there is turbulent. While the dye injected into the fourth turn remains perfectly unruffled for a long distance, indicating the laminar state of the flow in the helical coil.

1.2.2 Critical Reynolds number

It has been seen that, in helical pipes transition from laminar to turbulent flow regime takes place at a Reynolds number higher than that for a similar straight pipe. Correlations were proposed by Ito (1959), Schmidt (1967), Srinivasan (1970) et al., Janssen et al., (1978) etc. Critical Reynolds number obtained from the above correlations for a range of curvature ratio from 0.01 to 0.25 is plotted in fig. 2. In the lower range of curvature ratios ($\delta < 0.05$), all of the correlations provide approximately the same value for the Re_{cr} . Correlations provided by Ito et al and Schmidt et al. gives almost equal values of Re_{cr} for the entire range of curvature ratios which is of practical interest and these correlations are used in the present work for determination of flow regime.

1.2.3 Pressure drop in single-phase flow

It has already been seen that the flow phenomena in curved tubes are much more complex than that in a straight tube. The pressure drop occurring in a helical tube is found to be higher than that for straight tubes for the same flow rate.

Correlations for estimation of pressure drop was proposed by Ito (1959), Srinivasan et al. (1968), Tarbell & Samuels (1973), Ruffel (1974), Xin et al. (1997), Ju et al. (2001), Guo et al. (2001) etc. Ali (2001) and Naphon, & Wongwises (2006) has consolidated correlations for estimation of pressure drop for flow through helical pipes.

1.2.4 Heat transfer in single-phase flow

Heat transfer in helical coils has been experimentally investigated by Seban & McLaughlin (1963) both for laminar and turbulent flow regimes for flow of water with constant wall flux BC. Roger & Mayhew (1964) studied heat transfer to fluid flowing inside a helical pipe which was heated by steam. Mori and Nakayama (1967a) investigated forced convective heat transfer in turbulent regime for wall heat flux boundary condition. Variation of physical properties with temperature changes were not taken into account in their work.

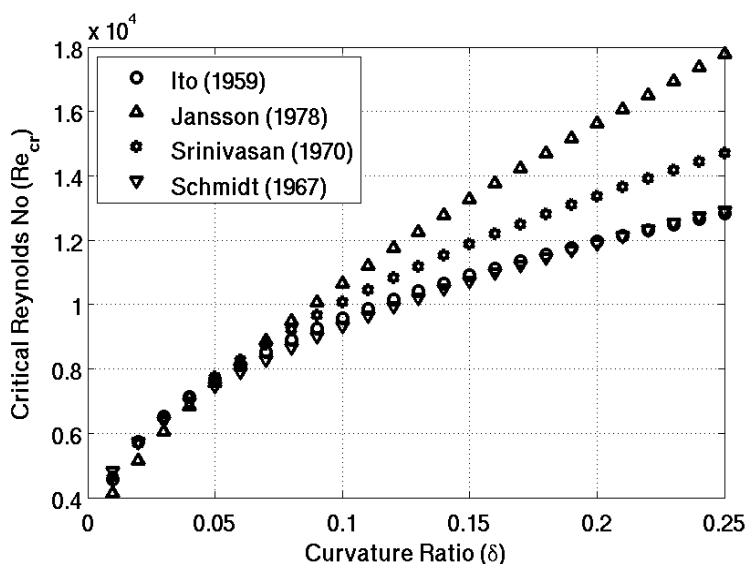


Fig. 2. Critical Reynolds number predicted by various correlations.

Mori and Nakayama (1967b) subsequently studied heat transfer under constant wall temperature boundary condition for the same helical coils. They had observed that the Nusselt number is remarkably affected by a secondary flow due to curvature. They had stated that the same formula used for estimation of heat transfer rates in wall flux boundary conditions can be used for the wall temperature boundary condition as well. Heat transfer and pressure drop in helical pipes was studied by Yildiz et al. (1997).

CFD study of helically coiled double pipe heat exchangers for laminar flow situations were carried out by Rennie and Raghavan (2005, 2006a). They have modelled the heat transfer from hot fluid to cold fluid using the CFD package PHOENICS 3.3 and found out the overall heat transfer coefficients for counter current and parallel flows. Pressure drop and heat transfer in tube-in-tube helical heat exchanger under turbulent flow conditions was studied by Vimal Kumar et al. (2006) using the CFD package FLUENT 6. However, no correlation for estimation of Nu was given in these papers.

Goering et al. (1997) has studied fully developed laminar convective heat transfer in curved pipes to investigate the dual influence of curvature and buoyancy. Direct numerical study on influence of curvature and torsion on turbulent flow in a helical pipe has been provided by Hüttel and Friedrich (2000). Later Hüttel and Friedrich (2001) have conducted a DNS study to bring out the details of the secondary flow in such systems. Recently Jayakumar et al. (2008a) have developed a correlation for estimation of inside heat transfer coefficient for flow of single-phase water through helically coiled heat exchangers. The correlation, which is validated against experiments, is applicable to a specific configuration of helical coil.

1.3 Pressure drop and heat transfer for air-water two-phase flow

Akagawa et al. (1971) measured pressure drop for two-phase gas liquid flow in helically coiled tubes for different curvature ratios. Kasturi & Stepanek (1972) carried out pressure

drop and void fraction measurement for two-phase counter current flow of gas and liquid in a helical coil. They compared the results with Lockhart-Martinelli correlation, Dukler's correlation and Hughmark's correlation and suggested that Lockhart-Martinelli parameter could be modified to obtain a better correlation. In their later work, Stepanek & Kasturi (1972) proposed correlations for void fraction and pressure drop in terms of new correlating parameters. Flow of air-water mixture through a helically coiled tube was studied by Whalley (1980) and the flow pattern transition between stratified and annular flow was examined. Rangacharyulu and Davies (1984) experimentally studied pressure drop and hold-up for counter-current upward flow of air-liquid system through copper coils. They proposed a new correlation for two-phase frictional pressure drop based on the modified Lockhart-Martinelli parameter. Flow of two-phase air-water mixture in helically coiled tube was studied by Watanabe et al. (1993). They found out the thickness of water film on the wall of the coil at different points around the circumference experimentally.

Czop et al. (1994) carried out experiments on water-SF₆ flow through a helically coiled tube of 19.8 mm id with 1170 mm coil diameter. It has been observed that the two-phase pressure drops are very much different from those calculated with Lockhart-Martinelli correlation but are in fairly good agreement with the Chisholm correlation. Awwad et al. (1995) carried out experimental investigations of air-water two-phase flow in horizontal helicoidal pipes. They have found that the pressure drop multiplier is strongly related to superficial velocities of air and water. The helix angle has almost no effect on pressure drop, even though coil diameter has certain effects at low flow rates. Xin et al. (1996) measured the pressure drop and void fraction for an air-water mixture flowing through vertical helicoidal pipes. In their later work, Xin et al. (1997) investigated the effect of coil geometries and flow rates of air and water on two-phase flow pressure drop in annular vertical and horizontal helical pipes. It has been observed that unlike two-phase flow through straight pipes, the pressure drop multipliers for helical pipes are dependent on the flow rates in addition to the Martinelli parameter.

Experimental investigations of oil-water-air three phase flows were carried out by Chen & Guo (1999) with an objective to separate gas-oil-water mixture. Murai et al. (2006) have experimentally studied the nature of flow patterns for flow of air-water mixture in a helically coiled tube. They established the effect of centrifugal acceleration on the flow regime map and brought out the spatial and temporal flow structure distribution. Jayakumar et al. (2010b) has reported numerical investigation of heat transfer to two-phase air-water mixture flowing through helical pipes. In that work, the variation of phasic velocity, temperature and void fraction at various cross-sections along the length of tube are presented. Influence of the coil parameters and inlet void fraction in heat transfer is also discussed in that paper.

1.4 Outline of the chapter

The chapter is organised as follows: Detailed characteristics and physics of fluid flow and heat transfer to single-phase water flowing through helical pipes are presented in next section. In the section 3, influences of various coil parameters on heat transfer for different boundary conditions are analysed. The results are used for generation of correlations to estimate the average and local values of Nusselt numbers. Nature of variation of Nusselt number at various positions along wall periphery is discussed in section 4. The generalised results are converted into an equation for estimation of local Nusselt number.

Sections 5 deal with analysis of two-phase flows through helical pipe. Details of numerical modelling employing the two-fluid model and validation are given. Factors influencing two-phase heat transfer are analysed and a correlation to estimate the heat transfer coefficient is recommended.

2. Heat transfer characteristics of single-phase flows

As a representative case, coil of $PCD = 200$ mm and coil pitch of 30 mm is considered for discussion. Diameter of the pipe used in the coil is 20 mm. Boundary layer mesh was generated for the pipe fluid volume. Optimised grid after the grid independency studies was used in the analysis. Pressure velocity coupling was done using the SIMPLEC scheme. Momentum equations were discretised using QUICK scheme. Power Law scheme of discretisation is used for turbulent kinetic energy and dissipation rate equations. Convergence criterion used was 1.0×10^{-5} for continuity, velocities, k , and ϵ . Temperature dependent properties as polynomial functions were used for water. For the energy equation third order QUICK discretisation scheme was employed. Convergence criterion for energy balance was 1.0×10^{-7} .

2.1 Property variation of the working fluid

Implication of using values of transport and thermal properties of the hot and cold fluids as functions of temperature is investigated (Jayakumar et. al 2008a). From the analysis, it can be seen that an error Nusselt number is about 24% when the properties at ambient conditions are used.

2.2 Data extraction

The results of simulation are exported as a CGNS (*CFD General Notation System*, www.cgns.org) file. The fields exported are pressure, temperature, velocity magnitude, x , y and z velocities, viscosity, density, specific heat, thermal conductivity of the fluid; wall temperature and wall heat flux.

For post-processing a visualisation package *AnuVi* developed by Computer Division, BARC, India is used. *AnuVi* is a cross-platform CFD post processor and Scientific Visualization Framework and is built on top of the open source software like *Python* (www.python.org), *Visualization Tool Kit* (VTK, www.vtk.org), *WxWidgets* (www.wxwidgets.org) and *FFmpeg* (www.ffmpeg.org). It can handle many standard file formats like CGNS, PLOT3D, VTK, STL, OBJ, BYU and PLY and has features to provide animation, extraction and derivation of data over many data components with advanced graphics (including shading, contouring, lighting and transparency). The package has features like Session Handling, Seamless Data integration, *Python* Language Scripting etc. Rendering is handled by *OpenGL* and can be accelerated with advanced graphics hardware. The feature of *Python* language scripting gives unlimited control to user which can be used for automation of data extraction and visualization.

For extraction of data and visualisation, the CGNS files are processed to create planes at desired spacing in the computational domain. Since the fluid properties are temperature dependent, the bulk fluid temperature at a cross section is evaluated using the relation,

$$T_b = \frac{\int u \rho C_p T dA}{\int u \rho C_p dA}, \quad (1)$$

Here dA is an elemental area of the pipe cross-section (see figure 5.1(b)). The wall temperatures at four locations (inner, outer, top and bottom of the pipe) in a cross section are also extracted. Using these data, values of local Nusselt number at four locations at that cross section are calculated using the formula,

$$Nu_{loc} = \frac{2r}{k} \left(\frac{q''}{T_w - T_b} \right). \quad (2)$$

The heat flux is calculated by, $q'' = k(\partial T / \partial n)_w$, where n is the normal direction.

As used by Lin and Ebadian (1997), average Nu at a cross section may be estimated by,

$$Nu_{av} = \frac{1}{2\pi} \int_0^{2\pi} (Nu_\phi) d\phi. \quad (3)$$

But this does not ensure that the Nusselt number so estimated is representative of the total heat flux in that cross-section. Hence, the mean Nusselt number is evaluated by;

$$Nu_{av} = \frac{2r}{k_m} \left(\frac{q_m''}{T_{w,m} - T_b} \right). \quad (4)$$

Here, $T_{w,m}$ and q_m'' are evaluated by the formula,

$$\varphi_m = \frac{\int_0^{2\pi} (\varphi \Delta A) d\phi}{\int_0^{2\pi} (\Delta A) d\phi}. \quad (5)$$

where, $\varphi = k, T_w$ or q'' as the case may be. Here ΔA is the area of elemental ring located along the wall to which the parameter is associated to. Thus the Nu_{av} is based on the average heat flux at a given cross-section and is evaluated using eqns. 4 and 5.

The above sets of operations are repeated at successive planes to cover the entire length of the pipe. All of the above processing have been done using Python scripts which runs on top of the AnuVi package. Various programs required to generate the cut planes etc was written in c++ programming language. MATLAB® has been extensively used for processing of the raw data, generation of 2D plots and for regression analysis. More details about the data extraction is available in Jayakumar (2009) and Jayakumar et al., (2010a).

The results of analysis carried out with constant wall temperature boundary condition and constant wall heat flux boundary condition is discussed in the following sections.

2.3 Analysis with constant wall temperature boundary condition

In this analysis, hot water at 330 K at a specified velocity of 0.8 ms^{-1} is entering the helical pipe at the top, where an inlet velocity boundary condition is specified. The flow velocity is such that the flow regime is turbulent. The fluid is made to cool down as it flows along the tube by specifying a wall temperature of 300 K. Temperature dependent values of fluid properties are used in this analysis. At the pipe wall, for the energy equation, a Dirichlet boundary condition and for momentum and pressure equations homogenous Neumann boundary condition are specified. At the outlet, a pressure outlet boundary is enforced.

Fig. 3 shows an overview of velocity contours at various sections along the length of the coil. The planes are identified by the angle (θ) which is the angle that the plane makes with the plane passing through the pipe inlet. In fig. 5 the first plane shown on the top is at 10° from the inlet (i.e., $\theta=10^\circ$) and the subsequent planes are 10° apart. Up to an angle of $\theta=35^\circ$, the velocity profile at a cross section is found to be symmetric. Subsequently, this uniform velocity pattern changes to a pattern with a high velocity region located at the outer side of the coil. This behaviour is seen predominantly by $\theta=45^\circ$ and continues to develop. It can be seen that by $\theta=135^\circ$, the high velocity region is present only in outer half cross-section. Area of high velocity region further reduces as the flow gets developed and covers approximately $\frac{1}{3}$ rd of the flow area by $\theta=240^\circ$. No significant change in flow pattern is observed downstream.

Temperature distribution at various planes along the length of coil is shown in fig. 4. At the inlet, temperature is uniform across the cross section. Since the wall is maintained at a lower temperature, the fluid cools down as it flows through the coil. Up to an angle of 20° , heat transfer is uniform along the periphery. In contrast to heat transfer in a straight tube, high temperature regions are seen on the outer side of the coil. This phenomena is predominant from the plane at angle $\theta=50^\circ$. This trend continues to develop and by 150° , clearly three regions viz., high temperature (327-330 K) at the outer side of the coil, intermediate temperature (321 to 324 K) at the centre and low temperature (311 to 314 K) on the inner side of the coil, are visible. As the fluid flows down the pipe, this temperature profile gets developed and the area of high temperature region decreases and by $\theta = 360^\circ$, a fully developed temperature profile is attained and the fluid continues to lose heat due to the lower wall temperature.

As the fluid flows through the helical coil, fluid particles undergo rotational motion. The fluid particles also undergo movement from inner side of the coil to the outer side and vice-versa. Fig. 5 shows particle trace for 10 fluid particles which are located along a line parallel to the X axis at the pipe inlet. It can be noted that these fluid particles are taking various trajectories and also move with different velocities. The particles, which were forming a line to begin with, are found to be totally scattered at the pipe exit. It can be clearly seen that the high velocity region oscillates as the fluid flows along the helical pipe. This causes fluctuations in the values of Nusselt number.

Variation of local Nusselt number along the length of the tube is presented in fig. 6. The X axis of the figure is the angle of the plane, starting from the pipe inlet. It is found that the Nusselt number on the outer side of the coil is higher than those at any other location at that cross-section. Due to the centrifugal forces, the velocity in the outer region is higher and this

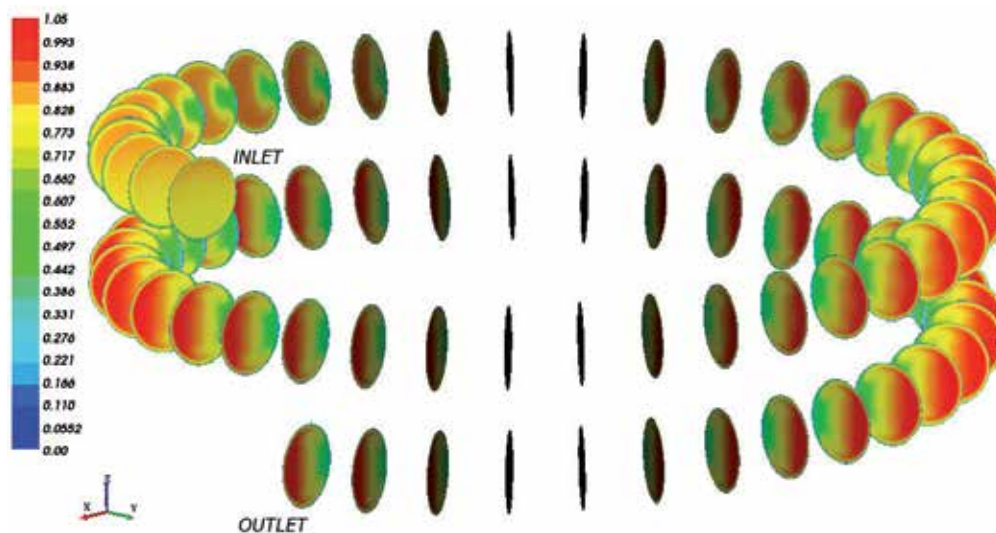


Fig. 3. Velocity (m s^{-1}) contours at various planes along the length of the coil.

leads to higher heat transfer coefficients. In a similar way, the Nu along the inner periphery of the coil is the lowest.

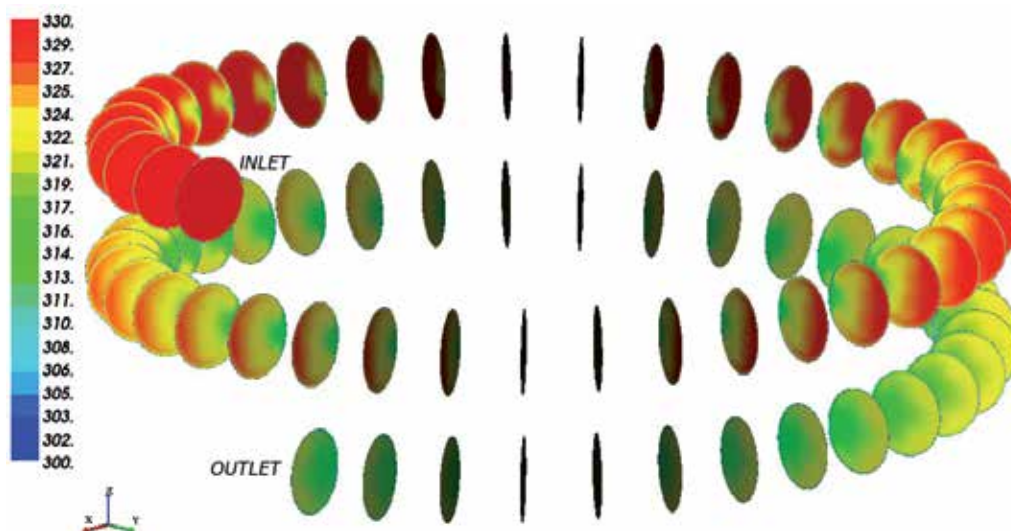


Fig. 4. Temperature (K) contours at various planes along the length of the coil.

The Nusselt numbers at the top and bottom side of the cross sections show prominent periodic behaviour in the developing region of the pipe. Oscillatory motion of fluid particles, as observed in fig. 5, influences heat transfer around the periphery. The fluctuational behaviour of the Nusselt number has been reported by other investigators as well (Lin and Ebadian, 1999; Liu, 1992; Patankar et al., 1974). In the later regions of the coil, the Nusselt number at the top and bottom differ only marginally. Figure 6 also shows average values of Nusselt number (eqn. (4)) along the length of the pipe. It is found that it

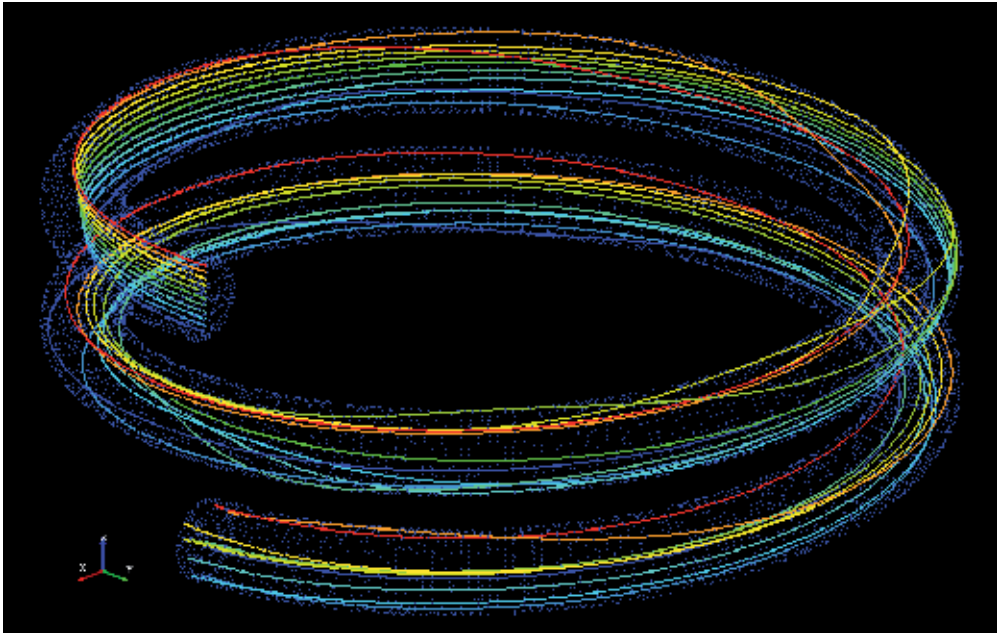


Fig. 5. Trace of fluid particles which are parallel to X axis at the inlet.

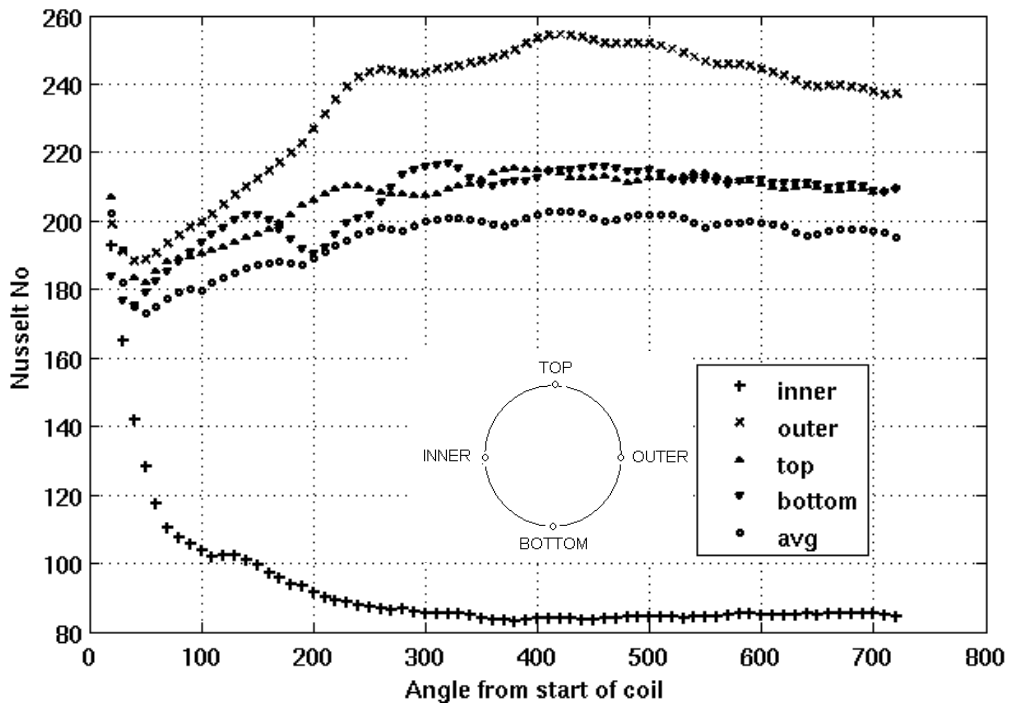


Fig. 6. Variation of Nusselt Number along the length coil.

attains an almost constant value by 300° . This constant value is used in the developing correlations for estimation of Nusselt number. Apart from the centrifugal action, buoyancy effects will move the hot particles upward and then downward as it loses heat (as can be seen in fig 5). This up and down movements together with centrifugal and inertial forces will lead to an overall spiral movement of the fluid. This may be attributed to the periodic behaviour of Nusselt number at top and bottom sides of the cross sections along the length of the pipe.

It may be noted that commercial CFD codes may not provide the value of bulk fluid temperature at different cross-section for estimation of the local Nusselt numbers. The user may be able to specify only a single value of bulk fluid temperature for the entire computational domain. This can lead to estimation of incorrect values of Nusselt numbers.

Variation of local values of Nusselt number along the periphery of the pipe wall at various locations of the pipe are shown in Fig. 7. In these figures, the angle θ refers to the angle which the current plane makes with the inlet plane. In the initial length of the pipe, up to an angle $\theta=10^\circ$, marginally higher rates of heat transfer is observed at the upper side of the pipe. Due to gravity effect, the hotter fluid will be present at the top and this result in higher values of Nusselt number at that location. As the flow gets developed, when the effect of centrifugal forces becomes appreciable, region of higher heat transfer shifts from angle 270° to 180° i.e. from the upper side of the pipe to outer side of the coil. This shift gets completed by $\theta=76^\circ$. It is observed that up to an angle of 140° , the percentage of circumference, which has a higher value of Nu is predominant. This percentage decreases and by $\theta=430^\circ$ onwards this region is so low that the average Nusselt number starts decreasing. Bai et al. (1999) has provided a figure showing ratio of local Nusselt number to average Nusselt number (only at 8 angular locations around the periphery) for turbulent heat transfer in a horizontally oriented helical coil. They have also obtained a similar pattern in the fully developed region as the one presented here.

3. Correlations for estimation of average Nusselt number

A correlation for estimation of inside heat transfer coefficient for flow of single-phase water through helically coiled heat exchangers is presented in previous section. (Jayakumar et al., 2008a). The correlation, which is validated against experiments, is applicable to the specific configuration of helical coil, since the research work was limited only to changes in flow rate of the streams. This section deals with the analysis of various configurations of helical coils. After establishing influence of the coil parameters, correlations for prediction of average Nusselt number have been developed. Subsequently correlation to predict the local values of Nusselt number as a function of angular location is presented.

CFD simulations are carried out by varying coil parameters such as (i) pitch circle diameter, (ii) tube pitch and (iii) pipe diameter and their influence on heat transfer has been studied. Helical coils of different configurations have been analysed for this purpose. The results of these computations (where temperature dependant fluid properties are used) are used for developing unified correlations for estimation of inside heat transfer coefficient for flow of single-phase water through helical coils. Since a large data set is considered, the correlation will be applicable to a wide range of coil configurations and Dean numbers. Analysis has been carried out with both constant wall temperature and constant wall heat flux boundary conditions in order to establish influence of the boundary condition on heat transfer coefficient.

3.1 Analysis with constant wall temperature boundary condition

The boundary conditions and the discretisation schemes used in this analysis are same as those given in section 2.3. The following sub-sections consider influence of each of the coil parameters separately. In all of the cases, average of the Nusselt number in the fully developed heat transfer region (where the Nu remains almost constant, see Fig. 6) is used as the representative value. Study has been carried out using the CFD package FLUENT 6.3 (3D, double precision). Each of the runs takes about 10 hours on a Xenon 2.4 GHz computer with 2 GB RAM.

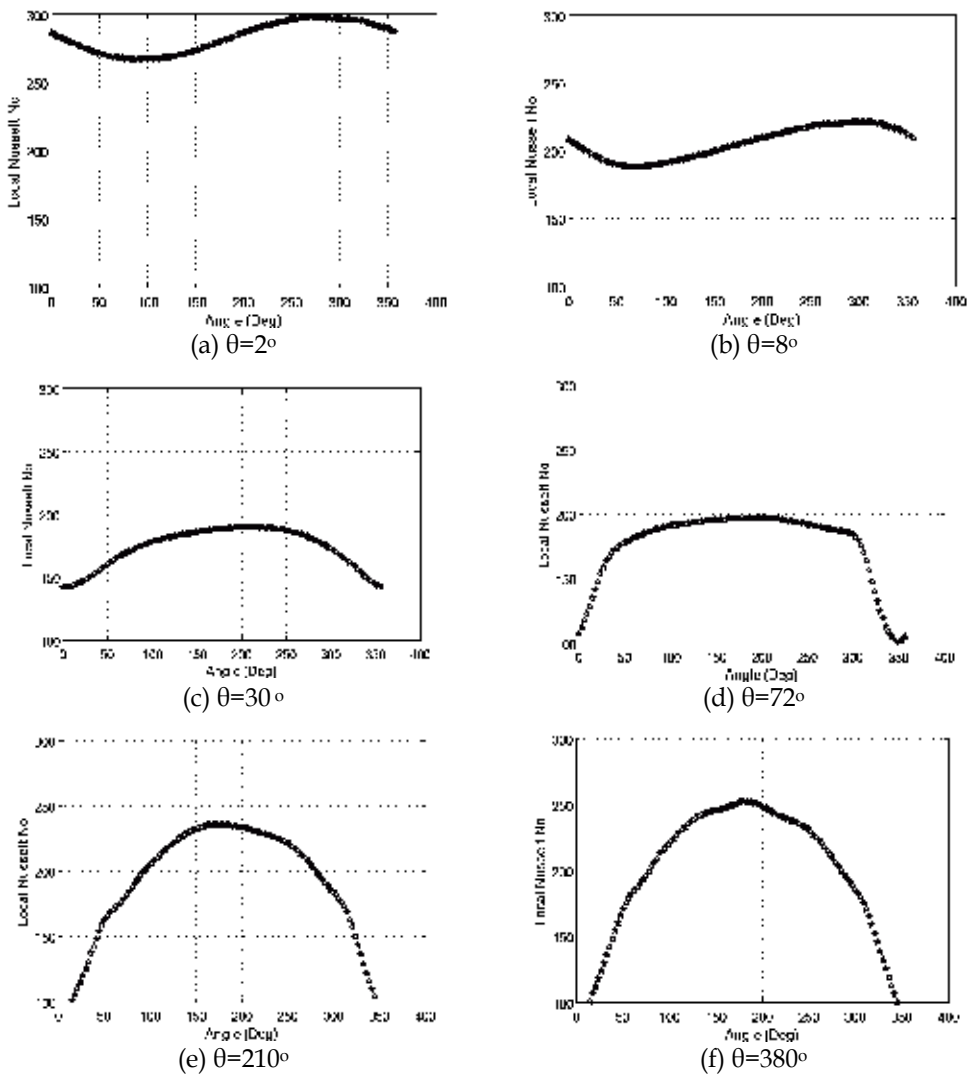


Fig. 7. Variation of Nu around the circumference at various cross section of the pipe ($0^\circ \Rightarrow$ Inner, $90^\circ \Rightarrow$ bottom, $180^\circ \Rightarrow$ Outer and $270^\circ \Rightarrow$ top).

3.1.1 Influence of Pitch Circle Diameter (PCD)

The coils with PCD 100 mm, 200 mm, 300 mm and 400 mm were analysed. In all these cases, the coil pitch and pipe diameter were kept at 30 mm and 20 mm respectively and the coils consisted of two turns (Jayakumar et al., 2010a).

The effect of PCD is to influence the centrifugal force on the moving fluid. This will in turn affect the secondary flows along the pipe cross section. As the PCD is increased, the effect of coil curvature on flow decreases and hence centrifugal forces play a lesser role in flow characteristics. For the coil with PCD=100 mm, the entrance effects are seen to be present up to an angle of 40°. While for PCDs 200, 300 and 400 this change to 20°, 10° and 6° respectively. For the case of coil with PCD=100 mm, the difference between Nusselt number at the inner and outer location in the fully developed heat transfer region is 200. As we move to coils of higher PCDs, this difference comes down and for a coil of PCD=400 mm, it reduces to 134. Thus the effect of centrifugal force on heat transfer is evident.

To correlate the average Nusselt numbers in the fully developed region Nu with pitch circle diameter of the coil, the dimensionless parameter curvature ratio δ ($=r/R_c$) is used. The correlation proposed is of the form $Nu = C(\delta)^n$. The Nusselt number can be correlated to curvature ratio as,

$$Nu = 265.65 (\delta)^{0.11}, \quad (6)$$

verifying the nature of the proposed correlation. The equation is found to give a good fit.

3.1.2 Influence of coil pitch (H)

In this analysis, a helical coil with a pipe of inner diameter ($2r$) 20 mm and pitch circle diameter (PCD) of 300 mm was considered. Analyses were carried out by changing the coil pitch. Coil with pitch of (i) zero, (ii) 15 mm, (iii) 30 mm, (iv) 45 mm and (v) 60 mm were analysed.

When the coil pitch is zero, local Nusselt numbers at the top and bottom points on the periphery of a cross section are almost the same. As the coil pitch is increased, the difference between them also increases. This difference is caused by torsion experienced by the fluid. As the pitch increases, the torsional effect also increases. However, variation of local Nu for the coils with pitch of 45 and 60 mm are identical. Average values of Nusselt number in the fully developed region is given in table 1.

H, mm	0	15	30	45	60
Nu_{avg}	189.24	191.08	191.75	192.27	192.55

Table 1. Average values of Nusselt number.

It is found that the Nu_{avg} increases marginally with increase in pitch and almost insensitive to its further changes at higher pitches. The percentage increase, when the pitch is changed from 0 mm to 15 mm is about 1% and this value changes to 0.2% when the pitch is changed from 45 mm to 60 mm. For any engineering application, the tube pitch has to be higher than pipe diameter and in that range the changes in Nu_{avg} due to changes in pitch are negligible.

Hence the effect of coil pitch on overall heat transfer for design purposes need not be considered for most of the practical applications with helical coils. However, it has implications in heat transfer in the developing region (ref. Fig. 7). The maximum difference in Nusselt number between the top and bottom locations is given in table 2. This clearly shows the extent of oscillatory behaviour. Another observation is the shift of the symmetry plane of temperature and velocity profiles with the change in coil pitch.

Pitch, mm	0	15	30	45	60
Max difference in values of Nu_{loc} between top and bottom locations	0	7	12	18	26

Table 2. Difference in values of Nusselt number.

3.1.3 Influence of pipe diameter (D)

In this analysis, the effect of pipe diameter on heat transfer in a helical coil is considered. The pipe diameters considered for analyses were, 10 mm, 20 mm, 30 mm and 40 mm. For all these cases, coil has a pitch of 45 mm and PCD of 300 mm and the coil consists of two turns.

For the coil with 10 mm diameter, Nusselt number in the top and bottom regions of the pipe are approximately equal. In the region of fully developed heat transfer, there is even uniform Nusselt number along the periphery of many planes. When the pipe diameter is low, the secondary flows are weaker and hence mixing is lesser. This produces nearly the same heat transfer in the upper half cross-section in a given plane.

When the diameter of the coil is changed to 20 mm, in contrast to the case where $d=10$ mm, heat transfer at the outer side of the coil remain the highest for all of the sections. As expected, the length of pipe needed for the heat transfer to attain a fully developed state has increased as the pipe diameter is increased. A straight line relationship is observed between Nusselt and pipe diameter. Regression analysis was carried out and the result verifies a linear relationship between Nu_{av} and pipe diameter.

3.1.4 Correlation for estimation of Nusselt number

The correlation for Nusselt number already consists of pipe diameter in terms of Reynolds number and curvature ratio. Hence the correlation can be of the form,

$$Nu = CRe^n Pr^{0.4} \delta^m, \quad (7)$$

where C , n and m are to be evaluated. If we use Dean number in the formulation, the curvature ratio term needs to be included twice. Hence Reynolds number is chosen in the general form of the equation for estimation of Nusselt number. In order to cover a wide range of Reynolds number, Dean number and curvature ratio, eight more cases, apart from those given above have been analysed.

Multiple-regression analysis based on the data generated from above case studies has been done using MATLAB®. The correlation so developed for estimation of Nusselt number is given by:

$$Nu = 0.116Re^{0.71}Pr^{0.4}\delta^{0.11} . \quad (8)$$

The applicable ranges of parameters for the equation 8 are: (i) $14000 < Re < 70000$; (ii) $3000 < De < 22000$; (iii) $3.0 < Pr < 5.0$; and (iv) $0.05 < \delta < 0.2$.

Fig. 8 gives a comparison of the Nusselt numbers predicted by eqn. (8) with Roger & Mayhew (1964) and Mori&Nakayama (1967b). It is found that present correlation is fairly in agreement with Nusselt number predicted by the experimental correlations. The earlier correlations are found to be under predicting the Nusselt number. This is attributable to the approximations used by the authors in data reduction and conservative nature of their approach.

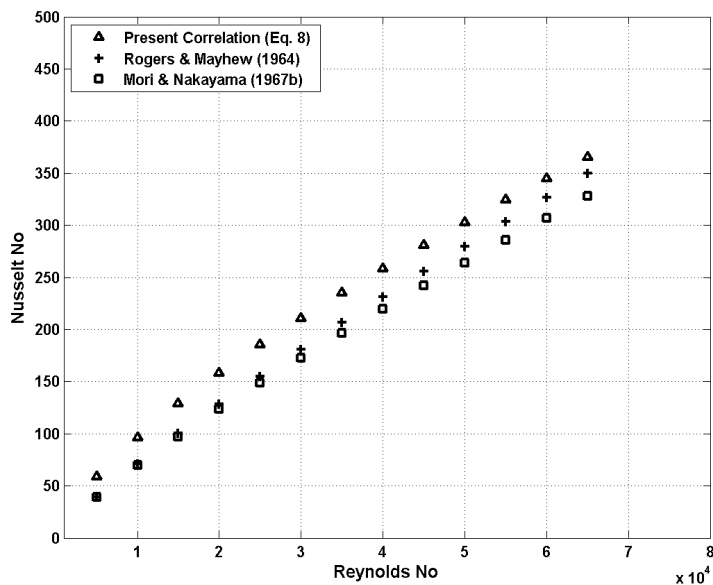


Fig. 8. Comparison of Nusselt number for the constant T_w B.C.

3.2 Constant wall heat flux boundary condition

This boundary condition is applicable to heat flux controlled surfaces such as electrically heated pipes, nuclear fuel elements etc. In these analyses, hot water at 330 K at a specified velocity of 0.8 ms^{-1} is entering the helical pipe at the top, where an inlet velocity boundary condition is specified. The fluid is made to cool down as it flows along the tube by specifying a wall heat flux of -150 kW m^{-2} .

Influence of parameters such as PCD , coil pitch and pipe diameter has been studied in this case also. They are found to be behaving in a manner similar to those described in section 3.1 and are not repeated here. Hence in this case also a correlation of the form given by eqn. (7) will be applicable. In order to cover a wider range of parameters, analysis of eight additional cases were also done.

Multiple regression analysis of the data obtained from the above 20 runs was performed to get a best fit of eqn. (7). The correlation resulted is,

$$Nu = 0.085Re^{0.74}Pr^{0.4}\delta^{0.1} \quad (9)$$

Nusselt number predicted by the correlation developed has been compared with the earlier works (Seban & McLaughlin, 1963 and Mori & Nakiyama, 1967a) and the results are presented in fig. 9. Seban and McLaughlin, (1963) have used constant values for transport and thermal properties of the working fluid. Also for data reduction, they considered the pipes to be straight. The authors themselves had stated that these approximations can lead to an error of 10% in the values of Nusselt number predicted. It has been shown that usage of constant properties for estimation of Nusselt number can lead to an error more than 20% (Jayakumar et. al 2008a). Thus the earlier correlations are found to be under-predicting the Nusselt number. A good match with the experimental results also verifies the simulation methodology, including the turbulence modelling.

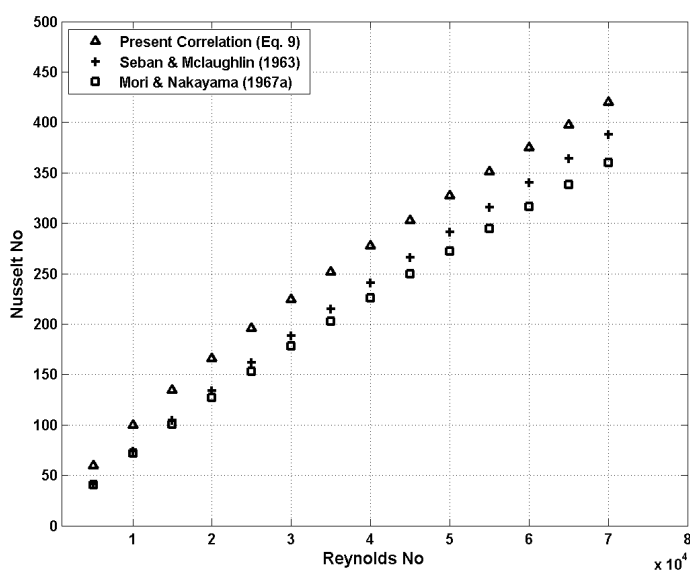


Fig. 9. Comparison of Nusselt number for the constant wall flux B.C.

A comparison of the Nusselt numbers generated from the correlations given by equations (8) and (9) is done. It is found that both the correlations give almost the same value of Nusselt number at lower values of Reynolds number. However, they show marginal difference when $Re > 50000$.

3.3 Conjugate heat transfer boundary condition

A correlation was developed for estimation of Nusselt number considering conjugate heat transfer (Jayakumar et. al 2008a). It was found that the percentage difference between conjugate heat transfer and constant wall flux boundary conditions is about 8%. Thus use of heat flux boundary condition is a good engineering approximation for estimation of heat transfer for the case of conjugate heat transfer. Since the effort required for analysing heat transfer with conjugate heat transfer may not be worth from design point of view, results of constant wall heat flux boundary condition can be used for the conjugate case as well.

4. Estimation of local Nusselt number

It has been shown that the heat transfer and hence the Nusselt number is not uniform along the periphery at any given cross-section of the helical pipe (Jayakumar, 2009). In section 3, the development of Nusselt number along the periphery was discussed. It will be useful to find out a relationship to predict the local values of Nusselt number Nu_{loc} as a function of the angular location and this is presented in this section.

4.1 Constant wall temperature boundary condition

Values of local Nusselt numbers in the fully developed heat transfer regime for the 20 simulations carried out in the previous section is used for this analysis. For each of the cases, a cross-sectional cut-plane in the fully developed heat transfer regime is created. Value of local Nusselt number has been calculated (at intervals of 3° around the periphery) for each of these cut-planes. The local Nusselt numbers are then normalised with the average Nusselt number Nu_{av} calculated using the equation (8) for that coil configuration and flow parameters.

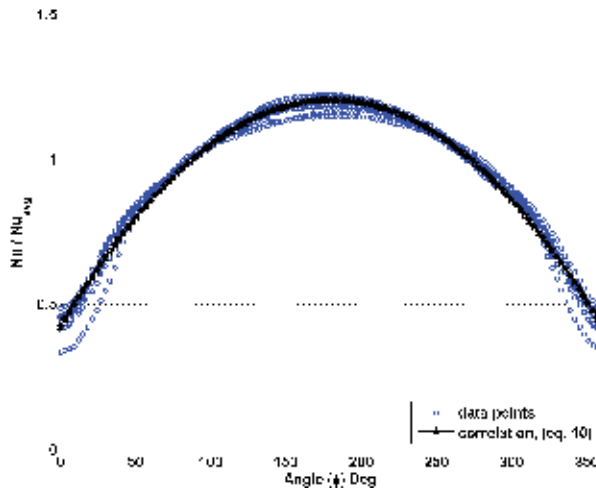


Fig. 10. Variation of local Nusselt number as function of angular position and average Nusselt number for constant T_w boundary condition.

Fig. 10 shows plot of ratio of local Nusselt number to the average Nusselt number (Nu_{loc}/Nu_{av}) as a function of angle (ϕ) for the different cases. The angle ϕ (in degrees) is measured anti-clockwise, starting from the inner side of the coil. It is observed that except in the regions close to the inner side of the pipe, the distribution of Nu_{loc}/Nu_{av} is almost independent of the coil geometry and Dean number. Utilising these $\frac{Nu_{loc}}{Nu_{av}} - \phi$ pairs of data

for the 20 simulations, the following correlation is developed for the prediction of local Nusselt number.

$$Nu_{loc} = Nu_{av} \left(-2.411e-05\phi^2 + 8.692e-03\phi + 0.4215 \right) \quad (10)$$

In this relation the angular location ϕ is to be expressed in degrees and the average Nusselt number Nu_{avc} is calculated using eqn. (8). Hence the applicability of equation 10 is same as that of eqn. (8).

4.2 Constant wall heat flux boundary condition

A similar exercise has been carried out to correlate the variation of local Nusselt number for the constant wall heat flux boundary condition. The plot of Nu_{loc}/Nu_{av} as a function of ϕ for the 20 different cases is shown in Fig. 11. The following correlation can be used for the prediction of local Nusselt number as a function of average Nusselt number and angular location.

$$Nu_{loc} = Nu_{av} \left(-2.331e-05\phi^2 + 8.424e-03\phi + 0.4576 \right) \quad (11)$$

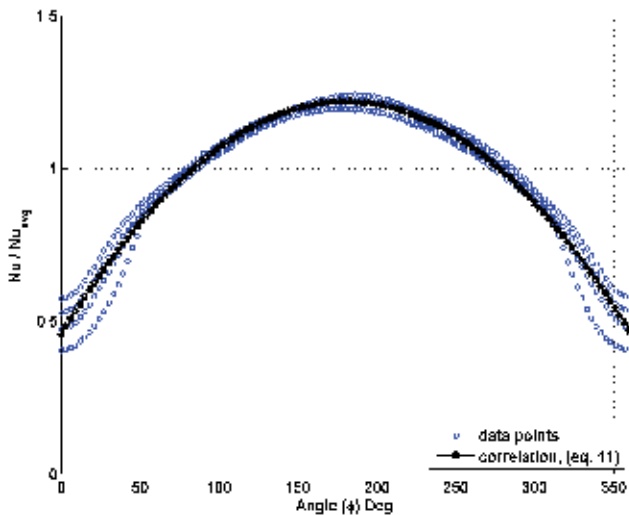


Fig. 11. Variation of local Nusselt number as function of angular position and average Nusselt number for constant q''_w boundary condition.

In this relation the angular location ϕ is to be expressed in degrees and the average Nusselt number Nu_{avc} is calculated using eqn. (9). Hence the applicability range of eqn. (11) is same as that of eqn. (9).

5. Air-water two-phase flow and heat transfer

Process requirements make some of the helically coiled heat exchangers to operate with air-water two-phase mixture as working fluid. As an example, there are situations of single-phase water and two-phase air-water mixture flowing through the helically coiled heat exchanger (Jayakumar and Grover, 1997). The characteristics of operation of such heat exchangers with two-phase working fluids are not well documented. There do exist a few experimental results on hydrodynamics of air-water flow through helical pipes. Experiments have been carried out to generate the pressure drop correlations for two-phase

flow of air-water through helical pipes. However numerical investigation, which can give much insight into the physics of the problem, is lacking. No work is reported on detailed numerical study of hydrodynamics and heat transfer characteristics for air-water two-phase flow through such systems. A numerical study can give much more insight into the phenomena and further, the influence of various parameters can also be studied. Jayakumar et al. (2008b, 2010b) have carried out heat transfer studies of flow of two-phase air-water mixture through helical coils. This paper gives a clear picture on the influence of velocity, temperature and void fraction on the coil parameters. The work also gives details of benchmarking for hydrodynamic and heat transfer analysis of air-water mixture through helical coils.

The modified Lockhart-Martinelli parameter (χ) is defined as,

$$\chi^2 = \left(\frac{dP}{dz} \right)_{l,H} / \left(\frac{dP}{dz} \right)_{g,H} \quad (12)$$

where, the subscript H refers to pressure drop in helical coils.

The Lockhart-Martinelli parameter (χ) was estimated and two-phase pressure drop is calculated using the functional relationships of two-phase friction multipliers, ϕ_l and ϕ_g .

$$\phi_l^2 = \left(\frac{dP}{dz} \right)_{TP,H} / \left(\frac{dP}{dz} \right)_{l,H} = f_1(X) \quad (13)$$

$$\phi_g^2 = \left(\frac{dP}{dz} \right)_{TP,H} / \left(\frac{dP}{dz} \right)_{g,H} = f_2(X) \quad (14)$$

5.1 Schemes for two-phase flow modelling

For modelling two-phase flows, one can use either Eulerian-Lagrangian model or Eulerian-Eulerian approach. The first one is generally used to trace the particles and hence is not appropriate to deal with gas-liquid flows in pipes. In the Eulerian-Eulerian approach, the phases are treated as interpenetrating and void fraction is used to distinguish the phases. There are 3 different schemes possible in this method, viz., Volume Of Fluid (VOF) model, the mixture model and the Eulerian model. The VOF is applicable when surface tracking is of importance and in the mixture model, pseudo properties of the mixture are used to solve a single set of conservation equations. However, in the Eulerian model, complete set of conservation equations are solved for each of the phases. Thus, either the mixture model or the Eulerian model may be applied for solution of two-phase flow through the helical coil system. Due to the centrifugal and coriolis forces generated during the flow in a helical pipe, a well-mixed gas-liquid region will not be probable and use of mixture properties for the flow will not yield a correct solution. Hence, it is decided to use the Euler scheme to be used for the modelling.

5.2 Governing equations for modelling Eulerian two-phase scheme

Heat transfer to flow of air-water mixture through a helical pipe, where the pipe wall has been kept at a constant temperature, is analysed with Eulerian model of two-phase flows

using the CFD package FLUENT. Conservation equations are solved for each of the phase k , viz., gas (g) and liquid (l). In describing the two-phase flow, which has been treated as interpenetrating continua, the concept of void fraction is used. The void fraction of any phase represents the fraction of volume (of the total volume) occupied by that phase. The volume of a phase k is defined as,

$$V_k = \int_V \alpha_k dV \quad (15)$$

where, the summation of the void fractions is unity.

$$\alpha_g + \alpha_l = 1 \quad (16)$$

5.2.1 Conservation of mass

The continuity equation for the phase k is expressed as,

$$\frac{\partial}{\partial t}(\alpha_k \rho_k) + \nabla \cdot (\alpha_k \rho_k \mathbf{u}_k) = \sum_{p=l,g} \left(\dot{m}_{pq} - \dot{m}_{qp} \right) + S_k \quad (17)$$

Here $\dot{m}_{pq} - \dot{m}_{qp}$ is the mass exchange between the liquid and gaseous phases. In the present case, since no mass exchange takes place between the phases, the source S_k is zero.

5.2.2 Conservation of momentum

The set of equations for conservation of momentum for the phase k is written as,

$$\begin{aligned} \frac{\partial}{\partial t}(\alpha_k \rho_k \mathbf{u}_k) + \nabla \cdot (\alpha_k \rho_k \mathbf{u}_k \mathbf{u}_k) = & -\alpha_k \nabla p + \nabla \cdot \boldsymbol{\tau}_k + \alpha_k \rho_k \mathbf{g} \\ & + \sum_{p=l,g} \left(\mathbf{R}_{pq} + \dot{m}_{pq} \mathbf{u}_{pq} - \dot{m}_{qp} \mathbf{u}_{qp} \right) \\ & + \mathbf{F}_k + \mathbf{F}_{lift,k} + \mathbf{F}_{vm,k} \end{aligned} \quad (18)$$

Here \mathbf{u}_{pq} is the interphase velocity and \mathbf{R}_{pq} is the interaction between the phases. \mathbf{F}_k is external body force, $\mathbf{F}_{vm,k}$ virtual mass force and $\mathbf{F}_{lift,k}$ is the lift force. The stress - strain tensor $\boldsymbol{\tau}$ is defined as:

$$\boldsymbol{\tau} = \alpha_k \mu_k (\nabla \mathbf{u}_k + \nabla \mathbf{u}_k^T) + \alpha_k \left(\lambda_k - \frac{2}{3} \mu_k \right) \nabla \cdot \mathbf{u}_k \mathbf{I} \quad (19)$$

In this relation, μ_k and λ_k are the shear and bulk viscosity of the phase k . The inter-phase force, \mathbf{R}_{pq} is evaluated from $\sum_{p=l,g} \mathbf{R}_{pq} = \sum_{p=l,g} \mathbf{K}_{pq} (\mathbf{u}_p - \mathbf{u}_q)$, where \mathbf{K}_{pq} is the inter-phase momentum exchange coefficient. The coefficient \mathbf{K}_{pq} can be estimated using the relation,

$$K_{pq} = \frac{\alpha_q \alpha_p \rho_p f}{\tau_p}, \quad (20)$$

where f is the drag function and τ_p is the particulate relaxation time. In the present analysis,

$$f = \frac{C_d \text{Re}}{24}, \quad (21)$$

where C_d is evaluated from the expression,

$$C_d = \begin{cases} 24(1 + 0.15 \text{Re}^{0.687}) / \text{Re} & \text{for } \text{Re} \leq 1000 \\ 0.44 & \text{for } \text{Re} > 1000 \end{cases} \quad (22)$$

and Re is the relative Reynolds number, which is evaluated using the expression,

$$\text{Re} = \frac{\rho_q |\mathbf{u}_p - \mathbf{u}_q| d_p}{\mu_q}, \quad (23)$$

for the primary phase. The particulate relaxation time is defined as

$$\tau_p = \frac{\rho_p d_p^2}{18\mu_q}, \quad (24)$$

Lift force on the secondary phase (droplets or bubbles) is due to the velocity gradient in the primary-phase flow field. The lift force acting on a secondary phase p in a primary phase q is computed using the relation,

$$\mathbf{F}_{lift} = -0.5\rho_q \alpha_p (\mathbf{u}_q - \mathbf{u}_p) \times (\nabla \times \mathbf{u}_q) \quad (25)$$

Virtual mass force, which occurs when the secondary phase (p) accelerates relative to the primary phase (q), is estimated using,

$$\mathbf{F}_{vm} = 0.5\rho_q \alpha_p \left(\frac{D\mathbf{u}_q}{Dt} - \frac{D\mathbf{u}_p}{Dt} \right), \quad (26)$$

where $\frac{D\phi}{Dt}$ is the material derivative of ϕ . Virtual mass effect is significant when the density of the secondary phase is much smaller than that of primary phase.

5.2.3 Conservation of energy

The energy balance equation for the phase k is expressed as,

$$\begin{aligned} \frac{\partial}{\partial t} (\alpha_k \rho_k h_k) + \nabla \cdot (\alpha_k \rho_k \mathbf{u}_k h_k) = & -\alpha_k \frac{\partial p_k}{\partial t} + \boldsymbol{\tau}_k : \nabla \mathbf{u}_k - \nabla \cdot \mathbf{q}_k + S_k \\ & + \sum_{p=l,g} \left(\dot{Q}_{pq} + \dot{m}_{pq} h_{pq} - \dot{m}_{qp} h_{qp} \right) \end{aligned} \quad (27)$$

In this equation, h_k is the specific enthalpy, \mathbf{q}_k is heat flux and S_k is the heat generation for the phase. Q_{pq} is the heat exchange between the phases and h_{pq} is interphase enthalpy.

5.2.4 Turbulence modelling

Turbulence is modelled using multiphase “mixture k - ε model” based on the realizable k - ε model. It has already stated that realizable model is the most appropriate one for flows with rotation, adverse pressure gradient etc. Usage of other models, viz., dispersed model and per phase model are computationally very expensive. The transport equations for the mixture k and ε are as follows.

$$\frac{\partial}{\partial t}(\rho_m k) + \nabla \cdot (\rho_m \mathbf{u}_m k) = \nabla \cdot \left(\frac{\mu_{t,m}}{\sigma_k} \nabla k \right) + G_{k,m} - \rho_m \varepsilon \quad (28)$$

and

$$\frac{\partial}{\partial t}(\rho_m \varepsilon) + \nabla \cdot (\rho_m \mathbf{u}_m \varepsilon) = \nabla \cdot \left(\frac{\mu_{t,m}}{\sigma_\varepsilon} \nabla \varepsilon \right) + \frac{\varepsilon}{k} (C_1 G_{k,m} - C_2 \rho_m \varepsilon) \quad (29)$$

where, the subscript m stands for the mixture. Production of turbulent energy is calculated from,

$$G_{k,m} = \mu_{t,m} (\nabla \mathbf{u}_m + (\nabla \mathbf{u}_m)^T) : \nabla \mathbf{u}_m \quad (30)$$

The mixture density and velocity are evaluated using $\rho_m = \sum_{k=l,g} \alpha_i \rho_i$ and $\mathbf{u}_m = \frac{\sum_{k=l,g} \alpha_i \rho_i \mathbf{u}_i}{\sum_{k=l,g} \alpha_i \rho_i}$

respectively. The turbulent viscosity is estimated using $\mu_{t,m} = \rho_m C_\mu \frac{k^2}{\varepsilon}$. The model constants are same as those used for the single-phase realizable k - ε model.

5.3 Estimation of two-phase heat transfer coefficient

Hydrodynamics of air-water two-phase flow through helical pipes are validated against the experimental results generated by previous researchers. Heat transfer calculations for the two-phase flow are validated against experimental results of flow through an annular pipe (Jayakumar et al., 2010b). In the section 3 details of heat transfer characteristics along the length of the pipe for single-phase fluid have been presented. These give us qualitative picture of various phenomena at various flow sections of the pipe. Quantitative studies of heat transfer with an objective to derive a heat transfer correlation are taken-up in the present chapter. For this 11 coil configurations were analysed.

The analyses have been carried out with a constant wall heat flux boundary condition. The wall heat flux imposed was -150 kW m^{-2} . In all cases, uniform inlet velocity of 0.8 m s^{-1} was specified for the phases. The air void fraction at the inlet was taken to be 0.2. The numerical schemes used in these analyses are same as those described in the previous chapter.

5.3.1 Influence of Pitch Circle Diameter (PCD)

In order to study the influence of PCD on heat transfer and pressure drop in two-phase flows, 4 cases were analysed. The results are presented in fig. 12(a). Values of two-phase heat transfer coefficient are estimated using the data extraction methods described in section 3. Mixture temperature and thermal conductivity are used in these computations. The figure also gives the values of single-phase heat transfer coefficient calculated as per the eq. 9. The single phase heat transfer coefficient is calculated assuming the entire flow (both liquid and gas) as water.

The ratio of two-phase heat transfer coefficient to single-phase heat transfer coefficient is presented in fig. 12(b). It is an important observation that the ratio is almost independent of the curvature ratio of the coil. Thus effect of curvature on two-phase heat transfer almost same as that for single-phase flow and it is well predicted by the single-phase heat transfer correlation.

5.3.2 Influence of coil pitch (H)

The influence of coil pitch on heat transfer rates of two-phase flows is studied by analysing five values of pitch, viz., 0, 15, 30, 45 and 60 mm. The values of heat transfer coefficient obtained from the analysis are shown in fig. 13(a). The ratio h_{tp}/h_s for different values of pitch are presented in fig 13(b). An almost constant value of the ratio indicates that the influence of pitch is similar to both single-phase and two-phase flows.

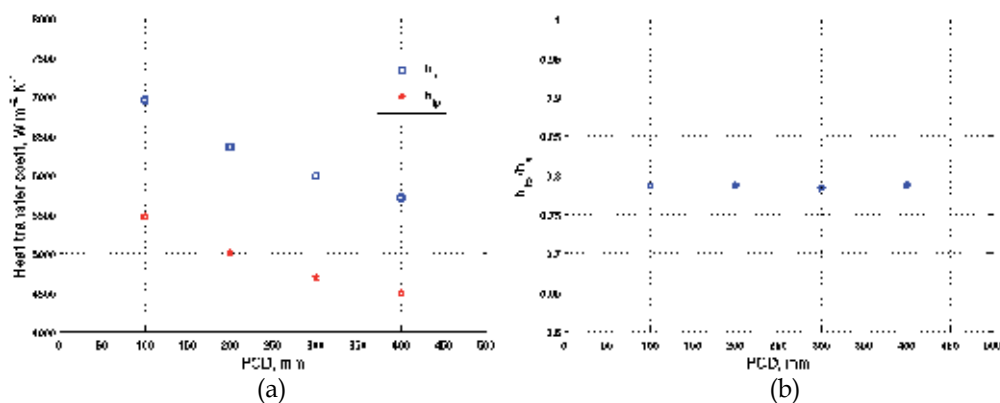


Fig. 12. (a) Variation of heat transfer coefficient and (b) Ratio h_{tp}/h_s as function of pitch circle diameter (PCD).

5.3.3 Influence of pipe diameter (2r)

In this study different coils having pipe diameters of 10, 20, 30 and 40 mm are analysed. In all of these analyses, the PCD was 300 mm and the coil pitch was 45 mm. The results of heat transfer coefficients are presented fig. 14(a). The ratio of two-phase to single-phase heat transfer coefficient for different values of pipe diameters is shown in fig. 14(b). It is clear from the figure that effects of pipe diameter for heat transfer in single-phase and two-phase flows are similar and the single-phase correlation is capable of predicting the heat transfer coefficient adequately.

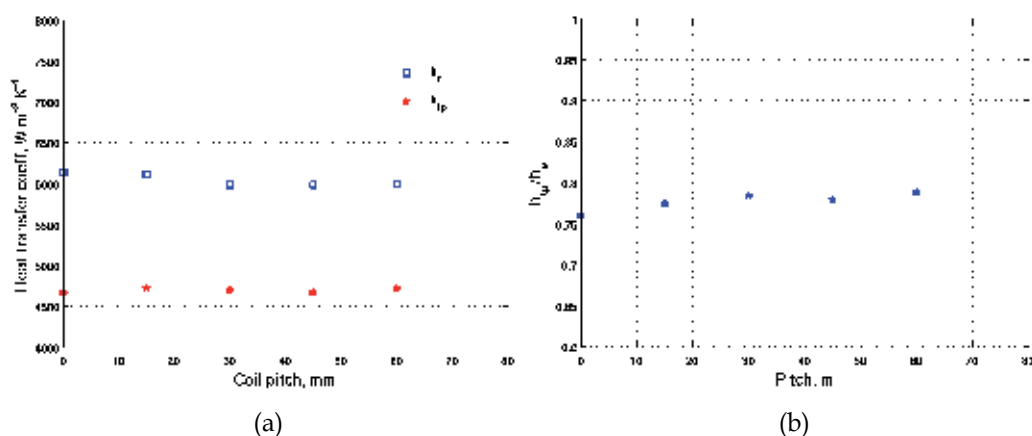


Fig. 13. (a) Variation of heat transfer coefficient and (b) Ratio h_{tp}/h_s as a function of coil pitch (H)

5.3.4 Influence of inlet void fraction (α)

After establishing the influence of coil parameters on two-phase flow and heat transfer, it is necessary to understand the influence of inlet void fraction on the heat transfer. The details of the helical coil chosen for these analyses are: diameter=12.8mm, PCD=450mm, and pitch=24mm. In this analysis, the inlet velocities considered were 0.8, 1.0, 1.5, 2.0 and 3.0 m s^{-1} . For each of the inlet velocities, air void fractions chosen were 0.01, 0.02, 0.04, 0.07, 0.1, 0.15 and 0.2. This leads to a total of 35 runs. Hot fluid (air-water mixture) flows into the coil at the upper face, where an inlet velocity boundary condition was specified. Inlet temperature of the fluid was taken as 360 K. A constant wall heat flux of -150 kW m^{-2} was used for inlet velocities 0.8 and 1.0 m s^{-1} . For the other three inlet velocities, a constant wall temperature boundary condition, $T_w = 300 \text{ K}$, was specified. The working fluid, after getting cooled, flows out through bottom face. An outlet pressure boundary condition is specified for this face. Temperature and pressure dependent properties of viscosity, density, thermal conductivity and specific heat were used for both air and water. In this analysis gravity effect was also taken into account. Each of these runs takes about 23 hrs of computer time on AMD Athlon X2 64 3.0 GHz computer and requires 4GB RAM and 1GB hard disk space. The system has an installed memory of 8 GB and runs on 64 bit Scientific Linux Operating System. There was difficulty in getting converged results for some of the runs. It had been found that the temperature equation is diverging after a few iterations. In order to overcome this problem, the analysis was started with an appropriate Dirichlet boundary condition, so that an approximate temperature field will be established. Then the analysis was restarted with the desired Neumann boundary condition (Jayakumar, 2009).

Fig. 15 shows the values of heat transfer coefficients. The two-phase (TP) heat transfer coefficient values are estimated by post-processing of the CGNS data file. The single phase (SP) heat transfer coefficient is calculated using the correlation developed in section 3. For estimation of single phase heat transfer coefficient, the entire flow is assumed to be liquid.

It is found that with an increase in void fraction, the two-phase heat transfer coefficient continuously decreases. A plot of the ratio of heat transfer coefficients as a function of inverse of Martinelli parameter is given in Fig. 16.

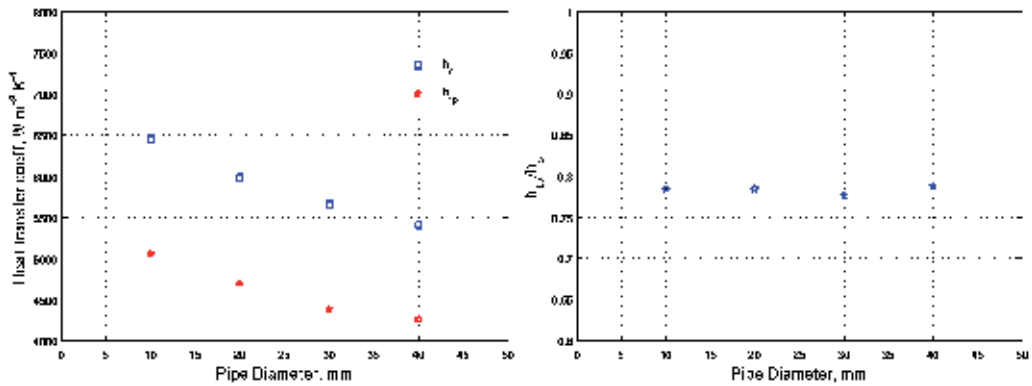


Fig. 14. (a)Variation of heat transfer coefficient and (b) Ratio h_{tp}/h_s as a function of pipe diameter (D).

5.3.5 Correlation for estimation of two-phase heat transfer coefficient

The data generated from the analysis reported in sections 5.3.1 to 5.3.4 is used to develop a correlation for prediction of two-phase heat transfer coefficient. Kim et al. (1999) has prepared a comparison of 40 two-phase heat transfer correlations and recommended the ones matching with the experimental results. A generalised heat transfer correlation for non-boiling gas-liquid flow in horizontal pipes has been proposed by Kim et al. (2006). Based on these results and discussion by Collier (2004), a correlation of the type,

$$\frac{h_{tp}}{h_s} = C\chi^n \tag{31}$$

is proposed. The values of Martinelli parameter, χ , is calculated using the pressure drop relations provided by Czop et al. (1994).

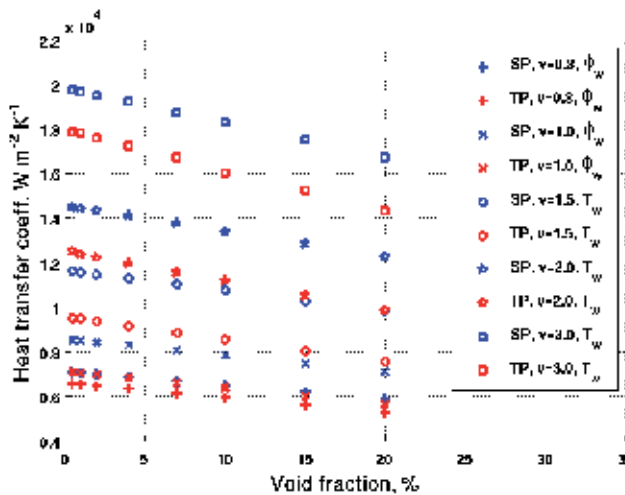


Fig. 15. Inside heat transfer coefficients for air-water flow.

Regression analysis was carried out using the entire set of two-phase heat transfer data. This leads to a correlation,

$$\frac{h_{tp}}{h_s} = 0.7\chi^{0.0424} \tag{32}$$

Fig. 17 shows the correlation along with the data points. The correlation is able to predict the data points within an error of $\pm 10\%$.

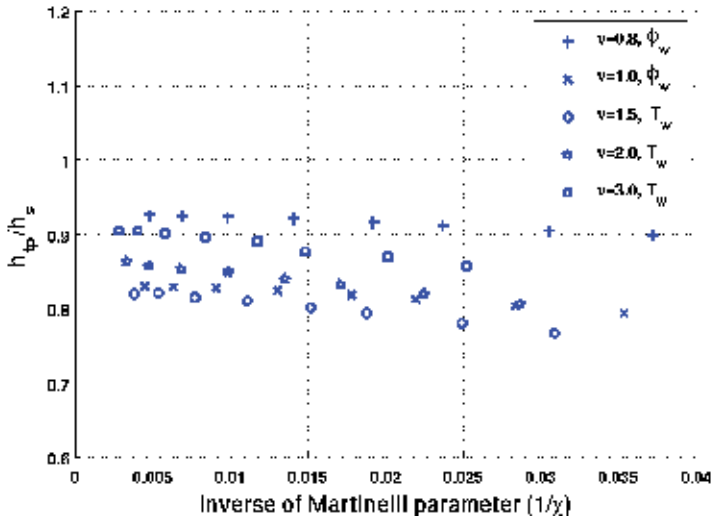


Fig. 16. Ratio h_{tp}/h_s as a function of χ .

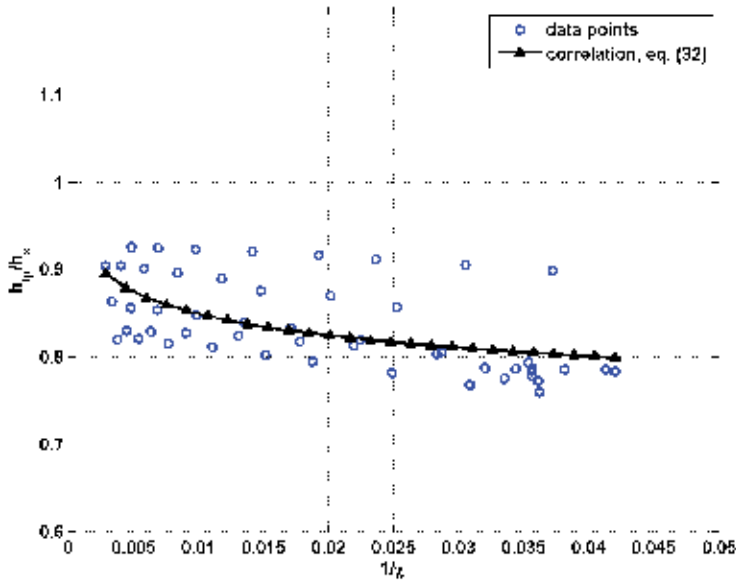


Fig. 17. Correlation for estimation of h_{tp}/h_s as a function of χ .

6. Conclusion

It is observed that the use of constant values for the thermal and transport properties of the heat transport medium results in prediction of inaccurate heat transfer coefficients. Heat transfer characteristics of the heat exchanger with helical coil are also studied using the CFD code. The CFD predictions match reasonably well with the experimental results within experimental error limits. Based on the results a correlation was developed to calculate the inside heat transfer coefficient of the helical coil.

Necessary Python codes, which run in the framework of AnuVi visualisation package, have been developed for accurate estimation of Nusselt number at any point on the heat transfer surface. The research work also includes development of various C++ and MATLAB® codes.

Characteristics of non-isothermal fluid flow and heat transfer under turbulent flow of single phase water through helical coils have been presented in detail. Analysis has been carried out both for the constant wall temperature and constant wall heat flux boundary conditions. Fluid particles are found to undergo oscillatory motion inside the pipe and this causes fluctuations in heat transfer rates.

Nusselt numbers at various points along the length of the pipe was estimated. Nusselt number on the outer side of the coil is found to be the highest among all other points at a specified cross-section, while that at the inner side of the coil is the lowest. Velocity profiles for the two boundary conditions were found to be matching, while the temperature profiles are different.

A number of numerical experiments have been carried out to study influence of coil parameters, viz., pitch circle diameter, coil pitch and pipe diameter on heat transfer. The coil pitch is found to have significance only in the developing section of heat transfer. The torsional forces induced by the pitch causes oscillations in the Nusselt number. However, the average Nusselt number is not affected by the coil pitch. After establishing the parametric influence, a correlation has been developed for estimation of average Nusselt number. This correlation is compared with those available in the literature and the deviations are within reasonable limits. It is also observed that these correlations are applicable for either of the boundary conditions. For most of the engineering applications, the correlations are applicable for conjugate heat transfer as well.

In the fully developed section, ratio Nu_{loc}/Nu_{av} is almost independent of coil parameters and Dean number. Correlations have been developed for prediction of local values of Nusselt number as a function of the average Nusselt number and the angular position of the point along the circumference.

CFD simulations of heat transfer to air-water two-phase mixture flowing through a helically coiled heat exchanger has been carried out. Studies have been carried out by varying (i) coil pitch, (ii) pipe diameter (iii) pitch circle diameter. Their influence on heat transfer and pressure drop has been brought out.

Unlike the flow through a straight pipe, the centrifugal force caused due to the curvature of the pipe causes heavier fluid (water-phase) to flow along the outer side of the pipe. High velocity and high temperature are also observed along the outer side. The torsion caused by pitch of the coil makes the flow unsymmetrical about the horizontal plane of coil. As the

pitch is increased, higher velocity and higher temperature regions are observed on the bottom half of the pipe.

Increase in pipe diameter, keeping the inlet velocity constant, causes higher heat transfer coefficient and lower pressure drop. This effect is due to the influence of secondary flows. As the PCD is increased, the centrifugal forces decreases and this causes reduction of heat transfer coefficient and pressure drop.

Estimation of inner heat transfer coefficient for the two-phase flow was carried out by changing the void fraction and flow velocity. Results indicate reduction in heat transfer coefficient with increase in void fraction.

The coil parameters, viz., PCD and pipe diameter and void fraction at inlet have significant effect on the heat transfer and pressure drop for two-phase flows through helical coils. However, the effect of pitch is negligible. It has been shown that the quantitative dependence of coil parameters on heat transfer is same for both single and two phase flows. Using the data generated from about 45 numerical experiments, a correlation to estimate two-phase heat transfer coefficient is developed.

7. Nomenclature

Symbol	Description and units
A	area, m ²
C _p	Specific heat, J kg ⁻¹ K ⁻¹
D _c	Pitch Circle Diameter, m
De	Dean number = $Re \sqrt{\frac{r}{R_c}}$ dimensionless
F	Force term, N
h	Heat transfer coefficient, W m ⁻² K ⁻¹
H	Tube pitch, m
k	Thermal conductivity, W m ⁻¹ K ⁻¹
L	Length, m
n	unit vector along outward normal
Nu	Nusselt number, dimensionless
p	Pressure, Pa
Pr	Prandtl number, dimensionless
Q	Heat transferred, W
q	heat flux, W m ⁻²
r	Inner radius of the tube, m
R	Resistance to the flow of thermal energy, W ⁻¹ m ² K
R _c	Pitch circle radius of the pipe, m
Re	Reynolds number, dimensionless
S	Source term in governing equations
T	Temperature, K
U	Overall heat transfer coefficient, W m ⁻² K ⁻¹
u	Velocity, m s ⁻¹
u	Velocity vector, m s ⁻¹
V	volume, m ³
Greek	
α	Void fraction, dimensionless

χ	Lockhart-Martinelli parameter, dimensionless
Δ	(temperature) difference, K
δ	Curvature ratio, dimensionless
ϕ	Angular location along the periphery of pipe cross-section
φ	Two-phase friction multiplier, dimensionless
λ	Non-dimensional pitch
μ	viscosity, $\text{kg m}^{-1} \text{s}^{-1}$
θ	Angle a cut plane makes with a plane passing through pipe inlet
ρ	Density, kg m^{-3}
τ	Stress tensor, Pa

Subscripts

av	Average
b	bulk
fi	Internal fouling
fo	External fouling
H	helical
i	internal
k	Phase, can be liquid (l) or gas (g)
lift	lift
LM	Log Mean
loc	local
m	mixture
o	external
ov	Overall
pq	from phase p to phase q
s	single-phase
TP	two-phase
vm	Virtual mass
w	wall

8. Acknowledgement

I express my sincere gratitude to Prof. Kannan N Iyer, Prof. S. M. Mahajani, Prof. J.C. Mandal and Prof. Vijayan P. K. for their meticulous guidance and extensive support during this research work.

9. References

- Abdulla M. A., 1994, A four-region, moving-boundary model of a once through, helical coil team generator, *Annals of Nuclear Energy*, 21(9), 541-562
- Akagawa, K., T. Sakaguchi, and M. Ueda. 1971, Study on a gas-liquid two-phase flow in helically coiled tubes. *Bulletin of the JSME*, Vol. 14 No. 72, pp 564-571.
- Akiyama, M., Cheng, K. C., 1792, Boundary vorticity method for laminar forced convection heat transfer in curved pipes, *Int. J. Heat Mass Transfer*, 15:1426-1431.
- Al-Hajeri M.H., A.M. Koluib, M. Mosaad, S. Al-Kulaib, 2007, Heat transfer performance during condensation of R-134a inside helicoidal tubes, *Energy Conversion and Management*, 48, 2309-2315
- Awwad, A., R. C. Xin, Z. F. Dong, M. A. Ebadian, and H. M. Soliman., 1995, Measurement and correlation of the pressure drop in air-water two-phase flow in horizontal helicoidal pipes. *Int. J Multiphase Flow*, Vol. 21, No. 4, pp 607-619.

- Bai, B., L. Guo, Z. Feng, and X. Chen. 1999, Turbulent heat transfer in a horizontally coiled tube. *Heat Transfer-Asian Research*, 28(5), 395-403.
- Berger S A, Talbot L and Yao L S, 1983, Flow in Curved Pipes, *Ann. Rev. Fluid Mech.*, 15, 461 - 512
- Chen, X. and L. Guo., 1999, Flow patterns and pressure drop in oil-air-water three-phase flow through helically coiled tubes. *Int. J Multiphase Flow*., Vol. 25, pp 1053-1072.
- Chisholm, D., 1967, Pressure gradient during the flow of incompressible two-phase mixtures through pipes, Venturies and Orifices, *Br. Chem. Eng.* 12(9), 1368-1371.
- Collier J.G., Thome J.R., 1994, *Convective Boiling and Condensation*, third ed. Clarendon Press, Oxford, England.
- Colorado D., D. Papini, J.A. Hernández, L. Santini, M.E. Ricotti, 2011, *International Journal of Thermal Sciences* 50, 569-580.
- Czop, V., D. Barbier, and S. Dong., 1994, Pressure drop, void fraction and shear stress measurements in an adiabatic two-phase flow in a coiled tube. *Nucl Eng Des*, Vol. 149, pp 323-333.
- Futagami, K., Aoyama, Y., 1988, Laminar heat transfer in helically coiled tubes, *Int. J. Heat Mass Transfer*, 31, 387-396
- Goering, D. J., Humphrey, J. C. A. and Greif, R., 1997, The dual influence of curvature and buoyancy in fully developed tube flows, *Int. J Heat Mass Transfer*, Vol 40, 2187 - 2199.
- Guo,L., Chen, X., Feng, Z. and Bai, B., 1998, Transient convective heat transfer in a helical coiled tube with pulsatile fully developed turbulent flow, *Int. J. Heat Mass Transfer*, 31, 2867-2875.
- Huttl, T.J. and Friedrich, R., 2000, Influence of curvature and torsion on turbulent flow in helically coiled pipes, *Int. J. Heat Fluid Flow*, 21, 345-353.
- Huttl, T.J. and Friedrich, R., 2001, Direct numerical simulation of turbulent flows in curved and helically coiled pipes, *Comp. Fluids*, 30, 591-605.
- Ito, H. 1959. Friction factors for turbulent flow in curved pipes. *Journal of Basic Engineering*, Transactions of the ASME, Vol. 81, 123-134.
- Janssen, L. A. M., Hoogendoorn, C. J., 1978, Laminar convective heat transfer in helical coiled tubes, *Int. J. Heat Mass Transfer*, 21, 1197-1206.
- Jayakumar J.S. and Grover, R.B., 1997, Two phase natural circulation residual heat removal, *Proc. 3rd ISHMT-ASME Heat and Mass Transfer Conference*, Kanpur.
- Jayakumar J. S., 1999, Analysis of two-phase natural circulation system under oscillatory conditions, M Sc.(Engg.) thesis, Indian Institute of Science, Bangalore, India.
- Jayakumar J. S., Grover, R. B. and Arakeri, V. H., 2002, Response of a two-phase system subject to oscillations induced by the motion of its support structure, *Int. Comm. Heat Mass Transfer*, 29, 519-530
- Jayakumar J. S., S.M. Mahajani, J.C. Mandal, P.K. Vijayan, Rohidas Bhoi, 2008a, Experimental and CFD estimation of heat transfer in helically coiled heat exchangers *Chemical Engineering Research and Design*, Volume 86, Issue 3, March 2008, Pages 221-232.
- Jayakumar J. S., Mahajani, S. M., Mandal, J. C. and Vijayan, P. K, 2008b, "Numerical Analysis of Heat Transfer to Air-Water Two-phase Flows in Helical Pipes", *Proceedings of ICHMT International Symposium on Advances in Computational Heat Transfer CHT-08*, May 11-16, Marrakech, Morocco, CHT-08-299.

- Jayakumar, J. S., 2009, CFD Analysis of single-phase and two-phase flow inside helically coiled tubes, Ph.D. Thesis, Indian Institute of Technology Bombay, Mumbai, India.
- Jayakumar J. S., S.M. Mahajani, J.C. Mandal, Kannan N. Iyer and P.K. Vijayan, 2010a, CFD analysis of single-phase flows inside helically coiled tubes, *Computers & Chemical Engineering*, Volume 34, Issue 4, April 2010, pp 430-446.
- Jayakumar J. S., S.M. Mahajani, J.C. Mandal, Kannan N. Iyer, P.K. Vijayan, 2010b, Thermal hydraulic characteristics of air-water two-phase flows in helical pipes, *Chemical Engineering Research and Design*, Volume 88, Issue 4, April 2010, pp 501-512.
- Jensen M. K. and Bergles A. E., 1981, *Trans. ASME* 103, 660-666
- Ju H, Huang Z, Xu Y, Duan B, Yu Y. Hydraulic performance of small bending radius helical coil-pipe. *J Nucl Sci Technol* 2001;18:826-31.
- Kang H.J., Lin C.X., Ebdadian M.A., 2000, Condensation of R134a Flowing inside helicoidal pipe, *International Journal of Heat and Mass Transfer* 43, 2553 - 2564
- Kasturi, G. and J. B. Stepanek. 1972, Two phase flow - I. Pressure drop and void fraction measurements in cocurrent gas-liquid flow in a coil. *Chem Eng Sci*, Vol. 27 pp 1871-1880.
- Kim, S. E., Choudhury, D. and Patel, B., 1997, Computations of Complex Turbulent Flows Using the Commercial Code FLUENT, *Proceedings of the ICASE/LaRC/AFOSR Symposium on Modeling Complex Turbulent Flows*, Hampton, Virginia.
- Lin, C. X., Ebdadian, M. A., 1997, Developing turbulent convective heat transfer in helical pipes, *Int. J. Heat Mass Transfer*, 40(16), 3861-3873
- Lin, C. X., Ebdadian, M. A., 1999, The effects of inlet turbulence on the development of fluid flow and heat transfer in a helically coiled pipe, *Int. J. Heat Mass Transfer*, 42, 739-751
- Liu, S, 1992, Laminar flow and heat transfer in helical pipes with finite pitch, Ph D thesis, University of Alberta, Canada.
- Lockhart, R.W. and Martinelli, R.C., 1956, "Proposed correlation of data for isothermal two-phase two-component flow in pipes", *Chem. Eng. Prog.*, 45, pp. 39.
- Manna, R., Jayakumar, J.S. and Grover, R.B., 1996, Thermal Hydraulic design of a condenser for a natural circulation system, *J. Energy, Heat and Mass Transfer*, 18, 39-46
- Mori, Y and Nakayama, W, 1967a, Study of forced convective heat transfer in curved pipes (2nd report), *Int. J. Heat Mass Transfer*, 10, 37-59.
- Mori, Y and Nakayama, W, 1967b, Study of forced convective heat transfer in curved pipes (3rd report), *Int. J. Heat Mass Transfer*, 10, 681-695.
- Murai, Y., Yoshikawa, S., Toda, S., Ishikawa, M., Yamamoto, F., 2006, Structure of air-water two-phase flow in helically coiled tubes, *Nuc Eng Des.*, Vol. 236, pp 94-106.
- Naphon P and Wongwises S., 2006, A review of flow and heat transfer characteristics in curved tubes, *Renewable and sustainable energy reviews*, 10, 463-490
- Patankar S., Pratap V. S. and Spalding D. B., 1974, *J. Fluid Mech.* 62, 539-551.
- Prabhanjan, D. G., T. J. Rennie, and G. S. V. Raghavan. 2004. Natural convection heat transfer from helical coiled tubes. *International Journal of Thermal Sciences*, 43(4), 359-365.
- Rangacharyulu, K. and G. S. Davies. 1984. Pressure drop and holdup studies of air-liquid flow in helical coils. *The Chem Eng J*, Vol. 29, pp 41-46.
- Rennie T J, Raghavan V G S, 2005, Experimental studies of a double-pipe helical heat exchanger, *Experimental Thermal and Fluid Science* 29, 919-924

- Rennie T.J., Raghavan, V. G. S., 2006b, "Effect of fluid thermal properties on heat transfer characteristics in a double pipe helical heat exchanger", *Int. J. Thermal Sciences*, 45, 1158-1165
- Rennie, T.J., Raghavan, V. G S, 2006a, Numerical studies of a double-pipe helical heat exchanger, *Applied Thermal Engineering*, 26, 1266-1273.
- Rennie, T.J., Raghavan, V.G.S., 2007, Thermally dependent viscosity and non-Newtonian flow in a double-pipe helical heat exchanger, *Applied Thermal Engineering* 27 (5-6), 862-868
- Rogers, G. F. C. and Mayhew, Y. R., 1964, Heat transfer and pressure loss in helically coiled tube with turbulent flow, *Int J Heat Mass Transfer*, 7, 1207-1216.
- Ruffel, A.E., 1974, The application of heat transfer and pressure drop data to the design of helical coil once-through boilers, *Multiphase Flow Systems Meet.*, Glasgow
- Schmidt E. F., 1967, Wfirmeeibergang und Druckverlust in Rohrschlangen, *G'zemieJng.-Tech.*, 39, 781-789.
- Seban, R. A., and McLaughlin, E. F., 1963, Heat transfer in tube coils with laminar and turbulent flow, *Int. J Heat Mass Transfer*, 6, 387-495.
- Shah, R. K. and Joshi, S. D. 1987, Convective heat transfer in curved ducts. *Handbook of Single-Phase Convective Heat Transfer*, S. Kakac, R. K. Shah, and W. Hung (eds.), Wiley Interscience, New York, Chapter 3.
- Sreenivasan K. R. and P. J. Strykowski, "Stabilization Effects in Flow Through Helically Coiled Pipes", *Experiments in Fluids* 1, 31-36 (1983)
- Srinivasan P.S., Nandapurkar, S.S. and Holland, F.A., 1968, Pressure drop and heat transfer in coils, *Chem. Eng.* 218, CE113-CE119
- Srinivasan, P. S., Nandapurkar, S. S. and Holland, F. A., 1970, Friction factor for coils, *Trans. Inst. Chem. Eng.*, 48, T156 - T161.
- Stepanek, J. B. and G. Kasturi. 1972. Two phase flow - II. Parameters for void fraction and pressure drop correlations. *Chem. Eng Sci*, Vol. 27, pp 1881-1891.
- Tarbell J M, Samuels M R. Momentum and heat transfer in helical coils. *Chem Eng J* 1973;5:117-27.
- Vimal Kumar, Supreet Saini, Manish Sharma and K D P Nigam, 2006, Pressure drop and heat transfer in tube-in-tube helical heat exchanger, *Chem. Eng. Sci.* 61, 4403 - 4416
- Watanabe, O., K. Nakajima and H. Fujita. 1993, Characteristics of liquid-film thickness of air-water annular two-phase flow in helically coiled tubes. *Heat Transfer - Japanese Research*, Vol. 22, No. 5, pp 447-461.
- Whalley, P. B. 1980, Air-water two-phase flow in a helically coiled tube. *Int J Multiphase Flow*, Vol. 6, No. 345-356.
- Xin RC, Awwad A, Dong ZF, Ebadian MA. 1997, An experimental study of single-phase and two-phase flow pressure drop in annular helicoidal pipes. *Int J Heat Fluid Flow*, 18, 482-488.
- Xin, R. C., A. Awwad, Z. F. Dong and M. A. Ebadian., 1996, An investigation and comparative study of the pressure drop in air-water two-phase flow in vertical helicoidal pipes. *Int J Heat and Mass Transfer*, Vol. 39(4), pp 735-743.
- Yang, G. and Ebadian, M. A., 1996, Turbulent forced convection in a helicoidal pipe with substantial pitch, *Int. J Heat Mass Transfer*, Vol 39(10), 2015 - 2032.
- Yildiz, C., Bicer, Y., Pehlivan, D., 1997, Heat transfer and pressure drop in a heat exchanger with a helical pipe containing inside springs, *Energy Convers. Mgmt.*, 38 (6), 619-624.

Fin-Tube Heat Exchanger Optimization

Piotr Wais

*Cracow University of Technology, Department of Thermal Power Engineering
Poland*

1. Introduction

Saving material and energy are common objectives for optimization. One of the important issues that should be defined during the design work, taking in consideration the cost of material, is the optimization of the heat efficiency. The optimization function can consider minimum weight for a specified heat flow, placement of individual fins to form channels or fin profile based on a set of specified conditions (for instance the dissipation from the fin faces, minimum mass, minimum pressure drop etc). In order to intensify the heat transfer from the heat exchanger surface to fluid, it is possible to increase convection coefficient (by growing the fluid velocity), widen temperature difference between surface and fluid or increase the surface area across which convection occurs. Extended surfaces, in the form of longitudinal or radial fins are common in applications where the need to enhance the heat transfer between a surface and an adjacent fluid exists.

Fins are commonly used in extended surface exchangers. Conventional fin-tube exchangers often characterize the considerable difference between liquids' heat transfer coefficients. In a gas-to-liquid exchanger, the heat transfer coefficient on the liquid side is generally one order of magnitude higher than that on the gas side. To minimize the size of heat exchangers, fins are used on the gas side to increase the surface area and the heat transfer rate between the heat exchanger surface and the surroundings. Both the conduction through the fin cross section and the convection over the fin surface area take place in and around the fin. When the fin is hotter than the fluid to which it is exposed then the fin surface temperature is generally lower than the base (primary surface) temperature. If the heat is transported by convection to the fin from the ambient fluid, the fin surface temperature will be higher than the fin base temperature, which in turn reduces the temperature differences and the heat transfer through the fin. Exchangers with fins are also used when one fluid stream is at high pressure. The temperature value is limited by the type of material and production technique. All above causes that finned tube heat exchangers are used in different thermal systems for applications where heat energy is exchanged between different media. Applications range from very large to the small scale (tubes in heat exchangers, the temperature control of electronic components).

The subject, which is investigated in the chapter, is inspired by the increasing need for optimization in engineering applications, aiming to rationalize use of the available energy. The performance of the heat transfer process in a given heat exchanger is determined for different fin profiles, considering the fluid flow as a variability often neglected for the fin optimization. The optimization task, defined in the chapter, is to increase heat transfer rates and reduce the

fin mass by means of changing the shape of the fin. The fin shape modification influences not only the mass of the heat exchanger, but also affects the flow direction that causes the temperature changes on the fin contact surfaces. The air flow is considered in all 3D models. The numerical outcome of heat transfer coefficient is compared to the results received from the empirical equation for the fin-tube heat exchanger of uniform fin thickness. The correlation function is cited and the procedure how to verify the models is described. For modified fin shapes, mass flow weighted average temperatures of air volume flow rate are calculated in the outlet section and compared for different fin/tube shapes in order to optimize the heat transfer between the fin material and the air during the air flow in the cross flow heat exchanger.

2. Heat transfer from fins

The analysis of heat transfer from finned surfaces involves solving second-order differential equations and is often a subject of researches including also the variable heat transfer coefficient as a function of temperature or the fin geometrical dimensions. To analyze the heat transfer problem, a set of assumptions is introduced so that the resulting theoretical models are simple enough for the analysis. Analytical investigations and search activities, which allow finding the optimal profile of the fin, are available under assumptions that simplify the problem of heat transfer. These basic assumptions are proposed by Murray (1938) and Gardner (1945) and are called Murray-Gardner assumptions (Kraus et al., 2001):

- the heat flow in the fin and its temperatures remain constant with time
- the fin material is homogeneous, its thermal conductivity is the same in all directions, and it remains constant
- the convective heat transfer on the faces of the fin is constant and uniform over the entire surface of the fin
- the temperature of the medium surrounding the fin is uniform
- the fin thickness is small, compared with its height and length, so that temperature gradient across the fin thickness and heat transfer from the edges of the fin may be neglected
- the temperature at the base of the fin is uniform
- there is no contact resistance where the base of the fin joins the prime surface
- there are no heat sources within the fin itself
- the heat transferred through the tip of the fin is negligible compared with the heat leaving its lateral surface
- heat transfer to or from the fin is proportional to the temperature excess between the fin and the surrounding medium
- radiation heat transfer from and to the fin is neglected

In general, the study of the extended surface heat transfer compromises the movement of the heat within the fin by conduction and the process of the heat exchange between the fin and the surroundings by convection.

2.1 Straight fin analysis

Straight fin is any extended surface that is attached to a plane wall (Incropera et al., 2006). It may be of uniform cross-sectional area, or its cross-sectional area may vary with the distance x from the wall. The fin of variable thickness is shown in Figure 1.

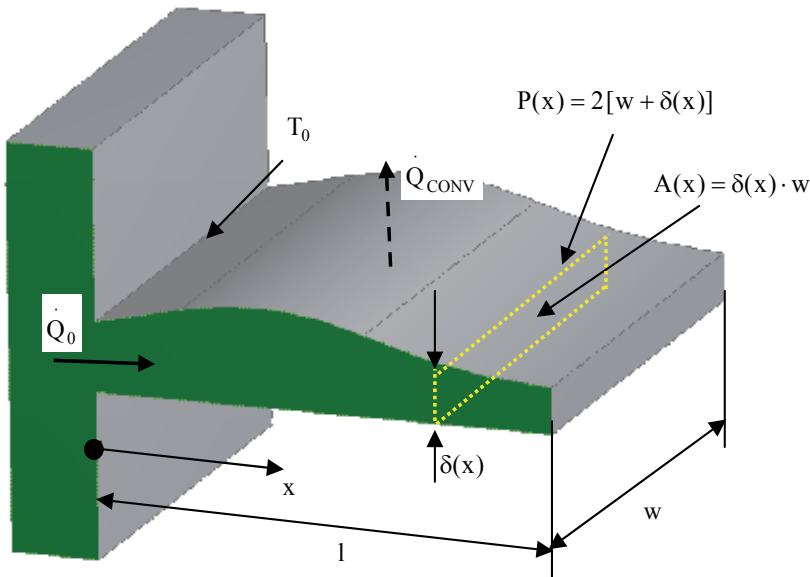


Fig. 1. Straight fin of variable cross section.

Both the conduction through the fin cross section and the convection over the fin surface area take place in and around the fin. When the fin temperature is lower than the base (primary surface) temperature T_0 , the heat is transferred from the fin to the surroundings (Shah & Sekulic, 2003).

The fin height is l , width is w , variable thickness $\delta(x)$. Its perimeter for surface convection depends on coordinate x and is $P(x) = 2[w + \delta(x)]$. Its cross-sectional area for heat conduction at any cross section is $A(x) = \delta(x) \cdot w$, where δ - fin thickness as a function of x , w - fin width.

The temperature distribution can be calculated taking into consideration an energy balance on a typical element between x and $x + dx$, shown in Figure 2.

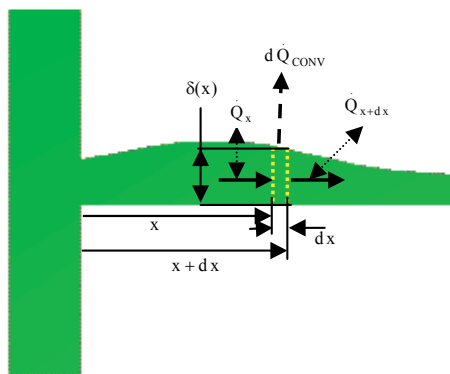


Fig. 2. Energy balance on a typical element.

The energy balance:

$$\dot{Q}_x - \dot{Q}_{x+dx} - d\dot{Q}_{CONV} = 0 \quad (1)$$

where

$$\dot{Q}_x = -k_f A_{k,x} \frac{dT}{dx} \quad (2)$$

$$\dot{Q}_{x+dx} = -k_f \left(A_{k,x} \frac{dT}{dx} + \frac{d}{dx} \left(A_{k,x} \frac{dT}{dx} \right) dx \right) \quad (3)$$

$$d\dot{Q}_{CONV} = h A_f (T - T_S) = h P dx (T - T_S) \quad (4)$$

Where

k_f - fin thermal conductivity

h - heat transfer coefficient

T_S - surrounding temperature

A_f - fin surface area

$A_{k,x}$ - cross-sectional area as a function of k and x

P - perimeter (function of x)

Then

$$k_f \frac{d}{dx} \left(A_{k,x} \frac{dT}{dx} \right) dx = h P dx (T - T_S) \quad (5)$$

and

$$\frac{d^2 T}{dx^2} + \frac{1}{A_{k,x}} \frac{dA_{k,x}}{dx} \frac{dT}{dx} - \frac{h P}{k_f A_{k,x}} (T - T_S) = 0 \quad (6)$$

or

$$\frac{d^2 T}{dx^2} + \frac{d(\ln A_{k,x})}{dx} \frac{dT}{dx} - m^2 (T - T_S) = 0 \quad (7)$$

where

$$m^2 = \frac{h P}{k_f A_{k,x}} \quad (8)$$

Both P and $A_{k,x}$ are the function of x or a variable cross section.

To simplify the equation, the new dependent variable is introduced:

$$\theta(x) = T(x) - T_s \quad (9)$$

where

θ - temperature difference between a point on a fin surface and the surroundings, $^{\circ}\text{C}$

Because the ambient (surrounding) temperature is assumed to be constant, then:

$$\frac{d\theta}{dx} = \frac{dT}{dx} \quad (10)$$

and

$$\frac{d^2\theta}{dx^2} + \frac{d(\ln A_{k,x})}{dx} \frac{d\theta}{dx} - m^2\theta = 0 \quad (11)$$

This second order, linear, homogeneous ordinary differential equation with nonconstant coefficients is valid for any thin fins of variable cross section. Once the boundary conditions and the fin geometry are specified, its solution will provide the temperature distribution and subsequently, the heat transfer rate through the fin (Shah & Sekulic, 2003)

2.2 Circular fin analysis

The fin of uniform thickness of circular fin that can be applied on the outside of a tube is shown in Figure 3. Such fins have extensive application in liquid-gas heat exchangers (Mills, 1995).

The energy balance on a typical element of circular fin between r and $r + dr$ can be written as:

$$(q \ 2\pi r \delta)|_r - (q \ 2\pi r \delta)|_{r+dr} - 2h(2\pi r)dr(T - T_s) = 0 \quad (12)$$

where

$$q = -k_f \frac{dT}{dr} \quad (13)$$

k_f - fin thermal conductivity

δ - fin thickness

T_s - surrounding temperature

then:

$$-\frac{d}{dr} \left(r \frac{\delta}{2} q \right) - hr(T - T_s) = 0 \quad (14)$$

$$\frac{d}{dr} \left(r \frac{dT}{dr} \right) - \frac{2hr}{\delta k_f} (T - T_s) = 0 \quad (15)$$

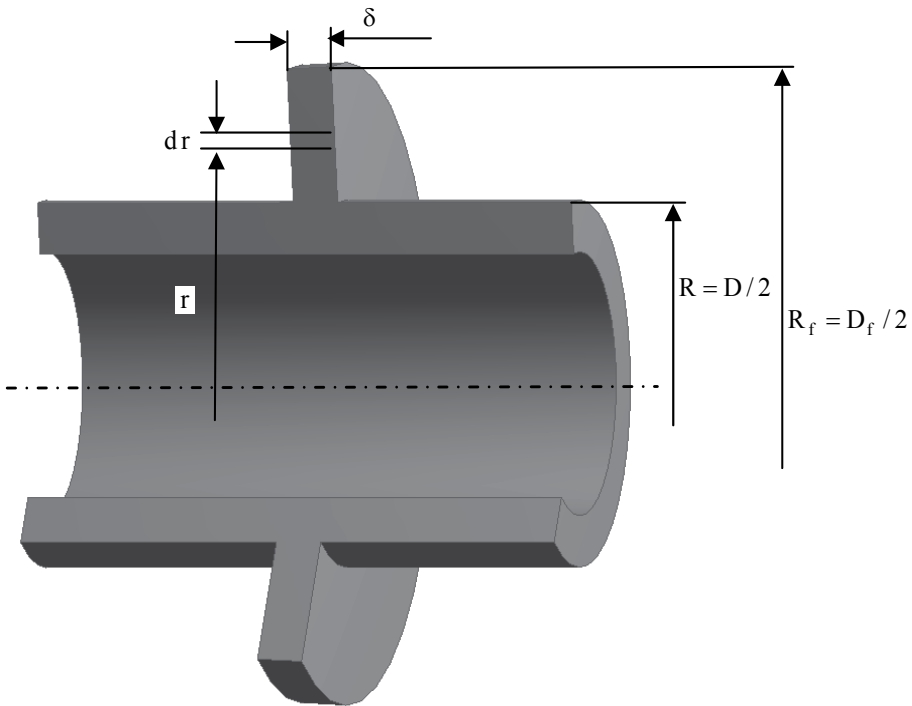


Fig. 3. Circular fin of uniform thickness.

To simplify the equation, the new dependent variable is introduced:

$$\theta(x) = T(x) - T_s \quad (16)$$

and constant value

$$m^2 = \frac{h P}{k_f A_k} = \frac{h 2(2\pi r)}{k_f (2\pi r) \delta} = \frac{2h}{k_f \delta} \quad (17)$$

Because the ambient (surrounding) temperature is assumed to be constant, then:

$$\frac{d\theta}{dr} = \frac{dT}{dr}, \quad \frac{d^2\theta}{dr^2} = \frac{d^2T}{dr^2} \quad (18)$$

and

$$\frac{d^2\theta}{dr^2} + \frac{1}{r} \frac{d\theta}{dr} - m^2\theta = 0 \quad (19)$$

The general solution of the equation is modified Bessel function of order zero:

$$\theta = C_1 I_0(mr) + C_2 K_0(mr) \quad (20)$$

where I_0 and K_0 are modified, zero-order Bessel functions of the first and second kind respectively.

Assuming the constant and known base temperature and zero heat flow through the tip of the fin:

$$r = R \rightarrow T = T_0 \rightarrow \theta_0 = T_0 - T_s \tag{21}$$

$$r = R_f \rightarrow \left. \frac{dT}{dr} \right|_{r=R_f} = 0 \rightarrow \left. \frac{d\theta}{dr} \right|_{r=R_f} = 0 \tag{22}$$

where

R_f - radial coordinate of fin tip ($R_f = D_f / 2$)

R - radial coordinate of fin base (external tube radius $R = D / 2$)

From the first condition:

$$\theta_0 = C_1 I_0(mR) + C_2 K_0(mR) \tag{23}$$

From the second condition and according to differentiation rules

$$\frac{d}{dr}[C_1 I_0(mr)] = C_1 m I_1(mr) \tag{24}$$

$$\frac{d}{dr}[C_2 K_0(mr)] = -C_2 m K_1(mr) \tag{25}$$

we obtain:

$$\left. \frac{d\theta}{dr} \right|_{r=R_f} = (C_1 m I_1(mr) - C_2 m K_1(mr)) \Big|_{r=R_f} = C_1 m I_1(mR_f) - C_2 m K_1(mR_f) = 0 \tag{26}$$

C_1 and C_2 can be evaluated to find a temperature distribution:

$$\frac{\theta}{\theta_0} = \frac{I_0(mr)K_1(mR_f) + K_0(mr)I_1(mR_f)}{I_0(mR)K_1(mR_f) + K_0(mR)I_1(mR_f)} \tag{27}$$

where

$I_1(mr) = \frac{d[I_0(mr)]}{d(mr)}$ and $K_1(mr) = \frac{d[K_0(mr)]}{d(mr)}$ are modified, first order Bessel functions of the first and second kind.

Heat dissipated by the fin and its efficiency can be expressed as:

$$\dot{Q} = -k_f A_k \left. \frac{dT}{dr} \right|_{r=R} = -k_f (2\pi R \delta) \left. \frac{d\theta}{dr} \right|_{r=R} \tag{28}$$

where δ is the fin thickness.

Then

$$\dot{Q} = 2\pi R \delta k_f \theta_0 m \frac{K_1(mR) I_1(mR_f) + I_1(mR) K_1(mR_f)}{K_0(mR) I_1(mR_f) + I_0(mR) K_1(mR_f)} \quad (29)$$

and fin efficiency

$$\eta_f = \frac{\dot{Q}}{h 2\pi (R_f^2 - R^2) \theta_0} = \frac{2R}{m(R_f^2 - R^2)} \frac{K_1(mR) I_1(mR_f) + I_1(mR) K_1(mR_f)}{K_0(mR) I_1(mR_f) + I_0(mR) K_1(mR_f)} \quad (30)$$

This result may be applied for an “active” tip (no zero heat flow through the tip of the fin) if the tip radius R_f is replaced by the corrected radius of the form $R_{f_COR} = R_f + \frac{\delta}{2}$ (Incropera et al., 2006). The fin tip area can be also neglected, taking into consideration the fact that the heat transfer at the fin tip is small. Some authors propose using simpler expressions for hand calculations (Shah & Sekulic, 2003).

2.3 Circular fin thickness optimization

The simple radial fin with a rectangular profile is sketched in Figure 3. The fin profile and its optimization issue is often the subject of research. Different authors eliminate some of Murray-Gardner assumptions in their investigations that make the problem more complex. The literature includes a large number of publications dealing with convective heat transfer for different surface geometry, fluid flow type, fluid composition, and thermal boundary conditions but without considering the fluid flow motion.

For the ideal case, if the convection is considered in a fin heat exchanger and the surrounding temperature is equal to T_s , the temperature difference between any point on the fin surface and the surrounding temperature can be written as:

$$\theta = T(r) - T_s \quad (31)$$

where:

$T(r)$ is the fin surface temperature that varies from the fin base to the fin tip

The optimized profile of the symmetrical radial fin of least material can be found from the generalized differential equation (Kraus et al., 2001):

$$f(r) \frac{d^2\theta}{dr^2} + \frac{f(r)}{r} \frac{d\theta}{dr} + \frac{df(r)}{dr} \frac{d\theta}{dr} - \frac{h}{k_f} \theta = 0 \quad (32)$$

assuming that the temperature excess changes linearly:

$$\theta = \theta_0 \left(1 - \frac{r - R_f}{R_f - R} \right) \quad (33)$$

and resolving above equation with two differential conditions

$$\frac{d\theta}{dr} = \frac{-\theta_0}{R_f - R} \quad (34)$$

$$\frac{d^2\theta}{dr^2} = 0 \quad (35)$$

the profile function is derived for the radial fin of least material (Kraus et al., 2001):

$$\frac{k_f f(r)}{h R_f^2} = \frac{1}{3} \left(\frac{r}{R_f} \right)^2 - \frac{1}{2} \left(\frac{r}{R_f} \right) + \frac{1}{6} \left(\frac{R_f}{r} \right) \quad (36)$$

The heat flux in a parabolic fin is less sensitive to the variation of the tip temperature than in the case of rectangular and trapezoidal fin profiles. This can be seen after resolving the differential equations analytically. Due to the manufacturing problem, the profile described by Equation (36) is not used.

3. Heat exchanger optimization

The analysis and design of heat exchangers consider problems in which the temperature of the fluid changes as it flows through a passage as a result of heat transfer between the wall and the fluid. For heat transfer and pressure drop analyses, at least the following heat transfer surface geometrical properties are needed on each side of a two-fluid exchanger: minimum free-flow area, core frontal area, heat transfer surface area which includes both primary and fin area, hydraulic diameter, and flow length. These quantities are computed from the basic dimensions of the core and heat transfer surface. Due to the complexity of calculations (heat transfer and flow characteristics) it is necessary to find the best possible design solution taking into consideration certain assumptions. In practice, flow maldistribution is common and influences the heat exchanger performance. It can be induced by heat exchanger geometry or heat exchanger operating conditions (e.g., viscosity, density). The objective function is defined within constraints and resolved afterwards.

The optimization of fin-tube heat exchanger is presented focusing on different fluid velocities and the consideration of aerodynamic configuration of the fin. It is reasonable to expect the influence of fin profile on the fluid streamline direction. In the cross-flow heat exchanger, the air streams are not heated and cooled evenly. The fin and tube geometry affects the flow direction and has the effect on the temperature changes.

To analyze the heat transfer problem, a set of assumptions is introduced so that the resulting theoretical models are simple enough for the analysis. One of the common assumptions in basic heat exchanger design theory is the uniform fluid distribution at the inlet of the exchanger on each fluid side. Firstly, calculations for circular fin-tube heat exchanger are done. To confirm the correctness of the numerical model, the results of heat transfer (outlet temperature) are reviewed and compared with the proper correlation (Hewitt et al., 1994) modified for one row crossflow tube-fin heat exchanger of rectangular profile and fin constant thickness.

3.1 Optimization and objective function

The optimization process should lead to project the heat exchanger that meets the stated criteria (for instance heat transfer required, minimum weight, heat exchanger efficiency or performance, allowable pressure drop etc).

There are different types of the optimization for radial fin heat exchangers. The optimization can consider (Kraus et al., 2001):

- minimum weight for a specified heat flow
- fin profile based on a set of specified conditions (for instance the dissipation from the fin faces and calculation of minimum volume as well as minimum profile area)
- placement of individual fins to form channels

One of the important issues that should be defined during the design work is the optimization of the heat efficiency, taking into consideration the cost of material and the whole heat exchanger.

As an example, the objective function is to maximize the heat transfer ratio for elementary heat exchanger mass (or volume for known material density) in fin-tube heat exchanger. It means that the fin profile is optimized to find the maximum value of function ξ , defined as the ratio between the heat removed from the tube/fin component to the tube/fin weight:

$$\xi = \frac{\dot{Q}}{m_s} \quad (37)$$

where

\dot{Q} - heat flow removed from the fluid to the fin and tube

m_s - tube and fin mass (solid).

Introducing c_f - fluid (air) specific heat capacity, \dot{m}_f - fluid mass flow rate, T_{IN} - fluid temperature in the inlet section, T_T - internal tube surface temperature, ρ_s - material density of solid (tube and fin), V_s - volume of tube and fin material, the ratio ξ is equal:

$$\xi = \frac{\dot{m}_f c_f (T_{IN} - T_{OUT})}{\rho_s V_s} \quad (38)$$

If the values of c_f , ρ_s do not change during the air flow, then the optimization problem can be resolved by finding the maximum value of the optimization function, ε :

$$\varepsilon = \frac{\dot{m}_f (T_{IN} - T_{OUT})}{V_s} = \frac{\dot{m}_f \Delta T_{Fluid}}{V_s} \rightarrow \max \quad (39)$$

where

$\Delta T_{Fluid} = T_{IN} - T_{OUT}$ - difference in fluid temperature between outlet and inlet section.

The temperature difference is found numerically and the solid volume is calculated for different fin profile shapes. The air temperature value is also computed numerically in the outlet section and the average air temperature is evaluated.

3.2 Numerical optimization of fin shape

To analyze the exchanger heat transfer problem, a model of heat exchanger is built under some assumptions:

- the heat exchanger operates under steady-state conditions
- heat losses to or from the surroundings are negligible
- there are no thermal energy sources or sinks in the exchanger walls or fluids,
- there is no thermal resistance between tube and fins,
- the physical properties of material and fluid do not depend on temperature (specific heat, density, heat conduction ...)
- the velocity and temperature of the fluid at the entrance of the heat exchanger are uniform over the flow cross section.
- the fluid flow rate is uniformly distributed through the exchanger
- there is no flow leakages in any stream.

The heat exchanger characteristic dimensions are written in Table 1:

	Fin and tube pitches
p_f (fin pitch), mm	3.0
p_t (tube pitch), mm	46
D (tube ext diam), mm	25
D_t (fin ext diam), mm	41

Table 1. Heat exchanger characteristic dimensions.

Calculations are done for circular fin-tube heat exchanger. Three-dimensional models are performed to find heat transfer characteristics between a finned tube and the air for different fin shapes in order to optimize the heat transfer between the air and fin material during the air flow in the cross flow heat exchanger. The model allows considering the heat transfer in three directions. The model is so defined that its output is compared with the results received from correlation formula. Correlation is described in Heading 3.3. Then, the main objective of this research is examined. The performance of a given heat exchanger for different fin profiles, with emphasis on the flow rates, is determined numerically by means of Ansys Workbench program (Ansys 12 Product Documentation).

A fin shape, used for the simulations, is shown in Figure 4 and the dimensions are presented in Table 2 where R_f - radial coordinate of fin tip, R - radial coordinate of fin base, R_{ch} - radial coordinate of chamfer. All profiles have the same radius R_f and thickness δ_f at the fin base (the thickness depends on angle β_1 and β_2 and changes along the fin height).

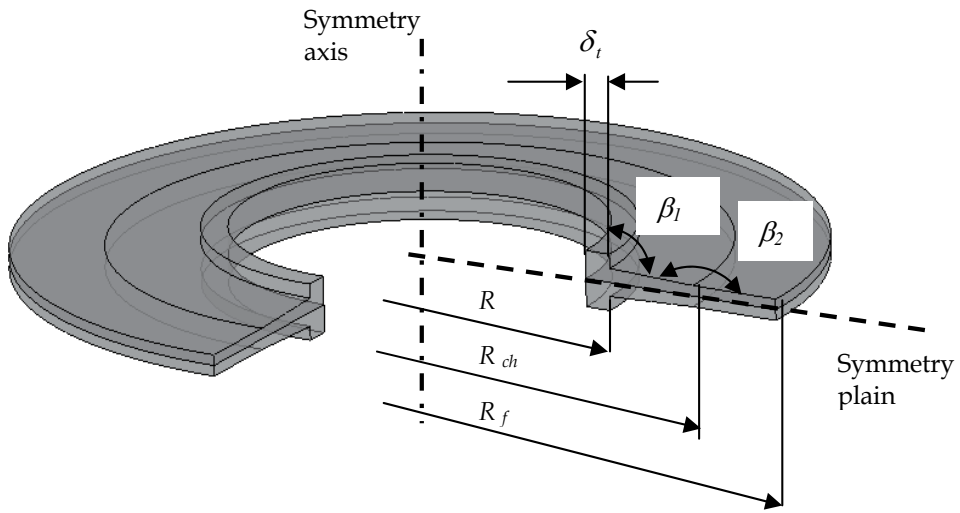


Fig. 4. Circular fin in optimization process.

	Fin version					
	(a)	(b)	(c)	(d)	(e)	(f)
R_f mm	20,5	20,5	20,5	20,5	20,5	20,5
R_{ch} mm	-	-	-	14,5	14,5	14,5
R mm	12,5	12,5	12,5	12,5	12,5	12,5
δ_f mm	2,0	2,0	2,0	2,0	2,0	2,0
$p_f/2$ mm	1,5	1,5	1,5	1,5	1,5	1,5
β_1 deg	90	90	90	92,9	95,7	98,5
β_2 deg	180	180	180	177,1	174,3	171,5
δ mm	constant 1,2	constant 1	constant 0,8	variable at R_f $d=1,0$ at R $d=1,2$	variable at R_f $d=0,8$ at R $d=1,2$	variable at R_f $d=0,6$ at R $d=1,2$

Table 2. Fin and tube dimensions.

The model sketch, including also an air volume attached to the fin and tube segment, is demonstrated in Figure 5 (Wais, 2010):

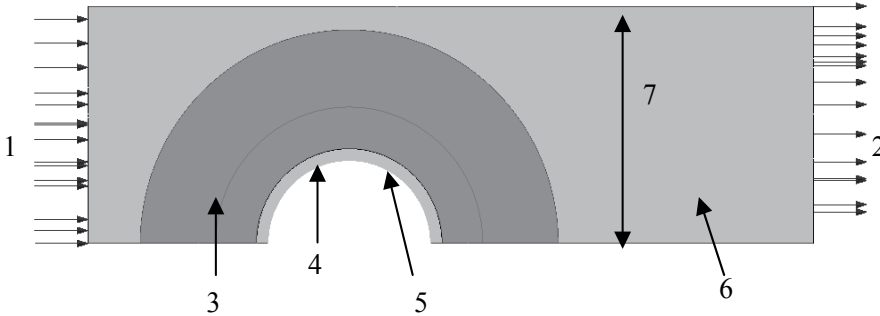


Fig. 5. Model used for CFD simulation.

where:

1. inlet area with constant air temperature $T_{IN} = 300 \text{ }^{\circ}\text{C}$ and unanimous air velocity distribution, normal to the section $v_{IN} = 4.0 \text{ m/s}$
2. outlet area
3. fin made of steel
4. tube made of steel
5. inner tube surface with constant temperature $T_T = 70 \text{ }^{\circ}\text{C}$
6. air volume
7. model width equal to $p_t/2$

3.3 Correlation for external heat transfer in cross-flow heat exchanger

The cross-flow heat exchanger is often used in process plants. Fins, applied in heat exchangers, assure greater surface area (contact area) per a unit volume and can reduce the size or cost of the unit. The negative feature of fins is the bigger pressure drop in the flowing fluid.

Finned tubes may be divided into two categories: low fin and high fin. The ratio of the fin height to external diameter of the tube is the determinant (Hewitt et al., 1994):

$$\text{low-fin tubes: } 0.05 > l/D_f > 0.33$$

$$\text{high-fin tubes: } 0.2 > l/D_f > 0.7$$

Similar to plain tubes, heat transfer correlations are based on maximum fluid velocity and additional terms for fin geometry. Average heat transfer coefficient \bar{h} is of more specific interest but it should be underlined that the surface temperature of the fins is not uniform. This is done by including the fin efficiency in deriving the effective heat transfer coefficient (Hewitt et al., 1994).

Therefore:

$$\text{Re}_D = \frac{\rho v_{\max} D}{\eta} \quad (40)$$

$$v_{\max} = \frac{\dot{m}_f}{S_{\min} \rho} \quad (41)$$

$$\overline{Nu} = \frac{\bar{h} D}{k_f} \quad (42)$$

where

D - external tube diameter,
 v_{\max} - maximum fluid velocity (in minimum flow area),
 ρ - fluid density,
 η - fluid dynamic viscosity,
 S_{\min} - minimum flow area,
 k_f - fin thermal conductivity,
 \bar{h} - average heat transfer coefficient

Typical fin-tube geometry, with surface area equation and minimum cross-sectional area, are presented in Figure 6.

Surface area of one sector (consists of fin and tube) are defined as:

$$\text{Surface area of fins: } A_f = \left[\frac{1}{2} \pi (D_f^2 - D^2) \right] + \pi D_f \delta$$

$$\text{Surface area of tube between fins: } A_t = \pi D s$$

$$\text{Total surface area: } A = \left[\frac{1}{2} \pi (D_f^2 - D^2) \right] + \pi D_f \delta + \pi D s$$

$$\text{Total tube surface (with fin removed): } A_T = \pi D (s + \delta)$$

Characteristic fin-tube heat exchanger configurations are shown in Figure 7.

Average heat transfer coefficient \bar{h} is of more specific interest for the whole process, which is correlated with the maximum velocity between tubes v_{\max} .

Total heat transfer can be calculated taking into consideration fin efficiency:

$$\dot{Q} = \bar{h} \Delta T (\eta_f A_f + A_t) = \bar{h}' \Delta T A \quad (43)$$

where

η_f - fin efficiency

\bar{h} - average heat transfer coefficient

\bar{h}' - effective heat transfer coefficient

ΔT - effective mean temperature difference,

A - total external area of the tubes and fins

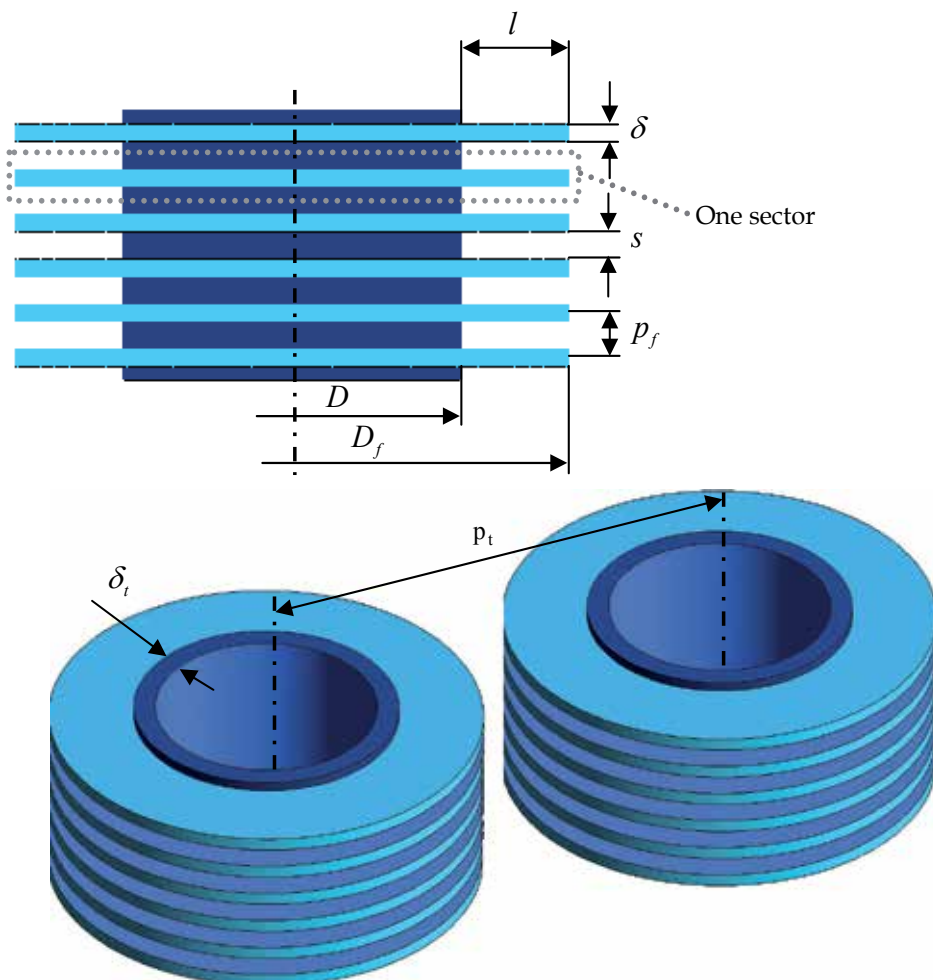


Fig. 6. Fin-tube geometry.

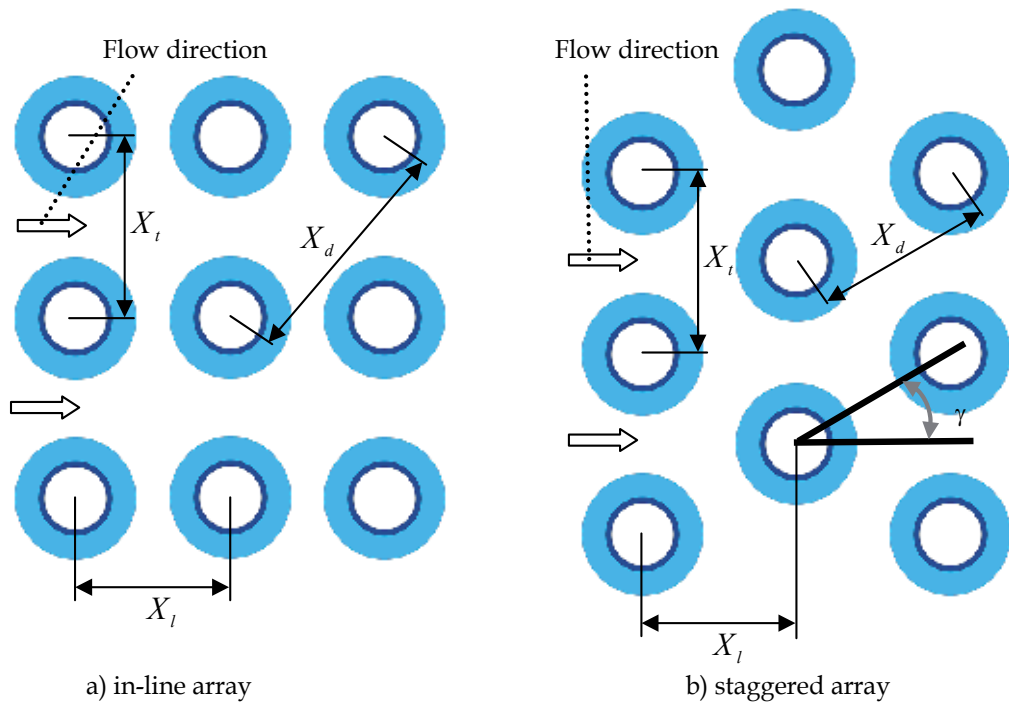


Fig. 7. Fin-tube patterns.

It is necessary to find the effective mean temperature difference to evaluate the heat transfer. Since the fluid temperatures change in fluid flow through the tube bank, the fluid temperature difference ΔT_{Fluid} can be calculated from energy exchanged as:

$$\dot{Q} = \bar{h} \Delta T (\eta_f A_f + A_t) = \dot{m}_f c_f \Delta T_{Fluid} \quad (44)$$

where

$$\Delta T = \frac{(T_0 - T_{OUT}) - (T_0 - T_{IN})}{\ln \frac{T_0 - T_{OUT}}{T_0 - T_{IN}}} \quad (45)$$

and

T_0 - temperature at the external tube surface (for diameter D)

T_{OUT} - average fluid temperature in the outlet section

T_{IN} - average fluid temperature in the inlet section

and for $T_{IN} > T_{OUT}$

$$\Delta T_{Fluid} = T_{IN} - T_{OUT} \quad (46)$$

After transformation

$$\Delta T_{Fluid} = \frac{\bar{h} (\eta_f A_f + A_t)}{\dot{m}_f c_f} \Delta T \quad (47)$$

$$T_{OUT} = T_{IN} - \frac{\bar{h} (\eta_f A_f + A_t)}{\dot{m}_f c_f} \Delta T \quad (48)$$

finally

$$\Delta T = (T_{IN} - T_0) \frac{1 - \exp\left(-\frac{\bar{h} (\eta_f A_f + A_t)}{\dot{m}_f c_f}\right)}{\frac{\bar{h} (\eta_f A_f + A_t)}{\dot{m}_f c_f}} \quad (49)$$

The value of heat transfer depends on local fluid velocity, fluid properties and details of the tube bank geometry. Correlations that allow calculating average heat transfer coefficient, \bar{h} , are derived from experimental data and take into account geometrical features.

Having calculated average heat transfer coefficient, \bar{h} , effective mean temperature difference, ΔT , and fin efficiency, η_f , the rate of heat transfer equals:

$$\dot{Q} = \bar{h} \Delta T (\eta_f A_f + A_t) \quad (50)$$

3.3.1 Correlation for low fin tube

The average Nusselt number for low fin tube can be calculated from below correlation (Hewitt et al., 1994):

$$\overline{Nu} = 0.183 \text{Re}^{0.7} \left(\frac{s}{l}\right)^{0.36} \left(\frac{X_t}{D_f}\right)^{0.06} \left(\frac{l}{D_f}\right)^{0.11} \text{Pr}^{0.36} \cdot F_1 \cdot F_2 \cdot F_3 \quad (51)$$

where

F_1 - factor for fluid property variation (significant only at high temperatures),

$$F_1 = \left(\frac{\text{Pr}_{Fluid_Ave}}{\text{Pr}_S}\right)^{0.26},$$

Pr_{Fluid_Ave} - Prandtl number of fluid for bulk temperature T_{Fluid_Ave}

Pr_S - Prandtl number of fluid for mean tube and fin surface temperature, \bar{T}_S

F_2 – factor for number of fin – tube rows
 for number of rows > 10 : $F_2 = 1.000$
 for number of rows = 8: $F_2 = 0.985$
 for number of rows = 6: $F_2 = 0.955$
 for number of rows = 4: $F_2 = 0.900$

F_3 – factor for staggered arrangement ($\gamma = 30^\circ, 45^\circ, 60^\circ$, see Fig. 5. for γ definition) $F_3 = 1$

F_3 – factor for in-line arrangement $F_3 = \frac{\overline{Nu} \text{ for plain tube (in-line)}}{\overline{Nu} \text{ for plain tube staggered array } (\gamma = 30^\circ)}$

Above recommended correlation is applicable for Reynolds number $10^3 \leq Re \leq 8 \cdot 10^5$,
 $0.19 < \frac{s}{l} < 0.66$, $1.1 < \frac{X_t}{D_f} < 4.92$, $0.058 < \frac{l}{D_f} < 0.201$ (Hewitt et al., 1994)

3.3.2 Correlation for high fin tube

Recommended correlation to calculate the average Nusselt number for staggered tube banks by Engineering Science Data (Hewitt et al., 1994) and Reynolds number range $2 \cdot 10^3 \leq Re \leq 4 \cdot 10^4$, $0.13 < \frac{s}{l} < 0.57$, $1.15 < \frac{X_t}{X_l} < 1.72$:

$$\overline{Nu} = 0.242 Re^{0.658} \left(\frac{s}{l}\right)^{0.297} \left(\frac{X_t}{X_l}\right)^{-0.091} Pr^{1/3} \cdot F_1 \cdot F_2 \quad (52)$$

where

F_1 – factor for fluid property variation (significant only at high temperatures)

F_2 – factor for number of fin – tube rows

1.0 for four or more rows,
 0.92 for three rows
 0.84 for two rows
 0.76 for one row

For high fin-tube and in-line array the correlation that can be applied for Reynolds number $5 \cdot 10^3 \leq Re \leq 10^5$, and $5 < \frac{A}{A_T} < 12$:

$$\overline{Nu} = 0.30 Re^{0.625} \left(\frac{A}{A_T}\right)^{-0.375} Pr^{0.333} \quad (53)$$

where

A_T – total tube surface area of one sector, $A_T = \pi D (s + \delta)$

A – total surface area of one sector, $A = \left[\frac{1}{2} \pi (D_f^2 - D^2) \right] + \pi D_f \delta + \pi D s$

Calculating the average Nusselt number, the fin efficiency value η_f can be achieved from (McQuiston & Tree, 1972):

$$\eta_f = \frac{\tanh(\sqrt{2\bar{h}/(\delta k_f)} \cdot \psi)}{\sqrt{2\bar{h}/(\delta k_f)} \cdot \psi} \quad (54)$$

where

$$\psi = \frac{D}{2} \left(\frac{D_f}{D} - 1 \right) \left(1 + 0.35 \ln \frac{D_f}{D} \right) \quad (55)$$

4. Results

The heat exchange optimization function is defined as the amount of dissipated heat to the heat exchanger weight for a one row heat exchanger (optimization parameter is the profile shape). The shape of the fin is modified to calculate heat transfer, reduce the total mass that refers to the cost of the whole heat exchanger. The performance of the heat transfer process in a given heat exchanger is determined for different fin profiles, considering the fluid flow. Fin geometry affects the heat transfer phenomenon between the plate itself and the air. Changing the fin profile, the fluid streamline can be modified in a way that it affects the temperature changes on the fin surface and heat convection conditions.

Numerical analyses are carried out to examine a modified finned tube heat exchanger. The tube material is kept fixed as well as the heat exchanger fin and tube pitches (spacing). No changes are done to the inlet and outlet temperature and pressure values. The shape of the fin and tube is modified to calculate heat transfer for different conditions, reduce the total mass that refers to the cost of the whole heat exchanger. The temperature difference is found numerically and the solid volume is calculated for different fin profile shapes.

To confirm the correctness of the numerical model, the results of the heat transfer are reviewed and compared with those received from the correlation recommended by Engineering Sciences Data Unit, Equation (52), modified for one row crossflow tube-fin heat exchanger of rectangular profile and fin constant thickness - fin profile (a), (b) and (c). Results are presented in Table 3.

Comparison, shown in Table 3, should be used only as a reference. Correlations for the heat transfer of air flow are expressed for at least 4 tube rows. Then factors are introduced to recalculate \overline{Nu} number for one row heat exchanger. The standard deviation of correlation for external flow is about 25% for laminar flow and 15% for turbulent flow (Hewitt et al., 1994). Presented correlation is used to check the model accuracy in relation to fin shape modifications.

After model verification, the fin of variable thickness is considered and the optimized function ε is calculated. The fin thickness δ near the tube is set up to be constant and equal to model (a) thickness (for manufacturing and operating reason) and the mass flow in outlet section m_f does not change in different models.

	Fin version		
	(a)	(b)	(c)
$\Delta T_{\text{model}} [^{\circ}\text{C}]$	45.5	44.7	43.9
$\Delta T_{\text{correl}} [^{\circ}\text{C}]$	45.7	43.3	41.4
$\frac{\Delta T_{\text{model}} - \Delta T_{\text{correl}}}{\Delta T_{\text{correl}}}$	-0.4%	3.2%	6.0%

Table 3. Results from numerical calculation and correlation.

The values of the optimization function are found and presented in Table 4 where:

$$\varepsilon = \frac{(T_{IN} - T_{OUT})}{V_s} \quad \text{from Equation (39) for constant } \dot{m}_f, \quad \Delta T_i = \frac{\Delta T_{\text{model}(i)} - \Delta T_{\text{model}(a)}}{\Delta T_{\text{model}(a)}},$$

$$\Delta \varepsilon_i = \frac{\varepsilon_{\text{model}(i)} - \varepsilon_{\text{model}(a)}}{\varepsilon_{\text{model}(a)}} :$$

	Fin version		
	(d)	(e)	(f)
$\Delta T_{\text{model}} [^{\circ}\text{C}]$	42,8	40,9	37,8
$\Delta T_{\text{model}(a)} [^{\circ}\text{C}]$	45,5	45,5	45,5
ΔT_i	-5,9%	-10,1%	-16,9%
$\Delta \varepsilon_i$	5,2%	13,6%	20,9%

Table 4. Results from numerical calculation for profile modification.

The results illustrate how the fin dimensions and configuration influence the heat transfer. The function $\Delta \varepsilon_i$ is higher for models with profile modification.

The same conclusion may also be drawn with flow analysis. Evaluating the streamlines for all models, the influence of fin shape on mass flow distribution is seen. To confirm the observation, the outlet area is divided into sections for which the mass flow distribution is calculated (Wais, 2010). The fin and tube surface orientation also affects the flow route and causes the variation of the air streamlines. In Figure 8 and 9, it is seen that the flow streams vary and change the flow direction depending on fin profile modification that has an impact on the fin surface temperature. The fin surface temperature is shown in Figure 10 and 11.

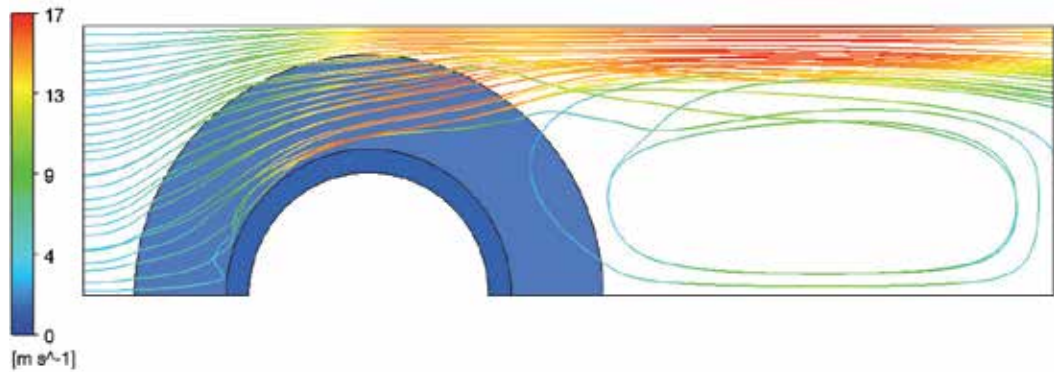


Fig. 8. Air streamlines for fin profile (a).

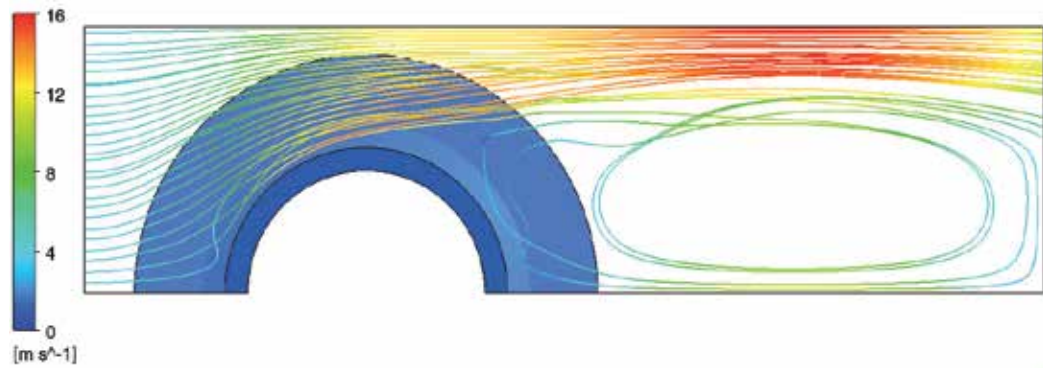


Fig. 9. Air streamlines for fin profile (f).

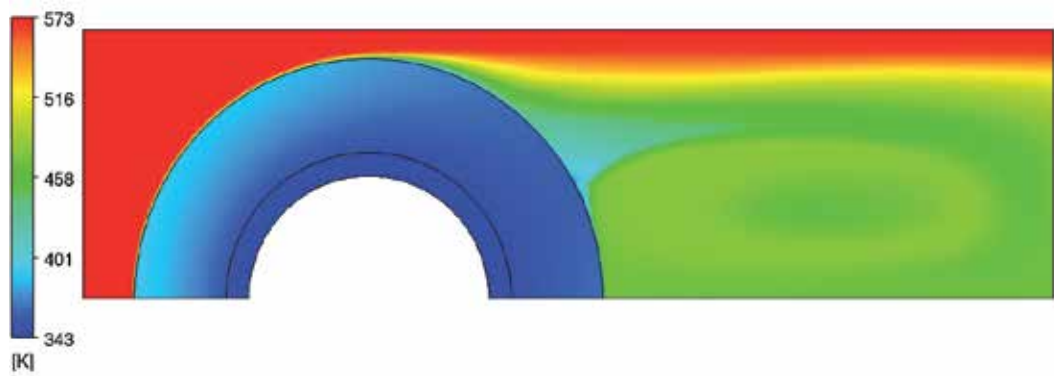


Fig. 10. Temperature on fin surface and flowing air temperature for fin profile (a).

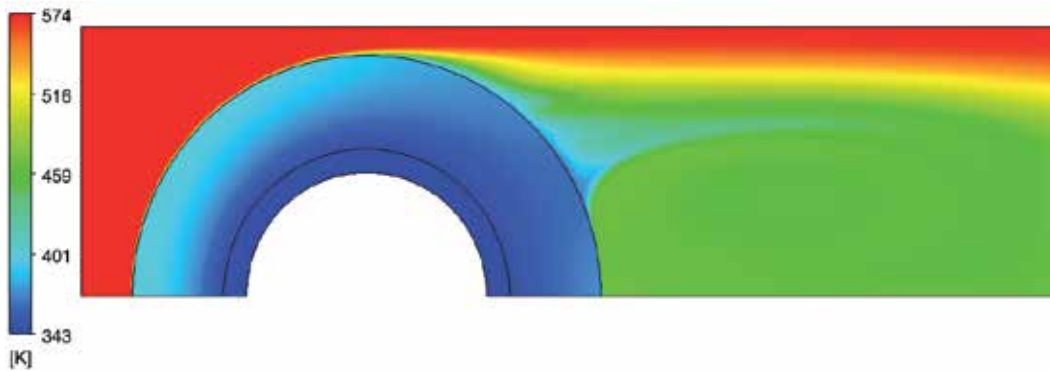


Fig. 11. Temperature on fin surface and flowing air temperature for fin profile (f).

5. Conclusion

The heat flux depends on the temperature difference between the local plate/tube and local air temperatures. In reality, these temperatures vary along the cross section of the air stream and along the fluid flow direction. All results are calculated considering the air flow and its streamline deviations caused by the plate and tube configuration and compared with the known correlation for circular fins of rectangular cross section. The model allows considering the heat transfer in three directions. This is an advantage, comparing to other optimization method, where the temperature profile is two-dimensional. The shape of the fin and tube is modified to calculate the heat transfer for different conditions, reduce the total mass that refers to the cost of the whole heat exchanger.

Described phenomena modify the conditions of the heat exchange between the plate and the fluid having the effect on the heat transfer. The rate of the heat transfer does not depend only on wall surface dimensions, heat transfer coefficient and the temperature difference between the fluid that surrounds the plate and the plate surface temperature. The air velocity and the fin shape are also essential because the fin profile influences the flow direction. For heat exchangers, built with many fins and designed for real industry, it is important to pay attention to and calculate the heat transfer considering the fluid flow and flow paths.

It should be also mentioned that if the fin is positioned into an air stream, the flow applies to a force from the fin tip surface in the direction of the oncoming flow (drag). The resistance of the body results in a pressure drop. The fin and tube surface orientation also modifies the resistance of the body that results in a pressure drop.

6. Nomenclature

- A – total external surface area of fins and tubes
- A_f – fin surface area
- $A_{k,x}$ – cross-sectional area as a function of k and x
- A_t – surface area of tube between fins

A_T	- total tube surface (with fin removed)
c_f	- fluid (air) specific heat capacity
D	- external tube diameter (also diameter of fin base),
D_f	- diameter of fin tip
\bar{h}	- average heat transfer coefficient
\bar{h}'	- effective heat transfer coefficient
I_0	- modified, zero-order Bessel function of the first kind
I_1	- modified, first-order Bessel function of the first kind
K_0	- modified, zero-order Bessel function of the second kind
K_1	- modified, first-order Bessel function of the second kind
k_f	- fin thermal conductivity,
l	- fin height
\dot{m}_f	- fluid mass flow rate
m_s	- tube and fin mass (solid).
\overline{Nu}	- average Nusselt number
P	- perimeter (function of x)
p_f	- fin pitch
p_t	- tube pitch
\dot{Q}	- heat flow removed from the fluid to the fin and tube
R	- radial coordinate of fin base (external tube radius $R = D / 2$)
R_{ch}	- radial coordinate of chamfer
R_f	- radial coordinate of fin tip ($R_f = D_f / 2$)
Re	- Reynolds number
S_{\min}	- minimum flow area
s	- spacing between adjacent fins
T_0	- temperature at the external tube surface (for diameter D)
T_{IN}	- fluid temperature in the inlet section
T_{OUT}	- average fluid temperature in the outlet section
T_S	- surrounding temperature
T_T	- inner tube surface temperature
V_s	- volume of tube and fin material
v_{IN}	- air velocity in the inlet section
v_{\max}	- maximum fluid velocity (in minimum flow area)
w	- fin width
X_d	- diagonal tube pitch ($\sqrt{X_t^2 + X_l^2}$)
X_l	- longitudinal (parallel to the flow) tube pitch

X_t – transverse tube pitch (perpendicular to the flow) tube pitch

Greek symbols

ΔT – effective mean temperature difference

ΔT_{correl} – difference in air temperature between inlet and outlet section calculated from correlation

ΔT_{model} – difference in air temperature between inlet and outlet section received from numerical computation

$\Delta T_{Fluid} = T_{IN} - T_{OUT}$ – difference in fluid temperature between outlet and inlet section

δ – fin thickness

δ_t – tube thickness

ε – optimization function

η – fluid dynamic viscosity,

η_f – fin efficiency

θ – temperature difference between a point on a fin surface and the surroundings

ξ – ratio between the heat removed from the tube/fin component to the tube/fin weight

ρ – fluid density

ρ_s – material density of solid (tube and fin)

7. References

- Ansys 12 Product Documentation, Available from ANSYS Customer Portal, <https://www1.ansys.com/customer/default.asp>
- Hewitt G. H., Shires G. L., Bott T. R. (1994). *Process Heat Transfer*, CRC Press Inc., ISBN 0-8493-9918-1, USA
- Incropera F. P., Dewitt D. P., Bergman T. L., Lavine A. S. (2006), *Fundamentals of Heat and Mass Transfer*, John Wiley & Sons, ISBN 978-0-471-45728-2, USA
- Kraus A., Aziz A., Welty J. (2001) *Extended surface heat transfer*, A Willey-Interscience Publication, ISBN 0-471-39550-1, USA
- Mills A. F. (1995), *Heat and Mass Transfer*, Richard D. Irwin Inc., ISBN 0-256-11443-9, USA
- McQuiston F. C., Tree D. R. (1972), *Optimum space envelopes of the finned tube heat transfer surface*, ASHRAE Transactions, Vol. 78, Part 2, pp. 144-152, ISSN: 0001-2505
- Shah R. K., Sekulic D. P. (2003), *Fundamentals of Heat Exchanger Design*, John Wiley & Sons, ISBN 0-471-32171-0, USA
- Wais P. (2010), *Fluid flow consideration in fin-tube heat exchanger optimization*, Archives of Thermodynamics, Vol. 31, No. 3, (September 2010), pp. 87-104, ISSN 1231-0956

Thermal Design of Cooling and Dehumidifying Coils

M. Khamis Mansour and M. Hassab
*Mechanical Engineering Department, Faculty of Engineering,
Beirut Arab University,
Lebanon*

1. Introduction

The cooling and dehumidifying coil is a critical component of air conditioning. Its performance has a strong bearing on the ultimate indoor environmental conditions, which in turn, has a significant impact on the indoor air quality. Decisions made to select a cooling coil influence the initial investment as well as the costs of installing, providing, and maintaining thermal comfort. The efficient thermal design of the cooling coil leads to a crucial reduction in the coil surface heat transfer area and of course, its capital cost and its weight. On the other hand, the enhancement in the coil thermal performance will usually be established at expense of the hydraulic performance of the cooling coil and in turn, its running cost. Because the cooling coil is an integral part of the air distribution system, its geometry — size, number of rows, fin spacing, and fin profile — contributes to the airside pressure drop and affects the sound power level of the fans. (Fan power needed to circulate air through the duct system may warrant extra sound attenuation at the air handler.) Cooling coils are an integral part of the chilled water system or the refrigeration unit, too. The extent to which coils raise the chilled water temperature or the evaporation temperature dramatically affects both capital investment in the cooling coil or the pumping power. Coil performance can even influence the efficiency of the chiller or Dx-unit. The focus of this chapter is on the description of the methodology should be used in thermal design of the cooling coil either chilled water coil or Dx-coil.

Methods to design the cooling and dehumidifying coil either chilled water coil or Dx evaporator coil are usually based on log mean enthalpy or log equivalent dry-bulb temperature difference [1]. In both methods, the cooling coil is treated as a single zone/region and hence the required surface area is determined [2]. This manner of the cooling coil design could lead to an imprecise design particularly when the cooling coil is partially wet. In this chapter, the numerical calculation using a discrete technique "row-by-row method" will be presented to calculate the detailed design of the cooling coil in order to enhance the calculation accuracy and trace the air and coil surface temperature locally.

2. Types of cooling coils

Cooling coils are classified to direct-expansion (DX) coils and chilled water coils as shown in Figure 1. Some coil manufacturers fabricate coils from 5/8 inch OD copper tubes, others

from 1/2 inch copper tube and still others use 3/8 inch tubes. Selection of the tube size is a matter of manufacturer's choice and market demand. Price, as always, plays a major part in the tube size selection.



Fig. 1. Description of the cooling coil for a)- Dx-cooling; b)- Chilled water coil (Aerofin heat transfer products).

3. Coil construction and geometry

In a coil, copper tubes are arranged parallel to one another, either in staggered pattern or non-staggered pattern, along the length L of the coil. A staggered pattern is more commonly used. For 5/8 inch tubes, the triangular pitch is 1.75 inch or 1.5 inch. For 1/2 inch tubes it is 1.25 inch. Plate or ripple fins are used to enhance the heat transfer area. Thus the primary surface area (outside area of bare copper tubes) is enhanced greatly by adding a secondary area of fins. The total area including fins is called outside surface area. The cross-section ($L \times H$) which the air flows is called the face area or the finned area. Thus L is finned length and H is fin height (see Figure 2). Fins are arranged perpendicular to the tubes. Where, the fin spacing varies between 8 and 16 fins per inch of tube.

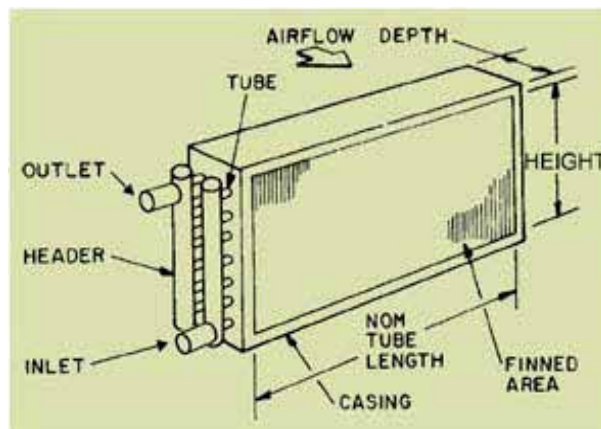


Fig. 2. Geometry configuration of the cooling coil (Aerofin heat transfer products).

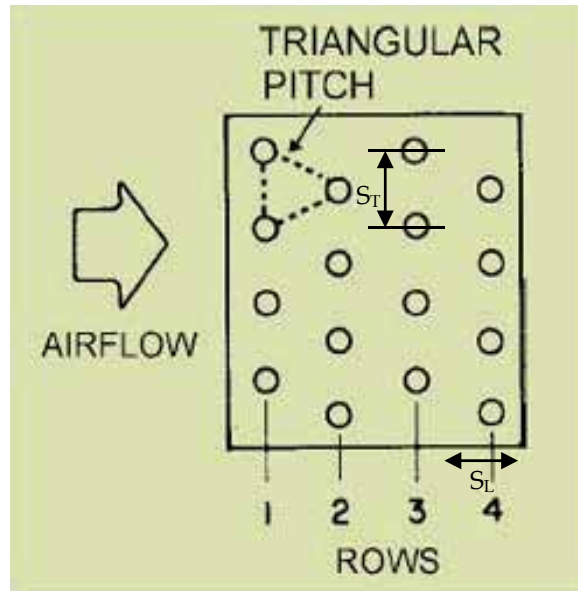


Fig. 3. A 4-row coil with a 4-tube face.

The average air velocity across the face area is called the coil face/frontal velocity and it is calculated as follows [3]:

$$\text{Face Velocity (m/s)} = \frac{\text{Air flow rate (kg/s)}}{\text{Face area (m}^2\text{)}}$$

The number of rows of tubes in the direction of air flow is termed as depth of coil (rows deep, D). Coils with 3, 4, 6 or 8 rows are commonly used. Refrigerant or chilled water enters the first row and leaves the coil from the last row. A coil in which chilled water or refrigerant is supplied to all the tubes in the first row (also referred to as tubes high or tubes in face) is called a maximum or full circuit coil (see Figure 3). Thus a typical coil of 17.5 inch (0.44 m) height which has 10 tubes in face (based on 1.75 inch (0.044 m) pitch) will have a maximum of 10 circuits. If the supply is given to alternate tubes in face, we get a half-circuit coil with 5 circuits as against 10 circuits. The U-bends at the end of the tubes can be arranged, at the time of manufacturing, to obtain the number of circuits desired. See Figure 4 for full and half circuit coils with 4 tube face.

Face velocity is restricted to 500 fpm (2.5 m/s) to avoid carryover of condensate from the coil. The value of 500 fpm (2.5 m/s) is very commonly used for coil sizing and it works very well for cfm/ton in the range of 500 to 600 (2.5 to 3 m³/s per ton). If cfm/ton ratio falls below 500 (2.5 m³/s per ton), this generally happens when room sensible heat factor goes below 0.8 due to high room latent load, a 4-row coil at 500 fpm (2.5 m/s) becomes inadequate. A 5-row coil is not very common. Hence by lowering face velocity, a 4-row deep coil can be selected at 400 fpm (2 m/s), when cfm/ton is about 400 (2 m³/s per ton).. As cfm/ton ratio reduces further, 6-row or 8-row coils have to be selected. This situation is encountered when the occupancy and/or fresh air components are high.

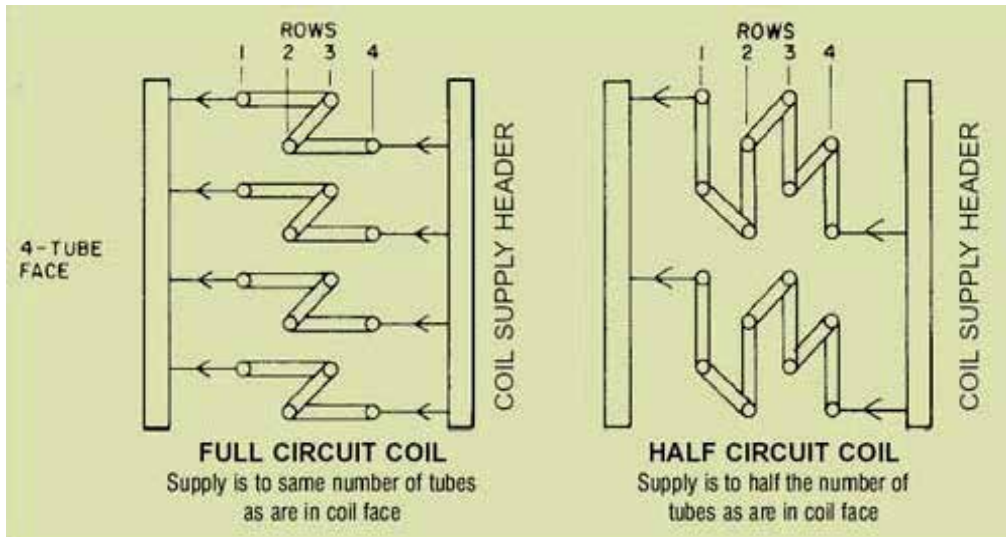


Fig. 4. Full circuit and half circuit four row coils with 4-tube face.

3.1 Fin patterns

There are three standard plate fin patterns that are usually used in the cooling coil: flat-plate, wavy-plate, and star-plate fin patterns, as shown in Figure 5. They are made of Aluminum, copper, and stainless steel or carbon steel. The fins are permanently attached to the tubes by expansion of each tube. Full fin collars allow for both precise fin spacing and maximum fin-to-tube contact. The flat-plate fin type has no corrugation, which results in the lowest possible air friction drop and lowest fan horsepower demands while the wavy-plate fin corrugation across the fin provides the maximum heat transfer for a given surface area, and is the standard fin configuration used. The star-plate fin pattern corrugation around the tubes provides lower air friction. This pattern is used when lower air friction is desired without a large decrease in heat transfer capacity.

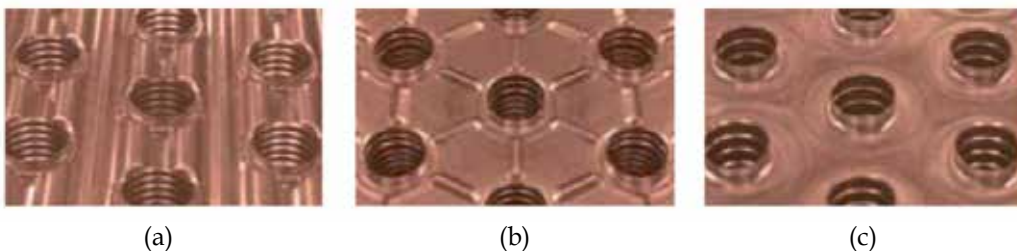


Fig. 5. (a) Wavy-plate fin; (b) Star-plate fin; (c) Flat-plate fin (*Aerofin heat transfer products*).

4. Simultaneous heat and mass transfer in cooling and dehumidifying coils

In the cooling coil, the coolant fluid "chilled water or refrigerant" flows inside the tubes and the air passes across the tube bundle. Since the coolant fluid temperature is less than the dew point temperature to ensure the dehumidification process there is possibility of heat

and moisture transfer between them. The directions of heat and moisture transfer depend upon the temperature and vapor pressure differences between air and wetted surface. As a result, the direction of the total heat transfer rate, which is a sum of sensible heat transfer and latent heat transfers. The concept of enthalpy potential [4] is very useful in quantifying the total heat transfer in these processes and its direction.

The sensible (Q_S) and latent (Q_L) heat transfer rates are given by:

$$Q_S = h_o A_S (t_i - t_a)$$

$$Q_L = h_{mass} A_S (W_i - W_a) h_{fg}$$

the total heat transfer Q_T is given by:

$$Q_T = Q_S + Q_L = h_o A_S (t_i - t_a) + h_{mass} A_S (W_i - W_a) h_{fg}$$

Where:

t_a = dry-bulb temperature of air, °C

t_i = temperature of water/wetted surface, °C

W_a = humidity ratio of air, kg/kg

W_i = humidity ratio of saturated air at t_i , kg/kg

h_o = convective heat transfer coefficient, W/m².°C

h_{mass} = convective mass transfer coefficient, kg/m²

h_{fg} = latent heat of vaporization, J/kg

Since the transport mechanism that controls the convective heat transfer between air and water also controls the moisture transfer between air and water, there exists a relation between heat and mass transfer coefficients, h_C and h_D as discussed in an earlier chapter. It has been shown that for air-water vapor mixtures,

$$H_{mass} \approx h_o / c_{pm} \text{ or } h_o / h_{mass} \cdot c_{pm} = \text{Lewis number} \approx 1.0$$

Where c_{pm} is the humid air specific heat ≈ 1.0216 kJ/kg.K. Hence the total heat transfer is given by:

$$Q_T = Q_S + Q_L = h_o A_S (t_i - t_a) + h_{mass} A_S (W_i - W_a) h_{fg} = (h_o A_S / c_{pm}) [(t_i - t_a) + (W_i - W_a) h_{fg}]$$

by manipulating the term in the parenthesis of RHS, it can be shown that:

$$Q_T = Q_S + Q_L = (h_o A_S / c_{pm}) [(h_i - h_a)]$$

The air heat transfer coefficient, h_o has been computed from the experimental correlations derived in [3]. The heat transfer parameter is written as Stanton number, St times Prandtl number, Pr to the 2/3 power. It is given as a function of Reynolds number, Re where the function was established through curve-fitting of a set of the experimental data as follow:

$$St \times Pr^{(2/3)} = 0.1123 \times Re^{-0.261}$$

Where these three dimensionless parameters are defined as:

$$St = \frac{(A_{min} \times h_o)}{(m_a \times c_{pm})}, Pr = \frac{(\mu_a \times c_{pm})}{k_a}, \text{ and } Re = \frac{(m_a \times d_o)}{(A_{min} \times \mu_a)}$$

Where,

- A_{\min} = minimum free-flow air area, (m²)
 m_a = mass flow rate of air through the cooling coil, (kg/s)
 μ_a =dynamic viscosity of air (kg/m.s)
 k_a =thermal conductivity of air (W/m. °C)
 d_o =outside diameter, (m)

5. Governing equations and methodology

The sizing of cooling coil requires solving the two energy equations of the air-side and coolant sides coupling with the heat and mass transfer equations. The design is accomplished through discretizing the cooling coil into N segments according to the number of the coil rows. The three governing equations are applied to each segment. By knowing the process data, coil geometry, and the design cooling load imposed on the coil the required surface area can be computed. The coil sizing is expressed by the face area and number of rows of a finned-tube coil for satisfying the design coil cooling load.

Process data:

- Room dB temperature/Return air dB temperature (°C)
- Fresh air dB temperature (°C)
- Dehumidified air flow (cfm or m³/s)
- Fresh air quantity (cfm or m³/s)
- Grand sensible heat factor (GSHF)
- Coil cooling load (kW)
- Apparatus dew point ADP (°C) (This denotes the average outside surface temperature of the coil.)

Coil geometry :

- Outside tube diameter, d_o (mm)
- Inside tube diameter, d_i (mm)
- Longitudinal tube spacing, S_L (mm) (see Figure 3)
- Transverse tube spacing, S_T (mm) (see Figure 3)
- No. of fins/m, N_f
- Aluminum fin thickness, t_f (mm)
- Exchanger compactness, surface area over exchanger volume, β (m²/m³)

Air-Side

$$\Delta Q_{ci} = m_a(h_{a_i} - h_{a_{i+1}}) \quad (1)$$

$$\Delta Q_{ci} = \frac{\eta_s}{c_{pm}} h_o \Delta A_o (h_{a_{mi}} - h_{s_{mi}}) \quad (2)$$

Water-Side

$$\Delta Q_{ci} = m_w c_{pw} (T_{w_{i+1}} - T_{w_i}) \quad (3)$$

$$\Delta Q_{ci} = h_i \Delta A_i (T_{s_{mi}} - T_{w_{mi}}) \quad (4)$$

Here,

$$ha_{mi} = \frac{(ha_i + ha_{i+1})}{2}, \quad ha_{i+1} = 2ha_{mi} - ha_i \quad (5)$$

$$Tw_{mi} = \frac{(Tw_i + Tw_{i+1})}{2}, \quad Tw_{i+1} = 2Tw_{mi} - Tw_i \quad (6)$$

Eliminate ha_{i+1} and Tw_{i+1} from Equation (1) & (3) respectively, the energy equations can be formulated;

$$\Delta Q_{ci} = 2m_a(ha_i - ha_{mi}) \quad (7)$$

$$\Delta Q_{ci} = 2m_w C_{pw}(Tw_{mi} - Tw_i) \quad (8)$$

Eliminate ha_{mi} between equations (2) & (7), it is yielded:

$$\Delta Q_{ci} = \frac{\eta_s h_o \Delta A_o / c_{pm}}{1 + \Delta NTU_o / 2} * (ha_i - hs_{mi}) \quad (9)$$

Similarly, eliminate Tw_{mi} between equations (4) and (8):

$$\Delta Q_{ci} = \frac{h_i \Delta A_i}{1 + \Delta NTU_i / 2} * (Ts_{mi} - Tw_i) \quad (10)$$

Now, by dividing equation (9) over equation (10):

$$\frac{ha_i - hs_{mi}}{Ts_{mi} - Tw_i} = R \quad (11)$$

Where,

$$R = \left[\frac{h_i c_{pm}}{h_o \eta_s} \left(\frac{\Delta A_i}{\Delta A_o} \right) \right] * \left[\frac{\left(\frac{1 + \Delta NTU_o}{2} \right)}{\left(\frac{1 + \Delta NTU_i}{2} \right)} \right] \quad (12)$$

$$\Delta NTU_o = \frac{\eta_s h_o \Delta A_o}{m_a c_{pm}}, \quad \Delta NTU_i = \frac{h_i \Delta A_i}{m_w C_{pw}}$$

Relation between hs and Ts :

a. Dry-Surface ($Ts > T_{dew}$ point)

$$hs_{mi} = h_a + c_p (Ts_{mi} - T_a) \quad (13)$$

b. Wet-Surface ($Ts < T_{dew}$ point)

When the coil is wet the enthalpy of saturated air hs_{mi} is a function of the temperature of the wetted surface Ts_{mi} , by curve fitting for psychrometric chart [2] of the saturated air enthalpy at different air temperatures of a range 3 to 11°C. The quadric equation is expressed as :

$$hs_{mi} = 10.76 + 1.4 Ts_{mi} + 0.046 Ts_{mi}^2 \quad (14)$$

Solution for Ts_{mi} :

Substituting for hs_{mi} from equations (14) into equation (11), we obtain a solution for Ts_{mi} as follows:

Wet Surface:

$$\begin{aligned} ha_i - hs_{mi} &= R(Ts_{mi} - Tw_i) \\ ha_i - (10.76 + 1.4 * Ts_{mi} + 0.046 * Ts_{mi}^2) &= R(Ts_{mi} - Tw_i) , \\ 0.046 Ts_{mi}^2 + (R + 1.4) * Ts_{mi} - (ha_i + R * Tw_i - 10.76) &= 0 \end{aligned}$$

The above equation can write as:

$$aTs_{mi}^2 + bTs_{mi} - c = 0$$

This quadratic equation can now be solved for Tsm as

$$Ts_m = \frac{-b \pm \sqrt{b^2 - 4ac}}{2a} \quad (15)$$

Where,

$$a = 0.046 \quad , \quad b = R + 1.4 \quad \text{and} \quad c = ha_i + R * Tw_i - 10.76$$

Solution of ΔQ_{ci} , ha_{i+1} , Tw_{i+1}

$$\Delta Q_{ci} = \frac{h_i \Delta A_i}{1 + \Delta NTU_i / 2} * (Ts_{mi} - Tw_i), \quad ha_{i+1} = ha_i - \frac{\Delta Q_{ci}}{m_a} \quad , \quad Tw_{i+1} = Tw_i - \frac{\Delta Q_{ci}}{m_w Cp_w}$$

Calculation of air dry-bulb temperature, Ta_{i+1}

The sensible heat transferred to the dry coil surface is written as:

$$\Delta Q_{ci} = m_a c_{pa} (Ta_i - Ta_{i+1}) \quad (16)$$

$$\Delta Q_{ci} = \eta_s h_o \Delta A_o (Ta_{mi} - Ts_{mi}) \quad (17)$$

or,

$$Q_{ci} = \eta_s h_o \Delta A_o \left(\frac{Ta_{i+1} + Ta_i}{2} - Ts_{mi} \right) \quad (18)$$

Eliminate ΔQ_{si} between equations (15) & (16) and Solving for Ta_{i+1}

$$Ta_{i+1} = \left[\frac{\left(1 - \frac{\Delta NTU_o}{2}\right)}{\left(1 + \frac{\Delta NTU_o}{2}\right)} \right] \times Ta_i + \left[\frac{\left(\Delta NTU_o\right)}{\left(1 + \frac{\Delta NTU_o}{2}\right)} \right] \times Ts_{mi} \quad (19)$$

Calculation of Wa_{i+1} :

$$Wa_{i+1} = \left[\frac{(ha_{i+1} - c_{pa} \times Ta_{i+1})}{(2501 + 1.8 \times Ta_{i+1})} \right] \quad (20)$$

Summary of final solution:

The final solutions for the coil capacity per row and for the states of air and water at the exit of any row within a chilled-water coil are given, in terms of the mean outer surface temperature of this row, as:

$$Ts_{mi} = \frac{-(R+1.4) + \sqrt{(R+1.4)^2 + 0.184 \times (ha_i + R \times Tw_i - 10.76)}}{0.092} \quad (21)$$

$$\Delta Q_{ci} = \frac{h_i \Delta A_i}{1 + \Delta NTU_i / 2} * (T_{S_{mi}} - T_{W_i})$$

$$T_{W_{i+1}} = T_{W_i} - \frac{\Delta Q_{ci}}{m_w C_{p_w}} \quad (22)$$

$$h_{a_{i+1}} = h_{a_i} - \frac{\Delta Q_{ci}}{m_a} \quad (23)$$

$$T_{a_{i+1}} = \left[\frac{\left(1 - \frac{\Delta NTU_o}{2}\right)}{\left(1 + \frac{\Delta NTU_o}{2}\right)} \right] \times T_{a_i} + \left[\frac{\left(\Delta NTU_o\right)}{\left(1 + \frac{\Delta NTU_o}{2}\right)} \right] \times T_{S_{mi}} \quad (24)$$

$$W_{a_{i+1}} = \left[\frac{\left(h_{a_{i+1}} - C_{pa} \times T_{a_{i+1}}\right)}{\left(2501 + 1.8 \times T_{a_{i+1}}\right)} \right] \quad (25)$$

Where,

$$R = \left[\frac{h_i C_{pa}}{h_o \eta_s} \left(\frac{\Delta A_i}{\Delta A_o} \right) \right] * \left[\frac{\left(1 + \frac{\Delta NTU_o}{2}\right)}{\left(1 + \frac{\Delta NTU_i}{2}\right)} \right] \quad (26)$$

$\Delta NTU_o = \frac{\eta_s h_o \Delta A_o}{m_a C_{pm}}$, $\Delta NTU_i = \frac{h_i \Delta A_i}{m_w C_{p_w}}$, and the total coil cooling load Q_C is: $Q_C = \sum_{i=1}^{N_r} \Delta Q_{ci}$

Calculation of the Number of Coil Rows, N_r :

The calculations of ($T_{W_{i+1}}$, $h_{a_{i+1}}$, $T_{a_{i+1}}$, and ΔQ_{ci}) are started from the first row until reaching the row number N_r at which its outlet water temperature is nearly equal to the given inlet water temperature to the coil, i.e. $T_{W_{N_r+1}} \cong T_{W_{in}}$.

Procedure of cooling coil design at a given cooling load Q_C :

1. The condition of the air leaving a chilled-water coil is nearly saturated, therefore, the relative humidity of the outlet air, ϕ_{out} from the coil can be assumed as 95 %.
2. Knowing [inlet air state, $CSHF = Q_S / Q_C$, and ϕ_{out}], the enthalpy of the outlet air $h_{a_{out}}$ from the coil can then be determined from the Psychometric Chart.
3. Knowing [Q_C , $h_{a_{in}}$, and $h_{a_{out}}$], then the air flow rate can be determined as:

$$m_a = \frac{Q_C}{(h_{a_{in}} - h_{a_{out}})} \quad \text{kg/s}$$

4. Knowing [Q_C , $T_{W_{in}}$, and $T_{W_{out}}$], the water flow rate can be determined as:

$$m_w = \frac{Q_C}{C_{p_w} (T_{W_{out}} - T_{W_{in}})} \quad \text{kg/s}$$

5. Knowing [m_a , V_{face} , ρ_a , β , and S_L], the outer surface area per row ΔA_o can be determined as:

$$\Delta A_o = \left[\frac{(\beta \times S_L \times m_a)}{(\rho_a \times V_{face})} \right] \text{m}^2$$

6. Starting the calculations of the unknowns [$T_{S_{mi}}$, ΔQ_{ci} , $h_{a_{i+1}}$, $T_{W_{i+1}}$, $T_{a_{i+1}}$, $W_{a_{i+1}}$] using in order equations (14, 10, 3, 1, 17, and 18), from the first row, $i=1$ to the row $i=N_r$ at which $T_{W_{N_r+1}} \cong T_{W_{in}}$. The calculations are then completed and as a final check, calculate the $CSHF$ and compare it with the given one.

6. Worked example of chilled-Water coils

Cross-counter flow chilled water cooling coil using corrugated plate-fins, has the flowing construction and operating design parameters:

Coil construction parameters:

Outside tube diameter, d_o	=13.41 mm
Inside tube diameter, d_i	=12.09 mm
Longitudinal tube spacing, S_L	=26.16 mm
Transverse tube spacing, S_T	=31.75 mm
No. of fins/m, N_f	=554
Aluminum fin thickness, t_f	=0.15 mm
Exchanger compactness, β	= 1060 m^2/m^3
Outside area/inside area, (A_o/A_i)	=23
$A_{\text{flow}}/A_{\text{face}}$ on the air-side, σ	=0.529
Finned-surface weighted efficiency, η_s	= 0.85
Number of tube-passes per water loop, N_p	= 6

Design operating Data:

Moist air

Total cooling load at full load, Q_c	=60 kW
Latent Load at full load, Q_L	=20 kW
Inlet air conditions	= t =Dry and wet bulb temperatures are: 26 °C, and 19 °C
Air face velocity, V_{face}	=2.8 m/s
Air heat transfer coefficient, h_c	=60 W/ ($\text{m}^2 \text{ } ^\circ\text{C}$)
Air mean specific heat, c_{pm}	=1.001 kJ/(kg. K)

Chilled water

Inlet water temperature, $T_{w_{\text{in}}}$	=6 °C
Water mass flow rate, m_w	=2.9 kg/s
Water inlet velocity, V_w	=1.25 m/s
Heat transfer coefficient on water side, h_i	=4000 W/ ($\text{m}^2 \text{ } ^\circ\text{C}$)
Number of tube-passes per water loop, N_{tp}	= 6
Exit water temperature, $T_{w_{\text{out}}}$	=11 °C
Water specific heat, CP_w	=4.14 kJ/(kg. K)

Under the above design full load conditions, calculate:

- The coil dimensions (tube length, finned width and coil depth).
- The number of coil rows and the total number of tubes.
- The exit air temperature.

Calculation Procedures

From psychrometric chart at inlet air conditions the inlet air properties are obtained represented by $h_{a_{\text{in}}}=54$ kJ/kg, $W_{a_{\text{in}}}=0.011$ kg_v/kg_a . and dew point temperature, $d_{\text{pt}} = 15.5^\circ\text{C}$. By knowing $Q_c=60$ kW, $\text{CSHF}=0.75$ ($=1- Q_L/Q_c$), and $\phi_{\text{out}} = 95\%$ using information from inlet point, the exit conditions can be determined as $h_{a_{\text{out}}}=33$ kJ/kg, $T_{a_o}=10.5$ °C, $W_{a_o} = 0.008936$ kg_v/kg_a

$$- m_a = \frac{Q_c}{(h_{a_{in}} - h_{a_{out}})} = \frac{60}{(54 - 33)} = 2.857 \text{ kg/s}$$

$$- m_w = \frac{Q_c}{Cp_w(Tw_{out} - Tw_{in})} = \frac{60}{4.14 * 5} = 2.90 \text{ kg/s}$$

Calculations of the coil design parameters:

$$\Delta A_o = \frac{\beta \times S_L \times m_a}{\rho_a \times V_{face}} = \frac{1060 * 0.02616 * 2.857}{1.16 * 2.8} = 24.39 \text{ m}^2$$

$$\Delta NTU_o = \frac{\eta_s h_o \Delta A_o}{m_a c_{pm}} = \frac{0.85 * 60 * 24.39}{2.857 * 1001} = 0.435$$

$$\Delta A_i = \left(\frac{A_i}{A_o} \right) \times \Delta A_o = \frac{24.39}{23} = 1.06 \text{ m}^2$$

$$\Delta NTU_i = \frac{h_i \Delta A_i}{m_w c_{pw}} = \frac{4000 * 1.06}{2.9 * 4114} = 0.355$$

$$R = \left[\frac{h_i c_{pa}}{h_o \eta_s} \left(\frac{\Delta A_i}{\Delta A_o} \right) \right] * \left[\frac{\left(1 + \frac{\Delta NTU_o}{2} \right)}{\left(1 + \frac{\Delta NTU_i}{2} \right)} \right] = 3.525 \text{ KJ/kg.K}$$

Row i=1:

$$Ts_{m1} = \frac{-(R+1.4) + \sqrt{(R+1.4)^2 + 0.184 * (ha_1 + R * Tw_1 - 10.76)}}{0.092} = 14.65 \text{ }^\circ\text{C}$$

$$\Delta Q_{c1} = \frac{h_i \Delta A_i}{1 + \Delta NTU_i / 2} \times (Ts_{m1} - Tw_1) = 13.15 \text{ kW}$$

Where, $h_i = 4000 \text{ W/m}^2.\text{C}$

$$Tw_2 = Tw_1 - \frac{\Delta Q_{c1}}{m_w c_{pw}} = 11 - \frac{13.15}{2.9 * 4.14} = 9.9 \text{ }^\circ\text{C}$$

$$ha_2 = ha_1 - \frac{\Delta Q_{c1}}{m_a} = 49.4 \text{ kJ/kg}$$

$$Ta_{i+1} = \left[\frac{\left(1 - \frac{\Delta NTU_o}{2} \right)}{\left(1 + \frac{\Delta NTU_o}{2} \right)} \right] \times Ta_1 + \left[\frac{\left(\Delta NTU_o \right)}{\left(1 + \frac{\Delta NTU_o}{2} \right)} \right] \times Ts_{m1} = 21.87 \text{ }^\circ\text{C}$$

$$Wa_2 = \frac{ha_2 - c_{pa} Ta_2}{2501 + 1.8 * Ta_2} = \frac{49.4 - 1(21.87)}{2501 + 1.8(21.87)} = 0.01083 \text{ kg}_v/\text{kg}_a$$

Row i=2

$$Ts_{m2} = \frac{-(R+1.4) + \sqrt{(R+1.4)^2 + 0.184 * (ha_2 + R * Tw_2 - 10.76)}}{0.092} = 13.28 \text{ }^\circ\text{C}$$

$$\Delta Q_{c2} = \frac{h_i \Delta A_i}{1 + \Delta NTU_i / 2} \times (Ts_{m2} - Tw_2) = 12.17 \text{ kW}$$

$$Tw_3 = Tw_2 - \frac{\Delta Q_{c2}}{m_w c_{pw}} = 9.9 - \frac{12.17}{2.9 * 4.14} = 8.89 \text{ }^\circ\text{C}$$

$$ha_3 = ha_2 - \frac{\Delta Q_{c2}}{m_a} = 45.14 \text{ kJ/kg}$$

$$Ta_3 = \left[\frac{\left(1 - \frac{\Delta NTU_0}{2}\right)}{\left(1 + \frac{\Delta NTU_0}{2}\right)} \right] \times Ta_2 + \left[\frac{\left(\frac{\Delta NTU_0}{2}\right)}{\left(1 + \frac{\Delta NTU_0}{2}\right)} \right] \times Ts_{m2} = 18.74 \text{ } ^\circ\text{C}$$

$$Wa_3 = \frac{ha_3 - CpaTa_3}{2501 + 1.8 \cdot Ta_3} = \frac{45.14 - 1(18.74)}{2501 + 1.8(18.74)} = 0.0104 \text{ kg}_v/\text{kg}_a$$

Row i=3

$$Ts_{m3} = \frac{-(R+1.4) + \sqrt{(R+1.4)^2 + 0.184 \cdot (ha_3 + R \cdot Tw_3 - 10.76)}}{0.092} = 12.0 \text{ } ^\circ\text{C}$$

$$\Delta Q_{c3} = \frac{h_i \Delta A_i}{1 + \Delta NTU_i/2} \times (Ts_{m3} - Tw_3) = 11.2 \text{ kW}$$

$$Tw_4 = Tw_3 - \frac{\Delta Q_{c3}}{m_w C p_w} = 8.89 - \frac{11.2}{2.9 \cdot 4.14} = 7.96 \text{ } ^\circ\text{C}$$

$$ha_4 = ha_3 - \frac{\Delta Q_{c3}}{m_a} = 41.22 \text{ kJ/kg}$$

$$Ta_4 = \left[\frac{\left(1 - \frac{\Delta NTU_0}{2}\right)}{\left(1 + \frac{\Delta NTU_0}{2}\right)} \right] \times Ta_3 + \left[\frac{\left(\frac{\Delta NTU_0}{2}\right)}{\left(1 + \frac{\Delta NTU_0}{2}\right)} \right] \times Ts_{m3} = 16.27 \text{ } ^\circ\text{C}$$

$$Wa_4 = \frac{ha_4 - CpaTa_4}{2501 + 1.8 \cdot Ta_4} = \frac{41.22 - 1(16.27)}{2501 + 1.8(16.27)} = 0.00986 \text{ kg}_v/\text{kg}_a$$

Row i=4

$$Ts_{m4} = \frac{-(R+1.4) + \sqrt{(R+1.4)^2 + 0.184 \cdot (ha_4 + R \cdot Tw_4 - 10.76)}}{0.092} = 10.8 \text{ } ^\circ\text{C}$$

$$\Delta Q_{c4} = \frac{h_i \Delta A_i}{1 + \Delta NTU_i/2} \times (Ts_{m4} - Tw_4) = 10.22 \text{ kW}$$

$$Tw_5 = Tw_4 - \frac{\Delta Q_{c4}}{m_w C p_w} = 7.96 - \frac{10.22}{2.9 \cdot 4.14} = 7.11 \text{ } ^\circ\text{C}$$

$$ha_5 = ha_4 - \frac{\Delta Q_{c4}}{m_a} = 37.64 \text{ kJ/kg}$$

$$Ta_5 = \left[\frac{\left(1 - \frac{\Delta NTU_0}{2}\right)}{\left(1 + \frac{\Delta NTU_0}{2}\right)} \right] \times Ta_4 + \left[\frac{\left(\frac{\Delta NTU_0}{2}\right)}{\left(1 + \frac{\Delta NTU_0}{2}\right)} \right] \times Ts_{m4} = 14.27 \text{ } ^\circ\text{C}$$

$$Wa_5 = \frac{ha_5 - CpaTa_5}{2501 + 1.8 \cdot Ta_5} = \frac{37.64 - 1(14.27)}{2501 + 1.8(14.27)} = 0.00925 \text{ kg}_v/\text{kg}_a$$

Row i=5

$$Ts_{m5} = \frac{-(R+1.4) + \sqrt{(R+1.4)^2 + 0.184 \cdot (ha_5 + R \cdot Tw_5 - 10.76)}}{0.092} = 9.68 \text{ } ^\circ\text{C}$$

$$\Delta Q_{c5} = \frac{h_i \Delta A_i}{1 + \Delta NTU_i/2} \times (Ts_{m5} - Tw_5) = 9.25 \text{ kW}$$

$$Tw_6 = Tw_5 - \frac{\Delta Q_{c5}}{m_w C p_w} = 7.11 - \frac{9.25}{2.9 \cdot 4.14} = 6.34 \text{ } ^\circ\text{C}$$

$$ha_6 = ha_5 - \frac{\Delta Q_{c5}}{m_a} = 34.40 \text{ kJ/kg}$$

$$Ta_6 = \left[\frac{\left(1 - \frac{\Delta NTU_0}{2}\right)}{\left(1 + \frac{\Delta NTU_0}{2}\right)} \right] \times Ta_5 + \left\{ \frac{\left(\frac{\Delta NTU_0}{2}\right)}{\left(1 + \frac{\Delta NTU_0}{2}\right)} \right\} \times Ts_{m5} = 12.59 \text{ }^\circ\text{C}$$

$$Wa_6 = \frac{ha_6 - c_p a Ta_6}{2501 + 1.8 \times Ta_6} = \frac{34.40 - 1(12.59)}{2501 + 1.8(12.59)} = 0.00864 \text{ kg}_v/\text{kg}_a$$

Row i=6

$$Ts_{m6} = \frac{-(R+1.4) + \sqrt{(R+1.4)^2 + 0.184 \times (ha_6 + R \times Tw_6 - 10.76)}}{0.092} = 8.645 \text{ }^\circ\text{C}$$

$$\Delta Q_{c6} = \frac{h_i \Delta A_i}{1 + \Delta NTU_i/2} \times (Ts_{m6} - Tw_6) = 8.3 \text{ kW}$$

$$Tw_7 = Tw_6 - \frac{\Delta Q_{c6}}{m_w c_{p_w}} = 6.34 - \frac{8.3}{2.9 \times 4.14} = 5.65 \text{ }^\circ\text{C}$$

$$ha_7 = ha_6 - \frac{\Delta Q_{c6}}{m_a} = 31.50 \text{ kJ/kg}$$

$$Ta_7 = \left[\frac{\left(1 - \frac{\Delta NTU_0}{2}\right)}{\left(1 + \frac{\Delta NTU_0}{2}\right)} \right] \times Ta_6 + \left\{ \frac{\left(\frac{\Delta NTU_0}{2}\right)}{\left(1 + \frac{\Delta NTU_0}{2}\right)} \right\} \times Ts_{m6} = 11.14 \text{ }^\circ\text{C}$$

$$Wa_7 = \frac{ha_7 - c_p a Ta_7}{2501 + 1.8 \times Ta_7} = \frac{31.50 - 1(11.14)}{2501 + 1.8(11.14)} = 0.0081 \text{ kg}_v/\text{kg}_a$$

$$Q_c = \sum_{i=1}^{N_r} \Delta Q_{ci} = (13.15 + 12.17 + 11.12 + 10.22 + 9.25 + 8.3)$$

The total calculated cooling load for 6-rows coil is: $Q_c = 64.31 \text{ kW}$

And coil sensible heat factor, $CSHF = \frac{Q_s}{Q_c} = \frac{m_a c_p (Ta_1 - Ta_7)}{64.31} = 0.66$

The calculated unknowns are listed row-by-row in the next Table; and the psychrometric process for the cooling and dehumidification process is represented by Figure 6.

Row number	Surface condition	$T_{s_{mi}}$ $^\circ\text{C}$	ΔQ_{Ci} kW	Tw_{i+1} $^\circ\text{C}$	ha_{i+1} kJ/kg	Ta_{i+1} $^\circ\text{C}$	Wa_{i+1} g _v /kg _a
Coil inlet	wet		0	11	54	26	11
1	wet	14.65	13.15	9.9	49.4	21.87	10.83
2	Wet	13.28	12.17	8.89	45.14	18.74	10.4
3	Wet	12	11.2	7.96	41.22	16.27	9.86
4	Wet	10.8	10.22	7.11	37.64	14.27	9.25
5	Wet	9.68	9.25	6.34	34.40	12.59	8.64
6	Wet	8.65	8.3	5.65	31.5	11.14	8.1

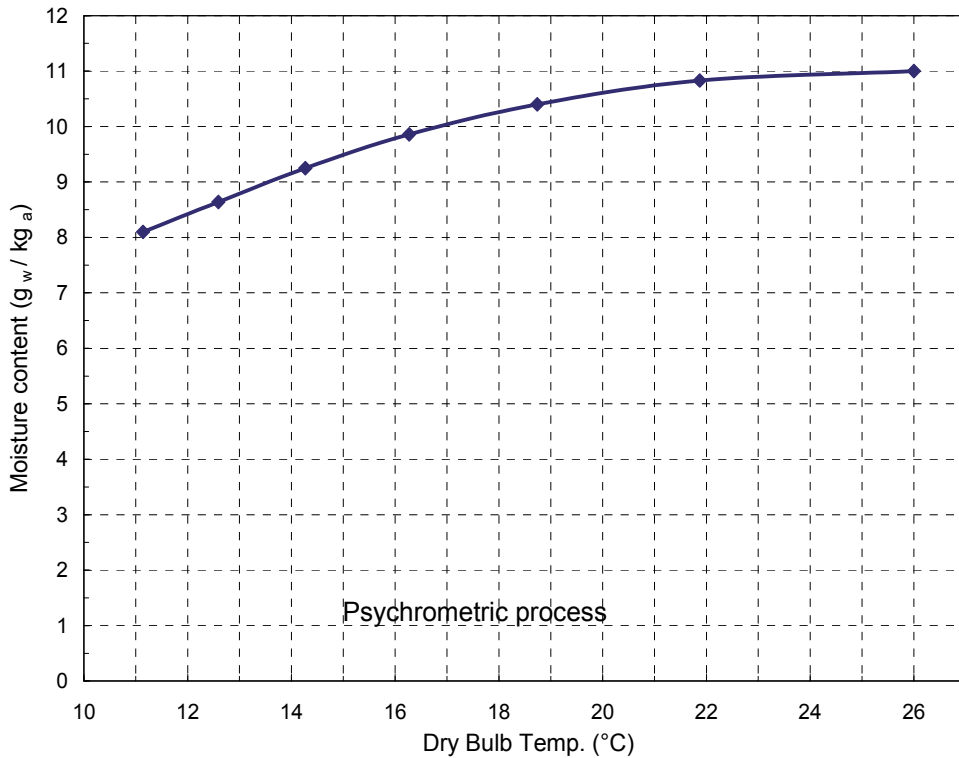


Fig. 6. Presentation of Cooling and dehumidifying process.

- a. Calculation of Coil number of tubes, N_t

$$N_r = \text{Number of coil rows} = 6$$

$$m_w = \frac{N_t}{N_p} \rho_w \left(\frac{\pi}{4} d_i^2 \right) V_w$$

$$N_t = \frac{4N_p m_a}{\pi \rho_w d_i^2 V_w} = 120 \text{ tubes}$$

- b. Calculation of Coil dimension (D, H, L)

$$N_t = N_r * N_c$$

$$N_c = \frac{120}{6} = 20$$

Height of the coil, $H = S_t * N_c = 0.635 \text{ m}$

$$A_o = \sum_{i=1}^{N_r} \Delta A_o = N_r * \Delta A_o = 6 * 24.39 = 146.34 \text{ m}^2$$

Given: $\frac{A_o}{A_i} = 23$

$$A_i = 6.363 \text{ m}^2 = N_t (\pi d_i L)$$

$$L = \text{Length of the coil} = \frac{A_i}{\pi N_t d_i} = 1.4 \text{ m}$$

$$D = \text{Coil depth} = N_c * S_L = 0.157 \text{ m}$$

c. Exit air temperature

$$T_{a_{out}} = 11.14 \text{ }^\circ\text{C}$$

Design of the cooling coil as single Region

In calculating the surface area of the cooling coil, the heat and mass transfer equations are applied on the entire coil surface. This approximation will greatly simplify the analysis. The obtained results (A_o , $T_{a_{out}}$) for one-section coil will be compared with the corresponding results obtained for N_r -sections coil.

Air-side

$$Q_c = m_a(ha_1 - ha_2) \quad (1)$$

$$Q_c = \frac{\eta_s}{c_p} h_o A_o (ha_m - hs_m) \quad (2)$$

Water-side

$$Q_c = m_w c_{p_w} (Tw_2 - Tw_1) \quad (3)$$

$$Q_c = h_i A_i (Ts_m - Tw_m) \quad (4)$$

Applying the heat transfer equations for the air and water at the inlet and exit sections of the coil, this leads to the following equation for T_s at these sections:

$$R = \frac{ha_1 - hs_1}{T_{s_1} - Tw_1} = \frac{ha_2 - hs_2}{T_{s_2} - Tw_2} \quad (5)$$

For an entire wet-surface, the saturated air temperature at the inlet and exit of the coil surfaces T_{s_1} and T_{s_2} are obtained, in a similar manner as done before for N -sections coil, as:

$$T_{s_1} = \frac{-(R+1.4) + \sqrt{(R+1.4)^2 + 0.184 * (ha_1 + R * Tw_1 - 10.76)}}{0.092} \quad (6)$$

$$T_{s_2} = \frac{-(R+1.4) + \sqrt{(R+1.4)^2 + 0.184 * (ha_2 + R * Tw_2 - 10.76)}}{0.092} \quad (7)$$

Where,

Tw_1 = inlet water temperature

Tw_2 = exit water temperature

$$R = \left[\frac{c_{p_a} h_i}{\eta_s h_o} \left(\frac{A_i}{A_o} \right) \right] \quad (8)$$

Knowing (T_{s_1} & Tw_1) and (T_{s_2} & Tw_2), the mean temperature difference between the chilled water and the coil surface can be assumed equal to the logarithmic mean temperature difference. ΔT_m can be determined from:

$$\Delta T_{W_m} = (T_{S_m} - T_{W_m}) = \frac{[(T_{S_1} - T_{W_1}) - (T_{S_2} - T_{W_2})]}{\ln\left[\frac{(T_{S_1} - T_{W_1})}{(T_{S_2} - T_{W_2})}\right]} \quad (9)$$

The area of the coil can now be determined from equation (4) as:

$$A_i = \frac{Q_c}{h_i * \Delta T_m} \quad (10)$$

The outer coil surface area A_o is determined from

$$A_o = \left(\frac{A_o}{A_i}\right) A_i \quad (11)$$

The volume of the cooling coil is given as:

$$\text{Volume} = \text{DHL}$$

$$\text{DHL} = \beta A_o \quad (12)$$

Number of Coil Tubes N_t :

$$m_w = \frac{N_t}{N_p} \rho_w \left(\frac{\pi}{4} d_i^2\right) V_w$$

$$N_t = \frac{4N_p m_a}{\pi \rho_w d_i^2 V_w} \quad (13)$$

The Length of the Tube (Coil), L:

$$L = \frac{A_i}{N_t \pi d_i} \quad (14)$$

The Coil Face Area, A_{face} :

$$A_{face} = HL = \frac{m_a}{\rho_a V_{face}} \quad (15)$$

From Equations (14) and (15) H can be determined as:

$$H = \left(\frac{m_a}{\rho_a V_{face}}\right) * \left(\frac{N_t \pi d_i}{A_i}\right) \quad (16)$$

Number of Rows, N_r :

$$N_r = \frac{W}{S_T} \quad (17)$$

Depth of the Coil D:

$$D = N_r * S_L \quad (18)$$

Calculation of exit air Temperature:

The temperature difference between the air stream and the coil surface is approximated as arithmetic mean temperature difference as shown from the heat transfer equation for the dry air.

$$Q_s = m_a C p_a (T a_1 - T a_2) \quad (19)$$

$$Q_s = \eta_s h_o A_o \left[\frac{Ta_1 + Ta_2}{2} - \frac{Ts_1 + Ts_2}{2} \right] \quad (20)$$

$$Ta_2 = \left[\frac{\left(1 - \frac{\Delta NTU_o}{2}\right)}{\left(1 + \frac{\Delta NTU_o}{2}\right)} \right] \times Ta_1 + \left[\frac{\left(\Delta NTU_o\right)}{\left(1 + \frac{\Delta NTU_o}{2}\right)} \right] \times \left(\frac{Ts_1 + Ts_2}{2} \right) \quad (21)$$

Worked Example

We will solve the previous worked problem using principal of treating the coil as single zone/section instead of multi-sections and compare the two results.

Calculation Procedures:

1. Knowing: [$ha_{in}=54$ kJ/kg, $Wa_{in}=0.011$ kg_v/kg_a, $Q_c=60$ kW, $CSHF=0.75$, $\phi_{out} = 95\%$], from the Psychrometric-chart we obtain:

Air Exit Condition: [$ha_{out}=33$ kJ/kg, $Ta_o=10.5$ °C, $Wa_o=0.86 \cdot 10^{-3}$ kg_v/kg_a]

2. $m_a = \frac{Q_c}{(ha_{in} - ha_{out})} = \frac{60}{54 - 33} = 2.857$ kg/s
3. $m_w = \frac{Q_c}{Cp_w(Tw_{out} - Tw_{in})} = \frac{60}{4.14 \cdot 5} = 2.90$ kg/s

$$R = \left[\frac{h_i Cp_a (A_i)}{\eta_s h_o (A_o)} \right] = 3.41 \text{ KJ/kg.K}$$

$$Ts_1 = \frac{-(R + 1.4) + \sqrt{(R + 1.4)^2 + 0.184 * (ha_1 + R * Tw_1 - 10.76)}}{0.092}$$

$$Ts_1 = 14.71 < T_{d.point} = 15 \quad [\text{Coil surface is wet}]$$

$$Ts_2 = \frac{-(R + 1.4) + \sqrt{(R + 1.4)^2 + 0.184 * (ha_2 + R * Tw_2 - 10.76)}}{0.092}$$

$$Ts_2 = 8.22 \text{ °C}$$

Calculation of ΔTw_m

$$\Delta Tw_m = (Ts_m - Tw_m) = \frac{[(Ts_1 - Tw_1) - (Ts_2 - Tw_2)]}{\ln \left[\frac{(Ts_1 - Tw_1)}{(Ts_2 - Tw_2)} \right]}$$

$$\Delta Tw_m = 2.52 \text{ °C}$$

Calculation of A_i & A_o

$$A_i = \frac{Q_c}{h_i \Delta T_m} = 5.95 \text{ m}^2$$

$$A_o = \left(\frac{A_o}{A_i} \right) A_i = 136.85 \text{ m}^2$$

Number of Coil Tubes N_t

$$N_t = \frac{4N_p m_w}{\pi \rho_w d_i^2 V_w} = 120 \text{ tubes}$$

The Length of the Tube (Coil), L:

$$L = \frac{A_i}{N_t \pi d_i} = 1.30 \text{ m}$$

Height of the Coil, H:

$$W = \left(\frac{m_a}{\rho_a V_{face}} \right) * \left(\frac{N_t \pi d_i}{A_i} \right) = 0.88 * 0.766 = 0.674 \text{ m}$$

Number of Rows, N_r

$$N_r = \frac{N_t}{N_c} = \frac{N_t * S_n}{W} = 5.65 \approx 6 \text{ rows}$$

Depth of the Coil, D:

$$D = N_r * S_L = 0.157 \text{ m}$$

Calculation of Exit air condition

$$Ta_2 = \left[\frac{(1 - \frac{\Delta NTU_0}{2})}{(1 + \frac{\Delta NTU_0}{2})} \right] \times Ta_1 + \left[\frac{(\Delta NTU_0)}{(1 + \frac{\Delta NTU_0}{2})} \right] \times \left(\frac{Ts_1 + Ts_2}{2} \right) = 10.95 \text{ }^\circ\text{C}$$

$$Wa_2 = \frac{ha_2 - cpaTa_2}{2501 + 1.8 * Ta_2} = 0.00874 \text{ kg}_v / \text{kg}_a$$

Calculation of Latent load and CSHF

$$Q_L Q_S = 60 - 2.857 * (26 - 10.95) = 17 \text{ kWkW}$$

$$CSHF = \frac{60 - 17}{60} = 0.717$$

Table-1 illustrates a comparison of the dimensions and exit air conditions for 60 kW cooling coil analyzed as only single-section and cooling coil divided to N_r -sections ($N_r=6$).

Physical quantity	Single-section coil	6-sections coil
Air exit temperature, °C	10.95	11.14
Number of tubes	120	120
Number of rows	6	6
Coil width ,m	0.674	0.635
Coil depth, m	0.157	0.157
Coil length, m	1.3	1.4
Coil SHF	0.717	0.67
Design cooling load, kW	60	60
Actual cooling load, kW	60	64.3

Table 1.

The results presented in Table-1 indicate that cooling coil analyzed as only one-section gives results with good agreement with those obtained with the coil analyzed as 6-sections. The maximum error is 7%.

7. Worked example of partially dry chilled-water coils

Cross-counter flow chilled water cooling coil using corrugated plate-fins, has the flowing construction and operating design parameters:

Coil construction parameters:

Outside tube diameter, d_o	=12.7 mm
Inside tube diameter, d_i	=12.0 mm
Longitudinal tube spacing, S_L	=26.16 mm
Transverse tube spacing, S_T	=31.75 mm
No. of fins/m, N_f	=554
Aluminum fin thickness, t_f	=0.38 mm
Exchanger compactness, β	= 1060 m^2/m^3
Outside area/inside area, (A_o/A_i)	=23
$A_{\text{flow}}/A_{\text{face}}$ on the air-side, σ	=0.529
Finned-surface weighted efficiency, η_s	= 0.85
Number of tube-passes per water loop, N_p	= 6

Design operating Data:

Moist air

Total cooling load at full load, Q_c	=60 kW
Latent Load at full load, Q_L	=20 kW
Inlet air conditions	= t =Dry and wet bulb temperatures are: 27 °C, and 17 °C
Air face velocity, V_{face}	=2.8 m/s
Air heat transfer coefficient, h_c	=60 W/ ($\text{m}^2 \text{ }^\circ\text{C}$)
Air mean specific heat, c_{pm}	=1.001 kJ/(kg. K)

Chilled water

Inlet water temperature, $T_{w_{\text{in}}}$	=6 °C
Water mass flow rate, m_w	=2.9 kg/s
Water inlet velocity, V_w	=1.25 m/s
Heat transfer coefficient on water side, h_i	=4000 W/ ($\text{m}^2 \text{ }^\circ\text{C}$)
Number of tube-passes per water loop, N_{tp}	= 6
Exit water temperature, $T_{w_{\text{out}}}$	=11 °C
Water specific heat, CP_w	=4.14 kJ/(kg. K)

Under the above design full load conditions, calculate:

- The coil dimensions (tube length, finned width and coil depth).
- The number of coil rows and the total number of tubes.
- The exit air temperature.

Calculation Procedures

From psychometric chart at inlet air conditions the inlet air properties are obtained represented by $h_{a_{\text{in}}}=48 \text{ kJ/kg}$, $W_{a_{\text{in}}}=0.0081 \text{ kg}_v/\text{kg}_a$, dew point temperature, $\text{dpt} = 10^\circ\text{C}$. By knowing $Q_c=60 \text{ kW}$, $\text{CSHF}=0.75$ ($=1- Q_L/Q_c$), and $\phi_{\text{out}} = 95\%$ using information from inlet point, the exit conditions can be determined as $h_{a_{\text{out}}}=30.6 \text{ kJ/kg}$, $T_{a_{\text{out}}}=10.5^\circ\text{C}$, $W_{a_{\text{out}}}= 0.0078 \text{ kg}_v/\text{kg}_a$

$$- m_a = \frac{Q_c}{(h_{a_{in}} - h_{a_{out}})} = \frac{60}{(48 - 30.6)} = 3.53 \text{ kg/s}$$

$$- m_w = \frac{Q_c}{c_{p_w}(T_{w_{out}} - T_{w_{in}})} = \frac{60}{4.14 \times 5} = 2.90 \text{ kg/s}$$

Calculations of the coil design parameters:

$$\Delta A_o = \frac{\beta \times S_L \times m_a}{\rho_a \times V_{face}} = \frac{1060 \times 0.0261 \times 3.53}{1.16 \times 2.8} = 29.95 \text{ m}^2$$

$$\Delta NTU_o = \frac{\eta_s h_o \Delta A_o}{m_a c_{p_m}} = \frac{0.85 \times 60 \times 29.95}{3.53 \times 1001} = 0.432$$

$$\Delta A_i = \left(\frac{A_i}{A_o}\right) \times \Delta A_o = \frac{29.95}{23} = 1.3 \text{ m}^2$$

$$\Delta NTU_i = \frac{h_i \Delta A_i}{m_w c_{p_w}} = \frac{4000 \times 1.3}{2.9 \times 4114} = 0.435$$

$$R = \left[\frac{h_i c_{p_a}}{h_o \eta_s} \left(\frac{\Delta A_i}{\Delta A_o} \right) \right] * \left[\frac{\left(1 + \frac{\Delta NTU_o}{2} \right)}{\left(1 - \frac{\Delta NTU_i}{2} \right)} \right] = 5.3 \text{ KJ/kg.K}$$

Row i=1:

$$T_{S_{m1}} = \frac{-(R+1.4) + \sqrt{(R+1.4)^2 + 0.184 * (h_{a1} + R * T_{w1} - 10.76)}}{0.092} = 13.5 \text{ }^\circ\text{C}$$

Since the mean coil surface temperature at the 1st row is 13.5 and it is larger than the inlet dew point temperature of the entering air, $d_{pt} = 10^\circ\text{C}$ the coil will be partially dry until the coil surface temperature reaches at least the dew point temperature. Therefore, the dry coil equations will be used here.

$$T_{S_{m1}} = \frac{(T_{a1} + R * T_{w1})}{(R+1)} = 13.6 \text{ }^\circ\text{C}$$

$$\Delta Q_{c1} = \frac{h_i \Delta A_i}{\left(1 - \frac{\Delta NTU_i}{2} \right)} \times (T_{S_{m1}} - T_{w1}) = 17.27 \text{ kW}$$

Where, $h_i = 4000 \text{ W/m}^2.\text{C}$

$$T_{w2} = T_{w1} - \frac{\Delta Q_{c1}}{m_w c_{p_w}} = 11 - \frac{14.5}{2.9 \times 4.14} = 9.8 \text{ }^\circ\text{C}$$

$$T_{a2} = T_{a1} - \frac{\Delta Q_{c1}}{m_a \times c_{p_a}} = 22.2 \text{ }^\circ\text{C}$$

$$W_{a2} = W_{a1} = 0.0081 \text{ kg}_v/\text{kg}_a$$

Row i=2

$$T_{S_{m2}} = \frac{(T_{a2} + R * T_{w2})}{(R+1)} = 11.81 \text{ }^\circ\text{C}$$

$$\Delta Q_{c2} = \frac{h_i \Delta A_i}{\left(1 - \frac{\Delta NTU_i}{2} \right)} \times (T_{S_{m2}} - T_{w2}) = 13.35 \text{ kW}$$

$$TW_3 = TW_2 - \frac{\Delta Q_{c2}}{m_w C p_w} = 9.8 - \frac{11.2}{2.9 \times 4.14} = 8.86 \text{ }^\circ\text{C}$$

$$Ta_3 = Ta_2 - \frac{\Delta Q_{c1}}{m_a \times C p_a} = 18.5 \text{ }^\circ\text{C}$$

$$Wa_3 = Wa_2 = 0.0081 \text{ kg}_v/\text{kg}_a$$

Row i=3

$$T_{sm3} = \frac{(Ta_3 + R \cdot TW_3)}{(R+1)} = 10.42 \text{ }^\circ\text{C}$$

$$\Delta Q_{c3} = \frac{h_i \Delta A_i}{(1 - \frac{\Delta NTU_i}{2})} \times (T_{sm3} - TW_3) = 10.36 \text{ kW}$$

$$TW_4 = TW_3 - \frac{\Delta Q_{c3}}{m_w C p_w} = 8.86 - \frac{8.7}{2.9 \times 4.14} = 8.13 \text{ }^\circ\text{C}$$

$$Ta_4 = Ta_3 - \frac{\Delta Q_{c1}}{m_a \times C p_a} = 15.6 \text{ }^\circ\text{C}$$

$$Wa_4 = Wa_3 = 0.0081 \text{ kg}_v/\text{kg}_a$$

Row i=4

$$T_{sm4} = \frac{(Ta_4 + R \cdot TW_4)}{(R+1)} = 9.34 \text{ }^\circ\text{C}$$

$$\Delta Q_{c4} = \frac{h_i \Delta A_i}{(1 - \frac{\Delta NTU_i}{2})} \times (T_{sm4} - TW_4) = 8 \text{ kW}$$

$$TW_5 = TW_4 - \frac{\Delta Q_{c4}}{m_w C p_w} = 8.13 - \frac{6.75}{2.9 \times 4.14} = 7.57 \text{ }^\circ\text{C}$$

$$Ta_5 = Ta_4 - \frac{\Delta Q_{c4}}{m_a \times C p_a} = 13.3 \text{ }^\circ\text{C}$$

$$Wa_5 = Wa_4 = 0.0081 \text{ kg}_v/\text{kg}_a$$

Row i=5

$T_{sm} < dpt$ therefore, the coil will act as a wet coil

$$ha_5 = 1.001 \times Ta_5 + Wa_5 \times (2501 + 1.8 \times Ta_5) = 33.76 \text{ kJ/kg}$$

$$T_{sm5} = \frac{-(R+1.4) + \sqrt{(R+1.4)^2 + 0.184 \times (ha_5 + R \cdot TW_5 - 10.76)}}{0.092} = 9 \text{ }^\circ\text{C}$$

$$\Delta Q_{c5} = \frac{h_i \Delta A_i}{(1 - \frac{\Delta NTU_i}{2})} \times (T_{sm5} - TW_5) = 9.5 \text{ kW}$$

$$TW_6 = TW_5 - \frac{\Delta Q_{c5}}{m_w C p_w} = 7.57 - \frac{7.97}{2.9 \times 4.14} = 7 \text{ }^\circ\text{C}$$

$$ha_6 = ha_5 - \frac{\Delta Q_{c5}}{m_a} = 31.1 \text{ kJ/kg}$$

$$Ta_6 = \left[\frac{\left(1 - \frac{\Delta NTU_0}{2}\right)}{\left(1 + \frac{\Delta NTU_0}{2}\right)} \right] \times Ta_5 + \left\{ \left[\frac{(\Delta NTU_0)}{\left(1 + \frac{\Delta NTU_0}{2}\right)} \right] \right\} \times Ts_{m5} = 11.7 \text{ }^\circ\text{C}$$

$$Wa_6 = \frac{ha_6 - CpaTa_6}{2501 + 1.8 \times Ta_6} = \frac{31.1 - 1(11.7)}{2501 + 1.8(11.7)} = 0.0077 \text{ kg}_v/\text{kg}_a$$

Row $i=6$

$$Ts_{m6} = \frac{-(R+1.4) + \sqrt{(R+1.4)^2 + 0.184 \times (ha_6 + R \times Tw_6 - 10.76)}}{0.092} = 8.1 \text{ }^\circ\text{C}$$

$$\Delta Q_{c6} = \frac{h_i \Delta A_i}{\left(1 - \frac{\Delta NTU_i}{2}\right)} \times (Ts_{m6} - Tw_6) = 7.31 \text{ kW}$$

$$Tw_7 = Tw_6 - \frac{\Delta Q_{c6}}{m_w Cpw} = 7 - \frac{6.37}{2.9 \times 4.14} = 6.4 \text{ }^\circ\text{C}$$

$$ha_7 = ha_6 - \frac{\Delta Q_{c5}}{m_a} = 30 \text{ kJ/kg}$$

$$Ta_7 = \left[\frac{\left(1 - \frac{\Delta NTU_0}{2}\right)}{\left(1 + \frac{\Delta NTU_0}{2}\right)} \right] \times Ta_6 + \left\{ \left[\frac{(\Delta NTU_0)}{\left(1 + \frac{\Delta NTU_0}{2}\right)} \right] \right\} \times Ts_{m6} = 10.3 \text{ }^\circ\text{C}$$

$$Wa_7 = \frac{ha_7 - CpaTa_7}{2501 + 1.8 \times Ta_7} = \frac{30 - 1(10.3)}{2501 + 1.8(10.3)} = 0.0076 \text{ kg}_v/\text{kg}_a$$

The total calculated cooling load for 6-rows coil is: $Q_C = \sum_{i=1}^{Nr} Q_{Ci} = 65.8 \text{ kW}$

And coil sensible heat factor,

$$CSHF = \frac{Q_S}{Q_C} = \frac{m_a Cp(Ta_1 - Ta_7)}{65.8} = 0.88$$

The calculated unknowns are listed row-by-row in the next Table; and the psychrometric process for the cooling and dehumidification process is represented by Figure 7.

Row number	Surface condition	Ts_{mi} $^\circ\text{C}$	ΔQ_{Ci} kW	Tw_{i+1} $^\circ\text{C}$	Ta_{i+1} $^\circ\text{C}$	Wa_{i+1} g_v/kg_a
Coil inlet	Dry		0	11	27	8.1
1	Dry	13.6	17.3	9.8	22.2	8.1
2	Dry	11.8	13.3	8.86	18.5	8.1
3	Dry	10.4	10.36	8.13	15.6	8.1
4	Dry	9.3	8	7.57	13.3	8.1
5	Wet	9.0	9.5	7	11.7	7.7
6	Wet	8.1	7.3	6.4	10.3	7.6

a. Calculation of Coil number of tubes, N_t

$$N_r = \text{Number of coil rows} = 6$$

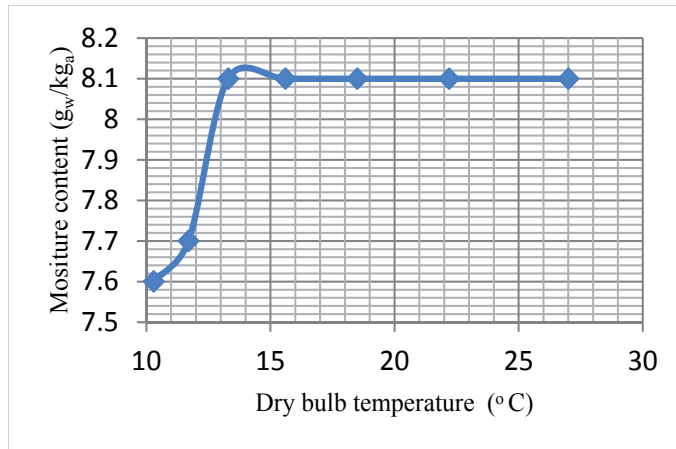


Fig. 7. Presentation of Cooling and dehumidifying process.

$$m_w = \frac{N_t}{N_p} \rho_w \left(\frac{\pi}{4} d_i^2 \right) V_w$$

$$N_t = \frac{4N_p m_a}{\pi \rho_w d_i^2 V_w} = 120 \text{ tubes}$$

b. Calculation of Coil dimension (D, H, L)

$$N_t = N_r * N_c$$

$$N_c = \frac{120}{6} = 20$$

Height of the coil, $H = S_t * N_c = 0.635 \text{ m}$

$$A_o = \sum_{i=1}^{N_r} \Delta A_o = N_r * \Delta A_o = 6 * 29.95 = 179.7 \text{ m}^2$$

Given: $\frac{A_o}{A_i} = 23$

$$A_i = 7.81 \text{ m}^2 = N_t (\pi d_i L)$$

$$L = \text{Length of the coil} = \frac{A_i}{\pi N_t d_i} = 1.71 \text{ m}$$

$$D = \text{Coil depth} = N_c * S_L = 0.157 \text{ m}$$

c. Exit air temperature

$$T_{a_{out}} = 10.3 \text{ } ^\circ\text{C}$$

Treating the cooling coil as a single zone "Worked Example"

We will solve the previous worked problem using principal treating the coil as single zone/section instead of multi-sections and compare the two results.

Calculation Procedures:

1. From psychrometric chart at inlet air conditions the inlet air properties are obtained represented by $h_{a_{in}} = 48 \text{ kJ/kg}$, $W_{a_{in}} = 0.0081 \text{ kg}_v/\text{kg}_a$, dew point temperature, $d_{pt} = 10^\circ\text{C}$.

By knowing $Q_C=60$ kW, $CSHF=0.75$ ($=1- Q_L/Q_C$), and $\phi_{out} = 95\%$ using information from inlet point, the exit conditions can be determined as $ha_{out}=30.6$ kJ/kg, $Ta_o=10.5$ °C, $Wa_o = 0.0078$ kg_v/kg_a

$$2. \quad m_a = \frac{Q_c}{(ha_{in}-ha_{out})} = \frac{60}{(48-30.6)} = 3.53 \text{ kg/s}$$

$$3. \quad m_w = \frac{Q_c}{cp_w(Tw_{out}-Tw_{in})} = \frac{60}{4.14*5} = 2.90 \text{ kg/s}$$

$$R = \left[\frac{h_i c p_a}{\eta_s h_o} \left(\frac{A_i}{A_o} \right) \right] = 3.41 \text{ KJ/kg.K}$$

$$Ts_1 = \frac{-(R + 1.4) + \sqrt{(R + 1.4)^2 + 0.184 * (ha_1 + R * Tw_1 - 10.76)}}{0.092}$$

$$Ts_1 = 13.74 > T_{d.point} = 10 \quad [\text{Coil surface is dry}]$$

$$Ts_1 = \frac{(Ta_1 + R * Tw_1)}{(R+1)} = 14.62^\circ \text{C}$$

$$Ts_2 = \frac{(Ta_2 + R * Tw_2)}{(R+1)} = 7.02$$

Calculation of ΔTw_m

$$\Delta Tw_m = (Ts_m - Tw_m) = \frac{[(Ts_1 - Tw_1) - (Ts_2 - Tw_2)]}{\ln \left[\frac{(Ts_1 - Tw_1)}{(Ts_2 - Tw_2)} \right]}$$

$$\Delta Tw_m = 2.05 \text{ }^\circ\text{C}$$

Calculation of A_i & A_o

$$A_i = \frac{Q_c}{h_i * \Delta T_m} = 7.31 \text{ m}^2$$

$$A_o = \left(\frac{A_o}{A_i} \right) A_i = 168.3 \text{ m}^2$$

Number of Coil Tubes N_t

$$N_t = \frac{4N_p m_w}{\pi \rho_w d_i^2 V_w} = 120 \text{ tubes}$$

The Length of the Tube (Coil), L:

$$L = \frac{A_i}{N_t \pi d_i} = 1.62 \text{ m}$$

Height of the Coil, H:

$$H = \left(\frac{m_a}{\rho_a V_{face}} \right) * \left(\frac{N_t \pi d_i}{A_i} \right) = 0.683 \text{ m}$$

Number of Rows, N_r

$$N_r = \frac{N_t}{N_c} = \frac{N_t * S_t}{H} = 5.5 \approx 6 \text{ rows}$$

Depth of the Coil, D:

$$D = N_r * S_L = 0.157 \text{ m}$$

$$NTU_o = \frac{h_o A_o \eta_s}{m_a c p_a} = 2.43$$

Calculation of Exit air condition

$$T a_2 = \left[\frac{\left(1 - \frac{NTU_o}{2}\right)}{\left(1 + \frac{NTU_o}{2}\right)} \right] \times T a_1 + \left[\frac{\left(NTU_o\right)}{\left(1 + \frac{NTU_o}{2}\right)} \right] \times \left(\frac{T_{S_1} + T_{S_2}}{2} \right) = 9.2^\circ \text{C}$$

$$W a_2 = \frac{h a_2 - c p a T a_2}{2501 + 1.8 * T a_2} = 0.008 \text{ kg}_v / \text{kg}_a$$

Calculation of Latent load and CSHF

$$Q_L Q_S = m_a (W a_2 - W a_1) \times 2501 = 0.88 \text{ kW}$$

$$CSHF = \frac{60 - 0.88}{60} = 0.98$$

Table-2 illustrates a comparison of the dimensions and exit air conditions for 60 kW cooling coil analyzed as only single-section and cooling coil divided to N_r -sections ($N_r=6$).

Physical quantity	Single-section coil	6-sections coil
Air exit temperature, °C	9.2	10.3
Number of tubes	120	120
Number of rows	6	6
Coil width, m	0.683	0.635
Coil depth, m	0.157	0.157
Coil length, m	1.62	1.71
Coil SHF	0.98	0.71
Design cooling load, kW	60	60
Actual cooling load, kW	60	65.8

Table 2.

The results presented in Table-2 indicate that cooling coil analyzed as only one-section gives results with good agreement with those obtained with the coil analyzed as 6-sections. The maximum error is 12%.

8. Worked problem on the thermal design of Dx-coils

Cross-counter flow Dx- evaporator coil using corrugated plate-fins, has the flowing construction and operating design parameters:

Coil construction parameters:

Outside tube diameter, d_o	=13.41 mm
Inside tube diameter, d_i	=12.09 mm
Longitudinal tube spacing, S_L	=26.16 mm
Transverse tube spacing, S_T	=31.75 mm

No. of fins/m, N_f	=554
Aluminum fin thickness, t_f	=0.15 mm
Exchanger compactness, β	= 1060 m^2/m^3
Outside area/inside area, (A_o/A_i)	=23
$A_{\text{flow}}/A_{\text{face}}$ on the air-side, σ	=0.529
Finned-surface weighted efficiency, η_s	= 0.85
Number of tube-passes per water loop, N_p	= 6

Design operating Data:

Moist air

Total cooling load at full load, Q_c	=60 kW
Latent Load at full load, Q_L	=20 kW
Inlet air conditions	= t = Dry and wet bulb temperatures are: 26 °C, and 19 °C
Air face velocity, V_{face}	=2.8 m/s
Air heat transfer coefficient, h_c	=60 W/ ($\text{m}^2 \text{ } ^\circ\text{C}$)
Air mean specific heat, c_{pm}	=1.001 kJ/(kg. K)

R-134a

Evaporating temperature, T_{ev}	=7 °C
Heat transfer coefficient on refrigerant side, h_i	=2000 W/ ($\text{m}^2 \text{ } ^\circ\text{C}$)
Number of tube-passes per water loop, N_p	= 6

Under the above design full load conditions, calculate:

- The coil dimensions (tube length, finned width and coil depth).
- The number of coil rows and the total number of tubes.
- The exit air temperature.

Calculation Procedures

- Knowing: [$h_{\text{a,in}}=54$ kJ/kg, $W_{\text{a,in}}=0.011$ kgv/kga, $Q_c=60$ kW, $\text{CSHF}=0.75$, $\phi_{\text{out}} = 95\%$], from the Psychometric-chart we obtain:

Air Exit Condition: [$h_{\text{a,out}}=33$ kJ/kg, $T_{\text{a,o}}=10.5$ °C, $W_{\text{a,o}}=0.86 \cdot 10^{-3}$ kgv/kga]

$$2. \quad m_a = \frac{Q_c}{(h_{\text{a,in}} - h_{\text{a,out}})} = \frac{60}{(54 - 33)} = 2.857 \text{ kg/s}$$

$$3. \quad R = \left[\frac{h_i c_{\text{p,a}}}{\eta_s h_o} \left(\frac{A_i}{A_o} \right) \right] = 1.7 \text{ KJ/kg.K}$$

$$T_{\text{S}_1} = \frac{-(R + 1.4) + \sqrt{(R + 1.4)^2 + 0.184 * (h_{\text{a}_1} + R * T_{\text{ev}} - 10.76)}}{0.092}$$

$$T_{\text{S}_1} = 14.23 < T_{\text{d,point}} = 15 \quad [\text{Coil surface is wet}]$$

$$T_{\text{S}_2} = \frac{-(R + 1.4) + \sqrt{(R + 1.4)^2 + 0.184 * (h_{\text{a}_2} + R * T_{\text{ev}} - 10.76)}}{0.092}$$

$$T_{\text{S}_2} = 9.21 \text{ } ^\circ\text{C}$$

Calculation of $\Delta T_{ev,m}$

$$\Delta T_{ev,m} = (T_{s,m} - T_{ev,m}) = \frac{[(T_{s_1} - T_{ev}) - (T_{s_2} - T_{ev})]}{\ln\left[\frac{(T_{s_1} - T_{ev})}{(T_{s_2} - T_{ev})}\right]}$$

$$\Delta T_{ev,m} = 5.33 \text{ } ^\circ\text{C}$$

Where, $\Delta T_{ev,m}$ = mean temperature difference on the refrigerant-side.

Calculation of A_i & A_o

$$A_i = \frac{Q_c}{h_i \cdot \Delta T_{ev,m}} = 5.63 \text{ m}^2$$

$$A_o = \left(\frac{A_o}{A_i}\right) A_i = 129.5 \text{ m}^2$$

Calculation of Exit air condition

$$T_{a_2} = \left[\frac{\left(1 - \frac{\Delta NTU_o}{2}\right)}{\left(1 + \frac{\Delta NTU_o}{2}\right)}\right] \times T_{a_1} + \left[\frac{\left(\Delta NTU_o\right)}{\left(1 + \frac{\Delta NTU_o}{2}\right)}\right] \times \left(\frac{T_{s_1} + T_{s_2}}{2}\right) = 10.75 \text{ } ^\circ\text{C}$$

$$\Delta NTU_o = \frac{\eta_s h_o A_o}{m_a C_{p_a}} = 2.30$$

Air is saturate at this temperature with $h_{a_2} = 31.5 \text{ kJ/kg}$

$$W_{a_2} = \frac{h_{a_2} - C_{p_a} T_{a_2}}{2501 + 1.8 T_{a_2}} = 0.00823 \text{ Kgv / kga}$$

Calculation of Latent load and CSHF

$$Q_c = m_a (h_{a_1} - h_{a_2}) = 64.28 \text{ kW}$$

$$Q_L = Q_c - Q_s = 64.28 - 2.857 * (26 - 10.72) = 20.62 \text{ kW}$$

$$\text{CSHF} = \frac{64.28 - 20.6}{64.28} = 0.68$$

Calculation of Dx-Coil Size

Number of Coil Tubes N_t

For DX-coil the number of tubes is determined by applying the continuity equation for the refrigerant at the exit of the coil where the velocity attains its maximum value at this exit section. Assuming the refrigerant as saturated vapor, and the maximum velocity of vapor $V_g \approx 10 \text{ m/s}$, N_t is given as:

$$m_r = \frac{Q_c}{x \cdot h_{fg}} = 0.33 \text{ kg/s} \text{ [Assume inlet dryness fraction, } x = 0.9\text{]}$$

$$N_t = \frac{4 N_p m_r}{\pi \rho_g d_i^2 V_g} \approx 96 \text{ tube}$$

The Length of the Tube (Coil), L

$$L = \frac{A_i}{N_t \pi d_i} = 1.54 \text{ m}$$

Height of the Coil, H

$$\text{Air face area, } A_{\text{face}} = \frac{m_a}{\rho_a V_{\text{face}}} = 0.88 \text{ m}^2$$

$$A_{\text{face}} = HL$$

$$H = \frac{A_{\text{face}}}{L} = 0.57 \text{ m}^2$$

Number of Rows, N_r

$$N_r = \frac{N_t}{N_c} = \frac{N_t * S_t}{W} = 5.35 \approx 6 \text{ rows}$$

Depth of the Coil, D:

$$D = N_r * S_L = 0.157 \text{ m}$$

9. Conclusion

In this chapter, simulation of the cooling coil using a discrete technique "row-by-row method" has been presented. The main advantage of this method is to trace the air and coil surface temperature locally. In addition, this method gives more accurate results for the cooling coil design or simulation compared with those given by ordinary method such as log mean enthalpy method. Step-by-step procedure has been introduced and worked examples are presented. The deviation between the two methods "numerical discrete method and treating the coil as a single zone" is around of 12%.

10. Nomenclature

A	= surface area, m ²
C _p	= specific heat, kJ/kg. C
h	= heat transfer coefficient, W/m ² . C
h _{mass}	= mass transfer coefficient, kg/m ² .S
NTU	= number of transfer unit
Q	= heat transfer, W
T	= temperature, °C
W	= humidity ratio, kg _v /kg _a

11. References

- [1] ASHRAE Systems and Equipment Handbook (SI), 2000, Chapter 21
- [2] Wibert Stoecker, and Jerold Jones. "Refrigeration & air-conditioning", 2nd, Ed., 1982, McGraw-Hill
- [3] ASHRAE Fundamental Handbook (SI), 2001, Chapter 6
- [4] Kays, W.M., and London A.L. Compact Heat Exchangers, 3rd edition, McGraw-Hill, New York. 1984
- [5] Threlkeld, J.L. Thermal Environment Engineering, Prentice-Hall Inc., New Work, NY. 1970.

Part 4

Plate Heat Exchangers

The Characteristics of Brazed Plate Heat Exchangers with Different Chevron Angles

Muthuraman Subbiah
*Higher College of Technology,
Oman*

1. Introduction

Plate heat exchangers (PHEs) were introduced in the 1930s and were almost exclusively used as liquid/liquid heat exchangers in the food industries because of their ease of cleaning. Over the years, the development of the PHE has generally continued towards larger capacity, as well as higher working temperature and pressure. Recently, a gasket sealing was replaced by a brazed material, and each thermal plate was formed with a series of corrugations (herringbone or chevron). These greatly increased the pressure and the temperature capabilities.

The corrugated pattern on the thermal plate induces a highly turbulent fluid flow. The high turbulence in the PHE leads to an enhanced heat transfer, to a low fouling rate, and to a reduced heat transfer area. Therefore, PHEs can be used as alternatives to shell-and-tube heat exchangers. Due to ozone depletion, the refrigerant R22 is being replaced by R410A (a binary mixture of R32 and R125, mass fraction 50 %/50 %). R410A approximates an azeotropic behavior since it can be regarded as a pure substance because of the negligible temperature gliding. The heat transfer and the pressure drop characteristics in PHEs are related to the hydraulic diameter, the increased heat transfer area, the number of the flow channels, and the profile of the corrugation waviness, such as the inclination angle, the corrugation amplitude, and the corrugation wavelength. These geometric factors influence the separation, the boundary layer, and the vortex or swirl flow generation. However, earlier experimental and numerical works were restricted to a single-phase flow. Since the advent of a Brazed PHE (BPHE) in the 1990s, studies of the condensation and/or evaporation heat transfer have focused on their applications in refrigerating and air conditioning systems, but only a few studies have been done. Much work is needed to understand the features of the two-phase flow in the BPHEs with alternative refrigerants. Xiaoyang *et al.*, [1] experimented with the two-phase flow distribution in stacked PHEs at both vertical upward and downward flow orientations. They indicated that non-uniform distributions were found and that the flow distribution was strongly affected by the total inlet flow rate, the vapor quality, the flow channel orientation, and the geometry of the inlet port Holger [2]. Theoretically predicted the performance of chevron-type PHEs under single-phase conditions and recommended the correlations for the friction factors and heat transfer coefficients as functions of the corrugation chevron angles. Lee *et al.*, [3] investigated the characteristics of the evaporation heat transfer and pressure drop in BPHEs with R404A and

R407C. Kedzierski [4] reported the effect of inclination on the performance of a BPHE using R22 in both the condenser and the evaporator. Several single-phase correlations for heat transfer coefficients and friction factors have been proposed, but few correlations for the two-phase flow have been proposed. Yan *et al.*, [5] suggested a correlation of condensation with a chevron angle of 30° for R134a. Yan *et al.*, reported that the mass flux, the vapor quality, and the condensation pressure affected the heat transfer coefficients and the pressure drops. Hieh and Lin [6] developed the correlations for evaporation with a chevron angle of 30° for R410A.

The main objective of this work was to experimentally investigate the heat transfer coefficients and the pressure drops during condensation of R410A inside BPHEs. Three BPHEs with different chevron angles of 45° , 35° , and 20° were used. The results were then compared to those of R22. The geometric effects of the plate on the heat transfer and the pressure drop were investigated by varying the mass flux, the quality, and the condensation temperature. From the results, the geometric effects, especially the chevron angle, must be considered to develop the correlations for the Nusselt number and the friction factor. Correlations for the Nusselt number and the friction factor with the geometric parameters are suggested in this study.

Experiments to measure the condensation heat transfer coefficient and the pressure drop in brazed plate heat exchangers (BPHEs) were performed with the refrigerants R410A and R22. Brazed plate heat exchangers with different chevron angles of 45° , 35° , and 20° were used. Varying the mass flux, the condensation temperature, and the vapor quality of the refrigerant, we measured the condensation heat transfer coefficient and the pressure drops. Both the heat transfer coefficient and the pressure drop increased proportionally with the mass flux and the vapor quality and inversely with the condensation temperature and the chevron angle.

Correlations of the Nusselt number and the friction factor with the geometric parameters are suggested for the tested BPHEs. In an effort to study and optimize the design of a plate heat exchanger comprising of corrugated walls with herringbone design, a CFD code is employed. Due to the difficulties induced by the geometry and flow complexity, an approach through a simplified model was followed as a first step. This simple model, comprised of only one corrugated plate and a flat plate, was constructed and simulated. The Reynolds numbers examined are 400, 900, 1000, 1150, 1250 and 1400. The SST turbulence model was preferred over other flow models for the simulation.

The case where hot water (60°C) is in contact with a constant-temperature wall (20°C) was also simulated and the heat transfer rate was calculated. The results for the simplified model, presented in terms of velocity, shear stress and heat transfer coefficients, strongly encourage the simulation of one channel of the typical plate heat exchanger, i.e. the one that comprises of two corrugated plates with herringbone design having their crests nearly in contact. Preliminary results of this latter work, currently in progress, comply with visual observations.

In recent years, compact heat exchangers with corrugated plates are being rapidly adopted by food and chemical process industries, replacing conventional shell-and-tube exchangers. Compact heat exchangers consist of plates embossed with some form of corrugated surface pattern, usually the chevron (herringbone) geometry[1].The plates are assembled being

abutting, with their corrugations forming narrow passages. This type of equipment offers high thermal effectiveness and close temperature approach, while allowing ease of inspection and cleaning [1],[2]. In order to be able to evaluate its performance, methods to predict the heat transfer coefficient and pressure drop must be developed. In this direction, CFD is considered an efficient tool for momentum and heat transfer rate estimation in this type of heat exchangers.

The type of flow in such narrow passages, which is associated with the choice of the most appropriate flow model for CFD simulation, is still an open issue in the literature. Due to the relatively high pressure drop, compared to shell-and-tube heat exchangers for equivalent flow rates, the Reynolds numbers used in this type of equipment must be lower so as the resulting pressure drops would be generally acceptable[1]. Moreover, when this equipment is used as a reflux condenser, the limit imposed by the onset of flooding reduces the maximum Reynolds number to a value less than 2000[3]. Ciofalo et al.[4], in a comprehensive review article concerning modeling heat transfer in narrow flow passages, state that, for the Reynolds number range of 1,500-3,000, transitional flow is expected, a kind of flow among the most difficult to simulate by conventional turbulence models.

On the other hand, Shah & Wanniarachchi[1] declare that, for the Reynolds number range 100-1500, there is evidence that the flow is already turbulent, a statement that is also supported by Vlasogiannis et al.[5], whose experiments in a plate heat exchanger verify that the flow is turbulent for $Re > 650$. Lioumbas et al.[6], who studied experimentally the flow in narrow passages during counter-current gas-liquid flow, suggest that the flow exhibits the basic features of turbulent flow even for the relatively low gas Reynolds numbers tested ($500 < Re < 1200$). Focke & Knibbe[7] performed flow visualization experiments in narrow passages with corrugated walls. They concluded that the flow patterns in such geometries are complex, due to the existence of secondary swirling motions along the furrows of their test section and suggest that the local flow structure controls the heat transfer process in such narrow passages.

The most common two-equation turbulence model, based on the equations for the turbulence energy k and its dissipation ε , is the $k-\varepsilon$ model[8]. To calculate the boundary layer, either "wall functions" are used, overriding the calculation of k and ε in the wall adjacent nodes[8], or integration is performed to the surface, using a "low turbulent Reynolds (*low-Re*) $k-\varepsilon$ " model[9]. Menter & Esch[9] state that, in standard $k-\varepsilon$ the wall shear stress and heat flux are over predicted (especially for the lower range of the Reynolds number encountered in this kind of equipment) due to the over prediction of the turbulent length scale in the flow reattachment region, which is a characteristic phenomenon occurring on the corrugated surfaces in these geometries. Moreover, the standard $k-\varepsilon$ model requires a course grid near the wall, based on the value of $y^+ = 11$ [9],[10], which is difficult to accomplish in confined geometries. The low-Re $k-\varepsilon$ model, which uses "dumping functions" near the wall[8],[9], is not considered capable of predicting the flow parameters in the complex geometry of a corrugated narrow channel[4], requires finer mesh near the wall, is computationally expensive compared to the standard $k-\varepsilon$ model and it is unstable in convergence.

An alternative to $k-\varepsilon$ model, is the $k-\omega$ model, developed by Wilcox[11]. This model, which uses the turbulence frequency ω instead of the turbulence diffusivity ε , appears to be more robust, even for complex applications, and does not require very fine grid near the wall[8].

However, it seems to be sensitive to the free stream values of turbulence frequency ω outside the boundary layer. A combination of the two models, $k-\epsilon$ and $k-\omega$, is the *SST* (Shear-Stress Transport) model, which, by employing specific “blending functions”, activates the Wilcox model near the wall and the $k-\epsilon$ model for the rest of the flow[9] and thus it benefits from the advantages of both models. Some efforts have been made towards the effective simulation of a plate heat exchanger. Due to the modular nature of a compact heat exchanger, a common practice is to think of it as composed of a large number of unit *cells* (Representative Element Units, *RES*) and obtain results by using a single cell as the computational domain and imposing periodicity conditions across its boundaries[4],[12]. However, the validity of this assumption is considered another open issue in the literature [4].

2. Experimental facility

The experimental facility is capable of determining in plate heat transfer coefficients and measuring the pressure drops for the refrigerants. It consists of four main parts: a test section, a refrigerant loop, two water loops, and a data-acquisition system. A schematic of the test facility used in this study is shown in Figure-1, and detailed descriptions of the four main parts are mentioned below.

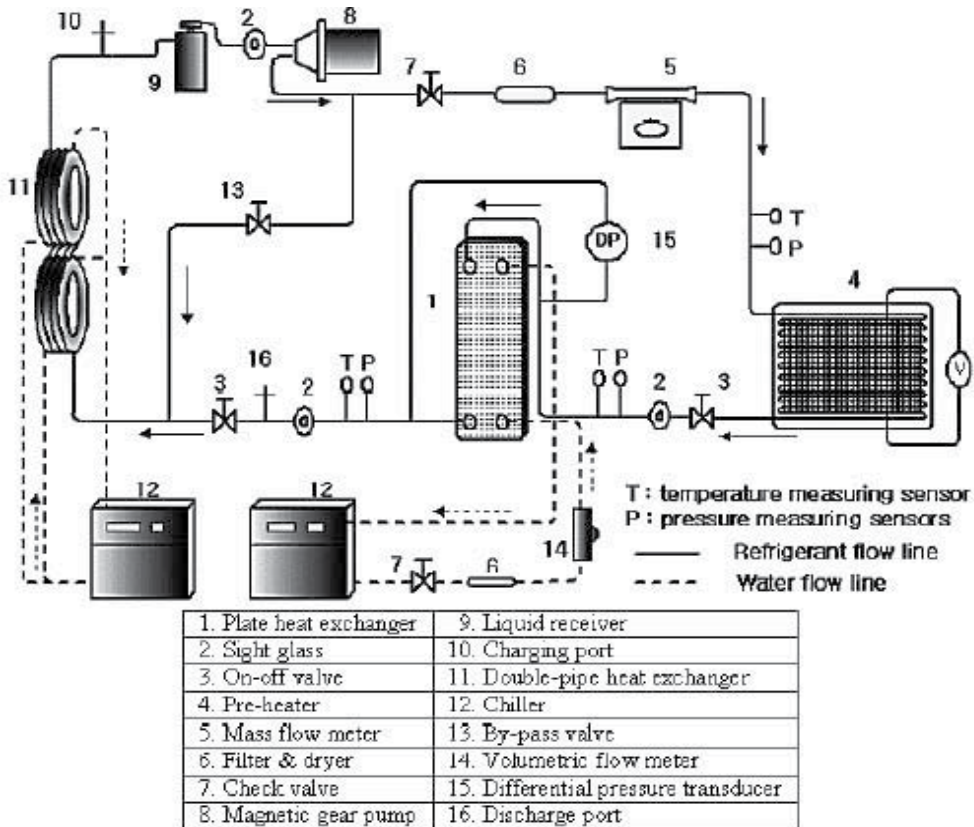


Fig. 1. Schematic diagram of the experimental system.

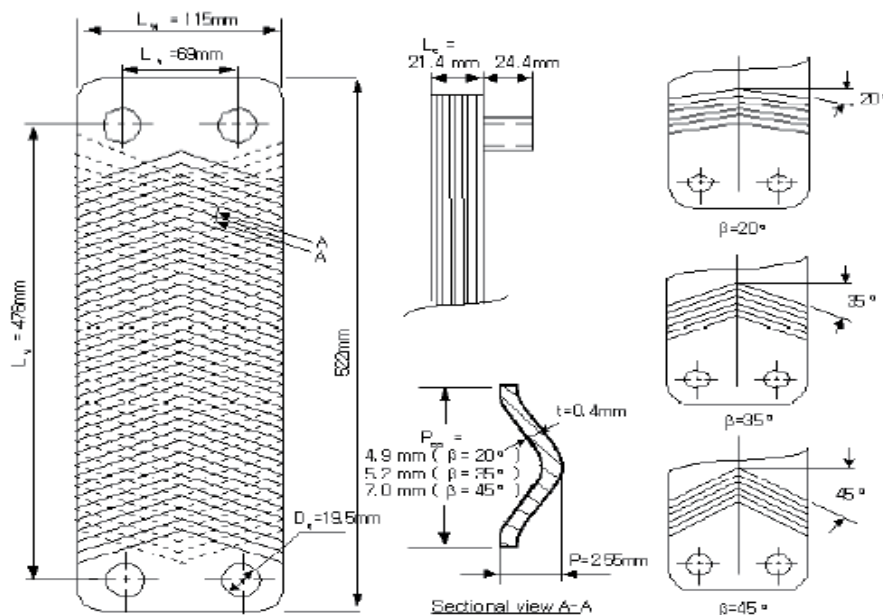


Fig. 2. Dimensions of the brazed plate heat exchangers.

2.1 Brazen plate heat exchangers

Three BPHEs with chevron angles of 45° , 35° , and 20° were used as the test sections. The angles of corrugation were measured from the horizontal axis. Each BPHE was composed of 4 thermal plates and 2 end plates, forming 5 flow channels. The dimensions of the BPHEs are shown in Figure-2. The refrigerant and cooling water were directed into the alternate passages between the plates through corner ports, creating counter flow conditions. The cooling water owed from the bottom to the top of every other channel on the basis of a central channel. On the other hand, the refrigerant owed from the top to the bottom in the rest of them.

2.2 Refrigerant loop

Refrigerant was supplied to the test section at specific conditions (i.e., temperature, flow rate, and quality) through the refrigerant loop. This loop contained a pre-heater, a double-pipe heat exchanger, a receiver, a magnetic gear pump, a differential pressure transducer, and a mass flow meter. Also included were thermocouples probes and pressure taps at the inlet/outlet of the test section. The refrigerant pump was driven by a DC motor which was controlled by a variable DC output motor controller.

The refrigerant flow rate was measured by using a mass flow meter installed between the magnetic gear pump and the pre-heater with an accuracy of 0.5 %. The pre-heater located before the test section was used to evaporate the refrigerant to a specified vapor quality at the inlet of the test section. The pressure drop of the refrigerant owing through the test section was measured with the differential pressure transducer, to an accuracy of 0.25 kPa. The refrigerant through the test section was subcooled at a double-pipe heat exchanger by

the water cooled by the chiller and went into a liquid receiver. The subcooled refrigerant returned to the magnetic gear pump and circulated through the refrigerant loop repeatedly. Calibrated T-type thermocouples were used to measure the temperatures of the refrigerant at the inlet/outlet of the test section. The entire loop was insulated with fiberglass to prevent heat transfer to the environment.

2.3 Water loop

There are two closed water loops in this facility. One is for determining the condensation heat flux at the test section. The other is for making the subcooled refrigerant state at two double-pipe heat exchangers before it enters the magnetic gear pump. The water flow rates of the test section were measured by using a turbine flow meter, and T-type thermocouples were installed to evaluate the gain of the heat flux of the water of the test section.

2.4 Data acquisition

The data were recorded by a computer-controlled data-acquisition system with 40 channels scanned at the speed of 30 data per minute. The temperature and the pressure of both fluids were continuously recorded, and the thermodynamic properties of the refrigerant were obtained from a computer program. After steady-state conditions had been reached in the system, all measurements were taken for 10 minutes.

3. Data reduction and uncertainty analysis

The hydraulic diameter of the channel, D_h , is defined as

$$D_h = 4 \times \text{Channel flow area} / \text{Wetted perimeter} = 4bL_w / 2L_w\phi \quad (1)$$

Where is $\phi = 1.17$. This value is given by the manufacturer.

The mean channel spacing, b , is defined as

$$b = p - t; \quad t = \text{Plate Thickness} \quad (2)$$

and the plate pitch p can be determined as, $N_t = \text{Total Number of plates}$

$$p = L_c / (N_t - 1) \quad (3)$$

The procedures to calculate the condensation heat transfer coefficient of the refrigerant side are described below. At first, the refrigerant quality at the inlet of the test section (x_{in}) should be selected to evaluate the condensation heat at a given quality. Its value is calculated from the amount of heat given by a pre-heater, which is the summation of the sensible heat and the latent heat:

$$\begin{aligned} Q_{pre} &= Q_{sens} + Q_{lat} \\ &= m_r C_{p,r} (T_{r,sat} - T_{r,pre,in}) + m_r i_{fg} x_{in} \end{aligned} \quad (4)$$

The refrigerant quality at the inlet of the test section can be written as

$$x_{in} = 1 / i_{fg} [Q_{pre} / m_r - C_{p,r} (T_{r,sat} - T_{r,pre,in})] \quad (5)$$

The power gained by the pre-heater is calculated by measuring the voltage and the current with a power meter. The change in the refrigerant quality inside the test section was evaluated from the heat transferred in the test section and the refrigerant mass flow rate (6)

$$\Delta x = x_{in} - x_{out} = Q_w / m_r X i_{fg} \quad (6)$$

The condensing heat in the test section was calculated from an energy balance with water:

$$Q_w = m_w C_{p,w} (T_{w,out} - T_{w,in}) \quad (7)$$

The heat transfer coefficient of the refrigerant side (h_r) was evaluated from the following equation:

$$1/h_r = (1/U) - (1/h_w) - R_{wall} \quad (8)$$

The overall heat transfer coefficient was determined using the log mean temperature difference

$$U = Q_w / A \times \text{LMTD}$$

$$\text{LMTD} = (T_{r,out} - T_{w,in}) - (T_{r,in} - T_{w,out}) / \ln \{ (T_{r,out} - T_{w,in}) / (T_{r,in} - T_{w,out}) \} \quad (9)$$

The heat transfer coefficient of the water side (h_w) was obtained by using Eq. (10). Equation (10) was developed from the single-phase water to water pre-tests by K_{im} [7]. If the least-squares method and the multiple regression method are used, the heat transfer coefficient of the water side is correlated in terms of the Reynolds number, the Prandtl number, and the chevron angle:

$$h_w = 0.295 (k_w / D_{Eq}) \text{Re}^{0.64} \text{Pr}^{0.32} (\pi/2 - \beta)^{0.09} \quad (10)$$

The thermal resistance of the wall is negligible compared to the effect of convection.

For the vertical downward flow, the total pressure drop in the test section is defined as

$$\Delta P_{total} = \Delta P_{fr} + \Delta P_a + \Delta P_s + \Delta P_p \quad (11)$$

And ΔP_{total} is measured by using a differential pressure transducer. The two-phase friction factor, f , is defined as

$$\Delta P_{fr} = f L_v N_{cp} G^2 E_q / D_h \rho_f \quad (12)$$

The port pressure loss in this experiment was less than 1 % of the total pressure loss. The static head loss can be written as and it has a negative value for vertical downward flow. The acceleration pressure drop for condensation is expressed as

$$\Delta P_p = 1.4 G^2 / (2 \rho_m) \quad (13)$$

An uncertainty analysis was done for all the measured data and the calculated quantities based on the methods described by Moffat [9]. The detailed results of the uncertainty analysis are shown in Table-1.

Parameters	Uncertainty
Temperature	±0.2 °C
Pressure	±4.7 Pa
Pressure Drop	±250 Pa
Water Flow Rate	±2%
Refrigerant mass flux	±0.5%
Heat flux of test section	±5.7%
Vapor Quality	±0.03
Heat Transfer coefficients of water side	±10.1%
Heat transfer coefficients of refrigerant	±9.1%

Table 1. Estimated uncertainty.

Where

$$G_p = 4m_{eq} / \pi D_p^2 \quad (14)$$

And

$$(1/\rho_m) = (x/\rho_g) + [(1-x)/\rho_l]. \quad (15)$$

The equivalent mass flow rate, m_{eq} , is defined as

$$m_{eq} = m [1-x+x(\rho_l/\rho_g)^{0.5}] \quad (16)$$

The port pressure loss in this experiment was less than 1% of the total pressure loss. The static head loss can be written as

$$\Delta P_s = -\rho_m g L_v \quad (17)$$

And it has a negative value for vertical downward flow, The acceleration pressure drop for condensation is expressed as

$$\Delta P_a = - [(G_{eq}^2 x / \rho_{fg})_{in} - (G_{eq}^2 x / \rho_{fg})_{out}] \quad (18)$$

4. Results and discussions

The condensation heat transfer coefficients and the pressure drops of R410A and R22 were measured in three BPHEs with chevron angles of 20°, 35°, and 45° by varying the mass flux (13 - 34 kg/m²s), the vapor quality (0.9 - 0.15), and the condensing temperature (20°C and 30°C) under a given heat flux condition (4.7 - 5.3 kW/m²). R22 was tested under identical experimental conditions for comparison with R410A.

4.1 Flow regime

Before the behaviors of heat transfer are considered, it is necessary to predict what flow regime exists at a given set of operating conditions. The detailed flow regime map for the PHE has not been proposed yet because of the difficulty of flow visualization. Vlasogiannis *et al.*, [10] suggested the criterion of a two-phase flow regime for a PHE in terms of

superficial liquid (j_f) and vapor velocities (j_g) by using water and air under adiabatic conditions. They only simulated a mixture of water and air as a two-phase fluid. According to their work, the flow patterns in a PHE are significantly different from those inside the vertical round tubes. They detected 3 types of flow patterns. The first was a gas continuous pattern with a liquid pocket at flow water flow rates ($j_f < 0.025$ m/s) over wide range of air flow rates.

The second was the slug flow pattern, which was detected at sufficiently high air ($j_g > 2$ m/s) and water flow rates ($j_f > 0.025$ m/s). Thirdly, the liquid continuous pattern with a gas pocket or a gas bubble at the high water flow rates ($j_f > 0.1$ m/s) and low air flow rates ($j_g < 1$ m/s). According to the flow regime map proposed by Vlasogiannis *et al.*, the expected flow pattern in this experimental study is the gas continuous flow pattern with liquid pockets. However, their flow regime map has a significant limitation for use since many important features, such as the phase-change, the heating or cooling conditions, the densities or specific volumes of the working fluids, the geometries of the PHEs, etc., were not considered in detail. According to the flow regime map proposed by Crawford *et al.* [11], which was developed for vertical downward flow in a round tube, all experimental flow patterns are located in the intermittent flow regime, but this flow regime can not represent the correct flow regime in a BPHE due to the different geometries.

4.2 Condensation heat transfer

Figure-3 shows the effects of the refrigerant mass flux, the chevron angle, and the condensation temperature on the averaged heat transfer coefficient for R410A. The term "averaged heat transfer coefficient" means the average of the heat transfer coefficients calculated by varying the quality of the refrigerant from 0.15 to 0.9, and the coefficients were obtained from Eq. (19):

$$H_{\text{averged}} = \frac{\sum h_{\text{local}} X_{\text{local}}}{\sum X_{\text{local}}} \quad (19)$$

Where h_1 is the local heat transfer coefficient at the local vapor quality. The experimental results indicate that the averaged heat transfer coefficients vary proportionally with the mass flux and inversely with the chevron angles and the condensation temperature. The small chevron angle forms narrow pitches to the flow direction, creating more abrupt changes in the velocity and the flow direction, thus increasing the effective contact length and time in a BPHE. The zigzag flow increases the heat transfer, and the turbulence created by the shape of the plate pattern is also important in addition to the turbulence created by the high flow rates. Increasing the mass flux at a given condensation temperature showed that the differences in the averaged heat transfer coefficients were significantly enlarged with decreasing chevron angle. This indicates that a PHE with the small chevron angle is more effective at a large mass flux ($G_c > 25$ kg/m²s) than at a small mass flux.

The averaged heat transfer coefficient of R410A decreases with increasing condensation temperature. The vapor velocity is a more influential factor than the liquid film thickness for the heat transfer. Vapor bubbles in the flow enhance the disturbance in the bubble wake as a turbulence promoter, and the turbulence induced by the vapor bubbles increases with the vapor velocity. Also, since the specific volume of the vapor increases with decreasing condensation temperature, the vapor velocity increases for a fixed mass flux and quality.

The vapor velocity at 20°C is faster than that at 30°C. The rates of the averaged heat transfer coefficients between condensation temperatures of 20°C and 30°C increased 5 % for a chevron angle of 45°, 9 % for 35°, and 16 % for 20°. These results show that different chevron angles lead partly to different flow pattern. Thus, we may conclude that the flow regime map should be modified by geometric considerations. The heat transfer coefficients in the high-quality region (fast velocity region) are larger than those in the low-quality region (slow velocity region). As mentioned above, this happens because the vapor velocity is the dominant effect on the heat transfer mechanism.

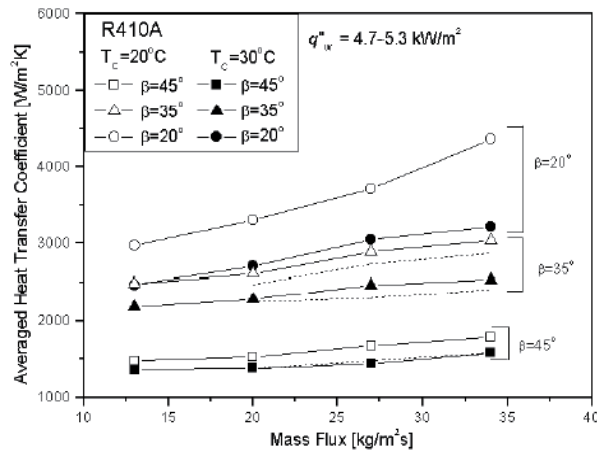


Fig. 3. Effect of mass flux on the averaged condensation heat transfer coefficient.

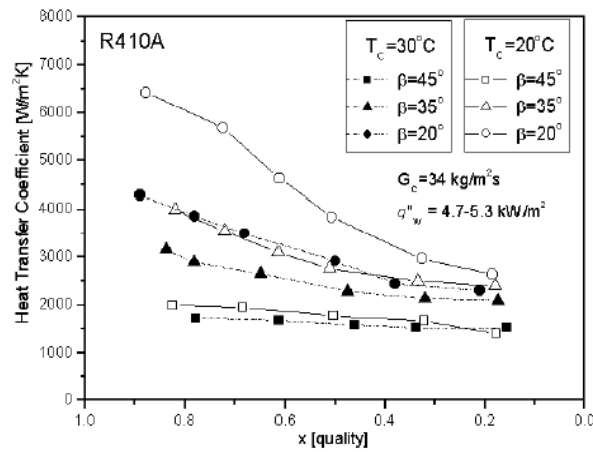


Fig. 4. Effect of quality on the condensation heat transfer coefficient.

Increasing the vapor quality at the same mass flux induces a faster bubble velocity, which increases the turbulence level and the convection heat transfer coefficient. The difference of heat transfer coefficients between the low-quality region and the high-quality region becomes larger with decreasing chevron angle. The PHE with a low chevron angle shows a better heat transfer performance in the high-quality region (i.e., the high vapor velocity region). Figure-4 also shows the variation of the heat transfer coefficients with the condensation temperatures. Like Figure-3, the heat transfer coefficients decreased with increasing condensation temperature. Also, the variations of the heat transfer coefficients with the condensation temperature are larger in the high-quality region. From the experimental results in Figures, 3 and 4, lowering the chevron angle and the condensation temperature gives the desired heat transfer effect.

4.3 Frictional pressure loss

The frictional pressure loss in a BPHE is obtained by subtracting the acceleration pressure loss, the static head loss, and the port pressure loss from the total pressure loss. Figure-5 shows the trend of the pressure drop along the mass flux, and Figure-6 shows the trend of the pressure drop along the quality at a mass flux of $34 \text{ kg/m}^2\text{s}$ and a heat flux of $4.7\text{-}5.3 \text{ kW/m}^2$. The frictional pressure drops in the BPHEs increase with increasing mass flux and quality and decreasing condensation temperature and chevron angle. This trend is similar to that of the condensation heat transfer. As mentioned above, since the vapor velocity is much faster than the liquid velocity during the two-phase flow in the tube, the vapor velocity is the dominant influence on the pressure drop, as well as the heat transfer. A high vapor velocity also tends to increase the turbulence of the flow. From Figures 3, 4, 5 and 6, we may concluded that since the trends of the the condensation heat transfer and the pressure loss in BPHEs are similar, those effects must be carefully considered in the design of a BPHE.

4.4 Comparison of R410A with R22

The ratios of R410A to R22 for the condensation heat transfer coefficients and pressure drops at a condensation temperature of 30°C are shown in the Figure-7. The ratios for the heat transfer coefficients are relatively constant in the range of 1 -1.1, regardless of the mass flux, while the ratios for the pressure drops decrease with increasing mass flux, except for the data at a chevron angle of 20° in the present experimental range. For a chevron angle of 20° , the heat transfer ratios of R410A to R22 are about 1.1, and the pressure drop ratios about 0.8, which is a 10 % higher heat transfer and a 20 % lower pressure drop. The smaller specific volume of the vapor of R410A relative to that of R22 makes the vapor velocity slower and yields a small pressure drop under the same conditions of the mass flux. While the two fluids have almost equal values of their latent heats, the liquid-phase thermal conductivity of R410A is larger than that of R22. The higher thermal conductivity for R410A helps to produce better heat transfer even if a reduction in the specific volume occurs. Also, a BPHE with a small chevron angle is known to have more effective performance from the ratios when replacing R22 with R410A.

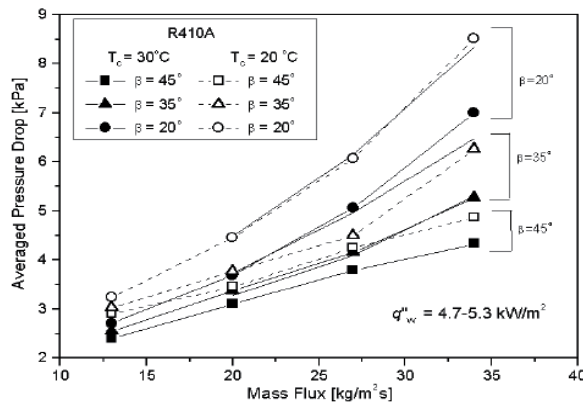


Fig. 5. Variation of the averaged condensation pressure drop with mass flux.

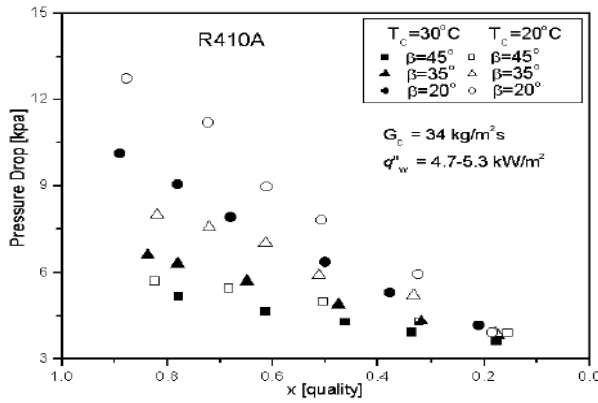


Fig. 6. Variation of the condensation pressure drop with quality.

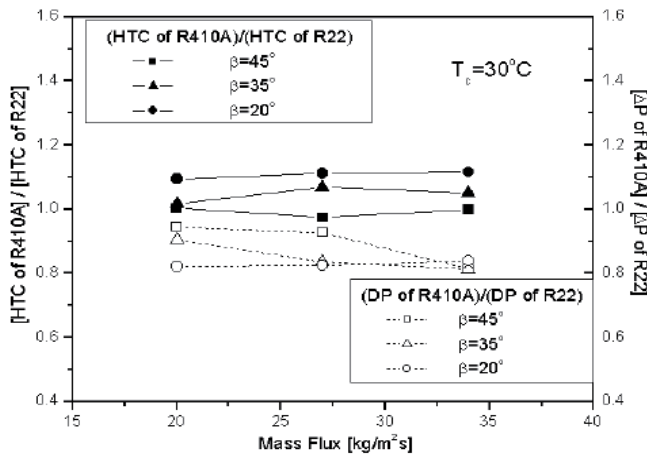


Fig. 7. Condensation heat transfer coefficient ratio and pressure drop ratio between R410A and R22.

4.5 Correlations of Nusselt number and friction factor for tested BPHEs

Based on the experimental data, the following correlations for Nu and f during condensation for the tested BPHEs are established: Where G_{e1} , G_{e2} , G_{e3} , and G_{e4} are non-dimensional geometric parameters that involve the corrugation pitch, the equivalent diameter, and the chevron angle. Re_{Eq} is the equivalent Reynolds number, and G_{Eq} the equivalent mass flux: where G_c is the channel mass flux. The suggested correlations for the Nusselt number and the friction factor can be applied in the range of Re_{Eq} from 300 to 4000. Figure-8(a) shows a comparison of the Nusselt number among the experimental data, the correlation proposed in this paper, and the correlation of Yan *et al.*, [5]. The correlation of Yan *et al.*, is

$$Nu = G_{e1} Re_{Eq}^{G_{e2}} Pr^{1/3} \quad (20)$$

$$G_{e1} = 11.22 (p_{co}/D_h)^{-2.83} (\Pi/2 - \beta)^{-4.5} \quad (21)$$

$$G_{e2} = 0.35 (p_{co}/D_h)^{0.23} (\Pi/2 - \beta)^{1.48} \quad (22)$$

$$f = G_{e3} Re_{Eq}^{G_{e4}} \quad (23)$$

$$G_{e3} = 3521.1 (p_{co}/D_h)^{4.17} (\Pi/2 - \beta)^{-7.75} \quad (24)$$

$$G_{e4} = -1.024 (p_{co}/D_h)^{0.0925} (\Pi/2 - \beta)^{-1.3} \quad (25)$$

$$Re_{Eq} = G_{Eq} D_h / \mu_f \quad (26)$$

$$G_{Eq} = G_c [1 - X + X(\rho_f / \rho_g)^{1/2}] \quad (27)$$

$$G_c = m / N_{ep} b L_w \quad (28)$$

and is obtained from one PHE with a chevron angle of 30° for R134a. Regardless of the BPHE types and refrigerants, most of the experimental data are within 20 % for the correlation proposed in this paper.

The correlation of Yan *et al.*(5), matched the data relatively well β for β : 20 and 35 within 30 %, but over-predicted the data quite a bit for 45. This discrepancy results from the correlation of Yan *et al.*, being developed for only a +30 PHE. Also, the correlation of Yan *et al.*

$$Nu = 4.118 Re_{eq}^{0.4} Pr^{1/3} \quad (29)$$

for the Nusselt number only adopted the equivalent Reynolds number and Prandtl number without any geometric parameters. Because a BPHE has a strong geometric effect, the correlation with geometric parameters must be developed for general applications. The root-mean-square (r.m.s.) of the deviations is defined as

$$r.m.s. = \sqrt{1 / N_{data} \sum (Nu_{pred} - Nu_{exp} / Nu_{exp})^2} \times 100(\%) \quad (28)$$

The r.m.s. deviation for the correlation of Yan *et al.*, [Eq. (29)] is 50.2 % and for Eq. (20), it is only 10.9 %. Figure-8(b) shows a comparison of the friction factor between the experimental

data and the proposed correlation. Similar to the correlation of the Nusselt number, the correlation of the friction factor includes the equivalent Reynolds number and the geometric parameters. Regardless of the BPHE types and refrigerants, most of the experimental data are within 15 % of the correlation proposed in this paper; the r.m.s. deviation for Eq. (23) is 10 %.

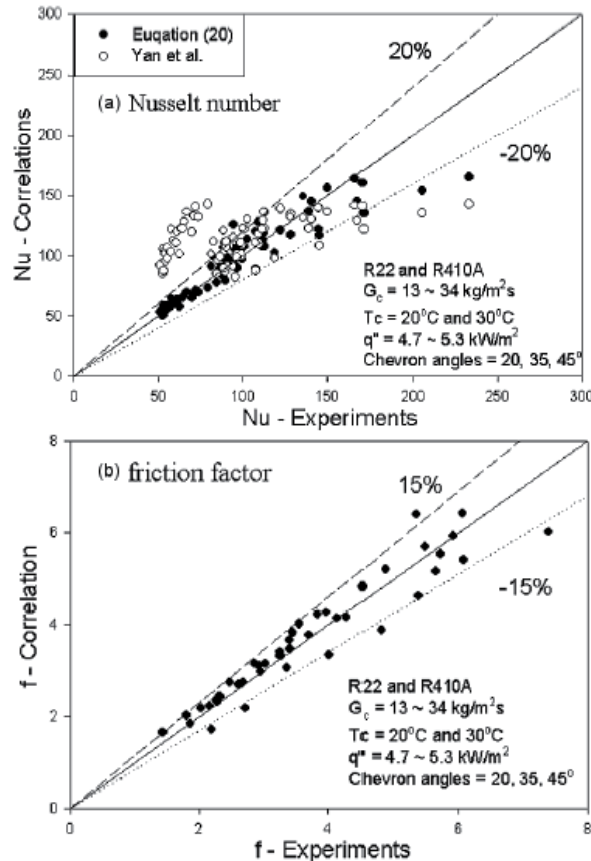


Fig. 8. Comparison of the correlations with the experimental data.

5. Study of a simplified geometry

In an effort to simulate the flow configuration, a **simple** channel was designed and constructed in order to conduct experiments and obtain formation on the flow pattern prevailing inside the furrows of the conduit. The flow configuration, apart from affecting the local momentum and heat transfer rates of a plate heat exchanger, suggests the appropriate flow model for the CFD simulation. A module of a plate heat exchanger is a single pass of the exchanger, consisting of only two plates. The simple channel examined is a single pass made of Plexiglas (**Figure 9**). It is formed by only **one** corrugated plate comprised of fourteen equal sized and uniformly spaced corrugations as well as a flat plate and it is used for pressure drop measurements and flow visualization. Details of the plate geometry are presented in **Table 2**. This model was chosen in an attempt to simplify the complexity of the

original plate heat exchanger and to reduce the computational demands. The geometry studied in the CFD simulations (similar to the test section) is shown in **Figure 10**. The Reynolds numbers examined are 400, 900, 1000, 1150, 1250 and 1400, which are based on the distance between the plates at the entrance ($d=10\text{mm}$), the mean flow velocity and the properties of water at 60°C . In addition to isothermal flow, heat transfer simulations are carried out for the same Reynolds numbers, where hot water (60°C) is cooled in contact with a constant-temperature wall (20°C). The latter case is realized in condensers and evaporators. Additionally, it is assumed that heat is transferred only through the corrugated plate, while the rest of the walls are considered adiabatic.

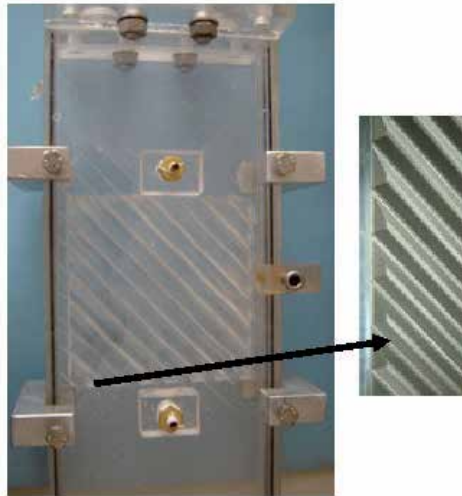


Fig. 9. Simplified model and detail of the corrugated plate.

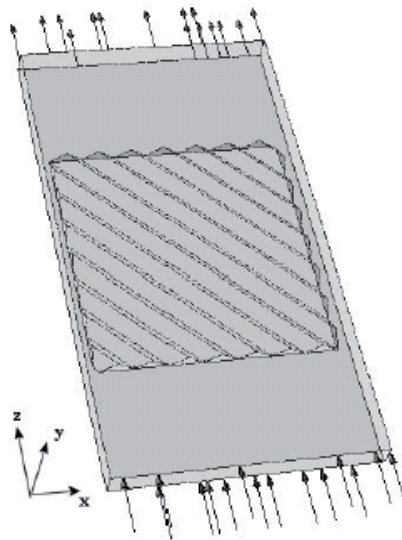


Fig. 10. CFD model.

A commercial CFD code, namely the *CFX* ® 5.6 code developed by *AEA Technology*, was employed to explore its potential for computing detailed characteristics of this kind of flow. In general, the models used in CFD codes give reasonably good results for single-phase flow systems. The first step in obtaining a solution is the division of the physical domain into a solution mesh, in which the set of equations is discretised.

The grid size used is selected by performing a grid dependence study, since the accuracy of the solution greatly depends on the number and the size of the cells. The resulting mesh was also inspected for inappropriate generated cells (e.g. tetrahedral cells with sharp angles) and fixed, leading to a total number of 870,000 elements. The *SST* model was employed in the calculations for the reasons explained in the previous chapter. The mean velocity of the liquid phase was applied as boundary condition at the channel entrance (i.e. Dirichlet BC on the inlet velocity) and no slip conditions on the channel walls. A constant temperature boundary condition was applied only on the corrugated wall, whereas the rest of the walls are considered adiabatic. Calculations were performed on a *SGI O2 R10000* workstation with a 195MHz processor and 448Mb RAM. The *CFX* ®5.6 code uses a finite volume method on a non-orthogonal body-fitted multi-block grid. In the present calculations, the *SIMPLEC* algorithm is used for pressure-velocity coupling and the *QUICK* scheme for discretisation of the momentum equations [31],[32].

Plate Length	0.200 m
Plate width	0.110 m
Maximum spacing between plates	0.010 m
Number of corrugations	14
Corrugation angle	45 °
Corrugation pitch	0.005 m
Corrugation width	0.014 m
Plate length before and after corrugations	0.050 m
Heat transfer area	$2.7 \times 10^{-2} \text{ m}^2$

Table 2. Simple Channel's plate geometric characteristics.

The results of the present study suggest that fluid flow is mainly directed inside the furrows and follows them (*Figure 11a*). This type of flow behavior is also described by Focke & Knibbe[7], who made visual observations of the flow between two superposed corrugated plates (*Figure 11b*). They confirm that the fluid, after entering a furrow, mostly follows it until it reaches the side wall, where it is reflected and enters the anti-symmetrical furrow of the plate above, a behavior similar to the one predicted by the CFD simulation. It seems that, in both cases, most of the flow passes through the furrows, where enhanced heat transfer characteristics are expected.

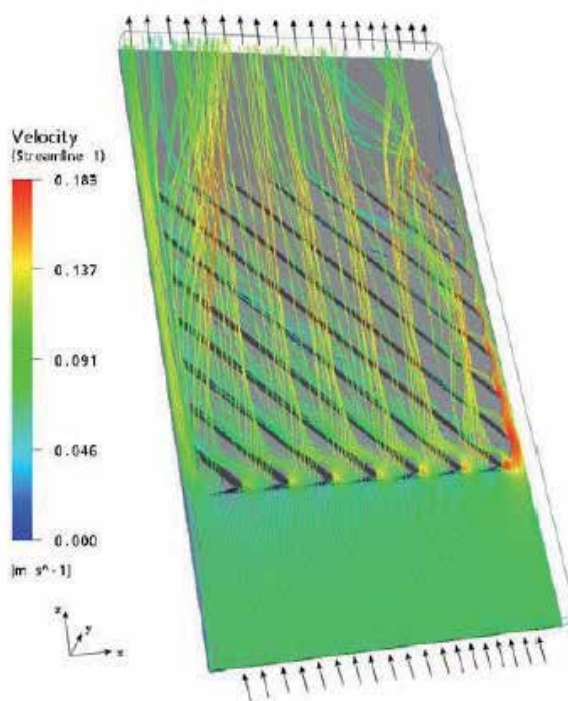


Fig. 11A. Typical flow pattern for the: a) simple channel, CFD results, $Re=900$.

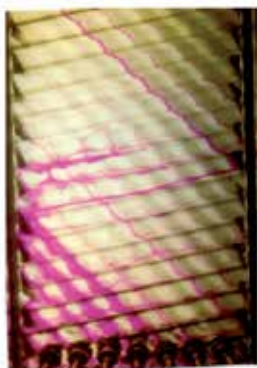


Fig. 11B. Flow visualization by Focke & Knibbe[7], $Re=125$.

Figure 12 shows details of the flow inside a furrow for the simple model, where swirling flow is identified. This secondary flow is capable of bringing new fluid from the main stream close to the walls, augmenting heat transfer rates. Focke & Knibbe[18], who performed visualization experiments in similar geometries, also describe this kind of swirling flow. The values of the z -component of shear stress (**Figure 13a**) increase with the Reynolds number –as expected– and the maximum value occurs at the crests of the corrugations. It may be argued that, during gas-liquid counter-current flow in such geometries, the shear stress distribution tends to prevent the liquid layer from falling over

the crest of the corrugations and to keep it inside the furrows. The visual observations of Paras et al.[14] seem to confirm the above behavior. The heat flux through the wall of the corrugated plate was calculated by the CFD code. In addition, the local Nusselt number was calculated (by a user-Fortran subroutine) using the expression:

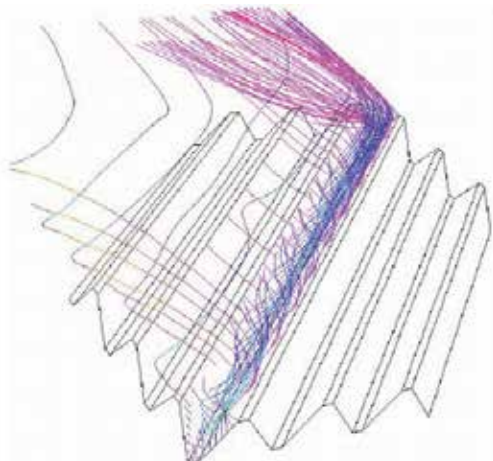


Fig. 12. Swirling flow inside a furrow; Re=900.

$$Nu_x = qd / (T_b - T_w) k \quad (31)$$

Where q' is the local wall heat flux, d the distance between the plates at the entrance, T_w the wall temperature, T_b the local fluid temperature and k the thermal conductivity of the fluid. In addition to the local Nusselt number, mean Nusselt numbers were calculated as follows:

* A *mean Nu* calculated by numerical integration of the local *Nu* over the *corrugated area only*, and

* An *overall average Nu* calculated using the total wall heat flux through the *whole* plate and the fluid temperatures at the channel entrance/exit.

The comparison of the values of the above Nusselt numbers shows that they do not differ more than 1%; therefore, the smooth part of the corrugated plate does not seem to influence the overall heat transfer. **Figure 13b** shows a typical local Nusselt number distribution over the corrugated wall for Re=900. All the Reynolds numbers studied exhibit similar distributions.

It is noticeable that local Nusselt numbers attain their maximum value at the top of the corrugations. This confirms the strong effect of the corrugations, not only on the flow distribution, but also on the heat transfer rate. To the best of author's knowledge, experimental values of heat transfer and pressure drop are very limited in the open literature for the corrugated plate geometry, since these data are proprietary. Therefore, the data of Vlasogiannis et al.[16] were used to validate the simulation results. These data concern heat transfer coefficients measurements of both single (Re<1200) and two-phase flow in a plate heat exchanger with corrugated walls and a corrugation inclination angle of 60°. Heavner et al.[14] proposed a theoretical approach, supported by experimental data, to predict heat transfer coefficients of chevron-type plate heat exchangers. **Figure 14** presents

the experimental friction factors, obtained from the Plexiglas test section of **Figure 9**, as well as the CFD predictions for the simple geometry studied, as a function of the Reynolds number. It appears that the experimental values follow a power law of the form:

$$f = m \text{Re}^{-n} \quad (32)$$

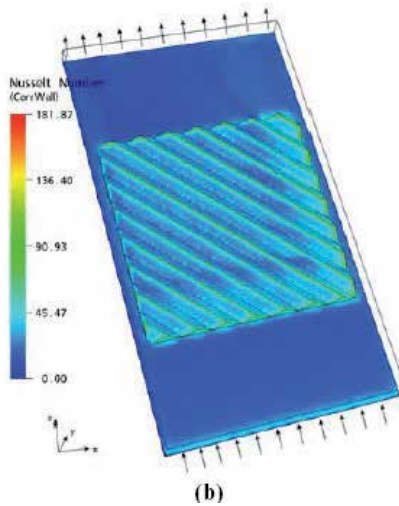
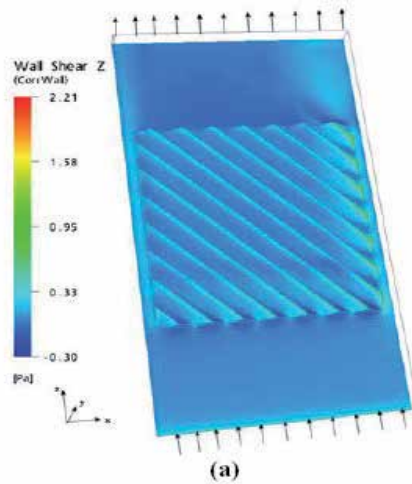


Fig. 13. Typical results of the CFD simulation for $\text{Re}=900$; distributions of: (a) z -shear stress component, (b) local Nusselt number.

Where m and n constants with values 0.27 and 0.14 respectively. Heavner et al.[14] proposed a similar empirical correlation based on their experimental results on a single pass of a plate heat exchanger with 45° corrugation angle, but with two corrugated plates. In spite of the differences in geometry, it appears that the present results are in good agreement with the experimental data of Heavner et al.[14] (0.687 and 0.141 for the variables m and n , respectively).

It must be noted that Focke et al.[15] , who also measured heat transfer coefficients in a corrugated plate heat exchanger having a partition of celluloid sheet between the two plates, reported that the overall heat transfer rate is the 65% of the corresponding value without the partition. **Figure 15** shows that the mean j -Colburn factor values calculated using the *overall* Nusselt number are practically equal to the 65% of the values measured by Vlasogiannis et al. This holds true for all Reynolds numbers except the smallest one ($Re=400$). In the latter case the Nusselt number is greatly overpredicted by the CFD code. This is not unexpected, since the *two-equation turbulence* model is not capable to predict correctly the heat transfer characteristics for such low Reynolds number. The CFD results reveal that the corrugations enhance the heat transfer coefficient, whereas the pressure losses due to the augmentation of friction factor f are increased (**Table 3**), compared to a smooth-wall plate heat exchanger. Additionally, comparison of the normalized values of Nusselt number and the friction factor, with respect to the corresponding values for the smooth plate (f_{sm} , Nu_{sm}), indicates that as the Reynolds number increases, heat transfer enhancement is slightly reduced, while the friction factor ratio, fff , is increased. This is typical for plate heat exchangers with corrugations [16].

Re	Nu_{vlasog}	65% Nu_{vlasog}	Nu_{all}	Nu_{sm}	Nu_{ave}/Nu_{sm}	F/f_{sm}
400	13.2	8.6	20.5	-	-	-
900	38.0	24.7	27.3	9.4	2.9	12.4
1000	41.2	26.8	28.6	10.2	2.8	12.8
1150	44.2	28.7	28.8	11.0	2.7	13.5
1250	46.8	30.4	30.9	11.7	2.7	13.9
1400	49.5	32.2	32.0	12.5	2.6	14.5

Table 3. Experimental values, calculated Nusselt numbers and normalised values of N_u and f

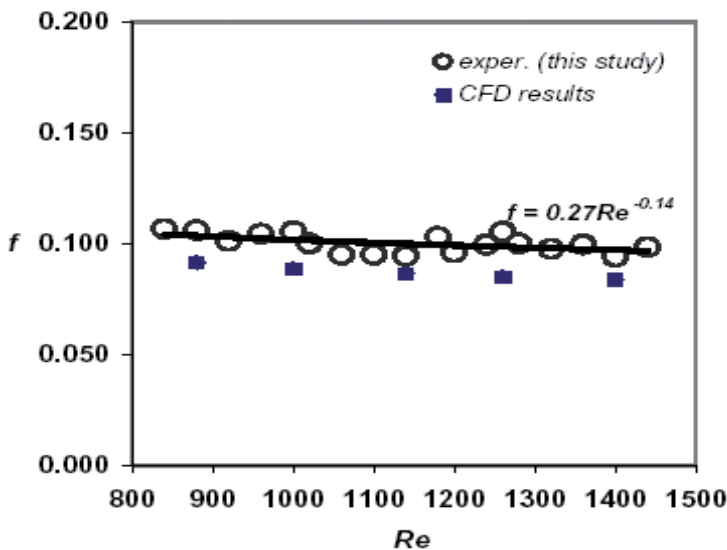


Fig. 14. Comparison of friction factor predictions (CFD) with experimental data.

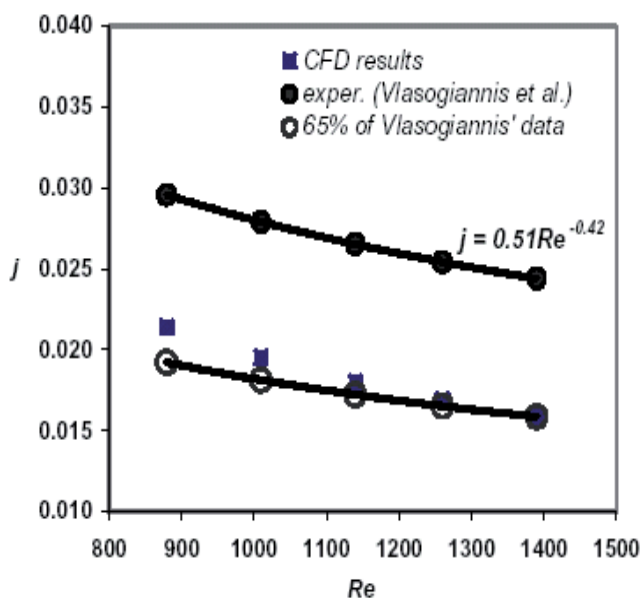


Fig. 15. Comparison of j -Colburn factor predictions (CFD) with experimental data.

6. Study of a heat exchanger channel

The results for the simplified geometry confirm the validity of the CFD code and strongly encourage the simulation of a module (pass) consisting of two corrugated plates of a compact heat exchanger (**Figure 16a**). In order to quantitatively evaluate the results of this simulation, the experimental setup of Vlasogiannis et al.[16] was used as the design model (**Figure 16b**). Due to the increased computational demands, an AMD AthlonXP 1.7GHz workstation with 1GB RAM was used. The geometric characteristics of the new model are presented in **Table 4**.

Plate length	0.430 m
Plate width	0.100 m
Mean spacing between plates	0.024 m
Corrugation angles	60°
Corrugation area length	0.352 m

Table 4. Geometric characteristics of the model with two corrugated plates.

Preliminary results of the present study, which is still in progress, are shown in **Figure 17**. It is obvious that the herringbone design promotes a symmetric flow pattern (**Figure 16b**). Focusing on the left half of the channel (**Figure 17a**), a close-up of the flow streamlines (**Figure 17b**) reveals a "peacock-tail" pattern as the liquid flows inside the furrows and over the corrugations. The same flow pattern, which is characteristic for this type of geometry, has also been observed by Paras et al.[14] in similar cross-corrugated geometries (**Figure 17c**), where "dry areas" of ellipsoidal shape are formed around the points where the

corrugations come into contact. The effect of fluid properties (e.g. surface tension, viscosity) on the shape and the extent of these areas, which are considered undesirable, will be examined in the course of this study.

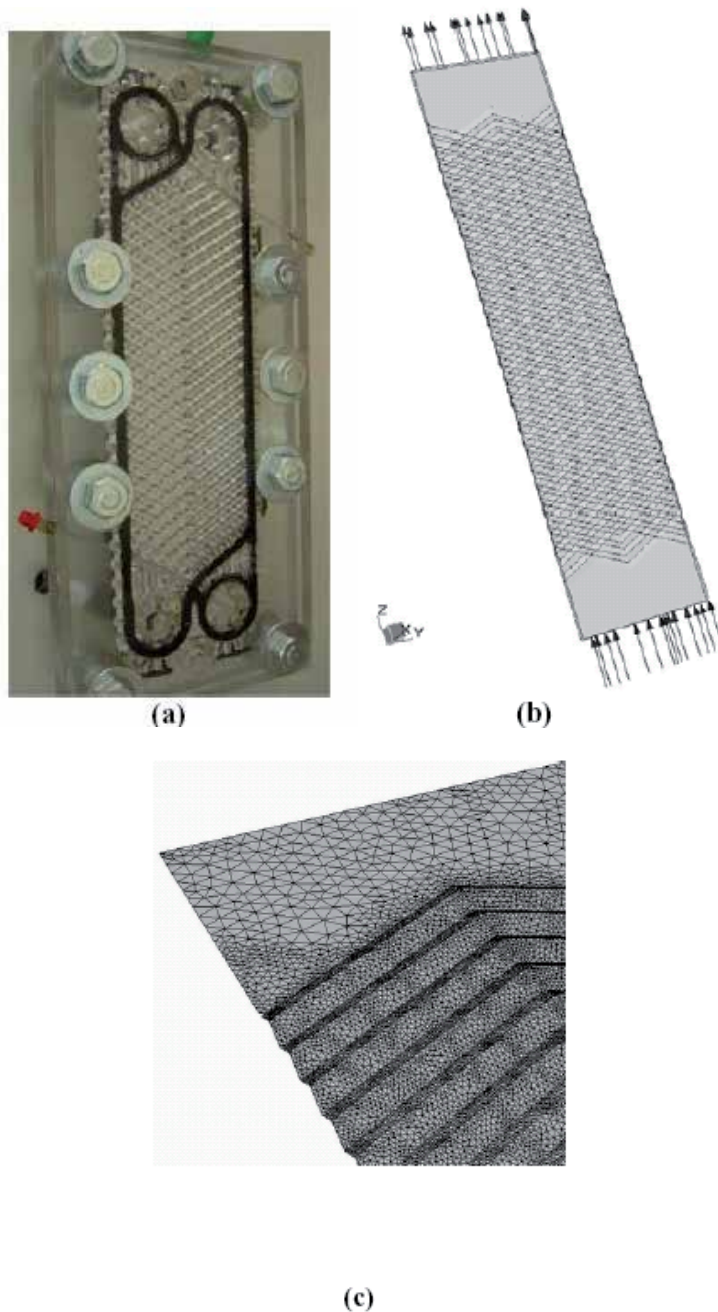
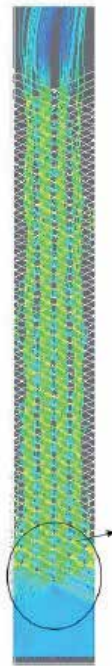
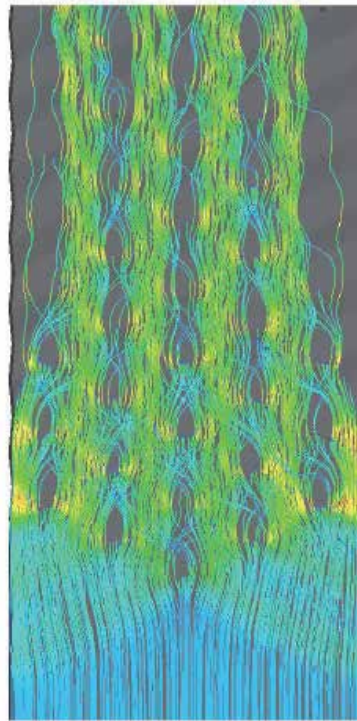


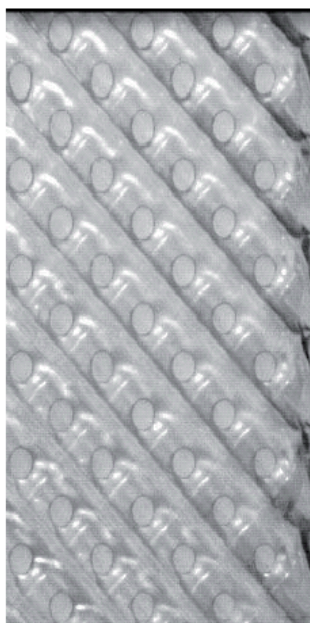
Fig. 16. (a) Module of a corrugated plate exchanger; (b) The CFD model and (c) Detail of the grid distribution over the corrugated wall.



(a)



(b)



(c)

Fig. 17. (a) Streamlines in the left half of the channel; (b) Close up of the flow pattern; (c) Photo of the flow in the cross-corrugated geometry [14].

7. Conclusion

An experimental investigation has been conducted to measure the condensation heat transfer coefficient and the pressure drop of R410A and R22 in BPHEs with chevron angles of 20, 35, and 45 degrees. The experimental data were taken at two different condensation temperatures of 20°C and 30°C in the range of mass flux of 14-34 kg/m²s with a heat flux of 4.7 -5.3 kW/m².

- Both the heat transfer coefficient and the pressure drop increased proportionally with the mass flux and the vapor quality and inversely with the condensation temperature and the chevron angle. Those effects must be carefully considered in the design of a BPHE due their opposing effects.
- A comparison of the data for R410A and R22 showed that the heat transfer coefficient for R410A was about 0 - 10 % larger and the pressure drop about 2- 21 % lower than those for R22. Therefore, R410A is a suitable alternative refrigerant for R22.
- Correlations for the Nusselt number and the friction factor with the geometric parameters were suggested for the tested BPHEs within 20 % (r.m.s. deviation: 10.9 %) for Nu and 15 % (r.m.s. deviation: 10 %) for f.

Although compact heat exchangers with corrugated plates offer many advantages compared to conventional heat exchangers, their main drawback is the absence of a general design method. The variation of their basic geometric details (i.e. aspect ratio, shape and angle of the corrugations) produces various design configurations, but this variety, although it increases the ability of compact heat exchangers to adapt to different applications, renders

it very difficult to generate an adequate 'database' covering all possible configurations. Thus, CFD simulation is promising in this respect, as it allows computation for various geometries, and study of the effect of various design configurations on heat transfer and flow characteristics.

In an effort to investigate the complex flow and heat transfer inside this equipment, this work starts by simulating and studying a simplified channel and, after gaining adequate experience, it continues by the CFD simulation of a module of a compact heat exchanger consisting of two corrugated plates. The data acquired from former simulation is consistent with the single corrugated plate results and verifies the importance of corrugations on both flow distribution and heat transfer rate. To compensate for the limited experimental data concerning the flow and heat transfer characteristics, the results are validated by comparing the overall Nusselt numbers calculated for this simple channel to those of a commercial heat exchanger and are found to be in reasonably good agreement. In addition, the results of the simulation of a complete heat exchanger agree with the visual observations in similar geometries.

Since the simulation is computationally intensive, it is necessary to employ a cluster of parallel workstations, in order to use finer grid and more appropriate CFD flow models. The results of this study, apart from enhancing our physical understanding of the flow inside compact heat exchangers, can also contribute to the formulation of design equations that could be appended to commercial process simulators. Additional experimental work is needed to validate and support CFD results, and towards this direction there is work in progress on visualization and measurements of pressure drop, local velocity profiles and heat transfer coefficients in this type of equipment.

8. Appendix

Nomenclature

A	heat transfer area of plate [m ²]
b	mean channel spacing [m]
C _p	constant pressure specific heat [J/kg K]
D	diameter [m]
f	friction factor
G	mass flux [kg/m ² s]
Ge	non-dimensional geometric parameter
g	gravitational acceleration [m/s ²]
h	heat transfer coefficient [W/m ² K]
i	enthalpy [J/kg]
j	superficial velocity [m/s]
L _c	distance between the end plates [m]
L _h	distance between the ports [m]
L _v	vertical length of the fluid path [m]
L _w	horizontal length of the plates [m]
LMTD	log mean temperature difference [°C]
m	mass flow rate [kg/s]
N _{cp}	number of channels for the refrigerant

N_{data}	total number of data
N_t	total number of plates
Nu	Nusselt number
Nu_{exp}	Nusselt number obtained from experiment
Nu_{pred}	Nusselt number obtained from correlation
p	plate pitch [m]
p_{co}	corrugation pitch [m]
Pr	Prandtl number [v]
Q	heat transfer rate [W]
q	heat flux [W/m^2]
Re	Reynolds number
T	temperature [$^{\circ}C$]
t	plate thickness [m]
U	overall ht coefficient [$W/m^2 K$]
x	quality

Subscripts

a	acceleration
c	channel
Eq	equivalent
f	liquid
fg	difference the liquid phase and the vapor phase
fr	friction
g	vapor
in	inlet
lat	latent
m	mean
out	outlet
p	port
pre	pre-heater
r	refrigerant
s	static
sat	saturated
sens	sensible
w	water

9. References

- [1] X. Rong, M. Kawaji and J.G. Burgers, Two-phase header flow distribution in a stacked plate heat exchanger, *Proceedings ASME/JSME FED-Gas Liquid Flows* 225 (1995), pp. 115-122.
- [2] H. Martin, 1996, A theoretical approach to predict the performance of chevron-type plate heat exchangers, *Chemical Engineering and Processing: Process Intensification*, Volume 35, Issue 4, Pages 301-310.
- [3] G. J. Lee, J. Lee C. D. Jeon and O. K. Kwon. 1999. In: Plate Heat Exchanger with chevron angles ,*Proceedings of the 1999 Summer Meeting of the SAREK*, edited by C. S. Yim (SAREK, Nov.). p. 144.

- [4] M. A. Kedzierski. 1997. Heat Exchanger Multiphase flow, Heat Transfer Engineering. Volume 5, issue 3 page 18: 25.
- [5] Y. Y. Yan, H. C. Lio and T. F. Lin. 1999. Different Chevron angles in plate heat exchanger, of Heat and Mass Transfer. Volume 11, issue 4 pages 42: 93
- [6] Y. Y. Hsieh and T. F. Lin. 2002.plate heat exchanger design theory, International journal of Heat and Mass Transfer. Volume 21, issue 9 pages 1033-45.
- [7] Y. S. Kim. 1999. Plate heat exchanger design, M.S. Thesis. Yonsei University.
- [8] S. Kakac and H. Liu. 1998. Heat Exchangers Selection, Rating and Thermal Design. CRC Press, Boca Raton. Volume 8, issue 9 pages 323-329
- [9] R. J. Mo. 1982. Model of plate heat exchanger, ASME Journal of fluid engineering, Volume 11, issue 9 pages 173-179
- [10] P. Vlasogiannis, G. Karajiannis. 2002. Compact heat exchangers, International journal Multiphase Flow.21, issue 9 pages 728: 757.
- [11] T. J. Crawford, C. B. Weinberger and J. Weisman. 1985. heat exchangers International journal Multiphase Flow.21, issue 9 pages 291: 297.
- [12] Shah, R.K., Wanniarachchi, A.S. (1991), Plate heat exchanger design theory, In: Buchlin, J.-M. (Ed.),Industrial Heat Exchangers, von Karman Institute Lecture Series 1991-04.
- [13] Kays, W.M. & London, A.L. (1998), Compact heat exchangers, 3rd Ed. Krieger Publ. Co., Florida.
- [14] Paras, S.V., Drosos, E.I.P., Karabelas, A.J, Chopard, F. (2001), "Counter-Current Gas/Liquid Flow Through Channels with Corrugated Walls-Visual Observations of Liquid Distribution and Flooding", World Conference on Experimental Heat Transfer, Fluid Mechanics & Thermodynamics, Thessaloniki, September 24-28.
- [15] Ciofalo, M. Collins, M.W., Stasiek, J.A. (1998), Flow and heat transfer predictions in flow passages of air preheaters: assessment of alternative modeling approaches, In: Computer simulations in compact heat exchangers, Eds. B. Sundén, M.Faghri, Computational Mechanics Publ. U.K.
- [16] Vlasogiannis, P., Karagiannis, G., Argyropoulos, P., Bontozoglou, V. (2002), "Air-water two-phase flow and heat transfer in a plate heat exchanger", Int. J. Multiphase Flow, 28, 5, pp. 757-772.
- [17] Lioumbas, I.S., Mouza, A.A., Paras, S.V. (2002), "Local velocities inside the gas phase in counter current two-phase flow in a narrow vertical channel", Chemical Engineering Research & Design, 80, 6, pp. 667-673.
- [18] Focke, W.W., Knibbe, P.G. (1986), "Flow visualization in parallel-plate ducts with corrugated walls", J. Fluid Mech., 165, 73-77.
- [19] Davidson, L. (2001), An Introduction to Turbulence Models, Department of Thermo and Fluid Dynamics, Chalmers University of Technology, Göteborg, Sweden.
- [20] Menter, F., Esch, T. (2001), "Elements of Industrial Heat Transfer Predictions", 16th Brazilian Congress of Mechanical Engineering (COBEM), 26-30 Nov. 2001, Uberlandia, Brazil.
- [21] AEA Technology (2003), CFX Release 5.6 User Guide, CFX International, Harwell, Didcot, UK.
- [22] Wilcox,D(1988), "Reassessment of the scale-determining equation", AIAA Journal, 26,11.

- [23] Mehrabian, M.A., Poulter, R. (2000), "Hydrodynamics and thermal characteristics of corrugated channels: computational approach", *Applied Mathematical Modeling*, 24, pp. 343-364.

Part 5

Energy Storage Heat Pumps Geothermal Energy

PCM-Air Heat Exchangers: Slab Geometry

Pablo Dolado, Ana Lázaro, José María Marín and Belén Zalba
*University of Zaragoza / I3A - GITSE
Spain*

1. Introduction

Energy efficiency and the search for new energy sources and uses are becoming main objectives for the scientific community as well as for society in general. This search is due to various environmental issues and shortages of conventional and non-sustainable energy resources, for example fossil fuels, that are essential to industrial development and to daily life. Free-cooling in buildings, bioclimatic architecture applications, demand and production coupling in renewable energy sources, as solar energy, are examples of thermal energy storage contributions to achieve these objectives. The application of Phase Change Materials (hereafter PCM) in Thermal Energy Storage (hereafter TES) is an expanding field due to the variety of materials being developed. There are four critical considerations for the technical viability of these applications: 1) The features of both the PCM and the encapsulation material must be stable during the system lifetime; 2) A reliable numerical model of the system to simulate different operational conditions; 3) The thermophysical properties of the PCM; 4) The cost of the system.

Specifically, the solid-liquid phase change phenomenon of the PCM is being widely studied in the field of TES, both experimentally and numerically, because this technology is of great interest among different fields: from applications in electronics, textile, transport... to applications in aerospace or thermo-solar power plants. The incorporation of these materials on the market, as stated before, is conditioned partly by its price. To cope with this situation, manufacturers often sell PCM as non-pure substances or mixtures which, on the one hand, lower their costs but, on the other hand, condition its thermophysical properties so that they are not as well established as in pure substances. Generally, this determining factor leads to a nonlinearity of the temperature dependence of the thermophysical properties of the PCM. This issue is another aspect to consider when simulating the thermal behaviour of these substances. Therefore, it is essential a good determination of these properties as they are input values to the theoretical models that simulate the thermal performance of devices based on these materials, some of which may strongly condition the results of the simulations.

When working at ambient temperatures, there are different situations where TES with PCM can be applied. Zalba et al., 2003, presented a comprehensive review on latent heat TES and its applications. The authors remarked that low values of λ_{PCM} can lead to real problems in the systems since there could be insufficient capacity to dispose of the stored energy quickly enough. Later, Sharma et al., 2009, presented another review highlighting that there was

scarce literature on the melt fraction studies of PCM used in the various applications for storage systems. Many of these applications have been studied widely in the last years; most are related to buildings and several to heat exchange between PCM and air as the heat transfer fluid:

- Ceiling cooling systems and floor heating systems including a PCM storage device were studied by authors like Turnpenny et al., 2001, and Yanbing & Yinping, 2003.
- Free-cooling has demonstrated to be an attractive application for latent heat storage using PCM. This application is reported in the work carried out by Butala & Stritih, 2009, and Lazaro et al., 2009a.
- Solar air heating systems are important in many industrial and agricultural applications, such as those reported in the papers by Kürklü, 1998.
- Other interesting possibilities are temperature maintenance/control in rooms with computers or electrical devices, and the pre-cooling of inlet air in a gas turbine (Bakenhus, 2000).

In any case, it is crucial to achieve efficient heat exchange between the heat transfer fluid and the PCM. This point is strongly affected by the heat exchanger geometry, as the TES unit has limited periods of time to solidify. Lazaro, 2009, compared the PCM-air heat exchange geometries studied by different researchers (Arkar et al., 2007; Turnpenny et al., 2000; Zalba et al., 2004; Zukowsky 2007). The author pointed out the difficulty of comparing between the different results provided by the authors, since each one show the results in its own way. Therefore, Lazaro concluded the need to standardize for proper comparison. Lazaro et al., 2009b, also presented experimental results for melting stage of real PCM-air heat exchangers pointing out the importance of the geometry. Geometry issues also affect the pressure drop of the TES unit and the air pumping requirements of the system, i.e., the electrical energy consumption. Regarding experimental studies, the evaluation of the thermal behaviour of the TES unit under statistical approaches or mathematical fitting leads to expressions that are very useful tools when designing such units. Among others, Butala & Stritih, 2009, and Lazaro et al., 2009b, followed this methodology when they evaluated their results.

In this chapter, a specific case study on slab geometry of a PCM-air heat exchanger is presented for temperature maintenance in rooms. However, the methodology posed here can be extrapolated to other different PCM geometries and system setups.

2. Pre-design: important factors

Since non-pure substances have lower costs than pure materials, they are used in commercial PCM. The characterization of the PCM and its encapsulation material are required to choose the optimal PCM and to design the heat exchanger for each application. The thermophysical properties of the PCM as a function of temperature are essential to the numerical model. Such information is not available for commercial PCM. This section therefore aims at the development of an adequate methodology to characterize PCM. Subsequently, the design of an experimental setup is explained, directed towards the determination of the enthalpy vs. temperature curves, by using the T-history method. The setup was built and a methodology was proposed to verify the T-history setups. The same methodology is applied to determine thermal conductivity, another essential thermal

property regarding heat transfer. As a result of the application of the existing methods to analyze the liquid and solid phases, the most suitable method is chosen and the setup was started up. Besides the energy storage capacity and the thermal conductivity as a function of temperature, other properties are also important to be known, such as the compatibility of the PCM with the encapsulation material.

2.1 Determination of enthalpy as a function of temperature

In order to obtain the most suitable method to determine enthalpy as a function of temperature during the solid-liquid phase change, two main thermal analysis methods were studied: differential scanning calorimetry (DSC) and adiabatic calorimetry. In addition, a customized method was studied: the T-history method. A complex review of the work on thermophysical properties was carried out with some conclusions being (Lazaro, 2009):

- DSC is the most used method for determining the storage capacity because it is the most common commercial device (Zhang D. et al., 2007).
- There are several problems with using DSC for non pure and low thermal conductivity substances (Arkar & Medved, 2005).
- The number of authors that use the enthalpy vs. temperature curves to express the storage capacity of PCM is increasing (Zalba et al., 2003).

DSC, adiabatic calorimetry and T-history method were studied and compared. Factors considered in the method selection are: sample size, heating and cooling rate, obtainability of the h-T curve, introduction to the market, easiness to build, cost, use, maintenance. The T-history method was selected as it provides the enthalpy vs. temperature curves and also uses sample sizes and heating/cooling rates similar to those used in real applications.

2.1.1 The T-history method

Zhang et al., 1999, developed a method to analyze PCM enthalpy. The T-history method is based on an air enclosure where the temperature is constant and two samples are introduced at a different temperature from the temperature in the air enclosure. During cooling processes, three temperatures are registered: the ambient (air enclosure) and those of the two samples. The two samples are one reference substance whose thermal properties are known (frequently water) and one PCM whose thermal properties will be determined with the results of the test. Figure 1 shows the basic scheme of the T-history method.

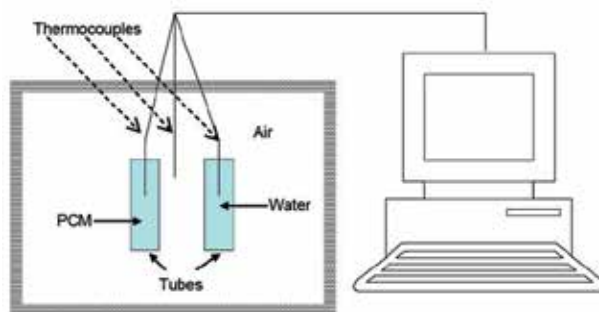


Fig. 1. Scheme of T-history installation.

The basic aspects of the T-history method are (Zhang et al., 1999):

- Heat transfer is one-dimensional in the radial direction since the samples containers are long cylinders.
- Containers with water and PCM samples are designed with $Bi < 0.1$ and therefore are considered capacity systems.
- Heat transfer occurs by free convection between the samples and air. Containers must be identical in order to have a very low and almost the same free convection coefficient.

To evaluate the temperature vs. time evolution, Zhang proposed three stages: liquid, phase change, and solid. Therefore, with this method it is possible to obtain $c_{p,liquid}$, $c_{p,solid}$ and h_{sl} . Marin et al., 2003, made improvements, based on the finite increments method, in order to obtain the h-T curves. Figure 2 shows how the calculations were carried out.

$$m_p \Delta h_p(T_i) + m_t c_{pt}(T_i)(T_i - T_{i+1}) = h A_t \int_{t_i}^{t_i + \Delta t_i} (T - T_{\infty, a}) dt = h A_t A_i \quad (1a)$$

$$\left[m_t c_{pt}(T) + m_w c_{pw}(T) \right] (T_i - T_{i+1}) = h A_t \int_{t^i}^{t^i + \Delta t^i} (T - T_{\infty, a}) dt = h A_t A_i \quad (1b)$$

$$\Delta h(T_i) = \left(\frac{m_w c_{pw}(T_i) + m_t c_{pt}(T_i)}{m_p} \right) \frac{A_i}{A_i'} \Delta T_i' \frac{m_t}{m_p} c_{pt}(T_i) \Delta T_i \quad (1c)$$

$$h_p(T) = \sum_{i=1}^N \Delta h_{pi} + h_{p0} \quad (1d)$$

$$c_p = \partial h / \partial T \quad (1e)$$

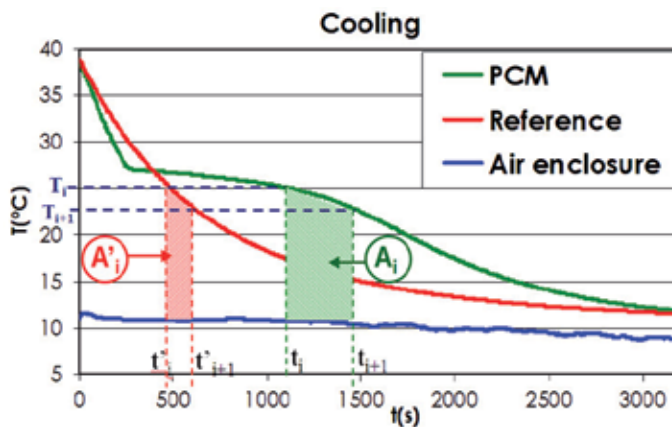


Fig. 2. Calculation of the improvements achieved by Marin et al., 2003.

The set of equations 1 summarize the calculations considering the improvements. There A_t denotes the tube lateral area, m_p the PCM mass, m_t the tube mass, c_{pt} the specific heat of the tube, c_{pw} the specific heat of water, h the convection coefficient whereas $h(T)$ denotes enthalpy. The little temperature steps, ΔT_i , varies in accord to the corresponding time intervals for the PCM ($\Delta t_i = t_{i+1} - t_i$) and for water ($\Delta t'_i = t'_{i+1} - t'_i$). The integral of the temperature difference against time, is the area under the curve in Figure 2 for the PCM (A_i) and for water (A'_i).

2.1.2 Design of a new installation to implement the T-history method

When analyzing errors with T-history, the most important factor is the precision in the temperature measurement. Thermal sensors used in previous implementations have been thermocouples, while Pt-100 was chosen for this new installation due to the higher precision: $\pm 0.05^\circ\text{C}$ with a 4 threads assembly. However, Pt-100 has a longer response time, but will not affect the results provided that the response time is the same for all temperature measurements. This objective is achieved by using Pt-100 of the same manufacture set, and characteristics will be identical. Enthalpy is expressed in a mass unit basis; therefore the precision in mass measurements is as important as the precision in temperature measurements. A 0.1 mg precision scale is used to measure the mass of samples. The sample containers have been designed so that the method standards are fulfilled ($Bi < 0.1$). Churchill-Chu (Marin & Monne, 1998) natural convection correlations for cylinders were used to calculate the suitable radius/length rate of the tubes. The chosen material was glass, since it allows the observation of the phase change process. Cylinders of 13 cm in length and 1 cm in diameter were used. A data logger was used with a RS-232 connection with 22 bits and 6 1/2 resolution. A thermostatic bath (0.1 K precision) was used to fix the initial temperature of the samples. A calculation software, especially developed in Labview, was used to obtain the h-T curves. The new T-history implementation based its improvements on:

- Obtainability of the h-T curves during cooling and heating.
- Horizontal position of samples in the air enclosure, minimizing convective movements.
- Utilization of more precise instrumentation.
- A program designed (Labview) for calculations and real time view of the measurements.
- A guarantee that there is no contribution of heat transfer by radiation.

Examples of T-history analysis applied to two typical PCM (organic and inorganic) are shown in Figure 3. Typical phenomena as hysteresis or sub-cooling can also be observed.

The objective of analyzing organic and inorganic substances is to confirm the expected differences in behaviour: the inorganic PCM presents the sub-cooling phenomenon that occurs during cooling, presenting more hysteresis and quite higher stored energy density when compared to organic PCM.

The procedure used was: mass measurements of the samples and sample containers using a precision scale, then the Pt-100 were introduced into the samples (one into the PCM and one into the water), and the tubes were inserted into the thermostatic bath at the desired initial temperature. The initial temperature depends on the PCM to be tested as well as if it is for a heating or a cooling test. For a heating test, the initial temperature must be lower than the phase change temperature. For a cooling test, it must be higher. Once the temperature inside

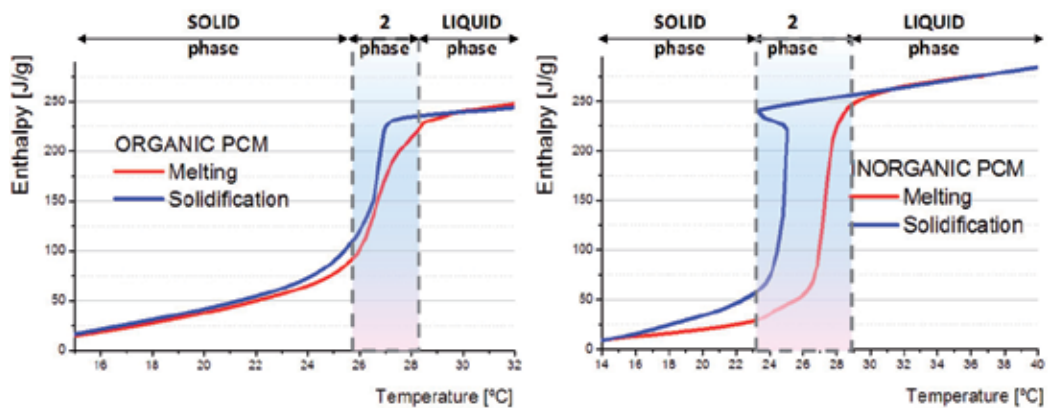


Fig. 3. T-history results for an organic PCM (left) and for an inorganic one (right).

the PCM and water is fixed, the tubes are inserted into the air enclosure and the measurement starts. The enthalpy was calculated as shown previously in equations 1.

Detailed information on the raw data and calculations can be found in Lazaro, 2009. An example of the outputs window (Labview application) of an arbitrary T-history test is shown in Figure 4.

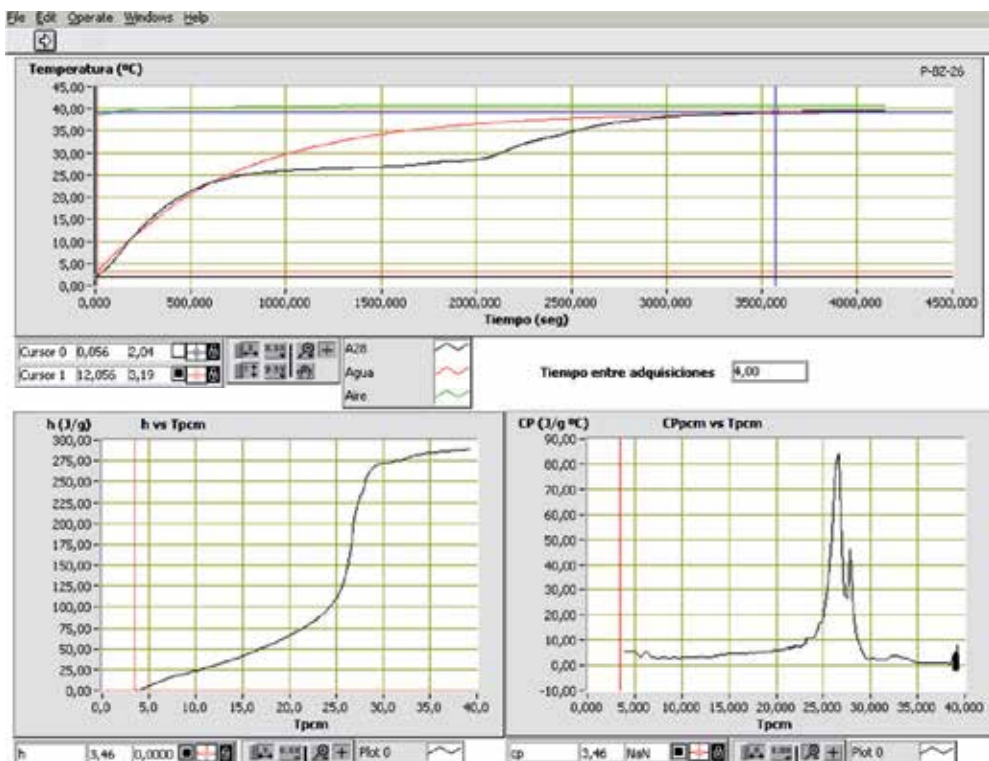


Fig. 4. Calculation outputs of a typical T-history test: measured temperatures (up), PCM enthalpy (down-left) and PCM specific heat (down-right).

2.2 Thermal conductivity

The same procedure to select the appropriate method to obtain the enthalpy vs. temperature curves was followed to find the method for thermal conductivity measurement in liquid and in solid phases. The most commonly used method is the hot wire method (Watanabe, 2002), nevertheless the temperature of the sample is measured with low accuracy and there is also the difficulty in measuring solid samples. A stationary parallel plate method (Mills et al., 2006) solves the problem of accuracy in temperature measurements, but in the liquid phase, convective movements affect the results. The Laser Flash is the only method that allows measuring the thermal diffusivity and sample temperature with accuracy, both in liquid and solid phases. It is based on a laser pulse that comes into contact with one surface of the sample and the temperature evolution on the opposite surface is measured by an infrared detector; therefore, the thickness of the sample must be perfectly determined. A mathematical evaluation of the temperature evolution allows the determination of the thermal diffusivity α of the sample (equation 2) and by measuring the heat capacity c_p with a DSC, also the thermal conductivity λ may be obtained:

$$\alpha = \frac{1.38 L^2}{\pi^2 t_{1/2}}, \quad (2)$$

$$\lambda = \alpha \rho c_p, \quad (3)$$

where L is the sample thickness and $t_{1/2}$ is the time elapsed until half the temperature increment is achieved, and ρ is the density.

2.3 Other properties to consider

Although we have focused on enthalpy and thermal conductivity, there are other important properties and issues to consider such as: encapsulation compatibility (plastic-paraffin; salt hydrated-metal), toxicity, flammability, corrosion, thermal cycling, rheology, density, and volumetric expansion.

2.4 Geometry

The specific study system corresponds to a PCM-air heat exchanger acting as a TES unit. The unit is basically composed of PCM plates, the casing, and a fan that blows the air that circulates inside the equipment between the plates (see Figure 5). Although the set up could be arranged horizontally to reduce pressure drop and electrical consumption, the vertical distribution was a requirement because of the very first application (for temperature maintenance in telecom shelters, it should be a stand-alone system, hooked outside the façade, with the ability to plug in with a conventional chiller).

An important aspect in the design of PCM-air heat exchangers is the selection of an appropriate geometry of the PCM macroencapsulation. It is necessary to consider what will be the requirements that the storage system must satisfy and that will depend on the application. The heat transfer rate (absorbed or released), and the operation time, are two of the factors that generally will be considered. At least there are three typical options to select the shape of the macroencapsulation: plates, cylinders, and spheres. Here, plate shape is

selected because it has been a deeply studied geometry since London & Seban, 1943. It involves: 1) Easy-to-control PCM thickness, which is a crucial design factor as it allows regulating elapsed times of the melting and solidification; 2) Uniformity of the PCM thickness and, therefore, of the phase change process; 3) Simplicity of the manufacturing process (both small scale and large scale) and versatility of handling (transportation, installation ...); 4) Commercial accessibility in a wide variety of plate-shaped encapsulations in different materials, both metallic and plastic.

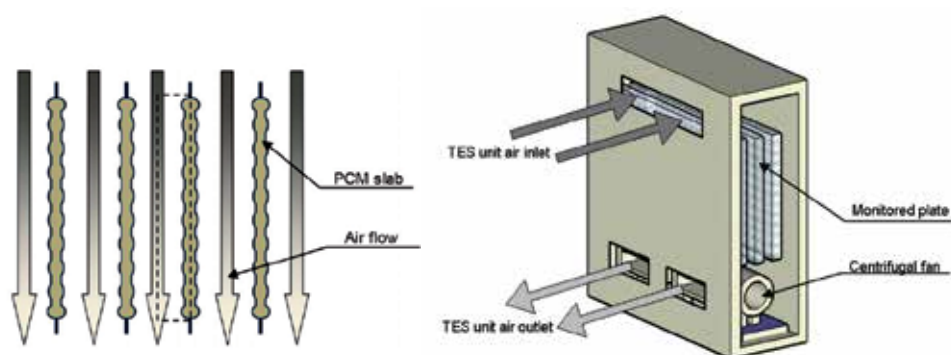


Fig. 5. PCM panels and air flow system (left); PCM-air heat exchanger (right).

Finally, the rigid metallic plate encapsulation has been selected to avoid both compatibility issues (Lazaro et al., 2006) as well as leakage problems detected previously (Lazaro, 2009) when using pouches.

2.5 Heat transfer mechanisms: basics

The basics of the heat transfer in PCM are compiled by Zalba et al., 2003, and discussed in a very understanding way by Mehling & Cabeza, 2008. The authors describe the basics of the heat transfer by means of: 1) Analytical models; 2) Numerical models; 3) Modelling; 4) Comparison of models vs. experimental; 5) Methods to improve the heat transfer.

3. Characterization of the heat exchanger

The main objectives of this section are:

1. How to test a prototype of PCM-air heat exchanger.
2. Gathering experimental results.
3. Analyzing data and obtaining empirical models.
4. Importance of the uncertainties in measurements and their propagation.

3.1 Experimental set up to test PCM-air heat exchangers

An experimental setup was designed to study different PCM-air heat exchangers (Dolado, 2011; Lazaro, 2009). A closed air loop setup was used to simulate indoor conditions. The setup design was based on the ANSI/ASHRAE STANDARD 94.1-2002 "Method of Testing Active Latent-Heat Storage Devices Based on Thermal Performance" (ANSI/ASHRAE, 2002). The setup is constituted of: 1) Inlet air conditioner allowing the simulation of different

operating modes (5 kW air chiller and 4.4 kW electrical resistance); 2) Air flow measurements; 3) Difference between inlet and outlet air temperature measurements (thermopile); 4) Inlet and outlet air temperature and humidity measurements; 5) PCM and air channels temperature measurements (31 thermocouples); 6) Data logger and data screening; 7) Air ducts and gates; 8) PID controller.

The energy balance of air between the prototype's inlet and outlet is utilized to evaluate the cooling (equation 4). As the main parameters are the air flow and the air temperature difference between the inlet and the outlet, the accuracy depends on the precision when measuring these parameters. The methods used are:

$$\dot{Q} = \dot{m}_{\text{air through HX}} \cdot \Delta h_{\text{air}} \approx \dot{m}_{\text{air through HX}} \cdot c_{\text{p,air}} \cdot \Delta T \quad (4)$$

- Air temperature difference: thermopile. There were difficulties to overcome in this measurement: a long period of time with little temperature difference; the temperature distributions along the air ducts due of its dimensions; and accuracy, which is required since it is a main parameter of evaluation. A thermopile was chosen as it is recommended by the ANSI/ASHRAE standard to overcome those difficulties.
- Air flow: energy balance of electrical resistances. The air temperature changes during tests, therefore most of air flow measurement methods are not suitable for transitory measurements. Mass flows depend only on the fan velocity; therefore they are measured by applying an energy balance to the electrical resistances.
- Air humidity: 2 sensors were used to measure air humidity at the inlet and outlet. Latent energy variation was negligible in the air energy balance for cooling power evaluation.

The reader can find more information on the experimental setup in Lazaro, 2009.

3.2 Two prototypes

Two real-scale prototypes of PCM-air heat exchangers were constructed and incorporated into the experimental setup to characterize them. Initially tests were conducted with the equipment filled with bags of a hydrated salt PCM (prototype 1). Subsequently, the bags were replaced by plates of a paraffin based PCM, and the unit was tested filled with plates. These two geometries were arranged vertically and parallel to the airflow. The casing of the heat exchanger unit used in both cases was the same. PCM thickness was a critical parameter to obtain the required cooling rates (Dolado et al., 2007). Vertical position was a requirement; therefore a metallic grid was used to force PCM thickness below a maximum in vertical position. The experimental setup built to test this kind of heat exchangers is shown in Figure 6. Tests using a constant inlet air temperature setpoint were accomplished.

Figure 7 (left) shows the cooling power evolution in prototype 1. Results showed that the cooling rates were very low and the total melting times were double the melting design time (2h). Different air flow rates were tested. As it can be seen in figure 8 (left), the air flow influence on melting times and cooling rates were negligible (in the figure *HH:mm* denotes time, hours:minutes). Cooling power does not increase by a rise of air flow rates. Indicating that, contrary to what was at first designed, heat transfer by conduction inside the PCM resistance is dominant. The prototype was opened to confirm the diagnosis, and PCM

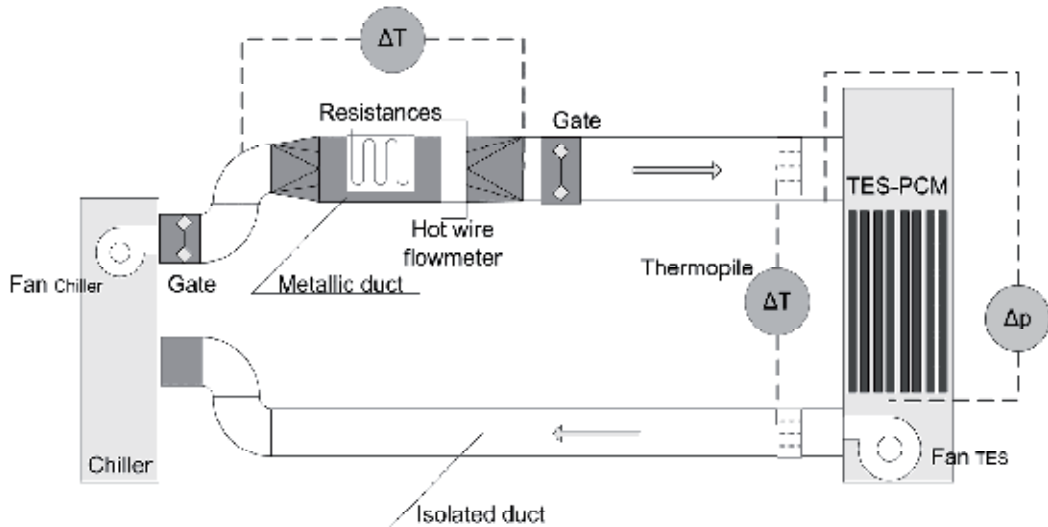


Fig. 6. Experimental installation arrangement to test PCM-air heat exchangers prototypes.

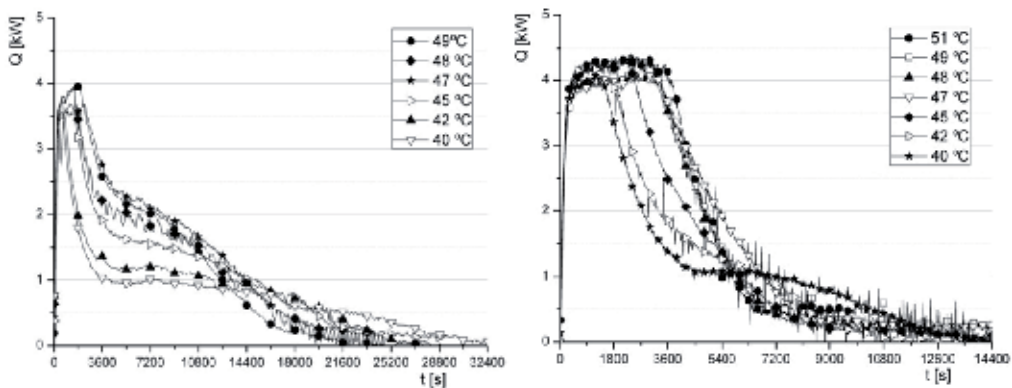


Fig. 7. Cooling rate evolution in prototype 1 during tests with different inlet air temperatures (left); in prototype 2 (right).

leakages were found out. Some pouches were torn and the metallic grid was deformed by the pushing force of the solidification process of the PCM inside pouches. PCM thickness was twice higher than the designed, causing a higher and dominant heat transfer resistance by conduction inside the PCM. Therefore melting times were higher and flow rate had almost no influence. This prototype did not fulfil melting time requirements and was discarded.

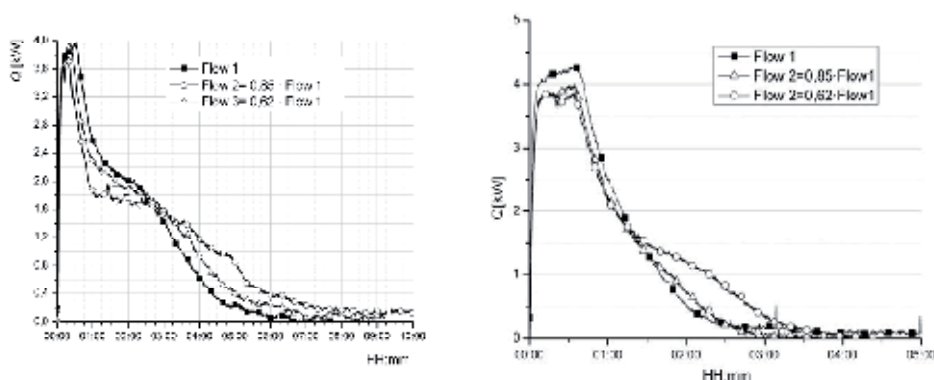


Fig. 8. Cooling rate evolution with constant inlet air temperature in prototype 1 during tests with different air flow rates (left); in prototype 2 (right); Flow 1 is the mass flow, equals to 0.34 kg/s.

Prototype 2 was designed using aluminium panels filled with organic PCM. Configuration was also vertical. Air flows were parallel to the panels from top to bottom. Due to the fact that the PCM in this prototype was organic, it presented lower thermal conductivity than PCM in prototype 1. Furthermore, the total stored energy in prototype 2 was also lower than in prototype 1. The first tests were accomplished using constant inlet air temperature. As it can be seen in figure 7 (right), cooling rates were higher than those obtained with prototype 1 and the melting times were half the melting times with prototype 1.

Different air flow rates in prototype 2 were tested. It was observed that it had influence on the melting time and cooling power. Figure 8 (right) shows that for the lowest air flow rate, the heat rate curve changes its shape and is more similar to prototype 1. This indicates that heat transfer by conduction inside the PCM starts to be relevant when compared to air convection. The first results of prototype 2 were satisfactory, so more test were planned to evaluate its behaviour under real conditions. Two types of experiments were accomplished: constant rise of inlet air temperature and constant heating power. Temperature rise ramps were then set into the resistances controller: results showed that faster the rise, higher cooling power and lower melting time. For constant power tests, different heating powers of electrical resistances were fixed. Results showed that prototype 2 was able to maintain a cooling capacity over 3 kW for approximately 1h 30' or approximately 1 kW for more than 3 h. This result is useful to design the optimal operation mode depending on the application.

3.3 Experimental results

The total energy exchanged during melting and solidification, as well as the time elapsed until total melting/solidification were determined from the heat rate curves experimentally obtained. The influence of the inlet air temperature and air flow was studied, and results showed that the continuous thermal cycling of the unit is a repetitive process: running experiments with similar conditions led to the same thermal behaviour; no degradation in the PCM properties was noticed. Pressure drop was measured for different air flows. Depending on the inlet air temperature, full solidification of the PCM could be achieved in less than 3 h for an 8 °C temperature difference between the inlet air and the average phase

change of the PCM. Average heat rates of up to 4.5 kW and 3.5 kW for 1 h were obtained for melting and solidification stages, respectively (Dolado et al., 2011b; Dolado, 2011; Lazaro, 2009; Lazaro et al., 2009a).

3.4 Empirical models

From experimental results, the empirical models were built aimed at simulating the thermal behaviour in the tested heat exchanger in different cases. These simulations were used to evaluate the technical viability of its application. Since the thermal properties of PCM vary with temperature, a PCM-air heat exchanger works as a transitory system and therefore, its design must be based on transitory analysis. This section shows that PCM selection criteria must include the power demand. The conclusions obtained for the PCM-air heat exchange can be useful for selecting PCM for other heat exchanger applications that use the tested geometry as well as for applications that use such technology: green housing, curing and drying processes, industrial plant production, HVAC, free-cooling.

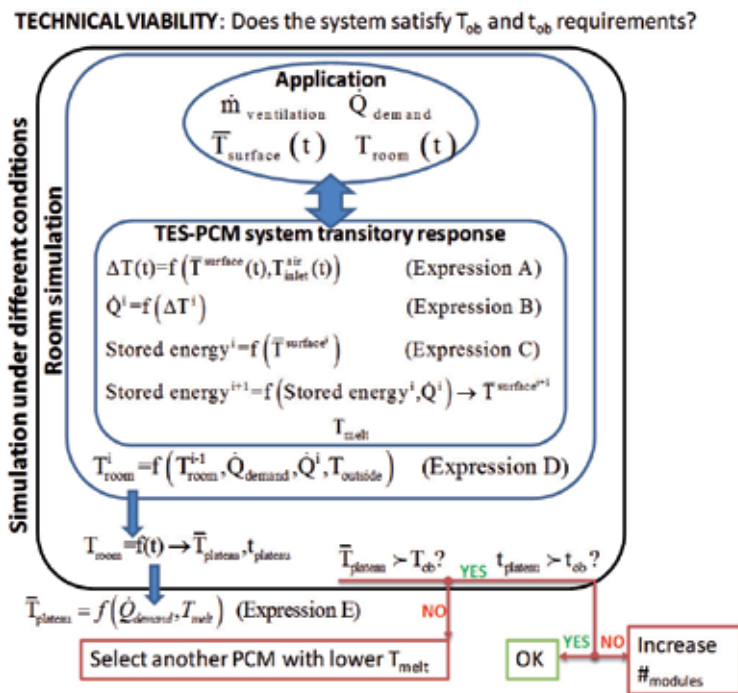


Fig. 9. Flow diagram to evaluate the technical feasibility of the system (Lazaro et al., 2009b).

The technical viability of TES with PCM systems depends on the capability to maintain the temperature below a maximum level (T_{ob}), during a specific period of time (Δt_{ob}). Figure 9 shows a flow diagram of the relevant parameters to test the technical viability of a system built with a specific geometry and an established air flow, for the heat exchange between air and PCM. To simulate a room under various conditions, the internal, external, and ventilation loads of the room, as well as the transitory response of the TES system using PCM must be known. Such transitory response was obtained by an empirical model built

from all experimental outcomes under real conditions. The results to test prototype 2 with constant heating power were evaluated and an average temperature was obtained for the air temperature plateau (\bar{T}_{plateau}). There was obtained a linear correlation (equation 5) between the average plateau temperatures and the heating power of the electrical resistances ($\dot{Q}_{\text{resistances}}$). The origin ordinate was the average phase change temperature of the PCM used.

$$\bar{T}_{\text{plateau}} = 26.6 + 1.58 \cdot \dot{Q}_{\text{resistances}} \quad (5)$$

$$\Delta T [\text{K}] = -1.4683 - 1.10943 \cdot \bar{T}_{\text{surface}} [^{\circ}\text{C}] + 1.10706 \cdot T_{\text{inlet}}^{\text{air}} [^{\circ}\text{C}] \quad (6)$$

The temperature on the surface of the PCM encapsulation was measured at 20 locations, distributed in such a way that the melting evolution can be studied and that any cold point can be detected. For each measurement, the average surface temperatures were obtained, as well as the plotting of the temperature difference between the inlet and the outlet (ΔT), the air temperature at the inlet of the TES unit ($T_{\text{inlet}}^{\text{air}}$) and the average surface temperatures (\bar{T}_{surface}). All locations come from experiments with the same airflow rate and heat exchange geometry. All measured locations were contained in a plane. A fitting tool was used to obtain the equation adjustment (equation 6). For the tested heat exchanger, expression A in figure 9 corresponds to equation 6. As it has been detailed, the heat exchanged with air was evaluated by an energy balance. The stored energy was then obtained for each measurement time step, as an accumulative result from the exchanged energy between air and PCM. The relationship between the stored energy and the average surface temperatures (\bar{T}_{surface}) corresponds to expression C in figure 9. Using the empirical model, different conditions were simulated, and the equations for the expressions shown in figure 9 were obtained, as well as various conclusions concerning PCM selection criteria (Lazaro et al., 2009b).

3.5 Uncertainties propagation

The guide EA-4/02 Expression of the Uncertainty of Measurement in Calibration, 1999, has been followed to estimate the uncertainty of measurements. Air flow was determined using an energy balance method that consists in applying an energy balance to the air flow that passes through the electrical resistances (equation 7). The air flow is measured with an accuracy of ± 0.026 kg/s (5.5% of measurement). Table 1 summarizes the expanded uncertainty estimation. The same procedure was followed to estimate the uncertainty of the cooling power determination. Equation 8 expresses the energy balance for the heat exchanger. Table 2 shows an example of uncertainty estimation in a cooling power measurement. In this case, the cooling power was measured with a ± 0.301 kW uncertainty (9%).

$$\dot{m}_{\text{air}} = \dot{Q}_{\text{resistances}} / (c_{\text{p,air}} \cdot \Delta T_{\text{thermopile}}) \quad (7)$$

$$\dot{Q}_{\text{HX}} = \dot{m}_{\text{air}} \cdot c_{\text{p,air}} \cdot \Delta T_{\text{inlet-outlet}} \quad (8)$$

	Expanded uncertainty	Standard uncertainty	Estimated value	Sensibility coefficient	Contribution to uncertainty
$\Delta T_{\text{thermopile}}[\text{K}]$	0.51	0.255	9.3	1	0.0008
Electrical power consumption of resistances [kW]	0.044	0.022	4.4	1	0.0000

Table 1. Air flow uncertainty of measurement estimation.

	Expanded uncertainty	Standard uncertainty	Estimated value	Sensibility coefficient	Contribution to uncertainty
$\Delta T_{\text{thermopile}}[\text{K}]$	0.51	0.255	7	1	0.0013
$\dot{m}_{\text{air}} [\text{kg/s}]$	0.026	0.013	0.47	1	0.0008
	Sum of contributions	Estimated value	Standard uncertainty	Expanded uncertainty	
$\dot{Q}_{\text{HX}} [\text{kW}]$	0.089	3.29	0.151	0.301	

Table 2. Example of cooling power uncertainty estimation.

The air temperature difference between the inlet and the outlet of the heat exchanger was measured using a thermopile and two Pt-100 in the centre of the air ducts. Measurements were compared during stationary periods in order to confirm the fact that a thermopile was more appropriate. Standard deviations of thermopile measurements are lower than the ones for Pt-100 differences and the mean values are all higher for the Pt-100 differences. This is due to the fact that Pt-100 are located at a specific point in the centre of the air duct whereas the thermopiles are distributed in the air duct cross surface.

4. Study of the heat transfer

In this section a theoretical model has been developed to perform the computer simulation of the thermal behaviour of a PCM-air heat exchanger, validating the theoretical model with the results obtained from the prototype in the experimental facility built for this purpose. In the archival literature, the approach of the solid-liquid phase change problem appears with different configurations, this section is focused on the case of macroencapsulated PCM, plate shape. Among the different numerical methods for solving the problem, in this section the energy equation is considered in terms of enthalpy as the governing equation can be applied at any stage, the temperature can be determined at each point, and therefore the values of the thermophysical properties can be evaluated. The PCM simulated are commercially available so the simulation involves, among other problems the non-linearity. The finite difference method for discretization of the governing equations is used. The models are based on 1D conduction analysis, using the thermo-physical data of the PCM measured in the laboratory. The models can take into account the hysteresis of the enthalpy curve and the convection inside the PCM, using effective conductivity when necessary.

4.1 Modelling the solid-liquid phase change

Modelling is a useful tool in a viability analysis of applications that involve TES by solid-liquid PCM. Therefore, there is a necessity to develop experimentally validated models that

are rigorous and flexible to simulate heat exchangers of air and PCMs. When developing a model, the trade-off between rigour and computational cost is crucial. There are many options reported in scientific literature to face the mathematical problem of phase change as well as to solve specific particularities such as hysteresis phenomena (Bony & Citherlet, 2007) or sub-cooling (Günther et al., 2007). In the review by Zalba et al., 2003, the authors presented a comprehensive compilation of TES with PCM. The authors remarked that although there is a huge amount of published articles dealing with the heat transfer analysis of the phase change, the modelling of latent heat TES systems still remains a challenging task. When working with commercially available PCM (or mixtures or impure materials), the phase change takes place over a temperature range and therefore a two-phase zone appears between the solid and liquid phases. In these cases, it is appropriate to consider the energy equation in terms of enthalpy (Zukowsky, 2007b). When the advective movements within the liquid are negligible, the energy equation is expressed as follows:

$$\rho \partial h / \partial t = \nabla (\lambda \cdot \nabla T) \quad (9)$$

The solution of this equation requires knowledge of the h-T functional dependency and the λ -T curve. The advantage of this methodology is that the equation is applicable to every phase; the temperature is determined at each point and the value of the thermo-physical properties can then be evaluated. In thermal simulations of PCM, the accuracy of the results relies on the material properties' data (Arkar & Medved, 2005). In the geometry studied in this work, the main properties were enthalpy and thermal conductivity, but notice that the rate of melting/solidification can also depend on other material properties such as viscosity or density (Hamdan & Elwerr, 1996). In the models developed here the variation of thermophysical properties with temperature in all phases was considered.

4.2 Development of a 1D finite differences equations model for PCM plates

A PCM plate model was developed with finite differences, one-dimensional, implicit formulation. Implicit formulation was selected because of its unconditional stability. The basis model assumed only conduction heat transfer inside the PCM plate, in a normal direction to the air flow. The model analyzed the temperature of the airflow in a one-dimensional way. Due to its symmetry, the analyzed system was a division of the prototype. In the present work, the model was implemented in Matlab R2008b. The software implements direct methods, variants of Gaussian elimination, through the matrix division operators, which can be used to solve linear systems.

The study system is the PCM-air TES unit (figure 5, right). The air inlet was located on the upper side of the TES unit. The air flowed downwards in the TES unit, circulating parallel to the PCM slabs, exchanging energy with the PCM, and eventually was blown outside the TES unit by a centrifugal fan. The system was studied from the point of view of a single slab. As the PCM zone of the TES unit was insulated as well as due to the distribution of the slabs inside the TES unit, some symmetry relationships could be considered so only the dotted domain in figure 5 (left) was modelled. The nodal distribution of the mathematical model is shown in figure 10. Depending on whether the encapsulation is considered or not, two more nodes have to be included between the PCM surface and the airflow. In the experimental study, the heat transfer processes that take place inside the TES unit between the air flowing through the slabs and the PCM inside the slabs were: forced convection in

the air, conduction in the shell of the aluminium slab, and conduction and natural convection in the PCM itself.

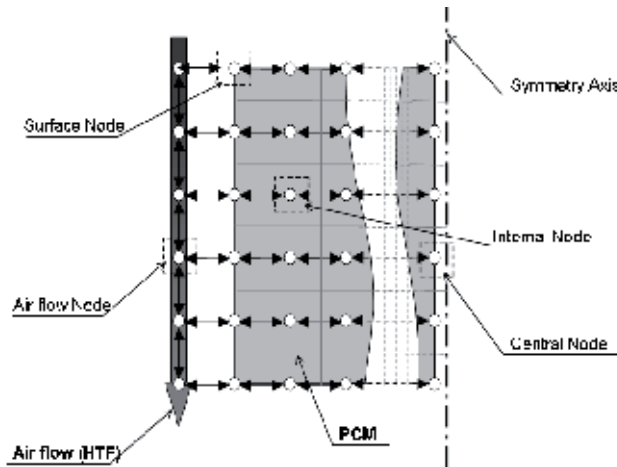


Fig. 10. Nodal distribution in the 1D plate system.

Nodes	Equations
Air Flow	$T_{air} = T_{air-1} - NTU_{air} (T_{air-1} - T_{surface})$
PCM Surface	$T_{surface} = (T_{PCM}^{t-1} + Fo T_{PCM+1} + Fo Bi T_{air}) / (1 + Fo + Fo Bi)$
PCM Inner	$T_{PCM} = [T_{PCM}^{t-1} + Fo (T_{PCM-1} + T_{PCM+1})] / (1 + 2Fo)$
PCM Central	$T_{PCM} = (T_{PCM}^{t-1} + 2Fo T_{PCM-1}) / (1 + 2Fo)$

Table 3. Node temperature equations not considering encapsulation.

Nodes	Equations
Air Flow	$T_{air} = T_{air-1} - NTU_{air} (T_{air-1} - T_{surface})$
Air Surface	$T_{surface} = \frac{[T_{surface}^{t-1} + 2(Fo_{enc} T_{enc} + Fo_{enc} Bi_{enc} T_{air})]}{[1 + 2(Fo_{enc} Bi_{enc} + Fo_{enc})]}$
Surface Encapsulation	$T_{enc} = \frac{[T_{enc}^{t-1} + 2(Fo_{enc-PCM} T_{surface} + 2Fo_{PCM-enc} T_{PCM})]}{[1 + 2(Fo_{enc-PCM} + 2Fo_{PCM-enc})]}$
Encapsulation PCM	$T_{PCM} = [T_{PCM}^{t-1} + Fo(2T_{enc} + T_{PCM+1})] / (1 + 3Fo)$
PCM Inner	$T_{PCM} = [T_{PCM}^{t-1} + Fo(T_{PCM-1} + T_{PCM+1})] / (1 + 2Fo)$
PCM Central	$T_{PCM} = (T_{PCM}^{t-1} + 2Fo T_{PCM-1}) / (1 + 2Fo)$

Table 4. Node temperature equations considering encapsulation.

The dominant resistance of the process could be convection on the air side and not always conduction-convection in the PCM. In this case the thermal resistance of the encapsulation was very low, and therefore it was not necessary to consider encapsulation in the node system, as the heat transfer process was controlled by the convection on the air side and/or by the conduction-natural convection in the PCM. However, in other cases it is not always possible to disregard the thermal influence of the encapsulation, and therefore two models were developed: the first model did not take into account the thermal behaviour of the encapsulation and the second model did, and it was developed in order to be used for general purposes. The node equations of the two models are summarized in tables 3 and 4. Important aspects to consider when dealing with the simulation of this type of heat exchanger are as follows: friction factor (rugosity of the encapsulation surface), convection coefficient, thermophysical properties of the PCM (as functions of temperature), hysteresis, natural convection inside the PCM, thermal losses/gains through the TES casing, etc. More detailed information can be found in Dolado et al., 2011a, and Dolado, 2011.

4.3 Experimental validation: applying the uncertainties propagation approach to the model

The validation stage of a theoretical model has become a fundamental objective to evaluate the precision, accuracy and reliability of computer simulations used in design. Uncertainties can be associated with the own theoretical model, as well as with the measurement systems used to characterize the process of interest or even with the manufacturing process of the equipment. Therefore, assessing the validity of an approximation of a theoretical model must be carried out based on stochastic measurements to ensure the trust of designers in the use of the model. This improved knowledge of the theoretical model helps to know what are the most critical factors as model inputs and, therefore, indicates what should be more controlled in its determination or measurement. It also allows establishing an uncertainty band set around the solution bringing more rigor to the model simulations. The methodology of uncertainties propagation is an external method used to analyze the system by means of the input-output analysis, instead of the traditional equation of uncertainties propagation applied to a known function. The whole methodology followed in is summarized in the next steps: 1) To select the variables under study; 2) To allocate the probability distributions of each variable; 3) To generate samples for the different runs of the theoretical model (by means of Latin hypercube sampling); 4) To run the program once per sample; 5) To analyze the relations between the inputs and the outputs; 6) To classify the variables; 7) To determine the uncertainty of the theoretical model results.

For the current study, the following parameters that introduce uncertainty in the results, were considered and classified into three groups:

- Material properties (parameterized enthalpy-temperature curve, $h-T$, and thermal conductivity curve, $\lambda-T$);
- Air conditions at the inlet of the TES unit (temperature and airflow);
- Geometric parameters (PCM plate thickness and width of the air gap between plates).

The parameterization and the range of uncertainty assumed for all these parameters are detailed in Dolado, 2011. The confidence level is 97.5%. Furthermore, as the probability distribution of the different parameters is unknown, a normal distribution is taken in all

cases. The study of uncertainties propagation is performed by numerical simulation of sets of input values of those parameters. Traditionally the random sampling technique has been used, which was followed by an improved version as the stratified sampling and subsequently the Latin hypercube (McKay et al., 1979) which is a valid technique used here. The variation range of the studied variable was analyzed. This result provides an estimate of the uncertainty range that would result as the TES unit is designed. This analysis sets the interval for the output variable of interest. For every particular time of the simulation the error was calculated as: 1) Histogram to the corresponding time of the results set of all simulations (the difference between the value in the current simulation and the reference case); 2) Function of the cumulative probability distribution; 3) Error in the given time at a certain confidence level; 4) Graphical representation of the reference case and of the error.

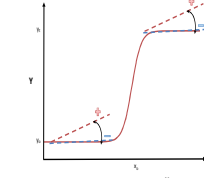
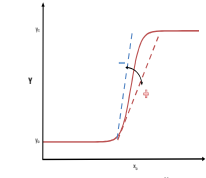
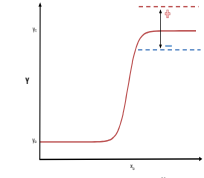
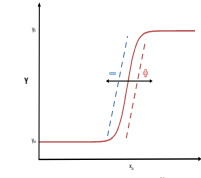
Parameter	b	ΔT	h_l	T_{sl}
Related with	Slope of the sensible heat	Thermal window	Latent heat	Average temperature of phase change
Reference value	3 kJ/(kg · K)	0.9 °C	170 kJ/kg	27 °C
Uncertainty	± 15 %	± 0.2 °C	± 20 kJ/kg	± 1 °C
Effect on h-T curve				

Table 5. Parameters setting of the enthalpy-temperature curve.

Variable	Reference value	Uncertainty
\dot{V}	1400 m ³ /h	± 86 m ³ /h
T	experimental curve of $T_{air,in}$, °C	± 0.6 °C

Table 6. Parameters setting of the inlet air.

The corresponding value for a cumulative relative frequency of 97.5% was taken as the uncertainty range in this approach. Running the theoretical model with the reference case conditions (tables 5 and 6) yielded to the results shown in figure 11. The figure shows that the heat rate has an initial plateau of about 4500 W, with a duration of 40 minutes, which reduces while reaching the complete melting of the PCM. The full melting takes place two hours after the start of the process. From these graphical results, the responses of interest were obtained. Among the responses of interest provided by the theoretical model, the analysis was focused on the following responses: average heat rate in the first hour ($\dot{Q}_{average,1h}$), and time until the air reaches 32 °C at the outlet ($t_{T_{air,out}=32^\circ C}$), as both responses pose a greater interest in practical operation of the TES unit. Immediately afterwards, applying the Latin hypercube sampling to run the numerical simulations, instead of getting a single result of $\dot{Q}_{average,1h}$, a complete distribution was obtained. Figure 11 shows the

evolution of the exchanged heat rate in the melting process with the associated uncertainty interval (97.5%) and also the results of the relative error in heat rate. It is observed that the relative error is below 10 % until the process is approaching the end of the melting stage. It then when the absolute values of heat rate are smaller and the relative error increases until the melting ends, as expected. This result is analogous in the solidification stage. As stated by Dolado et al., 2011b, and Lazaro et al., 2009a, considering the instrumentation used in the experimental setup, an uncertainty of 9 % in terms of the heat rate during the first hour of a typical test process is obtained. The calculations to determine the uncertainty in the measurement of the heat rate are shown in table 7. The uncertainty is estimated for each measurement so that, according to the EA Guide 4/02 Expression of the Uncertainty of Measurement in Calibration, 1999, a band of uncertainty associated with the experimental heat rate curve can be determined (figure 12).

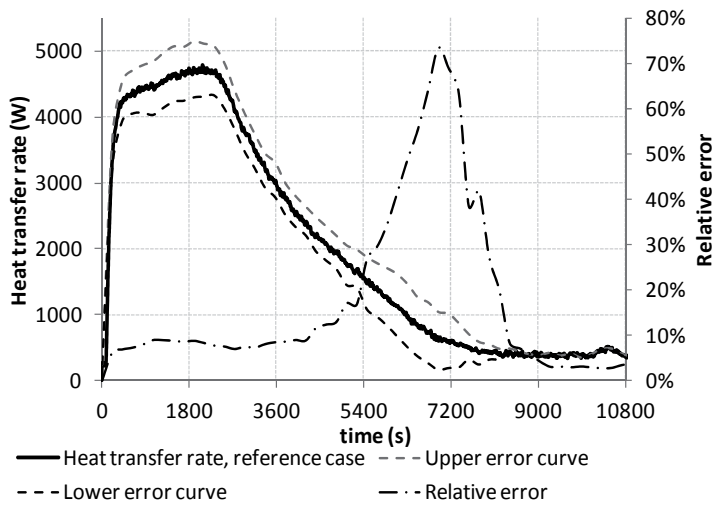


Fig. 11. Simulated heat rate, uncertainty bands and relative error (melting stage).

	Expanded uncertainty	Standard uncertainty	Estimated value	Sensibility coefficient	Contribution to uncertainty
$\Delta T_{\text{thermopile}}[\text{K}]$	0.51	0.255	ΔT_i	1	$(0.255 / \Delta T_i)^2$
\dot{m} [kg/s]	0.026	0.013	0.36	1	0.0013
c_p [J/(kg·K)]	2	1	1007	1	$9.86 \cdot 10^{-7}$
	Sum of contributions		Estimated value	Standard uncertainty	Expanded uncertainty
\dot{Q} [W]	$\text{SQRT} [(0.0013+9.86 \cdot 10^{-7}+(0.255/\Delta T_i)^2]$		\dot{Q}_i	$w_{\dot{Q}} \cdot \dot{Q}_i$	$2 \cdot w_{\dot{Q}} \cdot \dot{Q}_i$

Table 7. Uncertainties determination of the experimental heat rate.

As expected, the relative errors grow as the absolute value of the heat rate decreases (figures 11 and 12). This is because the expanded uncertainty associated with the measure of the thermopile is ± 0.51 °C (Lazaro, 2009) so that the error increases as the temperature difference between the air at the inlet and at the outlet of the TES unit decreases. Figure 12

shows the overlap between the experimental curve (including the lower and upper limits associated with its uncertainty) and the simulation (including the uncertainty of the response heat rate calculated applying the reported technique). The agreement is significant in most of the process, finding the more relevant discrepancies as the curve reaches the end of the corresponding stage of the cycle (i.e. as the heat rate values are smaller).

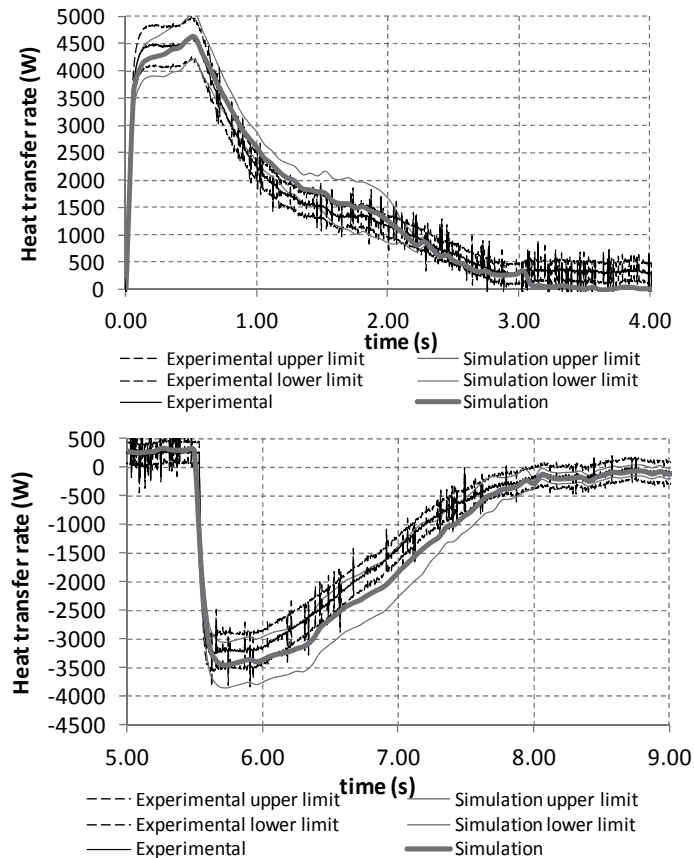


Fig. 12. Comparison of experimental and simulated results (including their corresponding uncertainty bands) for the melting (up) and solidification (down) of a thermal cycle.

5. Design focused on applications. Feasibility

This section will describe how to design the heat exchanger once an application is specified. Free-cooling and temperature maintenance in rooms with special requirements possess high potential for PCM application in different countries according to their climate. Until now, the low thermal conductivity of PCM and air hindered the development of suitable heat exchangers. This section has as the overall objective to apply methodologies to study PCM and PCM-air heat exchangers that allow the development of applications with technical and economical viability. Finally, using the combined technique of design of experiments (hereafter DOE) and simulations, the feasibility of the possible application of this type of equipment is studied for temperature maintenance in rooms. Because the simulation itself is

not a design tool, this methodology is proposed to size the equipment. This technique greatly reduces the time spent in performing the simulations required to find the optimal equipment (Del Coz Díaz et al., 2010) as well as and a potential cost saving on the experimental (Del Coz Díaz et al., 2010; Gunasegaram et al., 2009) if the prototype-model similarity relations are met. Moreover, contrary to a sequential analysis, it is reasonable to use a mathematical and statistical methodology that allows planning the sequence of experiments on the philosophy of maximum information with minimum effort.

5.1 Empirical model: simulations of a case study and modular design

An empirical model was built from the experimental results described in the previous section. The aim was to simulate the thermal behaviour of the tested heat exchanger in different cases. These simulations were used to evaluate the technical viability of application. The model describes the temperature evolution of a room with an internal cooling demand (\dot{Q}_{demand}), where the PCM-air heat exchanger is operating and there is a ventilation system. The enclosure temperature was considered to be the average between the outside temperature and the room temperature. A diagram of the room is shown in figure 13. Expression D in figure 9 is equivalent to equation 9, expressing the energy balance applied to the air inside the room.

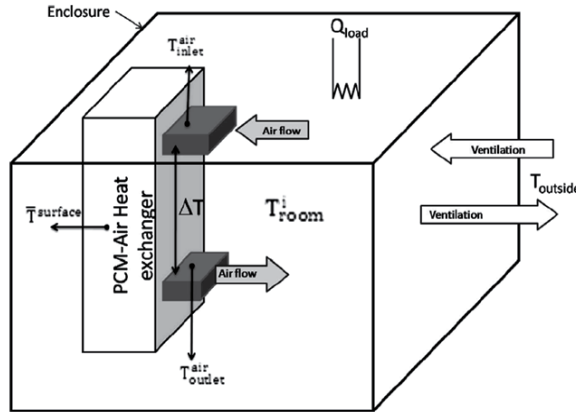


Fig. 13. Schematic diagram of the room in which the temperature is evaluated.

$$\begin{aligned} m c_{p,enclosure} \cdot \left[\left(\frac{T_{room}^i + T_{outside}}{2} \right) - \left(\frac{T_{room}^{i-1} + T_{outside}}{2} \right) \right] &= \rho_{air} \cdot V c_{p,air} \cdot (T_{room}^i - T_{room}^{i-1}) \\ &= \left[\dot{m}_{ventilation} c_{p,air} \cdot (T_{outside} - T_{room}^i) + \dot{Q}_{demand} - \dot{m}_{air\ HX} c_{p,air} \cdot \Delta T^{i-1} \right] \cdot \Delta t(i,i-1) \end{aligned} \quad (9)$$

where ΔT is obtained at each instant as a function of $\bar{T}_{surface}$ and the inlet air temperature, T_{inlet}^{air} (at instant i equal to T_{room}^i); and the $\bar{T}_{surface}$ at instant i is obtained from the stored energy evolution.

The real-scale PCM-air heat exchanger tested was constituted of 18 parallel modules ($\#_{modules}$ denotes de number of PCM modules in the heat exchanger). A module is constituted by a

metallic PCM container between two air channels. The pressure drop is the same for each module, and the air distribution through the air channels can be considered uniform. The unitary air flow through a module is the mass air flow ($\dot{m}_{\text{air HX}}$) divided by 18. Since the geometry and the air flow were maintained identical, the total stored energy for one module (E_t^{mod}) between two temperatures is the stored energy for the real-scale PCM-air heat exchanger between the two temperatures divided by 18 (equation 10). The total melting time depends on E_t^{mod} and on the cooling power demand (equation 11).

$$\text{Stored energy} = \#_{\text{modules}} \cdot E_t^{\text{mod}} \quad (10)$$

$$t_{\text{melt}} = \text{Stored energy} / \dot{Q}_{\text{demand}} = (\#_{\text{modules}} \cdot E_t^{\text{mod}}) / \dot{Q}_{\text{demand}} \quad (11)$$

$$\bar{T}_{\text{plateau}} = T_{\text{melt}} + 1.58 \cdot \dot{Q}_{\text{resistances}} = T_{\text{melt}} + 1.58 \cdot \dot{Q}_{\text{demand}} \cdot 18 / \#_{\text{modules}} \quad (12)$$

The 1.58 value in equation 13 comes from the linear correlation between the average plateau temperatures and the heating power ($\dot{Q}_{\text{resistances}}$) data obtained experimentally. The origin ordinate is the average phase change temperature of the PCM used. The relationship between the average phase change temperature (T_{melt}) and the cooling power demand (expression E in figure 9) is described in equation 12. Assuming that the origin ordinate in the adjustment equation 13 is T_{melt} , it is possible to define the number of modules and the T_{melt} needed for a given cooling power demand, as well as the T_{ob} and Δt_{ob} to maintain such a level (equations 14 and 15).

$$\Delta T [\text{K}] = -1.4683 - 1.10943 \cdot \bar{T}^{\text{surface}} [^{\circ}\text{C}] + 1.10706 \cdot T_{\text{inlet}}^{\text{air}} [^{\circ}\text{C}] \quad (13)$$

$$T_{\text{melt}} = T_{\text{ob}} - 1.58 \cdot \dot{Q}_{\text{demand}} \cdot 18 / \#_{\text{modules}} \quad (14)$$

$$\#_{\text{modules}} = \dot{Q}_{\text{demand}} \cdot \Delta t_{\text{ob}} / E_t^{\text{mod}} \quad (15)$$

For example, in the case where a 2 kW cooling power demand is required and a temperature level of 25 °C maintained during 2 h using a TES system, then 18 heat exchanger modules filled with a PCM of the same thermal properties of the one used in prototype 2 but with a T_{melt} of 21.8 °C would be needed. The same case with a cooling power of 4 kW would require a T_{melt} of 18.7 °C (see table 8).

\dot{Q}_{demand} [kW]	T_{ob} [°C]	t_{ob} [s]	T_{melt} [°C]	$\#_{\text{modules}}$
2	25	7200	21.8	18
4	25	7200	18.7	18

Table 8. Design conclusions for different cooling demands.

5.2 Theoretical model: DOE applied to simulations, improving design

The empirical model can give a very fast approach of relevant design parameters such as the PCM average phase change temperature. However, if we want to analyze the behaviour of

the equipment when modifying any other parameter or variable, or if we need to improve/optimize the design, we have to move to the numerical model.

As a starting point we will continue using the case brought by Lazaro, 2009, which provides that, for proper running of the electronic equipment, the maximum air temperature in the room should be between 38 °C and 48 °C, in particular we will establish it at 44 °C. The heat generation of the electronic equipment is 5 kW. For the evolution of temperature inside the room, an energy balance was stated with the following simplifications: 1) the cooling effect of the terrain was not considered. The ground floor area is supposed to be occupied by the equipment; 2) exterior ventilation is introduced only when it is favourable, and considering that the environment outside the house is 40 °C (worst case).

The idea behind this system is that after a failure of the conventional cooling system, the TES unit is intended to smooth the evolution of the temperature of the room so that it extends the time to reach a certain threshold temperature value. The aim is this period to be about two hours, so technicians have sufficient time to reach the place where the room is located and to repair the damage of the cooling system without having to stop the electronic equipment. A series of restrictions put on the TES system follow:

- Dimensions limitation due to the telecommunications shelter: the maximum length of the system is limited to 2.5 m (height of the shelter) which limits the section of the PCM to 1.25 m. Likewise, the width of the unit is also limited to 5 m due to the wall;
- Electrical power consumption limitation of the fan, so it can be supplied by batteries without being essential a connection to the grid. Pressure drop should be less than 30 Pa.

M_{PCM} [kg]	\dot{V} [m ³ /h]	e_{plate} [mm]	e_{air} [mm]	Finishing
132	1340	6.5	12	3

Table 9. Operating conditions.

The operating conditions are shown in table 9 and the simulation results with the theoretical model of the unit proposed by Lazaro, 2009, are shown in figure 14.

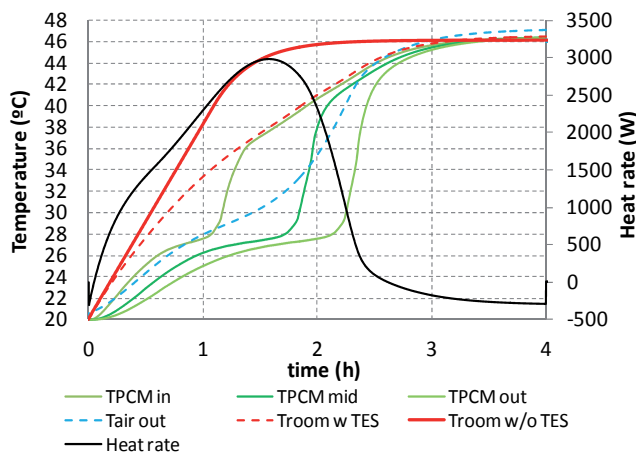


Fig. 14. Theoretical model simulated results of Lazaro’s case (2009).

As it can be seen in the results of the simulation the contribution of the storage equipment is remarkable: the time spent to reach the room 38 °C is 1h 40min (determined by the red dotted line), extending almost 40 minutes than if there was no storage system (red line). Table 10 compiles the main results.

%Melt	Investment [€]	$t_{\text{additional, } T=38^{\circ}\text{C}}$ [min]	$t_{\text{additional, } T=44^{\circ}\text{C}}$ [min]	Δp [Pa]
69.47	3924	36	61	36

Table 10. Main results of the simulation with Lazaro's case (2009).

Factors	Domain	
	Level (-)	Level (+)
M_{PCM} [kg]	100	200
\dot{v} [m ³ /h]	1000	2000
e_{plate} [mm]	6	14
e_{air} [mm]	10	20
Finish	1.5	2

Table 11. List of factors and their corresponding domain.

For the implementation of DOE the following factors and responses were considered:

- Factors (listed in table 11 along with their domain): mass of PCM, air flow, air channel width, thickness of the PCM plate, finishing of the plates (related to rugosity or to the presence of bulges in the surface of the plates).
- Responses: melting ratio in 3 hours, additional time for the air to reach a temperature of 38 ° C (compared with the evolution of temperature without unit TES) in the room, additional time for the air to reach a temperature of 44 ° C (compared with the evolution of temperature without TES unit) in the room, pressure drop, initial investment (mainly depending on the amount of PCM, the installed fan, the casing, and whether or not the plates have bulges on its surface).

5.2.1 Response optimization

Given that the main objective of the TES unit is to extend the time period during which the room temperature is below a certain temperature limit (in order to safeguard electronic equipment), the highest importance has set to that response. Table 12 lists the input parameters in the optimization. It has been considered that the most important requirement is to get the unit to extend as much as possible the time to reach the temperature limit of the air in the room, assigning the greatest importance to the maximum temperature limit (44 °C), $t_{\text{additional, } T=44^{\circ}\text{C}}$, and considering also important, but lesser, the time to reach the first temperature limit (38 °C), $t_{\text{additional, } T=38^{\circ}\text{C}}$, as well as the pressure drop, Δp (in order to be as lower as possible so that the electrical power consumption of the corresponding fan will be reduced). Also the investment and the melting ratio, %Melt, are interesting responses considered in the study, as they are related to economical and technical feasibility

respectively. Once the objectives are defined, each variable is assigned a weight (between 0.1 and 10) and an importance (also between 0.1 and 10).

In this approach to the optimization, each of the values of the responses is transformed using a desirability function. The weight defines the shape of this function for each response and is related to the emphasis on achieving the target:

- A value greater than one emphasizes the importance of achieving the goal;
- A unit value gives equal importance to the objective and the limits;
- A value less than one puts less emphasis on the goal.

After calculating the desirability for each response, the desirability composite is calculated (weighted geometric mean of the single ones) that allows to obtain the optimal solution.

In this case, the same weight is set to each of the answers assuming a unit value. This will set the target as important as any value within the limits for the corresponding answer.

On the other hand, assigning a value to the importance of each answer is related to the importance given to each of the answers, and if any of these responses is more important than the others (the most important is a 10, the less important is a 0.1). The optimization results are shown in figure 15.

Response variable	Objective	Weight	Importance
$t_{\text{additional, } T=44^{\circ}\text{C}}$	Maximize	1	10
Δp	minimize	1	5
$t_{\text{additional, } T=38^{\circ}\text{C}}$	Maximize	1	5
Investment	minimize	1	1
%Melt	Maximize	1	1

Table 12. Optimization parameters.

What is interesting of the optimized results is the value of composite desirability as well as its trend according to each of the factors considered. The composite desirability obtained in this case (0.919) indicates that the values determined by the optimization nearly fulfil the requirements of the response variables. The trends of composite desirability for each factor allow to adjust their value (usually due to physical or technological constraints) while keeping high desirability values. However, at least there are two drawbacks to use this configuration: first, it does not respect the width limitation (this unit has a width of more than 10 meters), and secondly, when manufacturing the TES unit it will be more feasible to use a PCM thickness higher than 0.5 mm (proposed in the optimization). Thus, moving in the optimization plot to a greater value of PCM thickness without reducing too much the composed desirability and rounding parameters, a value of 2.5 mm in thickness is selected (which also meets the width restriction). Table 13 shows the results of the corresponding simulation. The results of the last proposed unit are somewhat unfavourable compared to the optimized unit, but the proposed thickness of PCM is much more realistic than the optimized one. Yet the responses provided by the proposed unit represent a storage that improves the very first one. The comparison of these results against the ones of the initial

unit reflected that: a) Time to reach the target temperature of 44 °C increases: from 61 minutes it extends to 73 (19.7% improvement), being this a fundamental aspect of the application; b) The initial investment is reduced by 11%: from 3924 € to 3489 €; c) The PCM melting ratio is improved 23.2%; d) However, the volume occupied by the unit increments from 1.2 m³ to 3.8 m³.

Unit	%Melt	Investment [€]	t _{additional, T=38°C} [min]	t _{additional, T=44°C} [min]	Δp [Pa]
Proposed	92.64	3489	37	73	5
Optimized	100	3234	60	96	3

Table 13. Main results of the proposed and optimized units.

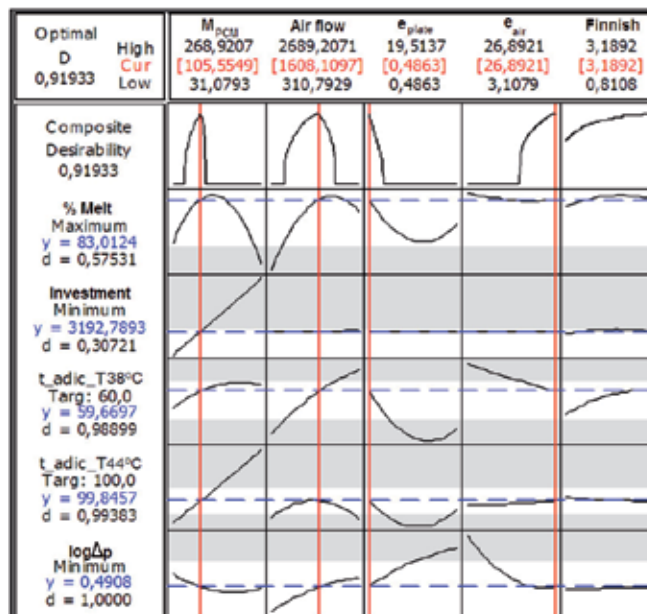


Fig. 15. Optimization plot results.

5.2.2 Model-prototype similarity

Dimensional analysis of these units show that the natural convection within the PCM is not going to be significant in any of the 2 units, being the heat transfer process by pure conduction for the second unit, and the ratio λ_{eff}/λ within the range of experimental validity for the other one (Dolado, 2011). Furthermore, since both Re and Bi numbers and NTU are within the range of experimental validity, the units can be used for design purposes.

5.3 Other applications

Keeping the temperature range, this type of heat exchanger can be applied in other different situations such as free-cooling, heat pumps, absorption solar cooling systems, greenhouses.

In any case, the DOE methodology proposed above could be followed to design a proper TES unit to the corresponding application (Dolado, 2011).

6. Conclusion

Methods to obtain enthalpy as well as the curves of thermal conductivity in the solid and liquid phases vs. temperature were proposed as a result of a critical analysis of the existing methods. A setup based on the T-history method was designed and built with significant improvements: 1) The possibility of measuring, for both organic and inorganic materials, cooling processes, therefore hysteresis and sub-cooling can also be studied; 2) The horizontal position decreases the error on enthalpy values since the liquid phase movements are minimized; 3) A Labview application allows the h-T curves to be directly obtained.

Results show that a heat exchanger using a PCM with lower thermal conductivity and lower total stored energy, but adequately designed, has higher cooling power and can be applied for free-cooling. Pressure drop is a key factor when designing any type of heat exchanger as it will determine the electrical energy consumption of the device. In the PCM-air heat exchangers with plates studied here, the pressure drop is ranged from 5 to 25 Pa. The analysis of the experimental data gathered accomplishes two aims: to develop empirical models of the TES unit and to come to a series of rules of thumb. Both are useful tools to design such kind of heat exchangers. For total energy storage strategy, the duration time of the cooling capacity of PCM heat exchanger depends on the cooling power demand. To validate the theoretical model developed, an uncertainties propagation analysis is proposed; here, the difference between the experimental and the simulation is less than 10% in terms of heat rate. The combined methodology of Design of Experiments applied to the numerical simulations seems to be a valid tool for design this kind of heat exchangers. When applied to the case study of temperature maintenance in a room, time to reach the maximum air temperature in the room was increased (19.7%), the initial investment was reduced by 11% and the PCM melting ratio was improved by 23.2%, as a drawback, the volume occupied by the unit was increased around 3 times.

7. Acknowledgment

The authors would like to thank the Spanish Government for the partial funding of this work within the framework of research projects ENE2005-08256-C02-02 and ENE2008-06687-C02-02. Pablo Dolado would specially like to thank the former Spanish Ministry of Education and Science for his FPI grant associated with the research project. The authors also wish to thank the company CIAT for the support given in the early stages of the experimental work. Special thanks are extended to Mr. Miguel Zamora, CIAT R&D Manager, for his collaboration.

8. Nomenclature

A	[m ²]	heat exchange area
A _t	[m ²]	tube lateral area
A _i	[m ²]	area under the T-t curve, for the PCM
A _i '	[m ²]	area under the T-t curve, for water
b	[J/(g · K)]	parameter associated with the slope of the curve in all-liquid phase and all-solid phase, sensible heat, heat capacity

$C_{air} = \rho_{air} \cdot \frac{\dot{V}_{air}}{2 \cdot N_{walls}} \cdot C_{p,air}$	[J/(s · K)]	heat capacity
C_p	[J/(kg · K)]	effective specific heat
$C_{p,air}$	[J/(kg · K)]	specific heat of air
$C_{p,liquid}$	[J/(kg · K)]	PCM effective specific heat in liquid phase
$C_{p,solid}$	[J/(kg · K)]	PCM effective specific heat in solid phase
C_{pt}	[J/(kg · K)]	specific heat of the tube
C_{pw}	[J/(kg · K)]	specific heat of water
d		desirability parameter (ranges from 0 to 1)
e	[m]	thickness
e_{plate}	[m]	thickness of the PCM plate
e_{air}	[m]	thickness of the air gap between two PCM plates
$E_{t,mod}$	[kJ]	total stored thermal energy for one module
h	[W/(m ² · K)]	convection coefficient (when standing alone)
h	[J/g]	enthalpy
h_{sl}	[J/g]	PCM solid-liquid phase change enthalpy
h_l	[J/g]	enthalpy value in liquid phase, just after finishing the solid-liquid phase change
h_s	[J/g]	enthalpy value in solid phase, just before the start of the solid-liquid phase change
L	[m]	sample thickness
m_p	[kg]	PCM mass
m_t	[kg]	tube mass
\dot{m}	[kg/s]	mass flow
$\dot{m}_{air \text{ through HX}}$	[kg/s]	air mass flowing through the heat exchanger
$\dot{m}_{ventilation}$	[kg/s]	ventilation air mass flow
M_{PCM}	[kg]	PCM mass
N		number of elements
$NTU_{air} = (h \cdot \Delta x \cdot w) / C_{air}$		number of transfer units
\dot{Q}	[W]	thermal power, heat transfer rate
$\dot{Q}_{average, 1h}$	[W]	average heat transfer rate in the first hour of storage unit operation
\dot{Q}_{demand}	[kW]	internal cooling demand
\dot{Q}_{HX}	[kW]	heat transfer rate in the heat exchanger
$\dot{Q}_{resistances}$	[kW]	heating power of the electrical resistances used in the experimental setup
t	[s]	time
t_{melt}	[s]	total melting time
$t_{additional, T=38^\circ C}$	[s]	elapsed time to reach 38°C in the room
$t_{additional, T=44^\circ C}$	[s]	elapsed time to reach 44°C in the room
$t_{1/2}$	[s]	time until the air reaches 32°C at the outlet of the storage unit
T	[K, °C]	time elapsed until half the temperature increment is achieved temperature

\bar{T}_{surface} [°C]	average surface temperature of the PCM
\bar{T}_{plateau} [°C]	average of air temperature during the plateau, obtained either from the evolution of room temperature when it is simulated or from the air temperature at the heat exchanger outlet when it is measured on the experimental setup
T_{room^i} [°C]	room temperature at i instant
T_{outside} [°C]	outdoors air temperature
T_{melt} [°C]	average PCM melting temperature
T_{ob} [°C]	air temperature plateau objective
T_{sl} [°C]	air temperature at the inlet of the storage unit
\dot{V} [m ³ /h]	average phase change temperature of PCM
w	volumetric flow
$\#_{\text{modules}}$	uncertainty contribution
%Melt	number of PCM modules in the storage unit
	ratio of PCM melted, percentage

Greek symbols:

α [m ² /s]	thermal diffusivity
λ [W/(m·K)]	thermal conductivity
λ_{eff} [W/(m·K)]	effective thermal conductivity
ρ [kg/m ³]	density
Δh [J/g]	enthalpy difference
Δp [Pa]	pressure difference
ΔT [K]	temperature difference
ΔT_i [K]	temperature step
$\Delta T_{\text{thermopile}}$ [K]	temperature difference of air between the inlet and outlet, measured using a thermopile
$\Delta t_i = t_{i+1} - t_i$ [s]	time interval for the PCM
$\Delta t'_i = t'_{i+1} - t'_i$ [s]	time interval for water
Δt_{ob} [s]	plateau time objective
$\Delta x, \Delta y$ [m]	node length and height respectively

Acronyms and definitions:

Bi	Biot number
Fo	Fourier number
Re	Reynolds number

$$Fo_{\text{enc}} = \frac{\lambda_{\text{enc}} \cdot \Delta t}{\rho_{\text{enc}} \cdot Cp_{\text{enc}} \cdot e^2}$$

$$Fo_{\text{PCM}} = \frac{\lambda_{\text{PCM}}(T) \cdot \Delta t}{\rho_{\text{PCM}}(T) \cdot Cp_{\text{PCM}}(T) \cdot \Delta y^2}$$

$$Fo_{\text{PCM-enc}} = \frac{\lambda_{\text{PCM}} \cdot \Delta t}{(\rho_{\text{enc}} \cdot Cp_{\text{enc}} \cdot e + \rho_{\text{PCM}} \cdot Cp_{\text{PCM}} \cdot \Delta y) \cdot \Delta y}$$

$$Fo_{\text{enc-PCM}} = \frac{\lambda_{\text{enc}} \cdot \Delta t}{(\rho_{\text{enc}} \cdot Cp_{\text{enc}} \cdot e + \rho_{\text{PCM}} \cdot Cp_{\text{PCM}} \cdot \Delta y) \cdot e}$$

$$Bi_{enc} = h_{air} \cdot e / \lambda_{enc}$$

DOE	Design of Experiments
DSC	Differential Scanning Calorimetry
HTF	Heat Transfer Fluid
HVAC	Heating, Ventilation, and Air Conditioning
PCM	Phase Change Material
PID	Proportional Integral Derivative
TES	Thermal Energy Storage
1D	One Dimensional

9. References

- ANSI/ASHRAE STANDARD 94.1-2002. (2006). *Method of Testing Active Latent-Heat Storage Devices Based on Thermal Performance* (ANSI approved), recently replaced by ASHRAE 94.1-2010.
- Arkar, C. & Medved, S. (2005). Influence of accuracy of thermal property data of a phase change material on the result of a numerical model of a packed bed latent heat storage with spheres. *Thermochim Acta*, (Aug 2005), Vol. 438, No. 1-2, pp. 192-201, 0040-6031.
- Arkar, C.; Vidrih, B. & Medved, S. (2007). Efficiency of free cooling using latent heat storage integrated into the ventilation system of a low energy building. *Int J Refrig*, (Jan 2007), Vol. 30, No. 1, pp. 134-143, 0140-7007.
- Bakenhus, B.H. (2000). Ice storage project. *ASHRAE J*, (May 2000), Vol. 42, No. 5, pp. 64-66, 0001-2491.
- Bony, J. & Citherlet, S. (2007). Numerical model and experimental validation of heat storage with phase change materials. *Energy Build*, (Oct 2006), Vol. 39, No. 10, pp. 1065-1072, 0378-7788.
- Butala, V. & Stritih, U. (2009). Experimental investigation of PCM cold storage. *Energy Build*, (Mar 2009), Vol. 41, No. 3, pp. 354-359, 0378-7788.
- Del Coz Díaz, J.J.; García Nieto, P.J.; Lozano Martínez-Luengas, A. & Suárez Sierra, J.L. (2010). A study of the collapse of a WWII communications antenna using numerical simulations based on design of experiments by FEM. *Eng Struct*, (Jul 2010), Vol. 32, No. 7, pp. 1792-1800, 0141-0296.
- Dolado, P.; Lazaro, A.; Zalba, B. & Marín, J.M. (2007). Numerical simulation of heat transfer in phase change materials (PCM) for building applications. *Proceedings of Heat transfer in components and systems for sustainable energy technologies*, 2-9502555-3-1, Chambéry, France, April 2007.
- Dolado, P.; Lazaro, A.; Marin, J.M. & Zalba, B. (2011a). Characterization of melting and solidification in a real-scale PCM-air heat exchanger: Numerical model and experimental validation. *Energy Conv Manag*, (Nov 2010), Vol. 52, pp. 1890-1907, 0196-8904.
- Dolado, P.; Lazaro, A.; Marin, J.M. & Zalba, B. (2011b). Characterization of melting and solidification in a real-scale PCM-air heat exchanger: Experimental results and empirical model. *Renew Energy*, (Apr 2011), Vol. 36, pp. 2906-2917, 0960-1481.

- Dolado, P. (2011). *Thermal Energy Storage with phase change. Design and modelling of storage equipment to exchange heat with air*. Thesis, University of Zaragoza, 978-84-694-6103-7, Zaragoza, Spain. Access by (in Spanish): <http://zaguan.unizar.es/record/6153>
- EA-4/02. (1999). *Expression of the Uncertainty of Measurement in Calibration*. European co-operation for Accreditation.
- Gunasegaram, D.R.; Farnsworth, D.J. & Nguyen, T.T. (2009). Identification of critical factors affecting shrinkage porosity in permanent mold casting using numerical simulations based on design of experiments. *J Mater Process Technol*, (Feb 2009), Vol. 209, No. 3, pp. 1209-1219, 0924-0136.
- Günther, E.; Mehling, H. & Hiebler, S. (2007). Modeling of subcooling and solidification of phase change materials. *Modell Simulat Mater Sci Eng*, (Dec 2007), Vol. 15, No. 7, pp. 879-892, 0965-0393.
- Hamdan, M.A. & Elwerr, F.A. (1996). Thermal energy storage using a phase change material. *Sol Energy*, (Feb 1996), Vol. 56, No. 2, pp.183-189, 0038-092X.
- Kürklü, A. (1998). Energy storage applications in greenhouses by means of phase change materials (PCMs): a review. *Renew Energy*, (Jan 1998), Vol. 13, No. 1, pp. 89-103, 0960-1481.
- Lazaro, A.; Dolado, P.; Marín, J.M. & Zalba, B. (2009a). PCM-air heat exchangers for freecooling applications in buildings: experimental results of two real-scale prototypes. *Energy Conv Manag*, (Mar 2009), Vol. 50, pp. 439-443, 0196-8904.
- Lazaro, A.; Dolado, P.; Marín, J.M. & Zalba, B. (2009b). PCM-air heat exchangers for freecooling applications in buildings: empirical model and application to design. *Energy Conv Manag*, (Mar 2009), Vol. 50, pp. 444-449, 0196-8904.
- Lazaro, A. (2009). *Thermal energy storage with phase change materials. Building applications: materials characterization and experimental installation to test PCM to air heat exchanger prototypes*. Thesis, University of Zaragoza, Zaragoza, Spain.
- Lazaro, A.; Zalba, B.; Bobi, M. & Castellón, C. (2006). Experimental Study on Phase Change Materials and Plastics Compatibility. *AIChE J*, (Feb 2006), Vol. 52, No. 2, pp. 804-808, 0001-1541.
- London, A.L. & Seban, R.A. (1943). Rate of ice formation. *Transactions of the ASME*, Vol. 65, pp. 771-778.
- Marin, J. M. & Monne, C. (1998). *Transferencia de calor (Heat transfer)*, Kronos, 8488502729, Zaragoza, Spain.
- Marin, J.M.; Zalba, B.; Cabeza, L.F. & Mehling, H. (2003). Determination of enthalpy-temperature curves of phase change materials with the temperature-history method: improvement to temperature dependent properties. *Meas Sci Technol*, (Feb 2003), Vol. 14, No. 2, pp. 184-189, 0957-0233.
- McKay, M.D.; Conover, W.J. & Beckman, R.J. (1979). A comparison of three methods for selecting values of input variables in the analysis of output from a computer code. *Technometrics*, Vol. 21, No. 2, pp. 239-245, 0040-1706.
- Mehling, H. & Cabeza, L.F. (2008). *Heat and cold storage with PCM. An up to date introduction into basics and applications*, Springer-Verlag, 978-3-540- 68556-2, Berlin-Heidelberg, Germany.
- Mills, A.; Farid, M.; Selman, J.R. & Al-Hallaj, S. (2006). Thermal conductivity enhancement of phase change materials using a graphite matrix. *Appl Therm Eng*, (Oct 2006), Vol. 26, No. 14-15, pp. 1652-1661, 1359-4311.

- Pérez Vergara, I.G.; Díaz Batista J.A. & Díaz Mijares, E. (2001). Simulation experiments optimized by response surfaces, *Centro Azucar*, (Jan 2001), Vol. 2, pp. 68-74.
- Sharma, A.; Tyagi, V.V.; Chen, C.R. & Buddhi, D. (2009). Review on thermal energy storage with phase change materials and applications. *Renew Sust Energ Rev*, (Feb 2009), Vol. 13, pp. 318-345, 1364-0321.
- Turnpenny, J.R.; Etheridge, D.W. & Reay, D.A. (2001). Novel ventilation system for reducing air conditioning in buildings. Part II: testing of prototype. *Appl Therm Eng*, (Aug 2001), Vol. 21, No. 12, pp. 1203-1217, 1359-4311.
- Watanabe, H. (2002). Further examination of the transient hot-wire method for the simultaneous measurement of thermal conductivity and thermal diffusivity. *Metrologia*, Vol. 39, No. 1, pp. 65-81, 0026-1394.
- Yanbing, K.; Yi, J. & Yinping, Z. (2003). Modeling and experimental study on an innovative passive cooling system e NVP system. *Energy Build*, (May 2003), Vol. 35, No. 4, pp. 417-425, 0378-7788.
- Zalba, B.; Marín, J.M.; Cabeza, L.F. & Mehling, H. (2004). Free-cooling of buildings with phase change materials. *Int J Refrig*, (Dec 2004), Vol. 27, No. 8, pp. 839-849, 0140-7007.
- Zalba, B.; Marín, J.M.; Cabeza, L. & Mehling, H. (2003). Review on thermal energy storage with phase change: materials, heat transfer analysis and applications. *Appl Therm Eng*, (Feb 2003), Vol. 23, No. 3, pp. 251-283, 1359-4311.
- Zhang, Y.; Jiang, Y. & Jiang, Y. (1999) A simple method, the T-history method, of determining the heat of fusion, specific heat and thermal conductivity of phase-change materials. *Meas Sci Technol*, (Mar 1999), Vol. 10, No. 3, pp. 201-205, 0957-0233.
- Zhang, D.; Tian, S.L. & Xiao, D.Y. (2007). Experimental study on the phase change behavior of phase change material confined in pores. *Sol Energy*, Vol. 81, No. 5, pp. 653-660, 0038-092X.
- Zukowski, M. (2007a). Experimental study of short term thermal energy storage unit based on enclosed phase change material in polyethylene film bag. *Energy Conv Manag*, (Jan 2007), Vol. 48, No. 1, pp. 166-173, 0196-8904.
- Zukowski, M. (2007b). Mathematical modeling and numerical simulation of a short term thermal energy storage system using phase change material for heating applications. *Energy Conv Manag*, (Jan 2007), Vol. 48, No. 1, pp.155-65, 0196-8904.

Ground-Source Heat Pumps and Energy Saving

Mohamad Kharseh

*Willy's CleanTech AB, PARK 124 Karlstad,
Sweden*

1. Introduction

The global warming itself and its consequences cause considerable problems. It results in extreme climate events such as droughts, floods, or hurricanes, which are expected to become more frequent. This puts extra strain on people and has great impact on public health and life quality especially in poor countries.

Internationally, there is a political understanding that global warming (or climate change) is the main challenge of the world for decades to come. Thus, all states must work together in order to overcome climatic change consequences.

Although, studies suggest that there is indeed relationship between solar variability and global warming (Lean and Rind, 2001), two causes of the warming have been suggested:

1. related to the accumulation of greenhouse gases in the Earth's atmosphere;
2. related to heat emissions (Nordell, 2003, Nordell and Gervet, 2009).

This implies that current warming is anthropogenic and caused by human activities, i.e. global use of non-renewable energy. So far, the total global energy consumption has already exceeded $15 \cdot 10^{10}$ MWh/year and it is projected to have an annual growth rate about 1.4 % until 2020 (EIA, 2010).

Much of the energy used worldwide is mainly supplied by fossil fuels (~85 % of the global energy demand while renewable energy sources supply only about 6 %) (Moomaw et al., 2011, Jabder et al., 2011, Jaber et al., 2011). Owing to global dependence on oil fuels has resulted in a daily oil consumption of 87.7 million barrels (Mbbl), Fig. 1 (IEA, 2010, EIA, 2007). Consequently, about $3 \cdot 10^{10}$ ton of carbon dioxide emissions are annually emitted into the atmosphere. In other word, for each consumed kWh about 205 kg of carbon dioxide is being emitted into the atmosphere.

Environmental reasons urge us to find more efficient ways in converting and utilizing the energy resources. From the environment point of view, there is now almost universal scientific acceptance that profligate energy use is causing rapid and dangerous changes in the global climate. There is mounting evidence that the mean global temperature has increased over the period 1880 to 1985 by 0.5 to 0.7 °C (Hansen and Lebedeff, 1987). While surface air temperature (SAT) compilations shows that SAT has increased 1.2 °C last century. If a current climatic change trend continues, climate models predict that the

average global temperature are likely to have risen by 4 to 6 °C by the end of 21st century (Gaterell, 2005). As climate change progresses, all the other environmental problems are becoming worse and harder to solve. Therefore, a sustainable future requires worldwide efforts to prepare for new energy sources and a more efficient use of energy.

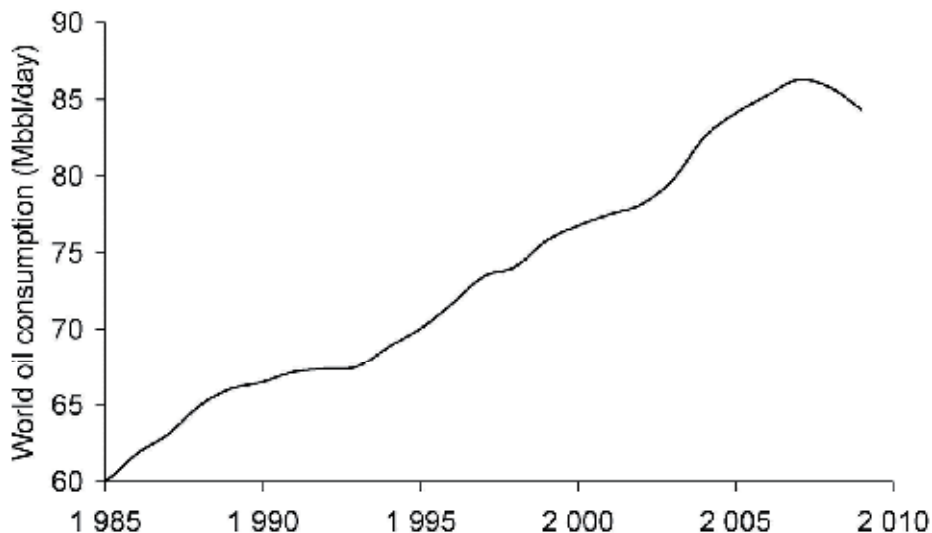


Fig. 1. World oil consumption.

Thanks to the awareness of the impact of global warming and its relationship with human activities, there has been a growing interest in reducing fossil energy consumptions. Specifically, more efficient use of energy and increased use of renewable energy seem to be our main weapon against the ongoing global warming.

Heating and cooling in the industrial, commercial, and domestic sectors accounts for about 40-50 % of the world's total delivered energy consumption (IEA, 2007, Seyboth et al., 2008). Although, buildings regulations aim to reduce the thermal loads of buildings, as the economic growth improves standards of living, the energy demand for heating and cooling is projected to increase. For example, in non-OECD nations, as developing nations mature, the amount of energy used in buildings sector is rapidly increasing. Consequently, the implementation of more efficient heating/cooling systems is of clear potential to save energy and environment. However, the use of renewable energy systems for heating and cooling applications has received relatively little attention compared with other applications such as renewable electricity or biofuels for transportation. Yet, renewable energy sources supply only around 2-3% of annual global heating and cooling (EIA, 2010). It is worth mentioning that a century or more ago renewable energy accounted for almost 100%. In other word, all current researches aim to approach what was the case in the past.

Nowadays, and due to its high thermal performance, the ground source heat pump (GSHP) has increasingly replaced conventional heating and cooling systems around the world. Such system extracts energy from a relatively cold source to be injected into the conditioned space in winter or alternatively, extracts energy from conditioned spaces to be injected into a relatively warm sink in summer.

Current work emphasizes the importance of using ground source heat pumps in reaching towards the renewable energy goals of climate change mitigation, and reduced environmental impacts.

2. Principle of GSHP systems

The ground source heat pump (GSHP) system are also known as ground coupled heat pump (GCHP), borehole systems or borehole thermal energy storage (BTES), and shallow geothermal system. Due to its high thermal performance, the ground source heat pump (GSHP) have increasingly replaced conventional heating and cooling systems around the world (IEA, 2007, Hepbasli, 2005, De Swardt and Meyer, 2001). Essentially GSHP systems refer to a combination of a heat pump and a system for exchanging heat from the ground. The GSHPs move heat from the ground to heat homes in the winter or alternatively, move heat from the homes to the ground to cool them in the summer. This heat transfer process is achieved by circulating a heat carrier (water or a water-antifreeze mixture) between a ground heat exchanger (GHE) and heat pump. The GHE is a pipe (usually of plastic) buried vertically or horizontally under the ground surface, Fig. 2 (Sanner et al., 2003). At the beginning of 2010 the totally installed GSHP capacity in the world was 50,583 MW producing 121,696 GWh/year with capacity factor and annual grow rate of 0.27 and 12.3%, respectively (Lund et al., 2010).

Heating mode: In this case, the GHE and the heat pump evaporator are connected together and the heat pump moves the heat from the ground into the conditioned space. The liquid of relatively low temperature is pumped through the GHE, collecting heat from the surrounding ground, and into the heat pump. Since the temperature of extracted liquid, which is around mean annual air temperature, is not suitable to be used directly for heating purpose, heat pump elevates the temperature to a suitable level (30-45 °C) before it is submitted to a distribution system.

Cooling mode: In this case, the GHE and the heat pump condenser are connected together and heat pump moves the heat from the conditioned space into the ground. The liquid of relatively high temperature is pumped through the GHE, dispersing heat into the surrounding ground, and into the heat pump.

As known, heat transfers from a warmer object to a colder one. Heat, as stated by the second law of thermodynamics, cannot spontaneously flow from a colder location to a hotter area unless work is done. The heat pump is simply a device for absorbing heat from one place and transporting it to another of relatively lower temperature. So, such device can be used to maintain a space temperature at desired level by removing unwanted heat (e.g. a fridge or air conditioning unit) or to transport heat to where it is wanted (space or water heating). In space conditioning application, heat pump system is composed of an indoor unite and an outdoor unite and the task of the heat pump is to transfer heat from one unite to the other. In order to keep inside temperature at comfort level in the winter, for example, the heat pump absorbs heat from outdoor and expels it into building. In the summer the reversed process occurs, i.e. the heat pump moves heat from indoor and expels it to outside.

The temperature difference between the indoor unite and outdoor unite is referred to as temperature lift. This temperature plays a major role in determining the coefficient of performance of heat pump ($COP = \text{delivered energy} / \text{driving energy}$). A smaller temperature

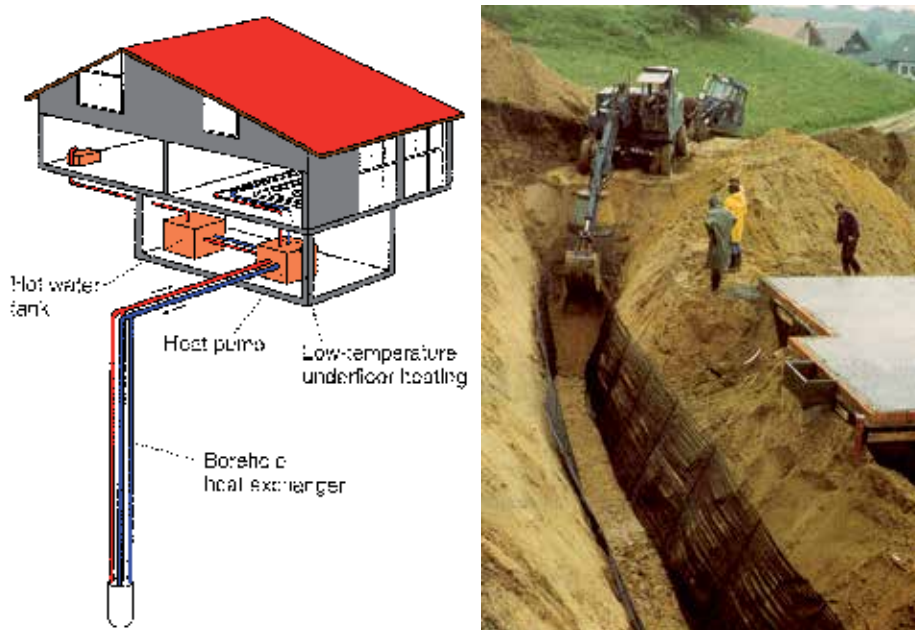


Fig. 2. Typical application of ground source heat pump system (Sanner et al., 2003).

lift results in a better COP. More specifically, extracting heat from a warmer medium during the heating season and injecting heat into a colder medium during cooling season leads to a better COP and, consequently, less energy use.

Fig.3 shows a schematic illustration of the components of assumed system as well as the thermodynamic cycle on diagrams temperature-entropy and pressure-enthalpy. Many techniques have been recently proposed in order to improve the cycle performance, more details are given by Wang, 2000, Chap.9 (Wang, 2000). In the current work, a heat exchanger has been added between the suction line and liquid line.

Like a heat engine but operating in reverse, the thermodynamics of the cycle can be analyzed on diagrams. In general COP is defined as the ratio between the delivered capacity and compressor capacity (Wang, 2000):

$$COP_c = \frac{Q_c}{W_{cp}} \quad (1)$$

$$COP_h = \frac{Q_h}{W_{cp}} \quad (2)$$

Where Q_h , Q_c , and W_{cp} represent the heating, cooling, and compressor capacity, respectively.

As shown in the Fig. 3, the heat exchanging operations in the evaporator and the condenser occurs at constant pressure processes (isobar). The compression process in the compressor befall at isentropic process theoretically, while the expansion operation in the expansion valve occurs at adiabatic process. With these in mind, as per the thermodynamics rules, the terms of Eq.1 and Eq.2 might be calculated as follows:

$$Q_h = m \cdot (h_3 - h_4) \quad (3)$$

$$Q_c = m \cdot (h_7 - h_6) \quad (4)$$

$$W_{CP} = m \cdot (h_2 - h_1) \quad (5)$$

Where, h and m represent enthalpy and refrigerant mass flow rate, respectively (see Fig. 3).

In order to accomplish the calculations, the following assumptions were made:

- Refrigerant R22
- Pressure drop at inlet and outlet of the compressor was assumed $P_8 - P_1 = 10$ and $P_2 - P_3 = 23$ KPa respectively, see Fig.3.
- The pressure drop through the pipe is negligible.
- The isentropic efficiency of the compressor is 80%.
- There is no sub-cooling in the condenser or useless superheat in suction line.
- Thermal efficiency of the heat exchanger, which expresses how efficient the heat exchanger utilizes the temperature difference, is 90%
- Heat loss factor of the compressor, i.e. ratio between heat loss of the compressor to the surroundings and the energy consumption of the compressor, is 15%.
- Regarding to the internal unite of the heat pump, in wintertime the condensation temperature was assumed 38 °C. In summertime, the evaporation temperature was assumed 8 °C.
- Heating/Cooling capacity assumed to be constant, thus a change in temperature will affect the flow rate of refrigerant through the cycle.

The calculation results are illustrated in Fig.4. Apparently, the COP of heating machine increases as the evaporation temperature rises. Likewise, the performance of cooling machine increases as the condensation temperature decreases.

The ground temperature below a certain depth is constant over the year. This depth depends on the thermal properties of the ground, but it is in range of 10-15 m, see section 3 below. Thus, the ground is warmer than the air during wintertime and colder than the air during the summertime. Therefore, use the ground instead of the air as heat source or as a heat sink for the heat pump results in smaller lift temperature and, consequently, better thermal performance. In addition to improve the COP, the relatively stable ground temperature means that GSHP systems, unlike ASHP, operate close to optimal design temperature thereby operating at a relatively constant capacity. It is good to mention here that in outdoor unite fan, in ASHP case, consumes more energy than that of the water pump in the GSHP case (De Swardt and Meyer, 2001). Therefore, the comparison would be even more favorable for the GSHP, if the fan energy consumption is considered in the COP calculation.

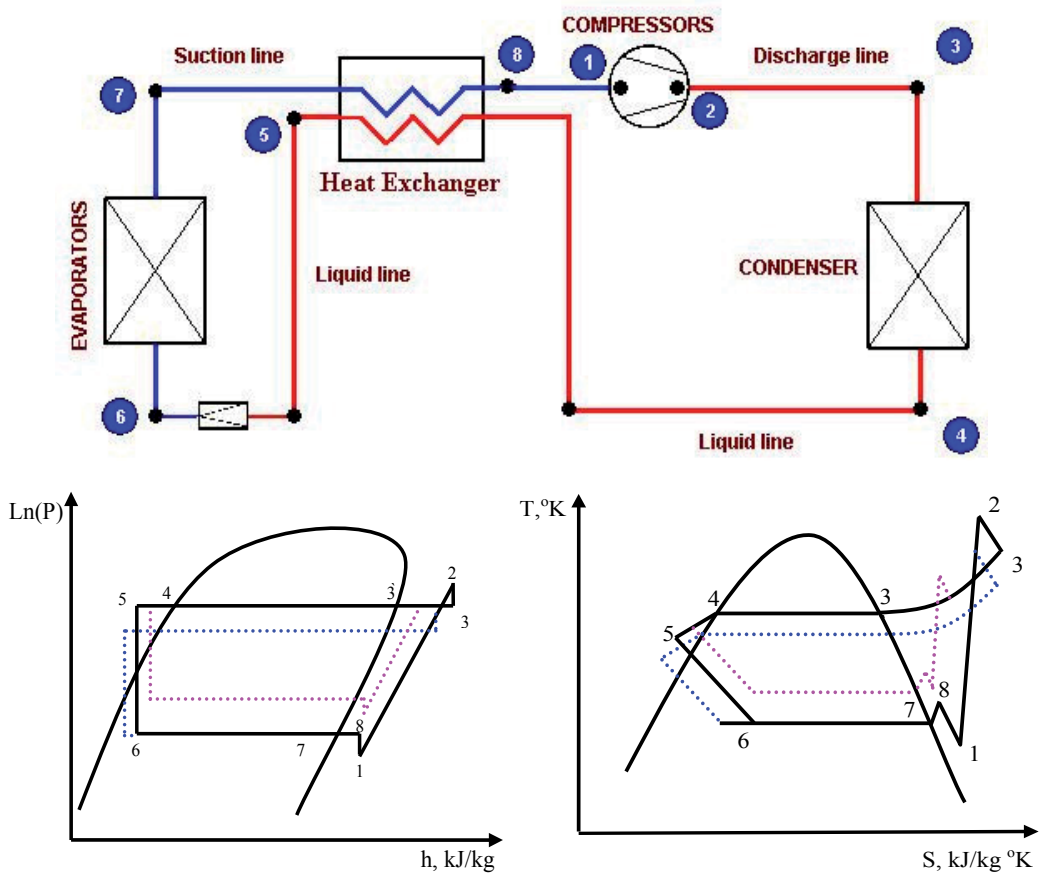


Fig. 3. Illustration of heat pump and the thermodynamic cycle on the LnP-h and T-S diagram.

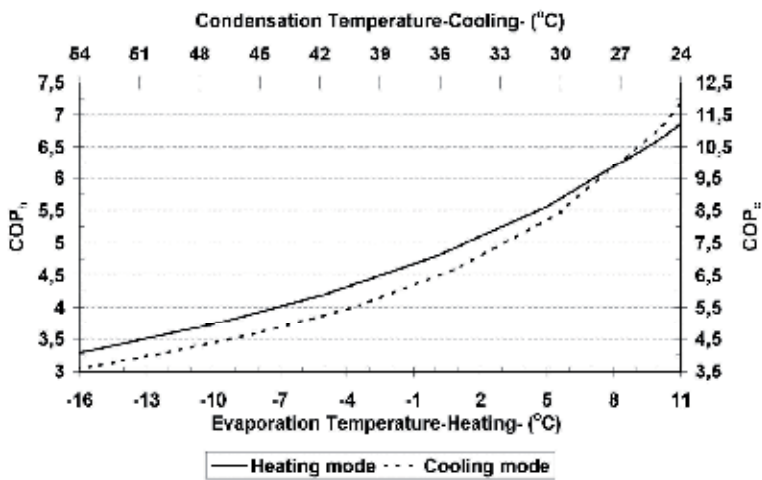


Fig. 4. Actual COP as a function of condensation /evaporation temperature.

3. Ground temperature

The ambient air temperature over the year or the day can be treated as a sinusoidal function around its average value T_a . This fluctuation might be expressed by:

$$T(t) = T_a + A_a \cdot \cos\left(2\pi \cdot \frac{t}{t_o}\right) \quad (6)$$

Where $T(t)$ is air temperature at given time t ; T_a is average air temperature for the period t_o , A_a is the air temperature amplitude (half of the difference between the maximum and minimum temperatures for the period), t_o is the time for one complete cycle (day or year).

Apparently, air temperature fluctuation generates variations in the ground temperature. In order to find out a mathematical expression of ground temperature, the equation to be solved is the one-dimensional heat conduction equation. The mathematical formulation of this problem is given as:

$$\frac{\partial^2 T(z,t)}{\partial z^2} = \frac{1}{\alpha} \cdot \frac{\partial T(z,t)}{\partial t} \quad (7)$$

Where α is the thermal diffusivity (m^2/s), z depth below the surface (m), t is the time. Note that for oscillating temperature at the boundary, we do not need an initial condition. The solution of Eq.12 can be found by Laplace transformation method (Carslaw and Jaeger, 1959):

$$T(t,z) = T_a + A_a \cdot e^{-\frac{z}{d_o}} \cdot \cos\left(2\pi \cdot \frac{t}{t_o} - \frac{z}{d_o}\right) \quad (8)$$

Where d_o is the penetration depth (m), which is defined as the depth at which the temperature amplitude inside the material falls to $1/e$ (about 37%) of the air temperature at the surface:

$$d_o = \sqrt{\frac{\alpha \cdot t_o}{\pi}} \quad (9)$$

Fig.5 shows the underground temperature as function of the depth at different seasons of the year. As shown, below a certain depth, which depends on the thermal properties of the ground, the seasonal temperature fluctuations at ground surface disappears and ground temperatures is essentially constant throughout the year. In other word, for depth below a few meters ground is warmer than air during the winter and colder than the air during the summer.

Eq. 8 shows that ground temperature amplitude decreases exponentially with distance from the surface at a rate dictated by the periodic time, mathematically we can write:

$$A_g = A_a \cdot e^{-\frac{z}{d_o}} \quad (10)$$

Where A_g is ground temperature amplitude ($^{\circ}\text{C}$).

In addition, Eq. 8 shows that there is a time lag between the ground and air oscillating temperature. In other words, the maximum or minimum ground temperature occurs later than the corresponding values at the surface. From the cosine term in Eq. 8 one can conclude that the time lag increases linearly with depth. The shifting time, ϕ , between surface and the ground at a given depth z is:

$$\phi = t_2 - t_1 = \frac{z}{2} \cdot \sqrt{\frac{C \cdot t_0}{\pi \cdot \lambda}} \quad (11)$$

Indeed, change in temperature of ambient air results in change in the undisturbed ground temperature. Measurements of borehole temperature depth profile (BTDP) evidently show that there are temperature deviations from the linear steady-state ground temperature in the upper sections of boreholes (Goto, 2010, Harris and Chapman, 1997, Lachenbruch and Marshall, 1986, Guillou-Frottier et al., 1998). Mathematical models have been used to simulate the change in ground temperature due to GW. Kharseh derived a new equation that gives the ground temperature increase in areas where the surface warming is known (Kharseh, 2011). The suggested solution is more user-friendly than other solutions. The derived equation was used to determine the average change of ground temperature over a certain depth and therefore the heat retained by a column of earth during the warming period. This average change of ground temperature is of great importance in the borehole system.

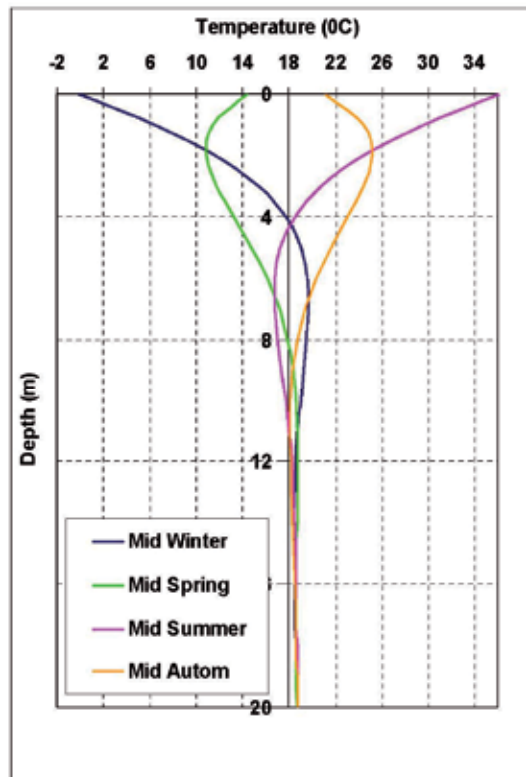


Fig. 5. Temperature profile through the ground.

4. Ground source heat pump systems and energy saving

4.1 Case study – the Kharseh chicken farm

The Kharseh chicken farm in Hama, Syria, was selected as a study case to show the contribution of ground source heat pumps in saving energy consumption of heating and cooling system. Even though the annual mean temperature in Syria is 15-18 °C, heating of such farm consumes considerable amounts of energy. The reason is that the air temperature is close to freezing during three winter months and that chickens require a relatively high temperature, 21-35 °C, depending on chickens' age as seen in Table. 1.

Age of chicken (weeks)	Temperature at 0.10-0.15 m level (°C)
1	35
2	32
3	29
4	27
5	24
6 (fully grown)	21

Table 1. Appropriate indoor temperature in chicken farms.

The chicken hangar is placed parallel to the main wind direction has a floor area of 500 m² (50 m x 10 m) in E-W direction. The total window area is 24 m².

4.2 Heating/cooling demand

The mean heating load composed of heat losses through the external walls and ventilation, while cooling load composed of heat gained through external walls, ventilation, solar radiation, and heat released by chickens. In current work the degree-hour method was used to estimate the thermal demand of the hangar (Durmayaz et al., 2000) using following assumptions:

- External wall's area, of thermal resistance 0.45 K.m²/W, is 336 m²
- Floor and ceiling area, of thermal resistance 5 and 0.45 K.m²/W, respectively, is 500 m²
- Windows's area, of thermal resistance 0.2 K.m²/W, is 24 m²
- Ventilation rate 20 m³/m²,h (ventilated area of chicken farm varies with chicken age)
- Heat release from chickens: 50 W/m² (varies with age)
- The capacity of the hangar is 5 cycles/year of 55 days the period of each cycle life. This mean that the hangar will be occupied 75% out of the entire year.
- During their first day, the chickens occupy about 85 m² of the building. This area is increased 14 m² per day until they occupy the entire area of the hangar after about one month. This mean the average occupied are during one cycle is 77% out of whole hangar's area.

- Heating season is 6 months, while cooling season is 4 months.
- 10 h of cooling and 24 hours of heating are required per a day during summer and winter, respectively.

Using these assumptions, the total heat loss coefficient of the hangar, L (W/K), can be calculated as follow:

$$L = \frac{(\rho C_p)_{air} \cdot I \cdot V}{3600} + \sum U \cdot A \quad (12)$$

Finally, annual heating demand, Q_h (MWh), is

$$Q_h = \frac{L \cdot DHh - 50 \cdot 500 \cdot 24 \cdot 30 \cdot 6}{10^6} \quad (13)$$

While the annual cooling demand, Q_c (MWh), is

$$Q_c = \frac{L \cdot DHc + 50 \cdot 500 \cdot 10 \cdot 30 \cdot 4}{10^6} \quad (14)$$

Where DHh and DHc is the total number of degree-hours of heating and cooling, respectively, which can be calculated as follow:

$$DHh = \sum_{j=1}^N (T_i - T_o)_j \quad \text{when is } T_o \leq T_b \quad (15)$$

While for cooling (DHc)

$$DHc = \sum_{j=1}^K (T_o - T_i)_j \quad \text{when is } T_o \geq T_b \quad (16)$$

Where T_b is the base temperature and T_i represents the indoor design temperature, T_o is the hourly ambient air temperature measured at a meteorology station, N is the number of hours providing the condition of $T_o \leq T_b$ in a heating season while K is the number of hours providing the condition of $T_o \geq T_b$ in a cooling season. In current work, and due to considering the big internal load, base temperature was assumed to be equal to T_i . Since the indoor temperature varies with the time during chickens cycle, the indoor temperature was assumed to be constant during one cycle and equals the average temperature i.e. $T_i = 28$ °C. Fig.6 shows that the estimated total annual heating demand is 230 MWh while the corresponding cooling demand is 33 MWh.

In order to determine the maximum required heating and cooling capacity, the required heating/cooling power as the chickens grow during the hottest and coldest period of the year were calculate. As shown in Fig. 7, during heating season, due to lowering the appropriate indoor temperature with age and due to increase the occupied area, the heating power increases with time until it peaks in the middle of the chickens' life cycle. This peak demand does not occur during the cooling season. The calculations showed that the maximum required heating and cooling capacity are 113 kW and 119 kW, respectively.

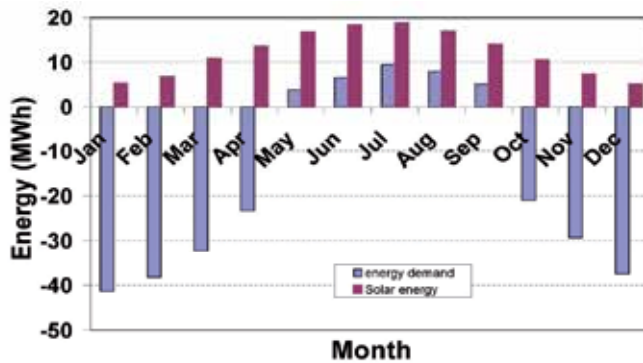


Fig. 6. Monthly heating/cooling demand and solar yield.

It should be noted that in Kharseh, 2009 the German DIN was used for the same aim. Therefore there is a small different in estimated thermal demand of the hangar.

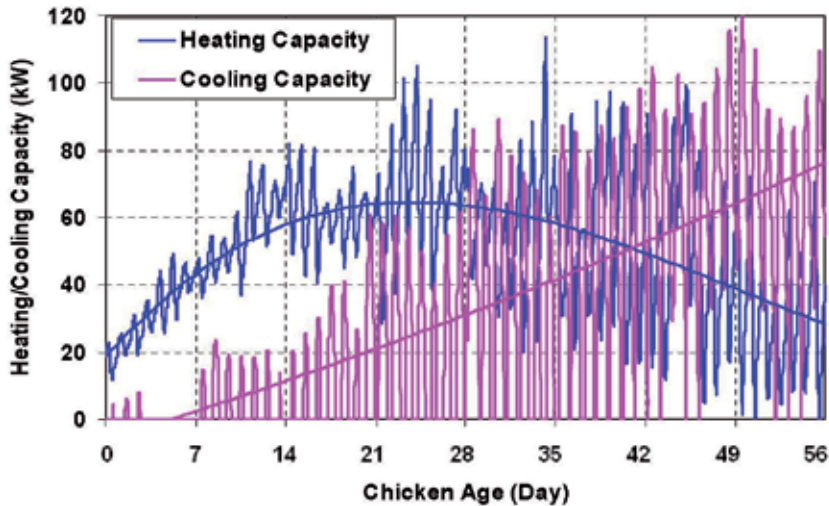


Fig. 7. Heating/cooling power as function of chicken age for one complete cycle during the hottest and coldest period.

4.3 System design and simulated operation

The EED (Earth Energy Design) model(EED, 2008) was used in pre-designing required borehole system to meet to estimated heating/cooling load at given conditions.

4.3.1 Borehole system

Specific data of the borehole system are given below:

- Number of boreholes: 10
- Borehole Diameter: 0.11 m
- Borehole Depth: 120 m

- Volumetric heat capacity: 2.16 MJ/m³.K
- Ground thermal conductivity: 3.5 W/m.K
- Drilling Configuration: open rectangle 175 (3 x 4)
- Borehole Spacing: 6 m.
- Borehole installation: Polyethylene U-pipe
- Fluid flow rate: 0.5 10⁻³ m³/s, borehole.

To keep the borehole temperature at steady state between the years extracted and injected heat from/to the ground were balanced by charging solar heat during the summer.

4.4 Solar collector

Since the annual heating demand of the hangar is much greater than annual cooling demand, which mean the energy extracted from the ground will be more than that injected into the ground, recharging the borehole filed by external energy resource is need. The amount of available solar energy in Syria means great potential for combined solar and GSHP systems. The estimated required solar collector area without considering heat yield from ground was:

$$A = \frac{Q_h \cdot \left(1 - \frac{1}{COP_h}\right) - Q_c \cdot \left(1 + \frac{1}{COP_c}\right)}{\eta \cdot \sigma} \quad (17)$$

Where

- Q_h Heating demand (MWh)
- COP_h Coefficient of performance for heating (in this case =5)
- Q_c Cooling demand (MWh)
- COP_c Coefficient of performance for free cooling (in this case =50)
- σ Yearly sun yield (in this case $\sigma=1.973$ MWh/m²)
- η Solar collector efficiency (in this case $\eta=0.86$).

In this case, the required solar collector area was 85 m². The solar heat is directly used when needed while the rest of the heat is stored to be used later (Fig.8).

4.5 Operation

During the wintertime Fig.8, water is pumped from the borehole through the solar collector to increase its temperature. The temperature increase, which is only 0.8 °C during the winter, is considerably greater during the summer. The heat pump cools the water before it is again pumped through the borehole, where it will be warmed up. The extracted heat is emitted into the hangar. Fig.9 shows that the lowest extracted water temperature from borehole is 11.5 °C. During summertime Fig.8, the ground temperature is cold enough for free cooling, so the water is pumped directly to the heat exchanger. Due to the heat exchange with indoor air, the water temperature will increase. After the heat exchanger, water passes though the solar collector and back to the borehole. Then, its temperature will decrease before pumped back to the hangar. Fig.9 shows that the highest extracted water temperature from borehole is 26.5 °C

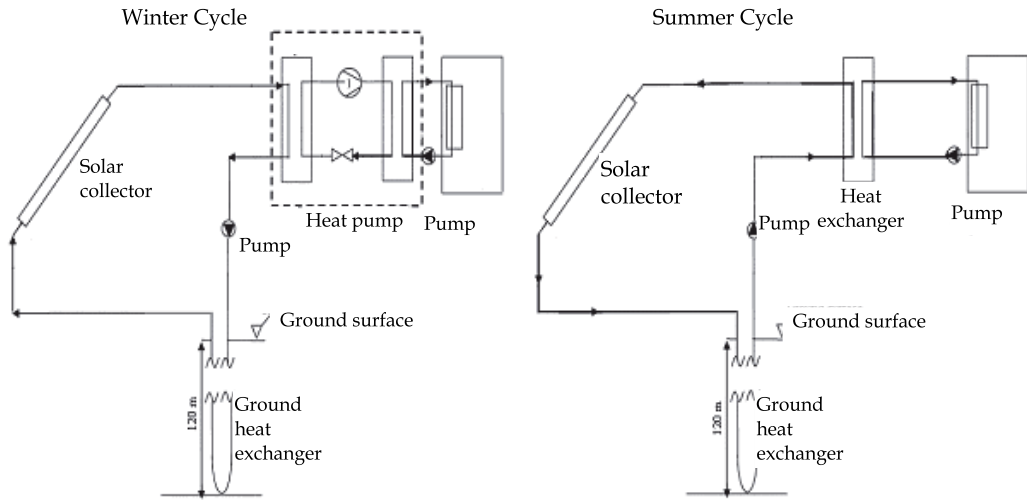


Fig. 8. Schematic of the solar coupled to ground source heat pump system.

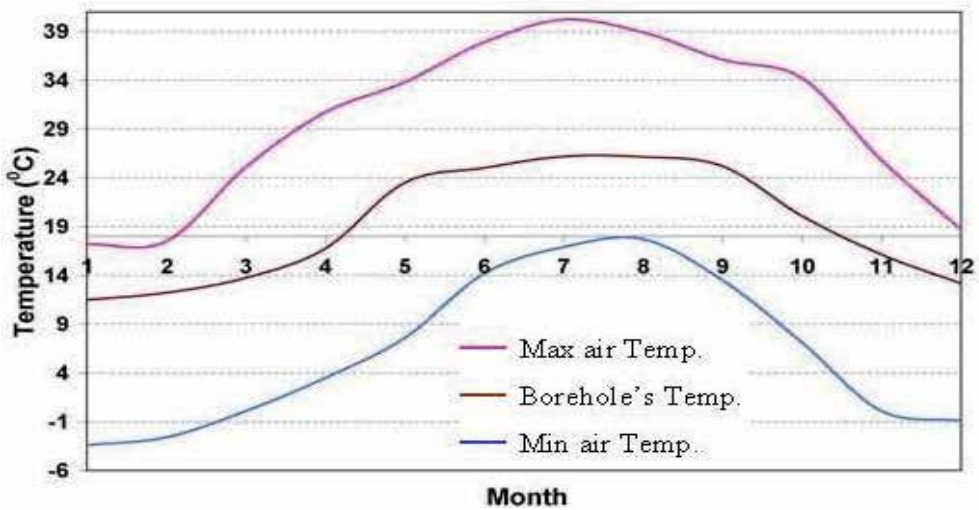


Fig. 9. Relevant temperatures for performed calculations.

5. Results and discussion

Present study was performed to determine the potential of GSHP, with solar collectors, for heating and cooling purposes in the Middle East. The Kharseh chicken farm in Syria of area 500 m² was chosen as a case study. The heating and cooling demands of the hangar were then used to estimate annual heating and cooling demands of the ideal chicken farm in Syria of area 200 m². The calculations showed the following results:

- A typical average size chicken house in Syria requires 92 MWh of heating and 13 MWh of cooling. Required heating and cooling powers are 45.2 kW and 47.7 kW, respectively, as shown in table 2.

Typical farm size Floor area 200 m ²			Totally for 13000 farms Floor area 2.6 Mm ²		
Meat production ton/year	Heating Energy MWh/year	Cooling Energy MWh/year	Total energy for heating GWh/y	Total energy for cooling GWh/y	Total Energy GWh/year
13	92	13	1196	170	1366

Table 2. Heating and cooling demand for chicken farms in Syria.

- 480 m of borehole with diameter 0.11 m and 34 m² of a solar collector were required to supply the heating and cooling of the typical chicken farms in Syria. In this case, the maximum fluid temperature delivered from the boreholes is 26.5 °C in the summer while the minimum mean fluid temperature was 11.5 °C during the winter.
- Table 3 shows the operation costs of coal furnace heating system combined with ASHP for cooling issue, diesel furnace heating system combined with ASHP for cooling issue, ASHP for both heating and cooling issue, and suggested GSHP heating/cooling system. Using Fig. 4, we found the COP_h and COP_c for the ASHP are 4 and 4.3, respectively, while the corresponding values for GSHP are 6.2 and 10. The conversion efficiency of conventional heater was assumed 85%. The calculations show that by using the GSHP, the annual operation costs can be reduced 38%, 69.2%, and 79.7 % compared to ASHP, coal heater combined with ASHP, and diesel heater combined with ASHP, respectively.
- Table 4 shows comparison between the required prime energy, i.e. tons of coal, of three different systems assuming the average annual efficiency of the power plant 32%. As shown, using the GSHP, the amount of fuel required is reduced 38% compared to ASHP or 57.2% compared to coal heater combined with ASHP. In other words, by use GSHP in all chicken farms in Syria, the annual coal consumption can be reduced 107.6·10³ ton compared to traditional existing system (coal heater combined with ASHP). Accordingly, the carbon dioxide emission can be reduced by the same percentages.

	Energy demand GWh/year	Energy Cost (MSP)			
		GSHP 3.5 SP/kWh	ASHP 3.5 SP/kWh	Coal Heater 8,141 kWh/kg, 13 SP/kg	Diesel Heater 10,1 kWh/1 25 SP/L
Heating	1196	675 (COP=6.2)	1047 (COP=4)	2247 ($\eta=0.85$)	3479($\eta=0.85$)
Cooling	170	60 (COP=10)	138 (COP=4.3)	138 (COP=4.3)	138 (COP=4.3)
Total	1366	735	1185	2385	3617
	Energy Cost SP/kWh	0.54	0.87	1.75	2.65

Table 3. Comparison between different heating/cooling systems for a typical chicken farm.

System	Required prime Energy GWh/y	Required Coal (10 ³ ton)
GSHP	210	80.6
ASHP	338	130
Coal Heater with ASHP	1446	188.2

Table 4. comparison between the required prime energy.

- The estimated installation cost of a borehole system for a typical chicken farm is \$15000. With current energy price in Syria the payback-time of GSHP is about 5.3, or 3 years compared to coal heater combined with ASHP, or diesel heater combined with ASHP, respectively.

6. Conclusions

The global energy oil production is unstable and will peak within a few years. Therefore, the energy prices are expected to rise and new energy systems are needed. In addition to this energy crisis the fossil fuels seems to be the main reason for climate change. There is a global political understanding that we need to replace fossil fuels by renewable energy systems in order to develop a stable and sustainable energy supply.

About half of the global energy consumption is used for space heating and space cooling systems. Ground source heat pump systems are considered as an energy system that can make huge contributions to reduce energy consumption and thereby save the environment.

7. Nomenclature

Q_c	cooling demand, (MWh)
Q_h	heating demand, (MWh)
W_{cp}	compressor capacity, (kW)
COP_c	coefficient of performance of cooling mode, (dimensionless)
COP_h	coefficient of performance of heating mode, (dimensionless)
h	enthalpy, (kJ/kg.K)
P	pressure, (Pa)
m	refrigerant mass flow rate, (kg/s)
$T(t)$	air temperature at given time t , (K)
T_a	average air temperature, (K)
A_a	the air temperature amplitude, (K)
A_g	ground temperature amplitude, (K).
t_o	the time for one complete cycle (day or year) of air temperature variation
z	depth below the surface, (m)
α	ground thermal diffusivity, (m ² /s)
d_o	penetration depth, (m)
ϕ	shifting time between the air and the ground temperatures variation,(s)
DH	degree-hour, (h.K)
CDH	cooling degree-hour, (h.K)
HDH	heating degree-hour, (h.K)
L	total heat loss coefficient of building, (W/K)
T_b	base temperature, (K)
T_o	outdoor temperature, (K)
Min T	minimum fluid temperature extracted from the borehole, (K)
Max T	maximum fluid temperature extracted from the borehole, (K)
σ	Yearly sun yield, (kWh/m ²)
η	Solar collector efficiency

8. References

- Carlaw, H. S. & Jaeger, J. C. 1959. *Conduction of heat in solids*, Oxford: Clarendon.
- De Swardt, C. A. & Meyer, J. P. 2001. A performance comparison between an air-source and a ground-source reversible heat pump. *International Journal of Energy Research*, 25, 899-910.
- Durmayaz, A., Kadioglu, M. & Sen, Z. 2000. An application of the degree-hours method to estimate the residential heating energy requirement and fuel consumption in Istanbul. *Energy*, 25, 1245-1256.
- EED. 2008. *Earth Energy Designer* [Online]. Available: www.buildingphysics.com/earth1.htm [Accessed].

- EIA. 2007. *Energy Information Administration* [Online]. Available: www.eia.doe.gov [Accessed].
- EIA 2010. *International Energy Outlook 2010*. Washington.
- Gaterell, M. R. 2005. The impact of climate change uncertainties on the performance of energy efficiency measures applied to dwellings. *Energy and Buildings*, 37, 982-995.
- Goto, S. 2010. Reconstruction of the 500-year ground surface temperature history of northern Awaji Island, southwest Japan, using a layered thermal property model. *Physics of the earth and planetary interiors*, 183, 435-446.
- Guillou-Frottier, L., Mareschal, J.-C. & Musset, J. 1998. Ground surface temperature history in central Canada inferred from 10 selected borehole temperature profiles. *Journal of geophysical research*, 103, 7385-7397.
- Hansen, J. & Lebedeff, S. 1987. Global Trends of Measured Surface Air-Temperature. *Journal of geophysical research: Atmospheres*, 92, 13345-13372.
- Harris, R. N. & Chapman, D. S. 1997. Borehole temperatures and a baseline for 20th-century global warming estimates. *Science*, 275, 1618-1621.
- Hepbasli, A. 2005. Thermodynamic analysis of a ground-source heat pump system for district heating. *International Journal Of Energy Research*, 29, 671-687.
- IEA 2007. *Renewables For Heating And Cooling*. Paris, France: International Energy Agency.
- IEA 2010. *International Energy Agency. Oil and Gas Markets*. Paris, France.
- Jabder, S. A. A., Amin, A. Z., Clini, C., Dixon, R., Eckhart, M., El-Ashry, M., Fakir, S., Gupta, D. & Haddouche, A. 2011. *Renewables 2011 Global Status Report*. Paris, France: Renewable Energy Policy Network for the 21st Century.
- Jaber, S. A. A., Amin, A. Z., Clini, C., Dixon, R., Eckhart, M., El-Ashry, M., Fakir, S., Gupta, D. & Haddouche, A. 2011. *Renewables 2011 Global Status Report*. Paris, France: Renewable Energy Policy Network for the 21st Century.
- Kharseh, M. 2011. Ground Response to Global Warming. *Journal of geophysical research*, Submitted.
- Lachenbruch, A. H. & Marshall, B. V. 1986. Changing Climate: Geothermal Evidence from Permafrost in the Alaskan Arctic. *Science*, 234, 689-696.
- Lean, J. & Rind, D. 2001. Earth's response to a variable sun. *Science*, 292, 234-236.
- Lund, J. W., Freeston, D. H. & Boyd, T. L. Year. *Direct Utilization of Geothermal Energy 2010 Worldwide Review*. In: *World Geothermal Congress 2010*, 25-29 April 2010 2010 Bali, Indonesia. 1-23.
- Moomaw, W., Yamba, F., Kamimoto, M., Maurice, L., Nyboer, J., Urama, K. & Weir, T. 2011. Introduction. In *IPCC Special Report on Renewable Energy Sources and Climate Change Mitigation*. Cambridge.
- Nordell, B. 2003. Thermal pollution causes global warming. *Global and planetary change*, 38, 305-312.
- Nordell, B. & Gervet, B. 2009. Global energy accumulation and net heat emission. *International Journal of Global Warming*, 1, 373-391.

- Sanner, B., Constantine Karytsasb, Dimitrios Mendrinosb & Rybachc, L. 2003. Current status of ground source heat pumps and underground thermal energy storage in Europe. *Geothermics*, 32, 579-588.
- Seyboth, K., Beurskens, L., Langniss, O. & Sims, R. E. H. 2008. Recognising the potential for renewable energy heating and cooling. *Energy Policy*, 36, 2460-2463.
- Wang, S. K. 2000. *Handbook of air conditioning and refrigeration*, New York, McGraw Hill.

The Soultz-sous-Forêts' Enhanced Geothermal System: A Granitic Basement Used as a Heat Exchanger to Produce Electricity

Béatrice A. Ledésert and Ronan L. Hébert
*Géosciences et Environnement Cergy,
Université de Cergy-Pontoise
France*

1. Introduction

The increasing need for energy, and electricity in particular, together with specific threats linked with the use of fossil fuels and nuclear power and the need to reduce CO₂ emissions leads us to look for new energy resources. Among them, geothermics proves to be efficient and clean in that it converts the energy of the earth into heating (domestic, industrial or agricultural purposes) or electricity (Lund, 2007). Numerous geothermal programs are producing energy at present and some of them have been performing for several decades in the USA (Sanyal and Eneedy, 2011), Iceland and Italy for example (Minissale, 1991; Romagnoli et al., 2010). From statistics presented in World Geothermal Congress 2010, the installed capacity of geothermal power generation reaches 10,715 MW in the world. It increased by nearly 20% in 5 years. Its average annual growth rate is around 4%. USA, Indonesia and Iceland increased by 530MW, 400MW and 373MW respectively. Many countries all around the world develop geothermal exploitation programs. As a consequence, scientists from the whole world meet each year at the Annual Stanford Workshop on Geothermal Reservoir Engineering to discuss new advances in geothermics.

Conventional geothermal programs use naturally heated groundwater reservoirs. In many sedimentary provinces, depths of a few hundreds of meters are enough to provide waters with a temperature around 90°C. Such resources give rise to low and very low enthalpy geothermics. Very low enthalpy geothermal resources are used through geothermal heat pumps for various purposes including hot water supply, swimming pools, space heating and cooling either in private houses or in public buildings, companies, hotels and for snow-melting on roads in Japan (Yasukawa and Takasugi, 2003). In 1999 the energy extracted from the ground with heat pumps in Switzerland reached 434 GWh. The same level of utilization in Japan would bring the Japanese figure to 8 TWh per year (Fridleifsson, 2000). Technically, heat pumps can be applied everywhere. It is the difference between surface (atmospheric) and underground temperatures at 20 m or deeper that provides the advantage of geothermal heat pumps over air-source heat pumps.

In volcanic zones (like in Iceland), geothermics depends on specific geological contexts that are rather rare on the earth even though quite numerous in specific zones e.g. in the vicinity

of subduction zones like around the Pacific Ocean as in Japan (Tamanyu et al., 1998) or in zones where the earth's crust is expanding like in Iceland (Cott et al., 2011). Such geothermics is called high enthalpy. It allows the production of electricity like in the Uenotai geothermal power plant in Japan which started operation in 1994 as a 27.5 MW electric power generation facility (Tamanyu et al., 1998). Electricity production from geothermal resources began in 1904 in Italy, at Larderello (Lund, 2004; Massachusetts Institute of Technology [MIT], 2006). Since that time, other hydrothermal developments led to an installed world electrical generating capacity of nearly 10,000 MWe and a direct-use, nonelectric capacity of more than 100,000 MWt (thermal megawatts of power) at the beginning of the 21st century from the steam field at The Geysers (California, USA), the hot-water systems at Wairakei (New Zealand), Cerro Prieto (Mexico), Reykjavik (Iceland), Indonesia and the Philippines (MIT, 2006).

Complementary to conventional geothermics, Enhanced Geothermal Systems (EGS; also called Engineered Geothermal Systems) aim to develop reservoirs in rocks where little (or no) water is available (Redden et al., 2010). This concept was invented, patented and developed in the early 1970s at Los Alamos National Laboratory and was first called Hot Dry Rock (HDR) geothermal energy. As defined by these early researchers, the practical HDR resource is the heat contained in those vast regions of the earth's crust that contain no fluids in place—the situation characterizing by far the largest part of the earth's drilling-accessible geothermal resource (Brown, 2009).

This concept was developed for electricity production in any kind of area at the surface of the earth even though the geodynamical context is not in favour of geothermics (Redden et al., 2010 and references therein).

However, because of the general low thermal gradient in the earth ($30^{\circ}\text{C}/\text{km}$ in sedimentary basins), reaching a temperature around $150\text{--}200^{\circ}\text{C}$ needed for the production of electricity make things more difficult than first considered. Technical and economical problems linked to such deep drillings (Culver, 1998; Rafferty, 1998) have restricted EGS to zones where the thermal gradient is high enough to reduce the depth of the exchanger. Now, EGS include all geothermal resources that are currently not in commercial production and require stimulation or enhancement (MIT, 2006).

Table 1 gives an overview of HDR/EGS programs in the world.

In such difficult technical conditions, one can wonder whether the geothermal energy resource and electricity production process are sustainable. According to Clarke (2009) and authors cited therein, the management and use of the geothermal resource (Rybach and Mongillo, 2006) and the environmental impacts during geothermal energy production (Bloomfield et al., 2003; Reed and Renner, 1995) were the first concern about sustainability of geothermal energy. These studies have shown that there is less impact on land use, air emissions including greenhouse gases, and water consumption from geothermal electricity generation than from fossil-fuel-based electricity generators. However, the environmental impacts from the construction of geothermal energy production facilities being less well understood, especially for enhanced geothermal systems (EGS) subsequent studies were conducted. The life-cycle analysis of the EGS technology (including pre-production process such as drilling, construction, production and transportation) had to be discussed, especially when the potential for large-scale development exists. Because of increased depth and decreased water availability, environmental impacts may be different from those of

Country	Site	Depth (m)	Dates	Production of electricity
France	Le Mayet		1975-1989	
	Soultz-sous-Forêts	5000 (3 boreholes)	1985-	1.5 MWe Since June 2008
Germany	Bad Urach	4500 and 2600	1976-	
	Falkenberg	300	1975-1985	
UK	Rosemanowes	2700	1975-1991	
Australia	Cooper Basin	4300	2001-	
USA	Fenton Hill	5000	1973-2000	
	Coso		2001-	
	Desert Peak	5420	2001-	
Japan	Hijori	2300	1987-	

MWe: MWelectricity (raw production minus consumption of electricity required for the production).
Data after MIT (2006), Davatzes and Hickmann (2009) and Genter et al. (2009)

Table 1. Overview of some HDR or EGS programs in the world.

conventional geothermal power generation. It is expected that EGS will produce less dissolved gas (mostly carbon dioxide CO₂ and hydrogen sulfide H₂S) than conventional energy by recovering the heat through a heat exchanger and reinjecting the fluid without releasing any gas during operation. As concerns subsurface water contamination it is unlikely because all the produced fluid is reinjected. EGS is also characterized by a modest use of land since with directional-drilling techniques, multiple wells can be drilled from a single pad to minimize the total wellhead area (MIT, 2006). EGS requires no storage and the plant is built near the geothermal reservoir because long transmission lines degrade the pressure and temperature of the geofluid as well as the environment. As a consequence EGS power plants require about 200 m²/GWh while a nuclear plant needs 1200 m²/GWh and a solar photovoltaic plant 7500 m²/GWh (MIT, 2006). Most of EGS developments are likely to occur in granitic-type crystalline rocks, at great depth. Careful management of the water resource is unlikely to induce subsidence (lowering of the ground's level as in shallow mining activity; MIT, 2006). Seismic activity linked to engineering of EGS reservoirs during hydraulic stimulation (injection of water under pressure to create or open pre-existing joints) has conducted managers of these sites to prefer chemical stimulations (use of chemicals to dissolve minerals responsible for the sealing of joints) in or close to urban areas (Hébert et al., 2011; Ledésert et al., 2009) in order to avoid earthquakes. Another force of the EGS technology is the possible use of CO₂ instead of water because of its favourable thermodynamic properties over water in EGS applications (Brown, 2000; Magliocco et al., 2011) thus leading to a possible sequestration of carbon dioxide produced by the use of fossil fuel. However EGS might have increased visual impact and noise levels compared to conventional geothermal power plants but no more than fossil fuel driven power plants (MIT, 2006). The highest noise levels are usually produced during the well drilling, stimulation, and testing phases (about 80 to 115 decibels). For comparison, congested urban areas typically have noise levels of about 70 to 85 decibels, and noise levels next to a major freeway are around 90 decibels. A jet plane just after takeoff produces noise levels of about 120 to 130 decibels (MIT, 2006). Finally, considering all these factors, EGS has a low overall

environmental impact when the production of electricity is considered compared to fossil or nuclear generation (MIT, 2006). As concerns the demand, supply and economic point of view, MIT (2006) provides a rather detailed analysis.

Geothermal energy and EGS in particular is studied world-wide and the annual Workshop on Geothermal Reservoir Engineering (Stanford, California, USA) allows scientists and industrials to compare data and improve renewable energy production. Proceedings of the workshop can be downloaded very easily and for free on the Internet. As a consequence, the latest advances in geothermal technology are available to the scientific community.

2. EGS technology

Flow rates on the order of $50 \text{ L}\cdot\text{s}^{-1}$ and temperatures of 150°C to 200°C are required to allow an economical generation of electrical energy from geothermal resources (Clauser, 2006). Heat source risk can be quantified via a detailed assessment of surface heat flow together with measurements of temperature in boreholes (for example, for the Desert Peak Geothermal area, at 0.9 to 1.1 km depth, the ambient temperatures is of ~ 180 to 195°C in rhyolite tuff and argillite; Hickman and Davatzes, 2010). Thermal insulation (measured on core or cuttings samples) together with precision surface heat flow measurements allows the prediction of temperature distribution at depth in one, two or three dimensions (Beardsmore and Cooper, 2009). For regions outside natural steam systems and high surface heat flow (for example Iceland, Indonesia, Turkey, etc.) conditions necessary for electricity production are met at depths below 3 km provided the underground rock heat exchanger is engineered in order to increase the paths available for the fluid flow. Such systems are called Engineered (or Enhanced) Geothermal Systems (EGS) or Hot Dry Rock (HDR). In these techniques, the host rock is submitted to stimulations (Economides and Nolte, 2000) in order to increase the heat exchange surface between the rock and the injected fluid. Stimulations are derived from petroleum technology where they have been used for decades. The first method consists in the injection of water under high pressure to create irreversible shearing and opening of fractures and is called hydraulic stimulation (Portier et al., 2009). The second method, called chemical stimulation (e.g. Nami et al., 2008; Portier et al., 2009) uses various kinds of chemical reactants to dissolve minerals and to increase permeability. Both methods have proven successful for enhancing permeability at depth but it is still a challenge to plan and control the stimulation process. Details about stimulations can be found in the abundant literature (e.g. Kosack et al., 2011; Nami et al., 2008; Portier et al., 2009 and references therein). During or after stimulations, tracers are used to assess the connectivity between the wells and the speed of fluid transfer. Many examples of use of tracers are found in the literature (e.g. Radilla et al., 2010; Redden et al., 2010; Sanjuan, 2006). In addition, prior to any stimulation or circulation test between the wells, in-situ stress and fracture characterization have to be considered with great attention in order to better constrain the geometry and relative permeability of natural or artificially created fractures (e.g. Hickman and Davatzes, 2010 for the Desert Peak geothermal field). A subsequent modelling of the 3D fracture network (Genter et al., 2009; Sausse et al., 2010, Dezayes et al., 2011) and of flow and transport along the fractures can be profitably performed (e.g. Karvounis and Jenny, 2011) to predict the behaviour of the thermal exchanger and ensure its financial viability. Such modelling is based on the accurate knowledge of the fracture network obtained through seismic records performed during stimulation or production tests (Concha et al., 2010) and

thanks to thorough characterization of the fracture network (Hébert et al., 2010, 2011; Ledésert et al., 2009). When the rock heat exchanger is finally operated, careful reservoir engineering and monitoring has to be performed to ensure the viability of the EGS (Satman, 2011). The produced hot fluid is continuously replaced by cooled injected water. After the thermal breakthrough time the temperature of the produced fluid decreases. However if after a time the field is shut-in the natural energy flow will slowly replenish the geothermal system and it will again be available for production. Therefore when operated on a periodic basis, with production followed by recovery, doublets are renewable and sustainable (Satman, 2011). Triplets (one injection and two production boreholes) are now considered as being the best configuration (MIT, 2006; Genter et al., 2009). However, it must be taken into consideration that when an EGS reservoir is developed through hydraulic fracturing, the size of the reservoir might extend too much and attendant high water losses might occur compromising the sustainability of the project as at Fenton Hill (MIT, 2006; Brown, 2009). When shearing occurs through reopening of pre-existing sealed fractures during hydraulic stimulation (e.g. at Fenton Hill; Brown, 2009) or when the mineral deposits are dissolved through chemical stimulation (e.g. at Soultz; Nami et al., 2008; Portier et al., 2009; Genter et al., 2009) the size of the exchanger is better constrained and fluid losses are limited.

Other risks such as technology (reliable supply of produced geofluids with adequate flow rates and heat content), finances (cost of construction, drilling, delays), scheduling, politics, etc...have to be estimated in order to make an EGS project viable. They are presented in MIT (2006) for the different stages of a project. In addition, seismic risk has to be fully taken into account where EGS programs are to be developed in urban areas in order to produce both electricity and central heating (Giardini, 2009): the Basel (Switzerland) experience (see section 4.4) had to be stopped because of a 3.4 magnitude earthquake generated by stimulation in a naturally seismic area. As a consequence to these numerous constraints, no financially viable EGS program is operating at present but the production of electricity that began at Soultz-sous-Forêts (France) in June 2008 is highly promising.

As a conclusion, Table 2 shows some forces and difficulties of EGS programs inferred from the literature.

Forces	Difficulties
Production of electricity	Deep drilling (technical and financial difficulties)
Sustainability of the resource provided its correct management	Risk of water loss in case of pure hydraulic fracturing
Low to no GHG emissions	Engineering of the reservoir to increase permeability
Low global environmental impact compared to fossil-fuel and nuclear electricity	Adequate flow rate and temperature
Available on continents worldwide	No financially viable program operating at present

Table 2. Forces and difficulties of EGS programs inferred from the abundant literature on the subject (see reference list). GHG: greenhouse gases.

3. The Soultz-sous-Forêts EGS

The Soultz-sous-Forêts' (called Soultz in the following) project began in the late eighties thanks to a particular geological context. Several zones in France are submitted to high heat flows, among which the Soultz area, because of the development of a rift system in northern Europe (Figure 1). Initiated by a French-German team (Gérard et Kappelmeyer, 1987), the Soultz program has been a European project with a significant Swiss contribution mainly supported by public funding between 1987 and 1995 and co-funded by industry from 1996 to present (Genter et al., 2009). The Soultz project represents a multinational approach to develop an EGS in Europe.

3.1 Geological context

The Soultz EGS site is located in the upper Rhine graben (Figure 2) where a high heat flow was measured at shallow depth in old oil wells (110 °C/km). Natural water being found in great amount at depth in the granitic heat exchanger, the project was not HDR anymore and was then called EGS since numerous stimulations (first hydraulic and then chemical with several steps and chemical reactants) were necessary to improve the connection between the 3 deep wells (around 5 000 m deep). First investigations of the fracture network showed that they are grouped in clusters separated by little or no-fractured zone, following a fractal organisation (Ledésert et al., 1993).

Figure 2 shows the more detailed location of the Soultz site and extension of the thermal anomaly related to the upper Rhine graben(URG) also showed on a geological cross section on which the Soultz horst can be distinguished.

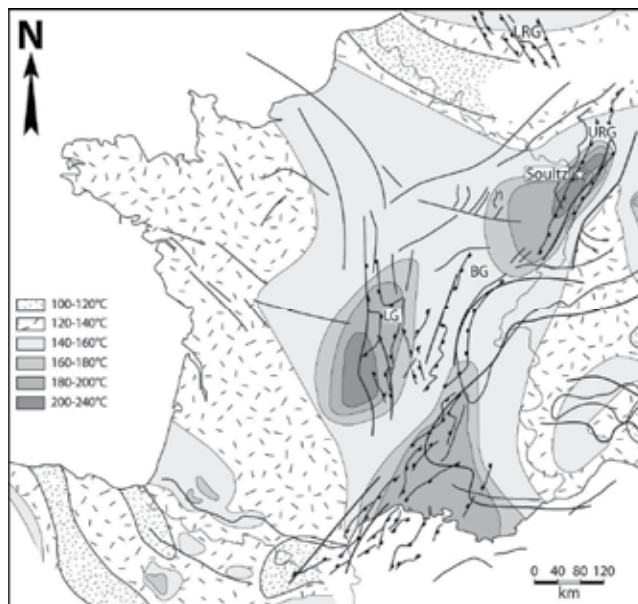


Fig. 1. Map of extrapolated temperatures at 5 km depth and location of some major structural structures (modified after Hurtig et al., 1992 and Dèzes et al., 2004). LRG : Lower Rhine Graben; URG : Upper Rhine Graben; BG : Bresse Graben; LG : Limagne Graben.

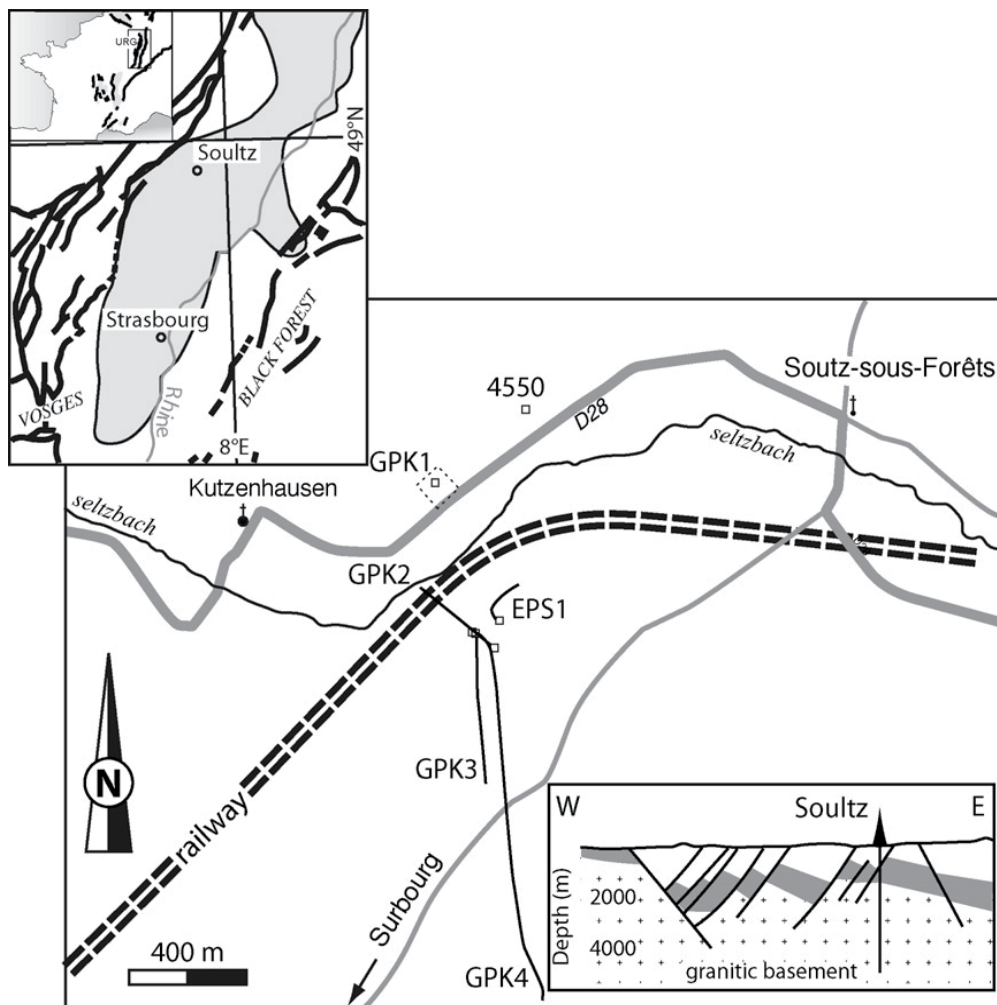


Fig. 2. Location map of the upper Rhine graben (URG) in eastern France and of the Soultz-sous-Forêts' site, 50 km North of Strasbourg, in a zone of high thermal anomaly (grey on the map). Six boreholes are present : 4550 (previous oil well), GPK1 (first HDR borehole), EPS1 (entirely cored scientific HDR borehole), GP2-GPK3-GPK4 (5 000m deep boreholes forming the triplet of the EGS). Their horizontal trajectories are shown on the main map. The E-W geological cross section shows the geometry of the upper Rhine graben and of the Soultz horst. Dots represent the granite while inclined grey and white layers correspond to the sedimentary cover. After Ledésert et al. (2010).

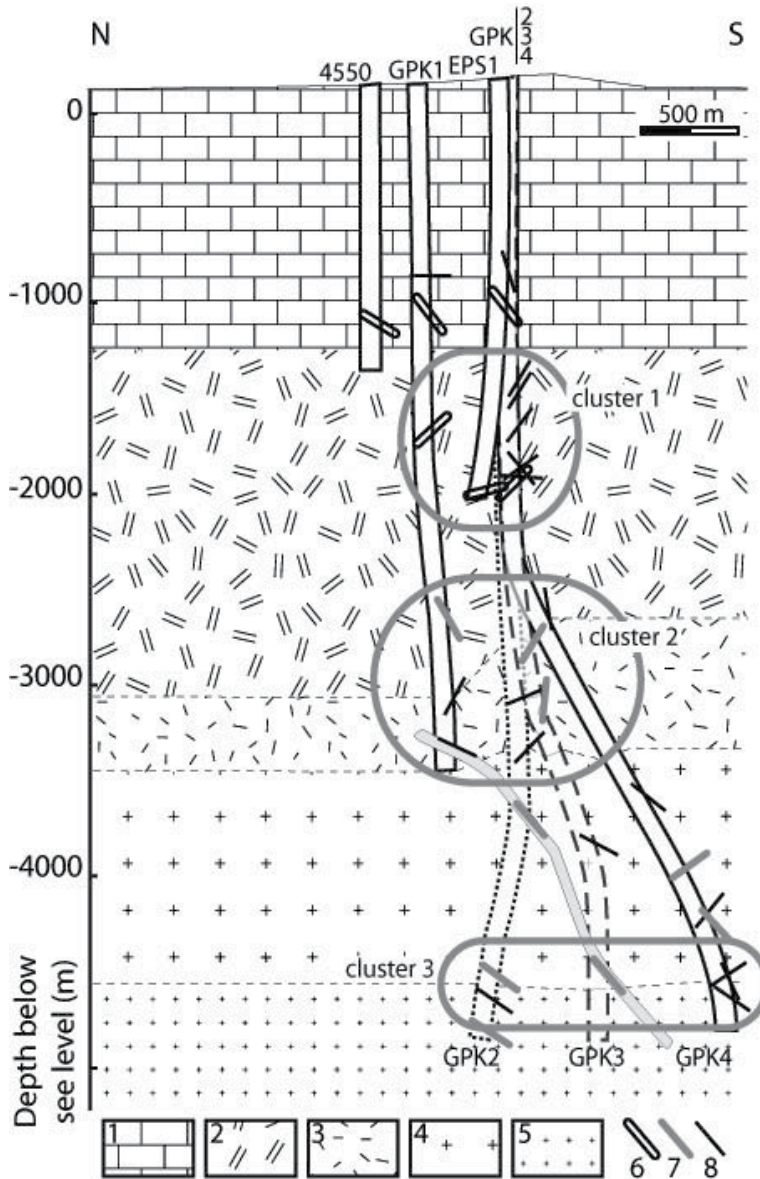


Fig. 3. Cross-section of the Soultz geothermal system. Note 3 zones intensely fractured and altered by natural fluids, noted cluster. A major drain is encountered in GPK1 near 3200m and is found in GPK2 around 3500m and GPK3 close to 4500m (represented with a light-grey curved wide line). 4550 (oil drill hole); EPS1 (cored scientific hole); GPK1 (scientific hole, destructive conditions, few core pieces). 1: sedimentary cover, 2: standard porphyritic Bt-Hbl granite, 3: standard granite with fractures and vein alteration, 4: Bt+Hbl - rich granite becoming standard granite at depth, 5: two-mica and Bt-rich granite, 6: Level 1 fracture, 7: Level 2 fracture, 8: Level 3 fracture. Figure modified after Dezayes and Genter (2008) and Hébert et al. (2011). Mineral abbreviations according to Kretz (1985), Bt : biotite, Hbl : hornblende.

3.2 Development of the Soultz EGS

The granite body is used as a heat exchanger in which the fracture planes are surfaces of heat exchange between the injected water and the hot rock mass. As a consequence, the knowledge about the fractures is necessary to better understand and predict the behaviour of the heat exchanger. This is why numerous studies have been performed on the natural fracture network (Ledésert et al., 1993; Genter et al., 1995; Sausse et al., 2007, 2008, 2009; Dezayes et al., 2008; Dezayes et al., 2011). Dezayes et al. (2010) have classified the fracture zones into three different categories (or levels) on the basis of their relative scale and importance as fluid flow paths (see complete review in Dezayes et al., 2010). Level 1 corresponds to major fracture zones, which were permeable prior to any stimulation operation (Figure 3) and were subject to important mud loss during the drilling operation. Fracture zones of level 2 are characterized by at least one thick fracture with a significant hydrothermal alteration halo. They showed a flow indication higher than 20% of fluid loss during stimulation. Fracture zones of level 3 show a poorly developed alteration halo and a fluid loss below 20% during stimulation. Figure 3 shows the location of the boreholes and that of fracture clusters that were reactivated during stimulations allowing connection between the wells.

According to the abundant literature on the subject, developing an EGS is a difficult and costly task that deserves thorough studies. The knowledge of the geometry of the fracture network being crucial as explained before, many methods are used to improve it. Concha et al. (2010) indicate that microseismic data can be used profitably in that they provide information about reservoir structure within the reservoir rock mass at locations away from boreholes, where few methods can provide information. They used microseismic events induced from production and hydrofracturing tests performed in 1993 as sources for imaging the Soultz EGS. These tests injected 45,000 m³ of water at depths between 2850 and 3490 m and resulted in over 12,000 microseismic events that were well recorded by a four station downhole seismic network. Concha et al. (2010) began by determining a three dimensional velocity model for the reservoir using Double Difference Tomography for both P and S waves. Then they analyzed waveform characteristics to provide more information about the location of fractures within the reservoir. Using such methods, it appears that the volume of the exchanger stimulated during operation of the Soultz EGS is approximately 1km³.

The Soultz EGS is characterized by three deep boreholes (CPK2, GPK3 and GPK4; ca 5000 m; Figure 3). They were drilled after GPK1 and EPS1 boreholes that could not be used for the EGS development because of technical problems, and oil wells such as 4550 (Figures 2 and 3).

Genter et al. (2009) provide an overview of the Soultz project. The first exploration of the geothermal Soultz site consisted in exploration by drilling at shallow depth (GPK1, 2 km). Then convincing results were obtained between 1991 and 1997 through a 4 month circulation test successfully achieved between 2 wells in the upper fractured granite reservoir at 3.5 km. Based on these encouraging results, 3 deviated wells (GPK2, GPK3, GPK4) were drilled down to 5 km depth between 1999 and 2004 for reaching down-hole temperatures of 200°C (Genter et al., 2009). They form the geothermal triplet. Geothermal water is pumped from the production wells (GPK2, GPK4) and re-injected together with

fresh surface water at lower temperature into the injection well GPK3. On a horizontal view, the 3 deep deviated wells are roughly aligned along a N170°E orientation (Figure 2) corresponding to the orientation of both the main fracture network and present-day principal maximal horizontal stress, allowing the best recovery of the injected water. The three deep boreholes were drilled from the same platform, about 6 m apart at the surface whereas at their bottom, the distance between each production well and the re-injection well is about 700 m. The 3 wells are cased between the surface and about 4.5 km depth offering an open-hole section of about 500 m length (Genter et al., 2009).

	GPK3 (injection well)	GPK2	GPK4
Pumping rates (L/s)	15	11.9	3.1
Arrival time for fluorescein (days)	injection	4	24
Volume of fluid	209 000	165 000	40 000
Permeability relative to GPK3 (m ²)		10 ⁻¹³	10 ⁻¹⁵
Quality of connection with GPK3		High	Low

Table 3. Results of circulation tests between the three deep wells showing the strong discrepancy between the two production wells, GPK2 and GPK4. Data in Sanjuan et al. (2006); Genter et al. (2009) and Kosack et al. (2011).

The geothermal wells were stimulated (hydraulically and chemically) between 2000 and 2007 in order to enhance the permeability of the reservoir that was initially low (Table 3) in spite of a large amount of fractures (up to 30 fractures/m; Ledésert et al., 1993; Genter et al., 1995). Figure 4 provides a synthetic view of the increase in the productivity/injectivity rates for each of the Soultz deep boreholes after hydraulic and chemical stimulations. A 5-month circulation test, carried out in 2005 in the triplet, showed similar results as in 1997 in terms of hydraulics (Nami et al., 2008): in both cases, a recovery of about 30% of the fluid mass was obtained at the production wells showing the open nature of the reservoir (Gérard et al., 2006). This result is opposed to the HDR concept where the reservoir is closed (Brown, 2009) and no water naturally exists in the reservoir prior to its injection. The limited recovered mass of injected fluid was continuously compensated by native brine indicating direct connections with a deep geothermal reservoir (Sanjuan et al., 2006). To give an example of stimulation test, from July to December 2005, about 209 000 m³ of fluid were injected into GPK3 and 165 000 m³ and 40 000 m³ were produced from GPK2 and GPK4 respectively (Sanjuan et al., 2006), yielding a nearly even mass balance. In addition, a mass of 150 kg of 85 % pure fluorescein was dissolved in 0.95 m³ of fresh water and was used as a tracer injected into GPK3 over 24 hours, while geochemical fluid monitoring started at GPK2 and GPK4. Fluorescein was first detected in GPK2, 4 days after the injection into GPK3. In GPK4, fluorescein was detected only 24 days after the injection. The average pumping rates were 11.9 L.s⁻¹ in GPK2, 15 L.s⁻¹ in GPK3, and 3.1 L.s⁻¹ in GPK4, already indicating a reduced water supply to GPK4 (Sanjuan et al., 2006; Genter et al., 2009). These results show that the hydraulic connection is very heterogeneous: it is rather easy between GPK3 and GPK2 while it is much more difficult between GPK3 and GPK4 (Table 3). The permeability in

most of the reservoir is on the order of 10^{-17} m². A good connection is naturally established between GPK2 and GPK3 with a mean permeability on the order of 10^{-13} m², while a barrier exists to GPK4 (Kosack et al., 2011).

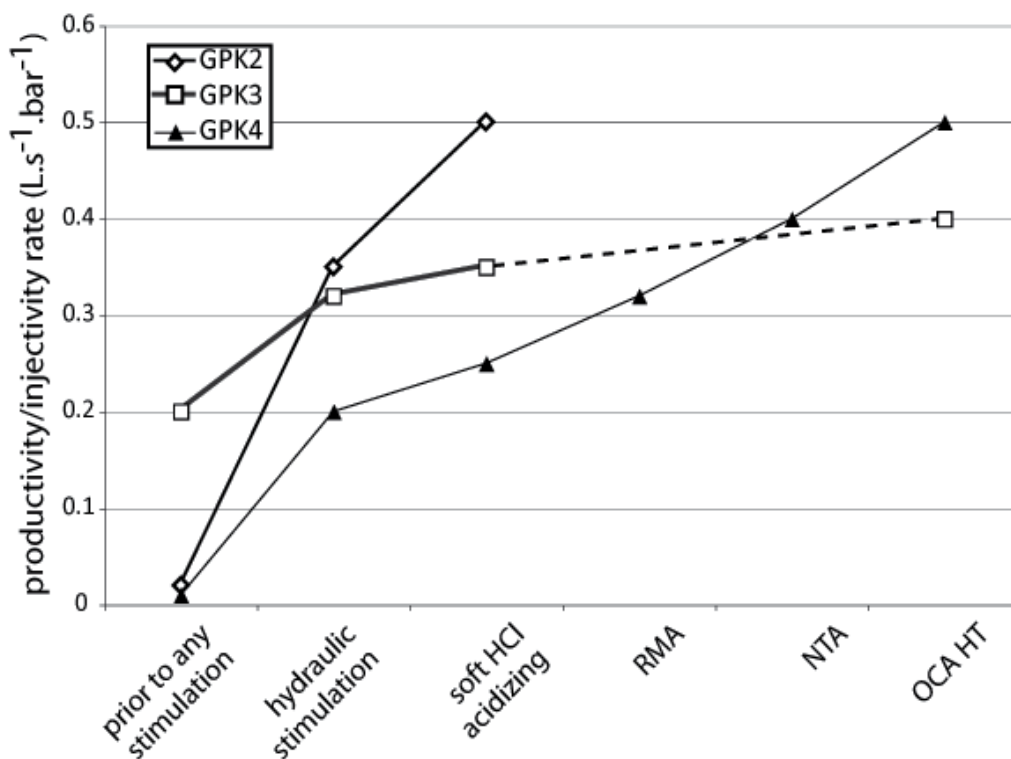


Fig. 4. Increase in the productivity/injectivity rates for each of the Soultz deep boreholes after hydraulic and various chemical stimulations (after Hébert et al., 2011). GPK3 had an initial rate higher than GPK2 and GPK4 (prior to any stimulation data). Because of its very low initial rate and different behaviour, GPK4 had to face multiple chemical stimulations and finally reached the same level as GPK2 even though its rate was only half that of GPK2 after the soft HCL acidizing. RMA : regular mud acid; NTA : nitrilo-triacetic acid (chelating agent); OCA HT : organic clay acid for high temperature.

Following processes run in oil-production wells to improve the permeability of a rock reservoir, two basic types of chemical stimulations can be conducted: matrix acidizing and fracture acidizing. Matrix stimulation is accomplished, for example in sandstones, by injecting a fluid (e.g. acid or solvent) to get rid of materials that reduce well productivity or injectivity. Fracture acidizing is used to develop conductive paths deeper into the formation. This treatment consists of injecting an acid fluid into the formation at a rate higher than the reservoir matrix will accept. This rapid injection produces a wellbore pressure build-up leading to a fracturing of the rock. Continued fluid injection increases the fracture's length and width (Portier et al., 2009).

At Soultz, thorough petrographic studies of the fracture network (Dubois et al., 2000; Genter et al., 1995; Hébert et al., 2010, 2011; Ledésert et al., 1999, 2009, 2010) have shown that more

than 90% of the fractures are sealed by minerals that precipitated because of natural fluid flow. K-Ar dating of illite (K-bearing clay mineral) found in a fractured and altered zone located at 2200 m in the Soultz granite (Bartier et al., 2008) indicate at least two episodic illitization at 63 Ma or slightly more for the coarsest particles and at 18 Ma or slightly less for the smallest. Other minerals precipitated at the same time (Bartier et al., 2008; Dubois et al., 2000; Ledésert et al., 1999), such as tosudite (Li-bearing mixed-layer clay mineral) and calcite (calcium carbonate). Calcite precipitated from the Ca-ions liberated by the dissolution of primary plagioclases present in rather great abundance in the granite (nearly 40% of 10%-Ca oligoclase; Ledésert et al., 1999; Table 4) during hydrothermal flow and from sedimentary brines enriched in Ca-ions during its flow within the calcareous Muschelkalk layers that penetrated into the granite (Ledésert et al., 1999).

Recently we have focused on calcite since this mineral is thought to impair the permeability between the 3 deep wells and especially between GPK3 and GPK4 (Hébert et al., 2010, 2011; Ledésert et al., 2009, 2010). To this aim, we performed a compared study of calcite-content, other petrographic data (alteration degree of the rock and illite content) and fluid flow from well-tests. Petrographic data were obtained on cuttings by mano-calcimetry (for the calcite content) and X-Ray diffraction (for the illite content). In the Soultz granite, like in many other granites (Ledésert et al., 2009), the base level of calcite amount is around 1.8 wt % (Hébert et al., 2010; Ledésert et al., 2009). As a consequence, calcite contents over 2% are considered as calcite anomalies by these authors.

The three deep wells show distinct behaviours in the deep part of the exchanger (open holes, below 4500m depth; Table 5).

In GPK2, two main groups of fracture zones are distinguished. The less conductive ones are characterized by low alteration facies, moderate illite content and low calcite content (below 2 wt.%) likely resulting from the early pervasive fluid alteration. It suggests that these fracture zones are poorly hydraulically connected to the fracture network of the geothermal reservoir. On the opposite, the fracture zones with the best conductivities match with high to moderate calcite anomalies (respectively 11, 8, ~5 wt.%), high to moderate alteration grade and high illite content. This suggests massive precipitation of calcite from later fluid circulations within the fractured zone. Thus, the calcite content seems possibly proportional to conductivity.

In GPK3, the less conductive fracture zones are concentrated in a zone that extends from ~ 4875 to ~ 5000 m measured depth (MD), where they correlate with a large and high calcite anomaly zone. The main fracture zone, which accommodates 63–78% of the fluid flow, has the lowest calcite anomaly (2.9 c wt.%) of all the fracture zones of this well. Nearly all the moderate calcite anomalies occur in the vicinity of fracture zones. In this well, regarding the fracture zones data and the calcite anomalies, it seems that the more calcite the less fluid flow and therefore calcite plays a major role in the reduction of the conductivity of the fracture zones of this well. Thus, in GPK3, the maximum fluid flow and significant calcite deposit are not correlated as it is observed in the open-hole section of GPK2.

The highest calcite anomaly of all three deep wells is found in GPK4 (18%). In GPK4, the fluid flow is mainly accommodated via a single zone. All the other fracture zones are considered to have a similarly low fluid flow and are characterized by moderate or high

Site	Habanero (Cooper Basin, Australia)	Hijori (Hijori caldera, Japan)	Soultz (Rhine graben, France)
Rock type	Granite	Tonalite/granodiorite	Granite
Quartz	39.3	35.3	28.4
Plasioclase	29.7	38.2	39.9 (oligoclase)
K-feldspar	18.1	2.1	18.8
Muscovite/Biotite	8.4	0.4	8.4 (biotite)
Carbonate	1.1	1.3	≤1.8-18
Chlorite/Clay M	0	6.5	<1
Sericite	0	9.5	<i>up to several % (illite)</i>
Pyroxene	2.2	0	4.5 (amphibole)
Epidote	0	1.8	< 1
Calcopyrite	1.1	0	0
Anhydrite	0	4.9	0
Total	100	100	100, depending on the zones

Table 4. Mineral composition of EGS rock bodies (mostly expressed in volume %). Data from Ledésert et al. (1999) and Yanagisawa et al. (2011). At Soultz, some zones are strongly fractured and altered by natural hydrothermal fluids. In such zones, the composition of the granite is strongly modified: primary quartz has been totally dissolved, oligoclase is replaced by illite or tosudite (clay minerals), biotite and amphibole by chlorite and epidote. Newly-formed minerals are indicated in italics.

	GPK2	GPK3	GPK4
Highly conductive fractures	High alteration High illite High calcite	Low calcite	Low calcite
relationship	Calcite proportional to conductivity : calcite is found in highly conductive fractures	The less calcite, the more fluid flow : calcite reduces conductivity	The less calcite, the more fluid flow : calcite reduces conductivity
Permeability	high	high	low
Connectivity	high	high	low

Table 5. Relationships between the amount of calcite and the intensity of fluid flows in the three deep Soultz wells. Comparison with permeability data (from table 3). The connectivity between the wells is deduced. No petrographic data (alteration degree and illite content) are available for GPK3 and GPK4 because of poor quality cuttings.

calcite anomalies. Therefore it seems that in GPK4, the highest the fluid flow, the lowest the calcite anomaly, as in GPK3.

However, GPK3 shows a high permeability while that of GPK4 is low (Table 5). Combining data of calcite content and permeability, one can infer that calcite may represent a serious threat to the EGS reservoir when the connectivity of the fractures is low while it does not impair the permeability when the connectivity is high. A solution can be brought by hydraulic fracturing that allows developing the extension of fractures. However, such process was employed in Basel (Switzerland) resulting in an earthquake of a 3.4 magnitude that scared the population in 2006. The EGS Basel project had to be stopped. At Soultz, an earthquake of 2.9 magnitude had been felt by local population during the stimulation of GPK3 in 2000 thus no further hydraulic stimulations were driven to prevent this problem. As a consequence, chemical stimulations had to be performed in order to improve the permeability and connectivity of the three deep wells. Particular efforts were put on GPK4. Figure 4 shows the results of chemical stimulations. The behaviour of the 3 deep wells has been largely improved. Given the good results of the circulation test conducted in 2005, and the improvement of the hydraulic performances of the three existing deep wells by stimulation, it was decided to build a geothermal power plant of Organic Rankine Cycle (ORC) type (using an organic working fluid). Thus, a first 1.5 MWe (electricity; equals 12 MW thermal) ORC unit was built and power production was achieved in June 2008 thanks to down-hole production pumps. The power plant was ordered to a European consortium made of Cryostar (France) and Turboden, Italy. A three year scientific and technical monitoring of the power plant has started on January 2009 focused on the reservoir evolution and on the technologies used (pumps, exchanger; Genter et al., 2009).

3.3 Technical data about the heat exchanger and the EGS (after Genter et al., 2009 and Genter et al., 2010)

The geothermal fluid is produced from GPK2 and GPK4 thanks to two different kinds of pumps and, after electricity production (or only cooling if electricity is not produced), it is reinjected in the rock reservoir through GPK3 and GPK1.

3.3.1 Pumps

It was necessary to install down-hole production pumps because the artesian production was not sufficient. Thus, two types of production pumps were deployed in the production wells: a Line Shaft Pump (LSP; in GPK2) and a Electro-Submersible Pump (ESP; in GPK4).

The LSP itself is in the well while the motor is at surface. The connection is obtained through a line shaft. The main advantage is to avoid installing the motor in hot brine, but the possible installation depth is limited and the line shaft has to be perfectly aligned. The LSP was supplied by Icelandic Geothermal Engineering Ltd. The length of the shaft is 345 m. The shaft (40 mm diameter) is put in an enclosing tube (3" internal diameter) with bearings every 1.5 m. The enclosing tube is set by means of centralisers in the middle of the LSP production column (6" internal diameter) which is put into the 8" casing. The pump itself is from Floway (USA) and made of 17 different stages of 20 cm (3.4 m total length). The LSP flow rate can be modulated until 40l/s with a Variable Speed Drive. The maximum rotation speed is 3000 rpm at 50 Hz. The surface motor is vertical. Metallurgy is cast iron and injection of corrosion inhibitor can be done at the pump intake by mean of coiled tubing. Shaft lubrication is made with fresh water injected from surface in the enclosing tube. The pump has been installed at 350 m depth into GPK2 that presents good verticality and is the

best producer. Due to hydraulic drawdown, the maximum flow rate expected with the LSP installed at 350 m is 35 l/s. During summer 2008, (07th July to 17th August), after six weeks of geothermal production (25 l/s, 155°C), scaling problems were observed within the lubrication part of the shaft. The fresh water used for lubricating the shaft was too mineralized and some carbonate deposits (calcite, aragonite) precipitated. Then, a poor lubrication occurred and the first axis of the shaft broke. Between mid August and November 2008, both the shaft and the pump were fully dismantled, analyzed and a demineralization water system was set up. The LSP pump was re-installed at 250 m depth in GPK2 and worked properly afterwards.

Both the ESP pump and its motor are installed into the GPK4 well at 500 m depth. The maximum expected flow rate from GPK4 equipped with ESP is 25 l/s but the pump is designed to a maximum flow rate of 40 l/s. The ESP was delivered by Reda/Schlumberger. Due to the expected maximum temperature (185°C) and the salty composition of the brine, specific design and noble metallurgy had to be used. The electrical motor is beneath the pump and connected to it through a seal section that compensates oil expansion and metallic dilatation. The motor is cooled by the pumped geothermal brine and internal oil temperature can reach 260°C. A fiber optic cable has been deployed with the ESP and allows monitoring the motor temperature and gives downhole information about the geothermal draw-down in the well. The first production tests from GPK4 with the ESP with an expected target of 25 l/s started on mid November 2008. After some days of production, GPK4 production decreased to 12.5 l/s at 152°C and the geothermal water was re-injected in GPK3 at 50°C. GPK2 flow rate was stabilized at 17.5 l/s for a temperature around 158°C. Both flows coming from GPK2 and GPK4 were re-injected under full automatism in GPK3 at 30 l/s. The ORC commissioning started for these geothermal conditions at around 155°C. GPK3 well-head pressure was maintained around 70-80 bars for reinjection.

3.3.2 Heat exchanger

A schematic view of the Soultz' binary power plant is given in Figure 5. As the purpose of the project was first to demonstrate the feasibility of power production, a binary system utilizing an organic working fluid called an Organic Rankine Cycle (ORC) technology was chosen. Due to the high salinity of the geothermal brine, the geothermal fluid cannot be vaporized directly into the turbine as occurs in classical "simple flash" power plants.

Then, a secondary circuit is used that involves a low boiling point organic working fluid (isobutane). As there is no easily accessible shallow aquifer around the geothermal site, an air-cooling system was required for the power plant, which also limits the impact on environment. It consists in a 9-fan system. The turbine is radial and operates around 13000 rpm. The generator is asynchronous and is running around 1500 rpm. The generator is able to deliver 11 kV and the produced power is to be injected into the 20 kV local power network.

The expected net efficiency of the ORC unit is 11.4%. Geothermal water may be cooled down to 80-90°C in the heat exchangers of the binary unit. After this cooling, the entire geothermal water flow rate is re-circulated in the reservoir. The system is built so that the production coming from one or two wells can easily be used to feed the power production loop. On surface, the pressure in the geothermal loop is maintained at 20 bars in order to

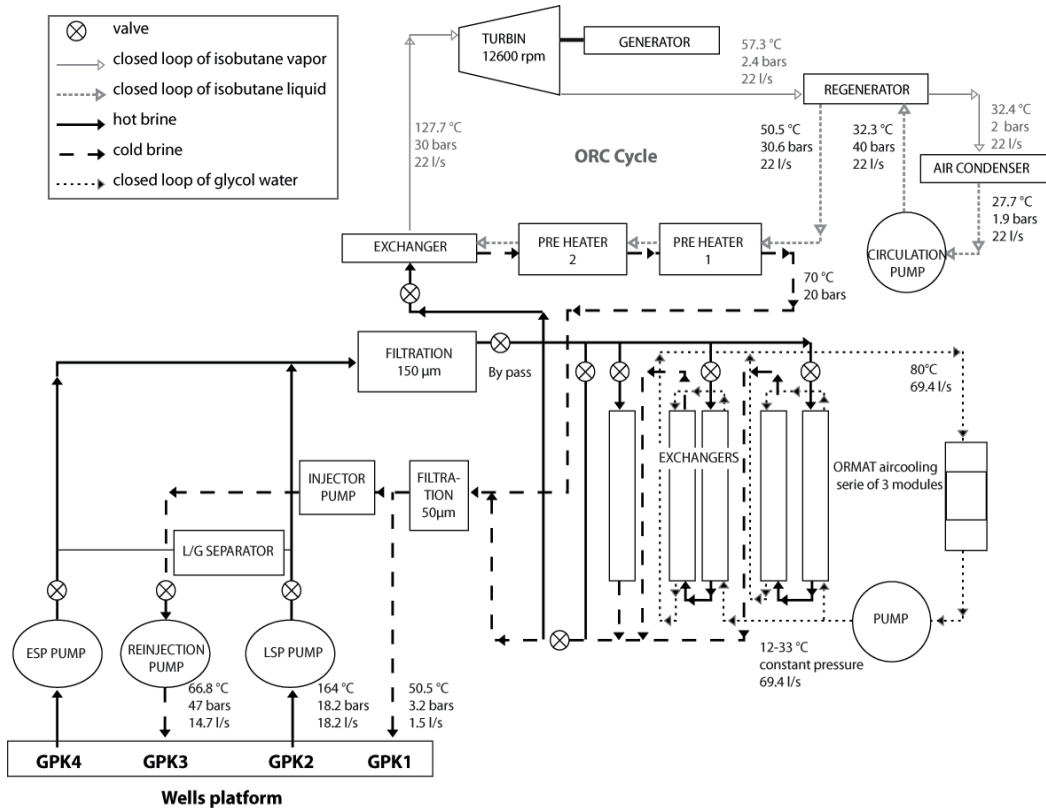


Fig. 5. Schematic view of the Soultz' binary power plant after Genter et al. (2010). Each production well can be run separately thanks to the valves. The hot geothermal fluid (around 165°C) is filtered (150 μm) before entering the surface network. After the complete cycle, the fluid is reinjected in the natural rock exchanger thanks to one or two wells : with a reinjection pump in GPK3 and in addition if necessary by gravity in GPK1. The temperature, pressure and flow figures indicated are those obtained during the 8 months circulation test performed in 2008. If the Organic Rankine Cycle dedicated to electricity production is not activated (the last valve being closed), the geothermal fluid goes through 5 exchangers in the cooling cycle (lower part of the figure with the ORMAT aircooling system) in order to be reinjected after filtration (50 μm) at low temperature (around 50 to 67°C). The last of these five exchangers is used only when necessary.

avoid mineral precipitations. Locally, in the filtering system, some scaling was observed with barite, celestine, iron oxides, galena and calcite mainly. In order to investigate corrosion and scaling, an innovative corrosion pilot was set up on the surface geothermal loop and tested for the first time between September 2008 and February 2009. Different kinds of steel were investigated for corrosion in the geothermal conditions of re-injection (20bars, < 80°C).

The liquid hot brine is pumped from the rock reservoir and first filtered in the surface geothermal loop in a self-cleaning 150μm filter. Whether the ORC cycle is or not in function, either the geothermal fluid feeds the ORC exchanger to produce electricity or it feeds the

Barriquand's exchangers to cool the brine to be reinjected. In that last case, the brine is injected in the 5 exchangers (Fig. 5). The fifth exchanger is used only when needed. The exchangers allow heat transfer between the brine and a fluid composed of water and mono propylene glycol.

3.4 Review of 20 years of research at Soultz

About 40 PhD theses have been written on the Soultz project in the last 20 years together with about 200 publications in international journals between 2001 and 2008. With this scientific background and the current production of electricity (1.5 MWe), the Soultz site is now a world reference for EGS. It appears that cooling 1 km³ of rock by only 20°C (initial temperature around 160-200°C) liberates as much energy as the combustion of 1 275 000 tons of oil and thus saves as much non-renewable fossil fuel (SoultzNet, 2011).

3.5 Future of the Soultz EGS

The total cost of the Soultz pilot operating now is 54 M€ (Soultznet, 2011). A prototype of 20-30 MWe will follow the first pilot presently in production (1.5 MWe). On a longer term, industrial units will be constructed (Soultznet, 2011). Large-scale production units inspired from the Soultz EGS might transform the world of energy since it is clean and sustainable. It preserves fossil fuels and limits the emissions of GHG and allows a continuous production of electricity 8000 hours/year, at night as well as at day, whatever the climate conditions (SoultzNet, 2011).

4. Other EGS programs in the world

The Soultz EGS is the only operating site at present. It benefited from the experience developed on other sites all around the world. The objective here is not to provide a complete review of these projects but to show the impact they had on the Soultz project. More details on these projects can be found in MIT (2006) and in the abundant literature easily available (e.g. Brown, 2000, 2009; Yanagisawa et al., 2011; Yasukawa and Takasugi, 2003). An overview of HDR/EGS programs in the world is given in table 6.

4.1 Fenton Hill (U.S.A.; after Brown, 2000, 2009; MIT, 2006)

The first attempt to extract the Earth's heat from rocks with no pre-existing high permeability was the Fenton Hill HDR experiment. It was initially totally funded by the U.S. government, but later involved active collaborations under an International Energy Agency agreement with Great Britain, France, Germany, and Japan. The Fenton Hill site is characterized by a high-temperature-gradient, a large volume of uniform, low-permeability, crystalline basement rock. It is located on the margin of a hydrothermal system in the Valles Caldera region of New Mexico, not far from the Los Alamos National Laboratory where the project was conceived.

The Fenton Hill experience demonstrated the technical feasibility of the HDR concept by 1980, but none of the testing carried out yielded all the performance characteristics required for a commercial-sized system (sufficient reservoir productivity, maintenance of flow rates with sufficiently low pumping pressures, high cost of drilling deep (> 3 km) wells in hard rock becoming the dominant economic component in low-gradient EGS resources).

Country	Site	Depth (m)	Temperature (°C)	Dates	Production of electricity
France	Le Mayet		22 (production)	1975-1989	
	Soultz-sous-Forêts	5000 (3 boreholes)	155 (production)	1985-	1.5 MWe Since June 2008
Germany	Bad Urach	4500 and 2600	180 (reservoir)	1976-	
	Falkenberg	300	13 (reservoir)	1975-1985	
Switzerland	Basel	4500	180 (reservoir)		
UK	Rosemanowes	2700	70 (production)	1975-1991	
Australia	Cooper Basin	4250	212 (production)	2003-	
USA	Fenton Hill	5000	191 (production)	1973-2000	
	Desert Peak	5420		2001-	
Japan	Hijori	2300	180 (production)	1981-1987	

MWe : MWelectricity (raw production minus consumption of electricity required for the production).
Data after MIT (2006), Davatzes and Hickmann (2009), Genter et al. (2009) and Wyborn (2011).
Temperatures are given for the production phase for successful EGS sites or for the reservoir when no production occurred.

Table 6. Overview of some HDR or EGS programs in the world.

The program was divided into two major phases. Phase I (1974 - 1980), focused on a 3 km deep reservoir with a temperature of about 200°C. Phase II (1979-1995) penetrated into a deeper (4.4 km), hotter (300°C) reservoir. The two separate, confined HDR reservoirs were created by hydraulic fracturing and were flow-tested for almost a year each. A major lesson learned from the Fenton Hill HDR experience is that the characteristics of the joint system are highly variable : the joint-extension pressure in the Phase I reservoir was only half that obtained for the Phase II reservoir (MIT, 2006). This pressure is controlled by the interconnected joint structure that cannot be discerned either from borehole observations or from the surface. Only microseismic observations might show the portion of the induced seismicity that is really related to the opening of the joints allowing the main flow paths. However, by the early 1980s, HDR projects (Table 6) showed that in most of the cases, hydraulic stimulation did not only create new fractures but also re-opened by shearing natural joints favourably aligned with the principal directions of the local stress field and generally sealed by mineral deposits.

Several lessons were learnt at Fenton Hill. First, deep (5 km) high-temperature (up to 300 °C) wells can be completed in hard, abrasive rock. Second, it was possible to create or reactivate large-scale fracture networks and thanks to seismic monitoring and directed boreholes to intercept them. It was also possible to circulate the fractures with fluids thanks to the boreholes. The first models of flow and heat transfer were developed and used to predict the behaviour of the EGS reservoir. However, if injection pressures were lowered to reduce water loss and reservoir growth, the flow rates were lower than expected. An expert panel of the Massachusetts Institute of Technology estimated in 2006 that EGS could provide up to 100 000 megawatts of electricity in the United States by 2050, or about 10% of the current national capacity (high proportion for an alternative energy source). Up to US\$132.9 million from the recovery act are to be directed at EGS demonstration projects.

4.2 Rosemanowes (UK; after MIT, 2006)

As a result of experience during Phase I at Fenton Hill, the Camborne School of Mines undertook an experimental HDR project at Rosemanowes (Cornwall, U.K.) in a granite. The project was funded by the U.K. Department of Energy and by the Commission of the European Communities. The temperature was restricted deliberately to below 100°C, to minimize instrumentation problems. This project was never intended as an energy producer but was conceived as a large-scale rock mechanics experiment about the stimulation of fracture networks. The site was chosen because of its clearly defined vertical jointing, high-temperature gradients between 30-40°C/km and its strike-slip tectonic regime.

Phase 1 of the project started in 1977, with the drilling of several 300 m wells dedicated to test fracture-initiation techniques. Phase 2 was characterized by the drilling of 2 wells that reached 2000 m and a temperature of nearly 80°C. Both were deviated in the same plane to an angle of 30 degrees from the vertical in the lower sections, and separated by 300 m vertically. Stimulation of the injection well was performed, initially with explosives, and then hydraulically at rates up to 100 kg/s and wellhead pressures of 14 MPa. A short circuit unfortunately developed between the two wells, which allowed cool injected water to return too rapidly to the production well: the temperature dropped from 80°C to 70°C. In phase 3A, with no further drilling, lowering the pressure in the production well seemed to close the joint apertures close to the borehole and increase the impedance. An experiment to place a proppant material (sand) in the joints near the production borehole was performed with a high viscosity gel and significantly reduced the water losses and impedance but also worsened the short circuiting and lowered the flow temperature in the production borehole even further. It was concluded that the proppant technique would need to be used with caution in any attempt to manipulate HDR systems. At Rosemanowes, it became clear that everything one does to pressurize a reservoir is irreversible and not necessarily useful for heat mining. For example, pumping too long at too high a pressure might cause irreversible rock movements that could drive short circuits as well as pathways for water losses to the far field (MIT, 2006). A packer assembly was placed close to the bottom of the borehole to seal off the short-cut and was successful but resulted in a subsequent low flow rate. This was interpreted as a new stimulated zone poorly connected to the previous one and demonstrated that individual fractures can have independent connections to the far-field fracture system leading to a globally poor connection of the reservoir.

4.3 Hijori (Japan; after MIT, 2006 and Yanagisawa et al, 2011)

This HDR project is located on Honshu island, on the edge of the Hijori caldera, where the high thermal gradient is related to a recent volcanic event (10 000 years old). The stress regime is very complex. The site was first drilled in 1989 after the results obtained at Fenton Hill to which Japan contributed. One injector and three producer wells were drilled from 1989 to 1991 between 1550 and 2151m. The temperature reached more than 225°C at 1500 m and 250°C at 1800 m. The spacing between the bottom of wells was about 40-55 m. The deep reservoir (about 2200 m), drilled from 1991 to 1995, was characterized by natural fractures. The distance between the wells, at that depth was 80 to 130 m. Hydraulic fracturing experiments began with injection of 2000 m³ of water. The stimulation was carried out in four stages at rates of 1, 2, 4 and 6 m³/min. A 30-day circulation test was conducted following stimulation. A combination of produced water and surface water was injected at

1-2 m³/min (17-34 kg/s), and steam and hot water were produced from 2 production wells. During the test, a total of 44500 m³ of water was injected while 13000 m³ of water were produced. The test showed a good hydraulic connection between the injector and the two producers, but more than 70% of the injected water was lost. The test was short and the reservoir continued to grow during the entire circulation period. After additional circulation tests in 1996, a one-year test began in 2000 for the shallow and the deep reservoirs with injection of 36°C water at 15-20 kg/s. Production of steam and water occurred at 4-5 kg/s at about 163-172°C. Total thermal power production was about 8 MWt. Test analysis showed that production was from both the deep and shallow reservoir. While the injection flow rate remained constant at about 16 kg/s, the pressure required to inject that flow decreased during the test from 84 to 70 bar. Total production from the two wells was 8.7 kg/s with a loss rate of 45%. Because of a dramatic cooling from 163°C to about 100°C, that long-term flow test was stopped. The measured change in temperature was larger than that predicted from numerical modelling. One lesson learnt from Hijori joined to Fenton Hill and Rosemanowes experiences was that it is better to drill a single well, stimulate it and map the acoustic emissions during stimulation, then drill additional wells into the acoustic emissions cloud rather than to try to drill two or more wells and attempt to connect them with stimulated fractures. In addition, injecting at low pressures for long time periods had an even more beneficial effect than injecting at high pressures for short periods. The Hijori project also showed how important it is to understand not only the stress field but also the natural fracture system. Both Fenton Hill and Hijori were on the edges of a volcanic caldera with very high temperature gradients (need for rather shallow wells, less expensive than deep ones) but also extremely complex parameters (geology, fractures, stress conditions) making these projects very challenging. The mineralogical composition of the Hijori EGS is close to that of Soultz and Habanero rock bodies and one can account for a rather similar chemical reaction with injected water, but the geological contexts are highly different resulting in different circulation schemes within the fracture networks.

4.4 Basel (Switzerland; after MIT, 2006 and Giardini, 2009)

Switzerland developed a Deep Heat Mining project to generate power and heat in Basel and Geneva. At Basel, in the southeastern end of the Rhine graben, close to the border with Germany and France, a 2.7 km exploration well was drilled, studied, and equipped with seismic instrumentation. A unique aspect of the Basel project is that drilling took place within city limits, and the heat produced by the system had the potential for cogeneration (direct use for local district heating as well as electricity generation). The project was initiated in 1996 and partly financed by the Federal Office of Energy together with private and public institutions. The plant was to be constructed in an industrial area of Basel, where the waste incineration of the municipal water purification plant provides an additional heat source. The core of the project, called Deep Heat Mining Basel, was a well triplet into hot granitic basement at a depth of 5 000 m. Two additional monitoring wells into the top of the basement rock were equipped with multiple seismic receiver arrays in order to record the fracture-induced seismic signals to map the seismic active domain of the stimulated reservoir volume. Reservoir temperature was expected to be 200°C. Water circulation of 100kg/s through one injection well and two production wells was designed to result in 30 MW of thermal power at wellheads. In combination with this heat source and an additional gas turbine,

a combined cogeneration plant would have produced annually up to 108 GWh of electric power and 39 GWh of thermal power to the district heating grid. North-northwest trending compression and west-northwest extension creates a seismically active area into which the power plant was to be located. Therefore, it was important to record and understand the natural seismic activity as accurately as possible, prior to stimulation of a deep reservoir volume characteristically accompanied by induced seismicity. The first exploration well was drilled in 2001 into granitic basement at 2,650 m. The next well was planned to the targeted reservoir depth of 5000 m. On December 8th, 2006, an earthquake of magnitude 3.4 occurred, responsible for 7 million CHF of property damage. It has been attributed to stimulation operations. In such a seismically active area, one has also to consider the likely impact of the geothermal reservoir on the occurrence of a large earthquake like the event that caused large damage to the city in 1356. As a consequence of this 2006 earthquake, the Basel project was totally stopped in 2009. Many newspaper articles can be found about this story.

4.5 Habanero (Australia; after MIT, 2006 and Wyborn, 2011)

Australia has the hottest granites in the world thanks to radioactive decay characterized by temperatures approaching 250°C at a depth of 4 km in the Innamincka granite (Cooper Basin, south Australia) where the Habanero EGS is developed. Like at Soultz, the Habanero EGS is based on 3 drillings reaching a 4250 m depth. In this white two-mica granite containing 75%SiO₂, biotite is widely chloritized, feldspar is also altered and calcite precipitated as secondary mineral as already described for the Soultz granite (see section 3). Some fractures intersected in the first well were overpressured with water at 35 MPa above hydrostatic pressure. The fractures encountered were more permeable than expected likely because of slipping improving their permeability and resulting in drilling fluids being lost into them. The well intersected granite at 3668 m and was completed with a 6-inch open hole. It was stimulated in November and December 2003. A volume of 20000 cubic meters of water was injected into the fractures at flow rates from 13.5 kg/s to 26 kg/s, at pressures up to about 70 MPa. As a result, a volume estimated from acoustic emission data at 0.7 km³ was developed into the granite body. A second well was drilled 500 m from the first one and intersected the fractured reservoir at 4325 m. During drilling pressure changes were recorded in the first well. The second well was tested in 2005 with flows up to 25kg/s and a surface temperature of 210°C was achieved. Testing between the two wells was delayed because of lost equipment in the second well. The first well was stimulated again with 20000 m³ of water and it appeared, thanks to acoustic emission, that the old reservoir was extended by another 50% and finally covered an area of 4 km². A third well was drilled 568 m from the first one and was stimulated in 2008. The well productivity was doubled. As a result of these stimulations, two parallel fracture planes with a 15°W dip developed separated by about 100 m around 4200-4400 m and 4300-4600 m depths. The open-loop test performed in 2008 injected 18.5 kg/s in the first well. The third well produced 20 kg/s of water at a temperature around 212°C thanks to flow in the main fracture plane cited before. The productivity obtained during this test was nearly similar to that obtained in the Soultz GPK2 well allowing electricity production from June 2008. The main challenges to future progress are the reduction of drilling costs, an increased rate of penetration for drillings in hard formations, increasing flow rate by improving well connection to reservoir and through development of multiple reservoirs

(Wyborn, 2011). The concept of a 25MWe commercial plant is now designed with 3 injection wells and 6 production wells. The ultimate potential is to supply up to 6500 MWe of long-term base-loadpower, equivalent to electrical supply from ~750 MT thermal coal (Wyborn, 2011).

5. Forthcoming developments and challenges of EGS projects

Many research teams are currently working on improvement of existing techniques of innovation developments to ensure better production rates and minimized constraints. Among these innovations, the following are particularly promising but of course non exhaustive.

5.1 CO₂ EGS

The use of supercritical CO₂ as a heat transfer fluid has been first proposed as an alternative to water for both reservoir creation and heat extraction in EGS (Brown, 2000). Numerical simulations have shown that under expected EGS operating conditions, CO₂ could achieve more efficient heat extraction performance than water (Magliocco et al., 2011). CO₂ has numerous advantages for EGS: greater power output, minimized parasitic losses from pumping and cooling, carbon sequestration and minimized water use. Magliocco et al. (2011) have performed laboratory tests of CO₂ injection while Plaskina et al. (2011) made a numerical simulation study of effects of CO₂ injection to provide a new method to improve heat recovery from the geopressured aquifers by combining the effects of natural and forced convection.

5.2 *In situ* formation of calcium carbonate as a diversion agent

During stimulation of EGS wells, water is injected in order to open sealed fractures through shear failure. When the fractures are open, the stimulation fluid flows into them and becomes unavailable for stimulation elsewhere. Fluid diversion agents can serve to temporarily plug newly stimulated fractures in order to make the injected water available to stimulate new fractures (e.g. Petty et al., 2011). The diversion agent is subsequently removed to allow flow from those previously sealed fractures. As demonstrated by Ledésert et al. (2009) and Hébert et al., (2010), calcite is found naturally in fractures of EGS reservoirs and prevents the fluid from flowing into fractures. The *in situ* precipitation of calcium carbonate was studied by Rose et al. (2010) for use as a diversion agent in EGS.

5.3 Use of oil and gas reservoirs for EGS purposes

A lot of oil and gas reservoirs have been or will be abandoned in petroleum industry. According to Li and Zhang (2008) these oil and gas reservoirs might be transferred into exceptional enhanced geothermal reservoirs with very high temperatures. Air may be injected in these abandoned hydrocarbon reservoirs and *in-situ* combustion will occur through oxidization. The efficiency of power generation using the fluids from *in-situ* combustion reservoirs might be much higher than that obtained by using hot fluids coproduced from oil and gas reservoirs because of the high temperature.

6. Conclusion

Enhanced Geothermal Systems experiences at Fenton Hill (USA), Rosemanowes (UK), Hijori (Japan) and Basel (Switzerland) allowed scientists to develop a European thermal pilot-plant producing electricity in Soultz-sous-Forêts (France) since June 2008. This project is the result of 20 years of active research based on geology (petrography, mineralogy, fracture analysis), geochemistry, geophysics (seismic monitoring, well-logging), hydraulics and modelling. Technical improvements were also necessary to allow deep drilling (down to 5000 m) in a hard (granite), highly fractured rock and circulation of water at great depth (between 4500 and 5000 m). The rock behaves as a heat exchanger in which cold water is injected. The water circulates in the re-activated fracture planes where it warms up. It is pumped to the surface and activates a 1.5 MWe geothermal Organic Rankine Cycle power plant that converts the thermal energy into electricity. In such a project challenges are numerous and difficult since the injected water must circulate at great depths between the 3 wells of the triplet with no or little loss and the flow rate and fluid temperature must be and remain high enough to allow production of electricity. Provided careful monitoring of the reservoir during operation, EGS are a sustainable, renewable and clean way to produce electricity. It has been proven that environmental impacts of EGS are lower than those of nuclear or fossil fuel power plants dedicated to the production of electricity. The Soultz EGS pilot plant is the first one in the world to produce electricity and it should be followed in the forthcoming years by industrial units that will produce electricity at a commercial scale. Many other EGS projects have begun all around the world and a lot of scientific and technical targets are in development to improve the production of energy (electricity and central heating through district networks).

7. References

- Baisch, S., Carbon, D., Dannwolf, U., Delacou, B., Devaux, M., Dunand, F., Jung, R., Koller, M., Matin, C., Sartori, M., Secanelli, R. & Uörös, R. (2009). Deep Heat Mining – Seismic Risk Analysis, *Departement für Wirtschaft, Soziales und Umwelt des Kantons Basel-Stadt, Armt für Umwelt und Energie*, Available at http://www.wsu.bs.ch/serianex_teil_1_english.pdf
- Bartier, D., Ledéser, B., Clauer, N., Meunier, A., Liewig, N., Morvan, G., Addad, A. (2008). Hydrothermal alteration of the Soultz-sous-Forêts granite (Hot Fractured Rock geothermal exchanger) into a tosudite and illite assemblage, *European Journal of Mineralogy*, 20 (1), 131-142.
- Beardsmore, G.R. & Cooper, G.T. (2009). Geothermal Systems Assessment- Identification and Mitigation of EGS Exploration Risk, *Proceedings of the Thirty-Fourth Workshop on Geothermal Reservoir Engineering*, Stanford University, Stanford, California, February 9-11, 2009, SGP-TR-187
- Brown, D.W. (2000). A Hot Dry Rock Geothermal Energy Concept Utilizing Supercritical CO₂ Instead of Water, *Proceedings of the Twenty-Fifth Workshop on Geothermal Reservoir Engineering*, Stanford University, Stanford, California, January 24-26, 2000, SGP-TR-165.

- Brown, D.W. (2009). Hot Dry Rock Geothermal Energy : Important Lessons from Fenton Hill, *Proceedings of the Thirty-Fourth Workshop on Geothermal Reservoir Engineering*, Stanford University, Stanford, California, February 9-11, 2009, SGP-TR-187
- Clauser, C. (2006), Geothermal Energy, in K. Heinloth (ed.), *Landolt-Börnstein, Group VIII Advanced Material and Technologies*, Vol. 3 Energy Technologies, Subvolume C, Renewable Energies, 480-595, Springer Verlag, Heidelberg-Berlin.
- Concha, D., Fehler, M., Zhang, H. & Wang, P. (2010). Imaging of the Soultz Enhanced Geothermal Reservoir Using Microseismic Data, *Proceedings of the Thirty-Fifth Workshop on Geothermal Reservoir Engineering*, Stanford University, Stanford, California, February 1-3, 2010, SGP-TR-188
- Culver, G. (1998) Drilling and Well Construction, Chapter 6, *Geothermal Direct Use Engineering and Design Guidebook*, Third Edition, Culver, Gene, Geo-Heat Center, Oregon Institute of Technology, Klamath Falls, OR, 1998.
<http://geoheat.oit.edu/pdf/tp65.pdf>
- Davatzes, N.C. & Hickman, S.H. (2009). Fractures, Stress and Fluid Flow prior to Stimulation of well 27-15, Desert Peak, Nevada, EGS Project, Clark, C. (2009). Pre-production Activity Impacts of Enhanced Geothermal Systems, *Proceedings of the Thirty-Fourth Workshop on Geothermal Reservoir Engineering*, Stanford University, Stanford, California, February 9-11, 2009, SGP-TR-187
- Dezayes, C. and Genter, A. (2008). Large-scale Fracture Network Based on Soultz Borehole Data, EHDRA Scientific Conference, *Proceedings of the EHDRA scientific conference*, 24-25 September 2008, Soultz-sous-Forêts, France.
- Dezayes C., Genter A., Valley B. (2010). Structure of the low permeable naturally fractured geothermal reservoir at Soultz, *Comptes Rendus Geosciences*, 342, 517-530.
- Dèzes, P., Schmid, S.M., Ziegler, P.A. (2004). Evolution of the European Cenozoic Rift System: interaction of the Alpine and Pyrenean orogens with their foreland lithosphere, *Tectonophysics*, 389, 1-33.
- Dubois, M., Ledésert, B., Potdevin, J.L. & Vançon, S. (2000). Détermination des conditions de précipitation des carbonates dans une zone d'altération du granite de Soultz (soubassement du fossé rhénan, France) : l'enregistrement des inclusions fluides, *Comptes Rendus de l'Académie des Sciences*, 331, 303-309.
- Economides, M.J. & Nolte, K.G. (2000). *Reservoir Stimulation*, Third Edition, Wiley, NY and Chichester
- Fridleifsson, I.B. (2000). Improving the Standard of Living, World Geothermal Congress 2000 Convention News 2, 1.
- Genter, A., Traineau, H., Dezayes, C., Elsass, P., Ledésert, B., Meunier, A. & Villemin. T. (1995). Fracture Analysis and Reservoir Characterization of the Granitic Basement in the HDR Soultz Project (France), *Geothermal Science and Technology*, 4(3), 189-214.
- Genter, A., Fritsch, D., Cuenot, N., Baumgärtner, J. & Graff J.J. (2009) Overview of the Current Activities of the European EGS Soultz Project : From Exploration to Electricity Production, *Proceedings of the Thirty-Fourth Workshop on Geothermal Reservoir Engineering*, Stanford University, Stanford, California, February 9-11, 2009, SGP-TR-187

- Genter, A., Cuenot, N., Goerke, X. & Sanjuan B., (2010). Programme de suivi scientifique et technique de la centrale géothermique de Soultz pendant l'exploitation, Rapport d'avancement Phase III : activité 2010, décembre 2010, rapport GEIE EMC RA05 001 P, 66 pp.
- Gérard, A. & Kappelmeyer, O. (1987). The Soultz-sous-Forêts project : Proceedings of the first EEC/US workshop on geothermal Hot dryRocks Technology, *Geothermics*, 393-399.
- Gérard, A., Genter, A., Kohl, Th., Lutz, Ph., Rose, P. & Rummel, F. (2006). The deep EGS (Enhanced Geothermal System) Project at Soultz-sous-Forêts (Alsace, France), *Geothermics*, 35, No. 5-6, 473-483.
- Giardini, D. (2009). Geothermal quake risks must be faced, *Nature*, 462, 848-849
- Hébert, R.L., Ledésert, B., Bartier, D., Dezayes, C., Genter, A., & Grall, C. (2010) The Enhanced Geothermal System of Soultz-sous-Forêts: A study of the relationships between fracture zones and calcite content, *Journal of Volcanology and Geothermal Research*, 196, 126-133.
- Hébert, R.L, Ledésert, B. , Genter, A., Bartier, D. & Dezayes, C. (2011) Mineral Precipitation in Geothermal Reservoir : the Study Case of Calcite in the Soultz-sous-Forêts Enhanced Geothermal System, *Proceedings of the Thirty-Sixth Workshop on Geothermal Reservoir Engineering*, Stanford University, Stanford, California, January 31 - February 2, 2011, SGP-TR-191
- Hickman, S. & Davatzes, N. (2010). In-Situ Stress and Fracture Characterization for Planning of an EGS Stimulation in the Desert Peak Geothermal Field, NV; *Proceedings of the Thirty-Fifth Workshop on Geothermal Reservoir Engineering*, Stanford University, Stanford, California, February 1-3, 2010, SGP-TR-188
- Hurtig, E., Cermak, V., Haenel, R. Zui, V. (1992). Geothermal Atlas in Europe, *Hermann Haak Verlagsgesellschaft mbH*, Germany.
- Karvounis D. & Jenny. P. (2011). Modeling of Flow and Transport in Enhanced Geothermal Systems, *Proceedings of the Thirty-Sixth Workshop on Geothermal Reservoir Engineering*, Stanford University, Stanford, California, January 31 - February 2, 2011, SGP-TR-191
- Kosack, C., Vogt, C., Marquart, G., Clauser, C. & Rath, V. (2011). Stochastic Permeability Estimation for the Soultz-sous-Forêts EGS Reservoir, *Thirty-Sixth Workshop on Geothermal Reservoir Engineering Stanford University*, Stanford, California, January 31 - February 2, 2011, SGP-TR-191
- Kretz, R. (1985). Symbols for Rock- forming Minerals , *American Mineralogist*, 68, 277-279.
- Ledésert, B., Dubois, J., Genter, A. & Meunier, A. (1993) Fractal analysis of fractures applied to Soultz-sous-Forêts Hot Dry Rock geothermal program, *Journal of Volcanology and Geothermal Research*, 57, 1-17.
- Ledésert, B., Berger, G., Meunier, A., Genter, A. and Bouchet, A. (1999). Diagenetic-type reactions related to hydrothermal alteration in the Soultz-sous-Forêts granite, *European Journal of Mineralogy*, 11, 731-741.
- Ledésert B., Hébert R., Grall C., Genter A., Dezayes C., Bartier D., Gérard A. (2009) Calcimetry as a useful tool for a better knowledge of flow pathways in the Soultz-

- sous-Forêts Enhanced Geothermal System, *Journal of Volcanology and Geothermal Research*, 181, 106-114.
- Ledésert, B., Hébert, R., Genter, A., Bartier, D., Clauer, N. & Grall C. (2010) Fractures, Hydrothermal alterations and permeability in the Soultz Enhanced Geothermal System, *Comptes Rendus Géosciences*, 342 (2010) 607-615.
- Li, K. & Zhang, L. (2008). Exceptional enhanced geothermal systems from oil and gas reservoirs, *Proceedings of the Thirty-Third Workshop on Geothermal Reservoir Engineering*, Stanford University, Stanford, California, January 28-30, 2008, SGP-TR-185
- Lund, J.W. (2007). Characteristics, Development and Utilization of Geothermal Resources, *Geo-Heat Center Quarterly Bulletin*, Vol. 28, No. 2, Geo-Heat Center, Oregon Institute of Technology, Klamath Falls, Or, Available from <http://geoheat.oit.edu/pdf/tp126.pdf>
- Magliocco, M., Kneafsey, T.J., Pruess, K. & Glaser, S. (2011) Laboratory Experimental Study of Heat Extraction from Porous Media by Means of CO₂, *Proceedings of the Thirty-Sixth Workshop on Geothermal Reservoir Engineering*, Stanford University, Stanford, California, January 31 - February 2, 2011, SGP-TR-191
- Minissale, A. (1991). The Larderello Geothermal Field: a Review, *Earth-Science Reviews*, Volume 31, Issue 2, Pages 133-151
- M.I.T (2006). The Future of Geothermal Energy: Impact of Enhanced Geothermal Systems (EGS) on the United States in the 21st Century, *Massachusetts Institute of Technology*, ISBN: 0-615-13438-6, Available from <http://geothermal.inel.gov>.
- Nami, P., Schellschmidt, R., Schindler, M. & Tischner, T. (2008) Chemical Stimulation Operations for Reservoir Development of the deep Crystalline HDR/EGS at Soultz-sous-Forêts (France), *Proceedings of the Thirty-Third Workshop on Geothermal Reservoir Engineering*, Stanford University, Stanford, California, January 28-30, 2008, SGP-TR-185
- Petty, S., Bour, D., Nordin, Y., Nofziger, L. (2011) Fluid Diversion in an Open Hole Slotted Liner – a First Step in Multiple Zone EGS stimulation, *Proceedings of the Thirty-Sixth Workshop on Geothermal Reservoir Engineering*, Stanford University, Stanford, California, January 31 - February 2, 2011, SGP-TR-191
- Plaksina, T., White, C., Nunn, J. & Gray, T. (2011). Effects of Coupled Convection and CO₂ Injection in Stimulation of Geopressured Geothermal Reservoirs, *Proceedings of the Thirty-Sixth Workshop on Geothermal Reservoir Engineering*, Stanford University, Stanford, California, January 31 - February 2, 2011, SGP-TR-191
- Portier, S., Vuataz, F.D., Nami, P., Sanjuan, B. & André Gérard, A. (2009). Chemical Stimulation Techniques for Geothermal Wells: Experiments on the Three-well EGS System at Soultz-sous-Forêts, France, *Geothermics*, 38, 349-359
- Radilla, G., Sausse, J., Sanjuan, B. & Fourar, M. (2010). Tracer Tests in the Enhanced Geothermal System of Soultz-sous-Forêts. What Does the Stratified Medium Approach Tells us about the Fracture Permeability in the Reservoir ? *Proceedings of the Thirty-Fifth Workshop on Geothermal Reservoir Engineering*, Stanford University, Stanford, California, February 1-3, 2010, SGP-TR-188

- Rafferty, K. (1998). Outline Specifications for Direct-Use Wells and Equipment, , Geo-Heat Center, Oregon Institute of Technology, Klamath Falls, OR, 1998. <http://geoheat.oit.edu/pdf/tp66.pdf>
- Romagnoli, P., Arias, A., Barelli, A., Cei, M. & Casini, M. (2010). An Updated Numerical Model of the Larderello-Travale Geothermal System, Italy, *Geothermics*, Volume 39, Issue 4, Pages 292-313
- Sanjuan, B., Pinault, J-L, Rose, P., Gérard, A., Brach, M., Braibant, G., Crouzet, C., Foucher, J-C, Gautier, A. & Touzelet S. (2006). Tracer Testing of the Geothermal Heat Exchanger at Soultz-sous-Forêts (France) between 2000 and 2005, *Geothermics*, 35, No. 5-6, 622-653.
- Sanval, S.K. & Eneedy, S. (2011) Fifty Years of Power Generation at the Geysers Geothermal Field, California - The Lessons Learned, *Proceedings of the Thirty-Sixth Workshop on Geothermal Reservoir Engineering*, Stanford University, Stanford, California, January 31 - February 2, 2011, SGP-TR-191
- Satman, A. (2011). Sustainability of Geothermal Doublets, *Proceedings of the Thirty-Sixth Workshop on Geothermal Reservoir Engineering*, Stanford University, Stanford, California, January 31 - February 2, 2011, SGP-TR-191
- Sausse, J., Dezayes, C., Genter, A. (2007). From geological interpretation and 3D modelling to the characterization of deep seated EGS reservoir of Soultz (France), *Proceedings European Geothermal Congress 2007*, Unterhaching, Germany, 30 May-1 June 2007, 7 pp.
- Sausse, J., Dezayes, C., Genter, A. & Bisset, A. (2008). Characterization of Fracture Connectivity and Fluid Flow Pathways Derived from Geological Interpretation and Modelling of the Deep Seated EGS Reservoir of Soultz (France), *Proceedings of the Thirty-Third Workshop on Geothermal Reservoir Engineering* Stanford University, Stanford, California, January 28-30, 2008, SGP-TR-185
- Sausse, J., Dezayes, Ch., Dorbath, L., Genter, A. & Place, J. (2009). 3D Fracture Zone Network at Soultz Based on Geological Data, Image Logs, Microseismic Events and VSP Results, *Geoscience*.
- Scott, S., Gunnarsson, I. & Stef, A. (2011). Gas Chemistry of the Hellisheiði Geothermal Field, SW-Iceland, *Proceedings of the Thirty-Sixth Workshop on Geothermal Reservoir Engineering*, Stanford University, Stanford, California, January 31 - February 2, 2011, SGP-TR-191
- SoultzNet (2011). <http://www.geothermie-soultz.fr>
- Rose, P., Scott Fayer, S., Susan Petty, S. & Bour, D. (2010). The In-situ Formation of Calcium as a diversion Agent for Use in Engineered Geothermal Systems, *Proceedings of the Thirty-Fifth Workshop on Geothermal Reservoir Engineering* Stanford University, Stanford, California, February 1-3, 2010, SGP-TR-188
- Tamanyu, S., Fujiwara, S., Ishikawa, J.I. & Jingu, H. (1998). Fracture System Related to Geothermal Reservoir Based on Core Samples of Slim Holes. Example from the Uenotai Geothermal Field, Northern Honshu, Japan, *Geothermics*, Volume 27, Issue 2, April 1998, Pages 143-166

- Wyborn, D. (2011). Hydraulic Stimulation of the Habanero Enhanced Geothermal System (EGS), South Australia, 5th BC Unconventional Gas Technical Forum April 2011, Geodynamics Limited, available from <http://www.em.gov.bc.ca/OG/oilandgas/petroleumgeology/UnconventionalGas/Documents/2011Documents/D%20Wyborn.pdf>
- Yanagisawa, N., Matsunaga, I., Ngothai, Y. & Wyborn, D. (2011) Geochemistry Change during Circulation Test of EGS Systems, *Proceedings of the Thirty-Sixth Workshop on Geothermal Reservoir Engineering*, Stanford University, Stanford, California, January 31 - February 2, 2011, SGP-TR-191
- Yasukawa, K. & Takasugi, S. (2003). Present Status of Underground Thermal Utilization in Japan, *Geothermics*, Volume 32, Issues 4-6, 609-618

Part 6

Fouling of Heat Exchangers

Fouling and Fouling Mitigation on Heat Exchanger Surfaces

S. N. Kazi

*Department of Mechanical and Materials Engineering,
Faculty of Engineering,
University of Malaya, Kuala Lumpur,
Malaysia*

1. Introduction

Heating or cooling of one medium by another medium is performed in a heat exchanger along with heat dissipation from surfaces of the equipment. In course of time during operation, the equipment receives deposition (Fouling) which retards heat exchanging capability of the equipment along with enhanced pressure loss and extended pumping power. Thus accumulation of undesired substances on a surface is defined as fouling. Occurrence of fouling is observed in natural as well as synthetic systems. In the present context undesired deposits on the heat exchanger surfaces are referred to fouling. With the development of fouling the heat exchanger may deteriorate to the extent that it must be withdrawn from service for cleaning or replacement.

The overall design of heat exchanger may significantly be influenced by fouling, use of material, process parameters, and continuous service in the system or process stream are all deliberately influenced by fouling phenomena. Preventive measures of fouling are highly encouraged as it keeps the service of heat exchanger for a longer time. However many mitigation techniques of fouling are harsh to the environment. A technique involving chemicals and means benign to the environment is the most desired approach and it could elongate the cleaning interval. On the other hand unique and effective arrangements may be required to facilitate satisfactory performances between cleaning schedules. As a result fouling causes huge economic loss due to its impact on initial cost on heat exchanging operation, operating cost, mitigation measures and performance. The present study focused on fouling phenomena, fouling models, environment of fouling, consideration of heat exchanger fouling in design and mitigation of fouling.

2. Fouling

Fouling is the resultant effect of deposition and removal of deposits on a heat exchanger surface. The process of fouling could be represented by the equation (2.1).

$$\frac{dm_f}{dt} = \dot{m}_d - \dot{m}_r \quad (2.1)$$

where \dot{m}_f , \dot{m}_d and \dot{m}_r are net deposition rates, deposition and removal rates respectively.

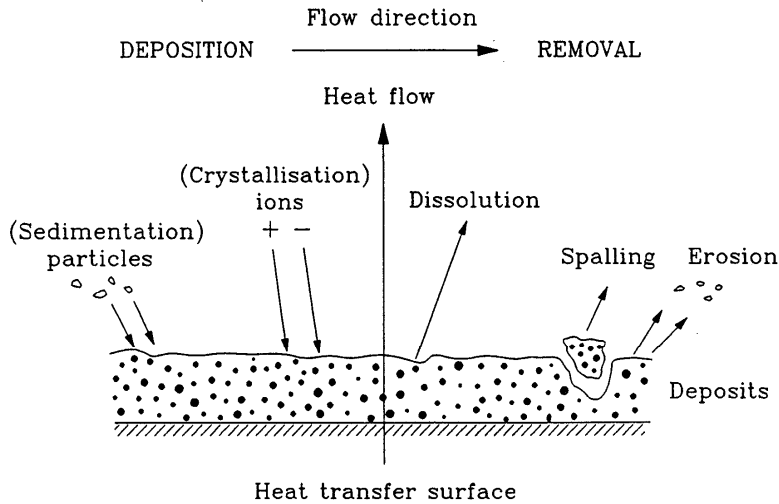


Fig. 2.1. Various deposition and removal processes during fouling.

Various deposition and removal processes for a typical system could be predicted as shown in Figure 2.1. The processes occur simultaneously and depend on the operating conditions. Usually removal rates increase with increasing amounts of deposit whereas deposition rates are independent of the amount of deposit but do depend on the changes caused by deposits such as increase in flow velocity and surface roughness. In the application of constant wall temperature or constant heat transfer coefficient boundary conditions, the interface temperature decreases as deposits build up which reduces the deposition rate.

Initiation period or time delay in heat exchanger fouling is considered the time when there is no deposition for some time after a clean heat exchanger has been brought into operation. Figure 2.2 illustrates this in detail. The initial growth of deposit can cause the heat transfer coefficient to increase rather than decrease resulting in a fouling resistance due to changing flow characteristics near the wall. At the initial stage the deposit penetrates the viscous sub-layer, the resulting turbulence increases the film heat transfer coefficient at the solid/liquid interface by changing flow characteristics near the wall. This increase in heat transfer coefficient may overcome the thermal resistance offered by the deposits and the net heat transfer coefficient may increase.

Several authors have reported negative fouling resistances [1, 2]. This process continues until the additional heat transfer resistance overcomes the advantage of increased turbulence. The time period from the beginning of the fouling process until the fouling resistance again becomes zero is called roughness delay time [3]. The time period from the beginning, when the formation of stable crystalline nuclei and their concretion to a compact fouling layer takes place is also called as induction period, which is in fact the roughness delay time and it ends up with the increase of fouling resistance above zero level.

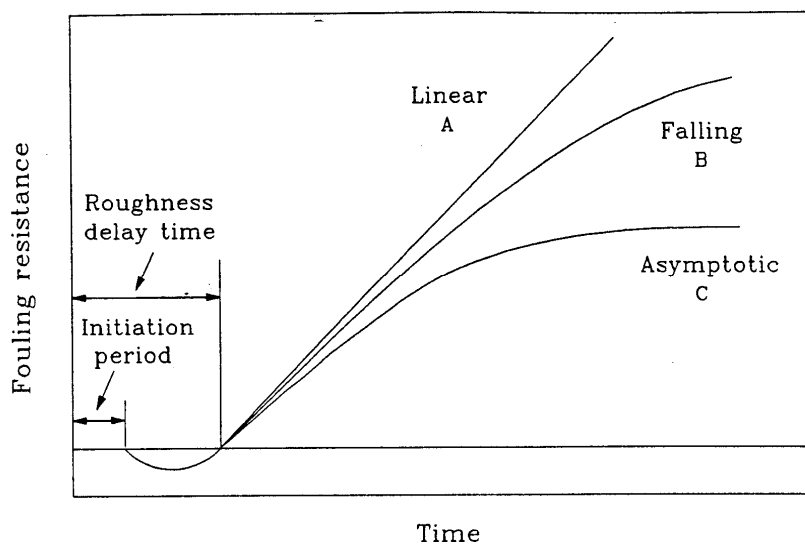


Fig. 2.2. Typical fouling curves.

The initiation period and the roughness delay time for particulate fouling are very small [4] in comparison to the fairly long delay time for crystallization fouling [5]. After the roughness delay time, the fouling curve can be classified into three categories, (a) Linear, (b) Falling, and asymptotic, as illustrated in Figure 2.2.

The linear fouling curve is obtained for very strong deposits where removal is negligible or in case where the removal rate is constant (and deposition is faster than removal). The falling rate curve is obtained from decrease in deposition and deposits with lower mechanical strength. The combined effect with time causes the net deposition or fouling rate to fall. Asymptotic fouling curve has been most commonly reported for different types of fouling. The removal rate increases with time for weak deposits and can eventually become equal to the deposition rate. The net rate is then zero as depicted in Figure 2.2.

Linear fouling curves have been presented by many authors for crystallization fouling [6-8]. However, there is some doubt as to whether the fouling rate may remain linear for a long time. For the constant heat flux situation, the net driving force may decrease with fouling. The increase in flow velocity due to the reduced cross-sectional area with deposit formation can increase the removal rate and the linear rate may change to a falling rate or even level-off completely [9]. Asymptotic behavior for crystallization fouling has reported by various authors [10, 5, 11-12]. Cooper et al. [13] found asymptotic behavior for calcium phosphate fouling (with some particulate fouling from suspended solids). For particulate fouling, asymptotic behavior is attained because particles do not adhere strongly to the wall and can be removed easily [4, 14].

A fouling process that follows a linear rate for constant heat flux can have falling or even asymptotic behaviour for constant temperature difference. The interface temperature decreases with deposit formation because of the extra resistance offered by deposit layer and enhanced flow velocities as flow passages are partially blocked by deposits. Thus the

thermal boundary conditions can result in different fouling curves which may give wrong impressions about the actual fouling mechanism.

2.1 Categories of fouling

Fouling can be categorised a number of different ways. These are (1) heat transfer service, (2) type of service fluid and (3) application. Most fouling situations are virtually unique. Fouling [15] can be classified into the following categories: (i) particulate, (ii) Precipitation, (iii) corrosion, (iv) biofouling and (v) chemical reaction.

2.2 Particulate fouling

Particulate fouling is evolved by the accumulation of solid particles suspended in the process stream onto the heat transfer surface. Heavy particles settle on a horizontal surface due to gravity and fine particles settle onto heat transfer surfaces at different inclinations due to suction force or other mechanisms. Unburned fuels or ashes deposition on boiler tubes, dust deposition on air cooled condensers etc. are examples of particulate fouling.

2.3 Precipitation fouling (sedimentation fouling)

This kind of fouling is also called crystallization fouling. Dissolved inorganic salts are normally present in fluid used in heat exchanger. There is a maximum amount of the salt (saturated) which can be dissolved in this fluid. During heating or cooling supersaturation occurs in the dissolved inorganic salts. The inverse solubility salts such as calcium and magnesium sulphate, carbonate, silicate, etc. have less solubility in warm water up to a certain temperature than in cold water. This may occur when the process condition inside the heat exchanger is different from condition at the entrance. A stream on a wall at a temperature above that of corresponding saturation temperature for the dissolved salts allows crystal formation on the surface. Normally crystallization starts at especially active points – nucleation sites – such as scratches and pits and often after induction period spread to cover the entire surface. This type of fouling is strong and adherent and requires vigorous mechanical or chemical treatment to be removed [16]. Fouling rate increases with the increase of salt concentration or surface temperature. These are often found in heat exchangers of process industries, boilers, evaporators etc.

2.4 Chemical reaction fouling

This type of fouling occurs when the depositions are formed as a result of chemical reaction resulting to produce a solid phase at or near the surface. In the present case carbonaceous material deposits due to thermal gradation of the components of a process stream on hot heat transfer surface. This type of fouling is often extremely tenacious and need special measure to clean off the deposits from heat exchanger surfaces to provide them satisfactory operation life [16].

2.5 Corrosion fouling

This type of fouling is also caused by some chemical reaction but it is different from chemical reaction fouling. This fouling is a reactant and it is consumed. In this case, the

surface reacts with the fluid and become corroded [15]. The corrosion products can foul the surface provided it is not dissolved in the solution after formation. pH value of the solution is one of the controlling parameter. Such as, presence of sulfur in fuel can cause corrosion in gas and oil fired boilers. Corrosion is often more prone in the liquid side of the heat exchanger. In some cases the product of corrosion may be swept away to downstream of a process loop and cause deposition on surfaces there.

2.6 Accumulation of biological fouling

On a heat transfer surface the growth of biological materials results in biofouling. In this case biological micro and macro organisms are stick to the heat transfer surface. When microorganisms (e.g., algae, bacteria, molds etc.) and their products grow they form microbial fouling. Seaweeds, waterweeds, barnacles develop microbial fouling. These fouling may occur simultaneously. The growth of attached organisms is one of the common problems [15] in heat exchanger operation. Food processing industries, power plant condensers using seawater, etc. are experiencing biofouling.

2.7 Fouling process

Fouling is a complex phenomenon due to involvement of a large number of variables. From a fundamental point of view the fouling mechanism follows certain stages in developing on a surface [17]. These are: Initiation, transport, attachment, removal and aging.

2.8 Initiation

Surface is conditioned in the initiation period. The initial delay induction period is influenced by the materials surface temperature, material, surface finish, roughness and surface coating. With the increase of degree of supersaturation with respect to the heat transfer surface temperature or increase of surface temperature the induction period decreases. During the induction period, nuclei for crystallization of deposit are also formed for biological growth. This period can take a long time, may be several weeks or a few minutes or even seconds.

The delay period decreases with increasing temperature in chemical reaction fouling due to the acceleration of induction reactions. If the initial period decreases with increasing surface temperature, crystallization fouling would be changed [18]. With the increase of surface roughness the delay period tends to decrease [19]. Additional sites are developed by the roughness projections, which promotes crystallization while grooves provide regions for particulate deposition.

2.9 Transport

In this part, fouling substances from the bulk fluid are transported to the heat transfer surface across the boundary layer. This is dependent on the physical properties of the system and concentration difference between the bulk and the surface fluid interface. Transport is accomplished by a number of phenomena including diffusion, sedimentation and thermophoresis [20, 21]. The local deposition flux \dot{m}_d on a surface can be expressed by equation (2.1).

$$\dot{m}_d = h_D(C_b - C_s) \quad (2.1)$$

Where, C_b and C_s are reactant concentration in the bulk fluid and that in the fluid adjacent to the heat transfer surface where as h_D is the convective mass transfer coefficient. From Sherwood number ($Sh = h_D d / D$), h_D could be evaluated. Sherwood number is dependent on the flow and the geometric parameters.

The phenomenon of transportation of a particulate matter in a fluid due to gravity on a horizontal or inclined surface is known as sedimentation. This is playing a vital roll where particles are heavy and fluid velocities are low.

2.10 Attachment

At this stage, the deposits are adhered to the surface and among itself. Salt ions approaching to the surface are attracted to it due to electro-magnetic forces and adhere to the surface to form nucleation and gradually it grows with time to form a fouling layer. Thus forces acting on the particles as they approach the surface are impotent in determining attachment. Properties of the materials, such as size, density and surface conditions are dominating the attachment phenomenon.

2.11 Removal

There is competition between removal and deposition of the foulants, up to the steady growth of the deposition on the surface. Shear forces at the interface between the fluid and deposited fouling are responsible for removal. The velocity gradients at the surface, the viscosity of the fluid and surface roughness are guiding the shear forces. Removal from the surface is performed through the mechanism of dissolution, erosion and spalling.

2.12 Aging

With the commencement of deposition ageing starts. During the ageing, there may be transformation of crystal to improve or decrease the deposition strength with time. During aging the mechanical properties of the deposit can change due to changes in the crystal or chemical structure. Alteration of the chemical composition of the deposit by a chemical reaction may change its mechanical strength. On the other hand the biofouling layer may become weak due to corrosion at the surface by slow poisoning of microorganisms.

2.13 Change in deposition thickness with time

Figure 2.3 is showing the growth rate of deposit on the surface [15]. Region A: fouling is initiated in the induction period. Region B: a steady deposit growth on the surface. The rate of removal of deposit was increased when the rates of deposition gradually retards. Region C: in this region the rate of removal and deposition seems equal and the thickness of deposition remains constant.

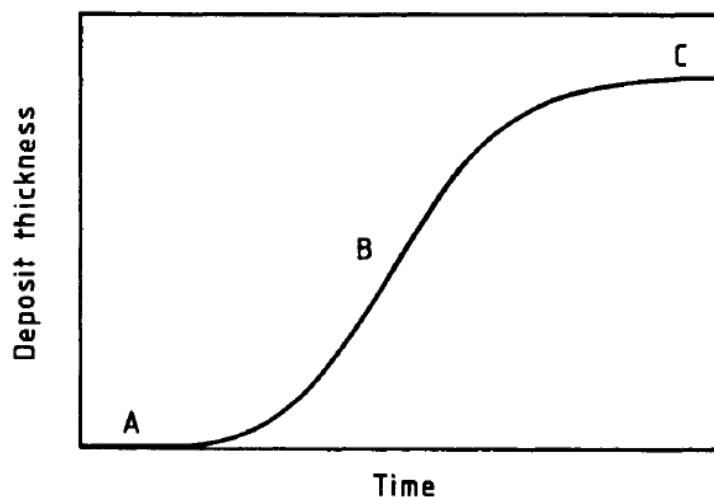


Fig. 2.3. Change in deposition thickness with time.

2.14 Composite fouling

Some of the common salts causes fouling are CaSO_4 , CaCO_3 and $\text{Mg}(\text{OH})_2$, and SiO_2 . Solubility, crystal structure and strength have impact on composite scale formation in fouling. Therefore, composite fouling needs more attention and further research [17].

3. Effects of fouling

Fouling phenomena imposes retardation on heat transfer and augmentation of frictional pressure drop which degrades the effectiveness of a heat exchanger. Some basic design aspects of heat exchangers along with mitigation of fouling are discussed in the present chapter.

3.1 Effect of fouling on heat exchanger design

A fixed value of fouling resistance could be assigned during the design stage although fouling is time dependent phenomenon. The cleaning schedule and operating parameters of the heat exchanger is dependent on the design fouling factor. Depending on application some heat exchangers require frequent cleaning whereas some need rear cleaning. Fouling rate is a dominating factor in designing a particular heat exchanger.

Fouling allowance: Provisions are during the design stage once fouling is anticipated. Different approaches are used to provide an allowance for fouling resistance. They all result into an excess heat transfer surface area. Updated methods include, specifying the fouling resistances, the cleanliness factor, or the percentage over surface.

A fouling resistance is prescribed on each side of the surface where fouling is anticipated. A lower overall heat transfer coefficient is resulted. To achieve the specified heat transfer, excess surface area is provided. Until the specified value of the fouling resistance is reached, the performance of the heat exchanger will be satisfactory. Depending on this fact, maintenance schedule could be planned to avoid unprecedented shut down for cleaning.

Tubular Exchanger Manufacturers Association (TEMA) [22] is referenced source of fouling factors used in the design of heat exchangers. Plant data, proprietary research data, personal and company experience etc. are other sources of fouling resistance data could be used in design.

Minimize Fouling by considering Design Features: Extent of fouling could be minimized by good design practice. Direct contact heat exchangers are considered where excess fouling is desired. In general a fouling prone fluid stream should be placed on the tube side as cleaning is easier. Generally higher fluid velocity and lower tube wall temperature retard fouling accumulation. Velocity of 1.8 m/s is a widely accepted figure for tube side flow of a heat exchanger. Heat Exchangers, operating over dew point for acid vapor and above freezing for fluids containing waxes prevent corrosion and freezing fouling. Fouling deposits are always found heavy in the region of low velocity at the vicinity of baffles in the shell side of the shell and tube heat exchangers.

Design features to facilitate fouling control: Full elimination of fouling may not be possible by good design practice alone. So, heat exchangers require cleaning at certain intervals. On-line cleaning can be employed to control fouling by extending cleaning cycle. Continuous fouling can ensure minimized fouling allowance. At construction and installation phase of a plant on-line cleaning system could be installed at ease. A heat exchanger with removable head and straight tube would be easy to clean and maintain. Space and provision for removal and cleaning of tube bundles are required to be available. On site cleaning facilities are to be provided with options of keeping isolation valves and connection provisions for cleaning hoses which could lead to chemical cleaning.

Fouling and operation of heat exchangers: Provision of excess surface area in heat exchangers for curbing fouling may lead to operation problem and fouling build. Generally high heat transfer area enhances total heat transfer which raises the outlet temperature. By changing process parameters such as flow, surface temperature leads to higher fouling.

Fouling control strategies: A number of strategies are applied for fouling control. In operating condition additives are added. On-line or off-line surface cleaning techniques are other options. To control fouling under different consequences are consolidated by some researchers as stated in Table 3.1 [23].

On-line techniques	Off-line techniques
Use and control of appropriate additives: Inhibitors, Antiscalants, Dispersants, Acids, Air jet	Disassembly and manual cleaning: Lances: Liquid jet, Steam, Air jet. Mechanical Cleaning:
On-line cleaning: Sponge balls, Brushes, Sonic horns, Soot blowers, Chains and scrapers, Thermal shock, Air bumping	Drills, Scrapers

Table 3.1. Various techniques adapted to control fouling.

Heat Exchanger with green additives: Many additives were developed for retardation of fouling but many of them found carcinogenic in nature. Now researchers are heading towards green additives. Chemistry and analysis are underway. Lab analysis and performances will be subsequently achieved. In near future users are looking for a breakthrough in this field.

3.2 Fouling effect on heat transport

Mineral scales deposited on heat exchanger surfaces are a persistent and an expensive problem in process industries, cooling water systems, steam generation units, desalination by evaporation etc. and also house hold equipment. Precipitation of mineral salts as a scale on the surface of the conduit and cause obstruction of fluid flow, impedance of heat transfer, wear of metal parts, localized corrosion attack and unscheduled equipment shutdown.

The deposit layer provides an additional resistance to heat transfer. Generally, the thermal conductivity of the deposit layer is very low compared with that of the material of the heat exchanger which may result in a much higher thermal resistance than the wall or film resistances. The deposit layer also reduces the flow area, which increases the pressure drop. This problem is quite severe and is further enhanced by the rough surface of the deposit. Both effects reduce the heat exchanger performance significantly. Additional energy requirements in terms of more heating or pumping power can hamper the economics of the process.

In a circular tube, fouling builds on the inside or outside of the tube depending on the flowing fluid. Fouling adds an insulating cover to the heat transfer surface. The overall heat transfer coefficient for a smooth tubular heat exchanger under deposited conditions, U_f can be obtained by adding the inside and outside thermal resistances:

$$U_f = \frac{1}{A_o / A_i h_i + A_o R_{fi} / A_i + A_o \ln(d_o / d_i) / 2\pi kL + R_{fo} + 1 / h_o} \quad (3.1)$$

where R_{fi} and R_{fo} represent resistances for the outer and inner surfaces of the tubes.

The thermal resistance due to fouling is evaluated generally based on experiments as difference in the overall specific resistances of the fouled and clean wall:

$$R_f = \left(\frac{1}{U_f} - \frac{1}{U_{cl}} \right) \quad (3.2)$$

Where, the overall heat transfer coefficient U_f can also be evaluated by using the rate equation:

$$U_f = \frac{\dot{Q}}{(A \times \Delta T_f)} \quad (3.3)$$

The heat flow rate \dot{Q}_f and temperature difference ΔT_f (the temperature difference between heated surface and the bulk liquid) are experimentally obtained. A is the exposed area of the heat exchanging surface to the liquid. The net rate of deposition of $\text{CaSO}_4 \cdot 2\text{H}_2\text{O}$ on metal

surface is estimated as $\frac{m}{t}$, where m is the total mass accumulation on a unit area and t refers to the amount of time the surface was exposed to the solution of the foulant.

Using the definition of heat transfer coefficient and fouling resistance, the equation (3.4) can be derived for constant heat duty.

$$\frac{A_{fouled}}{A_{clean}} = 1 + U_{clean} R_f \quad (3.4)$$

The required excess heat transfer area usually becomes excessive due to the higher clean heat transfer coefficients. It is often recommended that the additional surface should not exceed 25 percent of the heat transfer surface requirement for clean operation.

3.3 Effect of fouling on pressure drop

In heat exchangers pressure loss is considered more critical than loss in heat transfer due to fouling. Fouling results in a finite layer. Flow field, pressure drop are affected by the change in geometry of the flow passage. Thus in a tubular heat exchanger, the deposited layer roughens the surface, diminishes the inner and raises the outer dimension of the tubes. The inside diameter of the tube decreases and roughness of the tube increases due to fouling which, causes an increase in pressure drop. Pressure drop inside a tube of a heat exchanger under fouled and clean state can be correlated as follows:

$$\frac{\Delta P_f}{\Delta P_c} = \frac{f_f}{f_c} \left(\frac{d_c}{d_f} \right) \left(\frac{u_{mf}}{u_{mc}} \right)^2 \quad (3.5)$$

Considering that the mass flow rates under clean and fouled conditions are the same, the mass flow rate can be represented as:

$$\dot{m} = \rho u_m A_{cr} \quad (3.6)$$

Equation (3.5) thus becomes:

$$\frac{\Delta P_f}{\Delta P_c} = \frac{f_f}{f_c} \left(\frac{d_c}{d_f} \right)^5 \quad (3.7)$$

The magnitude of d_f of scaled tube can be obtained from equation (3.8).

$$d_f = d_c \exp \left(-\frac{2k_c R_f}{d_c} \right) \quad (3.8)$$

The thickness t_f of deposit layer can be obtained from:

$$t_f = 0.5d_c \left[1 - \exp\left(-\frac{2k_f R_f}{d_c}\right) \right] \quad (3.9)$$

For a known total fouling resistance, the tube diameter under fouled conditions can be evaluated on knowing the thermal conductivity of the deposits. Non-uniform thermal conductivity may result from the multi layers of fouling deposits. Approximate thermal conductivities of pure materials constituting fouling deposits are often used for estimation of thermal conductivity of the total deposits. Depending on situations the fouling layer is considered composed solely of one material. In some occasions to ease calculations f_f is considered equal to f_c .

4. Conditions influencing fouling

The conditions influencing fouling can be classified as: (A) operating parameters, (B) heat exchanger parameters, and (C) fluid properties. Among the operating parameters the important events which influencing fouling at a significant level are: (1) velocity, (2) surface temperature, and (3) bulk temperature.

Velocity influences fouling at a significant level. In diffusion controlled processes, increasing the fluid velocity causes more fouling [24]. In most cases, fouling decreases at higher fluid velocities [4, 13, 25]. Increasing flow velocity increases the fluid shear stress which causes more removal. This results in lower fouling rates which resulting to lower fouling resistance. For weak deposits (particulate fouling), increasing the flow velocity may completely eliminate fouling. For stronger deposits, increasing the flow velocity beyond a particular point may not decrease fouling significantly [25]. For very strong deposits, increasing the flow velocity may not have any effect at all [6].

Surface temperature may increase, decrease or have no effect on fouling [26]. The rates of chemical reaction and inverse solubility crystallization increase with an increase in temperature. For inverse solubility salts, higher surface temperature increases fouling due to higher concentration gradients and higher reaction rate constants. In case of normal solubility salts cooling results in more fouling.

The bulk temperature also effects on increase of fouling rate. In inverse crystallisation, when precipitation happens in the fluid bulk, increasing the temperature increases the rate of crystal formation and hence deposition. Thus bulk temperature has effects on chemical reaction rate and polymerisation rate.

The important heat exchanger parameters are classified as: surface material, surface structure (roughness), heat exchanger type and geometry [27]. Surface material is considered seriously for corrosion fouling because of the potential to react and form corrosion products. Different materials have different catalytic action and may promote or reduce fouling for different processes. The initial fouling rate and scale formation depends significantly on the surface roughness. Junghahn [28] proved theoretically that the free energy change associated with crystal nuclei formation was much less on a rough surface than on a smooth surface. Rough surfaces result in higher deposition due to protected zones in the cavities or pits where flow velocities are very low.

According to Rankin and Adamson [29], it is not the rate of nucleation but the nuclei attachment which is strongly dependent on the surface roughness. Chandler [30] also observed similar results. In general the rough surface causes more fouling which reduces the delay time for all types of fouling. Surface roughness increases turbulence near the surface, which in turn increases the removal rate of fouling on the surface. Better performance occurred due to the increase in surface roughness with deposit formation and has been reported by some authors [1, 2]. Marriott [31] reiterated that mirror finished surfaces in heat exchangers are used to reduce fouling in practice.

5. Heat exchanger type, geometry and process fluid influencing fouling

Shell and tube heat exchangers are used most commonly but they are not particularly suitable for fouling conditions. Fouling can be reduced with special baffle and tube design. Several studies [32-35] have shown that finned tubes foul less than plain tubes. Non-uniform thermal expansion leads to lower deposit strength and hence less deposition. Freeman et al. [36] found that tubes with longitudinal grooves on the outside had less particulate fouling (by alumina particles) than the plain tubes.

Fluidised-bed heat exchangers are used in several applications to reduce or even eliminate fouling completely. Fluidised particles remove deposits from the heat transfer surface. They also enhance the heat transfer efficiency as they interrupt the viscous sub-layer. These heat exchangers have been used successfully to reduce fouling by hard, adhering silica deposits [37]. Graphite heat exchangers are also reported to have less fouling. Direct contact heat transfer may be another alternative to reduce fouling [38]. Properties of the process fluid such as the nature and concentration of the dissolved constituents or suspended particles, presence of any living organisms, solution pH etc. affect fouling significantly.

Excessively high over-concentration of solids in the evaporating liquid may lead to carry-over in the steam and cause fouling in process heat transfer equipment. Corrosion is very important on the steam side of process equipment. Water pH, over-concentration of treatment chemicals in evaporating liquids and dissolved gases (mainly oxygen and carbon dioxide) are very important contributors to corrosion fouling [39]. The presence of living organisms causes biological fouling and makes biofilms. This can sometimes enhance other fouling mechanisms too, as microbial deposits may trap suspended particles. They may also change the chemistry of water and can cause scaling or corrosion [39].

6. Fouling models

A number of models have been proposed for different types of fouling. Analysis and model improvement is still progressing as there are difficulties due to the complex nature of deposit formation and lack of reproducible measurement of fouling resistance. Most of the models have been simplified with many assumptions [40] as stated below:

- Surface roughness is neglected.
- Change in surface roughness with deposit formation is also neglected.
- Only one type of fouling is usually considered.
- Changes in physical properties of the fluids are neglected in most of the cases.
- The fouling layer is assumed to be homogeneous.

- Changes in flow velocity with changing cross-sectional area due to fouling are usually neglected.
- The shape of deposits, e. g. crystals or particles is ignored.

It is also observed that few attempts have been made to model the initiation or roughness delay period. Almost all the models predict fouling (scaling) after the delay period. Some other notable parameters are neglected in modelling such as: (a) effect of simultaneous action of different fouling mechanisms, (b) equipment design, (c) surface parameters e.g. surface material and surface roughness, (d) increase in surface area with deposition, (e) properties of foulant stream, (f) nature of process, and the (g) fluctuations in operation.

Modelling is usually done taking into consideration only (a) flow velocity, (b) concentration, (c) wall and bulk temperature, and (d) time.

Watkinson and Martinez [11] developed a model, based on the fundamental material balance equation (2.1). For the deposition rate the following expression is adopted:

The deposition rate is expressed as shown in equation (6.1).

$$\frac{dx_f}{dt} = \frac{K_R}{\rho_f} (c_F - c_{Sa})^n \quad (6.1)$$

For sparingly soluble salts with inverse solubility (e.g. CaCO_3), the deposition rate is controlled by the slow reaction rate and the constant of reaction rate K_R that obeys the Arrhenius equation:

$$K_R = A_0 e^{\left(\frac{-E}{R_s T_f}\right)} \quad (6.2)$$

with T_f as the interface temperature.

Kern and Seaton [43] recommend for the removal rate the equation:

$$\dot{m}_r = a_8 \tau_f x_f \quad (6.3)$$

Where τ_f is the shear stress exerted by the liquid flow on the fouling film. Even though CaCO_3 deposits are much stronger than the particulate deposits considered by Kern and Seaton [43] the removal rate was assumed to be directly proportional to deposit thickness, which may not be correct for all the cases.

Kern and Seaton [41] proposed a model for particulate fouling which takes into account removal or re-entrainment of deposits. The mathematical model is based on a general material balance equation (2.1). Deposition and removal rates act separately and combine into a net deposition rate. The rate of deposition is expressed as:

$$\dot{m}_d = a_9 c' w \quad (6.4)$$

Where, c' is dirt concentration and w is constant weight flow of fluid. The removal rate is roughly proportional to the total depth of dirt deposited on the heat transfer surface as stated below.

$$\dot{m}_r = a_{10}\tau_f x_f \quad (6.5)$$

Combining the equations for deposition and removal rates (6.4) and (6.5) with the material balance equation (2.1), the fouling resistance expression is obtained:

$$R_f = R_f^*(1 - e^{-\theta t}) \quad (6.6)$$

where θ is a time constant and R_f^* is the asymptotic value of the fouling resistance. For these also the following equations are obtained.

$$R_f^* = \frac{a_9 c' w}{a_{10} \lambda_f \tau_f} \quad (6.7)$$

$$\theta = a_{10} \tau_f \quad (6.8)$$

Here, λ_f is the thermal conductivity of the deposits, a_9 and a_{10} are proportionality constants. This model predicts asymptotic fouling behaviour with R_f^* being the fouling resistance after an infinite time of operation. According to this model, no matter what the conditions, i.e. type of fluid, heat exchanger surface, temperature driving force, an asymptotic fouling value will be obtained sooner or later with removal rates becoming equal to deposition rates.

7. Cost imposed due to fouling

An additional cost is imposed by fouling of heat transfer equipment in industries. Few studies have been undertaken to determine the fouling related costs in industry. Fouling costs can generally be divided into four major categories, such as (1) increased capital expenditure, (2) energy costs, (3) maintenance costs, (4) cost of production loss and (v) extra environmental management cost.

Country	Fouling costs US \$ million	GNP (1984) US \$ million	Fouling costs % of GNP
USA (1982)	3860-7000 8000-10000	3634000	0.12-0.22 0.28-0.35
Japan	3062	1225000	0.25
West Germany	1533	613000	0.25
UK (1978)	700-930	285000	0.20-0.33
Australia	260	173000	0.15
New Zealand	35	23000	0.15
Total Industrial World	26850	13429000	0.20

Table 7.1. Estimated fouling costs incurred in some countries.

The heat transfer area of a heat exchanger is kept exaggerated to compensate retardation imposed by fouling. Oversized pumps and fans are selected to compensate design oversurfacing the enhanced pressure loss from reduction in the flow area.

In some occasions standby heat exchangers are kept in process design in order to ensure uninterrupted operation while a fouled heat exchanger is taken under cleaning maintenance. In-situ cleaning in some cases are recommended while chemical cleaning is preferred for others. All together, cost of cleaning, cleaning equipment, chemicals all are imposing extra to the capital cost of the plant.

Muller-Steinhagen [37] reported that total annual costs for highly industrialised countries such as the United States and the United Kingdom are about 0.25 percent of the countries gross national product (GNP). Even for a relatively less industrialised country like New Zealand, the total fouling costs are around 0.15 percent of its GNP. Muller-Steinhagen [37] has summarised the total fouling costs for various countries based on 1984 in Table 7.1.

8. Fouling mitigation

Gilmour [42] reported that the degradation of heat transfer performance due to fouling in shell and tube heat exchangers occurs mainly due to poor shell-side design. In recent years numerous methods have been developed to control fouling. These methods can be classified as: (1) chemical methods, (2) mechanical methods and (3) changing the phase of the solution. By adding foreign chemicals in a solution, reduction of fouling is achieved by chemical methods of fouling mitigation. Chemical additives developed by many companies have been extensively used to mitigate fouling in the industrial sector. Various additives can be used to prevent scaling [43-44]. Bott [45] specified that the additives used act in different ways, such as (a) sequestering agents, (b) threshold agents, (c) crystal modifiers and (d) dispersants. Some of the common water additives are EDTA (sequestering agent), polyphosphates and polyphosphonates (threshold agents) and polycarboxylic acid and its derivatives (sequestering and threshold treatment). Sequestering agents such as EDTA complex strongly with the scaling cations such as Ca^{++} , Mg^{++} , and Cu^{++} in exchange with Na^+ , thus preventing scaling as well as removing any scale formed previously. They are used effectively as antiscalants in boiler feed water treatment. Troup and Richardson [46] claimed that their use is uneconomical when hardness levels are high.

Polyphosphates and polyphosphonates as threshold agents are also used to reduce scaling in boilers and cooling water systems. Bott [45] said that they prevent the formation of nuclei thus preventing the crystallisation and mitigate fouling. Very small quantities of these agents are effective in reducing scaling from supersaturated salt solutions.

Crystal modifying agents (e.g. Polycarboxylic acid) distort the crystal habit and inhibit the formation of large crystals. The distorted crystals do not settle on the heat transfer surface, they remain suspended in the bulk solution. If their concentration increases beyond a certain limit, particulate fouling may take place. This is prevented either by using techniques to minimise particulate fouling or using dispersing agents along with crystal modifying agents.

Though crystallisation fouling may not be prevented completely using additives, the resulting crystalline deposits are different from those formed in the absence of any

additives. The layer loses its strength and can be removed easily. By controlling pH, crystallisation fouling can furthermore be minimised. The solubility of deposit forming components usually increases with decreasing pH. In many water treatment plants, sulphuric acid is added to maintain a pH between 6.5 and 7.5 [47]. In this case, addition of corrosion inhibitors may also be required which may enhance fouling again.

Seeding is used commercially to reduce crystallisation fouling. This method involves addition of seeds to the scaling fluid. Crystallisation takes place preferentially on these seeds rather than on the heat transfer surface. Calcium sulphate seeds are generally used to avoid calcium sulphate scaling [48-49]. These seeds need not be of the crystallising material, but they should have similar crystallographic properties, i. e. atomic arrangement and lattice spacing [50].

To mitigate particulate fouling by chemical means, dispersants are used to reduce the surface tension of deposits. It helps in disintegrating the suspended particles into smaller fragments that do not settle so readily.

Addition of certain chemicals can slow down or terminate chemical reactions. Dispersants are very helpful in keeping the foulants away from the surface. Some particles such as corrosion products may act as catalysts. Chemical reaction fouling could be suppressed by reducing the number of these particles. Corrosion inhibitors (chromates and polyphosphates) can be used to reduce corrosion fouling [47]. Usually a passivating oxide layer is desired to prevent corrosion of the surface. Corrosion fouling may promote other fouling mechanisms e. g. higher roughness of the corroded surface may enhance crystallisation fouling. The corrosion products may act as catalysts and promote chemical reaction fouling and also augments particulate fouling by depositing on the heat transfer surface.

Mitigation of fouling by chemical methods has several drawbacks. Fouling and corrosion inhibitors usually contain considerable amount of chlorine, bromine, chromium, zinc etc. Therefore, their concentration has to be monitored carefully. Treatment of fluid released from the plant to natural waterways is necessary to prevent harmful effects. Higher concentrations can be used in closed systems but overdosing may have negative effects and some components may precipitate. Using different additives at the same time may result in dangerous chemical reactions. Some additives have limited life and some degrade with time and lose activity.

Pritchard [51] has broadly classified mechanical methods into two categories according to their ways of action. (1) Brute force methods such as high-pressure jets, lances, drills etc. (2) Mild methods such as brushes and sponge balls. Muller-Steinhagen [37] has reported that several mechanical methods have been developed in recent years. The following mechanisms predict the modern methods:

- Breakage of deposits during brief overheating due to differential thermal expansions of heat transfer surface and deposits,
- Mechanical vibration of the heat transfer surfaces,
- Acoustical vibration of the surface,
- Increased shear stress at the fluid/deposit interface, and
- Reduced stickiness of the heat transfer surface.

Most liquid-side fouling mitigation techniques have been developed for the tube-side of shell and tube heat exchangers. The relevant techniques include:

1. increase in flow velocity,
2. reversal of flow direction,
3. heat transfer surface such as, surface roughness and surface materials,
4. fluidised bed heat exchangers,
5. pulsating flow,
6. turbulence promoters, and
7. transport of cleaning devices through tubes.

The deposits which are not strongly adhere to the surface can be removed by increasing the flow velocity. Muller-Steinhagen and Midis [4] reported that alumina deposits were removed completely when the flow velocity was increased for a short period of time after a fouling run. At higher flow velocity, the wall shear stress increases and causes more removal of deposits from the surface.

At a regular interval of time, the reversal of flow direction on the heat transfer surface could be another effective method of reducing fouling. This technique needs several modifications in the existing set-up. Muller-Steinhagen [37] stated that mitigation of fouling by increasing the flow velocity could be more effective than reversal of flow direction.

Surface material and surface roughness play an important role on fouling mitigation. Thus lowering the surface roughness retards the adhesion of deposits and the number of nuclei growth sites. Lower deposition rate also experienced with lowering surface energy of the material of heat exchanger. Using inert particles is an effective way of reducing or even eliminating fouling completely as practiced in fluidized bed heat exchangers. Pulsating flow in heat exchangers is a strategy to increase the level of turbulence [52-58]. Where, as a matter of fact heat transfer coefficient increases with the enhancement of deposit removal. Higher heat transfer reduces fouling by reducing the interface temperature which is beneficial for certain fouling mechanism such as crystallization fouling of inverse solubility salts. The higher level of turbulence augments the deposit removal rate.

Fracture of deposits by fatigue is enhanced by higher turbulence due to pulsation resulting to increase of removal rate. Generally the deposition rate of fouling phenomena [3] depends on the thickness of viscous and thermal sub-layers. Muller-Steinhagen [37] reported that by inserting turbulence promoters inside tubes or by using tube corrugations, the heat transfer coefficient can be increased by a factor of 2 to 15 by reducing the thickness of average thermal boundary layer. Turbulence promoters may reduce both the crystallisation and reaction fouling. Muller-Steinhagen [37] informed that particulate fouling will be enhanced if particulate or fibrous material already exists in the solution.

Middis [10] also reported fouling mitigation by adding natural fibre in the supersaturated solutions of concentration 3.6 g/L CaSO_4 . He observed that the rate of CaSO_4 fouling on heated metal tube surface decreases with the increase of fibre concentration in the fouling solution. Kazi [59] also got similar results by adding different types and concentrations of natural fibre in supersaturated solutions of CaSO_4 .

Some novel methods which do not fall under well reported categories, such as magnetic or electric treatment are also available in the market to reduce fouling. Usually magnetic treatment is carried out by inserting permanent magnets in a pipe before the heat exchanger.

Parkinson and Price [60] have reported significant reduction in fouling by the magnetic treatment as it helps in precipitating the salts. These salts stay suspended in the bulk liquid and are removed later. On the other hand Hasson and Bramson [61] informed that there is no effect of magnetic treatment at all on fouling. They observed that magnetic treatment neither decreased nor increased the rate of scaling. The nature of the deposits also remained unchanged. Bernadin and Chan [62] have also reported no influence of magnetic treatment on silica fouling. Muller-Steinhagen [37] has stated that magnetic mitigation devices in some cases actually increased fouling. Thus from the available information no conclusion can be made about the influence of the magnetic field on the scaling process.

9. Cleaning of heat exchangers

A decrease in the performance of a heat exchanger beyond acceptable level requires cleaning. In some applications, the cleaning can be done on line to maintain acceptable performance without interruption of operation. At other times, off-line cleaning must be used.

Garrett-Price et al. [27] presented some cleaning approaches for fouled heat exchangers. They specified on-line cleaning generally utilises a mechanical method designed for only tube side and requires no disassembly. In some applications flow reversal is required. Chemical feed can also be used as an on-line cleaning technique but may upset the rest of the liquid service loop.

On-line mechanical cleaning techniques are also in practice. On line tube side cleaning techniques are the sponge-ball and brush systems. The advantage of on-line cleaning is the continuity of service of the exchanger and the hope that no cleaning-mandated downtime will occur. The principal disadvantage is the added cost of a new heat exchanger installation or the large cost of retrofits. Furthermore there is no assurance that all tubes are being cleaned sufficiently.

Off-line chemical cleaning is a technique that is used very frequently to clean exchangers. Some refineries and chemical plants have their own cleaning facilities for dipping bundles or re-circulating cleaning solutions. In general, this type of cleaning is designed to dissolve the deposit by means of a chemical reaction with the cleaning fluid. The advantages of chemical cleaning approach include the cleaning of difficult-to-reach areas. Often in mechanical cleaning, there is incomplete cleaning due to regions that are difficult to reach with the cleaning tools. There is no mechanical damage to the bundle from chemical cleaning, although there is a possibility of corrosion damage due to a reaction of the tube material with the cleaning fluid. This potential problem may be overcome through proper flushing of the unit. Disadvantages of off-line chemical cleaning include corrosion damage potential, handling of hazardous chemicals, use of a complex procedure.

Off-line mechanical cleaning is a frequently used procedure. The approach is to abrade or scrap away the deposit by some mechanical means. The method includes high-pressure water, steam, lances and water guns. In off-line mechanical cleaning there are some advantages such as excellent cleaning of each tube is possible, good removal potential of very tenacious deposits. Disadvantages include the inability to clean U-tube bundles successfully, usual disassembly problem and the great labour needed.

Frenier and Steven [63] describe general methods for cleaning heat exchanger equipment, including both mechanical and chemical procedures. They have given guidelines for selecting between chemical and mechanical cleaning, and among the various types of chemical cleaning processes. They stated that water-based fluids can transport and deposit a wide variety of minerals, and corrosion products form due to the reaction of the aqueous fluids with the metals of construction. Hydrocarbon and petrochemical fluids transport and deposit a variety of organic scales. Common inorganic scale forming compound includes various iron oxides, hardness deposits (carbonates and silicates). They stated that the entire cleaning situation must be considered when choosing between mechanical and chemical cleaning, as well as the specific technique within the general category. The general categories of mechanical cleaning are abrasive, abrasive hydraulic, hydraulic and thermal [64].

Frenier and Barber [63] stated that, for chemical cleaning of the heat exchanger tubes, it is very beneficial to obtain a sample of the deposit so that its composition can be determined. Based on the chemical analysis of the deposit, an optimal treatment plan can be developed and the best solvent selected. They have classified the deposits generically, as organic (process-side) or inorganic (water-side).

They stated that the process side deposits may range from light hydrocarbon to polymers and generally they are similar to the fluids from which they originate. They mentioned that the general categories of solvents for process side scales include aqueous detergent solutions, true organic solvents and emulsions. Aqueous detergent formulations always contain a surfactant-type component. In addition they can contain alkaline agents, such as sodium hydroxide, sodium silicate, or sodium phosphate. Builder molecules such as ethylenediaminetetraacetic acid (EDTA) suppress the effects of hard water, and coupling agents such as glycol ethers, improve the dissolution of some organic deposits.

Detergent formulations are effective only for removing the lighter deposits. Refinery fluids, aromatics and terpenes are used to dissolve the organic deposits. N-methyl-2-pyrrolidinone also is a very effective polar solvent with low toxicity characteristics. They reiterated that the effectiveness of the application depends greatly on proper application conditions, such as flow rate and temperature. Combination of surfactants, organic solvents and water emulsions are good cleaning agents. Emulsions with an organic outer phase are particularly useful for cleaning large vessels. Oily rust deposits having both organic and inorganic compositions can be removed by acidic emulsions combining an acid and an organic solvent.

Water-side deposits usually contain minerals, such as iron oxides (corrosion products), hardness (Ca and Mg carbonates) and silica, in individual cases other minerals can also be found. The solvents for removing inorganic deposits usually contain mineral acids, organic acids or chelating agents.

Mineral acids used in chemical cleaning include hydrochloric acid (HCl), hydrofluoric acid (HF), sulphuric acid (H₂SO₄), phosphoric acid (H₃PO₄), nitric acid (HNO₃) and sulfamic acid (H₂NSO₃H). Hydrochloric acid is the most common and most versatile mineral acid. It is used on virtually all types of industrial process equipment at strengths from 5 percent to 28 percent (5-10 percent is the most usual range). It can be inhibited at temperatures up to about 180 °F. HCl will dissolve carbonates, phosphates, most sulphates, ferrous sulphide,

iron oxides and copper oxides. By using with appropriate additives, fluoride deposits, copper and silica can also be removed from surfaces with inhibited HCl. HCl is corrosive, so it has restricted use. HCl is not used to clean series 300 SS, free-machining alloys, magnesium, zinc, aluminium, cadmium, or galvanised steel because of the potential for generalised or localised attack. It is not desirable to contact the fouled metal with a strong mineral acid, because of the danger of damage to the equipment during or after cleaning. An alternative solvent family consists of aqueous solutions of chelating agents and organic acids with pH values of about 2 to 12.

Citric acid was one of the first organic acids used in industrial cleaning operations [65]. For removing iron oxide from steel surfaces, citric acid and a mixture of formic and citric acid could be used [66]. The mixture could hold more iron in solution than either of the acids alone could do. Ammonium citrate and sodium citrate solvents are currently used to clean a wide variety of heat transfer equipment, including boilers and various types of service water systems. The advantage of citric acid formulation is their low toxicity and ready biodegradability. EDTA is a versatile chemical that forms metal ion complexes with higher equilibrium constants than citric acid. As a result chemical cleaning solvents with pH values from 4.5 to about 9.2 have been formulated that can remove Fe and Cu, as well as Ca, Ni and Cr. The major advantage of the EDTA solvents is that they are much more aggressive than citric salts for removing very heavy iron oxide deposits especially if they contain copper. The disadvantage includes high cost per pound of metal removed and low biodegradability.

All of the chelating agents are also organic acids. Eberhard and Rosene [67] taught the use of solvents consisting of formic acid or citric acid for cleaning nondrainable tubes in super heaters. Reich [66] used a mixture of formic acid and citric acid to a proportion of 3:1, to remove iron oxide deposits. The advantage of these mixtures is that they avoid the precipitation of solids that formed in pure formic or citric acid solutions. Formulations of formic acid with hydroxyacetic acid and citric acid with hydroxyacetic acid can be used as a cleaning agent. Bipan [3] used acetic acid of concentration 3 percent to remove $\text{CaSO}_4 \cdot 2\text{H}_2\text{O}$ deposit on plate type SS heat exchangers. He said that with the increase in acid solution temperature the removal efficiency increases. Similar results were obtained by Kazi [68]. It reveals that a complete and systematic study of fouling on different metal surfaces and their mitigation by additives have been required to be done along with study of introducing a benign to environment technique for chemical cleaning of fouling deposits.

10. Nomenclature

A	Heat transfer area	m^2
A_0	Arrhenius constant	$\text{m}^3/\text{kg}\cdot\text{s}$
a_1 - a_{13}	Proportionality constant	-
c	Concentration	g/L or kg/m^3
c_p	Specific heat capacity	$\text{J}/\text{mol}\cdot\text{K}$
d	Pipe diameter	m
E	Activation energy	J/mol
ΔH	Head loss	$\text{m H}_2\text{O}$
h_c	Heat transfer coefficient	$\text{W}/\text{m}^2\cdot\text{K}$
K_R	Reaction rate constant (dimension depend on the order of n)	$\text{m}^4/\text{kg}\cdot\text{s}$
L	Length	m

\dot{m}	Mass flux	kg/m ² s
\dot{m}_d	Increase of solids mass present in the fouling film	kg/m ² s
\dot{m}_r	Decrease of solids in the fouling film	kg/m ² s
m_f	Solids deposited in the fouling film per unit area	kg/m ²
P	Pressure	kPa
P	Perimeter	m
P_c	Intercrystalline cohesive force	N
ΔP	Pressure drop	kPa/m
\dot{Q}	Heat flow	W
q	Heat flux	W/m ²
R	Ratio of the radius of inner and outer tubes of annulus	-
R_b	Bonding resistance	-
R_g	Universal gas constant	J/mol.K
R_f	Fouling resistance	m ² K/kW
R_f^*	Asymptotic value of the fouling resistance	m ² K/kW
r	Radius	m
r_H	Hydraulic radius	m
T	Temperature	°C
T_f	Temperature at the surface of the fouling film	°C
ΔT	Temperature difference	K or °C
t	Time	s
t_{ind}	Induction time	s
U	Overall heat transfer coefficient	W/m ² K
u	Velocity	m/s
\bar{u}	Local mean velocity	m/s
u^*	Friction velocity, $\sqrt{(\tau_w/\rho)}$	m/s
u^+	Dimensionless velocity, \bar{u}/u^*	-
u_t	Turbulent friction or shear velocity, $\bar{u}\sqrt{f/2}$	m/s
w	Constant weight flow of fluid	kg/s
x	Distance in x direction	m
x_f	Fouling film thickness	m
y	Distance in y direction	m
Greek		
α	Constant	-
β	Individual mass transfer coefficient	m/s
θ	Time constant	s
ε	Height of roughness	m

ε/d	Roughness ratio	-
f	Fanning friction factor	-
λ	Thermal conductivity	W/mK
λ_f	Thermal conductivity of the deposits	W/mK
μ	Dynamic viscosity	kg/ms
ρ	Density	kg/m ³
ρ_f	Density of the deposits	kg/m ³
τ	Shear stress	N/m ²
τ_w	Wall shear stress	N/m ²
τ_f	Shear stress exerted by the liquid flow on the fouling film	N/m ²
ν	Kinematic viscosity	m ² /s
ϕ	Friction factor	-
δ	Hydrodynamic boundary layer thickness	m
δ_c	Linear thermal expansion coefficient of the fouling film porosity	1/K
δ_t	Thermal boundary layer thickness	m
ξ	Ratio of thermal to hydrodynamic boundary layers	m

Dimensionless Numbers

Nusselt Number	$Nu = \frac{h_c \cdot d}{\lambda}$
Prandtl Number	$Pr = \frac{c_p \cdot \mu}{\lambda}$
Reynolds Number	$Re = \frac{\rho \cdot u \cdot d}{\mu}$

11. References

- [1] Bott, T. R. and Gudmundsson, J. S., Rippled Silica deposits in Heat Exchanger Tubes. 6th International Heat Transfer Conference. 1978.
- [2] Crittenden, B. D. and Khater, E. M. H., Fouling From Vaporising Kerosine. Journal of Heat Transfer, 1987. 109: p. 583-589.
- [3] Bansal, B., Crystallisation Fouling in Plate Heat Exchangers, PhD thesis, Department of Chemical and Materials Engineering, 1994, The University of Auckland: Auckland, New Zealand.
- [4] Muller-Steinhagen, H. M. and Middis, J., Particulate Fouling in Plate Heat Exchangers. Heat Transfer Engineering, 1989. 10(4): p. 30-36.

- [5] Bohnet, M., Fouling of Heat Transfer Surfaces. *Chemical Engineering Technology*, 1987. 10: p. 113-125.
- [6] Ritter, R. B., Crystallisation Fouling Studies. *Journal of Heat Transfer*, 1983. 105: p. 374-378.
- [7] Reitzer, B. J., Rate of Scale Formation in Tubular Heat Exchangers. *I & EC Process Design and Development*, 1964. 3(4): p. 345-348.
- [8] Hasson, D., Rate of Decrease of Heat Transfer Due to Scale Deposition. *DECHEMA Monograph*, 1962. 47: p. 233-282.
- [9] Bott, T. R. and Walker, R. A., Fouling in Heat Transfer Equipment. *The Chemical Engineer*, 1971: p. 391-395.
- [10] Middis, J., Heat Transfer and Pressure Drop For Flowing Wood Pulp Fibre Suspensions, PhD thesis, Chemical and Materials Engineering. 1994, The University of Auckland: Auckland, New Zealand.
- [11] Watkinson, A. P. and Martinez, O., Scaling of Heat Exchanger Tubes by Calcium Carbonate. *Journal of Heat Transfer*, 1975: p. 504-508.
- [12] Augustin, W., Verkrustung (Fouling) Von Wärmeübertragungsflächen, in *Institut für Verfahrens- und Kerntechnik*. 1992, Technische Universität Braunschweig: Germany.
- [13] Cooper, A., Suito, J. W. and Usher, J. D., Cooling Water Fouling in Plate Heat Exchangers. *Heat Transfer Engineering*, 1980. 1(3): p. 50-55.
- [14] Muller-Steinhagen, H. M., Reif, F., Epstein, N. and Watkinson, A. P., Influence of Operating Conditions on Particulate Fouling. *The Canadian Journal of Chemical Engineering*, 1988. 66: p. 42-50.
- [15] Bott, T.R., Fouling of Heat Exchangers. 1995: Elsevier Science & Technology Books. 529.
- [16] Bell, K.J. and A.C. Mueller, *Wolverine Heat Transfer Data book II*. 2001, Wolverine Tube, Inc.
- [17] Epstein, N., Heat Exchanger Theory and Practice, in: J. Taborek, G. Hewitt (eds.) *heat exchangers in Heat Exchanger Theory and Practice*, McGraw-Hill, 1983.
- [18] Epstein, N., Thinking about Heat transfer fouling: a 5 × 5 matrix. *heat Transfer Engineering*, 1983. 4: p. 43-46.
- [19] Epstein, N. (1981) Fouling in heat exchangers. In *Low Reynolds Number Flow Heat Exchangers*, S. Kakac, R. K. Shah, and A. E. Bergles (eds.). Hemisphere, New York.
- [20] Somerscales, E. F. C., and Knudsen, J. G. (eds.) (1981) *Fouling of Heat Transfer Equipment*. Hemisphere, New York.
- [21] Melo, L. F., Bott, T. R., and Bernardo, C. A. (eds.) (1988) *Fouling Science and Technology*. Kluwer, Dordrecht.
- [22] *Standards of the Tubular Exchanger Manufacturers Association* 7th ed. Tubular Exchanger Manufacturers Association, New York, 1988.
- [23] Chenoweth, J. M. (1988), General design of heat exchangers for fouling conditions. In *Fouling Science and Technology*, L. F. Melo, T. R. Bott, and C. A. Bernardo (eds.), pp. 477-494. Kluwer, Dordrecht.
- [24] Brusilovsky, M., Borden, J. and Hasson, D., Flux Decline due to Gypsum Precipitation on RO Membranes. *Desalination*, 1992. 86: p. 187-222.
- [25] Walker, G., *Degradation of Performance, Industrial Heat Exchangers- A Basic Guide*. 1982: Hemisphere Publishing Corporation. 213-272.

- [26] Gudmundson, J. S., Particulate Fouling, in Fouling of Heat Transfer Equipment, E.F.C. Somerscales and J.G. Knudsen, Editors. 1981, Hemisphere Publishing Corporation. p. 357-387.
- [27] Garrett- Price, B. A., Smith, S. A., Watts, R. L., Knudsen, J. G., Marner, W. J. and Suito, J. W., Overview of Fouling, Fouling of Heat Exchangers- Characteristics, Costs, Prevention, Control, and Removal. 1985, Noyes Publications: New Jersey. p. 9-20.
- [28] Junghahn, L., Methoden Zum Herabsetzen oder Verhindern der Krustenbildung. Chemie Ingenieur Technik, 1964. 36: p. 60-67.
- [29] Rankin, B. H. and Adamson, W. L., Scale Formation as Related to Evaporator Surface Conditions. Desalination, 1973. 13: p. 63-87.
- [30] Chandler, J. L., The Effect of Supersaturation and Flow Conditions on the Initiation of Scale Formation. Transactions of Institution of Chemical Engineers, 1964. 42: p. T24-T34.
- [31] Marriott, J., Where and How to Use Plate Heat Exchangers. Chemical Engineering, 1971. 78(8): p. 127-134.
- [32] Knudsen, J. G. and McCluer, H. K., Hard Water Scaling of Finned Tubes at Moderate Temperatures. Chem. Eng. Progress Symp. series, 1959. 55(9): p. 1-4.
- [33] Katz, D. L., Knudsen, J. G., Balekjian, G. and Grover, S. S., Fouling of Heat Exchangers. Petroleum Refiner, 1954. 33(4): p. 121-125.
- [34] Webber, W. O., Under Fouling Conditions Finned Tubes can Save Money. Chemical Engineering, 1960. 67(6): p. 149-152.
- [35] Sheikholeslami, R. and Watkinson, A. P., Scaling of Plain and Externally Finned Tubes. Journal of Heat Transfer, 1986. 108: p. 147-152.
- [36] Freeman, W. B., Middis, J. and Muller-Steinhagen, H. M., Influence of Augmented Surfaces and of Surface Finish on Particulate Fouling in Double Pipe Heat exchangers. Chemical Engineering Processing, 1990. 27: p. 1-11.
- [37] Muller-Steinhagen, H. M., Fouling: The Ultimate Challenge for Heat Exchanger Design. The sixth International Symposium on Transport Phenomena in Thermal Engineering. 1993. Seoul, Korea.
- [38] Muller-Steinhagen, H. M., Introduction to Heat Exchanger Fouling. Proceedings of Fouling in Heat Exchangers. 1988. The University of Auckland, Centre for Continuing Education, Auckland, New Zealand.
- [39] Garrett- Price, B. A., Smith, S. A., Watts, R. L., Knudsen, J. G., Marner, W. J. and Suito, J. W., Generic Industrial Fouling, in Fouling of Heat Exchangers- Characteristics, Costs, Prevention, Control, and Removal. 1985, Noyes Publications. p. 21-37.
- [40] Pinheiro, J. D. D. R. S., Fouling of Heat Transfer surfaces, Heat Exchanger Source Book, J.W. Palen, Editor. 1986, Hemisphere Publishing Corporation. p. 721-744.
- [41] Kern, D. Q. and Seaton, R. E., A Theoretical Analysis of Thermal surface Fouling. Brit. Chem. Eng., 1959. 4(5): p. 258-262.
- [42] Gilmour, C. H., No Fooling- No Fouling. Chem. Eng. Progr., 1965. 61(7): p. 49-54.
- [43] Harris, A. and Marshall, A., The Evaluation of Scale Control Additives, Conference on Progress in the Prevention of Fouling in Industrial Plant. 1981. University of Nottingham.
- [44] Krisher, A. S., Raw Water Treatment in the CPI. Chemical Engineering, 1978: p. 79-98.
- [45] Bott, T. R., The Fouling of Heat Exchangers. DSIR, Wellington, New Zealand., 1981.

- [46] Troup, D. H. and Richardson, J. A., Scale Nucleation on a Heat Transfer Surface and its prevention. *Chemical Engineering Communications*, 1978. 2: p. 167-180.
- [47] Muller-Steinhagen, H. M., Fouling of Heat Transfer Surfaces. VDI Heat Atlas, English Edition, VDI- Verlag GmbH, 1993: p. OC1-OC22.
- [48] Gaaney, R. J., Thorp, C. A. and Cadwallader, Calcium Sulphate Seeding Prevents Calcium sulphate Scaling. *Industrial and Engineering Chemistry*, 1963. 55(3): p. 39-43.
- [49] Rautenbach, R. and Habbe, R., Seeding Technique for Zero-Discharge Processes, Adaption to Electrodialysis. *Desalination*, 1991. 84: p. 153-161.
- [50] Telkes, M., Nucleation of Supersaturated Inorganic Salt Solutions. *Industrial and Engineering Chemistry*, 1952. 44(6): p. 1308-1310.
- [51] Pritchard, A. M., Cleaning of Fouled Surfaces: A Discussion, in *Fouling Science and Technology*, NATO ASI Series, Series E: Applied Science, Melo, L. F., Bott, T. R. and Bernardo, C. A., Editors. 1988. p. 721-726.
- [52] Keil, R. H., Enhancement of Heat Transfer by Flow Pulsation. *Industrial Engineering Chemistry: Process Design and Development*, 1971. 10(4): p. 473-478.
- [53] Ludlow, J. C., Kirwan, D. J. and Gainer, J. L., Heat Transfer with Pulsating Flow. *Chemical Engineering Communications*, 1980. 7: p. 211-218.
- [54] Karamercan, O. E. and Gainer, J. L., The Effect of Pulsations on Heat Transfer. *Industrial Engineering Chemistry Fundamentals*, 1979. 18(1): p. 11-15.
- [55] Herndon, R. C., Hubble, P. E. and Gainer, J. L., Two Pulsators for Increasing Heat Transfer. *Industrial Engineering Chemistry: Process Design and Development*, 1980. 19: p. 405-410.
- [56] Edwards, M. F. and Wilkinson, W. L., Review of Potential Applications on Pulsating Flow in Pipes. *Transactions of Institution of Chemical Engineers*, 1971. 49: p. 85-94.
- [57] Gupta, S. K., Patel, R. D. and Ackerberg, R. C., Wall Heat /Mass Transfer in Pulsatile Flow. *Chemical Engineering Science*, 1982. 37(12): p. 1727-1739.
- [58] Thomas, L. C., Adaptation of the surface Renewal Approach to Momentum and Heat Transfer for Turbulent Pulsatile Flow. *Journal of Heat Transfer*, 1974: p. 348-353.
- [59] Kazi, S. N., Heat Transfer to Fibre Suspensions-Studies in Fibre Characterisation and Fouling Mitigation, PhD thesis, Chemical and Materials Engineering. 2001, The University of Auckland: Auckland, New Zealand.
- [60] Parkinson, G. and Price, W., Getting the Most out of Cooling Water. *Chemical Engineering*, 1984: p. 22-25.
- [61] Hasson, D. and Bramson, D., Effectiveness of Magnetic Water Treatment in Suppressing Calcium Carbonate Scale Deposition. *Industrial Engineering Chemistry: Process Design and Development*, 1985. 24: p. 588-592.
- [62] Bernardin, J. D. and Chan, S. H., Magnetics Effects on Simulated Brine Properties Pertaining to Magnetic Water Treatment. *Fouling and Enhancement Interactions*, 28th National Heat Transfer Conference. 1991. Minneapolis, Minnesota, USA.
- [63] Frenier, W. W. and Barber, J. S., Choose the Best Heat Exchanger Cleaning Method. *Chemical Engineering Progress*, 1998: p. 37-44.
- [64] Gutzeit, J., *Cleaning of Process Equipment and Piping*. 1997, MTI Publication, Materials Technology Institute, St. Louis.
- [65] Loucks, C. M., *Organic Acids for Cleaning Power- Plant Equipment*. Annual Meeting of ASME. 1958. New York.

- [66] Reich, C. F., Scale Removal. 1961: U. S. A.
- [67] Eberhard, J. F. and Rosene, R. B., Removal of Scale Deposits. 1961: U. S. A.
- [68] Kazi, S. N., Duffy, G. G. And Chen, X. D., Mineral scale formation and mitigation on metals and a polymeric heat exchanger surface. Applied Thermal Engineering, 30 (2010): p. 2236-2242.

Fouling in Plate Heat Exchangers: Some Practical Experience

Ali Bani Kananeh and Julian Peschel
*GEA PHE Systems
Germany*

1. Introduction

Due to their compact size, Plate Heat Exchangers (PHEs) are widely used in industrial processes. They have higher heat-transfer performance, lower temperature gradient, higher turbulence, and easier maintenance in comparison with shell and tube heat exchangers. For minimizing material consumption and space requirements compact models have been developed over the last years. By using thin plates forming a small gap, these compact models impress with larger heat transfer coefficients and, thus, smaller required heat transfer area.

The advantages of compact heat exchangers over shell and tube ones at a glance:

- larger heat transfer coefficients
- smaller heat transfer surfaces required
- lower fouling due to high fluid turbulences (self-cleaning effect)
- significantly smaller required installation and maintenance space
- lighter weight
- simplified cleanability especially for GPHE
- lower investment costs
- closer temperature approach
- pure counter-flow operation for GPHE

In Figure 1, plate heat exchangers are compared with shell and tube heat exchangers regarding effectiveness, space, weight and cleaning time.

Deposits create an insulating layer over the surface of the heat exchanger that decreases the heat transfer between fluids and increases the pressure drop. The pressure drop increases as a result of the narrowing of the flow area, which increases the gap velocity (Wang et al., 2009). Therefore, the thermal performance of the heat exchanger decreases with time, resulting in an undersized heat exchanger and causing the process efficiency to be reduced. Heat exchangers are often oversized by 70 to 80%, of which 30 to 50% is assigned to fouling. While the addition of excess surface to the heat exchanger may extend the operation time of the unit, it can cause fouling as a result of the over-performance caused by excess heat transfer area; because the process stream temperature change greater than desired, requiring that the flow rate of the utility stream be reduced (Müller-Steinhagen, 1999). The deposits

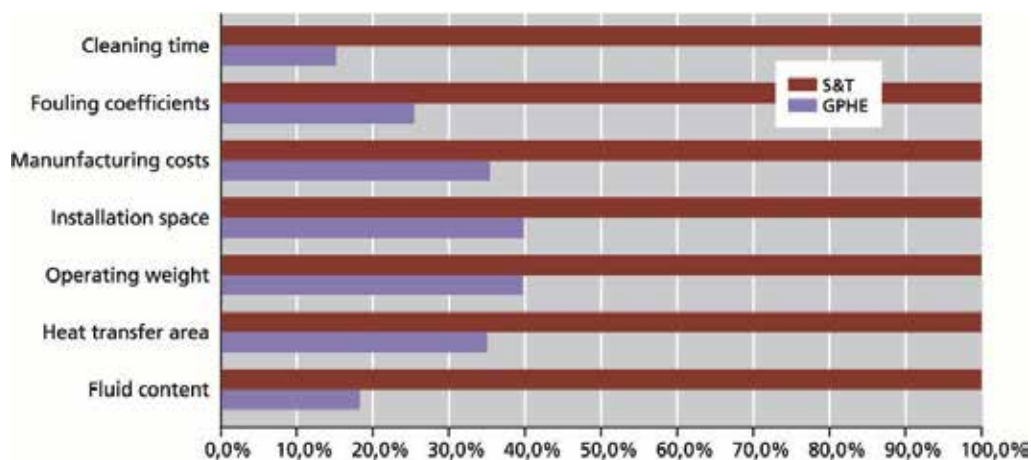


Fig. 1. Comparison of plate heat exchanger with shell and tube heat exchanger.

must be removed by regular and intensive cleaning procedures in order to maintain production efficiency.

As a result of the effects of fouling on the thermal and hydraulic performance of the heat exchanger, an additional cost is added to the industrial processes. Energy losses, lost productivity, manpower and cleaning expenses cause immense costs. The annual cost of dealing with fouling in the USA has been estimated at over \$4 billion (Wang et al., 2009).

The manner in which fouling and fouling factors apply to plate exchangers is different from tubular heat exchangers. There is a high degree of turbulence in plate heat exchanger, which increases the rate of deposit removal and, in effect, makes the plate heat exchanger less prone to fouling. In addition, there is a more uniform velocity profile in a plate heat exchanger than in most shell and tube heat exchanger designs, eliminating zones of low velocity which are particularly prone to fouling. Figure 2 shows the fouling resistances for cooling water inside a plate heat exchanger in comparison with fouling resistances on the tube-side inside a shell and tube heat exchanger for the same velocity. A dramatic difference in the fouling resistances can be seen. The fouling resistances inside the PHE are much lower than that inside the shell and tube heat exchanger.

Fouling inside heat exchanger can be reduced by:

- Appropriate heat-exchanger design
- Proper selection of heat-exchanger type
- Mitigation methods (mechanical and/or chemical)
- Heat exchanger surface modification/coating

The mechanics of deposits build-up and the impact of operating conditions on the deposition rate should be understood in order to select the appropriate method to reduce fouling (Müller-Steinhagen, 1999).

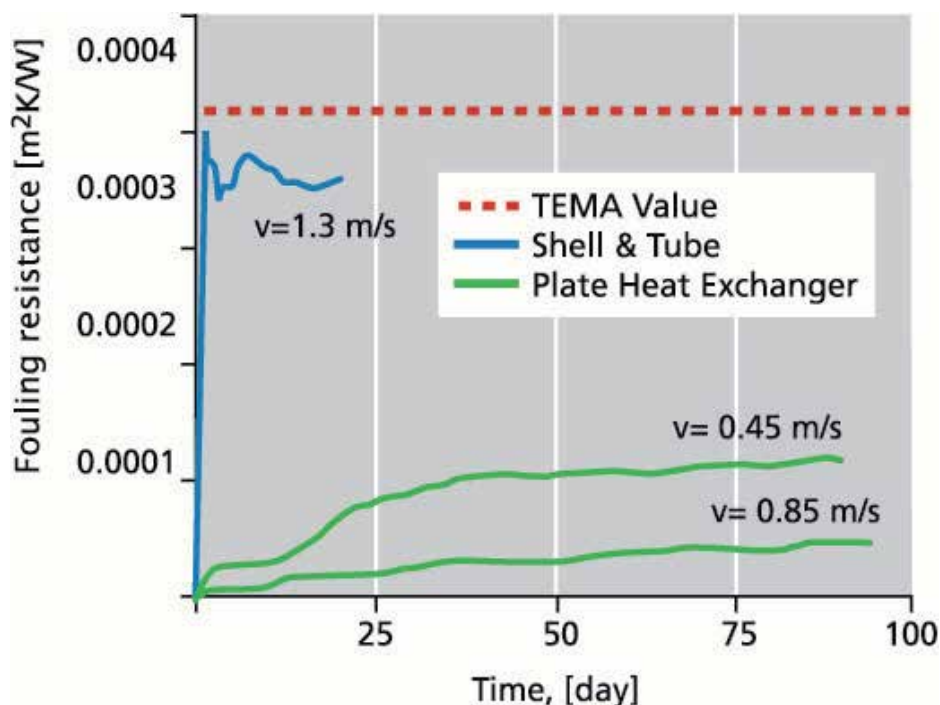


Fig. 2. Comparison of fouling resistance in PHE to tube-side fouling resistance (Müller-Steinhagen, 2006).

This chapter focuses on solving fouling problems in some industrial applications. The first section presents fouling problems with cooling water inside CO₂ coolers in different Egyptian fertilizer plants. The effect of heat exchanger geometry and flow patterns on the fouling behavior will be shown. Thermodynamic and hydraulic solutions are proposed like, redesigning of the plate heat exchangers and new plate geometries. The second section explains how fouling can be reduced inside gasketed plate heat exchangers used in food production using Nano-composite coatings. An antifouling coating with low surface energy (low wettability) can be used to avoid or minimize adhesion, improve process management, simplify cleaning processes with less resources and chemical use, and increase product reliability. The operational efficiency of the plant can be significantly improved and the intensity and frequency of cleaning can be substantially reduced.

2. Solving fouling problems by heat exchanger design modification

Fouling problems with cooling water inside CO₂ coolers in different Egyptian fertilizer plants were investigated. Thermodynamic and hydraulic solutions were proposed, which included redesign of the existing PHEs and new plate geometries. The main problems arose from the large surface margins required to meet pressure drop limits on the CO₂ side. Reducing the surface area of the heat exchanger increased the fluid velocity (shear stress from 5.31 to 10.84 Pa) inside the gaps and hence decreased fouling. Using computer-

modeled plate geometries from the new technology (NT) series with larger gap velocities due to better fluid distribution over the plates could decrease fouling and increase the availability of fertilizer plants.

2.1 Introduction

To guarantee production reliability in the complex urea fertilizer manufacturing process, PHEs are installed in several process chains including CO₂ cooling, residual gas scrubbing, and other process sections as were as in the primary urea production plant. Industrial processes commonly use water for cooling purposes. Open circuit cooling system is used in some processes, while closed loop system involving cooling towers is used in others. Closed loop systems usually cause less fouling than open ones, but they are more expensive (Kukulka and Leising, 2009). Cooling water normally contains dissolved or suspended solids like calcium carbonate and calcium sulphate. If the concentration of these dissolved solids exceeds certain limits, it leads to the accumulation of deposits on the heat exchanger surface (Müller-Steinhagen, 1999). These deposits create an insulating layer on the surface of the heat exchanger that decreases the heat transfer between the two fluids. The thermal performance of the unit decreases with time as the thickness of the deposit increases, resulting in an undersized heat exchanger and causing the process efficiency to be reduced (Kukulka and Leising, 2009). Deposit formation can be reduced either by changing the configuration of the heat exchanger or by regular cleaning procedures.

Deposit formation is influenced by the heat exchanger surface and geometry, cooling medium and the operating conditions. Its composition depends on the flow rate, temperature and chemical composition of the cooling medium (Kukulka and Leising, 2009). Pana-Suppamassadu et al. (2009) studied the effect of plate geometry (contact angle) and the gap velocity on calcium carbonate fouling in plate heat exchanger. They found that an increase in the gap velocity could reduce the fouling rate on the surface of plate heat exchanger.

In the present section, deposit formation on the surface of plate heat exchangers in different Egyptian fertilizer plants will be investigated. The effect of heat exchanger geometry and flow patterns on the fouling behavior will be shown.

2.2 Process description

Ammonia is the basic raw material in urea production. Ammonia plants in question operate using Uhde's proprietary ammonia process that is based on the well-established Haber-Bosch process. In the first stage, the raw material natural gas is desulphurized, then cracked into its individual chemical components catalytically by adding steam to generate the hydrogen required for ammonia synthesis. This process also generates carbon monoxide, carbon dioxide, hydrogen and residues of methane from the natural gas cracking process. In the next stage nitrogen is added to the process by combusting methane, CO and H₂ using air. With the addition of steam, carbon monoxide is converted to CO₂ using catalytic converters and then scrubbed out of the synthesis gas formed. The selectively scrubbed CO₂ is fed into the urea processing plant as the process medium together with the produced ammonia as starting material. The urea plants operate using the Stamicarbon process that was developed in the Netherlands [Uhde].

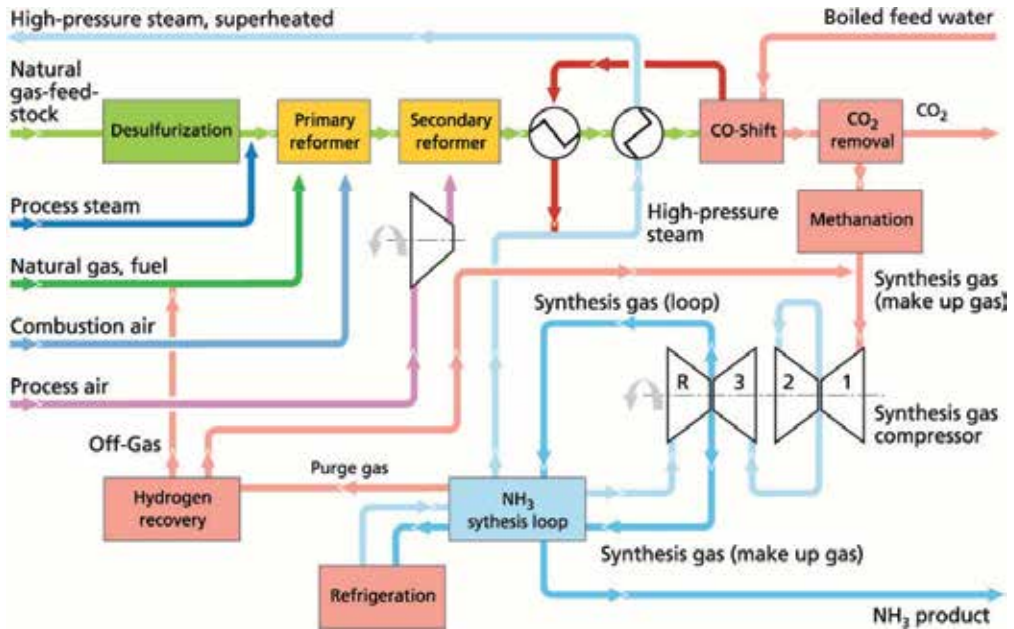


Fig. 3. Ammonia process [Uhde].

In the CO₂ scrubbing process three plate heat exchangers are switched in parallel, two in operation (A and B) and one in standby (C). Figure 4 shows the three coolers with their operating conditions. The CO₂ flows into the PHEs as a gas-steam mixture at 94 °C and is cooled down in a countercurrent process to 33 °C. Water at 30 °C is used as coolant. Each of the 10 tons and 3 meter high PHEs has 1000 m² of high-performance stainless steel (1.4539; AISI 904 L) VT-plates. The transferred heat capacity is 14.5 megawatts.

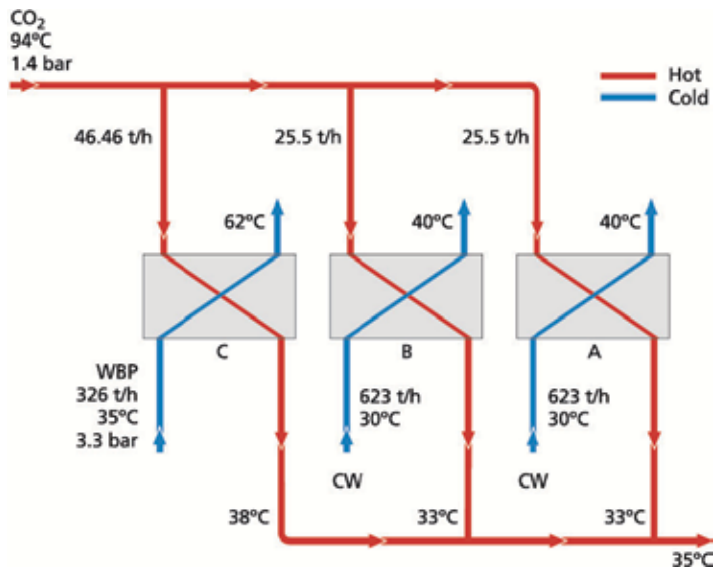


Fig. 4. CO₂ coolers used in the scrubbing process.

Nile river water treated by NALCO inhibitors is used in an open loop as the cooling medium for the CO₂ coolers, the specifications of the cooling water used is given in Table 1.

	CaH	Alkalinity	Chlorides	Inhibitors
Nile water	90 ppm	138	25 ppm	N-7356P: 30ppm, N-73203: 95ppm

Table 1. Cooling water specifications.

A typical analysis for Nile river water is shown in Table 2.

Substrate		Unit
Chloride	77.5	ppm
Ca	48	ppm
Mg	14.5	ppm
Na	60	ppm
K	9	ppm
Fe	0.1	ppm
SO ₄	57.5	ppm
SiO ₂	2	ppm
HCO ₃	180	ppm
KMnO ₄	10.1	ppm
Total hardness	172.5	ppm CaCO ₃
TDS	380	ppm
pH	7.8	-
Alkalinity	180	ppm CaCO ₃

Table 2. Nile river water analysis.

2.3 Problem description and observations

The cooling water flow rate on the CO₂ coolers (HP Scrubber) dropped from 500m³/hr to 300m³/hr due to fouling on the cooling water side, which caused operation problems in the Urea plant. The CO₂ outlet temperature was increasing with time and achieved about 50°C after 30 days of operation before the shutdown of the unit for mechanical cleaning. The CO₂ cooler was opened for mechanical cleaning; the PHE's inlet was plugged with plastic bags and pieces of bottles. Deposits were accumulated at an area about 20cm from the plate inlet and selectively covered the plate surface, as can be seen in Figure 5. They could plug the channels and restrict the water flow over the plate. These deposits accumulated due to the reduction of the gap velocity (shear stress) which increased the surface temperature.

A sample from the deposits was taken and analysed using ashing and X-ray Fluorescence (XRF). The sample was dried at 105 °C before ashing and XRF analysis. The results are shown in Table 3.

The ashing results showed that 14% of the sample was lost at a temperature below 500°C, which represents the organic material and can be considered as normal range. The XRF analysis showed that the main element in the deposits is zinc hydroxide as ZnO (38%) and

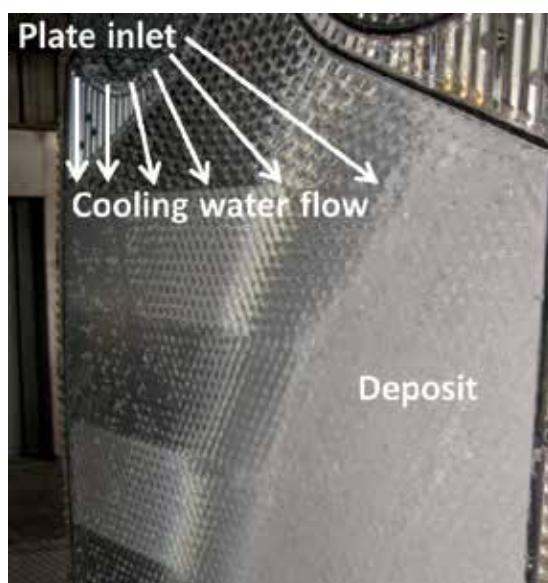


Fig. 5. Deposits formed on the surface of VT-plate.

the second is calcium phosphate (11%), which participated as a result of the increase of the plate surface temperature resulting from the reduction in the cooling water flow rate.

Loss at 500°C	14 %
Loss at 925°C	23 %

(a)

Substrate	Mass %
Magnesium (MgO)	3
Aluminium (Al ₂ O ₃)	1
Silicon (SiO ₂)	2
Phosphorous (P ₂ O ₅)	20
Sulphur (SO ₃)	1
Calcium (CaO)	11
Iron (Fe ₂ O ₃)	1
Zinc (ZnO)	38
Total oxides (normalized to loss 925 °C)	77

(b)

Table 3. (a) Ashing results, (b) Elemental analysis as oxides using XRF.

2.4 Technical solutions

2.4.1 Redesigning of the PHEs

The surface area of the CO₂ cooler was reduced by removing 86 plates out of 254 plates (the surface area was reduced by 34%). The average cooling water velocity inside the gaps was increased from 0.30 to 0.42 m/s, as can be seen in Table 4.

	Original Design	After modification
Plates number	254	168
Gap velocity [m/s]	0.30	0.42
Surface tension [Pa]	5.31	10.84
Reynolds number	3259	4599
Surface temperature [°C]	72	69

Table 4. Design modification for CO₂ cooler in Helwan fertilizer plant, Egypt.

The deposits formed on the surface of the plates were decreased as a result of the increase in the shear stress and the decrease of the surface temperature from 72 to 69°C. The surface temperature was calculated from the fluids temperatures, thermal conductivities and duties on both sides. The operation time for the cooler was increased from 30 days to 43 days and the plates were cleaned after more than 40 days of operation, as shown in Figure 6.

The CO₂ outlet temperature started to increase after about 23 days of operation due to the accumulation of deposits on the cooling water side which led to a reduction in the cooling water flow rate. The unit was opened after about 43 days for mechanical cleaning.

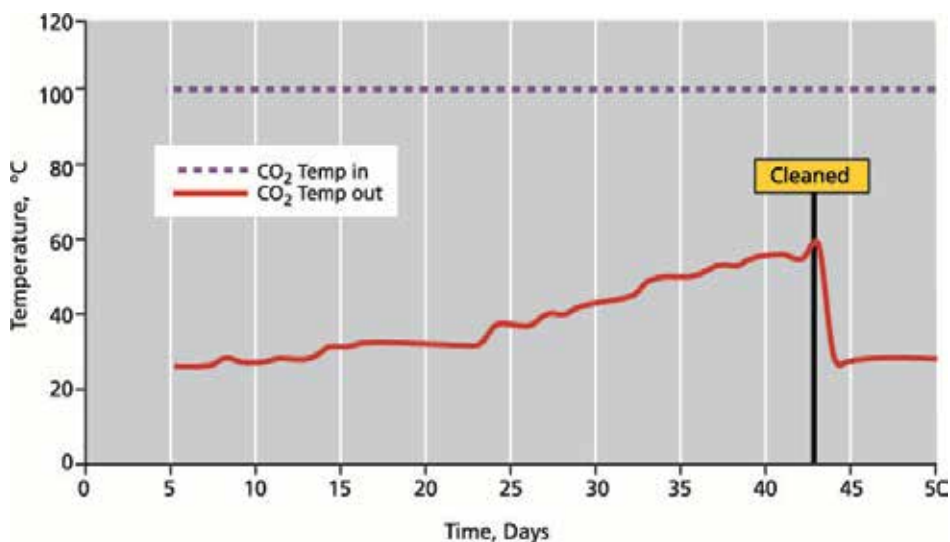


Fig. 6. Inlet and outlet CO₂ temperatures as a function of time.

2.4.2 New plate geometry

A new cooler with computer-modeled plate geometry from the NT (New Technology) series was installed in parallel with the existing two coolers. The NT Series sets new economic

standards with low investment costs, operation and maintenance. The optimized OptiWave plate design requires less heat transfer surface for the same performance. The new EcoLoc gaskets and installation methods simplify maintenance and ensure a perfect fit of the gasket and plate packs. The new plates have the advantage of higher gap velocities (shear stress) due to better fluid distribution over the plates and smaller gap size.

The advantages of the NT-plates at a glance:

- High heat transfer rates
- Low investment and service costs
- Optimized distribution of media
- Simplified handling
- Quick and safe gasket replacement
- Flexible solutions for special requirements
- Non-standard materials available
- Leading manufacturer's know-how

In conventional plates the fluid velocity over the plate's width is decreasing, the more the fluid is distributed from the inlet over the whole plate width. This is due to the higher pressure drop in longer flow channels. The optimized fluid distribution channels of the NT series lead to balanced velocity over the whole plate width and an equal distribution of the medium (Figure 7).

The flow channels of the NT-plates vary in their width and were optimized based on Computational Fluid Dynamics (CFD). The channels located further away from the inlet hole have bigger diameter than those closer to the inlet hole.

Fewer deposits were accumulated on the NT-plates due to the asymmetric flow distribution over the channels as can be seen in Figure 8. These deposits were formed because the unit was taken into operation in parallel with the old two VT-plates units and hence most of the cooling water was flowing inside them. The NT-plates unit was designed in principle to replace one of the VT-plates units so that the gap velocity could be increased.

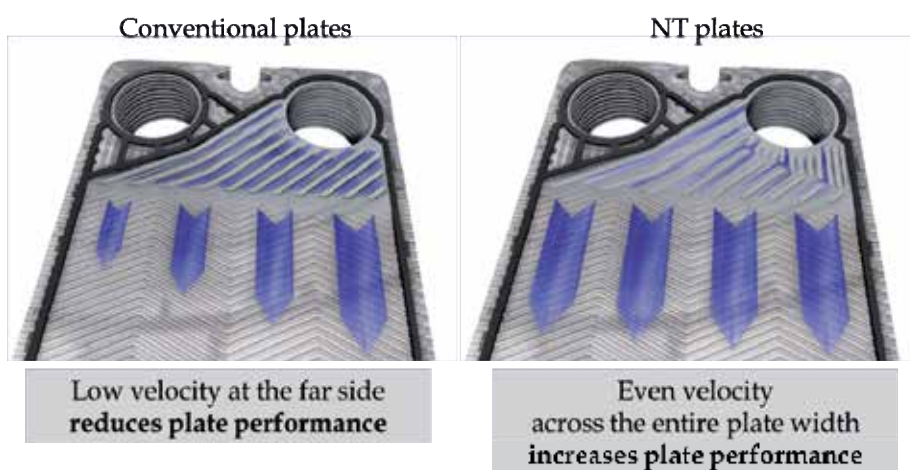


Fig. 7. Velocity distribution over the NT-plate compared with conventional plates.



Fig. 8. Deposits formed on the surface of NT-plate.

2.5 Conclusions

Nile water treated with NALCO inhibitors caused fouling problems inside CO₂ coolers in different Egyptian ammonia plants. Technical solutions including redesigning of the PHEs and new plate geometries were investigated. Reducing the surface area of the CO₂ coolers by 34% increased the gap velocity from 0.30 to 0.42 m/s (shear stress from 5.31 to 10.84 Pa) and hence decreased fouling. The operation time for the cooler was increased from 30 days to 43 days. NT-plates with asymmetric flow distribution over the channels decreased the rate of deposition on the surface of the plates.

3. Solving fouling problems by surface modification

In a recent study, Nano-composite coatings were used to reduce fouling inside gasketed plate heat exchangers involved in food production. An antifouling coating with low surface energy (low wettability) led to a hydrophobic and oleophobic effect. The goal of the project was the application of new surface coatings (nanotechnology) to avoid or minimize adhesion, improve process management, simplify cleaning processes with lesser resources and chemical use, and increase the product reliability.

The test facility constructed by the Institute of Environmental Process Engineering (IUV) at the University of Bremen in Germany used for the investigation of milk adhesion and the stability of the coatings on small cylindrical ducts. A number of coatings and surface treatments were tested. A pilot plant including a milk pasteurizer at the Institute of Food Quality LUFÄ Nord-West in Oldenburg-Germany was used for the thermal treatment of whey protein solutions. Heat exchanger plates coated with different nano-composites as well as electropolished plates installed in the heating section of the pasteurizer were tested. Significant differences were observed between coated and uncoated plates. The coated plates showed reduced deposit buildup in comparison with the uncoated stainless steel plates. Polyurethane-coated plates exhibited the thinnest deposit layer. Electro-polished

plates also reduced deposit buildup in comparison to the standard stainless steel plates and were almost comparable to the coated plates. The time required for cleaning in place (CIP) with the coated plates was reduced by 70% compared to standard stainless steel plates.

3.1 Introduction

Production problems, like decrease of production rate and increase in the intensity of cleaning procedure, arise in the dairy industry as a result of the deposit adhesion to the plate surface. The deposits must be removed by regular and intensive cleaning procedures in order to comply with hygiene and quality regulations for the dairy industry (Augustin et al., 2007). If not controlled carefully, deposits can cause deterioration in the product quality because milk cannot be heated up to the required pasteurization temperature. Milk deposits generally form so fast that heat exchangers must be cleaned regularly to maintain production efficiency and meet strict hygiene standards and regulations (Bansal and Chen, 2006). Energy losses, lost productivity, manpower and cleaning expenses cause immense costs (Beuf et al., 2003). In the dairy industry, fouling and the resulting cleaning of the process equipment account for about 80% of the total production costs (Bansal and Chen, 2006).

Gasketed plate heat exchangers with stainless steel plates are commonly used in the dairy industry. Stainless steel surfaces have high surface energies. The adhesion of product on solid surfaces is determined by the surface roughness and surface energy. The adhesion of deposits could be reduced by either decreasing the surface energy of the metal or by coating the metal surface with high anti-adhesion effect (low surface energy) materials, such as those made of nanoparticles (Gerwann et al., 2002). The application of nano-coatings with their anti-adhesion effects reduces the buildup of deposits on the surface of heat exchanger plates due to the reduction of adhesive forces. The operation efficiency of the plant can be significantly improved and the general hygienic situation of the product can increase. Additionally, intensity and frequency of cleaning can be substantially reduced to achieve the desired degree of product quality (Kück et al., 2007).

Beuf et al. (2003) studied the fouling of dairy product on modified stainless steel surfaces in a plate and frame heat exchanger. Different surface modifications, such as coatings (diamond like carbon [DLC], silica, SiOX, Ni-P-PTFE, Excalibur, Xylan) and ion implantation (SiF⁺, MoS₂) were analyzed. No significant difference was found between the modified stainless steels and the unmodified one. The cleaning efficiency of plates coated with Ni-P-PTFE was the best. The experimental results of Zhao et al. (2007) showed that the surface free energy of the Ni-P-PTFE coating had a significant influence on the adhesion of bacterial, protein and mineral deposits. The Ni-P-PTFE coating reduced the adhesion of these deposits significantly.

The fouling behavior of whey protein solutions on modified stainless steel (SS) surfaces coated with diamond-like carbon (DLC) and titanium nitride (TiN) have been studied by Premathilaka et al. (2007). They concluded that fouling decreased in the order DLC > SS > TiN and cleaning time decreased in the order TiN > SS > DLC.

The goal of the present work is to assess new surface coatings (developed by the Institute of New Materials, INM, in Germany) with low surface energy and low roughness to avoid or minimize adhesion of deposits, simplify cleaning processes, reduce resource and chemical

requirements, and increase product quality and consistency. The work will assess the deposit buildup during the thermal treatment of milk.

3.2 Experimental

3.2.1 Coated surfaces

The anti-adhesion nano-composite coatings, with hydrophobic and oleophobic effectiveness, used in this work were produced from commercially available polymer matrices such as epoxy, polyurethane or Polyamide systems which were reactively cross-linked with per-fluorinated monomers (or oligomers) and ceramic reinforcement particles. The coating material application was similar to wet chemical coating by spraying, and the required mechanical properties were obtained through a thermal cross linking step. The epoxy and polyurethane systems were hardened at 130 ° C for 1 hour, while the Polyamide systems were hardened at 200 °C for 2 hours, in order to ensure an optimum layer formation. Table 5 summarizes the plates used and their specifications.

Plate	Material	Contact angle Water [°]	Contact angle Milk [°]	Surface roughness [μm]
U1	Stainless steel	83.8	69.6	0.80
U1min,e	Electrically-polished stainless steel for one minute	61.7	93.5	0.50
U5min,e	Electrically-polished stainless steel for five minutes	60.3	87.8	0.22
A1	Epoxy-resin based coating of INM	97.6	94.5	0.92
A2	Epoxy-resin based coating of INM	91.0	97.6	0.95
A9	Polyurethane based coating of INM	92.2	88.3	0.23
A10	Polyurethane based coating of INM	93.4	95.5	0.06
A17	Epoxy-resin based coating of INM	95.8	95.1	1.14

Table 5. Contact angle and surface roughness of the sheets prepared by INM.

3.2.2 Laboratory scale testing

A laboratory facility was constructed by the Institute of Environmental Process Engineering (IUV), University of Bremen in Germany, for the investigation of milk adhesion. A heat exchanger was designed to enable thermal and hydraulic load measurements with variable designs. Its principal components were a double wall heated receiver tank, controllable pump, electromagnetic flow meter and the test cell (duct). A closed loop recirculation configuration was used to decrease the volume of the test medium required. Furthermore, a fast sample change by simple removal of the test cell (duct) was performed. Figure 9 shows the laboratory apparatus used and the test duct. The test channel employs an annular geometry, where the inner cylinder is engaged with an electric heater. The middle part (with the threaded ends) is made of stainless steel, while the coin section (right) and the fastener (left) are made from a high-performance plastic Polychlorotrifluoroethylene (PCTFE). This arrangement allows the middle section, which incorporates the heater, to be heated by thermal conduction without large heat losses. The coating material is applied to a small stainless steel tube which is pushed over the heater.

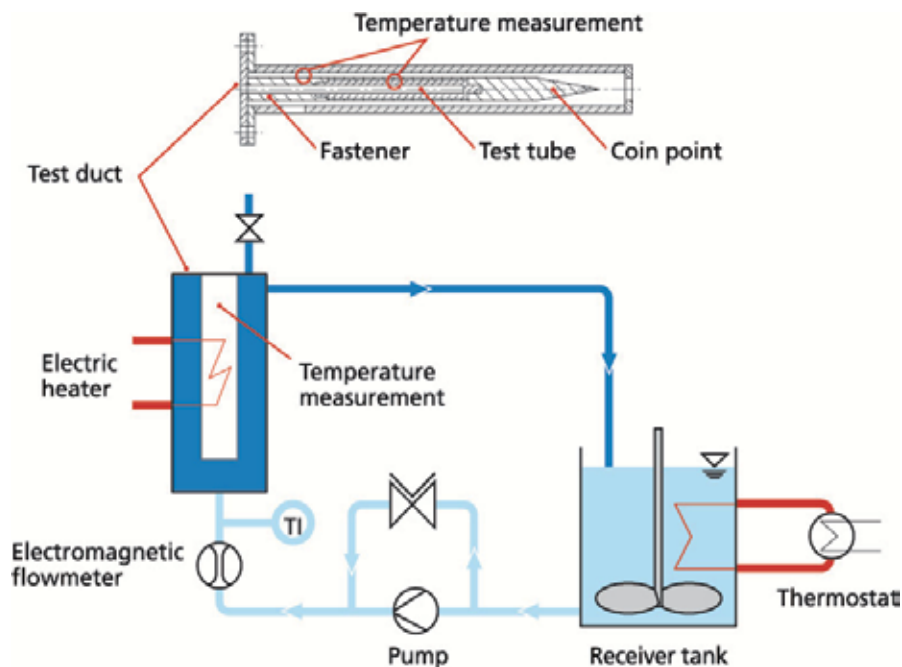


Fig. 9. Flowchart of laboratory heat exchanger apparatus (Institute of Environmental Process Engineering IUV, Universität Bremen).

For the experiments, a 10% (by weight) aqueous whey protein solution was set in the receiver tank. The solution was prepared by solving a whey protein concentrate WPC35 in water until the required concentration was obtained. The pH was adjusted to 6.0 using a 0.1 mol/liter HCl solution. Pre-heating was carried out to about 43 °C. The solution was pumped in the closed cycle of the experimental setup, the electric heater of the test channel was activated and the measuring procedure was started. After each trial, the whey protein solution was replaced to exclude any effect of heating on the ingredients. After each run, the tube was cleaned with 0.1 molar NaOH solution with cross flow velocity of 0.6 m/s. The experimental parameters were:

Volumetric flow rate: 0.036 - 0.37 m³/h
 Whey protein concentration: 10% (by weight)
 Average flow velocity in annulus: 0.2 m/s
 Fluid temperature (measuring section): 45 °C
 Temperature of the heating element: 230 °C
 Heat flux: 20 kW/m²
 Experimental time: 15 to 30 min.

3.2.3 Pilot plant testing

Industrial tests with milk were carried out on a small plant by the Institute of Food Quality LUFÄ-Oldenburg-Germany, with the support of the company GEA PHE Systems (Figure 10). The pilot plant can produce almost all dairy products. It is used for training purposes as well as technological support and procedure development to the food industry.

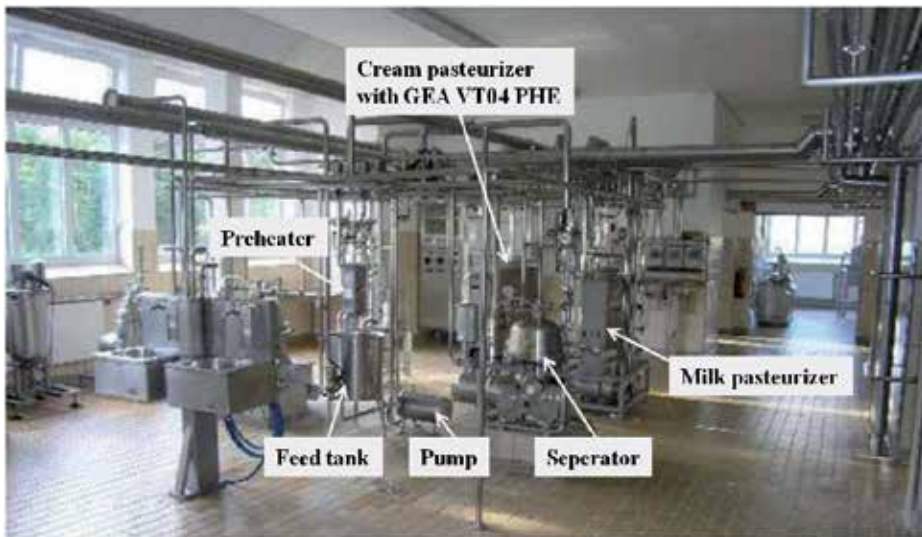


Fig. 10. Pilot plant used for practical tests (Institute of Food Quality LUFA-Oldenburg-Germany) with GEA Ecoflex VT04 plate heat exchanger.

The plate heat exchanger, in which coated and uncoated plates can be installed, consists of two cooling sections (deep cooler with 8 plates and pre-cooler with 10 plates), heat recovery section (with 12 plates), heating section (with 7 plates) and hot water section (with 6 plates). Before assembling the heat exchanger, selected plates in the heating and heat recovery sections were coated using the method described in section 3.2.1. As a reference, stainless steel, electro-polished and PTFE coated plates were also installed in the heat exchanger (Figure 11). Table 6 details the samples used and their specifications.

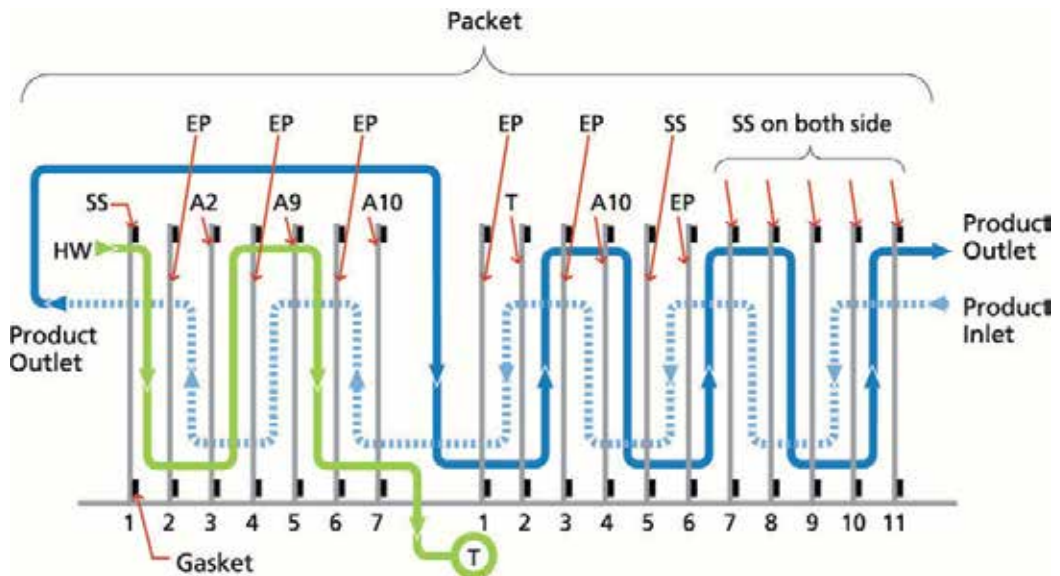


Fig. 11. Plates layout inside GEA Ecoflex VT04 plate heat exchanger.

Substrate	Material	Thickness [μm]
SS	Stainless steel	-
EP	Electrically-polished stainless steel	-
A2	Epoxy-resin based coating of INM	83.7
A9	Polyurethane based coating of INM	53.0
A10	Polyurethane based coating of INM	85.2
A67	Polyurethane based coating of INM	27.6
PTFE	Teflon	22.5

Table 6. Samples specifications used in the pilot plant experiments by LUFA.

The milk was pumped from the receiver tank through the pasteurizer at a constant flow rate. The process steps of heating, cooling and heat recovery were combined together. After a working time of 4 hours, the test was stopped and the plates of the heater and heat recovery sections were removed in order to measure deposit formation. Visual observations and mass investigations were done. Furthermore, the cleaning effectiveness was assessed.

3.3 Results and discussion

Technical investigations were carried out by IUUV and LUFA on the deposits formed from whey protein solution in both the laboratory facility and the pilot plant.

3.3.1 Laboratory tests by IUUV

Laboratory investigations were carried out by IUUV on the deposit of whey protein on the tube surface. Different stainless steel tubes were tested by IUUV using the laboratory heat exchanger apparatus described in section 3.2. Figure 12 shows the deposit accumulation rates of whey protein solution for the different tube surfaces.

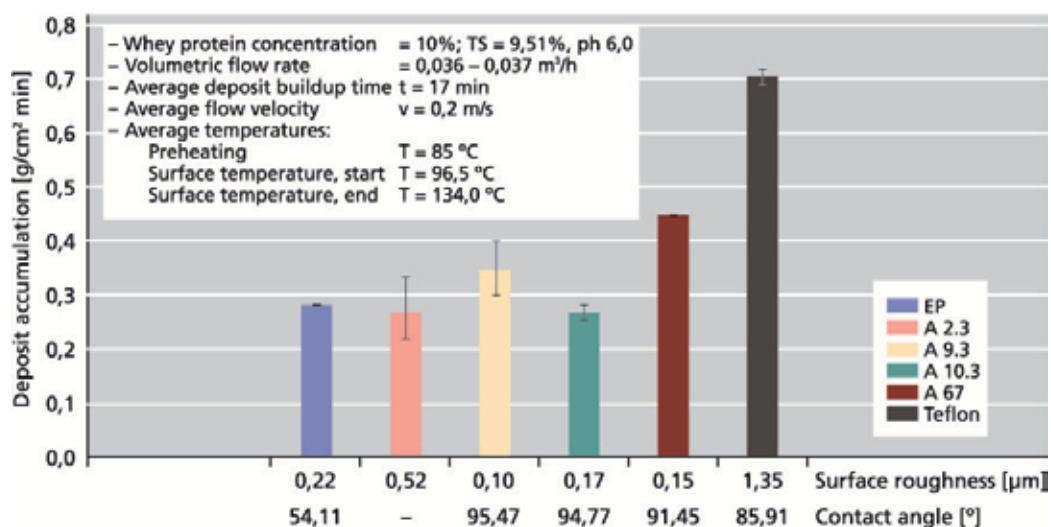


Fig. 12. Deposit accumulation rates for laboratory tests with whey protein on small coated cylindrical ducts. Plate characteristics are given in Table 6.

The Polyurethane-coated tubes gave the thinnest deposit layer, closely followed by the electropolished tubes. The laboratory cleaning tests showed that under the same hydrodynamic conditions, the cleaning time for test tube A9 is only 20% of that needed for the standard stainless steel tube.

3.3.2 Pilot plant tests by LUFA

In a test series LUFA Nord-West in Oldenburg-Germany examined the formation of deposit on test PHE plates which had undergone different treatments. Different coated plates were installed in the heating section of a pasteurizer, with PTFE coated plates next to electro-polished and standard stainless steel plates. The anti-fouling coatings were high-molecular polymers with implanted nano-particles which resulted in high hardness and scratch resistance. The pasteurizer was operated with a 10% (by weight) whey protein solution which was heated up to 85°C. Figure 13 shows the amount of residue, in g, for different surfaces in three tests. It is noteworthy that in these test conditions there is significant whey protein deposition on uncoated, electro-polished and A2-coated stainless steel.

The coatings A2 and A10 showed reduced deposit buildup (the PTFE coating gave more deposit buildup than the standard stainless steel plate). The plates coated with A10 coating had the lowest adhesion, which was similar to the laboratory test results. The deposit buildup on the electro-polished plates was lower than the standard stainless steel plate and almost comparable to the coated plates. Cleaning studies indicated that the cleaning in place (CIP) time, for all coatings was shorter than that for the standard stainless steel plate: PTFE coated plates down by 90%; coated plates down by 70%; electro polished plates down by 36%.

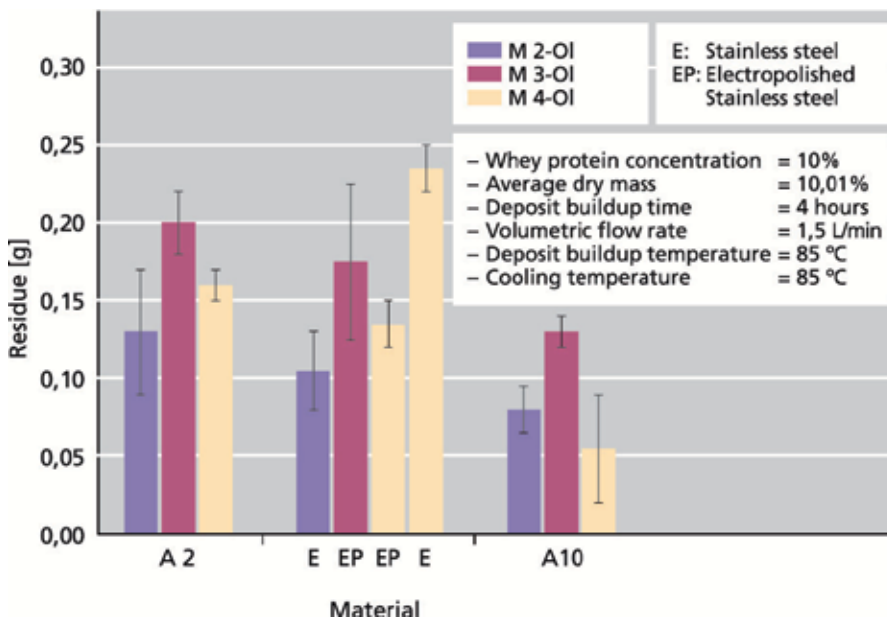


Fig. 13. Amount of deposits formed using whey protein solution, in three tests (m2, m3 and m4).

Figure 14 shows photographs for two different coated plates from the heating section in the heat exchanger after different experimental runs (A2 on left and A10 on right).

It is evident that the coatings have been locally destroyed at the contact points, as pointed by the red circles in the figure. The flow in the plate gap causes relatively high vibrations with particularly strong stresses to the contact points, which is added to the high thermal stresses. The coatings at the present stage of development could not withstand these stresses and need further development.



Fig. 14. Coated heat exchanger plates from heating section: (a) A2 coating, (b) A10 coating.

3.4 Conclusions

Nano-composites could be used as anti-fouling coatings to decrease fouling inside gasketed plate heat exchangers for the dairy industry. Industrial tests showed that the coatings A2 and A10 reduced fouling, though the PTFE coating showed higher fouling than the standard stainless steel plate. The deposit buildup on the electro-polished plates was lower than the standard stainless steel plates and almost comparable to the coated plates. A CIP time reduction was observed for all coatings: PTFE coated plates down by 90%; nano-composites coated plates down by 70%; electro polished plates down by 36%. Pilot plant testing indicated the coatings must be further developed so that they can withstand the thermal and mechanical stresses which arise in industrial operation.

4. Nomenclature

CIP	Cleaning in place
EP	Electrically-polished stainless steel
INM	Institute of New Materials
IUV	Institute of Environmental Process Engineering
LUFA	Institute of Food Quality
NT	New technology
PCTFE	Polychlorotrifluorethylene
PHE	Plate heat exchanger
PTFE	Polytetrafluorethene (Teflon)
SS	Stainless steel
VT	Varitherm
XRF	X-ray Fluorescence

5. References

- Augustin, W., Geddert, T., Scholl, S. (2007). Surface treatment for the mitigation of whey protein fouling, *Proceedings of 7th International Conference on Heat Exchanger Fouling and Cleaning*, pp. 206-214, ECI Symposium Series, Volume RP5Tomar, Portugal.
- Bani Kananeh, A., Scharnbeck, E., Kück, U. D. (2009). Application of antifouling surfaces in plate heat exchanger for food production, *Proceedings of 8th International Conference on Heat Exchanger Fouling and Cleaning*, pp. 154-157, Schladming, Austria.
- Bani Kananeh, A., Scharnbeck, E., Kück, U.D. and Rübiger, N. (2010). Reduction of Milk Fouling Inside Gasketed Plate Heat Exchanger Using Nano-Coatings. *Food and Bioproducts Processing*, Vol. 88, No. 4, (December 2010), pp. 349-356.
- Bansal, B., Chen, X. D. (2006). A critical review of milk fouling in heat exchangers, *Comprehensive Reviews in Food Science and Food Safety*, Vol. 5, No. 2, (April 2006), pp. 27-33.
- Beuf, M., Rizzo, G., Leuliet, J.C., Müller-Steinhagen, H., Yiantsios, S., Karabelas, A., Benezech, T. (2003). Fouling and cleaning of modified stainless steel plate heat exchangers processing milk products, *Proceedings of ECI Conference on Heat Exchanger Fouling and Cleaning: Fundamentals and Applications*, pp. 99-106, Vol. RP1, Article 14, Santa Fe, New Mexico, USA.
- Delplace, F., Leuliet, J. C. and Tissier, J.P. (1994). Fouling experiments of a plate heat exchanger by whey proteins solutions, *Transactions on IChemE C 72*, pp.163-9.
- Gerwann, J., Csögör, Z., Becker-Willinger, C. and Schmidt, H. (2002). Antimicrobial low surface-free energy nanocomposite coatings for medical applications, *Proceedings of Hygienic Coatings Conference*, Brussels.
- Kukulka, D. J. and Leising, P. (2009). Evaluation of Surface Coatings on Heat Exchangers. *Chemical Engineering Transactions*, Vol.18, (May 2009), pp. 339-344.
- Kück, U. D., Hartmann, D., Manske, S., Kück, A. and Rübiger, N. (2007). Entwicklung neuer Verarbeitungsprozesse für die Lebensmittelherstellung durch Anwendung von neuartigen funktionalen Materialoberflächen, *AiF-Abschlußbericht (AiF-Nr. 14228N/1)*, Bremen.
- Müller-Steinhagen, H. (1999). Cooling-Water Fouling in Heat Exchangers. *Advances in Heat Transfer*, Vol. 33, (1999), pp. 415-496.
- Müller-Steinhagen, H. (2006). Verschmutzung von Wärmeübertragerflächen. In: *VDI-Wärmeatlas Ausgabe 2006*, Verein Deutscher Ingenieure and VDI- Gesellschaft Verfahrenstechnik und Chemieingenieurwesen (GVC), pp. (Od1-Od30), Springer-Verlag Berlin Heidelberg, Germany.
- Pana-Suppamassadu, K., Jeimritiwong, P., Narataruksa, P. and Tungkamani, S. (2009). Effects of Operating Conditions on Calcium Carbonate Fouling in a Plate Heat Exchanger. *World Academy of Science, Engineering and Technology*, No. 53, (May 2009), pp. 1204-1215.
- Premathilaka, S. S., Hyland, M. M., X.D. Chen, X. D., Watkins, L. R., Bansal, B. (2007). Interaction of whey protein with modified stainless steel surfaces, *Proceedings of 7th International Conference on Heat Exchanger Fouling and Cleaning*, pp. 150-121 , ECI Symposium Series, Volume RP5, Article 21, Tomar, Portugal.
- Uhde GmbH, Available from: <http://www.uhde.eu/index_flash.en.epl>
- Wang, L., Sunden, B, Manglik, R.M. (2007). *Plate Heat Exchangers: Design, Applications and Performance*, WIT Press, ISBN 978-1-85312-737-3, Southampton, Great Britain.
- Zhao, Q., Liu, C., Liu, Y., Wang, S. (2007). Bacterial and protein adhesion on Ni-P-PTFE coated surfaces, *Proceedings of 7th International Conference on Heat Exchanger Fouling and Cleaning*, pp. 237-242, ECI Symposium Series, Volume RP5, Article 33, Tomar, Portugal.

Self-Cleaning Fluidised Bed Heat Exchangers for Severely Fouling Liquids and Their Impact on Process Design

Dick G. Klaren and Eric F. Boer de
KLAREN BV
The Netherlands

1. Introduction

The invention of the self-cleaning fluidised bed heat exchangers dates back to 1971 when the principal author of this chapter was involved in the discovery and development of a very unique Multi-Stage Flash (MSF) evaporator for the desalination of seawater. The condensers used in this thermal desalination plant used stationary fluidised beds in multi-parallel condenser tubes. The particles fluidised in these tubes consisted of glass beads of 2 mm diameter. These small glass beads knocked of scale crystals from the tube wall at their very early stage of formation and, moreover, the turbulence created by the stirring action of the glass beads in the liquid caused thinning of the laminar boundary layer. This dramatically improved the heat transfer film coefficient in spite of very low liquid velocities in the tubes and reduced pumping power requirements.

Since the early 80s, the chemical processing industries showed a lot of interest for this unique heat exchanger, which seemed to be able to solve any fouling problem, even those problems, which required cleaning of conventional heat exchanger every few days or even hours.

In the next paragraphs we will pay attention to the consequences of heat exchanger fouling and in particular its cost. We explain the self-cleaning fluidised bed technology and also present a couple of installations. We also show some examples where the benefits of the self-cleaning fluidised bed heat exchange technology are responsible for a much wider range of advantages with respect to process design than non-fouling heat exchange only.

2. Fouling of heat exchangers

2.1 Consequences of heat exchanger fouling

It can be stated that a general solution to heat exchanger fouling still does not exist. This is not surprising, as knowledge of underlying mechanisms of the fouling process remains limited. Moreover, fouling in heat exchangers often concerns different types of heat exchangers, each with its own unique characteristics. Also, there are large differences in physical properties of the fluids to be applied in the exchangers. The consequences of heat exchanger fouling are:

- Loss of energy,
- loss of production or reduced capacity operation,
- over sizing and / or redundancy of equipment,
- excessive maintenance cost,
- hazardous cleaning solution handling and disposal.

Over sizing of heat transfer equipment has become an accepted approach to increase the period of time necessary to reach the fouled state. The equipment is then cleaned (chemically or mechanically) to return the heat transfer surface to a near clean condition with recurring maintenance cost and the possibility of cleaning solution disposal problems. Later in this chapter, it will be shown that there are existing cases where over sizing of heat transfer surface can involve the installation of two to five times the surface required for the clean condition. Also, in these severe cases it may be necessary to carry out the cleaning procedure every two or three days, resulting in excessive downtime, maintenance costs and solution disposal problems. Sometimes the fouling problems are so severe that heat transfer performance reduces to almost zero in a matter of hours.

Experience has shown that the alternatives to recurring fouling problems associated with the cooling or heating of a severe fouling liquid are certainly limited. In the case of cooling applications unsuccessful attempts to recover energy from hot waste streams may lead to the total abandonment of an otherwise promising energy management program.

Frequently the only acceptable approach to heating severe fouling liquids will involve direct steam injection. This results in a loss of condensate and the dilution of the process stream, which often requires costly reconcentration later in the process. However, heating by direct steam injection does offer a unique opportunity to define the actual cost of fouling in terms of lost condensate and the subsequent cost of water removal. In the next paragraph we will pay attention to the very high cost of heat exchanger fouling on a global scale, and for one process in particular.

2.2 Cost associated with heat exchanger fouling

The heat exchangers in a crude oil train of a refinery for the distillation of crude oil in lighter fractions are often subject to severe fouling, and do represent globally a very high level of cost. In this sub-paragraph we like to explain this particular example in a nutshell. For a much more detailed explanation one is referred to Ref. [5].

Fig. 1 gives an schematic impression of the heating of crude oil in a crude oil train downstream the desalter and in the furnace, where after the oil is cracked in much lighter fractions in the distillation column. Fig. 2 gives an impression of the temperatures in this very much simplified example.

Fouling of the crude oil heat exchangers downstream the desalter, Ex4 up to and inclusive Ex8, is shown at first instance by a drop of the inlet temperature 271 °C of the crude oil in the furnace, which means that more heat has to be supplied into the furnace to meet the required outlet temperature 380 °C of the crude oil entering the distillation column. This, of course, a phenomenon caused by fouling of the heat exchangers, does requires extra fuel (i.e. extra energy) to be burned in the furnace to keep the distillation facility in operation. At a certain moment, the inlet temperature of the crude oil in the furnace has dropped to such an

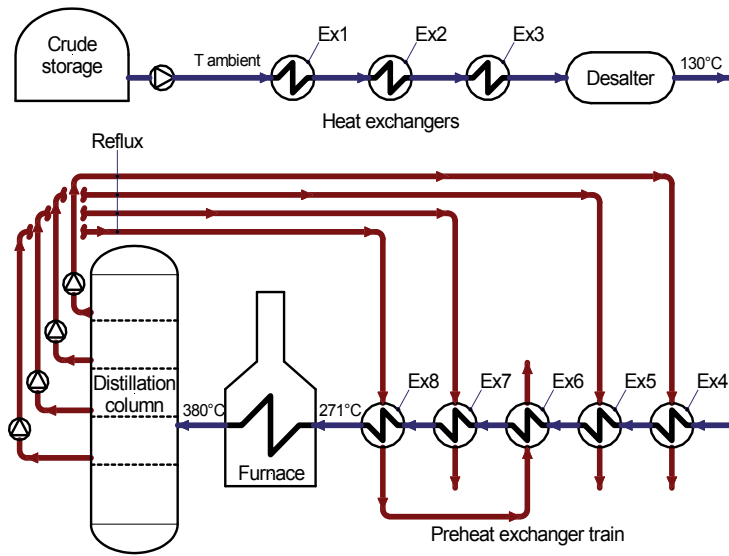


Fig. 1. Simplified flow diagram of a crude oil preheat train.

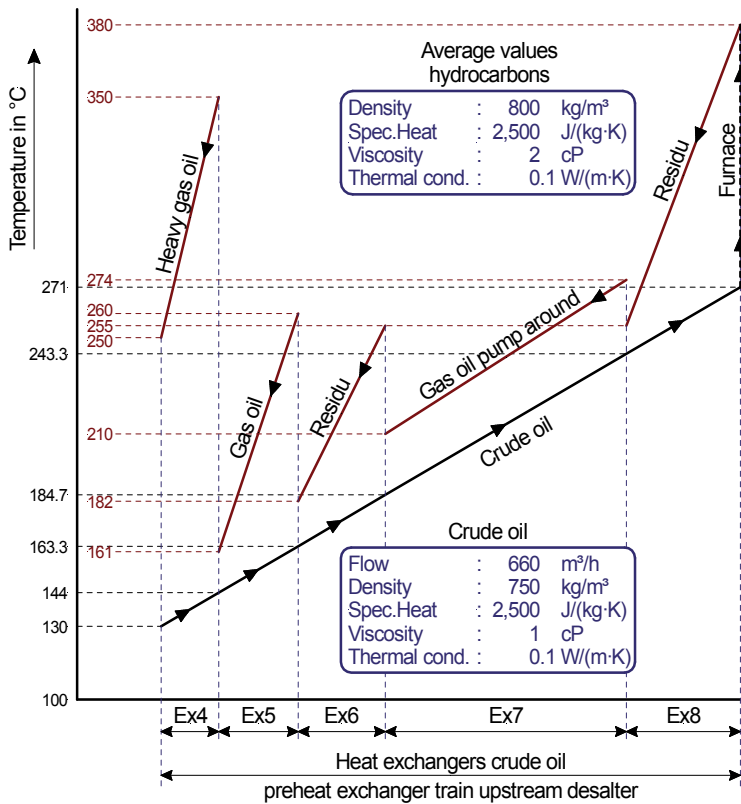


Fig. 2. Temperature diagram crude oil preheaters in simplified flow diagram shown in Fig. 1.

extent that the heating capacity of the furnace is insufficient to meet the required outlet temperature of the crude oil. This temperature can only be maintained by reducing the throughput of crude oil through the heat exchanger train, which, however, also reduces the production capacity of the refinery. This example shows very clearly that fouling of heat exchangers does cost extra energy and may also reduce the production capacity of an installation. For our crude oil preheat train, both facts, including the maintenance cost, increases the refining cost for each barrel of crude oil. What are these costs on a global scale?

At this moment (2011), the global production of crude oil amounts to approx. 85 million barrels per day (bpd). Table 1 has been derived from information given in Ref. [5], and gives an impression about the annual fouling cost for the crude oil being processed in the crude oil preheater trains of all refineries in the world as a function of the price per barrel crude oil.

	Crude oil price in US\$ per barrel			
	\$ 45	\$ 60	\$ 75	\$ 90
Fouling costs in billion US dollars	10.9	12.5	14.1	15.7

Table 1. Fouling costs crude oil trains as a function of crude oil price.

It is assumed that for a crude oil price of US\$ 60 / barrel, the total fouling cost in crude oil preheat trains processing the global crude oil production of 85 million bpd represents approx. 10 % of the worldwide fouling costs in heat exchangers, which costs include all kind of heat exchangers for both liquids and gases. From this statement and the numbers presented in Table 1, it can be concluded that the total cost the world has to pay annually for fouling of heat exchangers amounts to approx. US\$ 125 billion. In Ref. [1], Garrett-Price used a different approach and concluded that the fouling of heat exchangers do cost an industrialised nation approx. 0.3 % of its Gross National Product (GNP). If we apply this rule to the GNP of the whole world (2007) of US\$ 55 000 billion, then we find for the global fouling cost US\$ 165 billion. This is higher than US\$ 125 billion, but, very likely, because not all countries can be considered as sufficiently industrialised.

It is evident that the often excessive costs of heat exchanger fouling have led to a number of initiatives to develop some additional alternative solutions, often derived from research into the various fouling mechanisms. Over a period of forty years, the principal author Dr. Ir. Dick G. Klaren has participated in the development of one of the more promising alternatives: The self-cleaning or non-fouling fluidised bed heat exchanger. During this period the concept was taken from a laboratory tool to a fully developed heat transfer tool, which is now used to resolve severe fouling problems in a range of applications throughout the process industries.

3. Principle of the self-cleaning fluidised bed heat exchanger

Over the past 40 years, the principle of the fluidised bed heat exchange technology evolved from a type that applied a stationary fluidised bed into a more widely applicable concept

that uses a circulating fluidised bed. This section pays attention to both principles of which the circulating concept is more widely applicable in comparison with the stationary type.

In principle such a stationary fluidised bed heat exchanger consists of a large number of parallel vertical tubes, in which small solid particles are kept in a stationary fluidised condition by the liquid passing up the tubes. The solid particles regularly break through the boundary layer of the liquid in the tubes, so that good heat transfer is achieved in spite of comparatively low liquid velocities in the tubes. Further, the solid particles have a slightly abrasive effect on the tube wall of the exchanger tubes, removing any deposit at an early stage.

Fig. 3 shows a heat exchanger with a stationary fluidised bed, which means there is no change in position of the particles as a function of time. The inlet channel contains a fluidised bed and a flow distribution system which is of utmost importance to achieve stable operation of all parallel exchanger tubes, or said otherwise: Equal distribution of liquid and solid particles over all the tubes. This exchanger is characterised by the use of glass beads with diameters of 2 to 3 mm and very low liquid velocities in the tubes. The glass beads are fluidised along the tubes and form a shallow fluidised bed layer in the outlet channel. This exchanger is only suitable for operation on constant flow.

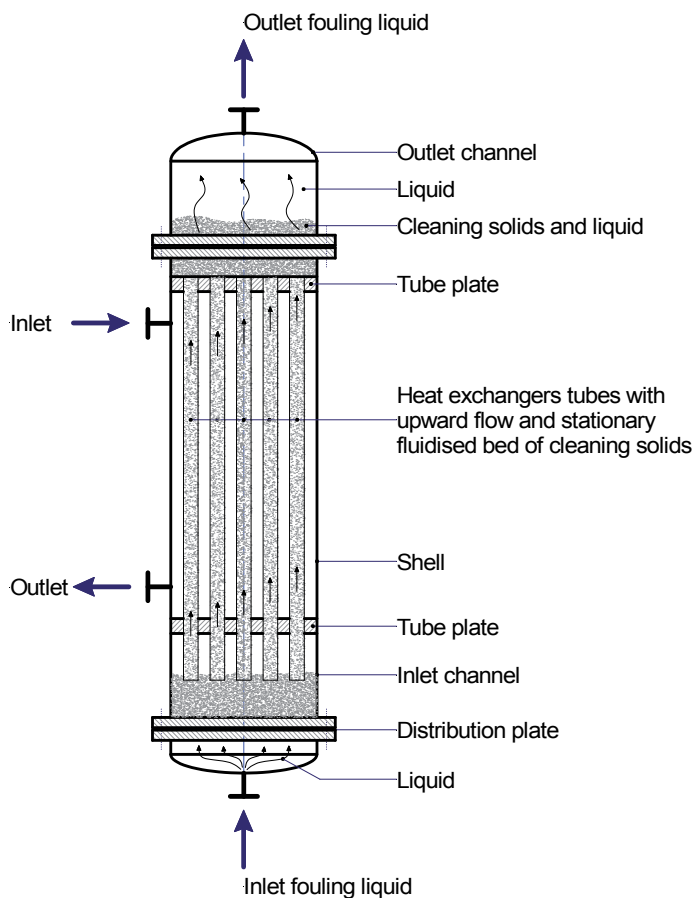


Fig. 3. Self-cleaning heat exchanger with stationary fluidised bed of cleaning solids.

Fig. 4 shows a heat exchanger with an 'internally circulating' fluidised bed. In this heat exchanger the liquid and particles flow through the tubes from the inlet channel into the widened outlet channel, where the particles disengage from the liquid and are returned to the inlet channel through multiple downcomer tubes, which are uniformly distributed over the actual heat exchanger or riser tubes. Now, the particles in the tubes experience a change of position with time. This heat exchanger can also use higher density materials like chopped metal wire as particles with dimensions up to 4 mm, and normally operates on higher liquid velocities in the tubes than the exchanger with the stationary fluidised bed. Depending on the design, this exchanger can also operate on a varying flow and in case of chopped metal wire particles; this exchanger represents the ultimate tool for handling the most severe fouling problems in liquid heat transfer.

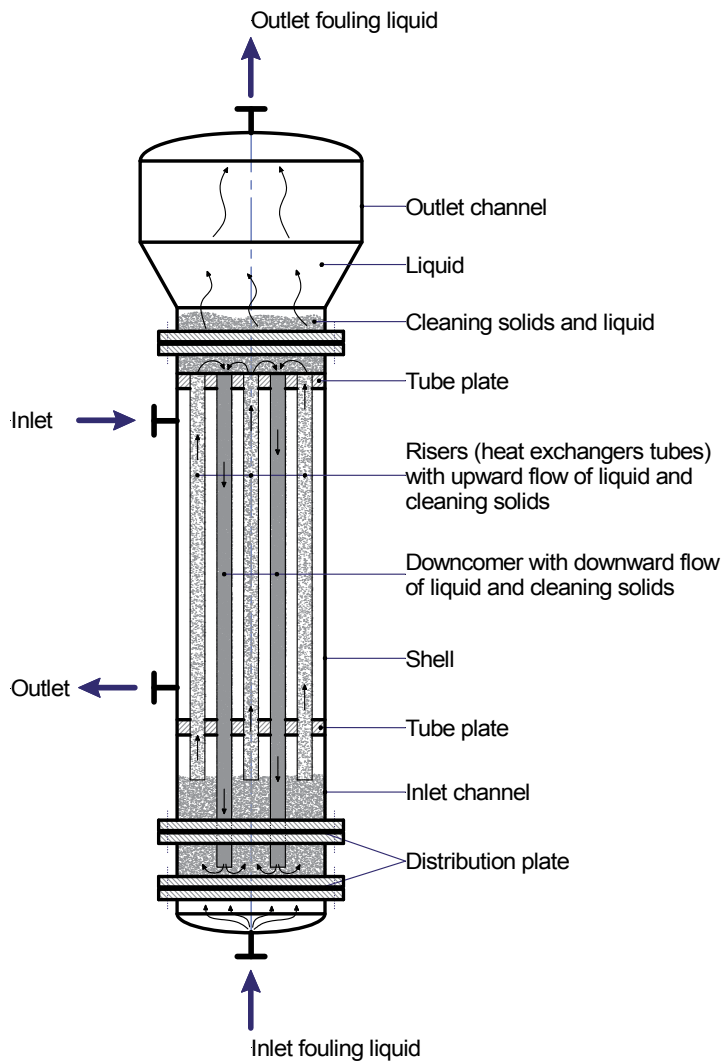


Fig. 4. Self-cleaning heat exchanger with internal circulation of cleaning solids.

The heat exchanger shown in Fig. 5 applies an 'externally circulating' fluidised bed. In this heat exchanger the liquid and particles flow from the outlet channel into an external separator where the particles are separated from the liquid, where after the particles flow from the separator into the inlet channel through only one downcomer and control channel. For hydraulic stability reasons, this heat exchanger has the advantage that it only uses one downcomer, and the flow through this external and accessible downcomer can be monitored, influenced and varied by the control flow through line 1B. This flow only represents approximately 5% of the feed flow through line 1 and shutting off this flow makes it possible to use the particles intermittently. This configuration also makes it possible to revamp existing severely fouling vertical conventional heat exchangers into a self-cleaning configuration as will be presented later in this chapter; this is a major advantage in comparison with the configuration shown in Fig. 4.

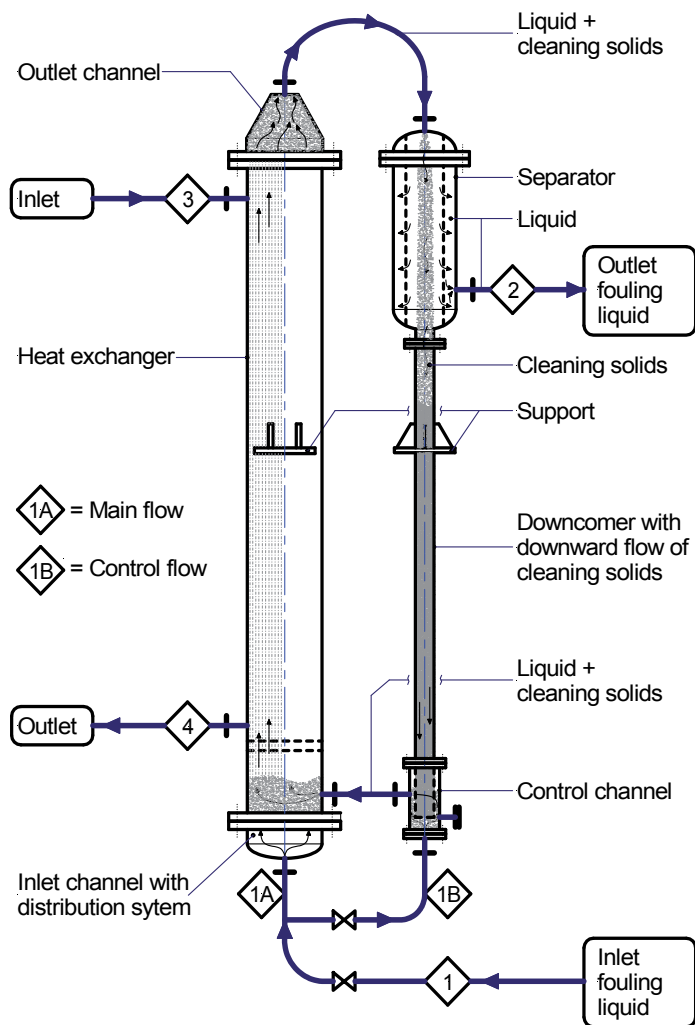


Fig. 5. Self-cleaning heat exchanger with external circulation of cleaning solids.

4. Performance of the self-cleaning fluidised bed heat exchanger

The performance of a self-cleaning fluidised bed heat exchanger and its design consequences have to be divided in the following subjects:

- Heat transfer correlation.
- Design consequences.
- Pumping power requirements.
- Fouling removal.
- Wear.

4.1 Heat transfer correlation

We briefly explain the composition of the tube-side heat transfer correlation for a heat exchanger which also applies recirculation of the particles and the liquid.

Fig. 6 shows the significant liquid velocities influencing the wall-to-liquid heat transfer coefficient for an exchanger with a circulating fluidised bed, such as:

- U_s = superficial liquid velocity in the tubes relative to the tube wall,
 $U_{b,w}$ = velocity of (moving) swarm of fluidised particles relative to the tube wall,
 $U_{l,s}$ = superficial liquid velocity relative to the boundary limits of the (moving) swarm.

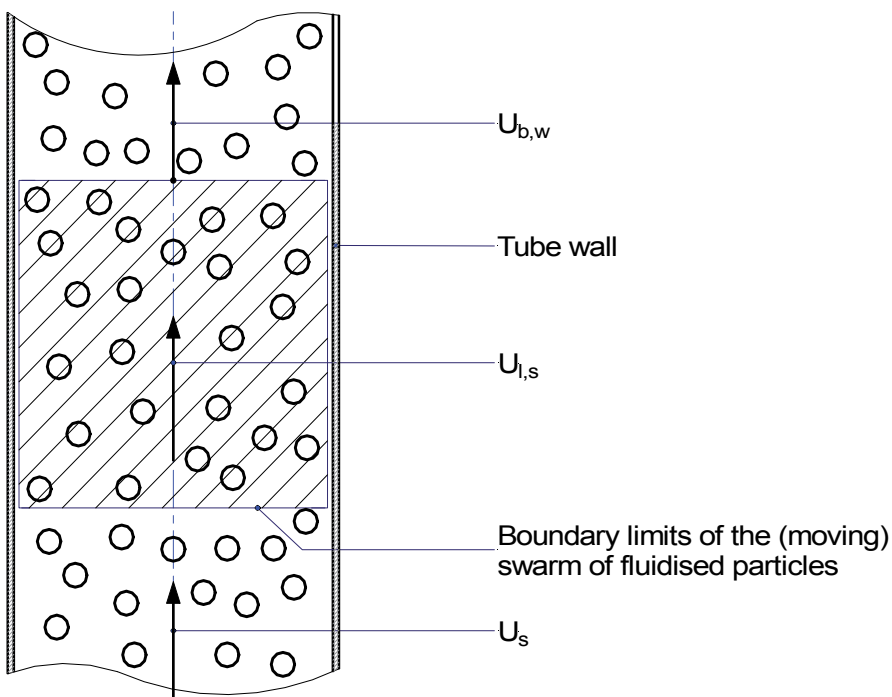


Fig. 6. Significant liquid velocities in tube of exchanger with circulating fluidised bed.

Where the superficial liquid velocity refers to the tube liquid velocity in the empty tube. From the explanation above, it follows:

$$U_s = U_{b,w} + U_{l,s} \quad (1)$$

For $U_{b,w} = 0$, the circulating fluidised bed satisfies the conditions of a stationary fluidised bed, which then yields:

$$U_s = U_{l,s} \quad (2)$$

where $U_{l,s}$ follows from the theory presented by Richardson and Zaki, Ref. [10].

The heat transfer coefficient $\alpha_{w,l}$ between the wall and the liquid of a circulating fluidised bed exchanger, is composed as follows:

$$\alpha_{w,l} = \alpha_l + \alpha_c \quad (3)$$

where:

α_l = wall-to-liquid heat transfer coefficient of a stationary fluidised bed with a superficial velocity $U_{l,s}$ related to the porosity ε of the bed

α_c = wall-to-liquid heat transfer coefficient for forced convection in a tube, taking into account a liquid velocity $U_{b,w}$, which actually corresponds with the velocity of the (stationary) fluidised bed moving along the tube wall

For the heat transfer coefficient α_l one is referred to Ruckenstein, Ref. [11], as long as superficial liquid velocities are calculated from porosities (ε) lower than 0.9. For porosities in the range $0.9 < \varepsilon \leq 1.0$, the following equation is suggested:

$$\alpha_l = \alpha_l|_{\varepsilon=1.0} + \frac{(1-\varepsilon)}{(1-0.9)} \times \{ \alpha_l|_{\varepsilon=0.9} - \alpha_l|_{\varepsilon=1.0} \} \quad (4)$$

The heat transfer coefficient $\alpha_l|_{\varepsilon=1.0}$ is calculated using the equation of Dittus and Boelter taking into account the liquid velocity in the tube which corresponds with the terminal falling velocity on one single particle in the tube, i.e. $\varepsilon = 1.0$, as the liquid velocity used in the Reynolds number.

The heat transfer coefficient α_c is also obtained using the equation of Dittus and Boelter with $U_{b,w}$ as the liquid velocity used in the Reynolds number.

Fig. 7 shows the wall-to-liquid heat transfer coefficients in an exchanger with a circulating fluidised bed as a function of the various process parameters using 2.0 mm glass particles. It should be noticed that in Fig. 7 the curve $U_s = U_{l,s}$ shows the relation between heat transfer coefficient and relevant parameters for the stationary fluidised bed bed.

It should be emphasised that this heat transfer correlation is only an attempt to produce some approximate numbers for the overall heat transfer coefficients for any preliminary design. The real numbers which should be used in the performance guarantee of the heat exchanger follow from experimental operation of a representative pilot plant. Such a pilot plant is anyhow necessary to demonstrate the non-fouling operation.

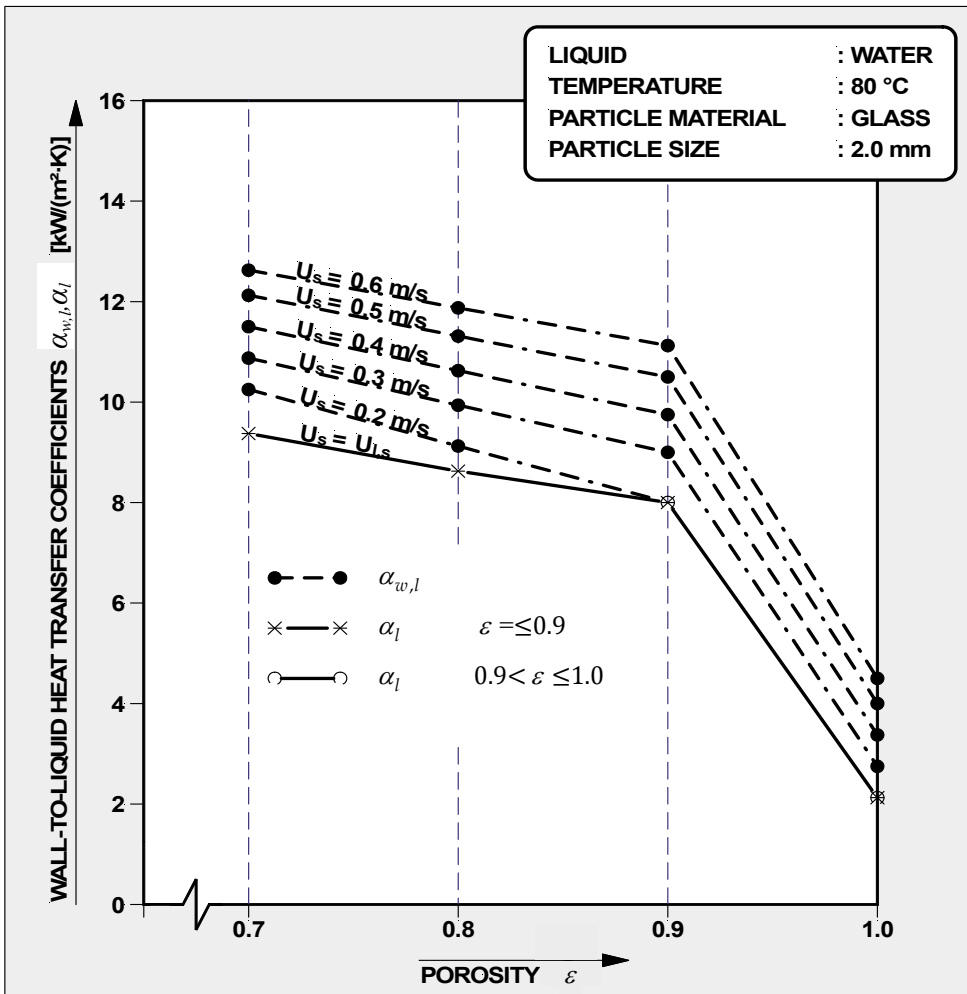


Fig. 7. Heat transfer coefficients in exchanger with circulating fluidised bed.

4.2 Design consequences

A fluidised bed exchanger offers the possibility to obtain heat transfer film coefficients at the tube-side of the same order of magnitude as normally achieved in conventional tubular exchangers, although at much lower liquid velocities. For example, a stationary fluidised bed heat exchanger using glass beads of only 2 mm with a porosity of the fluidised bed in the tubes of 75 % (i.e. the liquid volume fraction in the tube) can achieve heat transfer film coefficients of approx. 10 kW/(m²·K) at a superficial velocity of approx. 0.12 m/s, which can only be realised in a conventional tubular heat exchanger with a liquid velocity of approx. 1.8 m/s.

The design consequences of this unique behaviour for a fluidised bed heat exchanger can be best explained with the help of the equation below for a heat exchange tube, which has been derived from the conservation equations for mass and energy:

$$L_t = D_o \times \left(\frac{D_i}{D_o} \right)^2 \times \frac{\rho_l \times c_l \times V_l}{4 \times k} \times \frac{\Delta T}{\Delta T_{\log}} \quad (5)$$

Where:

L_t	=	Tube length	[m]
D_o	=	Outer diameter of the tube	[m]
D_i	=	Inner diameter of the tube	[m]
ρ_l	=	Density of the liquid	[kg/m ³]
c_l	=	Specific heat of the liquid	[J/(kg·K)]
V_l	=	Superficial liquid velocity in the tube	[m/s]
k	=	Overall heat transfer coefficient	[W/(m ² ·K)]
ΔT	=	Temperature difference of the liquid between tube inlet and tube outlet	[°C]
ΔT_{\log}	=	Logarithmic mean temperature difference across tube	[°C]

For a comparison of the tube length between different types of exchangers for the same duty and temperatures, Equation (5) can be simplified:

$$L_t = C_1 \times \frac{D_o \times V_l}{k} \quad (6)$$

Where C_1 is a constant for a particular installation / application.

Or in words: The length of the tubes L_t is directly proportional to the diameter of the tube D_o , the liquid velocity in the tubes V_l , but inversely proportional to the heat transfer coefficient k . It can be stated that the clean k -values for self-cleaning fluidised bed heat exchangers are always somewhat higher than for the conventional heat exchangers at their normally much higher liquid velocities, with the remark that the clean k -values for the self-cleaning fluidised bed heat exchangers correspond with the design values used for the full-size self-cleaning fluidised bed heat exchanger with no need for cleaning, while for the conventional heat exchangers due to fouling the design k -value may be 2, 3, 4 or even 5 times lower than the clean k -value and frequent cleanings may be still necessary.

What the design consequences of excellent heat transfer at very low liquid velocities do mean for a self-cleaning fluidised bed heat exchanger in comparison with a conventional heat exchanger for the same application can be best explained with the following striking example:

A conventional Multi-Stage Flash (MSF) evaporator for seawater desalination with a seawater velocity of 1.8 m/s in the condenser tubes of 19.05 × 1.21 mm and an average heat transfer coefficient of 2500 W/(m²·K) required a total length of the condenser tubes of 173 m. Depending on the design of this seawater evaporator, this tube length requires the installation of 8 evaporator vessels in series, each vessel with a length of 20 m or even more.

The same MSF desalination plant equipped with stationary fluidised bed heat exchangers required a seawater velocity in the tubes of only 0.125 m/s to maintain a fluidised bed in all parallel operating tubes with a porosity of 75 % using glass particles with a density of

2750 kg/m³ and a diameter of 2 mm. In spite of this low seawater velocity, an overall heat transfer coefficient of 2500 W/(m²·K) was achieved. From the equations above, it can be concluded that this desalination plant required only $0.125 / 1.8 \times 173 = 12$ m condenser tube length in series, which can be installed in only one vessel with an overall height of less than 15 m.

4.3 Pumping power requirements

Pumping power is influenced by the pressure drop across the heat exchanger and the pressure drop to support a stationary fluidised bed, which is determined by the following equation:

$$\Delta P_t = L_t \times (\rho_s - \rho_l) \times (1 - \varepsilon_t) \times g \quad (7)$$

Where:

ΔP_t	=	pressure drop across the tube due to bed weight	[N/m ²]
L_t	=	tube height	[m]
ρ_s	=	density of the material of the solid particles	[kg/m ³]
ρ_l	=	density of the liquid	[kg/m ³]
ε_t	=	liquid volume fraction in tube or porosity	[-]
g	=	earth gravity	[m/s ²]

For the MSF desalination plant with stationary fluidised bed condensers specified above, the pressure drop to support the bed weight amounts to 47 000 N/m². On top of this pressure drop we have to add a pressure drop caused by the flow distribution system of 4 000 N/m² for stabilisation of the flow through all tubes. Pressure drop due to wall friction has not to be taken into account because of the very low liquid velocities in the tubes of only 0.125 m/s. However, for this particular application, we have to add the lifting height for the liquid which requires an additional pressure drop of 120 000 N/m² resulting in a total pressure drop of $47\,000 + 4\,000 + 120\,000 = 171\,000$ N/m².

For the conventional MSF desalination plant we calculate a pressure drop of approx. 400 000 N/m² required by the wall friction in these very long condenser tubes with much higher liquid velocities, and when we take into account the losses in water boxes we end up with a total pressure drop of approx. 450 000 N/m².

It should be emphasised that for this particular application the pressure drop influencing the heat transfer coefficient and required by the condenser bundle installed in the conventional MSF is a factor $400\,000 / 51\,000 = 7.9$ (!!) higher than this pressure drop for the MSF equipped with stationary fluidised bed condensers. These differences in pressure drop directly influence the pumping power requirements for both installations. In general, when also considering 'circulating' fluidised bed heat exchangers operating at somewhat higher liquid velocities and using higher density solid particles, the differences in pumping power requirements will not be that much as presented above, although, for all applications, the differences in pumping power remain easily a factor 2 to 3 times lower for the fluidised bed heat exchanger compared to the conventional shell and tube heat exchanger.

4.4 Fouling removal

Fouling of heat exchangers is experienced by a gradual and steady reduction in the value of the overall heat transfer coefficient. A closer look into this phenomenon shows that there are always two causes:

1. Fouling of the actual heat transfer surface by the forming of an insulating layer of deposits, which reduces the heat transfer through the tube wall.
2. Clogging of flow distribution system in the inlet channel and / or the inlets of the heat exchanger tubes by large pieces of dirt or deposits broken loose from the wall of vessel and piping upstream the exchanger and present in the feed flow of the exchanger. Clogging of tubes removes heat exchanger tubes from participation in the actual process of heat transfer.

The first cause can be solved by the mild scouring action of the fluidised solid particles in the tubes. The second cause, at least of the same importance as the first cause but often neglected, can only be solved by the installation of a strainer upstream the self-cleaning fluidised bed heat exchanger. To minimise the cost for such a strainer and the ground area for the heat exchanger and its accessories, we have developed a proprietary self-cleaning strainer which forms an integral part with the inlet channel of the exchanger.

Now, let us pay attention to some of our fouling removal experiences in a fluidised bed heat exchanger and, therefore, we once more should pay attention to our MSF seawater evaporators:

It is known that natural seawater cannot be heated to temperatures above 40 to 50 °C because of the formation of calcium carbonate scale. Conventional MSF evaporators often operate at maximum seawater temperatures of 100 °C, but only after chemical treatment of the seawater feed which removes the bicarbonates from the seawater and prevents the forming of scale. Of course, this is a complication in the process and does cost money. The MSF evaporator equipped with the stationary fluidised bed condensers, using 2 mm glass beads, has convincingly demonstrated that it can operate at even much higher temperatures than 100 °C without scale forming on the tube walls. Although, the scale crystals are precipitating from the seawater on the tube walls these crystals are knocked off by the glass beads at an early stage, so that it never comes to the formation of an insulating scale layer and the tube walls remain clean and shiny. Here we have clearly demonstrated the fouling removal, self-cleaning or non-fouling behaviour of a fluidised bed heat exchanger operating under harsh conditions as the result of the scouring action of the fluidised particles. No doubt that this feature is of extreme importance for heat exchangers operating on severely fouling liquids.

Meanwhile, with many self-cleaning fluidised bed heat exchangers already installed in different industries, commercial operating experiences have shown that the self-cleaning fluidised bed heat exchanger, which can remain clean indefinitely, is a cost-effective alternative to the conventional heat exchanger which suffers from severe fouling in a couple of hours, days or weeks and even months. Any type of fouling deposit, whether hard or soft; biological or chemical; fibrous, protein, or other organic types; or a combination of the above can be handled by the self-cleaning fluidised bed heat exchanger. Moreover, later in this chapter it will be shown that the unique characteristics of this heat exchange technology allow for the introduction of major design changes of installations in traditional processes

and, therefore, the advantages of this heat exchange technology does reach much further than solving heat exchanger fouling problems only.

4.5 Wear

Now we have been informed about the remarkable effects of scouring particles on the heat transfer film coefficients at very low liquid velocities, low pumping power requirements and their potential to remove fouling, one might wonder what the consequences are of the scouring action of the particles with respect to wear and / or material loss of the heat exchanger tubes and the particles. After many years operating experiences we have come to the conclusion that only in case of the formation of a weak corrosion layer on tube and / or particle material, the scouring action of the particles may cause material loss due to the removal of this corrosion layer. For applications where corrosion of metal surfaces does not play a role, we present the following examples:

In a US plant, after one year of operation, the cleaning particles made of chopped stainless steel wire lost 2.5 % of weight. This is caused by the rounding-off effects of the sharp edged cylindrical particles. In the second year, being substantially rounded-off already during the first year of operation, the weight loss of the particles dropped to less than 0.5 %. Because the smooth stainless steel tube wall is not subjected to metal loss as a result of rounding-off effects, the material loss of the tubes should be much less than 0.5 % per year.

Similar experiences have been obtained in Japan with stainless steel tubes and particles. Again, after one year of operation a weight loss of approx. 2 % was measured. In the second year, this weight loss was negligible. Fig. 8 shows the rounding-off effects of chopped stainless steel wire as a function of operating time. The loss of approx. 2 % in the first year of operation as mentioned above can also be avoided by using particles which have already been rounded-off mechanically directly after their fabrication (chopping) process.

5. New installations equipped with self-cleaning fluidised bed heat exchangers

5.1 Multi-Stage Flash / Fluidised Bed Evaporator (MSF / FBE); most promising tool for thermal seawater desalination

As the development of this heat exchanger began in the early 70s with the application of stationary fluidised bed condensers in MSF evaporators, we like to begin this paragraph with what we may consider 'the origin of the fluidised bed heat exchange technology' as developed for seawater desalination, and referred to as Multi-Stage Flash / Fluidised Bed Evaporator or MSF / FBE. In the example below, we compare this evaporator with a conventional MSF. This comparison shows that the advantages of the self-cleaning fluidised bed heat exchange technology for the MSF are responsible for a much wider range of improvements than non-fouling heat exchange only.

A picture of the conventional MSF and its corresponding temperature diagram is shown in Fig. 9. The principle of this MSF can be best described as a large counter-current heat exchanger, where the cold feed is heated by the condensing vapour in the heat recovery section and the external heat supply takes place in the final heater. After leaving the final heat exchanger at its highest temperature, the liquid flashes through all stages, by way of

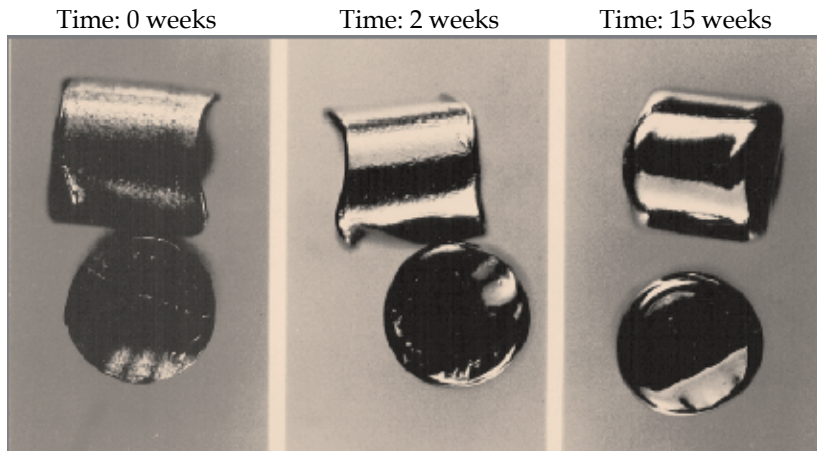


Fig. 8. Rounding-off effects of 2 mm stainless steel particles as a function of operating period.

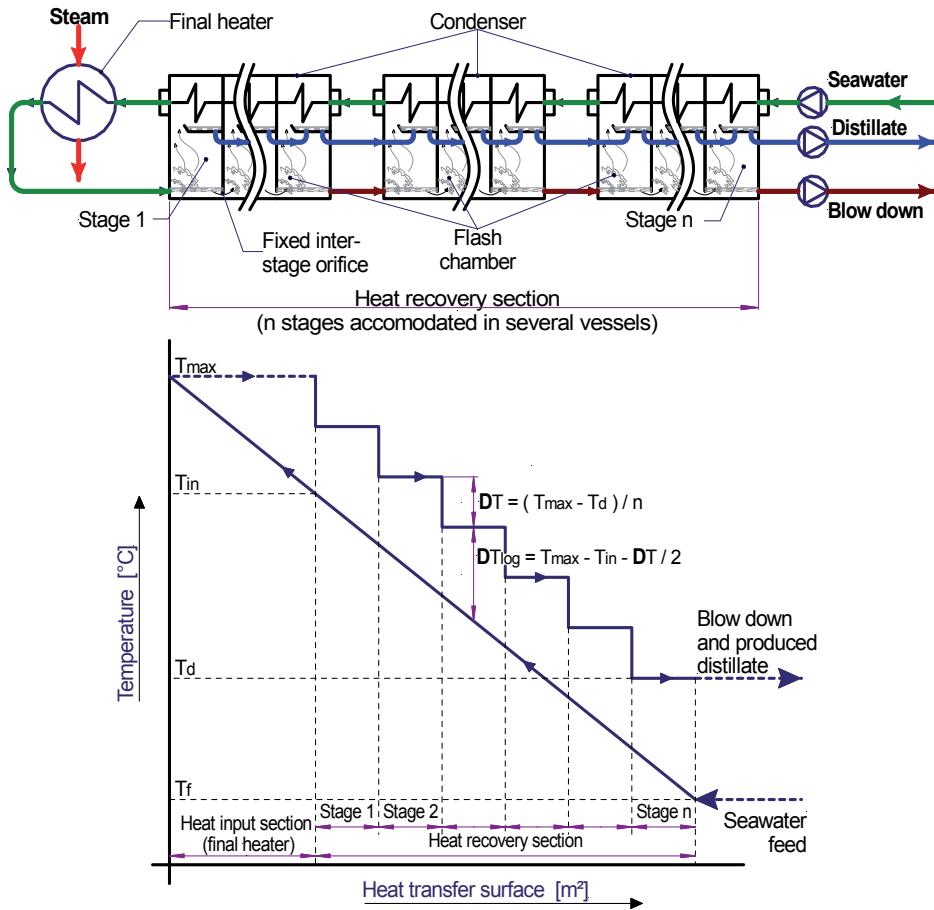


Fig. 9. Principle of conventional MSF and its temperature diagram.

openings in the bottom or intersection walls of the stages, and a gradual drop in saturation temperature takes place resulting in a partial evaporation of the liquid in each flash chamber. The flash vapour flows through the water-steam separators and finally condenses on the condenser surfaces, which are cooled by the colder incoming feed. The distillate is collected at the bottom of each stage and cascades down in the same way as the liquid in the flash chambers to the next stage. The plant has to be completed with pumps for the removal of the concentrated liquid or brine and distillate out of the coldest stage and for the feed supply. Dissolved gases and in-leaking non-condensables are removed from the feed by a vacuum line connected to a vacuum pump. The installation of the great length of horizontal condenser tubes in a conventional MSF requires the installation of several vessels in series.

The principle of the MSF / FBE is not much different from a conventional MSF, although, we have already shown that the total length of the vertical condenser tubes passing through all stages can be much shorter for an MSF / FBE than for a conventional MSF. This makes it possible to install all condenser tubes and flash chambers in only one vessel of limited height as is shown in Fig. 10.

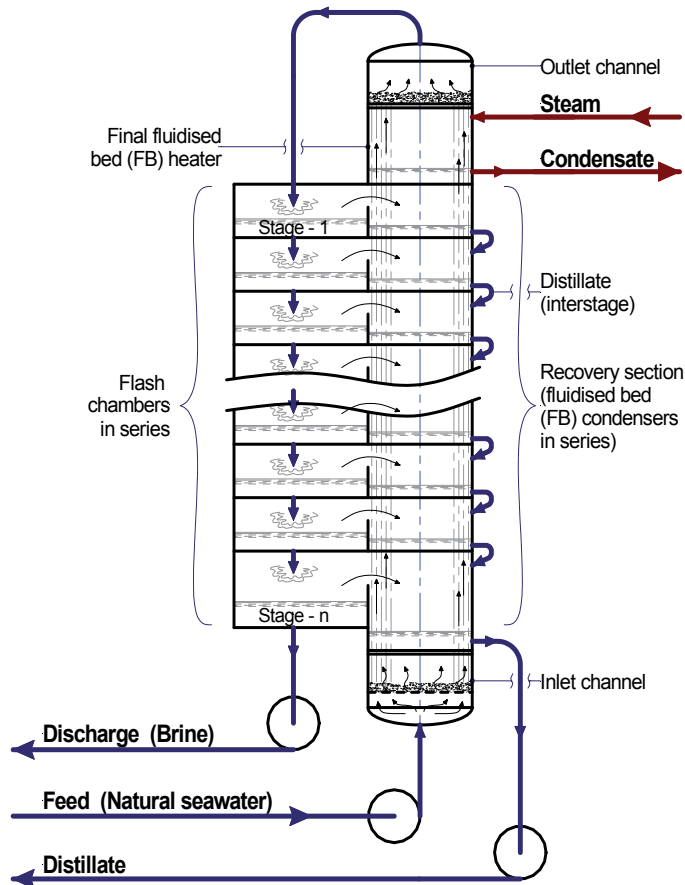


Fig. 10. Principle MSF / FBE.

As the result of the vertical layout of the MSF / FBE and the flashing down flow in the flash chambers with a height for each chamber of approx. 0.4 m, we are able to add a number of interesting improvements to the MSF / FBE in comparison with the conventional MSF, such as:

- It has already been mentioned that not only excellent heat transfer can be achieved at very low liquid velocities and very low pressure drop, but that the scouring action of the glass beads also remove scale deposits at an early stage. This makes it possible to operate the MSF / FBE at much higher maximum temperatures of the heated seawater than the conventional MSF without the need of chemicals to prevent scale. A higher maximum temperature increases the recovery of distillate from a particular seawater feed and makes it possible to design evaporators for a higher gain-ratio or lower specific heat consumption.
- *The vertical layout of the MSF/FBE* makes it possible to achieve a complete flash-off of the spraying brine flow in the flash chambers, which means that the evaporating liquid and produced vapours are in equilibrium with each other. Further, we do not need wire mesh demister for the separation of droplets from the vapour flowing into the condenser which reduces the pressure drop of the vapour flow on its way to the condenser. These advantages reduce the irreversible temperature losses in the heat transfer process, which makes it possible to save on heat transfer surface and / or reduce the specific heat consumption of the evaporator.
- *The vertical layout of the MSF/FBE* with a relatively short stage height, its high vapour space loadings, low brine levels in the flash chambers and no need for the installation of voluminous wire mesh demisters makes the flash chambers very compact, which reduces the plot area and the overall dimensions of the evaporator, and, consequently, its steel weight.
- *The vertical layout of the MSF/FBE* assures sufficient driving force for the interstage brine flow caused by the height of the brine level in the flash chambers only. Consequently, not much vapour pressure difference between stages is required to assure the interstage brine flow, which means that a large number of stages can be installed in a given flash range $\Delta T = T_{\max} - T_d$ shown in Fig. 9, which again makes it possible to reduce the specific heat consumption of the evaporator.
- *The vertical layout of the MSF/FBE* makes it possible to install interstage valves between all stages using only one activator. This valve system guarantees low brine levels in all stages at varying maximum temperatures or flash range of the evaporator. A varying maximum temperature or flash range makes it possible to vary the distillate production between 0 and 100 %, while still maintaining an excellent distillate quality.

Above, we have clearly shown that *the vertical layout of the MSF/FBE*, as the result of the integration of the vertical stationary fluidised bed condenser with the flash chambers, increases the advantages of this evaporator too such an extent, that this evaporator may be considered as the most promising tool for thermal seawater desalination in the future. Fig. 11 shows an MSF / FBE demonstration plant operating on natural seawater for a distillate production of 500 m³/d.

For more information about this fascinating evaporator, one is referred to the Ref. [8] and [9].



Fig. 11. MSF / FBE evaporator, Isle of Texel.

5.2 Reboiler at chemical plant; annual turnaround replaces cleaning every 4 to 5 days

A steam-heated evaporation system at a chemical plant in the United States recovers a volatile organic from a heavy organic solution laden with foulants. A hard black scale, that was forming in the upper 25 % of the tubes, was forcing the plant to switch two parallel once through rising film evaporators with a clean pair every four to five days.

When asked to increase throughput and simplify operations engineers considered installing a 190 m² falling film evaporator to operate in series with the existing rising film evaporators. Although the combination system was expected to run approximately 10 weeks between cleanings, a better solution was needed and found when engineers heard of an innovative self-cleaning fluidised bed heat exchanger technology being used at another chemical plant in the United States. The final decision in favour of the self-cleaning fluidised bed heat exchanger was made after the engineers viewed a 1 m tall, transparent desktop demonstration unit with six 12 mm up flow tubes and one 12 mm down flow (downcomer) tube.

The full-size exchanger with widened outlet channel shown in Fig. 12 at the right of the distillation column contains 73 m² of heat transfer surface. It applies internal circulation of 2.0 mm chopped stainless steel wire particles and uses 51 up flow and four down flow

(downcomer) tubes according to the design shown in Fig. 4. The process liquid circulated at a constant flow of 160 m³/h, is raised from about 120 to 150 °C with condensing steam at the shell-side. Back pressure is maintained on the process side of the exchanger to prevent vaporisation which would interfere with the fluidisation of the particles. Upon discharge from the exchanger, the heated liquid flashes across a control valve into the base of the recovery column.

Comments by the operators in September 1992 after the heat exchanger had been in service for over a year without any operating problems:

There have been no shutdowns for cleaning tubes and no process upsets, and maintenance has been nil. This is a significant cost cutting result from the higher recovery of acetic acid and the more concentrated residue in the bottoms. The self-cleaning fluidised bed heat exchanger appears capable for at least a full year between turnarounds. A sample of chopped metal wire particles taken from the unit after several months of operation indicated only normal rounding off of the edges. Under the new system, the reboiler circulation rate has been constant, thus providing uniform tower operation and more total throughput. If the alternative falling film evaporator had been installed, a shutdown would have been required every 10 weeks for a costly cleaning operation.

Today, July 2011, twenty years after the heat exchanger has been put in service and after 150 000 operating hours, the heat exchanger is still in operation using the same shiny tubes and to entire satisfaction of the operators. For more information, see Ref. [2].

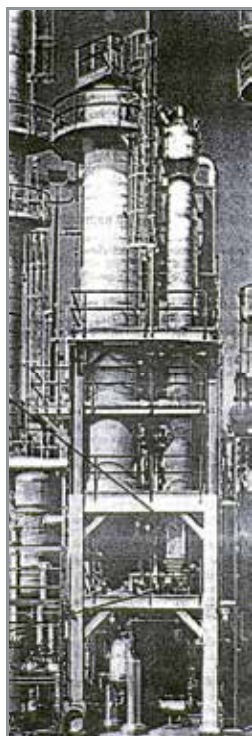


Fig. 12. Self-cleaning fluidised bed heat exchanger at chemical plant eliminates reboiler fouling.

5.3 Quench coolers at chemical plant; the real breakthrough of the self-cleaning fluidised bed heat exchange technology

A chemical plant in the United States cooled large quench water flows from a proprietary process in open cooling towers. This quench water released volatile organic compounds (VOCs) into atmosphere. As a consequence of environmental regulations the quench water cycle had to be closed by installing heat exchangers between the quench water and the cooling water from the cooling towers.

In August 1997, after considering other solutions using conventional shell and tube heat exchangers, plant management decided to carry out a test with a small self-cleaning fluidised bed heat exchanger and compared its performance with that of a conventional shell and tube heat exchanger, which suffered from a severe fouling deposit consisting of a tarry substance. Fig. 13 shows the results of this test, while Table 2 compares the design consequences for the self-cleaning heat exchangers and the conventional shell and tube exchangers. Plant management decided in favour of the self-cleaning fluidised bed heat exchange technology because of the above results and the dramatic savings on investment and operating cost.

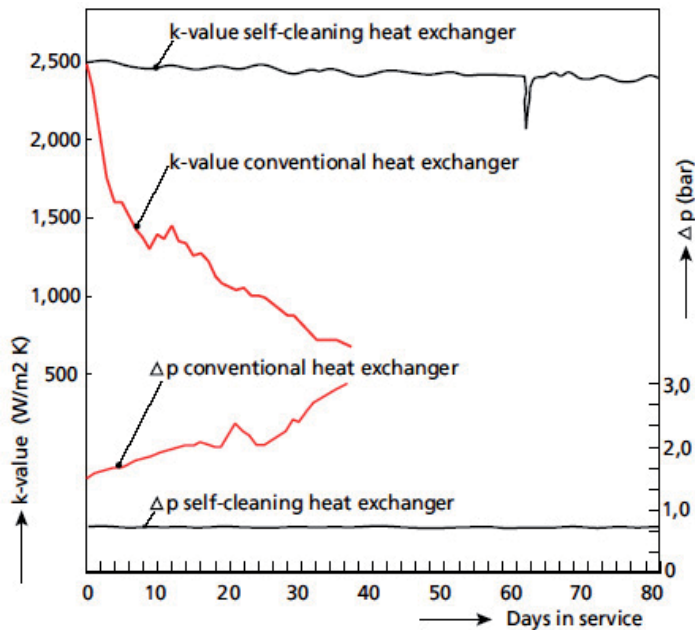


Fig. 13. Overall heat transfer coefficient (k-value) and pressure drop (Δp) as function of operating time.

	Unit	Conventional heat exchanger	Self-cleaning heat exchanger
Heat transfer surface	m ²	24 000	4 600
Total number of heat exchangers	-	24 × 1 000 m ²	4 × 1 150 m ²
Configuration	-	3 × 50 %	2 × 50 %
Pumping power	kW	2 100	840
Number of cleanings per year	-	12	0

Table 2. Comparison conventional heat exchanger versus self-cleaning fluidised bed heat exchanger.



Fig. 14. Installation of 4 600 m² self-cleaning surface replacing 24 000 m² conventional surface.

Fig. 14 shows the installation which serves two parallel production lines. In each production line two identical self-cleaning fluidised bed heat exchangers were installed handling 2 × 700 m³/h process liquid at the tube-side and 2 × 2100 m³/h cooling water at the shell-side. Each exchanger applies external circulation of the particles as shown in Fig. 5, has a shell diameter of 1 200 mm, a total height of 20 m and a heat transfer surface of 1 150 m², which surface consists of 700 parallel tubes with an outer diameter of 31.75 mm. Each exchanger uses 9 000 kg cut metal wire particles with a diameter of 1.6 mm.

The exchangers serving the first production line were put into operation in October 1998. Fig. 15 presents the trend of the overall heat transfer coefficient (k-value) after start-up till the end of April 1999. In spite of some fluctuations at the beginning, this figure shows a constant k-value of approximately 2 000 W/(m²·K). During a period of more than six months both exchangers operated continuously, with exception of a few short sops caused by interruptions in the power supply. The dotted line in Fig. 15 shows the trend of the k-

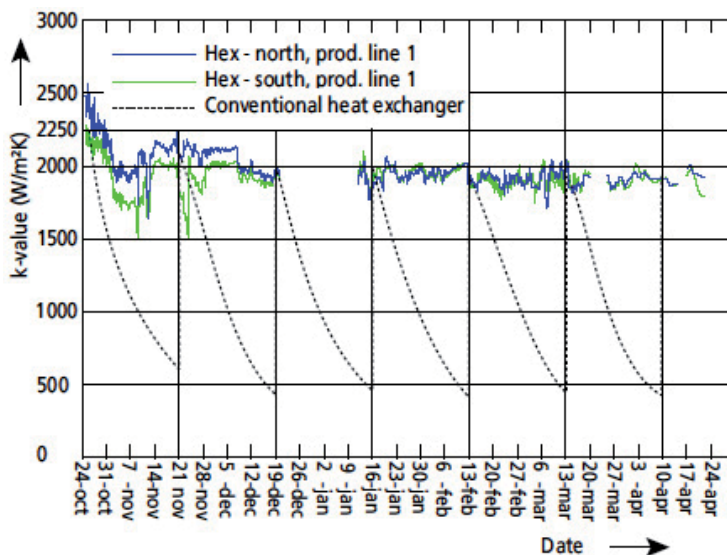


Fig. 15. k-values for self-cleaning heat exchangers of first production line, as a function of operating time and compared with the performance of conventional heat exchanger.

value for conventional shell and tube exchangers as derived from the test results shown in Fig. 13. The two exchangers of the second production line were put in operation in May 1999 and showed the same trend in k-value as the exchangers of the first production line. In December 2000, this chemical plant stopped production and the exchangers, after a final inspection, were mothballed and have never been put into operation again. This final inspection did not reveal any measurable wear of the tubes. All tubes were shiny and

	Unit	Conventional heat exchanger	Self-cleaning heat exchanger (1998)	Self-cleaning heat exchanger (2005)
Total heat transfer surface	m ²	24 000	4 600	3 332
Total number of heat exchangers	-	24 × 1 000 m ²	4 × 1 150 m ²	4 × 833 m ²
Configuration	-	3 × 50 %	2 × 50 %	2 × 50 %
Tube diameter / tube length	mm	25.4×1.65 / 12 000	31.75×1.65 / 16 000	15.88×1.21 / 8 700
Shell-side baffle type	-	segmented cross	segmented cross	EM
Total weight particles	kg	n.a.	36 000	20 000
Pumping power	kW	2 100	840	416
Number of cleanings per year	-	12	0	0

Table 3. Comparison conventional heat exchanger versus self-cleaning fluidised bed heat exchangers, state-of-the-art 1998 and 2005.

open. The cut metal wire particles showed a slight weight loss caused by rounding-off effects as discussed earlier. For more information about these fascinating heat exchange application, one is referred to Ref. [3].

In the first years of the new millennium, research and development concentrated on reducing the tube diameter of the self-cleaning fluidised bed heat exchangers in combination with rather large particles. A smaller tube diameter reduces the length of the heat exchanger tubes which creates a more compact heat exchanger with less height and, consequently, reduces the pumping power required for the process liquid. Then, we also paid attention to the installation of a novel type of baffle in the shell of the exchanger. This very innovative baffle is called the EM baffle and has been developed by Shell Global Solutions. The results of this redesign of the self-cleaning fluidised bed heat exchangers shown in Fig. 14 as far as heat transfer surface and pumping power are considered are presented in Table 3. For more information about this improved design, one is referred to Ref. [4].

6. Existing conventional severely fouling heat exchangers revamped into a self-cleaning fluidised bed configuration

The idea of changing internal circulation of particles as shown in Fig. 4 into the configuration where this circulation takes place through only one external downcomer shown in Fig. 5 was proposed by engineers of Shell in the early 90s. According to these engineers, this modification would make it possible to revamp existing vertical severely fouling conventionally designed reboilers into a self-cleaning configuration. Moreover, it would be an elegant and rather low cost but also a low risk approach to introduce a new technology due to the possibility of an immediate fallback from new technology to old proven technology. This idea is not only applicable for reboilers but also for evaporators and crystallisers and the constant circulating flow required by these unit operations corresponds with the preferred type of flow for the self-cleaning fluidised bed heat exchanger.

Moreover, also in this paragraph, it will be shown that this approach of introducing the self-cleaning heat exchange technology in existing plants could not only be an attractive solution for straight forward rather simple heat exchange applications suffering from severe fouling, but also for very complex industrial processes.

6.1 Reboiler

A typical example of a conventional reboiler that is suitable for revamping is shown in Fig. 16 with the revamped configuration shown in Fig. 17. Generally speaking, the requirements specified by plant management for the majority of revamps can be summarised as follows:

1. The same process conditions should be maintained as in the original installation, i.e. flow, temperatures and liquid velocity in the tubes.
2. The connections to the column should be maintained.
3. The installed pumps should be used and can be used because pumping power requirements are generally lower for the self-cleaning fluidised bed heat exchangers than for the conventional severe fouling shell and tube exchanger.

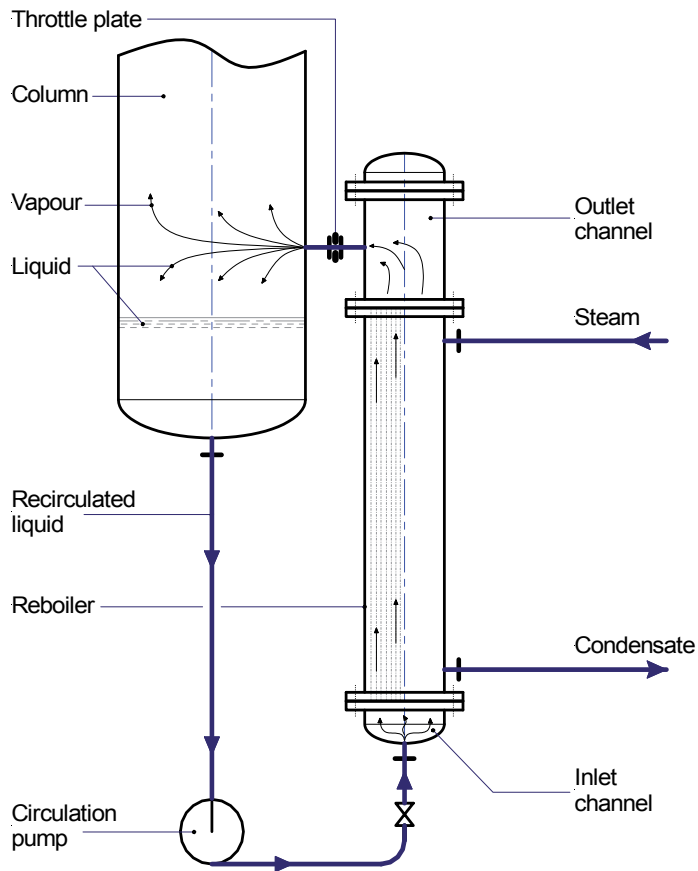


Fig. 16. Evaporator equipped with conventional heat exchanger.

4. As many components of the existing installation should be used in the revamped configuration like bundle, channels or maybe even modified channels.
5. The revamp must be carried out within the available space. This often means that a revamp can only be carried out when the existing installation has already a vertical position.

The advantages of most revamps are much lower maintenance cost, an increased production and 'smoother' operation.

6.2 Cooling crystallisation plant

A 2-stage cooling crystallisation plant in Egypt produces Sodium Sulphate. The chillers of both stages suffer from severe fouling caused by heavy deposits of crystals. Shutdown of the installation every 24 hours for melting out these deposits is common. The conventional cooling crystalliser is shown in Fig. 18, while Fig. 19 depicts this installation after its revamp into a self-cleaning configuration.

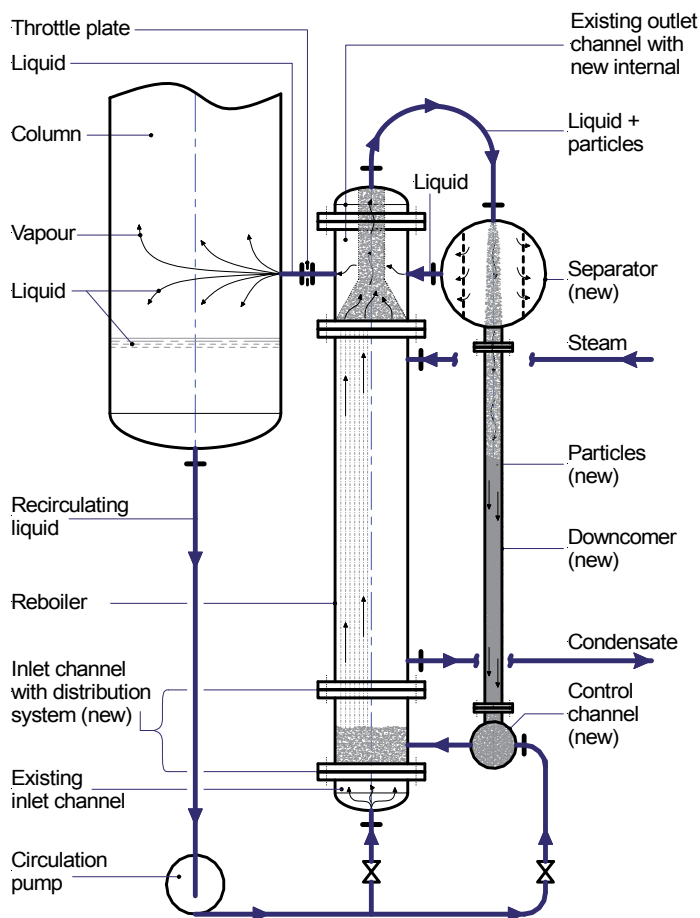


Fig. 17. Conventional evaporator revamped into a self-cleaning configuration.

Calculations have shown that the investments necessary for the modification of the existing installation into a self-cleaning configuration will be paid back by a substantially increased production in approximately six months.

Information about the reboiler, the cooling crystallisation plant and other applications discussed in this paragraph can be found in Ref. [7]

6.3 Evaporator for concentration of very viscous severely fouling slurry

In one of the Scandinavian countries, a production plant of a proprietary product operates a very large MVR evaporator for the concentration of a slurry up to approx. 70 % solids. Even at a temperature of 100 °C this slurry, which behaves non-Newtonian, has a very high viscosity varying between 50 and more than 200 cP. This very large shell and tube heat exchanger suffers from severe fouling which sometimes requires one month (!) of mechanical cleaning after only three months (!) of operation. In Fig. 20, the test plant in parallel with the existing evaporator is shown and the dimensions of the existing installation

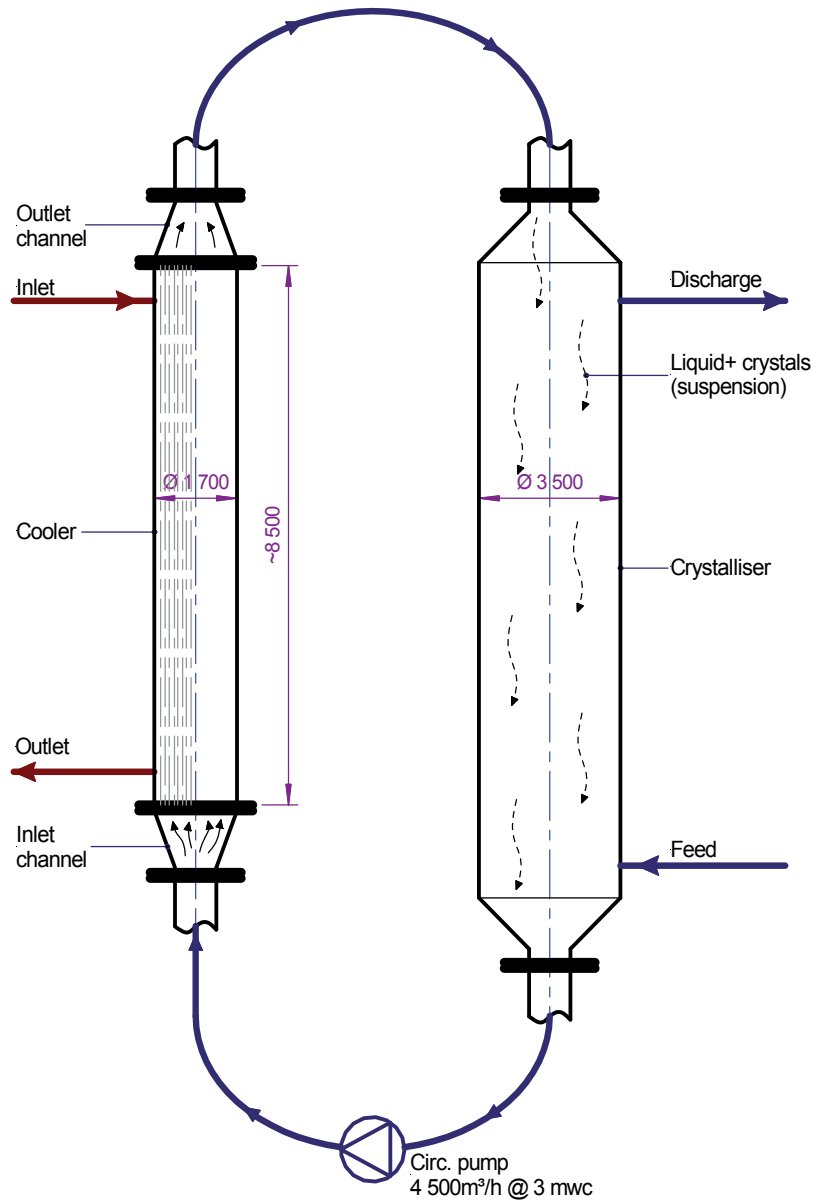


Fig. 18. Conventional cooling crystalliser.

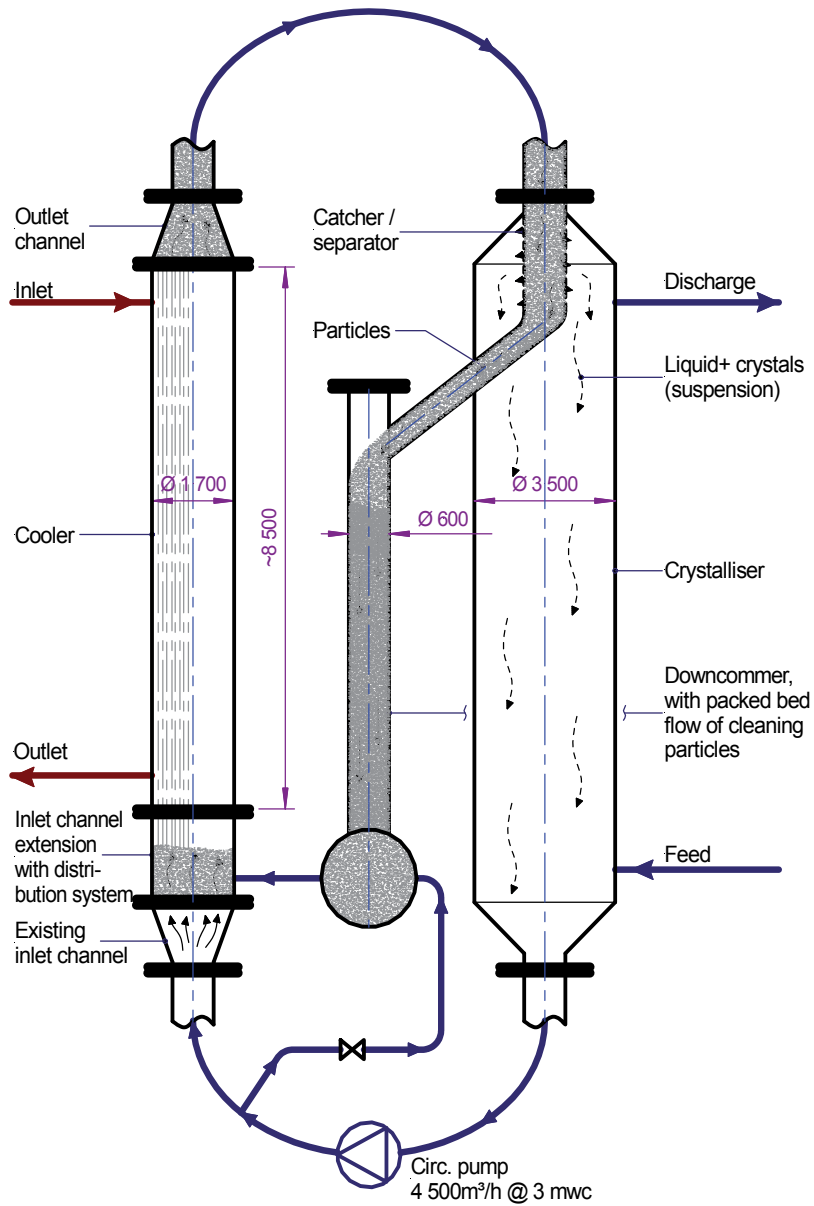


Fig. 19. Revamped into self-cleaning configuration of Fig. 18.

give a good impression about its size, although provided with relatively small diameter tubes with an ID of only 20 mm.

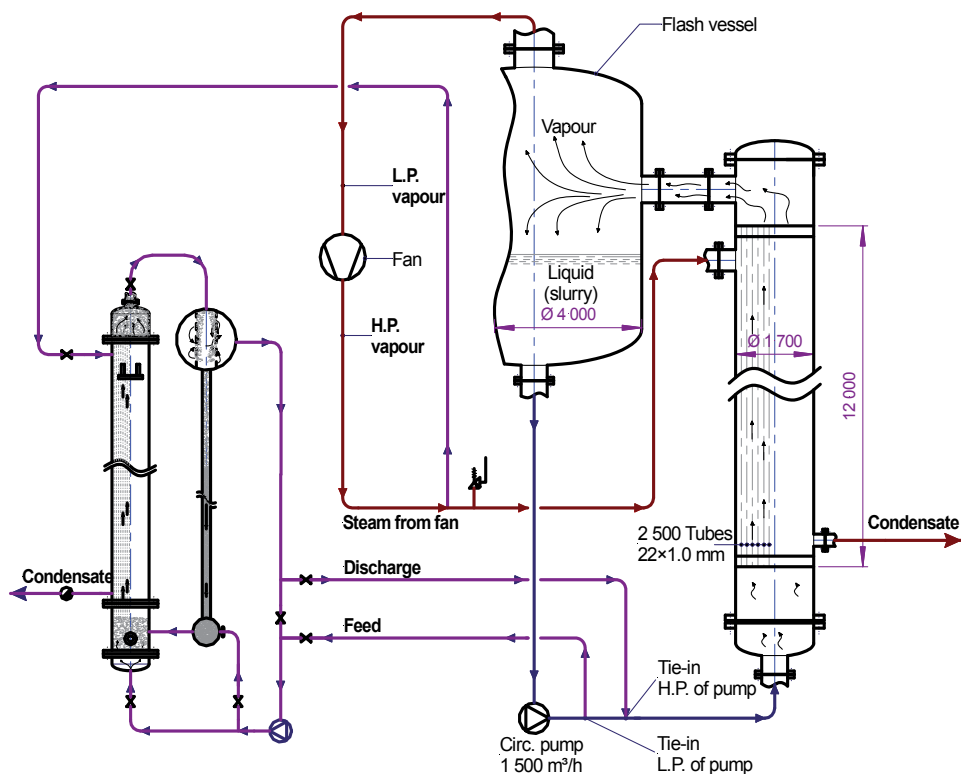


Fig. 20. Existing evaporator and test installation.

The proposal for the revamp of this installation is shown in Fig. 21 and uses a maximum of the very large existing components, including the circulation pump. The first series of experiments with the test installation are promising and shear-thinning effects caused by the increased turbulence of the slurry induced by the action of the fluidised particles are reducing the viscosity of the slurry substantially and have produced heat transfer coefficients or k -values between 1000 and 2000 W/(m²·K) depending on the concentration of the slurry without fouling. These coefficients should be compared with the clean heat transfer coefficients of approximately 600 W/(m²·K) for the conventional heat exchanger which, in a couple of months, reduces to only a fraction of its clean value due to by fouling.

This potential revamp reflects the benefits of recent developments which make it possible to operate a self-cleaning fluidised bed heat exchanger on a very viscous slurry and use rather large stainless steel particles (2.5 mm) in small tube diameter with an ID of only 20 mm.

6.4 Combination of preheater and thermal siphon reboiler

A chemical plant in the United States operates the preheater in series with the thermal siphon reboiler shown in Fig. 22. The 8-pass preheater with tubes with an O.D. of 25 mm, a

very high liquid velocity in the tubes of 4.5 m/s and heated by L.P. steam experiences severe fouling still requiring cleanings every two months, while the thermal syphon reboiler heated by M.P. steam requires cleanings every four months.

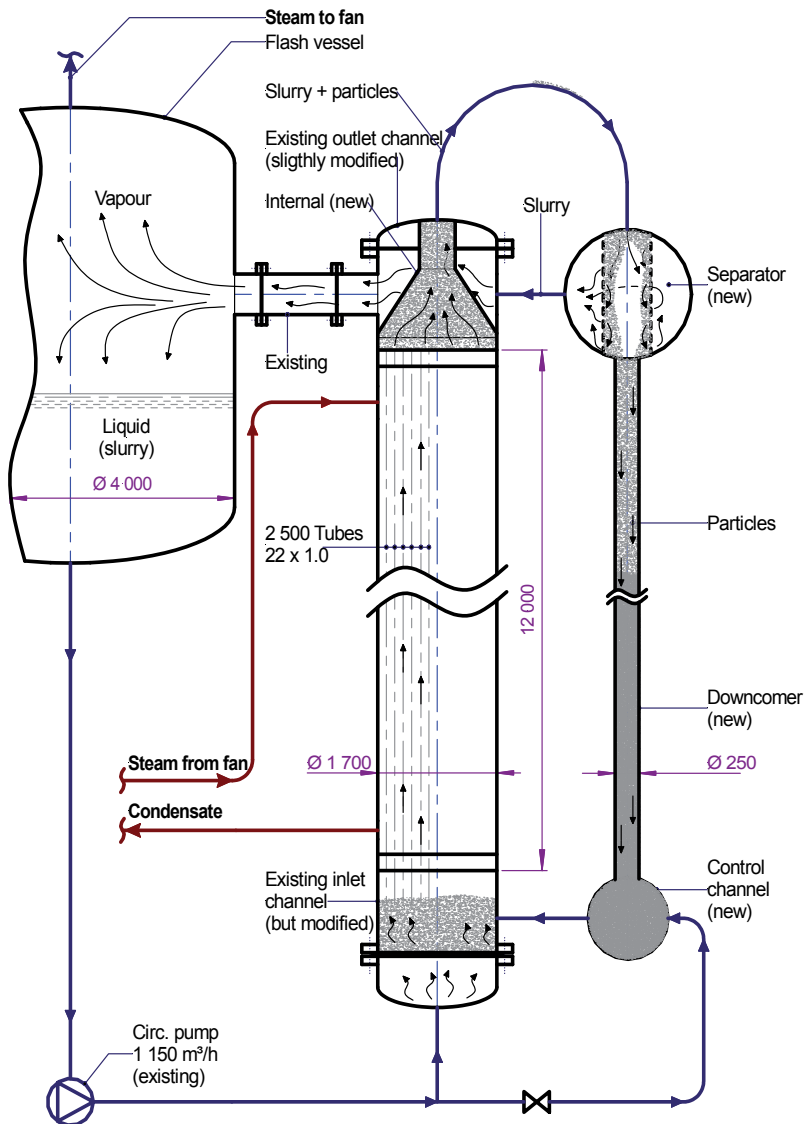


Fig. 21. Existing evaporator revamped into self-cleaning configuration.

The solution we are proposing to solve this problem is quite unique and explained in Fig. 23. As a matter of fact, we have increased the tendency of fouling in the preheater due to the precipitation of solids by increasing the outlet temperature of the preheater. This can be realised by adding M.P. steam to the shell of the preheater instead of L.P. steam. As a result of this temperature increase, the preheater will also partly contribute to the degassing

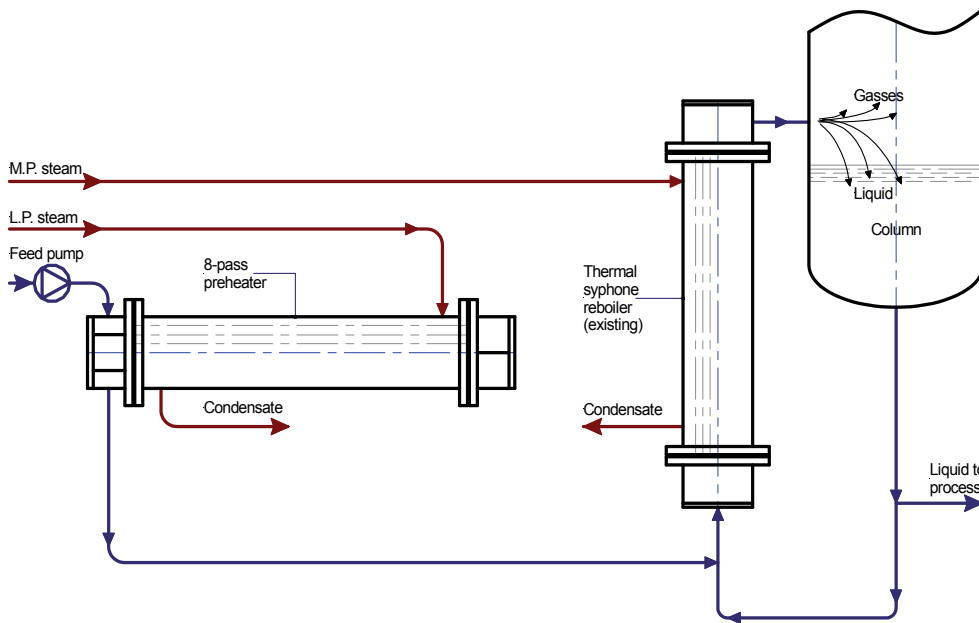


Fig. 22. Conventional preheater in series with thermal syphon reboiler.

of the liquid which is normally done in the reboiler. Above goals have been realised by revamping the existing 8-pass horizontal conventional heat exchanger into a vertical single-pass self-cleaning fluidised bed configuration using stainless steel cleaning particles with a diameter of 2.5 mm and also installing an extra circulation pump to maintain sufficient velocity in the tubes of our single-pass configuration for circulation of the cleaning particles. Although, we have indeed increased the tendency for fouling, we expect that the introduction of our self-cleaning technology will keep the preheater clean.

The separation of the gasses from the mixture of liquid and particles takes place in the widened outlet channel of the preheater, these gasses are fed into the reboiler and evenly distributed over all the tubes of the reboiler where they contribute to the (natural) circulation effect of this thermal syphon reboiler.

Considering the fact that a substantial fraction of the totally required degassing is not done anymore in the reboiler, the heat load of the reboiler can be reduced, which reduces the condensing steam temperature, the tube wall temperature and, consequently, the fouling of the reboiler.

The advantage of this approach is the revamp of the conventional preheater into a self-cleaning configuration at an increased heat load. An experiment with a single-tube self-cleaning pilot plant in parallel with the existing severely fouling preheater should demonstrate the non-fouling performance of the self-cleaning heat exchange technology. If this is indeed the case, then, we have not only solved the fouling problem of the preheater at an even higher heat load, but also reduced the fouling of the conventional thermal syphon reboiler.

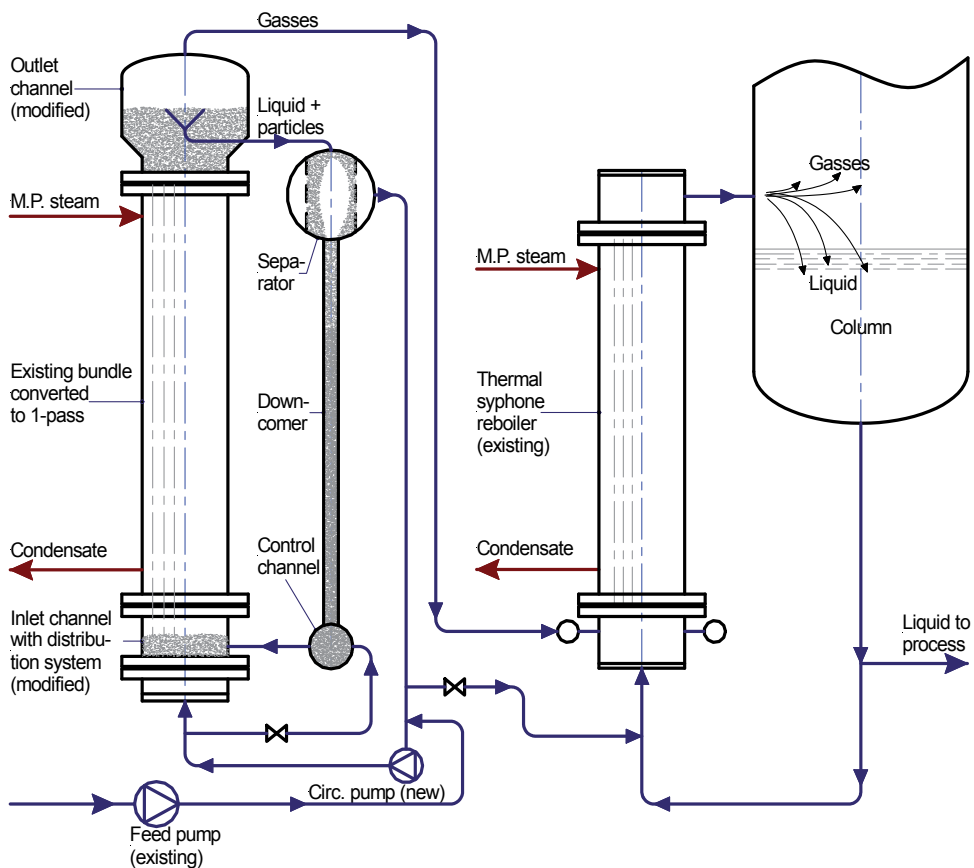


Fig. 23. Conventional preheater revamped into self-cleaning configuration and operating in series with thermal syphon reboiler.

For the proposed solution of this problem, we have introduced the concept of evaporation of a fraction of the liquid creating a mixture of liquid, vapour and particles in the tubes. We know that this is possible if certain design criteria are taken into account. Consequently, with this example, we have presented the possibility that our self-cleaning heat exchange technology can also be applied for applications where we even experience boiling or evaporation in the tubes.

6.5 Self-cleaning fluidised bed heat exchangers in existing 'directly heated' HPAL plants

There exist a strong drive to apply indirect heating (i.e. using heat exchangers) in High Pressure Acid Leach (HPAL) plants for the extraction of nickel and cobalt from laterite ore slurry, because of the benefits of indirect heating in comparison with direct heating (i.e. using steam injection or slurry / vapour mixing condensation), which benefits we summarise below:

- Increased autoclave production capacity.
- Reduced acid consumption.

Particularly, the high heat transfer coefficient and low slurry velocity do affect the total length of the installed heat exchange tubes. This follows from the Equation (5) for the tube length presented in paragraph 0 of his chapter, after substitution of the design and process parameters. As a consequence, the number of shells in series for the self-cleaning fluidised bed heat exchanger is a fraction (just one) in comparison with the large number of shells in series for the conventional shell and tube heat exchanger.

For this HPAL application, the scope of the benefits already mentioned at the beginning of this sub-paragraph increases when indirect heating is not only applied to the highest temperature stage of the installation but to all stages. It is not surprising that all major mining companies show much interest in the self-cleaning fluidised bed heat exchange technology for an even greater variety of applications than only HPAL for the extraction of metals from laterites.

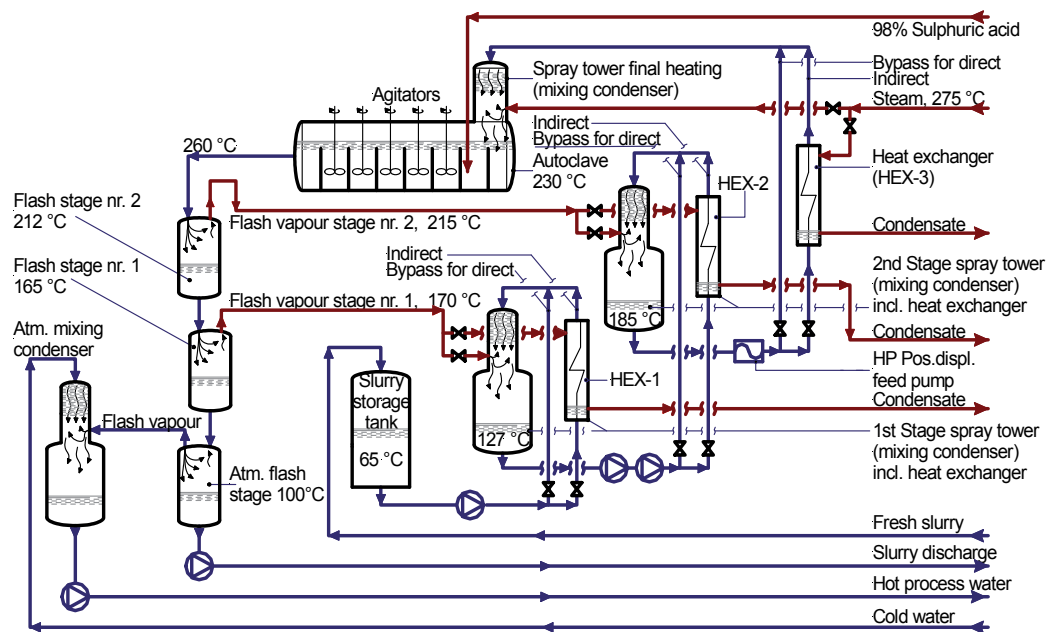


Fig. 25. HPAL plant for laterite nickel employing direct heat transfer revamped into indirect heated configuration.

For more information about the performance and the potential of HPAL plants equipped with self-cleaning fluidised bed heat exchangers, one is referred to Ref. [6].

	Unit	Conventional shell and tube	Self-cleaning fluidised bed
Inlet- / Outlet- / Steam temperature	°C	185 / 235 / 275	185 / 235 275
Density slurry	kg/m ³	1 340	1 340
Specific heat slurry [kJ/(kg K)]	kJ/(kg K)	3.6	3.6
Dynamic viscosity	cP	50 - 70	10 - 15
Tube velocity slurry	m/s	2.0	0.35
Diameter tube	mm	38 × 3.0	38 × 3.0
Diameter- / Material particles	mm	n.a.	4.0 / Titanium
Clean- / Design k-value	W/(m ² ·K)	~ 600 / 300	1 500 / 1 500
Tube length based on design k-values and Eq. (5)	m	166.8	5.84
Total number of shells in series for 1-pass tube-side and tube length per shell equal to 8 m	-	21	1
Total number of shells in series for 2-pass tube-side and tube length per shell equal to 8 m	-	11	n.a.
Pressure drop	bar	~ 6 - 10	< 1.0

Table 4. Comparison significant parameters for indirect heating of high temperature stage of HPAL plant of Fig. 25.

7. Final remarks

We have given an indication about the cost of fouling of heat exchangers on a global scale and we have shown that the self-cleaning fluidised bed heat exchange technology can play a significant role in battling these fouling cost, and does have even more potential that solving fouling problems only.

Particularly, the latter aspect has caught the attention of an increasing number of very large companies which are very much interested to implement the self-cleaning fluidised heat exchange technology for the upgrading of their existing proprietary processes, or even for the development of completely new processes.

8. References

- Garrett-Price, B.A., et al. (1985). *Fouling of Heat Exchangers*, Noyes Publications, Parkridge, New Jersey.
- Gibbs, R. & Stadig, W. (1992). *Fluidized bed heat exchanger eliminates reboiler fouling*, Chemical Processing, August.
- Klaren, D.G. (2000). *Self-Cleaning Heat Exchangers: Principles, Industrial Applications and Operating Installations*, Industrial Heat Transfer Conference, Dubai, UAE, September.
- Klaren, D.G. & de Boer, E.F. (2004). *Case Study Involving Severely Fouling Heat Transfer: Design and Operating Experience of a Self-Cleaning Fluidized Bed Heat Exchanger and its Comparison with the Newly Developed Compact Self-Cleaning Fluidized Bed Heat Exchanger with EM Baffles*, Presented at the Fachveranstaltung: Verminderung der Ablagerungsbildung an Wärmeübertragerflächen, Bad Dürkheim, Germany, October.
- Klaren, D.G., de Boer, E.F. & Sullivan, D.W. (2007). *Consider low fouling technology for 'dirty' heat transfer services*, Hydrocarbon Processing, Bonus Report, March.
- Klaren, D.G., de Boer, E.F. & Crossley, B. (2008). *Reflections on Indirect Heating of Laterite Ore Slurry in HPAL Plants Using Self-Cleaning Fluidized Bed Heat Exchangers*, Presented at ALTA 2008, Perth, Western Australia, June.
- Klaren, D.G. & de Boer, E.F. (2009). *Revamping existing severely fouling conventional heat exchangers into a self-cleaning (fluidised bed) configuration: New developments and examples of revamps*, International Conference on: Heat Exchangers Fouling and Cleaning-2009, Schladming, Austria.
- Klaren, D.G. and de Boer, E.F. (2010). *Multi-Stage Flash / Fluidized Bed Evaporator (MSF / FBE): A resurrection in Thermal Seawater Desalination?*, CaribDA Conference, Grand Cayman, June.
- Klaren, D. G. (2010). *Design, Construction and Operating Features of Multi-Stage Flash / Fluidized Bed Evaporators (MSF/FBE) for very large Capacities*, IDA Conference, Huntington Beach, California, USA, November.
- Richardson, J.F. and Zaki, W.N. (1954). *Sedimentation and fluidization: Part 1*, Trans. Inst. Chem. Eng., vol. 28, p. 35, 1954.

Ruckenstein, E. (1959). *On heat transfer between a liquid / fluidized bed and the container wall*, Rev. Roum. Phys., vol 10, pp. 235-246.



Edited by Jovan Mitrovic

Selecting and bringing together matter provided by specialists, this project offers comprehensive information on particular cases of heat exchangers. The selection was guided by actual and future demands of applied research and industry, mainly focusing on the efficient use and conversion energy in changing environment. Beside the questions of thermodynamic basics, the book addresses several important issues, such as conceptions, design, operations, fouling and cleaning of heat exchangers. It includes also storage of thermal energy and geothermal energy use, directly or by application of heat pumps. The contributions are thematically grouped in sections and the content of each section is introduced by summarising the main objectives of the encompassed chapters. The book is not necessarily intended to be an elementary source of the knowledge in the area it covers, but rather a mentor while pursuing detailed solutions of specific technical problems which face engineers and technicians engaged in research and development in the fields of heat transfer and heat exchangers.

Photo by Nomadsou11 / iStock

IntechOpen

